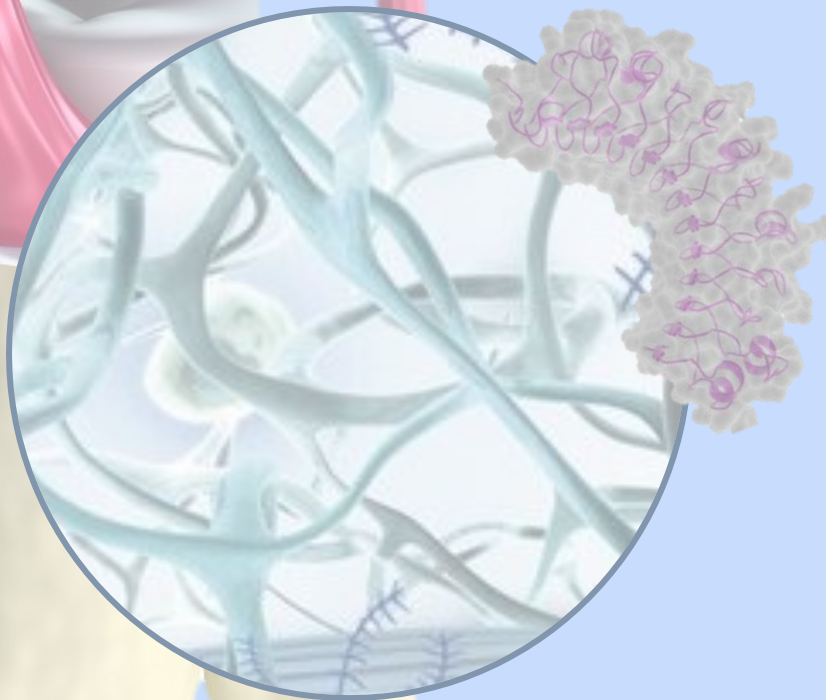


# **Lack of osteomodulin is associated with skeletal development abnormalities and osteoarthritis**

**Jérémie ZAPPIA**

**Thesis of Doctorate of Philosophy in  
Biomedical and Pharmaceutical Sciences**



**University of Liège**

**Academic year 2022-2023**

**musculoSkeletal Innovative research Lab – mSKIL**

**Center for Interdisciplinary Research on Medicines – CIRM**







# Lack of osteomodulin is associated with skeletal development abnormalities and osteoarthritis

Jérémie ZAPPIA

Graduated in Biological Sciences

musculoSkeletal Innovative research Lab – mSKIL

Center for Interdisciplinary Research on Medicines - CIRM

University of Liège

Academic year 2022-2023

A thesis submitted to obtain the degree of doctorate in Biomedical and Pharmaceutical Sciences.

*Promotor: Pr. Yves Henrotin*

*Co-promotor: Dr. Christelle Sanchez*

*President: Pr. Akeila Bellahcène*

*Secretary: Dr. Dominique de Seny*

*Jury members:*

- *Pr. France Lambert*
- *Dr. Marc Muller*
- *Pr. Pierre Drion*
- *Pr. Ruth Wittoek*
- *Pr. Martine Cohen-Solal*

This thesis was funded by the EOS program The Excellence of Science -Join-t-against-Osteoarthritis”, F.R.S.-FNRS and by the “Fonds Léon Fredericq”



# **L'absence d'ostéomoduline est associée à des anomalies du développement squelettique et à l'arthrose**

Jérémie ZAPPIA

Licencié en Sciences Biologiques

musculoSkeletal Innovative research Lab – mSKIL

Centre Interdisciplinaire de Recherche sur le Médicament - CIRM

Université de Liège

Année académique 2022-2023

Thèse présentée en vue de l'obtention du grade de doctorat en Sciences Biomédicales et Pharmaceutiques.

*Promoteur: Pr. Yves Henrotin*

*Co-promotrice: Dr. Christelle Sanchez*

*Présidente: Pr. Akeila Bellahcène*

*Secrétaire: Dr. Dominique de Seny*

*Membres du jury:*

- *Pr. France Lambert*
- *Dr. Marc Muller*
- *Pr. Pierre Drion*
- *Pr. Ruth Wittoek*
- *Pr. Martine Cohen-Solal*

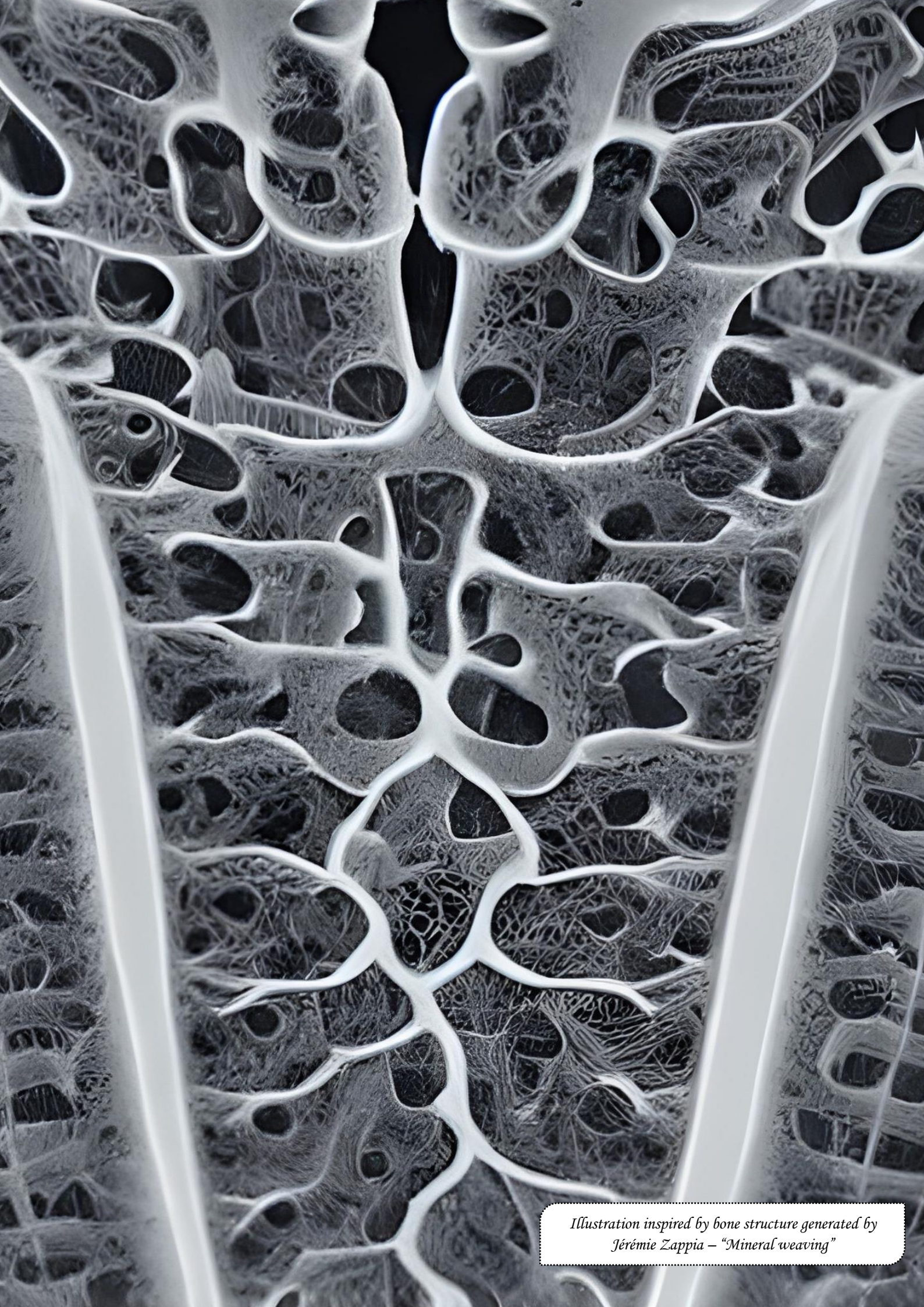
Cette thèse a été financée par le programme EOS The Excellence of Science -Joint-against-Osteoarthritis", F.R.S.-FNRS et par les "Fonds Léon Fredericq"





# Collaborations





*Illustration inspired by bone structure generated by  
J r mie Zappia – “Mineral weaving”*



# Remerciements-Acknowledgments

*“The key is to keep company only with people who uplift you, whose presence calls forth your best.”*

– Epictetus

*« La clef est de ne tenir compagnie qu'avec des personnes qui vous élèvent, dont la présence appelle le meilleur de vous-même »*

– Épictète

Je tiens tout d'abord à exprimer en premier lieu ma reconnaissance, merci Pr Yves Henrotin, pour l'opportunité qui m'a été donnée de m'épanouir en tant que chercheur dans votre laboratoire. Je suis heureux de la confiance témoignée envers ma personne ainsi que pour votre soutien lorsque je voulais explorer différentes facettes de mon projet de thèse ou lorsque je voulais vérifier mes hypothèses. Vous n'avez jamais refusé à ce que je développe ma curiosité scientifique, j'ai acquis ainsi un savoir-faire sur une multitude de techniques. Je vous remercie pour votre contribution dans ce travail de thèse qui n'aurait pas été le même sans vous, votre expertise, votre regard pointu, et vos relectures minutieuses. Vous avez joué un grand rôle durant le cours de mon doctorat et je vous en remercie. Merci également à ma co-promotrice, Dr Christelle Sanchez, tu m'as accompagné tout du long. Tu m'as fait confiance et tu m'as permis de gérer mon projet de façon personnelle assez rapidement, tout en veillant sur moi et en me suggérant de nombreux conseils, ce que j'ai beaucoup apprécié. Tu possèdes une grande expérience scientifique et, sans y paraître, rien ne t'échappait au labo et je te remercie pour t'en être souciee. Mes remerciements s'étendent par la même occasion à tout le labo mSKIL. Cécile, tu es le cœur du labo, tu te soucies de chacun et tu as un œil de lynx pour les petits détails et pour les différents aspects esthétiques. Je te remercie aussi pour tous les conseils que tu n'hésites pas à prodiguer. Prescilia, merci pour toutes tes anecdotes hilarantes, notamment durant nos dissections, et tes talents presque théâtraux qui captivent l'attention. Vous avez beaucoup participé à l'ambiance au labo. Je remercie tout le labo mSKIL pour leurs efforts et les échanges qui ont contribué à la personne que je suis devenue mais aussi pour leurs encouragements. En plus du cadre fourni par mon labo d'accueil, le fruit de cette thèse est également dû aux financements du FNRS, de la fondation Léon Fredericq et de la fondation arthrose que je remercie pour leur soutien. Je profite de cette occasion pour m'adresser tout particulièrement à toi Céline, membre crucial et co-fondatrice de la fondation arthrose, pour te remercier pour ta joie de vivre communicative et ton optimisme.

Pr Akeila Bellahcène, présidente du jury de thèse, je vous adresse ma reconnaissance, ainsi qu'à tous les membres du jury. Je vous remercie pour l'évaluation du manuscrit et pour toutes vos remarques constructives et bienveillantes qui ont visé à l'amélioration de ma thèse autant sur le fond que sur la forme. Je vous remercie pour votre perceptible enthousiasme qui a été communicatif. Merci Dr Dominique de Seny, pour les judicieux conseils afin de délivrer au mieux le message clef de ma thèse.

J'ai remercié ci-dessus le labo mSKIL, mais il est accompagné de tous les voisins incroyables du +5. Francois, Jean-Paul, Lucia, Jacobine, Laurence, Joël, Justine et Pauline, merci pour la bonne ambiance que vous créez à notre étage, merci pour toutes les conversations enrichissantes et tous les petits moments partagés. J'accorde une pensée particulière aux nouveaux doctorants Tiago et Margaux à qui je souhaite beaucoup de succès et qui ont ce petit côté facétieux qui nous égaye tous. Durant plusieurs années, j'ai eu la chance de te côtoyer Antoine, merci d'avoir été mon compagnon de thèse au sein du mSKIL.

J'aimerais remercier Artialis et toutes les personnes fantastiques qui s'y trouvent pour leur soutien scientifique, leur bonne humeur, et pour leurs encouragements à mon égard qui ont fait chaud au cœur.

Je ne peux évidemment pas manquer de revenir sur mon expérience avec toi, Marc ! Ton labo a été mon premier labo d'accueil et je ne peux que me risquer à imaginer ce qu'aurait été mon parcours si j'avais continué plus longtemps à tes côtés. Je pense que nos cerveaux auraient généré des feux d'artifices et des tempêtes (trop ?) créatives ! J'aime ta passion pour les sciences et l'originalité de ton approche scientifique. Tu auras été, toi aussi, d'une extrême bienveillance. Je te remercie pour tes conseils avisés, ton esprit critique et tes encouragements. Pour moi, plus qu'un mentor, tu es un ami. I am switching to English for the international members of Marc's group! Among the last PhD students, I had the opportunity to meet Gustavo, *mi pocho un poco (oops, demasiado!) loco*, Ratish, *बहुत सारे अंदरूनी चुटकुलों के साथ*, Thanh, *rất sáng tạo*, Que, *một trái tim đáng yêu với một sự trung thực tàn bạo*, and Hanh, *bạn sẽ luôn là "cun yeu" của tôi và giữa chúng ta luôn cảm thấy dễ dàng và tôi rất vui được làm bạn với bạn*. You did participate so much to the lab's atmosphere! Partis depuis longtemps du labo, je ne manquerai pas l'occasion d'adresser quelques mots à Thomas qui m'a appris énormément de choses, à Joerg, un exemple de rigueur scientifique et Rosanna si pétillante.

Durant cette thèse, j'ai aussi eu l'occasion de me lier d'amitié avec de nombreuses autres personnes en dehors de mon labo d'accueil mSKIL, qui m'ont fait grandir et qui ont étendu ma vision du monde. Tout d'abord, je pense à l'équipe du +1 ! Je pense à Déborah (si, si, c'est son vrai prénom !) aux cheveux si soyeux, à Marco (et google translate, *era così divertente!*) qui arbore toujours un magnifique sourire, à Marie (alors ces derniers épisodes de plan coeur ?) toujours complice, à Chiara (Gen Z ou Millennial ?!) d'une gentillesse incroyable, à Colin (long long Voldelolos) mon sang ou my blood pour les bilingues, Caroline (ce joli ptérosaure) qui possède un second degré et une autodérision que j'adore, et à Arthur (à l'allure d'ange, mais ne vous y fiez pas !) qui est d'une si agréable bonhomie. Vous êtes exceptionnels. Parmi les têtes familières du +1, je pense également à Marianne, Bernard, Isabelle et Ingrid, toujours si proches de leur équipe et à l'humour parfois caustique (que j'apprécie). En parlant d'Ingrid, je n'oublie pas Aurélie, dotée d'une grande sympathie et d'un bon flair apparemment ! Et parmi les têtes plus nouvelles, je pense à Lydie, Elisa, Manon et Romane venues compléter l'équipe. Au détour d'un couloir, ou d'un passage au -2 pour observer les zebrafish, je pense à vous Nadine, Latifa et Fabienne ! Toujours partantes pour une petite conversation et le partage d'un sourire.

As said previously, I could travel to many universities seeking the best way to answer the biological questions raised during my thesis. It was an extremely rewarding experience that I would do again. Everyone I have had the chance to meet has been wonderful and I am very grateful to them!

To begin with, at the university of Gent, I met Renée who is a student in a situation very close to mine. *Renée, je bent een buitengewoon empathische en briljante meid. Ik had me geen betere partner kunnen dromen om mee samen te werken bij gent. Voor mij ben je een vriend, allez pistolet!* At the KUL, where I spent many hours in this tiny room for scanning bones, I met Frederique and Carla. I am very grateful to both of you. *Jullie zijn twee uiterst bekwame wetenschappers en een plezier om mee samen te werken, bedankt! Frederique, ik sta vooral versteld van je nauwgezetheid en snelheid als het om DMM gaat.*

I flew over the English Channel to reach Chrissy Hammond's lab in Bristol. Chrissy, you were so welcoming and were able to put me at ease very quickly Thank you for everything you set in place to allow me to collect a maximum data during the time I was present. Thank you for your availability, your exceptional support, and your gift of creating a safe place within your team. I am also impressed by the eclecticism and original perspectives through which you look at sciences. In Bristol, I worked closely with Qiao, we became quite a team and we were not afraid of a science fest! We even discovered together a dinosaur, covered by scales, which takes on a most comical twist when you are part of a lab headed by Dr. Hammond (cfr Michael Crichton!). 乔，非常感谢你给予我的一贯支持！你有一颗友善纯洁的心，在远离亲人的日子里，你是我可以依靠的肩膀。你成为了我亲爱的挚友，一个让我信任，让我仰望，让我想保持亲近关系的人。我知道你偶尔会质疑自己，不要这样，因为你很聪明！我会永远铭记布鲁塞尔之行的美好回忆。 Thank you to you too Mengdi! We had a lot of good laughs! 你有滑稽的时机我爱！我们一起分享美好的乐趣，嘲笑我们多愁善感的生活！很遗憾我们没能一起去“洗澡”。你知道这意味着什么吗？下次我来英国时，我们将计划一次小型公路旅行，分享更多美好时光！感谢您在“布里斯托尔”欢迎我，您是我的朋友！ I also thank Erika with her unforgettable sense of hospitality. *Você veio ao laboratório com muita energia e bom humor para me guiar pela histologia da zebrafish. Seu encorajamento tocou meu coração, especialmente durante um período difícil. Sei que você é apaixonado por ciências e tenho certeza que muito sucesso virá para você, é merecido. Obrigado pela nossa conversa divertida em torno de uma cerveja e no parque!* I do not want to forget the other members of the lab that were so nice to me: Dylan, Lucy, Wahab, Georgie, Renata, and Joanna, thank you all!

En plus de tous ces échanges inter-universités, au sein même de Liège j'ai pu également collaborer avec de nombreuses personnes qui ont marqué mon esprit. Je pense au labo de Gabriel Mazzucchelli, qui a pris de son temps pour discuter avec moi d'approches protéomiques et dont l'équipe m'a accueilli à bras ouverts ; merci à vous Maximilien, Nancy et Lisette. Je remercie aussi Mireille Demoulin et son labo, avec Francesco et Joël, qui m'ont initié aux différentes étapes de la génération de nanobodies. Ce fût tout autant de moments enrichissants et très formateurs en ce qui concernent les compétences scientifiques. J'ai acquis aussi de nombreuses compétences grâce à ma collaboration au sein du labo de Marc

Muller que j'ai remercié précédemment. Pour les révisions de mon article principal, l'équipe du labo Majeb a été d'une grande aide et je remercie chaleureusement Michaël, Amélie et Raphaël.

Je tiens également à remercier les différentes plateformes qui m'ont alloué leurs services et qui ont été bénéfiques pour l'avancement de ma thèse, dont la plateforme zebrafish et la plateforme génomique pour leur aide concernant les RNA-seq. Je remercie Gaëlle et Olivier qui ont pris soin de nombreuses souris et qui ont été un plaisir aux côtés desquels travailler. Je remercie aussi la plateforme immunohistologie avec Tiffany, Hülya et Sevilay, trois filles formidables, pleines de vitalité et de bonne humeur, le tout supervisé par Chantal Humblet à l'image de son équipe.

Ensuite, il y a eu tous les étudiants qui ont collaboré à mon projet de thèse et que j'ai encadré. La première, Elisa, comment oublier ton entrée fracassante, merci pour ta spontanéité. Clémentine, le petit dragon, pleine de vie et d'entrain. C'est toi qui a passé le plus de temps à mes côtés pour ton stage et tu as été excellente et d'une aide incroyable. On n'oubliera pas non plus ces péripéties dans le train en revenant de la KUL. Puis mes derniers étudiants, venus en jumeaux, mes double troubles, Tiago et Juliane, venus à point pour m'aider à boucler mes travaux. On aura fait une très belle équipe et on aura bien avancé tous les trois !

Durant tout le parcours de ma thèse j'ai pu compter sur de nombreux amis et je ne peux manquer l'occasion de les citer et d'adresser quelques mots sincères à leur égard. Laura, créature aux 1001 noms, ma Lauramie brillante et incroyable qui d'un bond passe à une Lauranimale ou pire un Lauraptor. Toujours présente dans les bons et mauvais moments, je te remercie pour ton amitié inestimable et ta détermination. Douce et piquante, merci pour tous ces moments à rire, à pleurer et pleurer de rire. On aura vécu de grandes choses ensemble, mais parce qu'on était ensemble, c'était mieux et les choses devenaient plus faciles. On aura fait notre thèse en parallèle avec beaucoup de points communs, j'en suis fier et le plus important, heureux ! Je suis aussi tellement fier de tout ce que tu as réussi à accomplir. PS : tu vois je suis dans tes 10% de prédiction ! Merci Renaud mon ami vorace à qui personne ne résiste ! Tu es le chasseur, le monde est ta proie c'est bien pour ça que je suis heureux d'être ton ami car alors je suis en sécurité. Tu es redoutable et plus intelligent que tu n'en as l'air. Tu es le plus normal de mes amis, jamais vous ne m'entendez dire car cet homme est loin de l'être. Mais le génie ne réside-t-il pas dans la folie ? Merci aussi pour ton soutien, tu n'as pas changé depuis notre rencontre chez 'carte claire'. Adélaïde (ou Didier, on ne sait plus !), un grand merci pour toute ta douceur associée à ton attitude de warrior, *mi hervidora tan linda*, d'où Adébouilloire ! Te voir m'a toujours fait la sensation d'une bouffée d'air frais, tout est simple à tes côtés. Ton tourbillon créatif est inspirant, tu crées un espace où le monde serait plus beau. Mais ce n'est pas pour ça que je te laisserai t'en tirer à une prochaine battle de dance ! Merci à toi Morgane - MK, pour tous ces précieux moments de vie partagés. Tu es quelqu'un que je trouve d'un courage épatant et force le respect, ce qui pousse à nous dépasser nous-même. Merci pour toutes tes anecdotes sur tant d'aspects de la vie et de la culture, parfois contées en '*morganois*' mais c'est ce qui ajoute un twist dont on ne voudrait

se passer. Avec toi et Adé, au final ça ne m'étonne pas qu'on aille souvent à des JAMs et qu'on forme une si belle amitié. Aurélien, je te remercie aussi pour ton soutien et tes encouragements, et je te souhaite le meilleur. Surasa, noona, on aura passé aussi d'agréables moments. ฉันจำได้ว่าเมื่อเราพบกันฉันมีความสุขที่ได้พบคนน่ารักในห้องเรียนเดียวกันฉันมักจะรอคอยโอกาสใหม่ที่จะได้พบคุณ. J'ai aussi rencontré Paul au même moment que Surasa. *Hindi kita makakalimutan, lalo na ang iyong masasarap na pagkain. Ang aming goodby dinner ay nakatanim sa aking alaala. Sana maging maayos ang lahat sa tabi mo.* Les coïncidences de la vie nous ont amenés à partager une amie commune sans le savoir, ma Carolina. *Minha linda boneca, você é tão alegre, muito obrigada pelos bons momentos.* Lorsque j'ai commencé mes études en sciences biologiques je me suis lié de forte amitié à Marie-Ange, Sarah et Amélie, mes petites gauffres. On aura traversé nos études ensemble et j'en ai la tête remplie de bons souvenirs. Vous êtes toutes les trois des amies pour la vie ! Et bien sûr Yves que j'ai aussi connu à l'université et qui s'est lancé dans les galères de thèse en même temps que moi. Ton petit air goguenard que tu arbores me fait toujours autant rire. Jordane Blondie, petite fleur, tu es la chouchole comme tu dis ! On a les mêmes références et on se comprend. Je suis content d'avoir été ton voisin de travail et d'avoir développé une belle amitié avec toi. Tu trouves souvent le bon mot et je te remercie pour tes conseils et tes talents de cuisinières surtout pour ton dulce de leche. Carlos, merci pour tes encouragements, *eres mi guapo amigo y estoy muy feliz de haberte conocido a ti y a la dulce Verena. Vielen Dank auch an Sie für die sehr angenehmen gemeinsamen Abendessen.*

Nous arrivons aux derniers remerciements que j'aimerais adresser, mais ne nous détrompons pas, extrêmement importants à mes yeux, je les destine à ma famille. Papa, Maman, je vous remercie de tout cœur pour tout votre amour, bienveillance et le support inconditionnel à mon égard. Vous êtes exceptionnels et je vous suis tellement reconnaissant. Aymeric et Lauranne, bien sûr, tout autant encourageants et engagés dans ma réussite, vous êtes aussi extraordinaires et je suis heureux de vous écrire ces quelques lignes. J'ai beaucoup de chance de vous avoir auprès de moi, j'en ai pleinement conscience. Basile, farceur et espiègle, et Nola, aux magnifiques sourires, les plus beaux enfants sur cette terre (et oui je suis impartial et objectif), présents pour des moments pleins de joie et d'amour qui nous rappellent de vivre le moment présent. Merci Papy, merci Mamy, pour toutes ces années à mes côtés à croire en moi. Peu de mots peuvent exprimer la reconnaissance que je vous porte et à quel point je vous estime et vous aime. Je n'oublie pas le reste de ma famille qui a été fabuleuse et ne démerite pas.

Finally, or Finally, my last words are for you Prince, *મારી રાત્રિ નો ચંદ્રમાં અને હૃદય તો ટુકડો.* You shine and your light uplifts me. Nothing would have been the same without you. You have set an example of what a strong willed person is able to achieve and I admire you and what you are capable of. It was not always easy, but it is not supposed to be, then the success only taste sweeter. I felt very moved each time I could see you proud of me and I am very grateful to you for having cheered me up throughout my thesis. Prince you are simply the best, better than all the rest. I love you.



# Table of content

Summary-English.....	1
Résumé-Français .....	2
List of figures.....	3
List of tables.....	10
List of appendices.....	12
List of abbreviations .....	13
Preliminary table.....	17
Publications produced during the course of this thesis .....	18
<b>I.BACKGROUND.....</b>	<b>19</b>
<b>I.1 Global introduction on the skeleton.....</b>	<b>20</b>
<b>I.2 Cartilage biology .....</b>	<b>20</b>
I.2.1 The different types of cartilage .....	20
I.2.2 Chondrocytes and chondrogenesis .....	22
<b>I.3 Bone biology .....</b>	<b>24</b>
I.3.1 Osteogenesis .....	25
I.3.1.1 Intramembranous ossification .....	25
I.3.1.2 Endochondral ossification .....	26
I.3.2 Bone anatomy .....	29
I.3.2.1 Structural organization of bones.....	29
I.3.2.2 Bone matrix components.....	31
I.3.2.2.1 Inorganic.....	31
I.3.2.2.2 Organic .....	32
I.3.3 Bone remodeling .....	34
I.3.3.1 Osteoclast and osteoclastogenesis .....	34
I.3.3.2 Bone resorption and turnover .....	36
<b>I.4 Joint tissues biology .....</b>	<b>37</b>
I.4.1 Synovial joint anatomy.....	37
I.4.1.1 Articular cartilage .....	38
I.4.1.1.1 Articular chondrocytes .....	42
I.4.1.1.2 Matrix organization and composition .....	43
I.4.1.1.3 Calcified cartilage .....	48



I.4.1.2	Subchondral bone .....	49
I.4.1.3	Synovium .....	50
<b>I.5</b>	<b>Osteoarthritis.....</b>	<b>51</b>
I.5.1	Heterogeneity of OA, a complex disorder.....	52
I.5.2	Physiopathology of OA.....	57
I.5.2.1	Articular cartilage modifications .....	59
I.5.2.1.1	Biological mechanisms of cartilage degeneration .....	62
I.5.2.2	Subchondral bone modifications .....	65
I.5.2.2.1	Biological mechanisms of the subchondral bone sclerosis.....	68
I.5.3	Small Leucine-Rich Proteoglycans.....	71
I.5.3.1	SLRPs in OA.....	74
I.5.3.2	Osteomodulin.....	78
I.5.4	Models for studying OA.....	81
I.5.4.1	Mouse models .....	82
I.5.4.1.1	Spontaneous model .....	84
I.5.4.1.2	Destabilization of the medial meniscus .....	85
I.5.4.2	Zebrafish model .....	86
<b>II</b>	<b>OBJECTIVE &amp; STUDY DESIGN .....</b>	<b>91</b>
<b>III</b>	<b>MATERIAL &amp; METHODS .....</b>	<b>94</b>
III.1	Mouse strains and housing .....	95
III.2	Mouse model of OA .....	95
III.3	Knee joint histology and histomorphometry .....	96
III.4	Immunohistochemistry .....	101
III.5	Micro-computed tomography ( $\mu$ CT) and image analysis.....	101
III.6	Mechanical testing .....	104
III.7	CatWalk XT .....	105
III.8	Zebrafish husbandry and strains .....	108
III.9	Alcian blue staining in the Zebrafish .....	109
III.10	Alizarin red staining in the Zebrafish.....	109
III.11	Injection of mRNA of <i>omd</i> in the Zebrafish.....	110
III.12	Whole-mount <i>in situ</i> hybridization in the Zebrafish .....	111
III.13	Histology of the Zebrafish jaw joint .....	113
III.14	Zebrafish osteoclast assay in the caudal fin.....	113

III.15	TRAP staining of the Zebrafish scales.....	114
III.16	Regeneration of Zebrafish scales and second harmonic generation .....	114
III.17	Fourier transform infrared (FTIR) analysis .....	115
III.18	Human trabecular osteoblast culture for RNA-seq analysis .....	119
III.19	Human osteoblast culture for ALP assay and <i>in vitro</i> Alizarin red staining.....	122
III.20	ALP assay .....	123
III.21	Alizarin red staining of <i>in vitro</i> osteoblast culture .....	124
III.22	Solid phase binding assay.....	125
III.23	Mouse osteoclast culture .....	125
III.24	Assay in the serum for bone turnover markers .....	126
III.25	Western blot.....	126
III.26	Statistical analysis.....	127
<b>IV.MAIN RESULTS .....</b>		<b>128</b>
IV.1	General growth characteristics of <i>Omd</i> KO and UP mice.....	130
IV.2	OMD is mainly localized in bone and calcified cartilage in mouse knee joint tissues .....	132
IV.3	<i>Omd</i> influences bone and cartilage microarchitectures .....	134
IV.3.1	Effect of <i>Omd</i> on articular cartilage structure .....	134
IV.3.2	Effect of <i>Omd</i> on bone structure .....	138
IV.3.2.1	Metaphysis of the tibia.....	138
IV.3.2.2	Epiphysis of the tibia and the effect of <i>Omd</i> on the development of bone sclerosis. .....	145
IV.4	<i>Omd</i> may play a beneficial role against articular degradation and prevents subchondral bone sclerosis .....	148
IV.5	Loss of <i>Omd</i> expression induced gait abnormalities in mice .....	152
IV.6	<i>omd</i> is expressed in the zebrafish skeleton and its mutation induces articular cartilage lesions and impaired bone remodeling.....	154
IV.7	OMD inhibited osteoclastogenesis by binding to RANKL.....	160
<b>V.DISCUSSION OF MAIN RESULTS.....</b>		<b>166</b>
<b>VI.ADDITIONAL RESULTS &amp; DISCUSSION.....</b>		<b>173</b>
VI.1	Further characterization of the bone phenotype by $\mu$ CT in the mouse model .....	175
VI.2	Gait analysis of the DMM model .....	182
VI.3	Characterization of the functions of OMD in female mice .....	184

VI.3.1	General growth characteristics .....	184
VI.3.2	Characterization of the bone phenotype by $\mu$ CT in female mice of 16 months .....	186
VI.3.3	Characterization of the spontaneous development of OA in female mice of 16 months.....	194
VI.3.4	Gait analysis of female mice.....	199
VI.4	Further characterization of the loss of function of <i>omd</i> in the zebrafish .....	201
VI.4.1	Multiple alignment comparison .....	201
VI.4.2	Characterization of early stages of the mutant <i>omd</i> .....	203
VI.4.3	Characterization of the bone matrix components of the mutant <i>omd</i> .....	208
VI.4.4	Characterization of the regeneration of elasmoid scales of the mutant <i>omd</i> .....	213
VI.5	Additional data from <i>in vitro</i> models .....	217
VI.5.1	Effect of OMD treatment on human osteoblast culture .....	217
VI.5.2	Rescue of the sclerotic phenotype in cortical osteoblast culture .....	219
<b>VII.CONCLUSIONS &amp; FUTURE PERSPECTIVES .....</b>		<b>221</b>
<b>VIII.BIBLIOGRAPHY .....</b>		<b>229</b>
<b>IX.APPENDICES .....</b>		<b>252</b>

# Summary - English

**Purpose:** To investigate the roles of osteomodulin (OMD), a small proteoglycan known for controlling collagen fibrils organization in bone, in the development of osteoarthritis (OA) associated with subchondral bone sclerosis.

**Methods:** Loss of function and overexpressing mice for *Omd* aged 4, 8, and 16 months were used to study *Omd* roles in bone and cartilage metabolism and answer whether mice develop spontaneous OA. Surgical destabilization of the medial meniscus (DMM) model was performed to investigate its role in mechanically-induced OA. Additionally, we used *omd* overexpression as well as a mutant deficiency for *omd* in the zebrafish model to study *omd* effects on skeletal metabolism and cartilage development. Finally, *in vitro* models were used to further study OMD in osteoclastogenesis.

**Results:** *Omd* regulated bone and cartilage microarchitectures. Knock-out mice showed thinner calcified cartilage in the medial tibial plateau, and their growth plate was thicker at 16 months compared to WT. Both trabecular and cortical bone volume/total volume ratios were increased in the *Omd* knock-out mice and they showed a reduced percentage of porosity. The trabecular number of the knock-out mice was increased while their trabecular total volume was decreased. Further, their cortical bone showed increased thickness, and a higher whole bone strength. Knock-out mice were more prone to develop cartilage lesions spontaneously. Interestingly, *Omd* knock-out mice developed subchondral bone sclerosis spontaneously while overexpressing mice showed less subchondral bone sclerosis in the DMM OA model. At 16 months, *Omd*-overexpressing mice had the less trabecular number and a greater structure-model index for their trabecular bone geometry. The zebrafish model showed that the ectopic overexpression of *omd* induced developmental defects with abnormal cartilage structures. Further, we studied the development of OA in zebrafish, an animal model that develop OA features in the synovial jaw joint during aging and which is an excellent genetic model to study OA. We showed that adult zebrafish lacking *omd* were more prone to articular cartilage degeneration. Furthermore, mutant zebrafish showed increased mature osteoclasts generation and increased TRAP staining revealing a higher osteoclast activity. Impaired osteoclastogenesis might be involved in the defects involved during scale regeneration. Our zebrafish results are supported by our *in vitro* experiments where we demonstrated that OMD bound to RANKL and inhibited osteoclastogenesis.

**Conclusions:** OMD is a key factor in subchondral bone sclerosis associated with OA. This small proteoglycan participates in bone and cartilage homeostasis notably by acting on the regulation of osteoclastogenesis.

# Résumé-Français

**Objectif:** Étudier les rôles de l'ostéomoduline (OMD), un petit protéoglycane connu pour contrôler l'organisation des fibrilles de collagène dans l'os, dans le développement de l'arthrose associée à la sclérose osseuse sous-chondrale.

**Méthodes:** La perte de fonction et la surexpression d'*Omd* chez des souris âgées de 4, 8 et 16 mois ont été utilisées pour étudier les rôles d'*Omd* dans le métabolisme osseux et cartilagineux et déterminer si les souris développaient une arthrose spontanée. La déstabilisation chirurgicale du modèle de ménisque médial (DMM) a été réalisée pour étudier son rôle dans l'arthrose induite mécaniquement. De plus, nous avons utilisé la surexpression d'*omd* ainsi qu'un mutant déficient pour *omd* dans le modèle de poisson zèbre pour étudier les effets d'*omd* sur le métabolisme squelettique et le développement du cartilage. Enfin, des modèles *in vitro* ont été utilisés pour étudier OMD dans l'ostéoclastogénèse.

**Résultats:** Nous avons démontré qu'*Omd* régulait les microarchitectures osseuses et cartilagineuses. Les souris knock-out présentaient un cartilage calcifié plus mince dans le plateau tibial médian, et leur plaque de croissance était plus épaisse à 16 mois par rapport aux souris sauvages WT. Les rapports du volume d'os/volume total pour l'os trabéculaire et cortical étaient augmentés chez les souris *Omd* knock-out et leur porosité osseuse diminuée. Le nombre de trabécules des souris knock-out était plus élevé tandis que leur volume total trabéculaire était diminué. De plus, leur os cortical était plus épais et la résistance de leur os tibial accrue. Les souris knock-out étaient plus susceptibles de développer des lésions cartilagineuses spontanément. Les souris knock-out développaient spontanément une sclérose osseuse sous-chondrale, tandis que les souris surexprimant *Omd* ont montré moins de sclérose osseuse sous-chondrale dans le modèle DMM. À 16 mois, les souris surexprimant *Omd* avaient le plus petit nombre de trabécules et un indice de modèle de structure plus élevé pour leur géométrie osseuse trabéculaire. Le modèle de poisson zèbre a montré que la surexpression ectopique d'*omd* induit des défauts de développement avec des structures cartilagineuses anormales. En outre, nous avons étudié le développement de l'arthrose chez le poisson zèbre, un modèle qui développe des signes d'arthrose dans l'articulation synoviale de la mâchoire au cours du vieillissement. Nous avons montré que les poissons zèbres adultes dépourvus d'*omd* étaient plus sujets à la dégénérescence du cartilage articulaire. En outre, le poisson zèbre mutant a montré une génération accrue d'ostéoclastes matures et une augmentation de la coloration TRAP révélant une activité ostéoclastique plus élevée. Une ostéoclastogénèse altérée pourrait être impliquée dans les défauts observés lors de la régénération des écailles. Nos résultats sur le poisson zèbre sont étayés par nos expériences *in vitro* où nous avons démontré que l'OMD se liait à RANKL et inhibait l'ostéoclastogénèse.

**Conclusions:** L'OMD est un facteur clé de la sclérose osseuse sous-chondrale associée à l'arthrose. Ce petit protéoglycane participe à l'homéostasie osseuse et cartilagineuse notamment en agissant sur la régulation de l'ostéoclastogénèse.

## LIST OF FIGURES

**Figure 1:** Histological representation and schematic representation of the different types of cartilage with annotated structures. Hyaline cartilage (a); fibrocartilage (b); elastic cartilage (c). The illustration is available online from: <https://cnx.org/contents/tu2Wi4Fr@1/Histology-Module-4A-and-4B-Connective-Tissue> and provided by the Regents of University of Michigan Medical School © 2012.....**21**

**Figure 2:** Differentiation steps of chondrogenesis. Under the BMP pathway, MSCs express SOX9 to condense and proliferate and then RUNX2 to ensure the pre-hypertrophic and hypertrophic stages. SOX9 safeguards a pool of proliferating chondrocytes by inhibiting the effect of RUNX2 and delay the passage to pre-hypertrophic chondrocyte. The BMP pathway and RUNX2 trigger the expression of the transcriptional factor SP7. SP7 cooperates with RUNX2. Afterward, hypertrophic chondrocytes turn to apoptosis or transdifferentiate into osteoblast, for endochondral ossification. Figure adapted from [10,15,16] and designed by Jérémie Zappia with Biorender.....**23**

**Figure 3:** Schematic representation of the intramembranous and endochondral ossification [...]. Figure adapted from [40].....**28**

**Figure 4:** Structure of a long bone from the organ scale to the components [...][40].....**30**

**Figure 5:** (A) Illustration of the different steps of osteoclastogenesis. Myeloid precursor turns into pre-osteoclast under the action of M-CSF and starts to increase their RANK expression. Under, the action of RANKL, produced by stromal cells, osteoblasts and osteocytes as a soluble form or bound to the membrane, they are committed into osteoclasts. Mononuclear osteoclasts express a specific gene signature, namely TRAP and CTSK thanks to the NFAT pathway. They eventually fuse as functional osteoclasts and are polarized when active. Figure adapted from [46,53] and designed by Jérémie Zappia with Biorender. (B) The polarized osteoclast has distinct domains, the functional secretory domain for secretion of product waste, the basolateral domain, the zone of contact with bone named the sealing zone and the ruffled border, defining the resorption lacuna [58].....**35**

**Figure 6:** Illustration of the anatomy of the synovial joint. The end of two bones is covered by articular cartilage and is articulated thanks to an articular capsule. Inside the capsule, the synovial membrane is specialized in the secretion of synovial fluid to fill the cavity. <https://cdn.lecturio.com/assets/Articular-capsule-and-components.png>.....**38**

**Figure 7:** (A) Illustration of the architecture of the articular cartilage with the four domains: superficial zone, transitional or middle zone, deep zone and calcified cartilage. The tide mark is represented as a darker delimitation between the deep zone and the calcified cartilage, where the vascularization coming from the subchondral bone underneath stops. (B) Histological representation of the articular cartilage with the four above-mentioned domains. Each domain has different composition for its ECM. The water and proteoglycan contents are different across each domain with decreasing water content from the superficial zone to the lower domains and inversely for the proteoglycan content except for the calcified cartilage where the presence of proteoglycan is reducing again [69,75].....**41**

**Figure 8:** (A) Electron micrograph of an aggregate of proteoglycan. Hyaluronic acid makes up the axis where aggrecans are bound to. (B) Zoom on a specific region for its modelization showing the globular domains and link protein. (C) Network of collagen type II and aggrecans bound to hyaluronic acid. During the relaxed state, aggrecans are expanded and water is drawn inside the ECM, while the collagen is stretched to keep the equilibrium. Upon compression, water is moving out, aggrecans are getting closer and the swelling potential is increased until the compression force is removed [84,86].....**46**

**Figure 9:** Representation of the regions of the articular cartilage: superficial zone, middle zone, deep zone and calcified cartilage separated with the tidemark. Chondrocytes are represented with the different subcategories of ECM: pericellular zone, territorial zone and interterritorial zone. The representative composition of these ECMs is listed [90].....**48**

**Figure 10:** (A) Schematic representation of the microarchitectural characteristic of subchondral bone trabeculae located beneath the subchondral bone plate. The analysis was performed following the individual trabecular segmentation (ITS) from computed tomography. There are two trabecular geometry, either rod or plate adopting three possible orientations, longitudinal, oblique or transversal. (B) Trabeculae were isolated and the number of rod trabeculae is represented by the green bar plot and the number of plate trabeculae by the red bar plot. The measured elastic modulus in the three spatial orientations is represented by the grey bar plot. Data from bar plots are presented as mean standard deviation (SD) [98].....**50**

**Figure 11:** Representation of the diverse OA phenotypes, endotypes and molecular endotypes (inspired from v6). CRPM: C-Reactive Protein Metabolite; TNF: Tumor Necrosis Factor; IL: InterLeukin; VEGF: Vascular Endothelial Growth Factor; MMP: Matrix MetalloProteinase; TIMP: Tissue Inhibitor of Metalloproteinase; sICAM: serum InterCellular Adhesion Molecule; sVCAM: serum Vascular Cell Adhesion Molecule; MCP: Monocyte Chemoattractant Protein; SIRT: sirtuine. Illustration from [106]..**53**

**Figure 12:** Radar plot showing the profile of the three clusters describing the three main endotypes. In grey: cluster 1 corresponds to the low tissue turnover endotype. In orange: cluster 2 corresponds to the structural damage endotype. In blue: cluster 3 corresponds to systemic inflammation. The median biomarker concentrations for each cluster are represented with a circle (instead of a dot) when the difference between medians is statistically different. Values between 10% and 90% quantile are shown on the graph as percentages. Subsets of biomarkers are associated with different characteristics of OA: cartilage degradation, cartilage remodeling, bone formation, bone resorption, joint tissue degradation, and inflammation [109].....**55**

**Figure 13:** Illustration and comparison of the healthy joint and the pathological changes induced by OA on joint tissues [...] [114].....**58**

**Figure 14:** (Left) Healthy cartilage from a knee joint of a 43 years old human and (right) OA lesions of the articular cartilage of the knee joint of a 88 years old human [115].....**59**

**Figure 15:** Representation of the histological OARSI score with key characteristics. From grade 0 to 5. Grade 0: intact surface; grade 1: superficial fibrillations and cell abnormalities; grade 2: surface discontinuity and chondrocytes clusters; grade 3: branched clefts; grade 4: erosion; grade 5: denudation with subchondral bone being apparent at the surface. Pictures were taken with magnification 100X from [120].....**61**

**Figure 16:** Schematic representation of the effect of DAMPs in OA. [...] Illustration from [132] and designed by Jérémie Zappia.....**64**

**Figure 17:** Schematic representation of the microarchitectural modifications of the subchondral bone in OA [...] [98].....**67**

**Figure 18:** Schematic representation of the biological mechanisms involved in the subchondral bone with early-stage OA and late-stage OA [...] [163].....**70**

**Figure 19:** Effect of the binding of OMD on type I collagen. (A) Collagen without OMD. (B) Collagen with OMD. (C) Representation of the fibril formation without or with OMD leading to more various, larger and twisted fibrils or to more regular and straight fibrils respectively [246].....**80**

**Figure 20:** summary of the different models used in OA research [248].....**81**

**Figure 21:** Representation of the murine histological OARSI score with key characteristics. The medial femoral condyle can be observed at the top of the picture and the medial tibial plateau can be observed at the bottom. With the first score corresponding to the condyle and the second to the tibia, here is the attributed score for each image : (A) 0, 0.5; (B) 0, 1; (C) 0.5, 2; (D) 3, 3; (E) 0, 4; (F) 5, 6. Pictures are issued from [252].....**83**

**Figure 22:** (A) Revised phylogenetic tree replacing the synovial joint apparition (black asterisk) in a common ancestor of all bony vertebrates instead of the old model placing it with lungfish and tetrapods (grey asterisk). (B) Head of the zebrafish stained with Alcian blue with a focus on the jaw joint and pectoral fin joints. aa: anguloarticular; q: quadrate; sc: scapula; r: ray; pr: proximal radial; dr: distal radial. (C) Representation of the zebrafish histological OARSI score with key characteristics for the jaw joint. Grade 0: the surface of the cartilage is intact; grade 1: the cartilage is still intact but the surface is uneven with small fibrillations; grade 2: there are deeper fibrillations, matrix loss and surface abrasion; grade 3: there are vertical clefts extending to the deeper cartilage layers; grade 4: erosion of the superficial layer of the cartilage; grade 5: denudation of the cartilage with the subchondral bone surface being exposed; grade 6: the subchondral bone surface is exposed and deformed. Illustration adapted from [264].....**89**

**Figure 23:** Number of papers with “Osteomodulin” or “Osteoadherin” in their title published by year. The research was performed on Pubmed in February 2023.....**93**

**Figure 24:** Illustration of the ROI measured with QuPath for the histomorphometry analysis. (A, B) Toluidine Blue staining was used for uncalcified (1) and calcified (2) cartilage measurements. The yellow line was drawn to measure the plate length. Inside the yellow circle, the area of the growth plate was defined (3). (C) The Safranin-O Fast Green was used to measure the subchondral bone volume. The subchondral bone volume was measured inside the yellow box and calculated using the formula TV – (Bone marrow volume (4) + cartilage volume).....**100**

**Figure 25:** Photography of the Phoenix NanoTom M with its 180 kV/20 W ultra-high performance nanofocus X-ray tube from the KULeuven (source: <https://kuleuven.xct.be/ge-nanotom-m>).....**102**

**Figure 26:** Schematic representation of the distinct areas used for the analysis of the tibia (voxel size =3 µm) and for the femur (voxel size=10 µm). For the tibia, the 3D analysis was performed on 150 images for the trabecular bone and on 100 images for the cortical bone. For the femur, the 3D analysis was performed on 50 images for the trabecular bone, on 100 images for the cortical bone and on the whole area for the femoral head. Figure designed by Jérémie Zappia with Biorender.....**103**

**Figure 27:** Photography of the Instron 5565 tensile testing machine (from MaJEB sprl) with a tibia disposed to endure the three-point bending assay.....**104**

**Figure 28:** Illustration of the Catwalk XT device with the illuminated glass platform and with illuminated paws of a rodent, photography from <https://www.noldus.com/catwalk-xt/resources>.....**105**

**Figure 29:** (A) Illustration of a compliant runway from the Catwalk XT with marks showing the stride length, print position and base of support, illustration from <https://www.noldus.com/blog/automated-gait-analysis> (B) Schematic representation of a rodent body with marks showing the base of support of



<i>front and hind paws and with the graphical representation of stance (s), swing (s), stride length (cm), and step cycle (s), figure adapted from[275].....</i>	<b>106</b>
<b>Figure 30:</b> <i>Photography of injected zebrafish larvae at 24hpf with the representation under brightfield, green fluorescence showing the expression of GFP and red fluorescence showing the correct injection of rhodamine dextran.....</i>	<b>110</b>
<b>Figure 31:</b> <i>Representation of the TRAP staining analysis with the ZFBONE software available on FIJI..</i>	<b>114</b>
<b>Figure 32:</b> <i>Description of the selected areas of the caudal fin used for the FTIR analysis (a) Brightfield image of the caudal fin of the zebrafish, (b) schematic representation of the caudal fin composed of segmented bony rays which present bifurcation. (c) Schematic representation of the bifurcation and edge areas. Figure adapted from [280] and designed by Jérémie Zappia. (d) Brightfield images of the bifurcation and edge areas of the caudal fin of 3 months WT zebrafish and associated topographical distribution of collagen and phosphate groups. (e) Brightfield images of the bifurcation and edge areas of the caudal fin of 1 year WT zebrafish and associated topographical distribution of collagen and phosphate groups.....</i>	<b>118</b>
<b>Figure 33:</b> <i>Representative timeline of the in vitro culture of trabecular osteoblasts for RNA-seq analysis.....</i>	<b>120</b>
<b>Figure 34:</b> <i>Representative timeline of the in vitro culture of trabecula and cortical osteoblasts for the ALP assay (A) and the Alizarin red staining (B). For the Alizarin red, cultures were stopped at 17, and 21 days.....</i>	<b>123</b>
<b>Figure 35:</b> <i>Macro observations of the cartilage of the knee joint of male mice [...].</i>	<b>131</b>
<b>Figure 36:</b> <i>(A) Immunostaining of OMD (in brown) in the knee joint (medial tibial plateau) of KO, WT, and UP male mice at 4, 8, and 16 months [...].</i>	<b>133</b>
<b>Figure 37:</b> <i>Histomorphometry of the cartilage was performed with QuPath at 4, 8, and 16 months [...].</i>	<b>135</b>
<b>Figure 38:</b> <i>Histomorphometry of the cartilage was performed with QuPath at 4, 8, and 16 months [...].</i>	<b>137</b>
<b>Figure 39:</b> <i><math>\mu</math>CT analysis of the metaphysis of the tibia of the male mice at 4, 8 and 16 months [...].</i>	<b>140</b>
<b>Figure 40:</b> <i><math>\mu</math>CT analysis on the metaphysis of the tibia of the male mice at 4, 8 and 16 months [...].</i>	<b>142</b>
<b>Figure 41:</b> <i>Biomechanical testing of the tibia from 16 months mice [...].</i>	<b>144</b>
<b>Figure 42:</b> <i>(A) Histomorphometry of the subchondral bone on Safranin-O Fast Green of the knee joint of male mice at 8 and 16 months was performed with QuPath on the lateral and medial plateaus of the tibia separately [...].</i>	<b>146</b>
<b>Figure 43:</b> <i>Analysis of the development of OA lesions in the different genotypes after spontaneously occurring with age (left) or after the DMM (right) [...].</i>	<b>150</b>
<b>Figure 44:</b> <i>Analysis of the gait of 4, 8, and 16-month-old male mice with the CatWalkXT [...].</i>	<b>153</b>
<b>Figure 45:</b> <i>Whole mount in situ hybridization for the omd mRNA on WT zebrafish larvae at 48-hpf, 5-dpf and 8-dpf; and on omd<sup>-/-</sup> larvae at 5-dpf [...].</i>	<b>155</b>

<b>Figure 46:</b> Analysis of the overexpression of <i>omd</i> in the zebrafish [...]	<b>156</b>
<b>Figure 47:</b> The mutant deficient for <i>omd</i> was generated through CRISPR/Cas 9 [...]	<b>158</b>
<b>Figure 48:</b> RNA-seq analysis of primary human pre-osteoblast cultures treated with 10 ng/ml of rhOMD during 72-h with n=11 (6 men and 5 women). (A) Vulcano plot with Threshold $p_{adj} < 0.01$ and $\text{Log}_2\text{FoldChange}$ . (B) IBSP gene expression comparison.....	<b>161</b>
<b>Figure 49:</b> (A) Solid Phase binding assay on the capture of RANKL by OMD. RANKL was coated on a plate followed by OMD addition. On the left: Binding assay with different concentrations of OMD (1000 to 15.65 ng/ml by serial 2X dilution), with 0.2 $\mu\text{g/ml}$ of coated RANKL (red curve) and negative control without RANKL (blue curve). On the right: Binding assay with different concentrations of coated RANKL (800 to 6.25 ng/ml) and 0.5 $\mu\text{g/ml}$ of given OMD (pink curve); negative control without OMD (purple curve). Wilcoxon test was performed with differences being considered significant at $p\text{-values} < 0.05$ (* $p < 0.05$ , ** $p \leq 0.01$ ). (B) Assay of the effect of OMD on primary murine osteoclast culture. The peripheral blood mononuclear cells were collected from murine bone marrow and differentiated into osteoclasts with M-CSF and RANKL. Osteoclasts were counted after 4 days of differentiation following a TRAP staining. Each point represents a mouse, n=7. The osteoclast count was represented in percentage of cells with the corresponding control set as 100%. Blue arrows point at osteoclasts. Scale bar=50 $\mu\text{m}$ . The data were plotted as a box plot showing all points. One-way ANOVA was performed with differences being considered significant at $p\text{-values} < 0.05$ (* $p < 0.05$ ). (C) Level of P1NP and TRAcP 5b measured in the serum of KO, WT and UP mice [...]	<b>164</b>
<b>Figure 50:</b> $\mu\text{CT}$ analysis of the femur of male mice at 8 and 16 months with a zoom on the femoral head of 8 months mice [...]	<b>176</b>
<b>Figure 51:</b> $\mu\text{CT}$ analysis of the femur of 16 months male mice. For the analysis, the femoral head and the femoral shaft were separated [...]	<b>178</b>
<b>Figure 52:</b> $\mu\text{CT}$ analysis of the trabecular bone of the femoral head of 8 and 16 months male mice [...]	<b>180</b>
<b>Figure 53:</b> $\mu\text{CT}$ analysis of the cortical and trabecular bone of the femoral shaft of 16 months male mice [...]	<b>181</b>
<b>Figure 54:</b> Analysis of the gait with the Catwalk XT of male mice from the DMM model (represented by ●) with the SHAM group (represented by ▲) and non-operated mice of 8 months (represented by ◆) as controls [...]	<b>183</b>
<b>Figure 55:</b> Macro observations of the knee joint of female mice at 4, 8 and 16 months [...]	<b>185</b>
<b>Figure 56:</b> $\mu\text{CT}$ 3D rendering of the tibia of female mice of 16 months for each genotype, KO, WT and UP [...]	<b>187</b>
<b>Figure 57:</b> The bone parameters measured for the trabecular and cortical bone of 16 months female KO, WT and UP, were the bone volume (BV); the total volume (TV) and their ratio (BV/TV) [...]	<b>188</b>
<b>Figure 58:</b> Additional parameters for the trabecular bone parameters were reported for the 16 months female KO, WT and UP mice [...]	<b>190</b>
<b>Figure 59:</b> Additional parameters for the cortical bone were reported for the 16 months female KO, WT and UP mice [...]	<b>191</b>

<b>Figure 60:</b> Comparison of the main $\mu$ CT parameters between male and female mice at 16 months [...]	<b>193</b>
<b>Figure 61:</b> Analysis of the spontaneous OA development with the naturally occurring loss of proteoglycan at 16 months in female KO, WT and UP mice [...]	<b>195</b>
<b>Figure 62:</b> The spontaneous cartilage degradation of 16 months female mice was assessed from the knee joint sections that were stained with Toluidine Blue to score the loss of proteoglycan. The score (from 0 to 5) was attributed to the lateral and the medial tibial plateaus and to the lateral and medial condyles according to the OARSI recommendations. [...]	<b>196</b>
<b>Figure 63:</b> Comparison of the spontaneous cartilage degradation of 16 months male and female mice for the lateral and medial tibia [...]	<b>198</b>
<b>Figure 64:</b> Analysis of the gait of 4, 8, and 16-month-old female mice with the CatWalkXT [...]	<b>200</b>
<b>Figure 65:</b> Multiple alignment of the protein ostemodulin in homo sapiens, bos taurus, mus musculus, rattus norvegicus and danio rerio with Kalign and the associated identity matrix in percentage. The signal peptide, acidic patches, specific cysteines identified in [297] and key residues for collagen binding identified in [247] are highlighted in the sequences alignment.....	<b>202</b>
<b>Figure 66:</b> Alcian blue staining of 5 dpf WT and omd -/- larvae showing the whole larvae (Zoom 1,6X), scale bar=1mm; and the craniofacial cartilaginous structures in the lateral and ventral view (Zoom 6,3X), scale bar=200 $\mu$ m.....	<b>204</b>
<b>Figure 67:</b> Alcian blue staining of 8 dpf WT and omd -/- larvae showing the whole larvae (Zoom 1,6X), scale bar=1mm; and the craniofacial cartilaginous structures in the lateral and ventral view (Zoom 6,3X), scale bar=200 $\mu$ m.....	<b>205</b>
<b>Figure 68:</b> Alcian blue staining of 14 dpf WT and omd -/- larvae showing the whole larvae (Zoom 1,6X), scale bar=1mm; and the craniofacial cartilaginous structures in the lateral and ventral view (Zoom 6,3X), scale bar=200 $\mu$ m.....	<b>206</b>
<b>Figure 69:</b> Alizarin red staining of 8 dpf WT and omd -/- larvae showing the whole larvae (Zoom 1,6X), scale bar=1mm; and the craniofacial mineralized structures in the lateral and ventral view (Zoom 6,3X), scale bar=200 $\mu$ m.....	<b>207</b>
<b>Figure 70:</b> Study design of the FTIR analysis of the caudal fin of zebrafish [...]. Figure adapted from [280].....	<b>209</b>
<b>Figure 71:</b> FTIR analysis with the reported parameters being MM, C/P and COLL/P ratios from the bifurcation area and the edge of the caudal fin of 3 months zebrafish [...]	<b>211</b>
<b>Figure 72:</b> FTIR analysis with the reported parameters being MM, C/P and COLL/P ratios from the bifurcation area and the edge of the caudal fin of 1-year-old zebrafish [...]	<b>212</b>
<b>Figure 73:</b> Analysis of the elasmoid scales regeneration in 1.6-year-old zebrafish [...]	<b>214</b>
<b>Figure 74:</b> Multiphoton forward scattering (second harmonic generation (SHG), 880 nm wavelength) for the visualization of regenerating scales and zoom on the organization of collagen fibrils for the 1.6-year-old WT and omd -/- zebrafish. Red arrowheads highlight highly disorganized collagen fibrils area For each genotype, n=5. Scale bar=500 $\mu$ m.....	<b>216</b>
<b>Figure 75:</b> Primary human osteoblasts from cortical and trabecular bone were used for monolayer culture with osteogenic medium during 14 days. Osteoblasts were treated with 0, 10 or 40 ng/mL of	

*rhOMD during 3 days prior to the analysis of the ALP activity reported in percentage. Each point represents a unique patient and paired one-way ANOVA was performed with differences being considered significant at p-values<0.05 (\*p<0.05, \*\*p≤0.01).....218*

**Figure 76:** *Alizarin red staining on cortical osteoblasts, either from the non-sclerotic area or the neighboring sclerotic subchondral bone, after 17 days and 21 days of differentiation in osteogenic medium. Sclerotic osteoblasts were treated with 2.5 or 10 ng/mL of rhOMD, or none (CTL), during their 3 last days of differentiation. For 17-days, n=2, and for 21-days, n=1..... 220*

**Figure 77:** *Graphical representation of the effect of the lack of OMD in the murine knee joint [...]......228*

## LIST OF TABLES

<b>Table 1:</b> Nomenclature for the gene and protein associated to its species. The nomenclature indicates the writing rules to refer correctly to different species.....	<b>17</b>
<b>Table 2:</b> Classification of bones and associated features, adapted from [25].....	<b>29</b>
<b>Table 3:</b> Non-collagenous proteins of the bone matrix and associated functions, adapted from [51].....	<b>33</b>
<b>Table 4:</b> Types of collagen represented in articular cartilage with the composition of structural collagen chains, expressing genes, classification based on supramolecular assembly, percentage found in articular cartilage, and distribution in articular cartilage; adapted from [81].....	<b>44</b>
<b>Table 5:</b> Identification of molecular and clinical features related to four different OA subtypes with a proposed adapted treatment for the patient, adapted from [111].....	<b>56</b>
<b>Table 6:</b> Classification of the SLRP family in five classes; BGN: Biglycan; DCN: Decorin; ASP: Asporin; ECM2: Extracellular Matrix Protein 2; ECMX: Extracellular Matrix Protein X; LUM: Lumican; KTN: Keratocan; FMOD: Fibromodulin; OMD: Osteomodulin; PRELP: Proline/arginine-rich end leucine-rich repeat protein; EPN: Epiphycan; OGN: Osteoglycin; OPTC: Opticin; CHAD: Chondroadherin; NYX: Nyctalopin; TSK: Tsukushi; PODN: Podocan; PODNL: Podocan like protein. Classification is based on the N-end cysteine cluster and a 3D representation of a representative member generated with the PyMol software (Schrödinger LCC, version 2.1.1) is illustrated with lateral asparagines (N shown in red). X-Ray crystallographic analysis for the SLRP Family members of class III and class IV are not yet available. The different post-translational modifications, GAG type, glycosylation and other features are listed. LRR: leucine-rich repeat. The table is from [50] and was designed and generated by Jérémie Zappia.....	<b>72</b>
<b>Table 7:</b> Summary of the skeletal phenotypes of SLRPs deficient mouse and their association with OA. Table generated and designed by Jérémie Zappia.....	<b>75</b>
<b>Table 8:</b> Comparison of skeletal features in humans, rodents and zebrafish, adapted from [263].....	<b>87</b>
<b>Table 9:</b> Safranin-O Fast-Green staining.....	<b>97</b>
<b>Table 10:</b> Toluidine Blue staining.....	<b>98</b>
<b>Table 11:</b> OARSI guidelines for histological scoring, with Safranin-O Fast-Green staining, of murine OA modifications.....	<b>98</b>
<b>Table 12:</b> OARSI guidelines for histological scoring, with Toluidine Blue staining, of murine loss of proteoglycan associated with OA.....	<b>99</b>
<b>Table 13:</b> Guidelines adapted from OARSI for histological scoring, with Toluidine Blue staining, of OA modifications in the zebrafish.....	<b>113</b>
<b>Table 14:</b> RNA-Seq analysis of primary human pre-osteoblasts treated with 10 ng/ml of rhOMD during 72-h. List of differential gene expression, upregulated and downregulated genes sorted according to their padj. Genes with significant differential gene expression are highlighted in yellow with differences being considered significant at padj<0.05.....	<b>162</b>
<b>Table 15:</b> Summary of the bone parameters over time in the male mouse models.....	<b>222</b>

**Table 16:** Summary of the cartilage parameters over time in the male mouse models.....**222**

**Table 17:** Summary of OA parameters in the male mouse models (Spontaneous & DMM).....**222**

**Table 18:** Summary of the characterization of the zebrafish models, with the microinjection of *omd* mRNA (UP) and the mutant (KO).....**222**

**Table 19:** Summary of the *in vitro* models (murine and human primary cell culture).....**222**

# LIST OF APPENDICES

- Appendix 1:** Review on the SLRP family in the skeletal tissues.....
- Appendix 2:** Main paper “Osteomodulin down-regulation is associated with osteoarthritis development” .....
- Appendix 3:** Supplemental table of the CatWalk XT analysis.....
- Appendix 4:** Multiple alignment parameters.....
- Appendix 5:** Western blot from commercially available antibodies against OMD.....

## LIST OF ABBREVIATIONS

Acan: aggrecan

ASIC3: acid-sensing ion channel 3

ADAMTS: A disintegrin and metalloproteinase with thrombospondin motifs

ALP: alkaline phosphatase

Bglap: osteocalcine

BMD: bone mineral density

BMI: body mass index

BML: bone marrow lesion

BMP: bone morphogenetic protein

BSA: bovine serum albumin

BV: bone volume

COL1: type I collagen

COL2: type II collagen

COL10A1: type X collagen  $\alpha$  1 chain

COLL/P: collagen-to-phosphate index

C/P: carbonate-to-phosphate index

CRISPR: clustered regularly interspaced short palindromic repeat

CTSK: cathepsin K

DAMP: damage-associated molecular pattern

DC2: decalcifiant medium

DCC: deleted in colon cancer

DLL4: notch/delta-like protein 4

DMEM: Dulbecco's modified eagle medium

DMM: destabilization of the medial meniscus

DNA: deoxyribonucleic acid

    cDNA: complementary deoxyribonucleic acid

    gDNA: genomic deoxyribonucleic acid

DPF: day post fertilization



ECM: extracellular matrix  
FBS: fetal bovine serum  
FDR: false discovery rate  
FGF: fibroblast growth factor  
FPA: focal plane array  
FTIR: Fourier transform infrared  
GAG: glycosaminoglycan  
GFP: green fluorescent protein  
IGF1: insulin-like growth factor 1  
ITS: individual trabecular segmentation  
HAP: hydroxyapatite  
HEPES: 2-[4-(2-Hydroxyethyl)piperazin-1-yl]ethane-1-sulfonic acid  
HPF: hour post fertilization  
HIF-1 $\alpha$ : hypoxia-inducible factor 1-alpha  
HMG: high-mobility group  
HRP: horseradish peroxidase  
IR: infrared  
KO: knock-out for *Omd*  
LRR: leucine-rich repeat  
MAPK: mitogen-activated protein kinase  
M-CSF: macrophage stimulating factor  
MM: mineral-to-matrix index  
MMP: matrix metalloproteinase  
MRI: magnetic resonance imaging  
MSC: mesenchymal stem cell  
mTORC: mammalian target of rapamycin complex  
NFAT: nuclear factor of activated T cells  
NGF: nerve growth factor  
NGS: next-generation sequencing

OA: osteoarthritis

OARSI: osteoarthritis research society international

OMD: osteomodulin

OPG: osteoprotegerin

OSX: osterix

PCR: polymerase chain reaction

PBS: phosphate-buffered saline

PBST: phosphate-buffered saline tween

PDGF: platelet derived growth factor

PFA: paraformaldehyde

PGE2: prostaglandin E2

PLR: perilacunar/canalicular remodeling

RANK: receptor activator of nuclear factor kappa-B

RANKL: receptor activator of nuclear factor kappa-B ligand

RIN: RNA integrity number

ROI: region of interest

RNA: ribonucleic acid

mRNA: messenger ribonucleic acid

rRNA: ribosomal ribonucleic acid

shRNA: short hairpin RNA

tRNA: transfer ribonucleic acid

RPM: rotation per minute

RUNX2: runt-related transcription factor 2

SD: standard deviation

Shh: sonic hedgehog

SAMP8: senescence-accelerated mice prone 8

SASP: senescence-associated secretory phenotype

SHG: second harmonic generation

SLRP: small leucine-rich proteoglycan

SMI: structure model index

SOST: sclerostin

SOX : sex determining region Y (SRY)-related high-mobility group (HMG) box

SLIT3: slit guidance ligand

TBS: tris-buffered saline

TGF- $\beta$ : transforming growth factor beta

TMB: 3,3',5,5'-tetramethylbenzidine

TNF- $\alpha$ : tumor necrosis factor  $\alpha$

TLR: toll-like receptor

TRAP: tartrate-resistant acid phosphatase

TRPV1: transient receptor potential vanilloid 1

TV: total volume

UP: overexpressing *Omd*

VEGF: vascular endothelial growth factor

Wnt: wingless-related integration site

WT: wild type

YFP: yellow fluorescent protein

$\alpha$ MEM: alpha minimum essential medium eagle

$\mu$ CT: micro-computed tomography

## PRELIMINARY TABLE

Table 1: Nomenclature for the gene and protein associated to its species. The nomenclature indicates the writing rules to refer correctly to different species.

Species	Common name	Gene	Protein
<i>Homo sapiens</i>	Human	<i>OMD</i>	OMD
<i>Mus musculus</i>	Mouse	<i>Omd</i>	OMD
<i>Danio rerio</i>	Zebrafish	<i>omd</i>	Omd

## Publications produced during the course of this thesis

- **Jérémie Zappia**, Marc Joiret, Christelle Sanchez, Cécile Lambert, Liesbet Geris, Marc Muller, and Yves Henrotin. "From translation to protein degradation as mechanisms for regulating biological functions: a review on the SLRP family in skeletal tissues." *Biomolecules* 10, no. 1 (2020): 80.
- Antoine Florin, Cécile Lambert, Christelle Sanchez, **Jérémie Zappia**, Nancy Durieux, Antonio Martins Tieppo, Ali Mobasheri, and Yves Henrotin. "The secretome of skeletal muscle cells: A systematic review." *Osteoarthritis and Cartilage Open* 2, no. 1 (2020): 100019.
- Cécile Lambert, **Jérémie Zappia**, Christelle Sanchez, Antoine Florin, Jean-Emile Dubuc, and Yves Henrotin. "The damage-associated molecular patterns (DAMPs) as potential targets to treat osteoarthritis: perspectives from a review of the literature." *frontiers in Medicine* 7 (2021): 607186.
- Christelle Sanchez, **Jérémie Zappia**, Cécile Lambert, Jacques Foguene, Yvan Dierckxsens, Jean-Emile Dubuc, Jean-Pierre Delcour, André Gothot, and Yves Henrotin. "Curcuma longa and Boswellia serrata extracts modulate different and complementary pathways on human chondrocytes in vitro: deciphering of a transcriptomic study." *Frontiers in Pharmacology* 13 (2022).

Main paper issued from this thesis:

- **Jérémie Zappia**, Qiao Tong, Renée Van der Cruyssen, Frederique Cornelis, Cécile Lambert, Tiago Pinto Coelho, Juliane Grisart, Erika Kague, Rik J. Lories, Marc Muller, Dirk Elewaut, Chrissy L. Hammond, Christelle Sanchez, and Yves Henrotin. "Osteomodulin down-regulation is associated with osteoarthritis development." (2023). **Under review in Bone research**

# **I. BACKGROUND**

### **I.1 Global introduction on the skeleton**

The skeleton is among the largest organ in the human body, constituting roughly 15% of the body weight with bone, cartilage, ligaments and tendons making up skeletal tissues. The skeleton assumes several functions. It provides structural support for soft tissues and protection. It is the attachment site for tendons and ligaments for locomotion and joints are specific structures allowing mobility. For mammals, bone marrow is found inside bones and is the hematopoiesis site, supporting blood cellular components production. The skeleton is an incredible source of minerals and serves as a calcium and phosphorus reservoir, but it also absorbs toxins for their clearance. Finally, the skeleton can be considered as an endocrine organ. It produces factors and hormones to control mineral balance, glycemic and lipidic metabolism, sexual hormones biosynthesis and even cognition [1–5].

### **I.2 Cartilage biology**

The cartilage is a firm and flexible non-vascularized connective tissue containing cells in lacunae called chondrocytes which are embedded in a highly hydrated extracellular matrix (ECM). Its nutrients come from the densely vascularized and innervated neighboring tissue, the perichondrium. The function of the cartilage is to bear mechanical stress and constraint of the body, and provide support for skeletal growth [6,7].

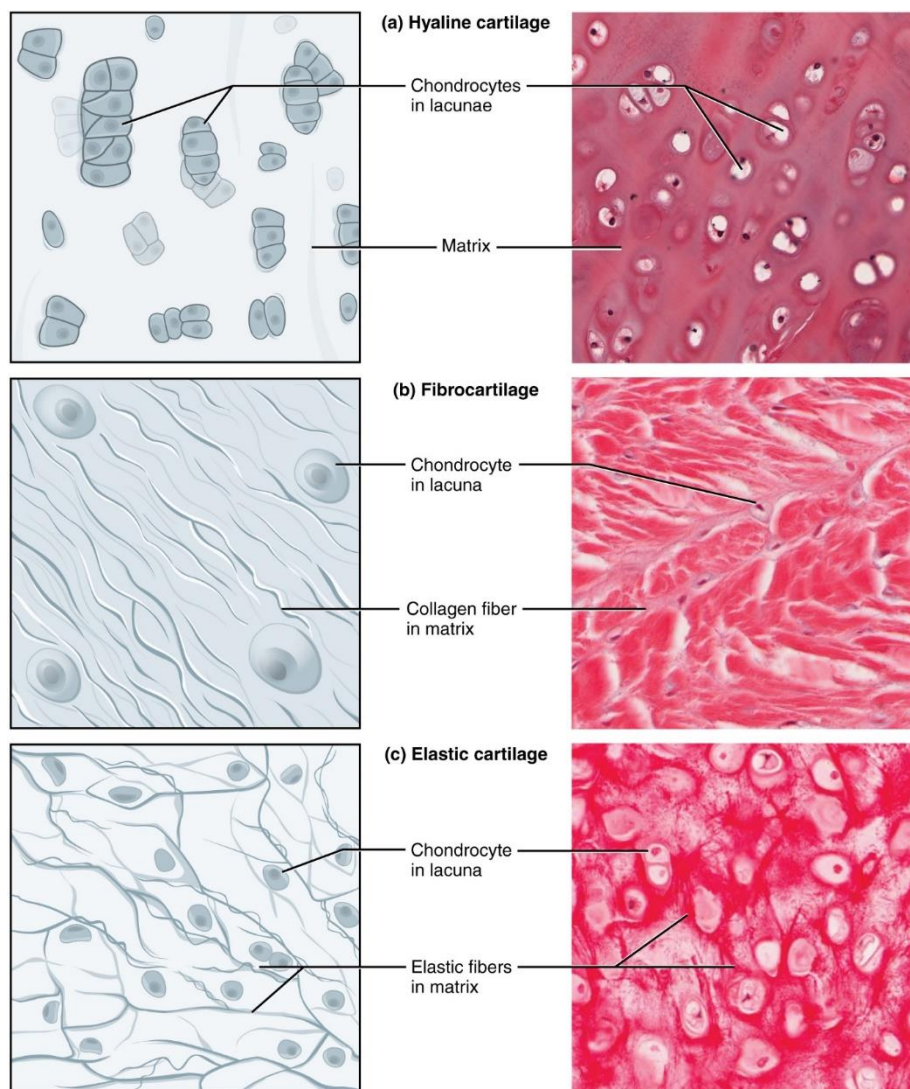
#### **I.2.1 The different types of cartilage**

Different types of cartilage are found throughout the body and have distinct properties. Among them, there are hyaline, elastic, and fibrocartilaginous cartilages (Fig 1).

The hyaline cartilage presents an extensive and homogenous ECM rich in proteoglycans and collagens, typically of type II, considered the most common hallmark of cartilage. During the

## I. BACKGROUND

development, the hyaline cartilage makes up the initial scaffold, called anlagen, from which starts the endochondral ossification and results in the replacement of the cartilage template with bone. In adults, it is namely found in the nose, larynx, trachea, costal cartilage, the growth plate of long bones and articular cartilage. It is the most abundant cartilage [6,7].



*Figure 1: Histological representation and schematic representation of the different types of cartilage with annotated structures. Hyaline cartilage (a); fibrocartilage (b); elastic cartilage (c). The illustration is available online from: <https://cnx.org/contents/tu2Wi4Fr@1/Histology-Module-4A-and-4B-Connective-Tissue> and provided by the Regents of University of Michigan Medical School © 2012.*

The fibrocartilage combines features of hyaline cartilage and dense connective tissues. Its cells have been named fibrochondrocytes as they present both chondrocyte and fibroblast characteristics. Its ECM is less rich in proteoglycans than the hyaline cartilage and is mainly



made of collagen of type I and type II specifically oriented parallelly to the direction of the stress plane. Fibrocartilaginous tissues are more dense and strong than other types of cartilage, providing excellent support for bearing weight, but also for the resistance of compression, tensile and shear forces. In adults, it is namely found in the intervertebral disc, meniscus, acetabular labrum and temporomandibular joint [6].

The elastic cartilage includes elastic fibers in addition to collagens and proteoglycans. It confers strength, elasticity and flexibility to allow deformation. It is namely found in the ear, epiglottis and larynx [6].

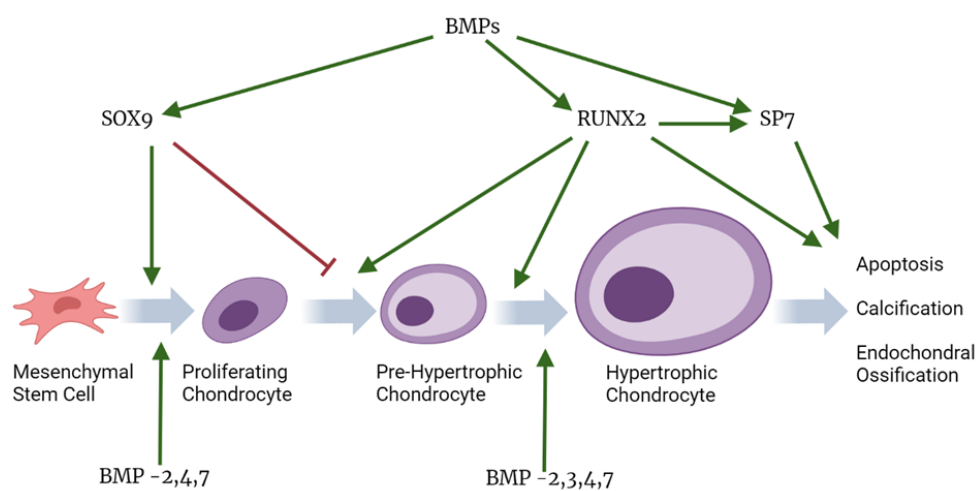
### **I.2.2 Chondrocytes and chondrogenesis**

Chondrogenesis is the process resulting in the development of the cartilage and is also required for the development of the skeleton via endochondral ossification (Fig 2). It is starting during embryogenesis but is pursued in adulthood. Mesenchymal stem cells (MSCs) are recruited and migrate to condensate and eventually become chondroprogenitor cells, forming the initial analgen scaffold. There are three possible origins of MSCs: neural crest cells of the neural ectoderm, the paraxial mesoderm cells and the lateral plate mesodermal cells. The neural crest cells give rise to the craniofacial cartilage, the paraxial mesoderm is at the initiation of the axial skeleton and the lateral plate mesoderm forms the appendicular cartilage [8]. MSCs are recruited through the Bone morphogenetic pathway (BMP), which controls several steps of chondrogenesis [9]. Cell-to-cell and cell-to-matrix interactions trigger the condensation phenomenon with increased adhesion proteins, such as aggrecan which is considered cartilage-specific [6,8].

Chondroprogenitors condition their ECM and secrete cartilaginous matrix proteins such as the cartilage hallmark collagen II and several growth factors and transcriptional factors which are

## I. BACKGROUND

crucial for the following steps of differentiation [8,10]. Among early factors, SOX transcriptional factors are upregulated in the condensed cells. In the SOX family, SOX9 is considered a key regulator in chondrogenesis induction and chondrocyte survival. It binds to HMG-box sites in DNA to induce the expression of type II collagen and aggrecan and its own expression. SOX9 is necessary for the conservation of the chondrocyte phenotype [8,11–13]. SOX9 is itself under the control of the BMP pathway with BMP-2 being the first member characterized in its regulation [14]. Several additional BMP members, BMP-4 and BMP-7, induce SOX9 expression during the initiation of the chondrogenesis [10]. Other pathways and conditions increase SOX9 expression, namely sonic hedgehog (Shh), transforming growth factor- $\beta$  (TGF- $\beta$ ), hypoxic conditions and HIF-1 $\alpha$ , fibroblast growth factors (FGFs), the inhibition of Notch, the inhibition of Wnt, making it extremely complex for a tight spatiotemporal regulation [7,11].



*Figure 2: Differentiation steps of chondrogenesis. Under the BMP pathway, MSCs express SOX9 to condense and proliferate and then RUNX2 to ensure the pre-hypertrophic and hypertrophic stages. SOX9 safeguards a pool of proliferating chondrocytes by inhibiting the effect of RUNX2 and delay the passage to pre-hypertrophic chondrocyte. The BMP pathway and RUNX2 trigger the expression of the transcriptional factor SP7. SP7 cooperates with RUNX2. Afterward, hypertrophic chondrocytes turn to apoptosis or transdifferentiate into osteoblast, for endochondral ossification. Figure adapted from [10,15,16] and designed by Jérémie Zappia with Biorender.*

## ***I. BACKGROUND***

Further, SOX9 and BMPs are involved in chondrocyte proliferation [10,13]. In the growth plate, chondrocytes proliferate linearly and form columns where chondrocytes are lining up as they are maturing. During bone formation, this mechanism promotes their elongation [17].

Following their differentiation, chondrocytes become pre-hypertrophic and then hypertrophic by adopting a large volume, the latter being the end stage. SOX9 inhibits the transition from proliferation to pre-hypertrophic chondrocytes. Because of the *SOX9* switch-off, the inhibitory brake is lifted on the transcription factor *RUNX2*. Under the control of the BMP-2,3,4,7, *RUNX2* expression increases and stimulates hypertrophy [10]. *RUNX2* can act in partnership with *SP7*, also known as *OSX*, to promote cartilage mineralization. *RUNX2* target genes are namely *MMP13*, for cartilaginous matrix degradation, *ALP* and *COL10A1* which promote matrix mineralization. Under *RUNX2*, hypertrophic chondrocytes initiate terminal apoptosis or transdifferentiate into osteoblasts, which leads to endochondral ossification (Fig. 2) [16,18–22] as it will be described later on.

### **I.3 Bone Biology**

Bone is a hard highly mineralized tissue composed of 60% inorganic component, 10% water, and 30% organic component. Bone presents three major cell types: osteoblast, osteocyte and osteoclast. Its ECM is mainly produced by osteoblasts which once they are embedded in their own matrix are called osteocytes. On the opposite, osteoclasts are specialized bone-resorbing cells. Both functions are meticulously coupled for a correct bone remodeling process, vital for bone homeostasis [2]. Bones are categorized and classified following their shape as long bones, short bones, flat bones, irregular bones and sesamoid bones. The femur, tibia and fibula are notably from the long bones category. Bones can be formed through

intramembranous ossification or endochondral ossification with a supportive anlagen template. The latter is the path taken during limb development. [23–25].

### **I.3.1 Osteogenesis**

#### **I.3.1.1 Intramembranous ossification**

It is by the intramembranous ossification that long bones grow radially and that most of the flat bones are generated (Fig 3A). During the intramembranous ossification, there is bone development not from cartilage template but directly from osteogenic MSCs condensation and their subsequent differentiation into osteoblasts and production of bone matrix. Firstly, osteoblasts disposed in a cluster called the ossification center produce and lay down an osteoid matrix. An osteoid matrix is a bone-specific organic matrix, rich in collagens, and not yet mineralized. The mineralization follows up within ossification centers, and embedded inside their matrix, osteoblasts become osteocytes [3,26].

In condensed MSCs, BMPs and FGFs are critical for osteoblast differentiation. BMPs induce the expression of *RUNX2* and *SP7*, two transcription factors needed for the regulation of proteins of the bone matrix. The collagen of type I, *COL1*, which is the most abundant collagen in bone is then secreted in the matrix [3,26–28] (Fig 3A). As the chondrogenesis/endochondral ossification and the intramembranous ossification share the same master regulator *RUNX2* and regulatory pathways, it is the level of *SOX9* and *RUNX2* that determine which path being adopted [29]. FGFs control the early steps of differentiation and proliferation but also the maturation of osteoblasts [3].

First avascular, the bone matrix is invaded by capillaries. The vascularization is under the control of the angiogenic factor VEGF [30] The intramembranous ossification is stimulated as

well in a paracrine manner through VEGF action. Following the vascularization, minerals are transported to the ECM and the mineralization begins (Fig 3A) [26]. Interestingly, mineral clusters from intramembranous and endochondral ossification show some structural differences but no change in their composition. In intramembranous ossification, mineral clusters issued from mice are ten times smaller than in endochondral ossification [31].

### **I.3.1.2 Endochondral ossification**

Endochondral bones are numerous in the human body and make up the axial and appendicular skeleton with namely the femur and tibia. For the endochondral ossification (Fig 3B), MSCs are recruited but need to condense and form an anlagen template as described by the process explained in the section “*I.2.2 Chondrocytes and chondrogenesis*”. The anlagen presents the approximate shape of the future bone and its cartilaginous template is replaced by bone during ossification. The chondrogenesis, via chondrocyte proliferation and matrix production, allows the growth of bones. In long bones, the endochondral ossification starts from the center of the anlagen template, the central ossification center in the diaphysis, and spreads bidirectionally outwards for the elongation. This process resumes the primary ossification [32,33]. Around the anlagen in the perichondrium, another condensation occurs and gives rise to osteoblasts forming the bone collar. The bone collar supports cortical bone development [33].

Hypertrophic chondrocytes also ensure cartilaginous matrix mineralization through the expression of *COL10A1* and *ALP*. They remodel the ECM through the production of MMPs together with the activity of specialized mature osteoclasts involved in cartilage degradation known as chondroclasts [22,34]. The vascularization of the matrix is regulated by VEGF, which engages the loss of hypoxic conditions that was favoring chondrogenesis, and recruits

## ***I. BACKGROUND***

osteoblasts. There are two types of blood vessels invading the cartilage, classified based on morphological, structural and functional criteria: the type H and type L. Osteoblasts are mainly found close to the type-H endothelium that preserves a pool of osteoprogenitor. Interestingly, the type-H endothelium plays an important role in cartilage resorption in endochondral ossification thanks to a distinct subtype of osteoclasts named vessel-associated osteoclasts [35,36]. Along with vascularization, marrow elements start to be integrated inside the bone in development. Hypertrophic chondrocytes at the end of the growth plate undergo apoptosis and die or transdifferentiate into osteoblasts. After apoptosis, empty lacunae are welcoming blood vessels and osteoblasts for bone production. Hypertrophic chondrocytes, from the anlagen and the growth plate, have also the ability to start the expression of *COL1A1* and *SP7* and transdifferentiate into osteoblasts (Fig 3B). Lineage tracing experiments were able to show that hypertrophic chondrocytes are a major source of osteoblasts as possibly 60% of them come from this origin in the femur in 3 and 4-week-old mice [37,38]. Yet, mechanisms behind the regulation of transdifferentiation are still poorly understood. Regulatory factors such as the  $\beta$ -catenin from the Wnt pathway, the tyrosine-protein phosphatase non-receptor type 11, and the *BMPR1a*, a receptor from the BMP pathway, are reviewed in [39].

During the primary ossification, the cartilaginous matrix is substituted by bones, and cartilage is located only in the extremities. There, chondrogenesis is preserved and assures bone elongation. Then, in the epiphysis, the secondary ossification takes place with neovascularization. A cartilaginous structure, the growth plate keeping ongoing chondrogenesis, remains between the metaphysis and the epiphysis [33] (Fig 3B).

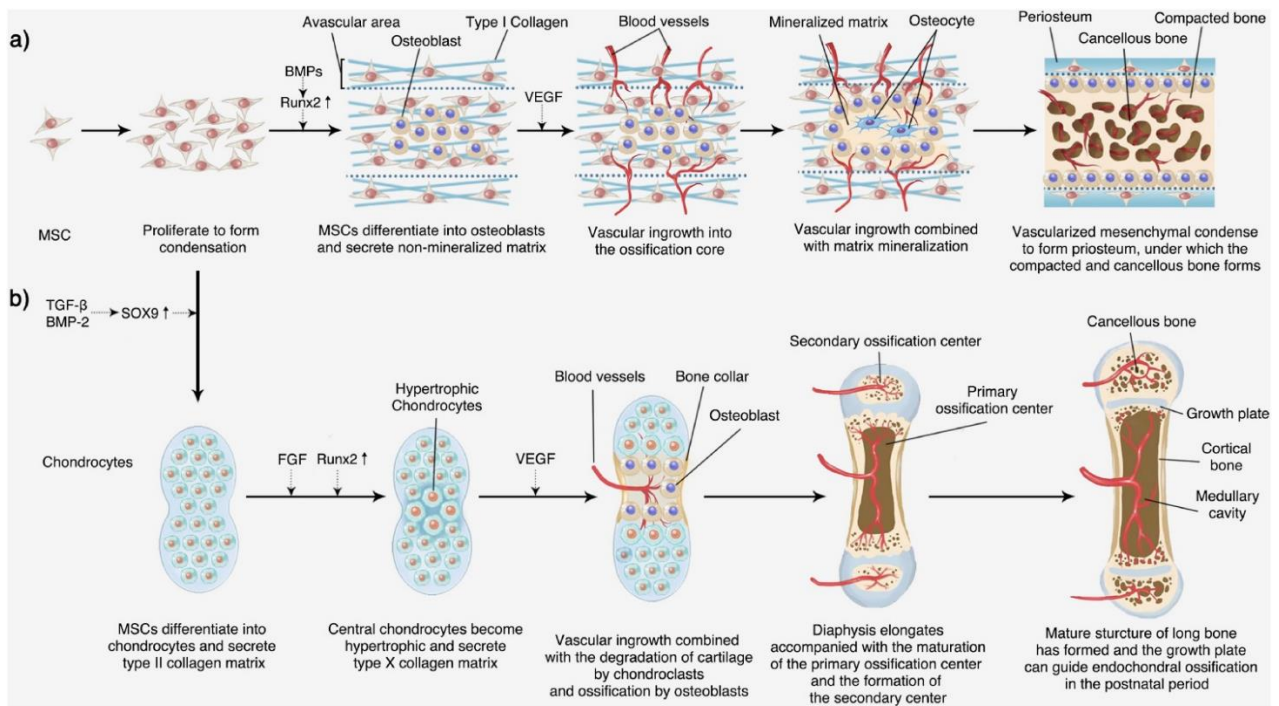


Figure 3: Schematic representation of the intramembranous and endochondral ossification. A) Intramembranous ossification. MSCs are recruited and proliferate and then condense in order to enter the following steps either in the intramembranous or endochondral ossification. In the former process, under the BMP pathway that activates the expression of RUNX2, MSCs eventually differentiate into osteoblasts in ossification centers, directly without any cartilage support needed. Osteoblasts secrete an avascular osteoid matrix, rich in collagen I. Later, under the regulation of VEGF, blood vessels invade the ECM and the mineralization starts. As the mineralization and osteoblasts surround blood vessels, it shapes the trabeculae. Once trapped into their own matrix, osteoblasts turn into osteocytes. The periosteum is the membrane derived from the condensed mesenchyme around the mineral matrix. Facing its inner side, osteoblasts secrete new layers of bone matrix forming together the cortical bone embracing the trabecular/cancellous bone. B) Endochondral ossification starts with MSCs condensation. Under the BMP pathway and SOX9, MSCs enter into chondrogenesis and become chondrocytes that generate a cartilaginous matrix rich in collagen II. Then, RUNX2-expressing chondrocytes become hypertrophic and eventually undergo apoptosis. The empty lacunae are invaded by blood vessels and osteoblasts. Hypertrophic chondrocytes can also take a second path and transdifferentiate into osteoblast. The cartilaginous matrix is remodeled and osteoblasts generate a bone matrix that is vascularized and mineralized. The primary ossification starts in the diaphysis and then elongates at the extremities. The secondary ossification occurs in the epiphysis again with the same mechanism of invasion of the cartilage with blood vessels and osteoblasts. Altogether, it achieves the mature structure of the long bone, with remaining chondrocytes located in the growth plate structure between the epiphysis and metaphysis. Figure adapted from [40].

**I.3.2 Bone anatomy**

**I.3.2.1 Structural organization of bones**

In this section, I will focus on the structure of a typical long bone (Fig 4). Bones can be classified according to their structural organization. In humans, there are two main types: woven bone and lamellar bone. Their structural characteristics and properties are summarized in table 2 with examples for each type.

*Table 2: Classification of bones and associated features, adapted from [25].*

<b>Structure</b>	<b>Structural characteristics</b>	<b>Subtype</b>	<b>Physical properties</b>	<b>Examples</b>
<b>Woven bone</b>	Random collagen fibers	Immature	Weaker More flexible	Embryonic skeleton Fracture callus
	Not stress oriented	Pathological	Weaker	Fibrous dysplasia
	No lamellae		More flexible	Paget’s disease
	Rapid turnover More cells			
<b>Lamellar bone</b>	Stress oriented Lamellae	Cortical – Lamella into osteons	Higher Young’s modulus More resistant to bending and torsion	Tibial shaft
	Predominately matrix	Cancellous – Lamella into parallel sheets	Lower Young’s modulus Less resistant to bending and torsion	Tibial metaphysis

Woven bones are found during development in the growing metaphysis, during fracture and in pathological bones. Features of woven bones are their lack of orientation for their collagen fibrils, irregular mineralization, and the presence of numerous cells. As collagen fibrils go in every direction, it results in a uniform distribution of mechanical loading and a more flexible structure as opposed to the more organized lamellar bone. The flexibility is enhanced by its rich cell composition and higher water content [25,41].



## I. BACKGROUND

Lamellar bones are more structured, with an apposition of lamella made of a mineralized collagen matrix of a thickness between 4 to 12  $\mu\text{m}$  (Fig 4). Osteoblasts from lamellar bones produce a thin layer of a matrix with homogenous mineralization and with collagen fibrils adopting the same orientation and arranged according to lines of stress. Because of this high structural level, mechanical properties differ along lamellar bones, it depends on the orientation of the applied force [25,41]. Regarding the orientation of each lamella, their collagen fibrils direction alternates in way of a plywood arrangement, as confirmed by 3D Raman mapping [42]. The lamellar bone which is the mature bone turns out to be the constituent of cortical and trabecular bones.

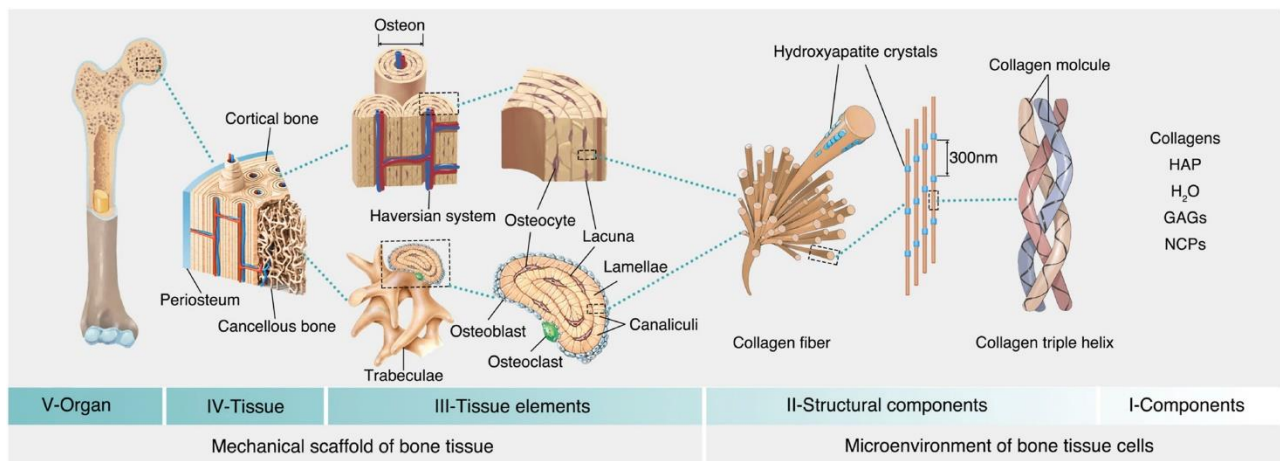


Figure 4: Structure of a long bone from the organ scale to the components. The bone is made of the diaphysis, metaphysis and epiphysis with the outer layer being the periosteum. Cortical bone is the dense compact outer bone and the cancellous bone is the highly porous bone arranged in a mesh structure. Both cortical and trabecular bone are made of lamellae but presents distinct structure. The cortical bone unit is the osteon, with the central Haversian canal connected by the perpendicular Volkmann's canal. Trabecular bone is made of trabeculae made of stacked lamellae. The main bone cells, osteoclasts, osteoblasts and osteocytes are found in both cortical and trabecular bone. Osteocytes are inside lacunae in between lamellae and connected through canaliculi. The bone matrix of lamellae is made of inorganic compounds, mainly hydroxyapatite crystals, and organic compounds, mainly collagen fibers. Collagen fibers display a high organizational level with the association of the collagen triple helix; other bone components such as water, crystals of hydroxyapatite (HAP) and non-collagenous proteins (NCP) with glycosaminoglycan (GAGs) [40].

### **I.3.2.2 Bone matrix components**

In the bone matrix, there are two main categories of constituents: the inorganic and organic parts. Inorganic elements constitute around 60% of the bone matrix leaving the residual 40% to the organic elements and water. It is interesting to pinpoint that ECM composition is dynamic and differs according to age, sex and health conditions [25,43]. We should think about it like our fingerprint, in a stiffer form.

#### **I.3.2.2.1 Inorganic**

When it comes to the inorganic elements of the bone matrix, the main compound is hydroxyapatite with the following chemical formula :  $(Ca_{10}(PO_4)_6OH_2)$ . It is rich in calcium and phosphorus and is responsible for biomineralization. The density and the size of hydroxyapatite crystals affect the degree of mineralization and consequently bone stiffness [25,44]. Among the properties that can be reported from the mineralization aspect of the bone, the Ca/P ratio is a marker of bone quality [45].

Regarding the biomineralization process, the ALP enzyme produced by osteoblasts uses the pyrophosphate (PPi), which is not bioavailable under this form, to cleave it in inorganic phosphate that can be incorporated in a collagen scaffold in combination with  $Ca^{2+}$  ions. PPi are even inhibitors of mineralization and by the increased Pi/PPi ratio, the process is pushed toward mineralization. Hydroxyapatite crystals are incorporated within and between collagen fibrils [25,44].

### **I.3.2.2.2 Organic**

The predominant constituent is the type I collagen making up around 90% of the organic composition. Non-collagenous proteins represent around 5% of the organic phase and lipids around 2% [46].

Type I collagen is the major representative of the collagen family, yet other collagens are involved in the composition of the bone matrix such as the type III, and IV collagens with their own functions. Type I collagen is namely distinguishable thanks to its large fibril diameter. Collagens are the template serving for bone mineralization but they also provide tensile strength and bind other macromolecules [25,47,48].

Non-collagenous proteins play critical roles in the bone as well, not only structurally but also in the regulation of the cell, matrix and mineral associations. Their scope of action is relatively wide as they regulate the fate of cells too. They safeguard bone metabolism and homeostasis and can be associated with musculoskeletal disorders [49] (Table 3). The functions of non-collagenous proteins are still not fully understood, yet current knowledge positions them, and *a fortiori* the matrisome, as key regulators of organs' physiology. One family, the Small Leucine-Rich Proteoglycan (SLRP), are of special interest to this manuscript because it includes osteomodulin (OMD). I have discussed the SLRP family in the skeletal tissues in the following review [50] that you can read in "Appendix 1" (From translation to protein degradation as mechanisms for regulating biological functions: a review on the SLRP family in skeletal tissues). Furthermore, their specific association with OA is described in the chapter "5.3.1 SLRPs in OA" where they will be presented in more detail.

Table 3: Non-collagenous proteins of the bone matrix and associated functions, adapted from [51].

<b>PROTEOGLYCANS AND GLYCOSAMINOGLYCANS</b>	
<b>Heparan sulfate</b>	Produced by osteoclasts and osteoblasts Plays important roles in cell-cell interactions
<b>Hyaluronan</b>	Non-sulfated glycosaminoglycan Hyaluronan in periosteum, endosteum, and around cells CD44 is the cell surface hyaluronan receptor and plays a role in the development
<b>Biglycan</b>	Found in pericellular location undergoing morphological delineation Upregulated in osteoblasts and may act as shear sensors when found in osteocytes Binds collagen and TGF- $\beta$
<b>Decorin</b>	Found in pericellular location undergoing morphological delineation Upregulated in osteoblasts and may act as shear sensors when found in osteocytes Binds collagen and TGF- $\beta$ Inhibits cell attachment to fibronectin
<b>Fibromodulin</b>	Binds collagen and TGF- $\beta$
<b>Versican</b>	Found in osteoid May capture space destined to be bone
<b>GLYCOPROTEINS</b>	
<b>Alkaline phosphatase</b>	Potential Ca <sup>2+</sup> carrier Hydrolyzes inhibitors of mineral deposition such as pyrophosphates Loss of functions leads to hypophosphatasia Bone formation marker Non-specific and bone-specific forms
<b>Fibronectin</b>	Produced during the early stages of bone formation Binds cells in an RGD-independent manner May be involved in the proliferation
<b>Thrombospondin</b>	Role in development Found in the early stages of bone formation Antiangiogenic
<b>Vitronectin</b>	Involved in cell attachment and spreading Shows specificity for osteopontin
<b>SIBLING FAMILY OF GLYCOPROTEINS</b>	
<b>Bone sialoprotein</b>	Limited pattern of expression Marks late stage of differentiation and early stage of mineralization
<b>Dentin matrix acidic phosphoprotein 1</b>	Expressed by osteocytes and osteoblasts Has affinity for hydroxyapatite and the N-terminus of type I collagen Regulates mineralization
<b>Matrix extracellular phosphoglycoprotein</b>	Expressed by osteocytes and osteoblasts Regulates mineralization Negative regulator of osteoblast activity
<b>Osteopontin</b>	Secreted in early stages of osteogenesis Promotes adhesion Inhibits mineral formation and crystal growth
<b>OTHER IMPORTANT NON-COLLAGENOUS PROTEINS</b>	
<b>Osteocalcin</b>	Expressed by osteocytes and osteoblasts Enhances calcium binding, controls mineral deposition Bone remodeling marker Overexpressed in cancer and some autoimmune diseases
<b>Osteonectin</b>	Binds to collagen Hyaluronic acid, and vitronectin Located at site of mineral deposition (possible nucleator) May play a role in osteoblast proliferation

### **I.3.3 Bone remodeling**

The bone remodeling process is the mechanism orchestrating the balance between bone formation and bone resorption in order to replace old bone with new bone. Osteoblasts are cells in charge of the bone matrix deposition while osteoclasts are specialized cells resorbing the bone [52].

#### **I.3.3.1 Osteoclast and osteoclastogenesis**

Osteoclasts are giant multinucleated cells issued from the myeloid line. Precursor cells start expressing macrophage colony-stimulating factor (*M-CSF*) and turn into osteoclast precursors, which present the receptor activator of NF- $\kappa$ B (RANK) on their surface. RANK is the receptor of the receptor activator of NF- $\kappa$ B ligand (RANKL), considered the master regulator of osteoclastogenesis [53,54]. RANKL induces the activation of NF- $\kappa$ B and mitogen-activated protein kinase (MAPK) pathways. Following their maturation, committed mononuclear osteoclasts express the nuclear factor of activated T cells, cytoplasmic 1 (*NFAT*) that induces the expression of tartrate-resistant acid phosphatase (*TRAP*) and cathepsin-K (*CTSK*), two other osteoclast marker genes. Ultimately, osteoclasts fuse together and generate the typical giant multinucleated cells [53–56] (Fig 5A). Multinucleated osteoclasts actively resorbing bone matrix display a cellular polarization. Starting from the apical domain, there are the functional secretory domain, then the basolateral domain followed by the sealing zone, where osteoclasts are attached to the matrix, and the ruffle border [57] (Fig 5B).

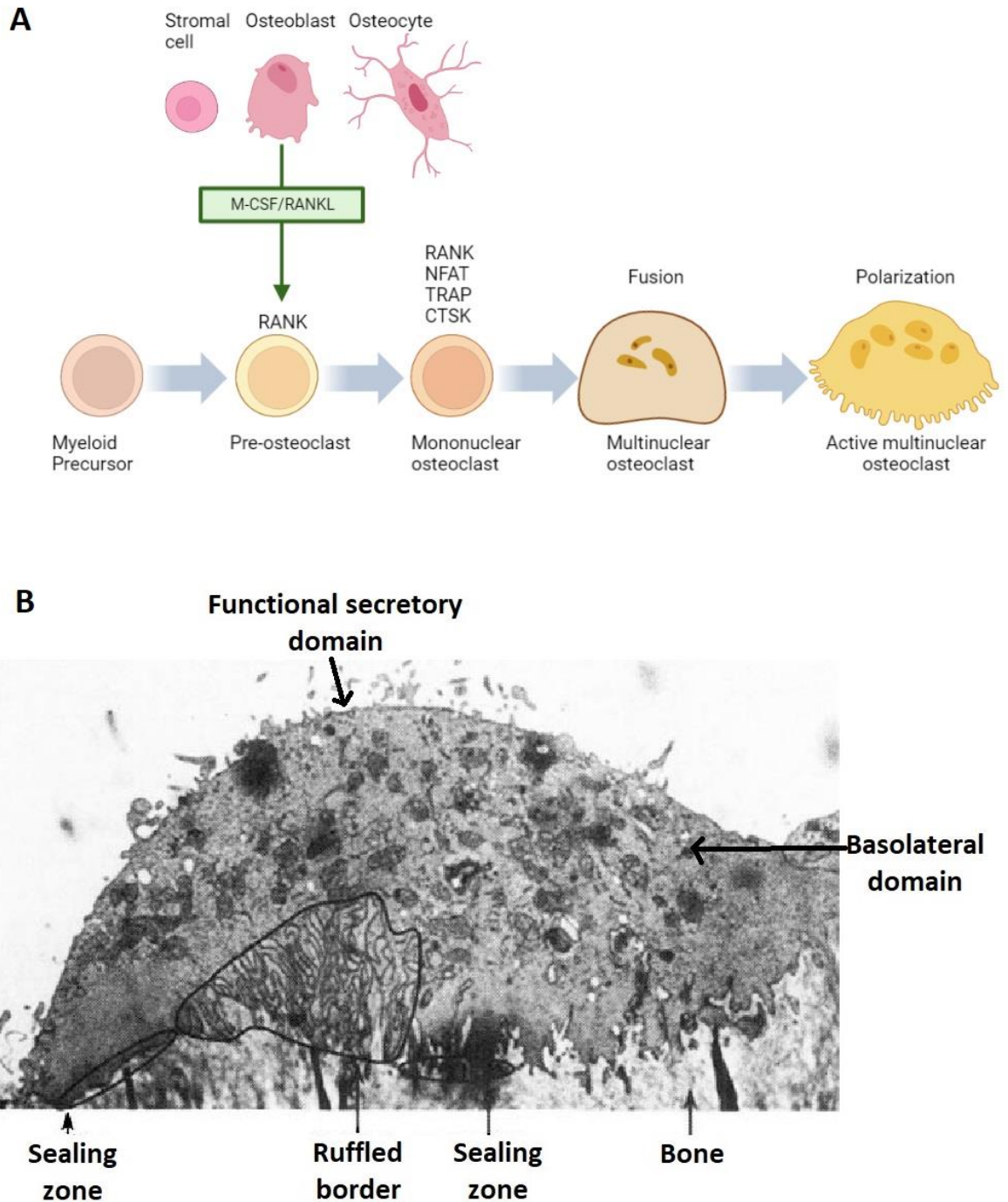


Figure 5: (A) Illustration of the different steps of osteoclastogenesis. Myeloid precursor turns into pre-osteoclast under the action of M-CSF and starts to increase their RANK expression. Under the action of RANKL, produced by stromal cells, osteoblasts and osteocytes as a soluble form or bound to the membrane, they are committed into osteoclasts. Mononuclear osteoclasts express a specific gene signature, namely TRAP and CTSK thanks to the NFAT pathway. They eventually fuse as functional osteoclasts and are polarized when active. Figure adapted from [46,53] and designed by Jérémie Zappia with Biorender. (B) The polarized osteoclast has distinct domains, the functional secretory domain for secretion of product waste, the basolateral domain, the zone of contact with bone named the sealing zone and the ruffled border, defining the resorption lacuna [58].

Multinucleated osteoclasts can also undergo into a fission and give smaller and more motile daughter cells called osteomorphs. Osteomorphs keep their ability to fuse back into osteoclasts. While osteoclasts are mainly found on the bone surface, osteomorphs are located in the bone marrow and blood and they express a distinct transcriptome. This suggests specific functions associated with osteomorphs that need further extensive research to deepen our knowledge of bone homeostasis and associated pathologies [59].

To keep the bone remodeling balanced, there are negative feedback mechanisms affecting osteoclastogenesis, namely through the RANKL/RANK association and osteoprotegerin (OPG) competing with RANK to bind to RANKL. The RANKL/OPG interaction prevents the activation of downstream pathways involved in osteoclast formation [54].

### **I.3.3.2 Bone resorption and turnover**

Bone is highly dynamic and bone remodeling is continuously occurring throughout our entire life. It is a major mechanism for establishing correct bone architecture, preserving the homeostasis of calcium and phosphorous metabolism, repairing bone microdamage and eventually avoiding bone fractures [60,61]. Besides, the apoptosis of osteocytes induces RANKL production by the neighboring cells and triggers bone remodeling [62,63]. Each year, the bone turnover enables the renewal of approximately 5% of the cortical bone and 20% of the trabecular bone.

To proceed to the resorption of bone, osteoclasts adhere to the bone surface through the sealing zone which delimits an actin ring, marker of active osteoclasts, and a region underneath defining the resorption lacuna also called Howship's lacuna. At the ruffled border, which extensively increases the contact surface, massive vesicle trafficking occurs for bone resorption. Osteoclasts dissolve the mineral composition of the bone matrix by the

acidification of the lacuna. They also secrete proteinases such as TRAP, CTSK and MMPs for the degradation of organic components. TRAP dephosphorylates bone matrix proteins [64] and generates reactive oxygen species [65], and CTSK degrades ECM [66]. Degradation products are following endocytosis on the ruffle border and are transported to the secretory domain for their secretion. Once their function is fulfilled and resorption is complete, osteoclasts can undergo apoptosis [60].

After the degradation of bone, there is a renewal with new bone formation. Bone matrix being resorbed, cytokines are released and lead to the recruitment and differentiation of osteoblasts. Osteoblasts specifically attach to resorption pits that are covered with binding proteins for leading bone formation on targeted sites [61].

### **I.4 Joint tissues biology**

There are three categories of joints classified according to their composition and their motility. Fibrous or synarthroses, which are not motile, cartilaginous or amphiarthroses, that allow few movements, and synovial or diarthroses, that allow movements [67].

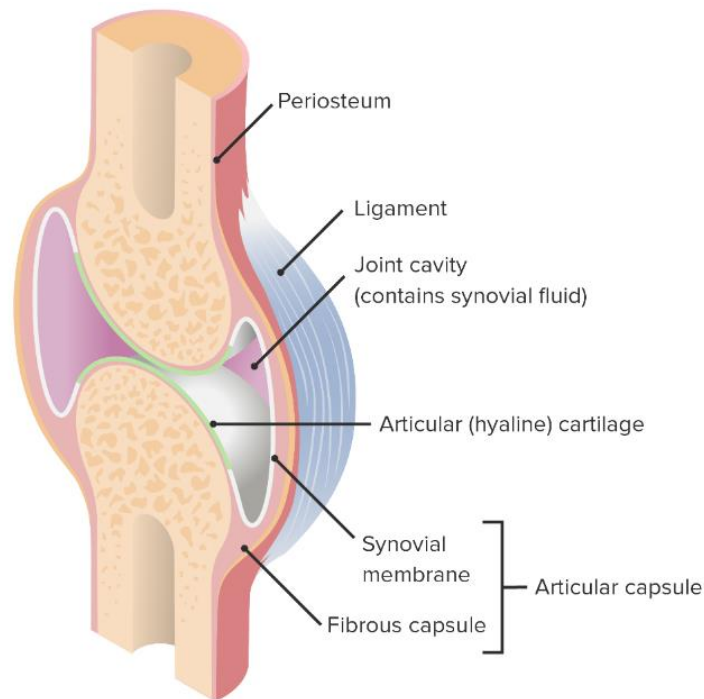
In this manuscript, I will only cover the synovial joint which is the category represented by the knee joint.

#### **I.4.1 Synovial joint anatomy**

The synovial joint (Fig 6) is characterized by a cavity surrounded by a fibrous articular capsule. The synovial membrane is located on the inner surface of the capsule and with the articular cartilage, they define the joint cavity. The cavity is filled with synovial fluid secreted by the synovial membrane for serving lubrication to the joint. Between articular cartilage, the meniscus is inserted, and with the intra-articular and lateral ligaments, they stabilized the



joint. Altogether, the different articular tissues allow specific mechanical properties for smooth movements between the bones whilst reducing friction [67].



*Figure 6: Illustration of the anatomy of the synovial joint. The end of two bones is covered by articular cartilage and is articulated thanks to an articular capsule. Inside the capsule, the synovial membrane is specialized in the secretion of synovial fluid to fill the cavity. <https://cdn.lecturio.com/assets/Articular-capsule-and-components.png>*

### **I.4.1.1 Articular cartilage**

The articular cartilage is made of hyaline cartilage, but contrary to other hyaline cartilage, it has no perichondrium. With the absence of the perichondrium, articular chondrocytes assume their nutrition by diffusion of the synovial fluid for the upper region and by diffusion of blood elements coming from the subchondral bone for the deeper layer [68,69].

It is a white, smooth and soft structure of typically around 2 to 4 mm of thickness. The functions of the articular cartilage are to transfer and absorb mechanical loading and shock, and to assure the correct distribution of mechanical stress exerted on the joint. It displays a

## ***I. BACKGROUND***

protective function for the stiffer load-bearing bone underneath. Together with the synovial fluid, it assures free movements of the joint with low friction [70,71].

The architecture of the articular cartilage presents four different zones: the superficial zone, the transitional or middle zone, the deep zone and the calcified zone. Each zone presents distinct biochemical and anatomical features (Fig7). The superficial zone represents around 10-20% of the thickness of the articular cartilage. It has the highest content of water and collagen with collagen fibers oriented parallel to the surface and tightly packed. The chondrocytes appear flat and thin. In this zone, cellular density is high. The superficial zone has fewer proteoglycans than other zones [70,72]. The superficial zone produces lubricin, under the expression of the *PRG4* gene, in order to lubricate the joint [73,74]. The superficial zone protects the zones underneath from shearing stress and is in direct contact with the synovial fluid. It is itself covered and protected by the lamina splendens, which is a thin acellular fibrous membrane. If this zone is damaged, the whole joint integrity is at risk and there is a high probability to develop osteoarthritis (OA) [71,72].

The transitional or middle zone represents 40-60% of the articular cartilage. In this zone, chondrocytes are bigger and spherical, collagens fibers are thicker and oriented obliquely in a network. The amount of proteoglycan is increasing in comparison to the superficial zone. The middle zone gives the structure to absorb compressive force [70,71].

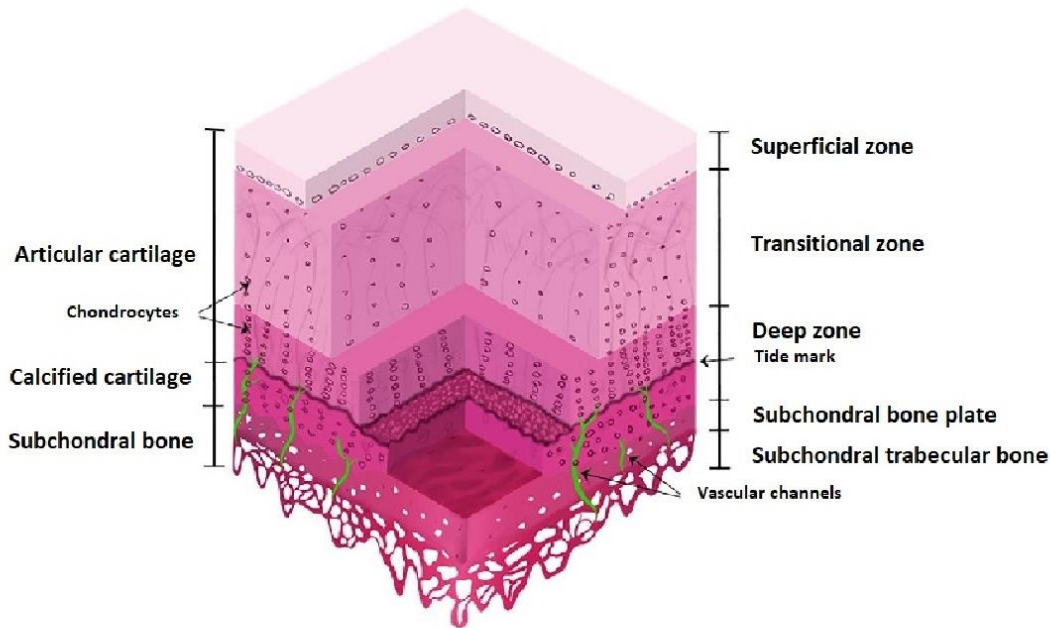
The deep zone represents around 30% of the articular cartilage and is the richest in proteoglycans but its water concentration is low. Its collagen fibers are the thickest and are oriented perpendicular to the articular surface; then the global structure of collagens is creating an arcade. Thanks to this structural arrangement and its composition, the deep zone

## ***I. BACKGROUND***

is the greatest to absorb compressive forces. Alongside the collagen fibers, chondrocytes are arranged in columns [70,71].

The calcified zone, in contact with the subchondral bone, represents 5-10% of the articular cartilage. It is delimited by the tidemark, which separates this zone from the deep zone. The tidemark is a basophil demarcation stopping the invasion of capillaries coming from the subchondral bone. There are fewer chondrocytes and they can shift to the hypertrophic phenotype. The calcified zone anchors the collagen fibers from the deep zone into the subchondral bone [69].

**A**



**B**

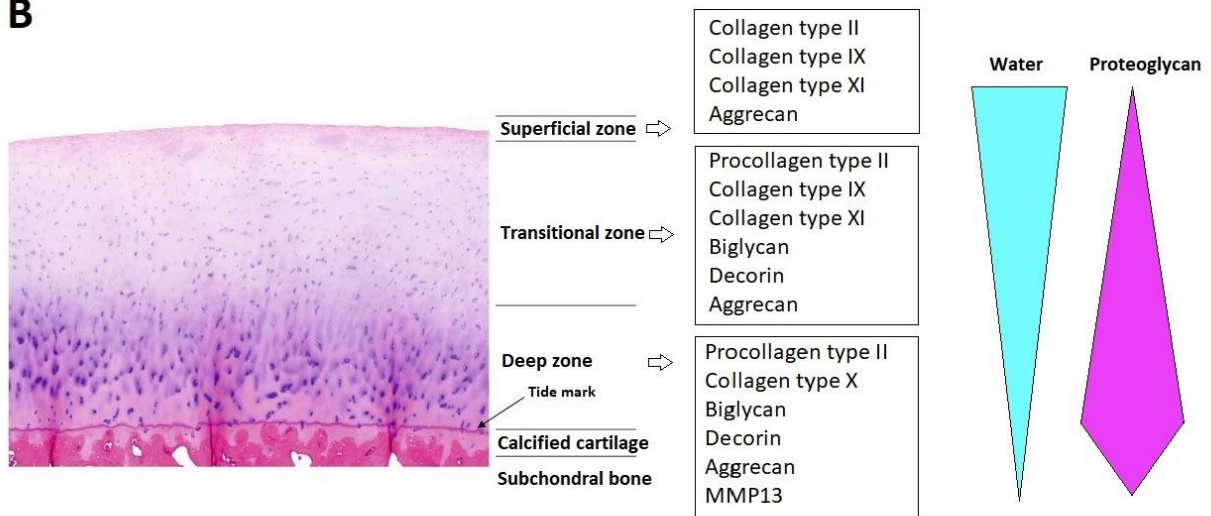


Figure 7: (A) Illustration of the architecture of the articular cartilage with the four domains: superficial zone, transitional or middle zone, deep zone and calcified cartilage. The tide mark is represented as a darker delimitation between the deep zone and the calcified cartilage, where the vascularization coming from the subchondral bone underneath stops. (B) Histological representation of the articular cartilage with the four above-mentioned domains. Each domain has different composition for its ECM. The water and proteoglycan contents are different across each domain with decreasing water content from the superficial zone to the lower domains and inversely for the proteoglycan content except for the calcified cartilage where the presence of proteoglycan is reducing again [69,75].

### **I.4.1.1.1 Articular chondrocyte**

Chondrocytes are the main cell type present in the articular cartilage but constitute only 2% of the total articular cartilage. They are highly specialized and more often quiescent. There is typically a single chondrocyte by lacuna but it happens that one lacuna hosts two of them. They are trapped in their own matrix and they generate and modulate their microenvironment. They regulate the turnover of the matrix. Even if isolated, intercellular communications remain between chondrocytes thanks to voltage-gated gap junctions which exchange glucose and essential amino-acids, establishing a functional network for their correct metabolism [76].

Chondrocytes show the ability to modulate their gene expression according to mechanical stimuli. By this mechanism, they are adapting accordingly to their environment. For instance, under dynamic compression, they upregulate the aggrecan and type II collagen expressions while under static compression they downregulate them [77]. Among other stimuli acting on chondrocytes, one can mention growth factors, piezoelectric forces, and hydrostatic pressures [70].

Even though being the only representing cell type of the cartilage, a recent single-cell analysis highlighted the heterogeneity among chondrocytes. It is firstly observed by their different anatomy across the zones of the articular cartilage, flatter, wider, in hypertrophy. Chondrocytes display distinct transcriptomes as well and nine clusters, or subtypes, of chondrocytes, were identified. The characterization was made from healthy knee cartilage of 10-week-old mice, out of 1625 cells expressing high levels of *Sox9*, *Col2a1*, and *Aggrecan*. As expected, clusters can adequately discern chondrocytes based on their morphology and localization, but also on ECM gene expression, such as various collagen types, collagen

processing enzymes, proteoglycans and namely the lubricin and the SLRP family with *Omd*. Subtypes of chondrocytes can be related to different biological functions as indicated by their specific enrichment for ontology terms [78]. Murine subtypes of chondrocytes are substantially similar to human subtypes characterized by single-cell analysis. However, every murine feature does not perfectly translate to human and some distinctions remain. As the single-cell from human samples was performed from cartilage issued from OA patients undergoing knee arthroplasty surgery, dissimilarities are either due to the pathology and/or are species-specific [78,79]. More studies on the functional characteristics of those subtypes of chondrocytes are needed for a better understanding of the articular cartilage's physiology and how they could be related to the onset of joint pathologies.

### **I.4.1.1.2 Matrix organization and composition**

The articular cartilage matrix is mainly composed of water which represents 60-80% of the matrix. Out of the 20-40% of macromolecules (wet weight), collagens make up 50-60% and proteoglycans 30% of the dry weight [69].

The localization of water is either intra-fibrillar or extra-fibrillar, water is not 'trapped' by proteins but is rather freely exchangeable [80]. Water also interacts with proteoglycans as it is drawn to the matrix by their negative charges attracting water dipole. The high percentage of water is a functional adaptability, it protects chondrocytes and the subchondral bone from compressive forces and it allows the diffusion of nutrients and the elimination of biological waste [70].

Regarding collagens, many types are found in cartilage but the type II is the major collagen and is characteristic of the cartilage matrix. Type II collagen constitutes 90-95% of collagens found in cartilage, and generates a fibrillar network associated with proteoglycan, necessary

## I. BACKGROUND

to endure shear and tensile forces. Other collagens are labeled as minor type collagens. Even if they are scarcely distributed in the ECM, they endorse the function to bring stability and elasticity by generating crosslinks with the type II collagen. Table 4 summarizes the different collagens found in articular cartilage.

*Table 4: Types of collagen represented in articular cartilage with the composition of structural collagen chains, expressing genes, classification based on supramolecular assembly, percentage found in articular cartilage, and distribution in articular cartilage; adapted from [81].*

Collagen	Chains	Genes	Classification	%*	Distribution in articular cartilage
<b>Type I</b>	$[\alpha 1(I)]_2\alpha 2(I)$	COL1A1 COL1A2	Fibril forming	0	Fibrocartilage
<b>Type II</b>	$[\alpha 1(II)]_3$	COL2A1	Fibril forming	90-95	ECM of all zones
<b>Type III</b>	$[\alpha 1(III)]_3$	COL3A1	Fibril forming	Na	Na
<b>Type IV</b>	$[\alpha 1(IV)]_2\alpha 2(IV)$ $\alpha 3(IV)\alpha 4(IV)\alpha 5(IV)$ $[\alpha 5(IV)]_2\alpha 6(IV)$	COL4A1 COL4A2 COL4A3 COL4A4 COL4A5 COL4A6	Network forming	Na	PCM
<b>Type V</b>	$[\alpha 1(V)]_2\alpha 2(V)$	COL5A1 COL5A2	Fibril forming	Na	PCM
<b>Type VI</b>	$\alpha 1(VI)\alpha 2(VI)\alpha 3(VI)$ $\alpha 1(VI)\alpha 2(VI)\alpha 4(VI)$ $\alpha 1(VI)\alpha 2(VI)\alpha 5(VI)$ $\alpha 1(VI)\alpha 2(VI)\alpha 6(VI)$	COL6A1 COL6A2 COL6A3 COL6A4 COL6A5 COL6A6	Beaded filament	1-2	PCM
<b>Type IX</b>	$\alpha 1(IX)\alpha 2(IX)\alpha 3(IX)$	COL9A1 COL9A2 COL9A3	FACIT: Fibril-associated collagens with interrupted triple helices	1-5	ECM of all zones and growth plate in adults
<b>Type X</b>	$[\alpha 1(X)]_3$	COL10A1	Network forming	1	Calcified zone and hypertrophic cartilage
<b>Type XI</b>	$\alpha 1(XI)\alpha 2(XI)\alpha 3(XI)$	COL11A1 COL11A2 COL11A3	Fibril forming	1-5	ECM of all zones and PCM

\*: Percentage of collagen in healthy articular cartilage; Na: no studies have been found to support it

Proteoglycans are complex macromolecules made of a core protein that is covalently decorated by glycosaminoglycan (GAG). GAGs are long unbranched polysaccharides made of repeated disaccharide units made of an amino sugar (N-acetylgalactosamine or N-acetylglucosamine) and a uronic acid (glucuronic acid or iduronic acid). GAGs are negatively charged and consequently attract water dipole or ions, highly useful for the physicochemical

## ***I. BACKGROUND***

properties of the cartilage and its integrity [82,83]. There are four types of GAGs: hyaluronan, chondroitin sulfate and dermatan sulfate, heparan sulfate, and keratan sulfate. Chondroitin sulfate makes up 65-90% of GAGs of the cartilage. In articular cartilage, there are two main types of proteoglycan: aggrecan and small proteoglycans. Aggrecans were named according to their ability to aggregate. They are made of three globular domains, G1, G2 and G3 and present domains rich in chondroitin sulfate (CS1 and CS2), containing around 100 chondroitin sulfate chains, and keratan sulfate domain, containing around 30 of them. Multiple aggrecan molecules bind to hyaluronic acid, thanks to a glycoprotein “link protein”, resulting in an aggregate necessary for supporting the cartilage’s integrity (Fig 8 A, 8B). Aggrecan bound to the hyaluronic acid attracts water in the environment and they expand within the ECM. Collagen fibers, providing a network, maintain this expansion and stretch to balance the forces generated by the swelling. This conformation is also advantageous upon compression as water dispersion induces convergence of aggrecan and it increases their swelling potential. Then, it limits water diffusion and when the compression is dissipated, water is moving back until the balance of the relaxed state is achieved [84](Fig 8C).

Besides aggrecans, there are the SLRPs such as biglycan, decorin, and fibromodulin, which bind directly to collagens playing a role in fibrillogenesis and organizing the ECM. Proteoglycans have the ability to bind to cytokines and growth factors to regulate their bioavailability and constitute a reservoir. This function is dependent on the numerous post-translational modifications they could undergo [50]. Several other non-collagenous and non-proteoglycan proteins make up the composition of articular cartilage and fine-tune its structural organization, physiology, and communication with other tissues [85].



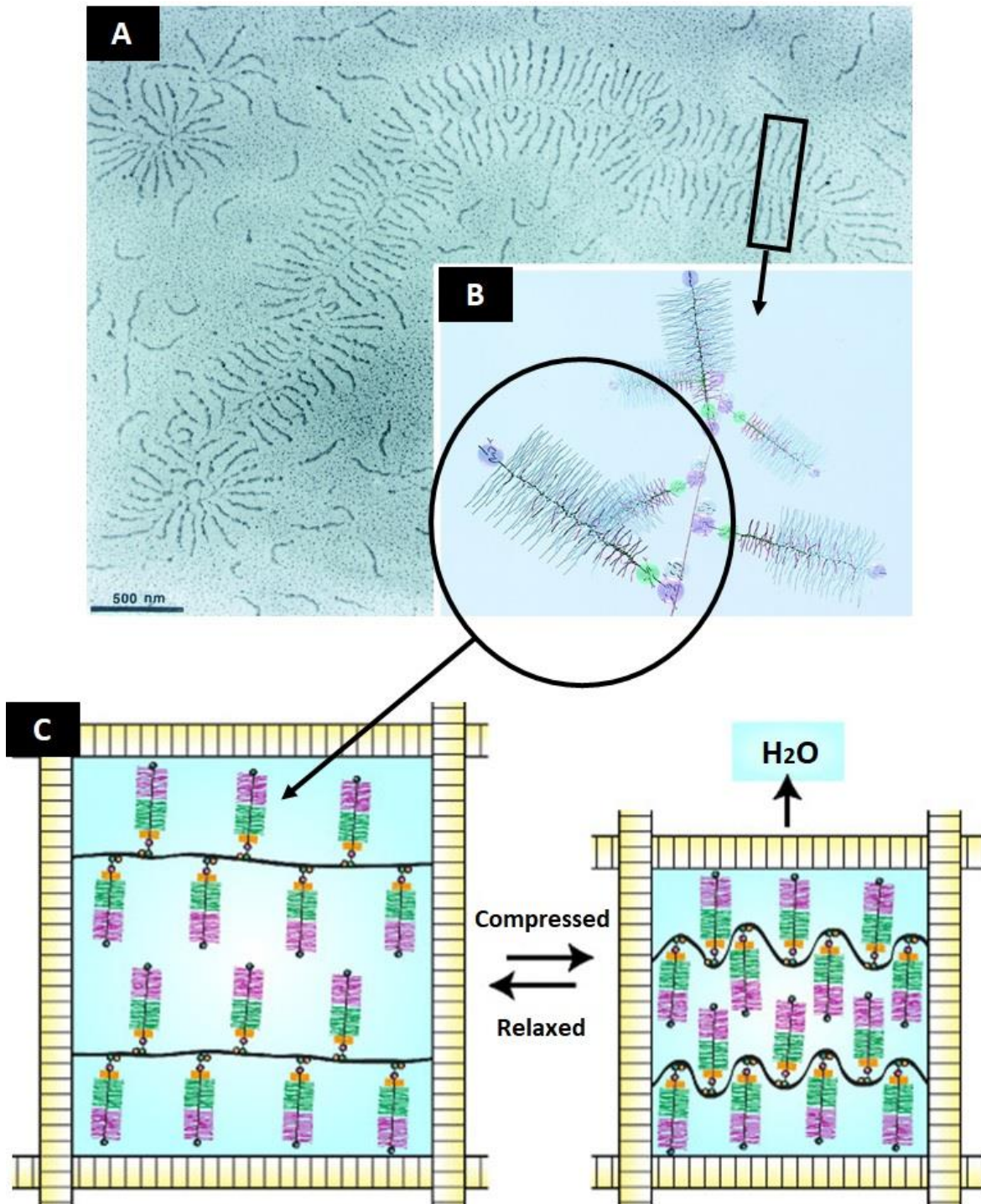
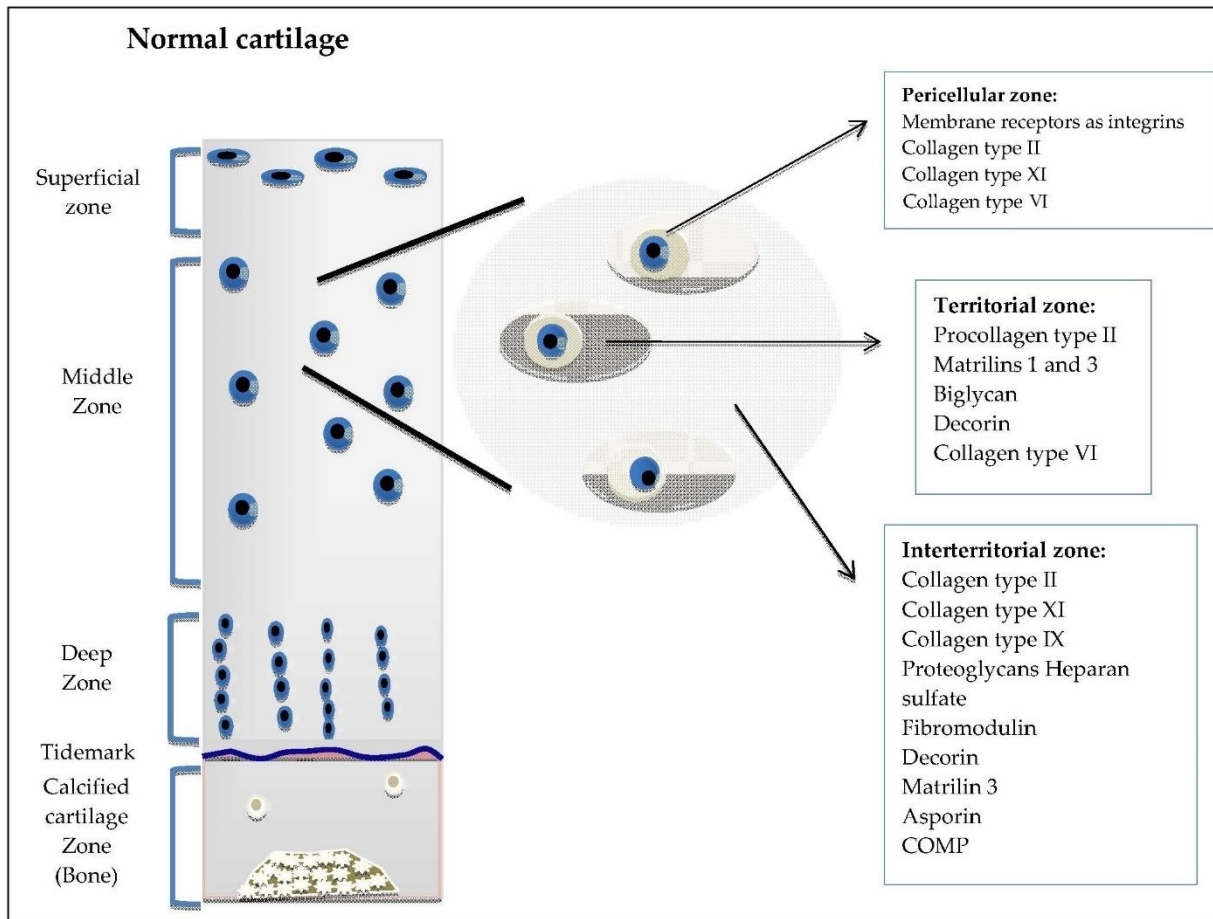


Figure 8: (A) Electron micrograph of an aggregate of proteoglycan. Hyaluronic acid makes up the axis where aggrecans are bound to. (B) Zoom on a specific region for its modelization showing the globular domains and link protein. (C) Network of collagen type II and aggrecans bound to hyaluronic acid. During the relaxed state, aggrecans are expanded and water is drawn inside the ECM, while the collagen is stretched to keep the equilibrium. Upon compression, water is moving out, aggrecans are getting closer and the swelling potential is increased until the compression force is removed [84,86].

## ***I. BACKGROUND***

To go even deeper into the articular cartilage, there is a structural hierarchy within the ECM, with the pericellular matrix, the territorial, and the interterritorial regions (Fig 9). This classification is based on the proximity with chondrocytes, and each region has its own composition and organization. The pericellular matrix is the closest to chondrocytes and surrounds them. It is a matrix rich in proteoglycans and glycoproteins. Its major collagen is the type VI collagen, which is only present in the pericellular matrix in adults. Biomechanical and biochemical signals are transmitted to chondrocytes through the pericellular matrix [87,88]. The territorial matrix, further from chondrocytes, surrounds the pericellular matrix. It is a region where collagen fibers form a basket-like structure around the cell. This may serve as a protective region for chondrocytes. The interterritorial matrix makes up most of the articular cartilage matrix. It is a region rich in aggrecan and has large collagen fibers arranged either parallel, obliquely or perpendicular to the joint surface, accordingly to their localization on the four domains of the articular cartilage. Consequently, it is a key region for the articular biophysical properties [70,89].



*Figure 9: Representation of the regions of the articular cartilage: superficial zone, middle zone, deep zone and calcified cartilage separated with the tidemark. Chondrocytes are represented with the different subcategories of ECM: pericellular zone, territorial zone and interterritorial zone. The representative composition of these ECMs is listed [90].*

#### **I.4.1.1.3 Calcified cartilage**

The calcified cartilage is the deepest zone of the articular cartilage. The particularity of this zone is the presence of hypertrophic chondrocytes secreting ALP, type X collagen, type I collagen. It is responsible for ECM mineralization with an increasing percentage of minerals with aging but always lower than bone [69,91,92]. There is a large discontinuity of stiffness between the hyaline cartilage and the subchondral bone, the calcified cartilage mediates a transition and helps to reduce shear stress of the osteochondral unit playing the role of a soft-to-hard bridge [68]. The presence of nanochannels between calcified cartilage and

subchondral bone is an additional indicator of the importance of calcified cartilage for the crosstalk and for the solute and signal exchange between both tissues. The nanochannels are a parallel to the bone canaliculi but smaller [93,94]. The calcified cartilage is continuously remodeled and its mineralization and thickness change with aging [95].

### **I.4.1.2 Subchondral bone**

The subchondral bone is referred here as the bone laying down the calcified cartilage and separated from it with the cement line, comprising the subchondral bone plate made of cortical bone and the subchondral trabecular bone [96]. The articular cartilage intertwines with the subchondral bone in complex ways, defining comb-like insertion. The subchondral bone supports the articular cartilage for mechanical loading and is a nutrient source as it is richly vascularized [96]. Hence, numerous genes involved in subchondral bone homeostasis are mechanosensitive [97].

The subchondral bone displays a specific microarchitecture revealing that trabeculae adopt more often the rod geometry than the plate geometry (Fig 10). The direction of rod trabeculae is predominantly transversal while there are two main orientations for plate trabeculae being either transversal or longitudinal. This microarchitecture allows the subchondral bone to have a uniform elastic modulus along spatial planes. It suggests that the subchondral bone is optimized to physically support the articular cartilage [98].

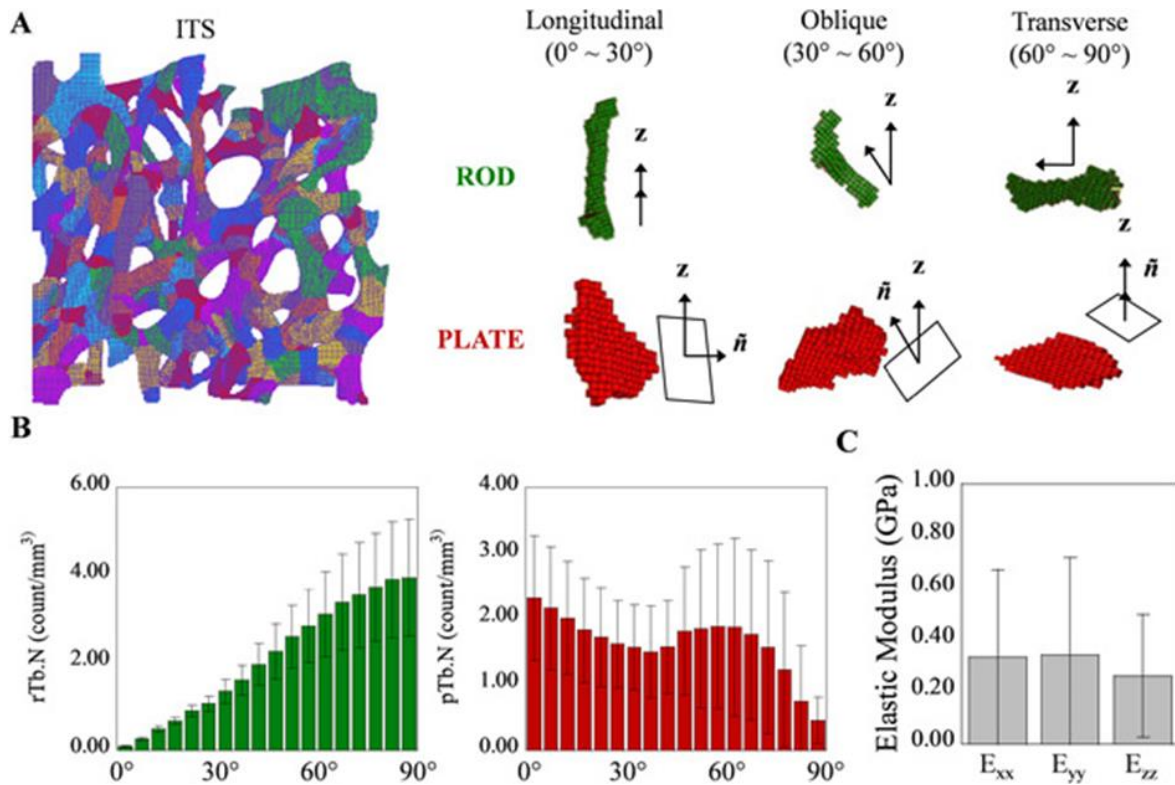


Figure 10: (A) Schematic representation of the microarchitectural characteristic of subchondral bone trabeculae located beneath the subchondral bone plate. The analysis was performed following the individual trabecular segmentation (ITS) from computed tomography. There are two trabecular geometry, either rod or plate adopting three possible orientations, longitudinal, oblique or transversal. (B) Trabeculae were isolated and the number of rod trabeculae is represented by the green bar plot and the number of plate trabeculae by the red bar plot. The measured elastic modulus in the three spatial orientations is represented by the grey bar plot. Data from bar plots are presented as mean standard deviation (SD) [98].

### I.4.1.3 Synovium

The synovium is a vascularized conjunctive tissue covering the inner joint cavity, except for the cartilage. It can be arranged in villousities. About its structure, the synovium is subdivided into the superficial lining layer called the intima, facing the joint space, and the sublining layer called the subintima. Blood vessels, lymphatics, nerves and fat tissues are contained in the subintima. Synoviocytes are located in the intima where they undertake key functions of the synovium. There are type A synoviocytes or macrophage-like and type B synoviocytes or fibroblast-like. Type A is in charge of endocytosis of biological debris and protection of the

joint cavity keeping it aseptic. Type B secretes the synovial fluid, bringing nutrients to chondrocytes and lowering the coefficient of friction due to its thickness for joint lubrication [99,100].

### **I.5 Osteoarthritis**

Worldwide, 527.8 million of people are suffering of OA according to a study from 2019. Globally, it corresponds to an increase of 113.25% from 1990 [101]. It is a degenerative disease of high prevalence and a major source of handicap. Then, it is a public health challenge and it is of rising interest as the global life expectancy is increasing in our aging populations.

According to the OARSI ([www.oarsi.org](http://www.oarsi.org)), OA is defined as followed: “Osteoarthritis is a disorder involving movable joints characterized by cell stress and extracellular matrix degradation initiated by micro- and macro-injury that activates maladaptive repair responses including pro-inflammatory pathways of innate immunity. The disease manifests first as a molecular derangement (abnormal joint tissue metabolism) followed by anatomic, and/or physiologic derangements (characterized by cartilage degradation, bone remodeling, osteophyte formation, joint inflammation, and loss of normal joint function), that can culminate in illness.”

OA is a disorder that involved pathologic changes in all the joint tissues including subchondral bone, cartilage, meniscus, synovium, and muscles. The main risk factor associated with OA is age, yet other factors such as sex, prior joint injury, obesity, genetic predisposition, and mechanical factors may be involved [102]. OA is a heterogenous disease and it originates from factorial causes with different subtypes of patients associated to distinct phenotypes. Ultimately, tissular damages provoke joint pain, anatomical changes, swelling and impaired mobility [103,104]. It is also categorized as primary OA, or spontaneous, when there is no

apparent cause or as secondary OA in the case of an identified apparent cause such as trauma, obesity, inflammation, genetic factors, or systemic diseases [83,105].

The multifactorial nature of OA contributes to various symptoms and makes it a challenging disease for researchers lacking understanding of the big picture.

### **I.5.1 Heterogeneity of OA, a complex disorder**

The different phenotypes within OA can be explained by the heterogeneity of the physiopathological mechanisms involved in the onset and progression of the disease and of the comorbidities associated with OA. A better understanding of those phenotypes and, *a fortiori*, of the correlated underlying mechanisms would undoubtedly lead to more adequate intervention for the patient, and personalized medicine with optimized treatments. Let us not forget that OA was previously described as a homogenous non-inflammatory disease affecting the integrity of the cartilage. Since then, our representation of OA changed dramatically. We are far from stopping our progress in the understanding of OA, or as I should refer after this allocution, our understanding of “OA<sub>s</sub>”.

A systematic review from [106], investigated on the OA phenotypes and reported their classification (Fig 11). Six different phenotypes were reported: aging-driven, cartilage-driven, metabolic syndrome-driven, subchondral bone-driven, inflammatory/immune/synovitis-driven, and mechanical injury-driven. For the inflammatory phenotype, patients overexpress inflammatory cytokines such as IL-1 $\beta$ , IL-6, and IL-8 among others. They show specific biomarkers in their serum and have a higher sensitivity to pain at the baseline. Specific biomarker signature is also found in patients associated with a higher prevalence of metabolic factors such as obesity, diabetes, or hypertension; defining a metabolic phenotype profile. Alterations of bone and cartilage metabolism also occur in subgroups of patients with well-

## I. BACKGROUND

defined biomarkers for both tissues. Concerning the mechanical injury-driven phenotype, it appears that abnormal mechanical loading seems to be responsible for 12-22% of knee OA and is one of the main mechanisms [103]. However, identifying and studying OA phenotypes turns out to be challenging as they are connected and constitute more of a spectrum than clearly defined categories [106,107]. Another work corroborated the heterogeneity of OA and proposed to consider patient's and disease's characteristics such as pain sensitization, psychological distress, radiographic severity, BMI, muscle strength, inflammation, comorbidities, gender, and pattern of cartilage damage to help in the phenotyping OA difficulty [108].

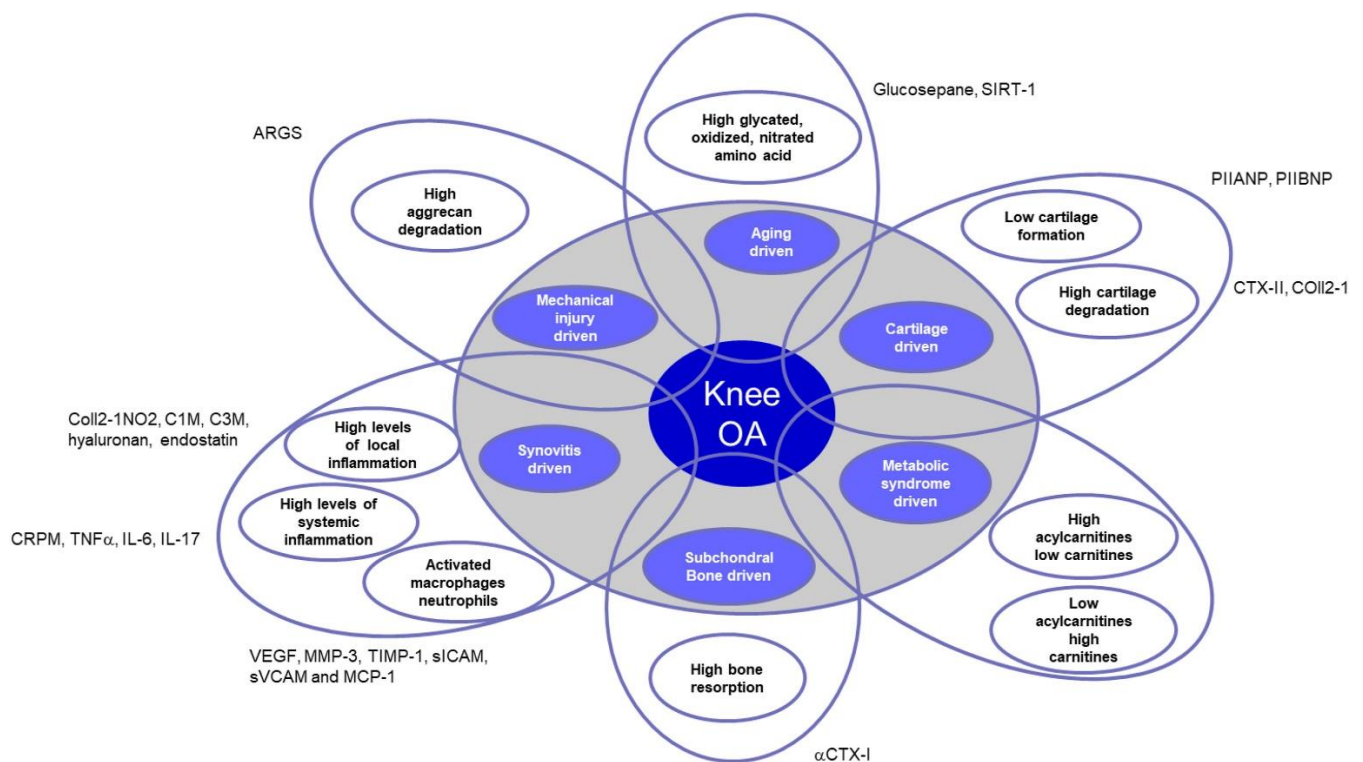


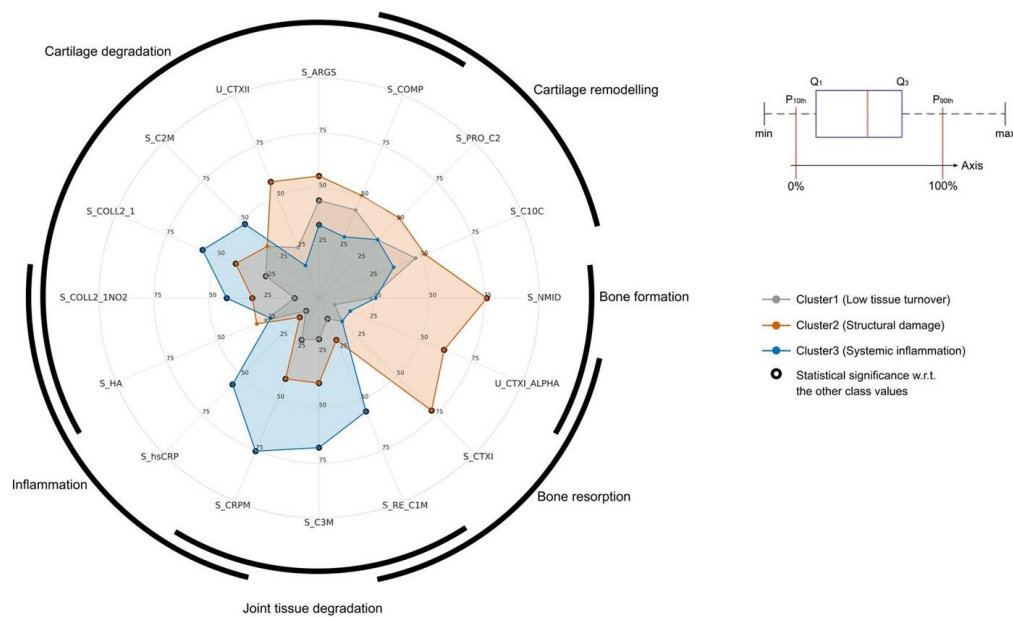
Figure 11: Representation of the diverse OA phenotypes, endotypes and molecular endotypes (inspired from v6). CRPM: C-Reactive Protein Metabolite; TNF: Tumor Necrosis Factor; IL: InterLeukin; VEGF: Vascular Endothelial Growth Factor; MMP: Matrix MetalloProteinase; TIMP: Tissue Inhibitor of Metalloproteinase; sICAM: serum InterCellular Adhesion Molecule; sVCAM: serum Vascular Cell Adhesion Molecule; MCP: Monocyte Chemoattractant Protein; SIRT: sirtuine. Illustration from [106].



## ***I. BACKGROUND***

The aforementioned phenotypes result from molecular modifications appearing years prior to the macroscopic alterations and which define what are called the endotypes of the disease. Again, various endotypes were described for OA and, as they overlap (especially in older patients), they result in phenotypes of OA as described by [107] (Fig 11).

Past studies and meta-analysis enlightened us on the importance to grant to OA phenotypes and endotypes. Deeper investigations conducted on OA cohort were able to detect and characterize subsets of patients corresponding to endotypes. A study conducted on the IMI-APPROACH cohort achieved the characterization of three main endotypes associated with three phenotypes for knee OA: low tissue turnover (low repair and articular cartilage/subchondral bone turnover), structural damage (high bone formation/resorption, cartilage degradation) and systemic inflammation (joint tissue degradation, inflammation, cartilage degradation) (Fig 12). Furthermore having different biomarker profiles for each cluster, they also displayed other statistical differences with, for example, more women in the structural damage and systemic inflammation clusters, and higher BMI and pain when standing in the systemic inflammation cluster [109,110].



Biochemical markers analyzed in the APPROACH cohort sampled from serum (S) and urine (U)

Name	Inter and intra coefficient of variation	Detection range	Description
S_C3M	<15%	1-85 ng/mL	MMP-mediated type III collagen degradation fragment. Type III collagen is a major collagen of connective tissues, including synovial membrane. C3M has been shown to be released from synovial membranes in the presence of proinflammatory cytokines which activate MMPs.
S_CRPM	<15%	1-110 ng/mL	MMP-mediated C reactive protein (CRP) degradation fragment. CRP is an acute reactant elevated in chronic inflammatory diseases. CRPM is a metabolite of CRP.
S_ARGS	<15%	0.01-0.4 pmol/mL	ADAMTs-mediated aggrecan degradation products. Aggrecan is the major proteoglycan of articular cartilage. Like MMPs, ADAMTs are expressed and activated in the presence of proinflammatory cytokines.
S_C10C	<15%	500-7500 ng/mL	CTSK mediated type X collagen degradation fragment.
S_C2M	<15%	0-10 ng/mL	MMP-mediated type II collagen degradation fragment.
S_COLL2_1	<15%	200-2200 nM	Typ II collagen degradation fragment similar, but from a different domain compared with C2M
S_COLL2_1_NO2	<15%	150-6000 pg/mL	Inflammation-related (nitrated) type II collagen degradation fragment. Nitrosylation is a post-translational modification induced by an increase in oxidative stress associated with inflammation.
S_COMP	<15%	1-50 units/L	Cartilage oligomeric matrix protein (COMP) is an articular cartilage protein, which is released when cartilage is turned over.
S_CTXI	<10%	0-3 ng/mL	Cross-linked, isomerized and CTSK-generated fragment of type I collagen C-terminal telopeptide. It is a marker of bone resorption.
S_HA	<15%	10-800 ng/mL	Hyaluronic acid is a glycosaminoglycan distributed widely across connective, epithelial and neural tissues, including articular cartilage. It is released as part of tissue remodeling and turnover induced by, for example, inflammation.
S_hsCRP	<10%	0-60 mg/mL	High-sensitive C reactive protein (hsCRP) is an acute reactant elevated in chronic inflammatory diseases and used as a diagnostic marker in different rheumatic diseases.
S_PRO_C2	<10%	5-1000 ng/mL	Type IIB collagen propeptide (synthesis). When new type II collagen is expressed by cartilage cells, PRO_C2 is released and is a reflection of cartilage formation.
S_NMID	<10%	1-180 ng/mL	Bone gamma-carboxyglutamic acid-containing protein.
S_RE_C1M	<15%	10-500 ng/mL	MMP-mediated type I collagen degradation. See S_C3M and S_CTXI I.
U_CTXI_ALPHA	<15%	0-10 µg/mmol	CTSK generated fragment of type I collagen C-terminal telopeptide (corrected for creatinine) is a non-isomerized version of S_CTXI and therefore believed to reflect degradation of young bone in contrast to the isomerized which measures old bone.
U_CTXII	<15%	10-2500 ng/mmol	MMP and CTSK-mediated type II collagen degradation fragment (corrected for creatinine). See CTXI and C2M as well.

Figure 12: Radar plot showing the profile of the three clusters describing the three main endotypes. In grey: cluster 1 corresponds to the low tissue turnover endotype. In orange: cluster 2 corresponds to the structural damage endotype. In blue: cluster 3 corresponds to systemic inflammation. The median biomarker concentrations for each cluster are represented with a circle (instead of a dot) when the difference between medians is statistically different. Values between 10% and 90% quantile are shown on the graph as percentages. Subsets of biomarkers are associated with different characteristics of OA: cartilage degradation, cartilage remodeling, bone formation, bone resorption, joint tissue degradation, and inflammation [109].

## I. BACKGROUND

The democratization of high throughput omic technologies is helping the deeper phenotyping effort put nowadays for OA. A transcriptome atlas was built from a total of 131 OA patients to deconstruct the complexity of OA and to decipher the crosstalk between articular tissues. By the technique of cluster generation, they identified four subtypes of OA presenting distinct metabolism: GAG metabolic disorder, collagen metabolic disorder, activated sensory neurons, and inflammation. Clusters have obviously specific genetic profiles and marker genes but the tissular joint crosstalk is also impacted differently. Interestingly, one of the clusters is enriched for the ossification and osteoblast regulation pathways. The same cluster correlates with a narrowing of the joint space [111]. Two other studies performed on smaller patient samples successfully identified subtypes of OA. They corroborated the inflammation and the ECM-related cluster and all studies associated the inflammation cluster with a narrower joint space even though their study design was independent [112,113].

The efficiency of OA treatments is mostly unpredictable as we could expect from such a heterogenous and complex disorder. The principal aim of the studies listed here is to develop personalized medicine and successful treatments for OA. Currently, we are witnessing the first steps toward this approach. For instance, first suggestions of treatments could be proposed based on the newly classified OA [111] (Table 5).

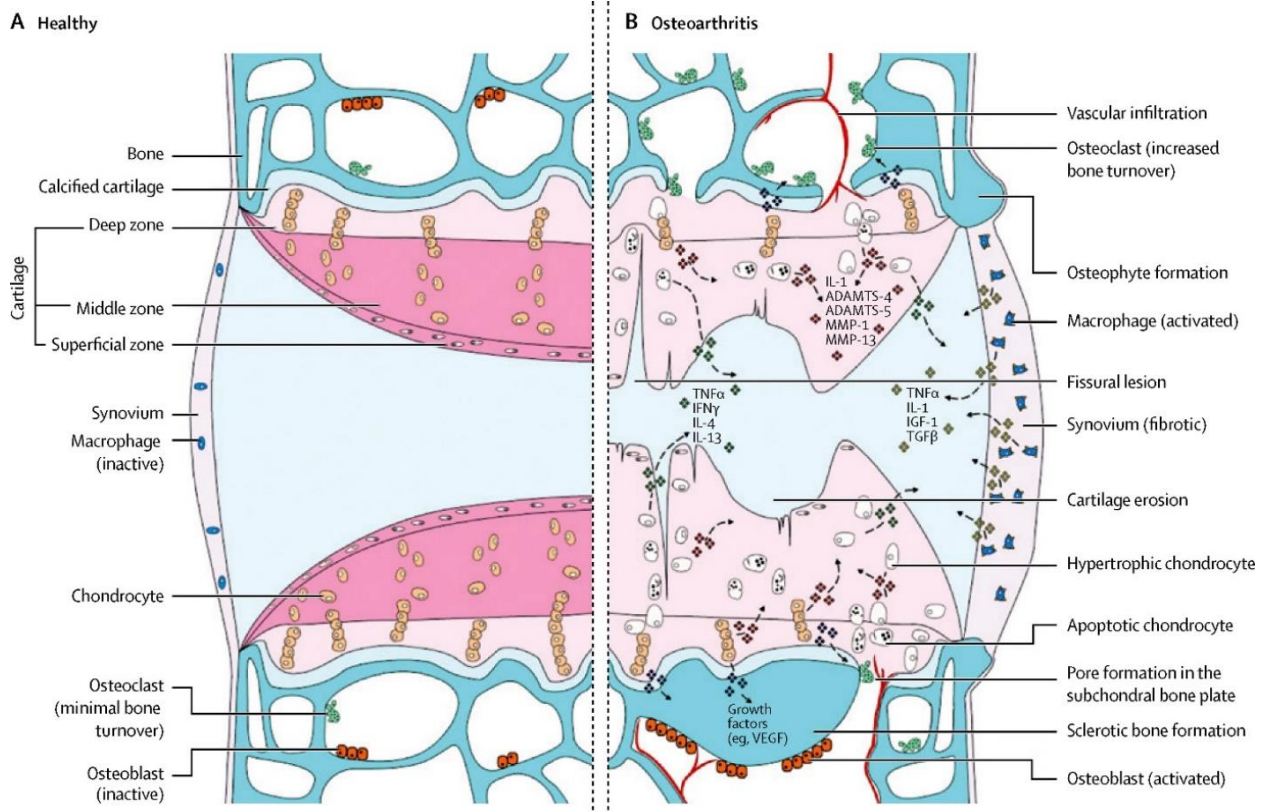
*Table 5: Identification of molecular and clinical features related to four different OA subtypes with a proposed adapted treatment for the patient, adapted from [111].*

Feature	GAG metabolic disorder	Collagen metabolic disorder	Activated sensory neurons	Inflammation
<b>Molecular</b>	PCOL CE2/ACAN ↑ VCAN ↓ GAG metabolic ↑	TGF-β/COL6A1 ↑ Collagen catabolic ↑	GRIK2/GRM7 ↑ Synapse assembly ↑	TMSB4X/CD34 ↑ Immune response ↑
<b>Clinical</b>	Typical symptom	Severe osteophyte	Younger age of KRS	Apparently narrow joint space
<b>Treatment principles</b>	GAG supplement	Collagen supplement	Analgesia	Anti-inflammation
<b>Drugs</b>	Hyaluronic acid Hyaluronic Glucosamine	Gelatin Hyaluronic collagen Undenatured collagen	NGF-inhibitor (tanezumab) Acetaminophen Opioids	NSAIDs Corticosteroids IL-1 inhibitor (canakinumab) TNF-α inhibitor (adalimumab, infliximab, etanercept)

### **I.5.2 Physiopathology of OA**

OA is characterized by pathological changes in all tissues of the joint. It induces degradation and loss of the articular cartilage, inflammation of the synovium, abnormal subchondral bone remodeling leading to sclerosis and osteophytes, joint shape alteration, degeneration of ligaments and menisci and hypertrophy of the joint capsule [102]. A schematic illustration of the global picture is represented by figure 13.

Each periarticular tissue modification could be reviewed in great details as they all have been extensively investigated. Yet, with the purpose of summarizing, I will go further with the cartilage and subchondral bone pathological changes.



*Figure 13: Illustration and comparison of the healthy joint and the pathological changes induced by OA on joint tissues. Chondrocytes are represented in the cartilage matrix colored in red to represent its composition rich in GAGs which are loss in OA and correspond to a loss of staining. The integrity of the cartilage is lost, articular cartilage is damaged and eroded, and chondrocytes become hypertrophic during the development of OA and even undergo apoptosis. Inflammation markers and proteases are secreted by chondrocytes. The synovium shows a pathological phenotype, and its macrophages are activated. There is an increased vascularization of the subchondral bone which upregulates the expression of VEGF. Osteoclasts and osteoblasts are activated in the subchondral bone and the bone remodeling process is impaired and generates subchondral bone sclerosis and ectopic bone formation leading to osteophytes [114].*

### **I.5.2.1 Articular cartilage modifications**

Articular cartilage degradation is the hallmark of OA and the cartilage undergoes deep metabolic and physiological modifications. From macro-observations, modification of the cartilage is clearly visible with the fresh white and translucent healthy cartilage turning yellowish and with a distinct texture due to the fibrillations. Ultimately, there is a complete erosion of the cartilage and the subchondral bone that was beneath becomes visible (Fig 14).



*Figure 14: (Left) Healthy cartilage from a knee joint of a 43 years old human and (right) OA lesions of the articular cartilage of the knee joint of a 88 years old human [115].*

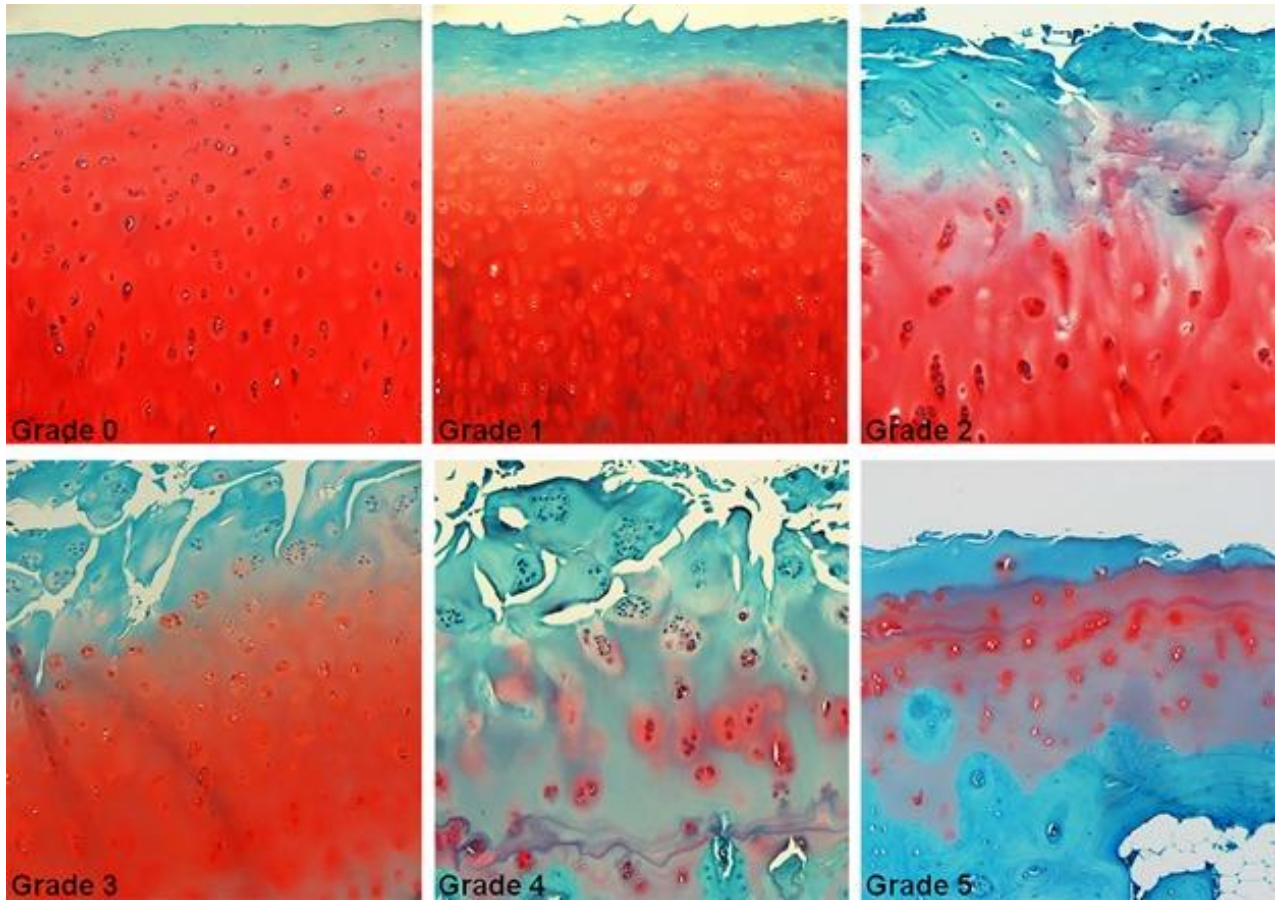
As the degradation of cartilage is a key feature of OA, there are several scores assessing its damage. The gold standard is the “osteoarthritis research society international” (OARSI) score described by [116] (Fig 15). It is divided from grade 0 to grade 6 with grade 0 representing an intact surface and intact cells; grade 1 still shows an intact surface but which is uneven with superficial abrasion and may have chondrocytes death, proliferation and generation of

## ***I. BACKGROUND***

clusters or hypertrophy; grade 2 displays a surface discontinuity with deeper fibrillations, a loss of histological staining for the Safranin-O Fast Green/ Toluidine Blue and a disorientation of chondrocytes; grade 3 is marked by vertical fissures/clefts through the middle zone that can be branched when more severe; grade 4 is the erosion of the cartilage, there is cartilage loss; grade 5 is the denudation step with apparent subchondral bone at the joint surface; grade 6 is the most severe and correspond to the deformation, the subchondral bone is apparent and remodeled, it shows microfractures. The OARSI score is particularly relevant to distinguish early to mild OA and has been validated in human and animal studies [117–119]. The severity of the OARSI score correlates with the loss of biomechanical properties of the articular cartilage [120].

Other articular cartilage modifications correlate with the development of OA such as the duplication of the tidemark. Its area is increased and starts to be innervated and capillary vessels penetrate the tidemark and modify the environment of chondrocytes. The angiogenesis of the cartilage and the hypertrophic phenotype are regulating each other positively in an interdependent way [121,122]. The duplication of the tidemark is the consequence of the activation of the endochondral ossification mechanism and the mineralization supervised by hypertrophic chondrocytes [123,124].

## I. BACKGROUND



*Figure 15: Representation of the histological OARSI score with key characteristics. From grade 0 to 5. Grade 0: intact surface; grade 1: superficial fibrillations and cell abnormalities; grade 2: surface discontinuity and chondrocytes clusters; grade 3: branched clefts; grade 4: erosion; grade 5: denudation with subchondral bone being apparent at the surface. Pictures were taken with magnification 100X from [120].*



### **I.5.2.1.1 Biological mechanisms of cartilage degeneration**

In OA, previously quiescent chondrocytes become more active, they proliferate and form clusters; this process is mimicking what is occurring during skeletal development. The cartilage turnover is increased and in response to mechanical stress or inflammation, chondrocytes upregulate their production of collagenase and aggrecanase. The main degrading enzymes are from the MMPs and A Disintegrin and Metalloproteinase with Thrombospondin Motifs (ADAMTS). From the MMP family, MMP-13 is particularly efficient against type II collagen [102,125]. Chondrocytes increase their production of chemokines and cytokines contributing to the inflammation of the cartilage. There are several upregulated cytokines but the main one is IL-1 $\beta$ . IL-1 $\beta$  was shown to have a key incidence in the development of pathological modifications. In OA chondrocytes culture in alginate, the stimulation by IL-1 $\beta$  was considerably increasing the expression of MMPs and downregulating the aggrecan, favoring the degradation outcome [126]. Other *in vitro* experiments showed that IL-1 $\beta$  was able to inhibit proteoglycan synthesis [127]. Tumor necrosis factor  $\alpha$  (TNF- $\alpha$ ) is a second crucial cytokine enhancing the catabolic pathway. Both IL-1 $\beta$  and TNF- $\alpha$  inhibit the type II collagen and aggrecan synthesis and stimulate the production of reactive oxygen species and MMPs [128,129].

Following the aging process or after trauma, chondrocytes enter into senescence and secrete various factors grouped as senescence-associated secretory phenotype (SASPs). SASPs are secreted in the microenvironment where they induce senescence and inflammation to the neighboring cells, promoting cartilage damage and OA [130,131]. The breakdown of the cartilage results in damage-associated molecular patterns (DAMPs) released from the ECM.

## ***I. BACKGROUND***

DAMPs contribute to the initiation of the inflammation and its perpetuation by triggering synovial inflammation. It induces neo-angiogenesis, activation of macrophages, which polarize preferentially into M1 leading to a higher M1 to M2 ratio (M1 being proinflammatory macrophage and M2 being anti-inflammatory), and the subsequent production of inflammatory mediators which are released back into the joint cavity, promoting further cartilage degradation [132–134] (Fig 16). DAMPs come from the cleavage of a wide variety of proteins and namely from fibronectin, hyaluronan, lubricin, SLRPs with OMD included, and collagens [132,135–143]. They play predominant intracellular roles but they are also released into the joint cavity either passively by damaged cells or cells under necrosis or even through exosomes [144].

Further, it is proposed that the early degeneration of the cartilage is related to the ectopic hypertrophy of chondrocytes, another key feature of OA. The damage caused by MMPs and ADAMTS is correlated with the expression of terminal differentiation-marker genes such as *COL10A1* and *MMP-13* [125]. Articular chondrocytes that have switched into hypertrophy contribute to the destabilization of the articular integrity. They are involved in the mineralization of the cartilage by the expression of *ALP* and can later enter the cellular death pathway [145–147].

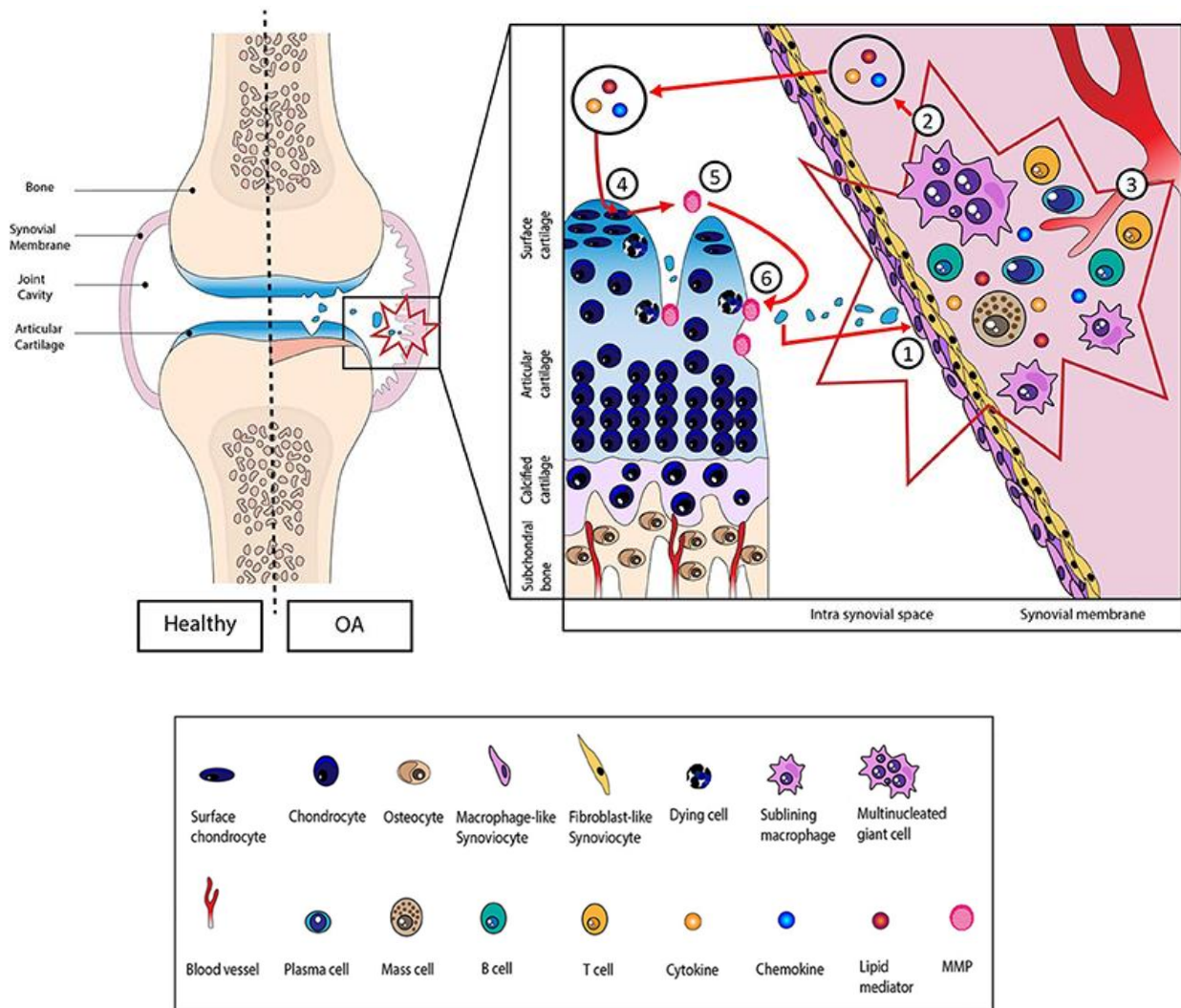


Figure 16: Schematic representation of the effect of DAMPs in OA. (1) The articular cartilage releases DAMPs in the joint cavity during degradation. (2) It triggers the proliferation of the lining cells and inflammatory cells infiltrate the tissue alongside (3) neo-vascularization. (4) Inflammatory mediators, cytokines, chemokines and lipid mediators, and DAMPs are released back into the joint cavity maintaining the inflammatory cycle through (5) the activation of chondrocytes which increases MMPs production leading (6) to more cartilage damage. Illustration from [132] and designed by Jérémie Zappia.

Changes in the pericellular matrix is preceding the early shifting of phenotype presented by chondrocytes in OA and, later, the pericellular matrix becomes loosely organized. The pericellular matrix is the closest ECM to chondrocytes, and it implies that their closest cellular environment is transformed with the disease, impairing biochemical and biomechanical cell responses. Several proteins of the matrix, SLRPs included, act as reservoirs of growth factors and regulate their bioavailability. For instance, in the pericellular matrix, fibrillin and fibulin

sequester TGF- $\beta$  while biglycan and syndecan modulate the Wnt pathway. However, both TGF- $\beta$  and Wnt are activated during OA [50,148]. Most of the Wnts induce cartilage degeneration, they promote chondrocyte differentiation and hypertrophy but also the upregulation of *MMPs* culminating in the promotion of OA [149–153]. Concerning TGF- $\beta$ , it can promote the expression of *MMPs* and, in long-term exposure, the loss of proteoglycan in the deep layer of the cartilage. However, the scope of action of the Wnt and TGF- $\beta$  pathways is highly complex and as pleiotropic factors their influence is multifactorial and the outcome of their activation can be positive for the integrity of the cartilage [154,155].

### **I.5.2.2 Subchondral bone modifications**

The cartilage damage was the first modification to be widely studied for the understanding of OA pathophysiology, but overall the subchondral bone is however not to be neglected and has aroused the interest of researchers, especially in recent years.

Bone marrow lesions (BMLs), sometimes described as bone marrow edema, are modifications of the subchondral bone which are identified by an abnormal signal on MRI. BMLs are associated with different pathologies including OA and they are related to different features such as bone marrow necrosis, fibrosis, microfractures and fibrovascular ingrowth [156,157]. According to [158], out of 710 people above 50 years old, without any radiographic evidence of knee OA, 52% displayed BML. The prevalence of BML increases with age and there is a strong correlation between cartilage damage from OA and BML with 88% of BMLs correlating with denuded cartilage or severe cartilage damage [158,159]. BMLs are associated with higher OARSI histological score than non-OA and OA with no BML, and they are associated with microarchitectural modifications of the subchondral bone, the plate thickness is increased, there is higher bone volume, more numerous trabeculae with their geometry shifting to plate-

## ***I. BACKGROUND***

like structure, and the bone mineral density (BMD) is significantly increased at BML locations. Subregions of the knee joint show different relations to BMLs and associated joint modifications with the anterior medial region being the more prone to develop BMLs [160,161]. BMLs are induced by repetitive mechanical stress and they represent the subchondral bone response, which turns to increase the bone remodeling to attempt to repair the damage, leading to pathophysiological modifications for both bone and cartilage [160,162].

Even though subchondral bone sclerosis was commonly identified in advanced OA, studies highlighted subchondral bone modifications preceding cartilage damage (Fig 17). With mechanical overload, there are abnormal bone resorption and microdamage that affect rod trabeculae. At first, with increased bone resorption, the subchondral bone may get thinner and more porous with less trabecular bone and thereafter evolves into thicker and sclerotic bone [163]. There are fewer rod trabeculae, thus there is a thickening of the trabeculae to keep on the mechanical demand, and plate trabeculae become over-represented with the consequence of altered mechanical properties of the subchondral bone becoming stiffer. The orientation of plate trabeculae in OA also differs from healthy subchondral trabeculae worsening the global mechanical properties. The osteochondral unit is impaired and the articular cartilage starts to display OA pathological degeneration. Human and spontaneous OA guinea pig model studies showed that subchondral microarchitecture modifications occur before cartilage degradation, suggesting that subchondral bone structural changes are initiating cartilage degradation [98,164]. Modifications of the subchondral bone were confirmed *in vivo* in humans, in 20 women, by [165], showing a strong correlation between Kellgren-Lawrence grade and the subchondral bone microarchitecture of the medial tibial

## I. BACKGROUND

plateau, with higher bone volume, increased trabecular thickness with a shift toward plate trabeculae in the medial tibial plateau than in the lateral.

Moreover, a direct effect from osteoblasts on chondrocytes was identified *in vitro*, in a co-culture design. Osteoblasts from the sclerotic area of the subchondral bone in OA patients accelerated the hypertrophic differentiation of chondrocytes and induced the mineralization of their ECM [166].

Altogether, these findings indicate a bone-driven phenotype for OA, with the subchondral bone playing a major function in the initiation of OA, at least for a subtype of patients (Fig 17).

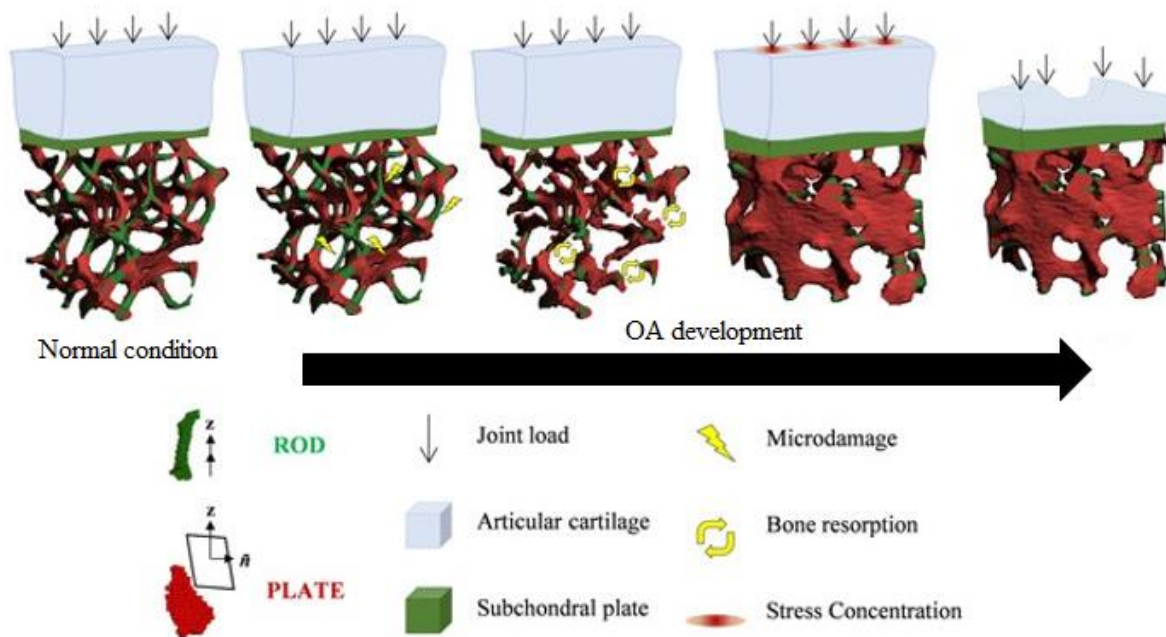


Figure 17: Schematic representation of the microarchitectural modifications of the subchondral bone in OA. In early OA, the cartilage is still intact but the beginning of alterations of the subchondral bone can be observed. Mechanical overloading affects mostly rod trabeculae. Because of microdamage and abnormal bone resorption, the number of rod trabeculae is reduced and, in an attempt to compensate, there is a thickening of the subchondral trabeculae. It results in an impaired rod-to-plate trabeculae ratio and a thickening of the subchondral plate which generates a locally stiffer bone. The undermined subchondral bone is impeded in its support function for the articular cartilage and further mechanical stress contributes to its degradation in advanced OA [98].

### **I.5.2.2.1 Biological mechanisms of the subchondral bone sclerosis**

Subchondral bone sclerosis derives from an unbalanced bone remodeling which disturbs both the bone resorption and bone deposition functions (Fig 18). Abnormal stress conditions in the subchondral bone conduct to higher osteoclast activity. It was shown that TRAP staining was increased in subchondral bone in the murine model and in human [167,168]. The pro-resorptive environment is helped by osteocytes adjacent to microdamage which undergo apoptosis and secrete pro-osteoclastic molecules during the early stage of OA development [62,169].

In reaction of the bone resorption, there is a locally higher concentration of TGF- $\beta$ 1, which recruits MSCs leading to aberrant bone formation and angiogenesis helping OA progression (Fig 18). In humans, TGF- $\beta$ 1 concentration was higher in subchondral bone associated with OA compared to healthy controls. *In vitro*, it was confirmed that TGF- $\beta$ 1 from osteocytes activates Smad2/3 and that TGF- $\beta$ 1 level correlates with subchondral BMD modification, and *ALP* and osteopontin expression. Furthermore, when TGF- $\beta$  is inhibited in MSCs from the subchondral bone, it has a protective effect on chondrocytes, showing once more the importance of osteochondral crosstalk [167,168]. In parallel, osteocytes from the subchondral bone stimulate the mineralization process through the activation of the Wnt pathway and the decrease of the production of sclerostin (SOST), a Wnt antagonist [170,171].

The behavior of osteocytes in regard to their surrounding bone matrix is altered. Osteocytes can actively resorb their bone matrix through the perilacunar/canalicular remodeling (PLR) to maintain bone homeostasis. However, lacunocanicular networks are disrupted by OA in subchondral bone from the human knee and it was associated with reduced MMP13 and CTSK,

## ***I. BACKGROUND***

two PLR enzymes. In mice, the mutation of *MMP-13* in osteocytes mediated the suppression of PLR, they had increased subchondral bone volume and it compromised the cartilage with premature OA [172].

Results from hip-OA showed also subchondral bone sclerosis associated with the disease, with a higher trabecular number, a shift from rod to plate trabecula and thicker trabeculae. Interestingly, they showed that the bone remodeling process is impaired with higher osteoclast number in subchondral bone in OA but most importantly, a higher number of SP7 and osteocalcin positive osteoblasts. Even though there is higher bone resorption, as the bone formation is superior, the outcome leads to subchondral bone sclerosis [173].

Subchondral bone sclerosis is also associated with neo-angiogenesis of the cartilage, and specifically increased of type-H vessels promoting OA (Fig 18). The activation of the mammalian target of rapamycin complex (mTORC) pathway in chondrocytes stimulates the production of VEGF in bone and was shown to be sufficient for the development of type-H vessels in the subchondral bone. The development of type-H vessels supports further sclerosis of the subchondral bone by regulating bone resorption and the stimulation of factors implied in osteogenesis [35,36,174]. Osteoblasts also display activation of mTORC in the subchondral bone leading to its sclerosis and OA. Again, TGF- $\beta$ 1 reveals itself as a master regulator of the sclerotic phenotype as its activation elevates the neo-angiogenesis by enhancing VEGF synthesis [122,167,175–178].

The biological mechanisms involved in subchondral bone sclerosis including the uncoupled bone remodeling, neo-angiogenesis and impaired osteochondral crosstalk were reviewed in [163]. They illustrated the modifications occurring in the subchondral bone in early OA and late OA (Fig 18).



# I. BACKGROUND

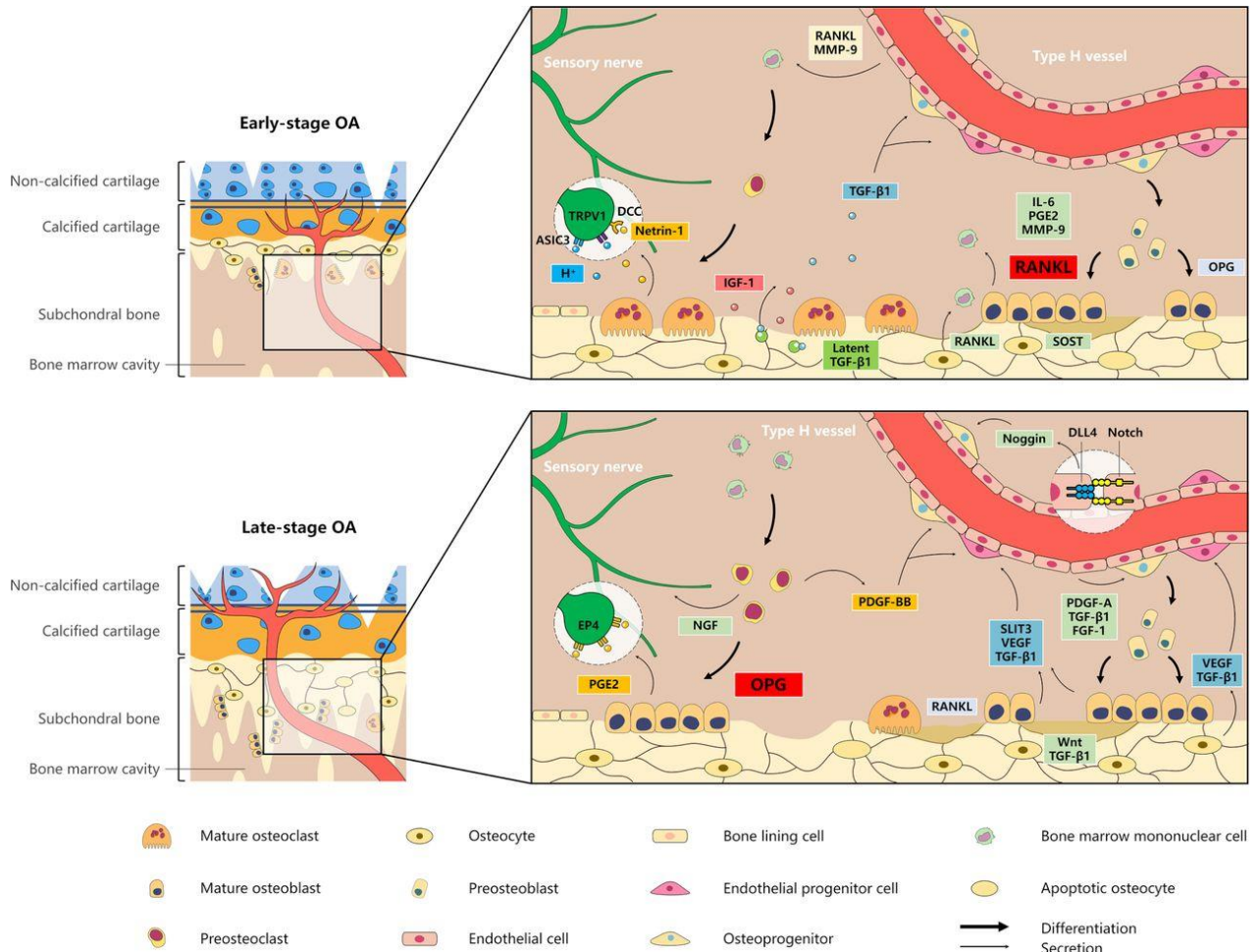


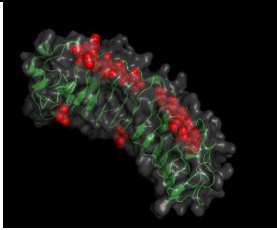
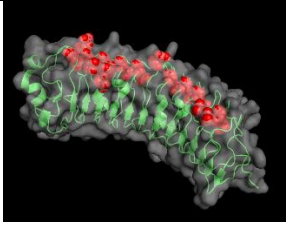
Figure 18: Schematic representation of the biological mechanisms involved in the subchondral bone with early-stage OA and late-stage OA. In early-stage OA, there is abnormal bone resorption with the upregulation of RANKL and downregulation of OPG by osteoblasts increasing the number of osteoclasts in the subchondral bone. The production of prostaglandin E2 (PGE2), IL-6, MMP9 and VEGF enhances the pro-osteoclastic environment. This effect is reinforced by the type-H vessels producing RANKL and MMP9. The enhanced bone resorption releases cytokines from the bone matrix, such as insulin-like growth factor 1 (IGF1) and TGF-β1. It is followed by the neo-angiogenesis of the subchondral bone and its invasion by type-H vessels and, consequently, the osteogenesis is stimulated and enhanced as well. Type-H vessels are surrounded by osteoprogenitors and stimulate their proliferation and differentiation namely by expressing platelet-derived growth factor A (PDGF-A), TGF-β1 and FGF-1. Osteoclasts secrete Netrin-1 and H<sup>+</sup> promoting sensory innervation with the expression of acid-sensing ion channel 3 (ASIC3); deleted in colon cancer (DCC); and transient receptor potential vanilloid 1 (TRPV1) which are pain-related. In late-stage OA, the mineralization is enhanced namely with the activation of the Wnt and TGF-β1 pathways. Osteocytes also reduce the production of SOST, an inhibitor of the Wnt pathway, to increase the mineralization outcome. Osteoblasts and osteocytes are still contributing to the capillary invasion through the production of VEGF, slit guidance ligand 3 (SLIT3), and TGF-β1. Pre-osteoclasts help the angiogenesis too by producing PDGF-BB. The invasion of type-H vessels is maintained and their endothelial cells communicate through the intercellular Notch/delta-like protein 4 (DLL4) pathway and it leads to the induction of Noggin, a BMP inhibitor, for the correct differentiation of the osteoprogenitors. A subgroup of osteoblasts promotes subchondral bone sclerosis through the expression of PDGF-A, TGF-β1 and FGF-1. Sensory innervation is supported by nerve growth factor (NGF) and PGE2 coming from pre-osteoclasts and osteoblasts respectively. PGE2 is the ligand of Prostaglandin E2 receptor 4 (EP4), mediating the pain response and inflammation as well [163].

**I.5.3 Small Leucine-Rich Proteoglycans**

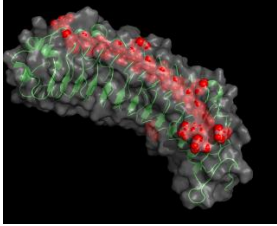
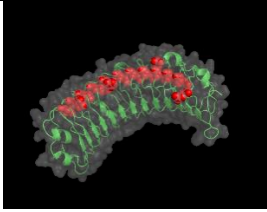
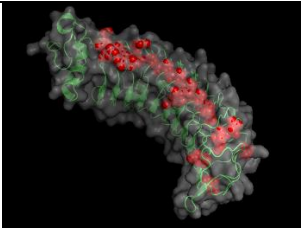
Numerous collagens, glycoproteins and proteoglycans compose the ECM and they constitute what is called the “core matrisome”. Among the proteoglycan of the matrisome, a specific family, the SLRP, includes OMD but also 17 other members with the well-known biglycan, and decorin, classified in five classes. SLRPs are composed of a core protein covalently decorated by GAGs. The core protein is characterized by a variable number of central leucine-rich repeat (LRR) domains, each made of one  $\alpha$ -helix and one  $\beta$ -strand structuring SLRPs as solenoid-like proteins with a horseshoe shape ideal for protein–protein interaction helping their functions in fibrillogenesis, cytokines reservoir in the ECM, and binding to cellular receptors. SLRP members display distinct features, such as different LRR lengths, glycosylation patterns, the nature of their GAG chains or even the composition of their N-terminal domain containing four cysteines spaced by a varying number of amino acids which were used to classify them (Table 6) [50].

## I. BACKGROUND

Table 6: Classification of the SLRP family in five classes; BGN: Biglycan; DCN: Decorin; ASP: Asporin; ECM2: Extracellular Matrix Protein 2; ECMX: Extracellular Matrix Protein X; LUM: Lumican; KTN: Keratocan; FMOD: Fibromodulin; OMD: Osteomodulin; PRELP: Proline/arginine-rich end leucine-rich repeat protein; EPN: Epiphycan; OGN: Osteoglycin; OPTC: Opticin; CHAD: Chondroadherin; NYX: Nyctalopin; TSK: Tsukushi; PODN: Podocan; PODNL: Podocan like protein. Classification is based on the N-end cysteine cluster and a 3D representation of a representative member generated with the PyMol software (Schrödinger LCC, version 2.1.1) is illustrated with lateral asparagines (N shown in red). X-Ray crystallographic analysis for the SLRP Family members of class III and class IV are not yet available. The different post-translational modifications, GAG type, glycosylation and other features are listed. LRR: leucine-rich repeat. The table is from [50] and was designed and generated by Jérémie Zappia.

Class	N-end cysteine motif	3D representation and PDB ID	Member	GAG type/ Glycosylation	Other
I	CX <sub>3</sub> CXCX <sub>6</sub> C	 ID: 1XKU	BGN	Chondroitin sulfate Dermatan sulfate N-linked oligosaccharides	Only ECM2 has a peculiarity in its motif with only 2 conserved cysteines.
		 ID : 2FT3	DCN	Chondroitin sulfate Dermatan sulfate N-linked oligosaccharides O-linked oligosaccharides	
			ASP	N-linked oligosaccharides Potential O-linked oligosaccharides Acid aspartic sulfation	
			ECM2 ECMX		
II	CX <sub>3</sub> CXCX <sub>9</sub> C		LUM KTN	Keratan sulfate poly-lactosamine N-linked oligosaccharide Tyrosine sulfation	tyrosine cluster that can be sulfated

## I. BACKGROUND

		 <p>ID : 5MX0</p>	FMOD	poly-lactosamine Keratan sulfate N-linked oligosaccharides Tyrosine sulfation acidic patch	
		 <p>ID : 5YQ5</p>	OMD		
			PRELP	N-linked oligosaccharide	
III	CX <sub>2</sub> CXCX <sub>6</sub> C		EPN	Chondroitin sulfate Dermatan sulfate O-linked oligosaccharides N-linked oligosaccharides acidic patch	LRRs with only 7 repeats.
			OGN	Keratan sulfate Chondroitin sulfate Dermatan sulfate N-linked oligosaccharides	
			OPTC	O-linked oligosaccharides Tyrosine sulfation	
IV	CX <sub>3</sub> CXCX <sub>6-17</sub> C	 <p>ID: 5MX1</p>	CHAD	Keratan sulfate (existence of potential site)	
			NYX TSK	(existence of potential site)	
V	CX <sub>3-4</sub> CXCX <sub>9</sub> C		PODN	(existence of potential site) acidic patch	High number of LRR with 20 repeats for POD and 21 repeats for PODNL
			PODNL	(existence of potential site)	

### **I.5.3.1 SLRPs in OA**

SLRPs were demonstrated to play key functions in the ECM and were related to various pathological conditions. Several members of the SLRP family were investigated from the OA perspective and related to its development or onset. Firstly, biglycan, decorin, asporin, lumican, keratocan, fibromodulin, osteomodulin, PRELP, epiphygan, osteoglycin, opticin, chondroadherin, tsukushi and podocan-like protein were observed and/or were shown to have functions in skeletal tissues [179–183]. Most of them bind to the collagen network and regulate fibrils organization and diameter while protecting collagens to be enzymatically cleaved by collagenases. However, in pathological conditions such as OA, there is an extensive degradation of SLRPs by MMPs with specific fragmentation patterns associated with the severity or localization of tissues affected by OA. SLRPs are not only affected by protein degradation but their gene expression is also modified with OA [50,184–191]. In addition, several SLRPs bind to TGF- $\beta$  and BMPs, which are deeply connected to the cartilage integrity and the onset of subchondral bone sclerosis, influencing the cellular response [192–199]. They are also involved in the inflammatory response as they are included in the DAMPs identified in OA. They bind to Toll-like receptors (TLRs) and they activate the complement pathway [132,138,139,191].

The *in vivo* functions of SLRPs in OA were extensively investigated thanks to mouse models with single and double SLRPs deficiency, represented in table 7. The deficient mouse models showed that SLRPs maintain the integrity of the skeletal tissues *in vivo* including the joint which was developing OA in the absence of biglycan, fibromodulin, decorin, epiphygan and associated double knock-out mice. The microarchitectures of bone and cartilage, in addition to the collagen fibrils, were affected in mostly all the SLRP-deficient models. In consequence,

the biophysical properties of the joint are impaired because of the degenerative changes and the joint is less suitable to endure mechanical loading (Table 7).

*Table 7: Summary of the skeletal phenotypes of SLRPs deficient mouse and their association with OA. Table generated and designed by Jérémie Zappia.*

<b>SLRPs</b>	<b>Skeletal Phenotypes</b>	<b>OA</b>	<b>Ref</b>
<b>Biglycan</b>	<ul style="list-style-type: none"> <li>- Low bone mass</li> <li>- Ectopic ossification in tendons, menisci and cruciate and patellar ligaments</li> <li>- Abnormal collagen fibrils in bone and tendons</li> <li>- Collagen loss in articular cartilage</li> <li>- Torn cruciate ligaments</li> <li>- Altered subchondral bone microarchitecture</li> <li>- Decreased nucleus pulposus</li> <li>- Early disc degeneration</li> <li>- Phenotype aggravated with age</li> </ul>	<ul style="list-style-type: none"> <li>- Premature knee OA and subchondral bone sclerosis, observed from 3 months in [200] and from 6 months in [201]</li> <li>- Altered subchondral bone microarchitecture in the DMM model</li> </ul>	[200–206]
<b>Fibromodulin</b>	<ul style="list-style-type: none"> <li>- Ectopic ossification in ankles, tendons, menisci and cruciate and patellar ligaments</li> <li>- Abnormal collagen fibrils in tendons</li> <li>- Decreased tendon stiffness</li> <li>- Torn cruciate ligaments</li> <li>- Phenotype aggravated with age</li> </ul>	<ul style="list-style-type: none"> <li>- Premature knee OA and subchondral bone sclerosis, observed from 9 months</li> </ul>	[200,204,207,208]
<b>Decorin</b>	<ul style="list-style-type: none"> <li>- Abnormal collagen fibrils in bone</li> </ul>	<ul style="list-style-type: none"> <li>- Accelerated cartilage damage and osteophyte formation in the DMM model with alignment of collagen fibrils</li> </ul>	[203,206,209]
<b>Lumican</b>	<ul style="list-style-type: none"> <li>- Abnormal collagen fibrils in tendons</li> </ul>		[208]
<b>Epiphycan</b>	<ul style="list-style-type: none"> <li>- lighter and shorter femur</li> <li>- Phenotype aggravated with age</li> </ul>	<ul style="list-style-type: none"> <li>- Premature knee OA, observed from 9 months</li> </ul>	[201]
<b>Osteoglycin</b>	<ul style="list-style-type: none"> <li>- Higher bone mass</li> <li>- Altered bone microarchitecture</li> <li>- Decreased osteoclast number</li> <li>- Abnormal collagen fibrils in tendon</li> </ul>		[183,210]
<b>Opticin</b>	<ul style="list-style-type: none"> <li>- Abnormal collagen fibrils in articular cartilage</li> </ul>	<ul style="list-style-type: none"> <li>- Prevent cartilage damage in DMM model</li> </ul>	[211]
<b>Chondroadherin</b>	<ul style="list-style-type: none"> <li>- Altered bone and cartilage microarchitectures</li> </ul>		[212,213]

	<ul style="list-style-type: none"> <li>- Altered bone and cartilage mechanical properties</li> <li>- Abnormal collagen fibrils in cartilage</li> </ul>	
<b>Tsukushi</b>	<ul style="list-style-type: none"> <li>- Shorter skeleton</li> <li>- Lower bone mass and altered bone and cartilage microarchitectures</li> </ul>	[181]
<b>Biglycan/ Fibromodulin</b>	<ul style="list-style-type: none"> <li>- Lower bone mass</li> <li>- Shorter long bones</li> <li>- Decreased flexibility of knee and ankle joints</li> <li>- Ectopic ossification in ankles, menisci and cruciate and patellar ligaments</li> <li>- Abnormal collagen fibrils in tendons</li> <li>- Torn cruciate ligaments</li> <li>- Altered subchondral bone microarchitecture</li> <li>- increased articular chondrocytes apoptosis</li> <li>- Increased osteoclast activity</li> <li>- Phenotype aggravated with age</li> </ul>	<ul style="list-style-type: none"> <li>- Premature knee OA and subchondral bone sclerosis, observed from 3 months</li> <li>- Premature temporomandibular joint OA, observed from 5 months</li> </ul>
<b>Biglycan/ Decorin</b>	<ul style="list-style-type: none"> <li>- Shorter and wider long bones</li> <li>- Low bone mass</li> <li>- Abnormal collagen fibrils in bone</li> <li>- Altered subchondral bone microarchitecture</li> </ul>	<ul style="list-style-type: none"> <li>- Accelerated cartilage damage and osteophyte formation in the DMM model with altered subchondral bone microarchitecture and alignment of collagen fibrils</li> </ul>
<b>Lumican/ Fibromodulin</b>	<ul style="list-style-type: none"> <li>- Joint laxity and hypermobility</li> <li>- Misaligned knee patella and overgrowth of the metaphyseal bone</li> <li>- Bowed legs and gait abnormalities</li> <li>- Decreased tendon stiffness</li> </ul>	<ul style="list-style-type: none"> <li>- Premature knee OA, observed from 5 months</li> </ul>
<b>Biglycan/ Epiphygan</b>	<ul style="list-style-type: none"> <li>- Shorter long bones</li> <li>- Ectopic ossification in tendons and ligaments</li> <li>- Collagen loss in articular cartilage</li> <li>- Deficiency of superficial articular chondrocytes</li> <li>- Phenotype aggravated with age</li> </ul>	<ul style="list-style-type: none"> <li>- Premature knee OA, subchondral bone sclerosis and osteophytes, observed from 4 months</li> </ul>

## ***I. BACKGROUND***

Further, detrimental phenotypes and OA were more severe in the double knock-out models, indicating the synergy of SLRPs and their likely overlapping functions (Table 7). Besides, as a result of the mutation of an SLRP gene, compensation mechanisms can arise with the upregulation of other SLRPs to alleviate the deleterious outcome [200,201,203,204,206,208]. Concerning the beneficial effect of the lack of opticon after DMM, it results from the upregulation of lumican and epiphycan, but a decrease of fibromodulin, preventing joint damage [211]. However, even if most of the reported SLRP-deficient mouse models develop OA, they are progressing in their own fashion. For instance, more severe spontaneous articular damage is observed in biglycan-deficient mouse than with fibromodulin or epiphycan deficient models; or with no subchondral bone sclerosis associated with decorin-deficient mouse in a DMM model [200,201,209]. Therefore, distinct biological mechanisms are associated with SLRP members, despite compensation mechanisms being present and then with some anticipated limitations.

The regulation of the bioavailability of cytokines was also investigated in mouse models to identify mechanisms leading to OA. In mouse lacking biglycan and fibromodulin, the sequestration of TGF- $\beta$ 1, which can be bound by both SLRP, is decreased in the ECM leading to the overactivation of the pathway and later to the degradation of the cartilage. The increased availability of TGF- $\beta$ 1 was corroborated *in vitro*, alongside the resulting upregulation of MMPs and ADAMTS in the absence of biglycan and fibromodulin [218]. The biglycan and fibromodulin regulate bone remodeling as well through the direct binding of RANKL, the master differentiation factor of osteoclasts. While RANKL sequestration is decreased in the double deficient mice, its expression is increased and the expression of its receptor TNF $\alpha$  too. This is enhancing osteoclastogenesis, with elevated osteoclast number in the double deficient SLRP mice. The promoted bone resorption is coupled with higher osteogenic potential and



more active osteoblasts are conditions supporting the development of subchondral bone sclerosis associated with OA [219]. The lumican controls similar functions by inhibiting osteoclastogenesis but promoting pre-osteoblast viability and differentiation *in vitro* [220,221].

### **I.5.3.2 Osteomodulin**

Osteomodulin (OMD), also known as osteoadherin, was the target of the research led in the present thesis. A detailed description of this SLRP is therefore opportune, with particular attention to its functions in skeletal tissues.

OMD is from the second class of the SLRP family and is decorated by keratan sulfate chains. It was discovered in 1995, from bovine bone extract with a concentration of 0.4mg/g of tissue wet weight. It was first associated with bone tissue and teeth, it is strongly expressed by osteoblasts and binds to them through integrin  $\alpha_v\beta_3$ . Moreover, OMD presents a large acidic patch in the C-terminal domain increasing its affinity for mineralized tissues with hydroxyapatite crystals and displays different glycosylation patterns according to the development of bone with more substitution of keratan sulfate during the initiation of the mineralization [50,222–227]. However, recent investigations demonstrated that *OMD* is expressed in other cell types and tissues such as articular chondrocytes, pre-hypertrophic chondrocytes and fibro chondrocytes; aortic arteries; brain; or even umbrella cells in bladder epithelia indicating broader functions than primarily expected [228–232]. It is noteworthy to highlight that OMD is associated with ectopic mineralization, with cardiovascular calcification [233–235].

Most of the studies performed on OMD analyzed its function on skeletal tissues and mineralization. Its expression is upregulated in the osteogenic condition/osteoblast

## ***I. BACKGROUND***

differentiation and OMD improves the osteogenic fate of cells cultured *in vitro*; it is correlated to the increased expression of *SP7* and *RUNX2*, improved ALP activity and mineralization. The silencing of OMD by shRNA confirmed its functions and showed a decreased osteogenic induction. Further, the expression of *OMD* by osteoblasts is enhanced under osteoclast activity and a mouse model with reduced osteoclastogenesis has a downregulated expression of *OMD*. It establishes a correlation between osteoblast maturation, bone remodeling and the expression of *OMD*. Mechanistically, OMD has a high affinity for BMP-2 and BMP receptors, the formation of this cluster facilitates and stabilizes the binding of BMP-2 with its receptor and activates the canonical BMP pathway leading to the promoted osteogenic profile whereas the absence of OMD induces the downregulation of the BMP pathway. Furthermore, there is a positive feedback via the BMP pathway as SMAD-4 binds to the promotor of *OMD* to stimulate its expression [195,236–241]. However, the effect of TGF- $\beta$ 1 takes the opposite path and downregulates the expression of *OMD* [242]. In parallel of leading cells to an osteogenic fate, OMD helps in the regulation of apoptosis and proliferation. The overexpression of *OMD* enhanced cell viability *in vitro* by decreasing the activity of Caspase-3/7 while its knock-down promoted apoptosis [236,243].

Concerning OA-related features, *OMD* was shown to be upregulated in BMLs, which are premonitory signs of the development of subchondral bone sclerosis [223,244]. OMD is deeply connected to the subsequent subchondral bone sclerosis, but inversely, observations from our laboratory demonstrated its protein production and gene expression downregulated by osteoblasts in monolayer culture coming from sclerotic areas of OA patients compared to non-sclerotic areas [187]. Its downregulation by osteoblasts presenting the sclerotic phenotype is consistent with the uprising activation of TGF- $\beta$ 1 in such conditions and with its previously described negative feedback on OMD [167,168,187,242]. The decreased level of OMD in

## I. BACKGROUND

subchondral bone associated with OA was validated by an independent study enrolling ten patients with primary OA. The same study showed a reduction of OMD in a rat model followed by surgically-induced OA compared to normal rats [245]. The depletion of OMD in the subchondral bone may affect its properties and increase its fragility as OMD directly binds to type I collagen to regulate fibrils formation and their diameter. OMD reduces the diameter of collagen fibrils and allows a better organization of the collagen network with fewer twisted fibrils by controlling the rate of fibril formation [246,247] (Fig 19). There is also an increased fragmentation pattern of OMD from OA patients indicating enhanced degradation of OMD. This phenomenon may promote inflammation given that OMD binds directly to factor to the complement pathway for its activation [139].

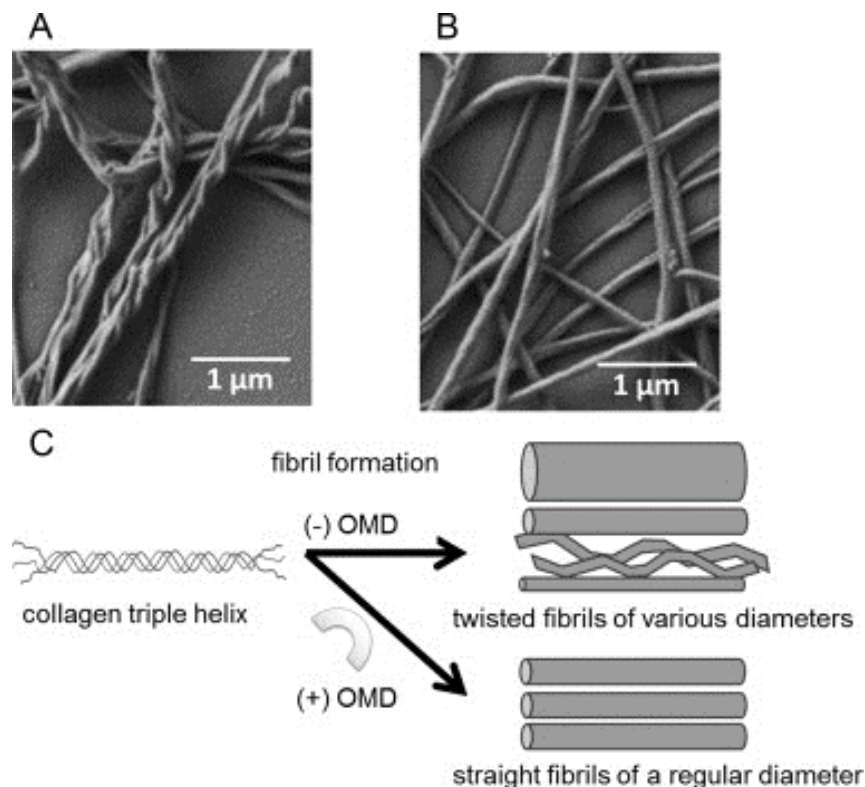


Figure 19: Effect of the binding of OMD on type I collagen. (A) Collagen without OMD. (B) Collagen with OMD. (C) Representation of the fibril formation without or with OMD leading to more various, larger and twisted fibrils or to more regular and straight fibrils respectively [246].

**I.5.4 Models for studying OA**

Either *in vitro* or *in vivo*, there is a large repertoire of models for OA, each one with its perk and inconvenient (Fig 20). The biological response of tissues can be predicted by *in vitro* models that allow to investigate research hypothesis in a simplified model. Cells from the different tissues of the joint can be used for *in vitro* monolayer culture and even 3D cultures. The study of the crosstalk between different cell types can be achieved with more complex co-culture models [248].


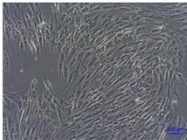







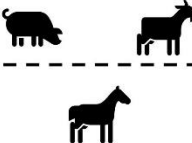

<p style="text-align: center;"></p> <p><b>Monolayer culture</b> Large cells number Low cost</p> <p><b>Co-culture</b> Cell-cell interplay</p> <p><b>3D organoid</b> Mimic <i>in vivo</i> microenvironment Cell-cell interaction Tissue like organisation Chondrocyte phenotype stabilisation</p>	<p style="text-align: center;"><b>In vitro models</b></p> <p>Monolayer culture Co-culture</p>  <p>3D culture/organoid</p> 	<p style="text-align: center;"></p> <p><b>Monolayer culture</b> Rapid dedifferentiation of chondrocytes Far from the original tissue</p> <p><b>Co-culture</b> Different growing methods</p> <p><b>3D organoid</b> Large cells number required Right scaffold need More difficult to achieve</p>
<p style="text-align: center;"></p> <p>Easy genetic manipulations, useful in OA genes studies Small, transparent embryos and juveniles High throughput drug screening Have synovial-like joints</p>	<p style="text-align: center;">Zebrafish</p> 	<p style="text-align: center;"></p> <p>Not mammals Small size of the joints Extra whole genome duplication Limited availability of antibodies</p>
<p style="text-align: center;"></p> <p>Deciphering molecular mechanisms Rapid development Low cost Availability</p> <p>Mechanism/development of OA similar to that in humans Similar cartilage characteristics No spontaneous regeneration</p>	<p style="text-align: center;"><b>In vivo models</b></p> <p>Small models</p>  <p>Large models</p> 	<p style="text-align: center;"></p> <p>Experimental OA far from human OA</p> <p>Higher cost Difficult implementation Small cohort</p> <p>High sensitivity</p>

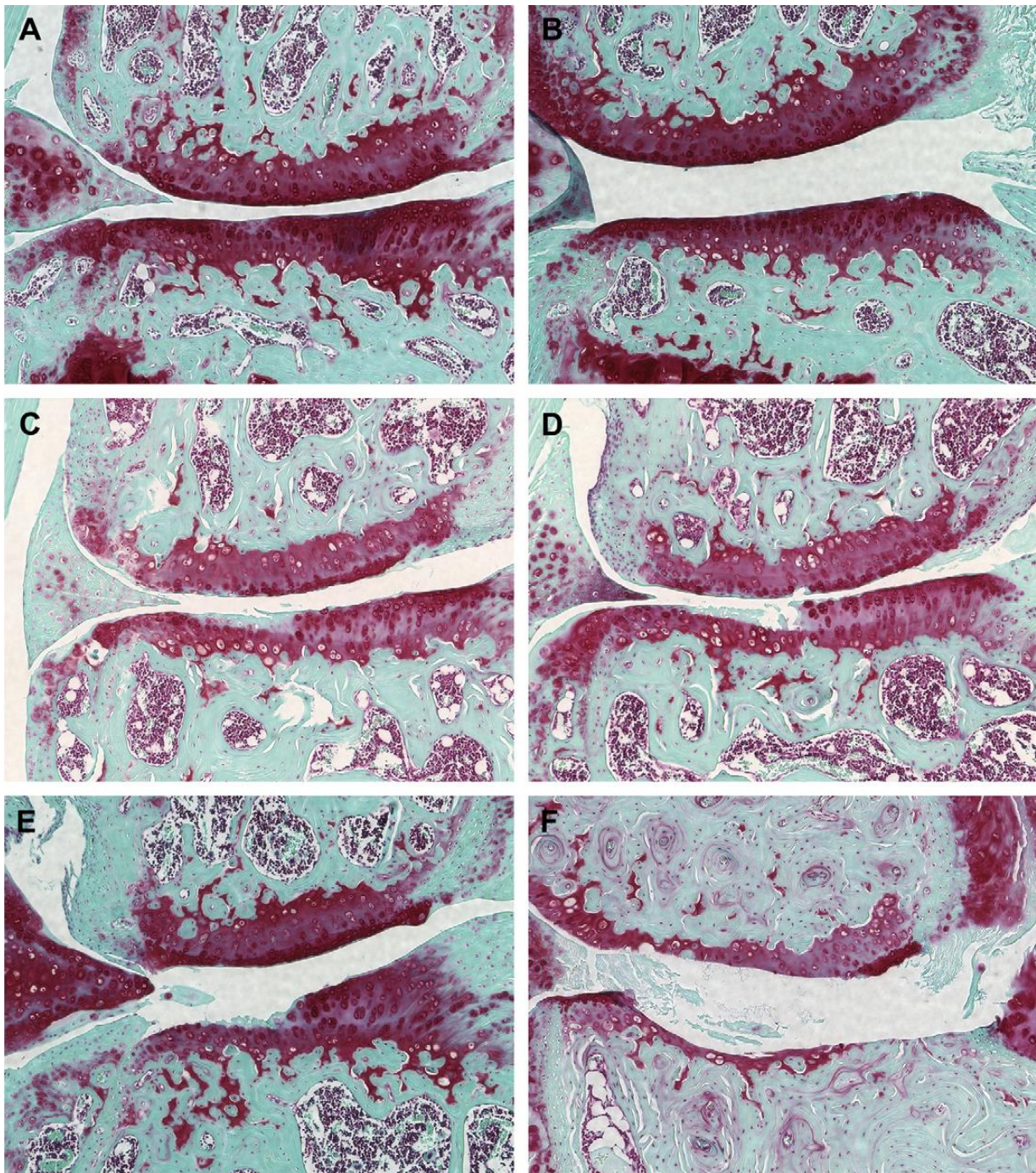
Figure 20: summary of the different models used in OA research [248].

However, animal models are useful for studying the joint morphology, the development and onset of OA. There are at least 18 different species of animal that can be used to study the physiopathology of OA including guinea pigs, mice, rats and even zebrafish which were added to the list recently [249]. For experimental studies, small animals are easier and cheaper to handle but their anatomy, histology and molecular aspects are different enough to raise the question of reliability when it comes to translate the outcome to humans. For instance, the murine cartilage thickness, of 0.03 mm on average, is 70 times smaller than in humans with 2.2 to 2.5 mm of articular cartilage thickness on average. One of the main benefits presented by the mouse model is the easier opportunity to generate genetically modified lines to study genetic disease pathways [250].

### **I.5.4.1 Mouse models**

As previously introduced, OA is a complex disorder, and it can be classified into primary or secondary OA according to the origin of the disease. In animal models, there are naturally occurring, or so-called, spontaneous OA models translating primary OA and several surgically-induced models. For instance, the destabilization of the medial meniscus (DMM) is a model for secondary OA [251].

In parallel to humans, a cartilage integrity OARSI score was designed for the murine model and divided into 6 grades (Fig 21). The grade 0 represents a healthy and intact cartilage; grade 0.5 represents a loss of proteoglycan; grade 1 has still an intact articular cartilage but with small fibrillations; grade 2 displays vertical clefts and partial loss of surface lamina; grade 3 goes approximately until 25% of the erosion of the cartilage to the calcified cartilage while grade 4 encompasses between 25 and 50% and grade 5 from 50 to 75%, the final grade 6 corresponds to the erosion extending 75% of the articular cartilage or its complete loss [252].



*Figure 21: Representation of the murine histological OARSI score with key characteristics. The medial femoral condyle can be observed at the top of the picture and the medial tibial plateau can be observed at the bottom. With the first score corresponding to the condyle and the second to the tibia, here is the attributed score for each image : (A) 0, 0.5; (B) 0, 1; (C) 0.5, 2; (D) 3, 3; (E) 0, 4; (F) 5, 6. Pictures are issued from [252].*

### **I.5.4.1.1 Spontaneous models**

Mice develop OA spontaneously with aging, which is a close equivalent to human primary OA. It was reported that the incidence of OA was increasing with age and in 16 months C57Bl/6, 80% of them were showing signs of OA. There was a loss of proteoglycan associated with defects of the Golgi apparatus [253]. The medial plateau always shows the most severe OA lesions with increased chondrocytes cell death associated with aging [254]. However, designing experiments with spontaneously occurring OA lesions in mice can appear challenging and time-consuming.

Although mice develop OA naturally, the specific STR/ort strain, derived from a serendipitous generation, offered the opportunity of a newly interesting model because of its naturally fast development of OA. Male mice display OA from 18 weeks of age. While rapidly generating OA, this strain displays cartilaginous lesions with key hallmarks such as proteoglycan loss, cartilage clefts, osteophytes and subchondral bone sclerosis. Subchondral bone sclerosis is even one of the first modifications reported in STR/ort mice. However, compared to C57Bl/6 mice, STR/ort mice have a higher bone mass for both the cortical and trabecular bone. The bone phenotype of this strain is associated with a greater osteoblast number, which are more active, impaired osteoclast function and endochondral ossification defects. Other peculiarities than bone and cartilage physiology can be reported from the STR/ort strain, namely for immune cells and their metabolism [255].

Recently, investigations on a new model of spontaneous OA in mouse was reported. Senescence-accelerated mice prone 8 (SAMP8) mouse have a fast aging process with a reduced lifespan and develops OA faster, starting to exhibit mild lesions at 14 weeks. Concerning the subchondral bone, first modifications were reported at 6 weeks with a thicker

subchondral plate and increased angiogenesis. These observations report modifications of the subchondral bone prior to the cartilage damage in the primary OA model of SAMP8 male mice [256–258].

### **I.5.4.1.2 Destabilization of the medial meniscus**

OA can be surgically induced and namely through the destabilization of the medial meniscus (DMM). This surgery allows the gradual development of OA, still resembling the human pathology. The study of OA following the DMM corresponds to the observation of post-traumatic OA. An incision is made through the skin and the patellar ligament to section the medial menisco-tibial ligament without removing the meniscus [251].

This surgery induces OA with high reproducibility. The result of the DMM surgery is dependent on the time left post-surgery to allow the progression of OA. It is also age-dependent with exacerbated severity of cartilage degradation, subchondral bone sclerosis, and osteophyte in older mice. This phenomenon could be explained by the fact that the skeleton is highly dynamic and different events occur during its development. The DMM is not only accompanied by cartilaginous lesions but also by impaired bone remodeling with elevated osteoclast number and subchondral bone sclerosis. [259,260].



### **I.5.4.2 Zebrafish Model**

Even if small mammals with mouse and rat are still the preferred models, the zebrafish gained popularity in the 80's as a model for toxicology, developmental biology, and biomedical and genetic research. It became a fashionable model due to numerous advantages reviewed in [261] and namely its easy genetic manipulation to screen numerous genes of interest. The zebrafish is a small vertebrate of freshwater and a bony fish from the Teleostei infraclass. Although being further to human than its rodent models counterparts, the zebrafish remains a very reliable model as 71.4% of human genes have at least one ortholog in the zebrafish. Furthermore, from this pool of genes, there are 82% of disease-associated genes related to at least one orthologue in the zebrafish [261,262].

Concerning bone and cartilage biology, the zebrafish presents the same skeletal development, cell types and gene expression as mammals with few exceptions (Table 8). Because of the shared similarities and the ease of genome editing, a burst of zebrafish strains emerges in order to model a vast range of skeletal disorders like osteoporosis, craniosynostosis, Ehlers-Danlos syndrome, fibrodysplasia, ossificans progressiva, osteogenesis imperfecta to name only the most famous ones. Recently, researchers have even used the zebrafish as an OA model, which is of great interest to us in the specific context of this thesis [261,263].

Table 8: Comparison of skeletal features in humans, rodents and zebrafish, adapted from [263].

<b>Skeletal feature</b>	<b>Human</b>	<b>Rodent</b>	<b>Zebrafish</b>
<b>Bone types</b>	Dermal Compact Spongy	Dermal Compact Spongy	Dermal Compact Tubular (spongy)
<b>Skeletal cell types</b>	Chondrocytes Osteoblasts Osteocytes Osteoclasts (multinucleate)	Chondrocytes Osteoblasts Osteocytes Osteoclasts (multinucleate)	Chondrocytes Osteoblasts Osteocytes Osteoclasts (multinucleate and mononucleate)
<b>Ossification types</b>	Endochondral Intramembranous Perichondral	Endochondral Intramembranous Perichondral	Endochondral Intramembranous Perichondral
<b>Development</b>	<i>In utero</i>	<i>In utero</i>	<i>In ovo</i>
<b>Average brood size</b>	n/a	6-8	100-150
<b>Mineralization begins</b>	4-5 weeks	About 2 weeks	3-4 dpf
<b>Skeletal maturity</b>	Up to 30 years	4-5 months	2-4 months
<b>Direction of loading</b>	Axial	Orthogonal	Axial
<b>Repair after fracture</b>	Yes	Yes	Yes
<b>Regeneration after amputation</b>	Limited (digit tip)	Limited (digit tip)	Yes
<b>Gene conservation (vs humans)</b>	100%	85%	75%
<b>Bone marrow</b>	Yes	Yes	No
<b>Visualization of cell dynamics of bone</b>	No	Limited (intravital imaging)	Transparency in mutants. Larval stages and fin regenerates, adult scale regeneration
<b>BMD assessment</b>	CT(fixed/live); high resolution peripheral quantitative CT (HRpQCT, fixed/live); ultrasound (live); DXA (live)	$\mu$ CT (fixed); DXA (live)	$\mu$ CT (fixed)
<b>Drug screening</b>	<i>In vitro</i>	<i>In vitro</i>	<i>In vivo</i>
<b>Ex vivo/ in vitro study of bone</b>	<i>In vitro</i> differentiation of stem cells <i>Ex vivo</i> culture of primary cells	<i>In vitro</i> differentiation of stem cells <i>Ex vivo</i> culture of primary cells	<i>Ex vivo</i> scale culture <i>Ex vivo</i> culture of primary cells

## ***I. BACKGROUND***

The zebrafish, as mammals, presents synovial lubricated joints, with the jaw joint and joints of the pectoral fin. Histology of the joint shows a complex structure with distinct layers of flattened articular chondrocytes, and with hypertrophic chondrocytes located beneath the articular surface. The articular cartilage is itself laying on the subchondral bone (Fig 22 A, B). The synovial joint of the zebrafish expresses the different markers found in mammals, such as aggrecan, type II collagen, type X collagen and lubricin. The expression of those markers conserves their spatial features between the superficial and deeper layers of the cartilage. A single-cell analysis confirmed the distinct characteristics of the different cartilage layers. Interestingly, the expression of lubricin was proven to be essential for the maintenance of the cartilage with mutants showing cartilage degeneration resembling OA. The shared OA features encouraged researchers to develop a translational OARSI score (Fig 22C) [264,265]. Several genes associated with OA were characterized in the zebrafish, as well as transgenic lines marking chondrocytes at different maturation stages, establishing the zebrafish as a new excellent model for OA [266–268].

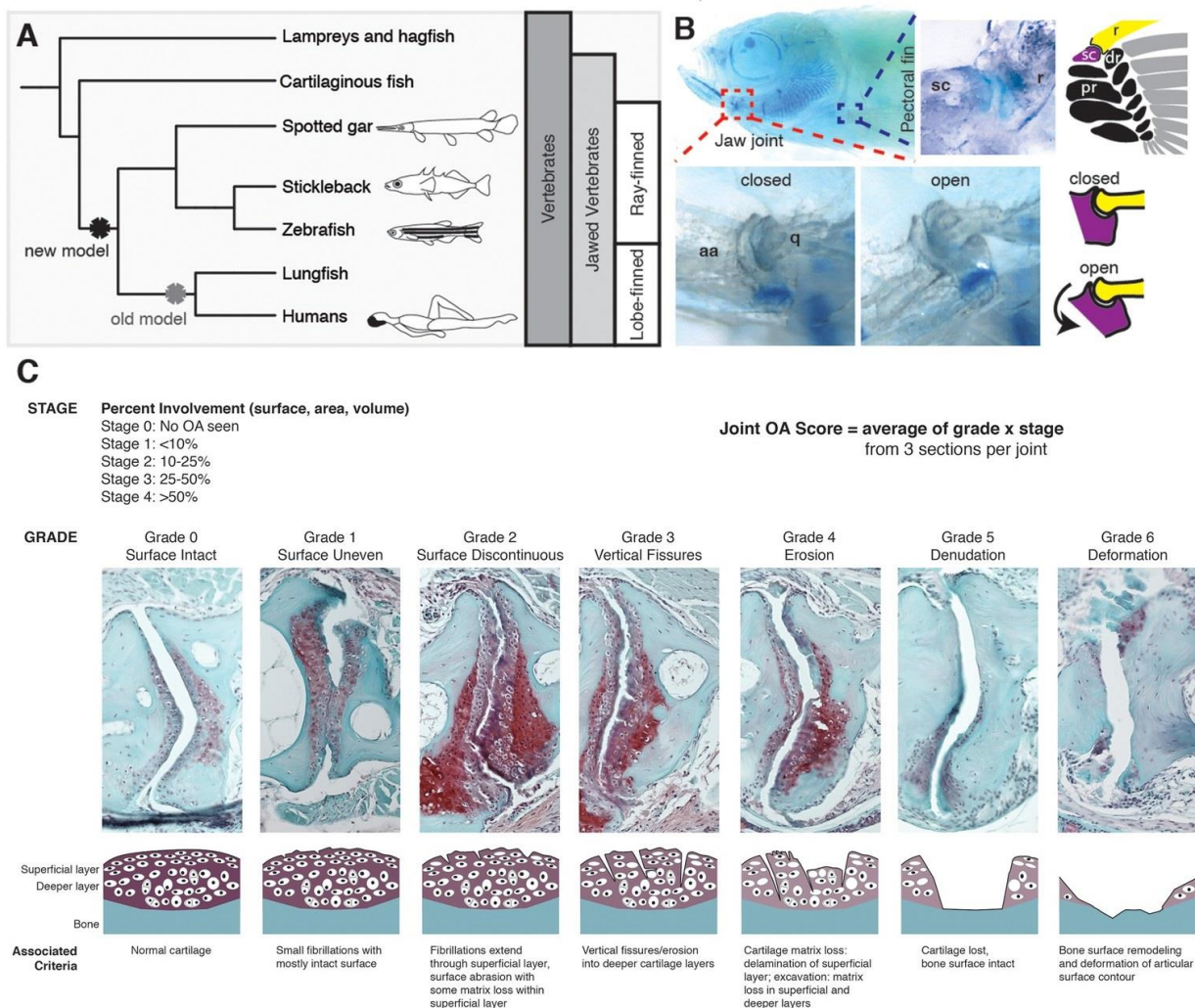


Figure 22: (A) Revised phylogenetic tree replacing the synovial joint apparition (black asterisk) in a common ancestor of all bony vertebrates instead of the old model placing it with lungfish and tetrapods (grey asterisk). (B) Head of the zebrafish stained with Alcian blue with a focus on the jaw joint and pectoral fin joints. aa: anguloarticular; q: quadrate; sc: scapula; r: ray; pr: proximal radial; dr: distal radial. (C) Representation of the zebrafish histological OARSI score with key characteristics for the jaw joint. Grade 0: the surface of the cartilage is intact; grade 1: the cartilage is still intact but the surface is uneven with small fibrillations; grade 2: there are deeper fibrillations, matrix loss and surface abrasion; grade 3: there are vertical clefts extending to the deeper cartilage layers; grade 4: erosion of the superficial layer of the cartilage; grade 5: denudation of the cartilage with the subchondral bone surface being exposed; grade 6: the subchondral bone surface is exposed and deformed. Illustration adapted from [264].

## ***I. BACKGROUND***

In parallel to surgically-induced OA in rodents, a surgery sectioning the interopercular–mandibular ligament was developed in the zebrafish. It induces joint destabilization followed by articular cartilage degeneration of the jaw joint. The OARSI score was attributed to injured jaw joints compared to uninjured ones for 1-year-old fish, showing a significant increase of the histological score 14 days post-surgery. The zebrafish, being a highly regenerative organism, showed complete recovery of the OA lesions by 28 and 42 weeks post-surgery [265]. In contrast to mammals with low to inexistent regenerative capacities, the zebrafish, with full regeneration of the articular cartilage after induced OA, opens new perspectives of research and offers unique advantages to explore cartilage regeneration/repair mechanisms.

Another specificity of the zebrafish, and other bony fish, is their exoskeleton composed of elasmoid scales, being part of the dermal skeleton. Elasmoid scales are mainly made of an outer calcified layer encapsulating type I collagen fibrils, and they are covered by osteoblasts and osteoclasts. Transcriptomic analysis showed their strong osteogenic expression and studies reported them as a valuable model for basic bone biology, skeletal diseases, bone remodeling and bone repair mechanisms. Elasmoid scales can be plucked to study regenerative abilities *in vivo* or to use them in *ex vivo* culture [261,263,269–271].

## **II. OBJECTIVE & STUDY DESIGN**

## ***II. OBJECTIVE & STUDY DESIGN***

My host laboratory, the musculoSkeletal Innovative research Lab (mSKIL), has acquired expertise in the field OA and namely has investigated on the bone-driven phenotype of OA by focusing on the subchondral bone and its osteoblasts. Previous observations reported the specific phenotype of osteoblasts from sclerotic and neighboring non-sclerotic areas of OA patients. The secretome analysis displayed a different proteomic signature associated with the sclerotic phenotype of osteoblasts. OMD showed the greatest diminution of secretion in the supernatant of sclerotic osteoblasts and its gene expression was also downregulated. The quantification of OMD by western blot on human serum confirmed its reduction in OA patients as well as the reduction of its minor fragmented forms. Further, the competitive Elisa assay against OMD in human serum in 22 healthy persons and 22 severe OA patients supported the decreased OMD level in OA patients, indicating the strong correlation between OMD and the disease [187].

OMD was selected as an interesting target to explore in OA and more precisely in bone-driven OA. However, the challenge had to be tackled almost from scratch as very few information had been gathered on OMD and its functions. The extent of our knowledge was very poor, and it is even more graphic to represent the number of annual publications on OMD (Fig 23). Therefore, I had the opportunity to study OMD from its fundamental aspects and to uncover its function on bone and cartilage.

Our hypothesis was that OMD is strongly correlated to OA and was an active player in its development. As OMD was mostly associated with mineralized tissues and more precisely with bone, it would safeguard the bone structure and homeostasis of the ECM. With the concept of phenotypes/endotypes of OA in mind, this work could set OMD as a factor part of the “bone-driven” OA phenotype. Its downregulation and/or absence might lead to

## II. OBJECTIVE & STUDY DESIGN

subchondral bone sclerosis and promote OA. Until now, it remains unclear how OMD could affect the joint. Besides, the functions of OMD were never been studied *in vivo*, leaving a blank canvas to investigate. To answer these questions, I used different models, murine-zebrafish-*in vitro* primary cultures, taking advantage of their specificities. For *in vivo* models, the functions of OMD were explored through a loss of function and gain of function in order to be as complete as possible. In this manuscript the mutant loss of function in the mouse model is referred to as “KO mouse” and the overexpressing line as “UP mouse”.

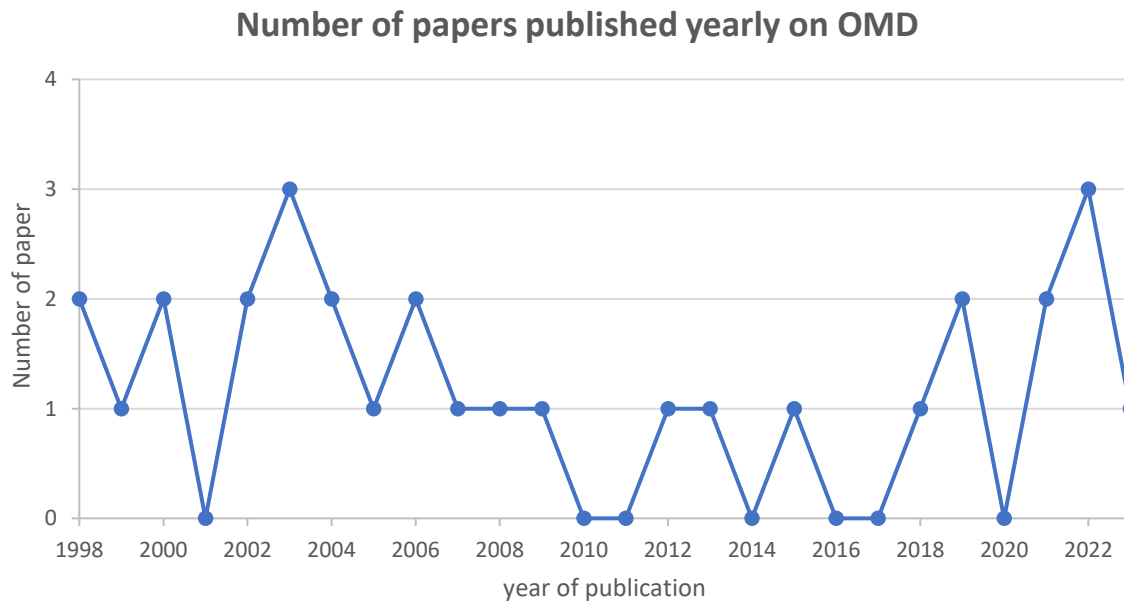


Figure 23: Number of papers with “Osteomodulin” or “Osteoadherin” in their title published by year. The research was performed on Pubmed in February 2023.



# **III. MATERIAL & METHODS**

#### **III.1 Mouse strains and housing**

The mutant mouse strain deficient for *Omd* used for this research project, C57BL/6 *Omd*<sup>tm1Lex</sup>/*Mmucd*, RRID: MMRRC\_011749-UCD, was obtained from the Mutant Mouse Resource and Research Center (MMRRC) at the University of California at Davis, an NIH-funded strain repository, and was donated to the MMRRC by Lexicon Genetics Incorporated. The mutation targeted the coding exons 1 and 2 by homologous recombination. The genotyping protocol from MMRRC was applied. The overexpressing mouse strain for *Omd* used for this research project, C57BL/6 *Tg(Bglap-Omd)1Kieg*, EMMA ID EM:02120, was obtained from the European Mouse Mutant Archive (EMMA), a repository supported by the national research programs and by the EC's Research and Innovation programme Horizon 2020. The transgenic line expressed *Omd* under the osteocalcin promoter in addition to its natural expression, hence *Omd* overexpression is only osteoblast specific. Strains were crossed with the wild-type (WT) C57BL/6 to maintain the line. Transgenic, WT, and mutant mice were maintained on a 12-hour-light/dark cycle with food and water supplied *ad libitum* in rooms maintained at 18-24°C; with humidity levels maintained at 45-65% and cardboard houses being replaced every week for their enrichment. To ease the nomenclature in the paper, we refer to the *Omd* deficient mice as “KO” and to the *Tg(Bglap-Omd)* as “UP”. The ethical committee of the University of Liège approved all experimental procedures (reference no. 19-2090).

#### **III.2 Mouse model of OA**

Post-traumatic OA was induced by DMM on UP, WT, and KO strains at 16 weeks, only on male mice. The surgical transection of the medial menisco-tibial ligament of the right knee was performed to induce mild instability of the knee [251]. The mice were euthanized 12 weeks

### **III. MATERIAL & METHODS**

after surgery and their knees were histologically analyzed. For spontaneous OA, UP, WT, and KO mice were euthanized at 16 months and their knees were histologically analyzed.

*Remark concerning the experimental design:*

*The surgical model including only male mice requires an aside on sex-inclusivity in biomedical research. A main concern raised by the NIH, from the notice number NOT-OD-15-102, is the integration of the consideration of key biological variables, such as sex, to improve the global quality of biomedical research. Most of the preclinical research reported their studies from male animals, omitting the observation of females while observations from both sexes is crucial to turn discoveries into health opportunities. This problematic results in a biased perspective for the understanding of mechanisms or diseases affecting both sexes. Therefore, the NIH encourages researchers to improve their experimental design by the addition of female animals in their research strategy or to provide justifications to study only one sex when applicable. Since the NIH reformed its grant policy in 2016 taking into account sex as a biological variable, there was an improvement toward the inclusivity of both sexes [272]. Following the NIH recommendations, both sexes were studied to characterize the functions of Omd, except for the DMM model. This experimental strategy was motivated by much more moderate OA lesions developed by female mice in this surgical model [259] which was not meeting our expectation to observe severe OA development.*

#### **III.3 Knee joint histology and histomorphometry**

Knee joints of the mice, at 4, 8, 16 months, and 28 weeks from the DMM model, were fixed for 24 hours in 4% paraformaldehyde (PFA) at 4°C, followed by decalcification in hydrochloric acid (DC2 medium; Labonord) for 2 hours and 30 minutes at 4 °C then washed in milliQ water

### III. MATERIAL & METHODS

overnight at 4°C before embedding in paraffin. Coronal sections of 5 µm were cut within the central area with 3 sections of at least 80 µm apart selected for the analysis with the Safranin-O Fast-Green staining (Table 9). An additional central section was used for the Toluidine Blue staining (Table 10). Each compartment of the knee joint was scored by two readers following OARSI guidelines for the mouse model as described in [252] and the mean score from the 3 sections was calculated (Table 11, 12).

Table 9: Safranin-O Fast-Green staining.

Solutions	Timing (min)
Safesolv	15
Safesolv	1
Methanol 100%	1
Methanol 95%	1
Methanol 70%	1
Methanol 50%	2
Methanol 30%	2
MilliQ water	2
Ehrlich Hematoxylin	15
MilliQ water	30 sec
MilliQ water	30 sec
Methanol 30%	2
Methanol 50%	2
Methanol 70%	2
Methanol 70% - HCl 1%	30 sec
Methanol 70%	2
Methanol 70% NH <sub>4</sub> OH 1%	4
Methanol 70%	2
MilliQ water	2
Fast-Green 0,165%	30 sec
Acetic acid 1%	5 sec
Safranin-O 0,05% - Ammonium acetate 0.1M	4
Methanol 100%	1
Methanol 100%	1
Safesolv	2
<b>Mounting with Safemount</b>	

### III. MATERIAL & METHODS

Table 10: Toluidine Blue staining.

Solutions	Timing (min)
Safesolv	15
Safesolv	1
Methanol 100%	1
Methanol 95%	1
Methanol 70%	1
Methanol 50%	1
MilliQ water	2
Toluidine Blue 0.04%	10
MilliQ water	10 sec
MilliQ water	10 sec
MilliQ water	5
<b>Drying</b>	
Safesolv	5
<b>Mounting with Safemount</b>	

Table 11: OARSI guidelines for histological scoring, with Safranin-O Fast-Green staining, of murine OA modifications.

OARSI guidelines	
Score	OA cartilage damage (Safranin-O Fast-Green)
0	Normal
0.5	Loss of Safranin-O without structural changes
1	Small fibrillations without loss of cartilage
2	Vertical clefts down to the layer immediately below the superficial layer and some loss of surface lamina
3	Vertical clefts/erosion to the calcified cartilage extending to <25% of the articular surface
4	Vertical clefts/erosion to the calcified cartilage extending to 25-50% of the articular surface
5	Vertical clefts/erosion to the calcified cartilage extending to 50-75% of the articular surface
6	Vertical clefts/erosion to the calcified cartilage extending >75% of the articular surface

### III. MATERIAL & METHODS

Table 12: OARSI guidelines for histological scoring, with Toluidine Blue staining, of murine loss of proteoglycan associated with OA.

OARSI guidelines	
Score	Loss of cartilage proteoglycan (Toluidine Blue)
0	Normal staining of non-calcified cartilage
1	Decreased but not complete loss of Toluidine Blue staining over 1-100% of the articular surface
2	Complete loss of Toluidine Blue staining in the non-calcified cartilage extending to <25% of the articular surface
3	Complete loss of Toluidine Blue staining in the non-calcified cartilage extending to 25-50% of the articular surface
4	Complete loss of Toluidine Blue staining in the non-calcified cartilage extending to 50-75% of the articular surface
5	Complete loss of Toluidine Blue staining in the non-calcified cartilage extending to >75% of the articular surface

Histomorphometry of the sections was performed with the software QuPath version 0.3.2 [273]. The sections were photographed at 10X magnification and high resolution. The cartilage histomorphometry analysis was performed on the section stained with Toluidine Blue. The total cartilage, the calcified cartilage, the plate length, and the growth plate area were measured. For the growth plate, the area was measured inside a consistent circle of a fixed size under the articular plateau. The subchondral bone area analysis was performed on the 3 sections stained with the Safranin-O Fast-Green. The bone area was measured under the tibial plateau according to its length and the bone marrow area was removed. The measured regions of interest (ROI) are explained in the figure 24.

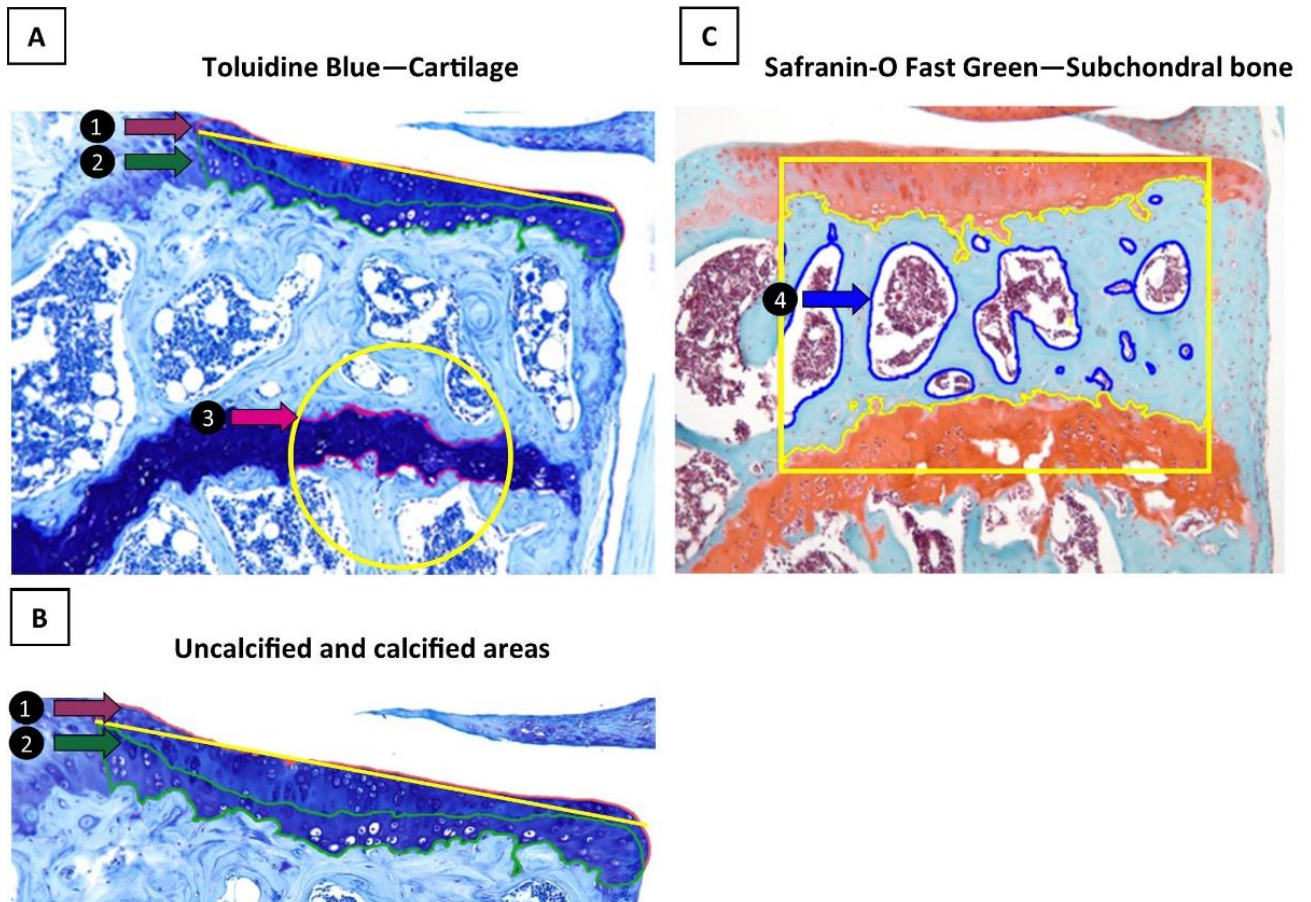


Figure 24: Illustration of the ROI measured with QuPath for the histomorphometry analysis. (A, B) Toluidine Blue staining was used for uncalcified (1) and calcified (2) cartilage measurements. The yellow line was drawn to measure the plate length. Inside the yellow circle, the area of the growth plate was defined (3). (C) The Safranin-O Fast Green was used to measure the subchondral bone volume. The subchondral bone volume was measured inside the yellow box and calculated using the formula  $TV - (\text{Bone marrow volume (4)} + \text{cartilage volume})$ .

The scripts generated for the histomorphometry analysis using QuPath are deposited in GitHub and publicly accessible for the cartilage (Toluidine Blue) and the bone (Safranin-O Fast Green) analysis respectively at:

- <https://doi.org/10.5281/zenodo.7898818>
- <https://doi.org/10.5281/zenodo.7899774>.

#### **III.4 Immunohistochemistry**

Epitope retrieval was performed using the chondroitinase ABC (50 units/mL, Sigma-Aldrich) in 60mM sodium acetate and 100mM Tris (pH 8) for 30 min at 37°C. Animal-Free Blocking Solution (Cell Signaling Technology, dilution 5X) was used to block the sections before overnight incubation with the primary polyclonal goat antibodies anti-mouse OMD (R&D systems, AF3308, 0.8 µg/mL) in Antibody diluent (Dako, S2022). The sections were then incubated for 30 minutes with the secondary polyclonal rabbit antibody anti-goat coupled with horseradish peroxidase (HRP) (DakoP0449, dilution 1:400) diluted in Antibody diluent. The revelation of the secondary antibody was determined by using DAB (Cell Signaling Technology, 8059) for 2 minutes. Sections were counterstained by the Hematoxyline of Carazzi (Sigma-Aldrich) for 4 minutes.

#### **III.5 Micro-computed tomography (µCT) and image analysis**

Tibiae and femurs from mice were dislocated and fixed for 24 hours in 4% PFA at 4°C and transferred into phosphate-buffered saline (PBS) for storage, at 4°C. Samples were imaged using the Phoenix NanoTom M (GE Measurement and Control Solutions, Germany) (Fig 25). A target of diamond was applied, and scans were operated at a voltage of 60 kV and a current of 170 µA, voxel size of 3 µm and 10 µm for the tibia and the femur respectively. A filter of aluminum of 0.2 mm was used to reduce beam hardening during the acquisition. The exposure time was 500 ms, and 1800 images were acquired over 360° using the fast scan mode (frame averaging = 1; image skip = 0). During reconstruction (Datos|x, GE Measurement, and Control Solutions), we applied a beam hardening correction of 8. After reconstruction, scans were oriented in the same plane, using DataViewer (Bruker MicroCT, Kontich, Belgium). Images were analyzed using CTAn (Bruker MicroCT, Kontich, Belgium).





Figure 25: Photography of the Phoenix NanoTom M with its 180 kV/20 W ultra-high performance nanofocus X-ray tube from the KULeuven (source: <https://kuleuven.xct.be/ge-nanotom-m>).

For the tibial trabecular architecture, we selected 150 images (450  $\mu\text{m}$  height) starting at 30  $\mu\text{m}$  below the growth plate level. Using 3D analysis, the trabecular bone volume (BV), total ROI volume (TV), number of trabeculae, porosity, trabecular separation, and the structure model index (SMI) were calculated. For the cortical architecture, we selected 100 images (300  $\mu\text{m}$  height) starting at 1500  $\mu\text{m}$  below the growth plate level and corresponding to the mid-shaft. Using 3D analysis, the BV, TV, cortical thickness, porosity and tibial crest length were calculated. 3D visualization was performed using CTVox (Bruker MicroCT, Kontich, Belgium). The subchondral bone of the tibia, showing a coronal view of the medial and lateral plateaus, was also visualized in 3D using CTVox and a 2D visualization was generated using DataViewer.

For the femur, the whole bone was scanned with a voxel size of 10  $\mu\text{m}$  and BMD was obtained from  $\text{Al}_2\text{O}_3$  (3.85  $\text{g}/\text{cm}^3$ ) and borosilicate (2.23  $\text{g}/\text{cm}^3$ )  $\mu\text{CT}$  phantoms. For the femoral trabecular architecture, we selected 50 images (500  $\mu\text{m}$  height) starting below the growth

### III. MATERIAL & METHODS

plate level. Using 3D analysis, the BV, TV, number of trabeculae, porosity, and trabecular separation were calculated. For the cortical architecture, we selected 100 images (1000  $\mu\text{m}$  height) at the mid-shaft. Using 3D analysis, the BV, TV, cortical thickness, and porosity. For the femoral head, the whole region was assessed and the trabecular BV, TV, number of trabeculae, porosity, and the trabecular separation were calculated by 3D analysis. 3D visualization was performed using CTVox (Bruker MicroCT, Kontich, Belgium).

Concerning the porosity parameter, bone is a naturally porous material, and the volume of all open and closed pores was measured as a percent of the total VOI volume. With a voxel size of 3  $\mu\text{m}$ , the porosity is addressing the bone vasculature while it is unlikely taking the lacunar-canalicular porosity into account, and the osteocyte network, with lacunae ranging roughly around 10  $\mu\text{m}$  [274], cannot be analyzed with confidence above a 1  $\mu\text{m}$  resolution (Bruker personal communication). A schematic representation of the  $\mu\text{CT}$  analysis design is represented in figure 26.

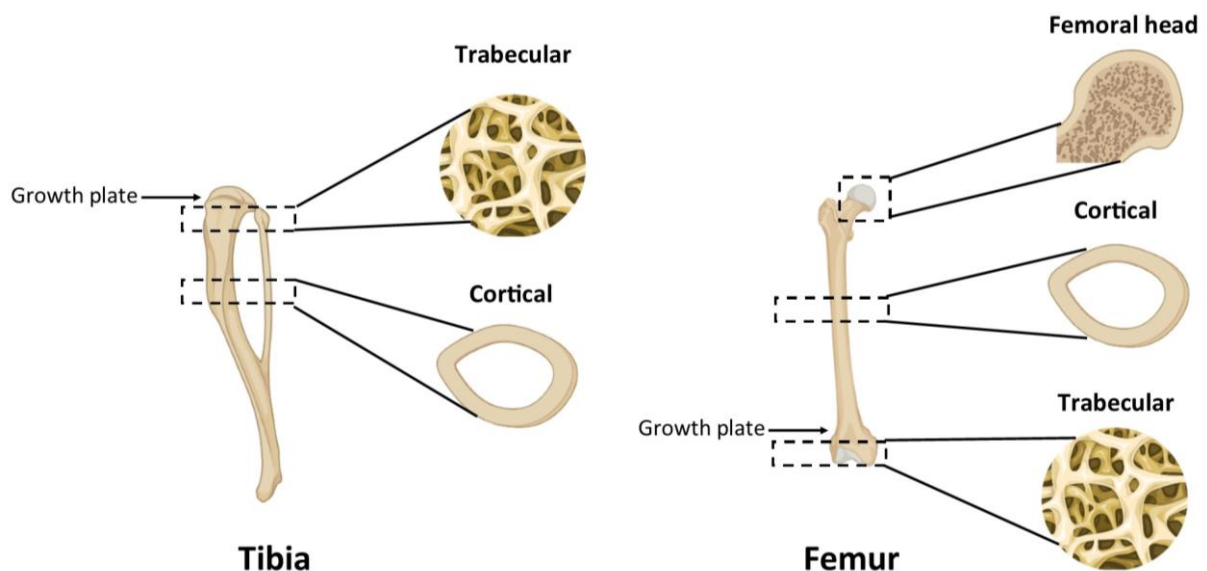
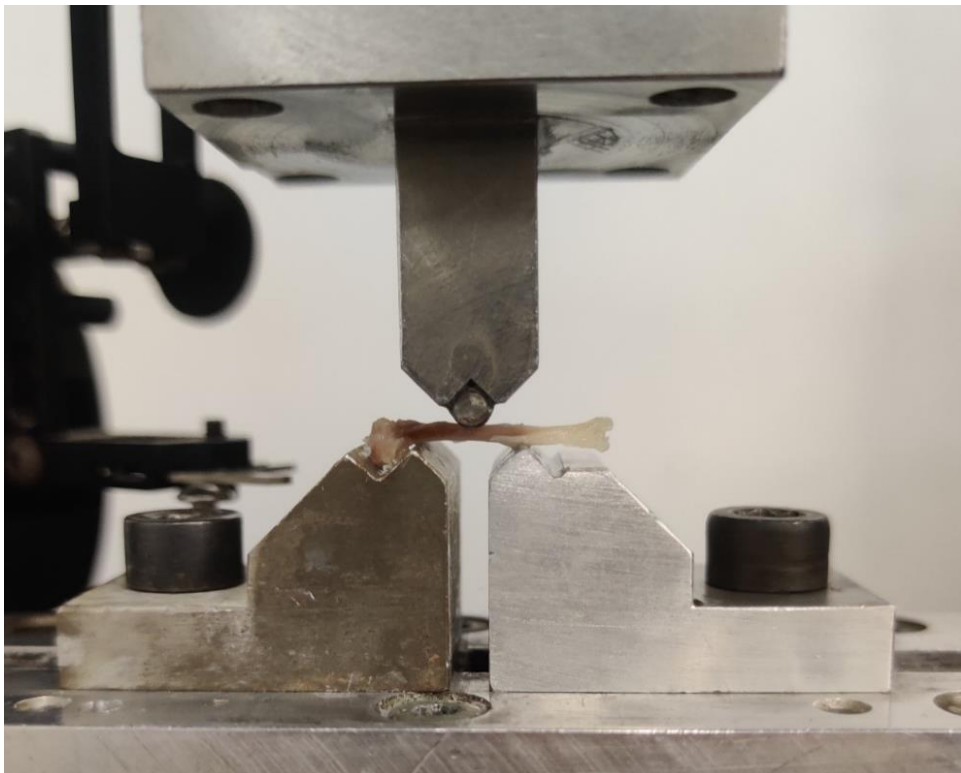


Figure 26: Schematic representation of the distinct areas used for the analysis of the tibia (voxel size=3 $\mu\text{m}$ ) and for the femur (voxel size=10  $\mu\text{m}$ ). For the tibia, the 3D analysis was performed on 150 images for the trabecular bone and on 100 images for the cortical bone. For the femur, the 3D analysis was performed on 50 images for the trabecular bone, on 100 images for the cortical bone and on the whole area for the femoral head. Figure designed by Jérémie Zappia with Biorender.

#### **III.6 Mechanical testing**

The biomechanical properties of the tibia of 16 months mice were determined using a three-point bending test in an Instron 5565 tensile testing machine (Fig 27). Tibiae were stored in PBS, and the remaining soft tissues and fibulae were carefully removed. The samples were assessed at room temperature on a special holding device on their anteroposterior axis. Force was applied on the midpoint of the tibia diaphysis with a 100 N load cell, at 8 mm separation (span length) with a perpendicular constant speed of 0.05 mm/s and with a preload of 1 N, until it fractured. From the load-deformation curve, the values for the maximal load (N) and stiffness (N/mm) were obtained. The stiffness was calculated as the slope of the initial linear uploading portion of the curves [275].



*Figure 27: Photography of the Instron 5565 tensile testing machine (from MaJEB sprl) with a tibia disposed to endure the three-point bending assay.*

#### III.7 CatWalk XT

The gait analysis of the mice was performed using the CatWalk XT System (Noldus, Netherlands; software version XT 10.5) (Fig 28). The CatWalk XT platform was placed in a dark and silent environment to enhance the quality of the recording and reduce animal stress. The walkway consists of a glass plate suspended above a camera and narrowed by two perpendicular black panels defining a passage for the mouse. A green LED light, situated at the edge, lights up the glass platform of the walkway and the light refracted correlates with the contact intensity of the paw. The ceiling possesses a red LED light contrasting the body of the mouse.

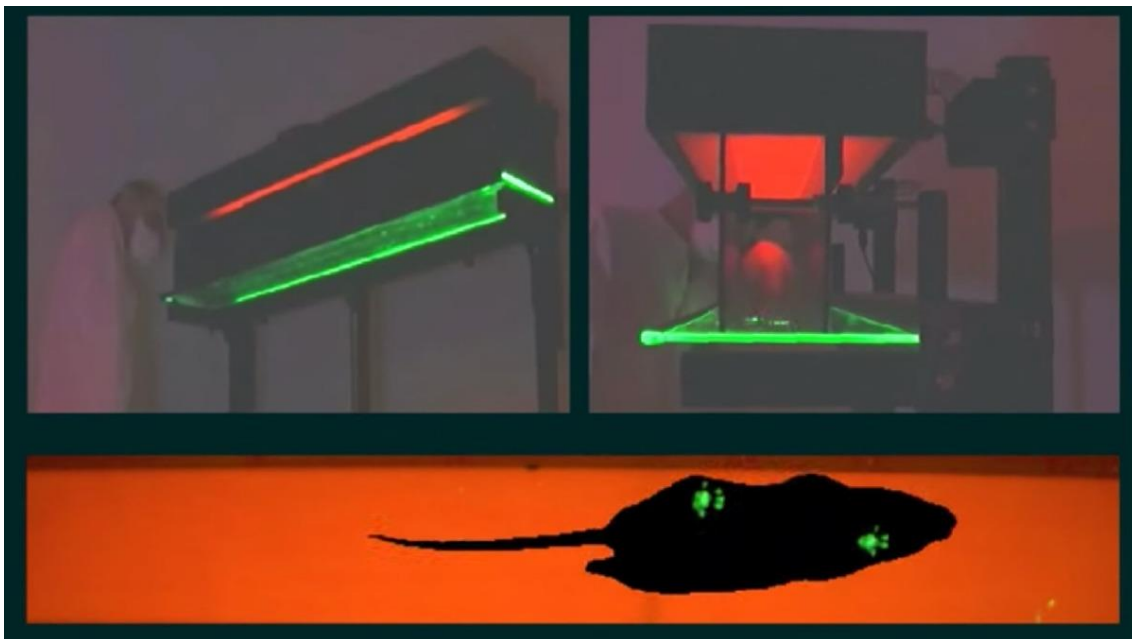


Figure 28: Illustration of the Catwalk XT device with the illuminated glass platform and with illuminated paws of a rodent, photography from <https://www.noldus.com/catwalk-xt/resources>.

The Catwalk XT was calibrated before the beginning of every session. The same detection settings were used for each mouse: camera gain of 18.99 dB, green intensity threshold of 0.1, detection threshold of 0.1 a.U, red ceiling light of 17.2 V, and green walkway light of 16.5 V. The setting were optimized for mice allowing consistent recording and gait parameters

### III. MATERIAL & METHODS

evaluation. The gait was recorded, and the CatWalk XT software automatically labeled the footprint and generated the various associated gait parameters for the compliant runs (Fig 29). A compliant run was defined as a run where the mouse did not stop while going through the walkway with at least 12 footprints, the maximum variation was set at 60% and the speed was comprised between 10 and 45 cm/s. These criteria were selected in order to minimize the variation between the run of each mouse. At least 3 runs for each mouse were recorded and the data represent the mean value. The data of the left and right paws were pooled for the front and hind paws to simplify the run parameter visualization (except for the DMM model where only the values from the right paws, correlating to the side of the surgery, were reported). Thus, the value for the front and hind paws represent the average of 6 different values. Every run was manually checked and corrected if needed.

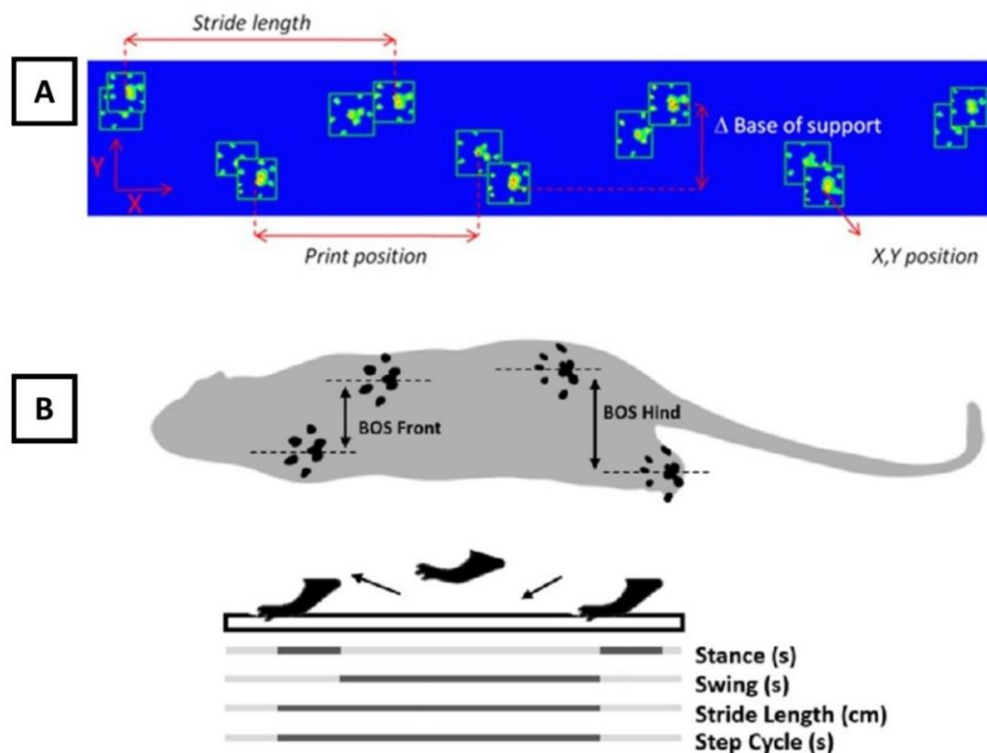


Figure 29: (A) Illustration of a compliant runway from the Catwalk XT with marks showing the stride length, print position and base of support, illustration from <https://www.noldus.com/blog/automated-gait-analysis> (B) Schematic representation of a rodent body with marks showing the base of support of front and hind paws and with the graphical representation of stance (s), swing (s), stride length (cm), and step cycle (s), figure adapted from [276].

### **III. MATERIAL & METHODS**

After the classification of the paw print, the following parameters were reported (definition from the manual of instruction of the Catwalk XT):

- Base of support: Indicates the average width between the contralateral paws. It is expressed in cm.
- Initial dual stance: The duration (in seconds) of ground contact for both contralateral paws simultaneously.
- Max contact area: Indicates the maximum area of a paw that comes into contact with the glass plate. It is expressed in cm<sup>2</sup>
- Max contact mean intensity (referred to as intensity): Describes the mean intensity of a paw at maximum contact.
- Print area: Indicates the area of the complete print (not only at Max contact but for all frames that make up a stance). It is expressed in cm<sup>2</sup>.
- Stand: Indicates the duration of the stance phase. It is expressed in seconds.
- Stand index: Indicates the speed with which the paw loses contact with the glass plate.
- Swing: Indicates the duration of the absence of paw contact toward the walkway between two consecutive steps. It is expressed in seconds.
- Stride length: Indicates the distance between successive placements of the same paw. It is expressed in cm.
- Step cycle (s): Indicates the time in seconds between two consecutive initial contacts of the same paw.
- Swing speed: Indicates the speed of a swing. It is computed from stride length and swing duration. It is expressed in cm/seconds.

- Terminal Dual Stance: Indicates the second step in a step cycle of a hind paw that the contralateral hind paw also makes contact with the glass plate.

#### **III.8 Zebrafish husbandry and strains**

Zebrafish (*Danio rerio*) were raised in standard conditions, in a recirculating system from Techniplast (Buguggiate, Italy). The temperature and characteristics of the water were controlled as follows: pH=7.4, nitrates ( $\text{NO}_3^{2-}$ ) <50 mg/L, nitrites ( $\text{NO}_2^-$ ) <0.8 mg/L, ammonium ( $\text{NH}_3$ ) <2 mg/L, carbonate hardness (KH) 3-10°KH, total hardness (GH) 6-16°GH, and temperature=28 °C. The light cycle was controlled with 14h of light and 10h in the dark. Fish were fed twice daily with dry powder (ZM fish food<sup>®</sup>, Zebrafish Management Ltd, Winchester, UK) with size of the powder adapted to their age, and once daily with fresh nauplii from *Artemia salina* (ZM fish food<sup>®</sup>) and larvae aged less than 14 days were also fed twice daily with a live paramecia culture. Embryos are reared in E3 medium (5 mM NaCl, 0.17 mM KCl, 0.33 mM  $\text{CaCl}_2$ , 0.33 mM  $\text{MgSO}_4$ , and 0.00001% methylene blue) in Petri dishes at 28°C and they are fed with paramecia starting from 5 days post fertilization (dpf).

Mutant lines deficient for *omd* were generated using CRISPR-Cas9 mutagenesis with the guide RNA 5'-CAA-GAG-CTG-CGC-CAA-TG-TCA-3'. The gRNAs targeting *omd* were incubated with Cas9 protein (Thermo Fisher Scientific) before microinjections into 1-cell stage zygotes. The mutation targeted the START codon. The reporter line used to visualize osteoclasts is the transgenic line *TgBAC(ctsk:Citrine)* and was kindly provided by Prof. Stefan Schulte-Merker. The ethical committee of the University of Liège approved all experimental procedures (references no. 16-1961 and 19-2133).

#### **III.9 Alcian blue staining in the Zebrafish**

Zebrafish larvae were fixed with 4% PFA during 2 hours at room temperature. and rinsed with PBS-Tween (PBST) for 10 minutes three times. The staining is carried out using an Alcian blue solution (0.04% Alcian Blue, 10 mM MgCl<sub>2</sub>, 80% ethanol) for 18 hours with gentle stirring. In order to remove nonspecific staining, larvae were washed with a solution of 80% ethanol, 10 mM MgCl<sub>2</sub> during 3 days under gentle agitation. Following the staining step, larvae were rehydrated by passing them successively in 5 minutes baths of decreasing ethanol concentration (80%-50%-25%-water). Natural pigmentation of the larvae was bleached out with a solution of hydrogen peroxide/potassium hydroxide (H<sub>2</sub>O<sub>2</sub> 3%, KOH 0.5%) for 20 to 60 minutes. Larvae are then rinsed with a 25% glycerol solution (25% glycerol, 0.1% KOH) during 10 minutes three times and lastly for 30 minutes. Then, one wash of 10 min is carried out with a 50% glycerol solution (50% glycerol, KOH 0.1%), and finally, larvae are stored at 4°C and protected from light.

#### **III.10 Alizarin red staining in the Zebrafish**

Zebrafish larvae were fixed with 4% PFA during 2 hours at room temperature. and rinsed with PBST for 10 minutes three times. The embryos (10-50/ependorf tube) at the desired stage must have been suitably euthanized and fixed with 4% PFA. Natural pigmentation is directly removed with a solution of hydrogen peroxide/potassium hydroxide (H<sub>2</sub>O<sub>2</sub> 3%, KOH 0.5%) for 20 to 60 minutes. Larvae are then rinsed with a 25% glycerol solution (25% glycerol, 0.1% KOH) during 10 minutes three times and lastly for 30 minutes. The staining is carried out with a 0.05% Alizarin red S (Sigma Aldrich) solution for 30 minutes with gentle shaking and protected from light. Larvae are then rinsed with 50% glycerol (50% glycerol, 0.1% KOH) during 10 minutes twice, stored at 4°C and protected from light.



#### III.11 Injection of mRNA of *omd* in the Zebrafish

For *omd* overexpression, zebrafish *omd* mRNA and *GFP* mRNA, serving as a control, were microinjected into 1-cell stage zygotes. The following primers were used to generate the *omd* mRNA: forward 5'-CGA GAG AGA TAT TCA ATC CCA CAG-3' and reverse 5'-TCA ACC AAC AAG GAA TGG AAG-3'. The T7 promoter sequence for *in vitro* mRNA synthesis with the kit mMessage mMACHINE®T7 Ultra (Invitrogen) was added afterward with a nested PCR- using the forward primer : 5'-GCG AAT TGT AAT ACG ACT CAC TAT AGG GCC ACC ATG ACA TTG GCG CAG-3'. The *GFP* mRNA was synthesized with the kit mMessage mMACHINE®SP6 Ultra from the linearized pCS2 plasmid containing the coding sequence of the GFP. The yielded mRNAs were purified with the kit AllPrep DNA/RNA Mini (QIAGEN) and quantified with the Nanodrop. Fertilized eggs were injected with either 0.4 ng or 0.8 ng of mRNA in combination with 1.6 U/ $\mu$ L of rRNasin and 0.5% of rhodamine dextran allowing to control the correct injection of larvae thanks to its red fluorescence (Fig 30). Phenotypic characterization was performed at 24-hour post fertilization (hpf) and 4-dpf. At 4-dpf, the larvae were fixed with 4% PFA overnight at 4°C and then stained with Alcian blue as described in the section III.9.

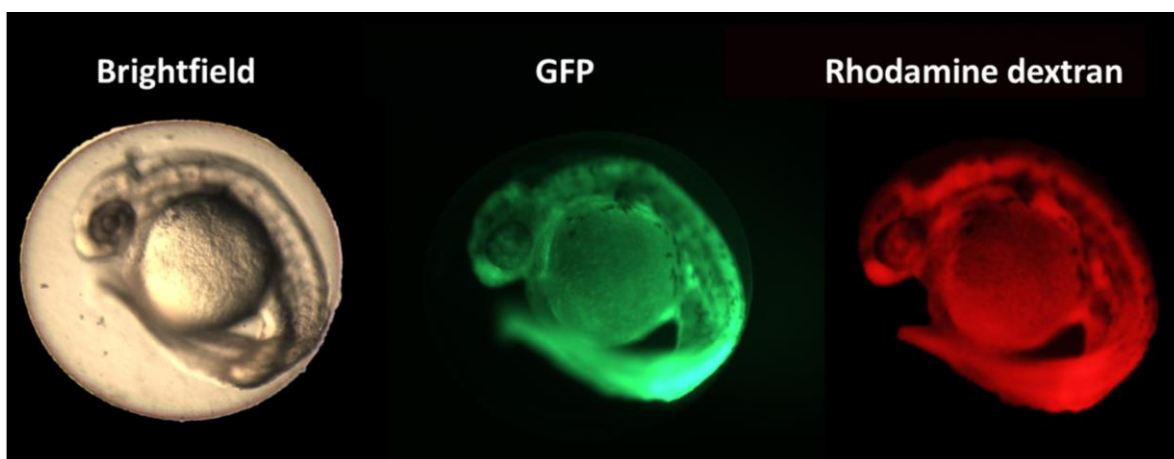


Figure 30: Photography of injected zebrafish larvae at 24hpf with the representation under brightfield, green fluorescence showing the expression of GFP and red fluorescence showing the correct injection of rhodamine dextran.

#### **III.12 Whole-mount *in situ* hybridization in the Zebrafish**

Zebrafish larvae at 48-hpf, 5-dpf and 8-dpf were used for whole-mount *in situ* hybridization. Larvae were raised in presence of 0.003% of 1-phenyl-2-thiourea until 5-dpf to avoid pigmentation development. Larvae were fixed overnight in 4% of PFA at 4°C and stored in 100% methanol at -20°C until use. Visible *in situ* hybridizations were performed throughout several days starting with the rehydration by successive incubations for 5 minutes in 75%methanol/25%PBST, 50%methanol /50%PBST, 25%methanol /75%PBST and three times in 100% PBST. If necessary, a bleaching of larvae can be carried out to remove natural pigmentation with a solution of hydrogen peroxide/potassium hydroxide (3% $H_2O_2$ , 0.5%KOH). Larvae are then digested with proteinase K (Thermo Scientific) at 40  $\mu$ g/ml during 30 minutes at 37°C for the 48-hpf larvae, at 50  $\mu$ g/ml during 30 minutes at room temperature for the 5-dpf, at 40  $\mu$ g/ml during 50 minutes at room temperature for the 8-dpf larvae. After the digestion, larvae are fixed for 20 minutes with 4% PFA and then washed five times for 5 minutes in PBST. The pre-hybridization is carried out for 2 up to 5 hours of incubation at 65°C. in HybMix+ (50%formamide, 5X SSC, 0,1%Tween20, 50  $\mu$ g/ml of heparin, and 500 $\mu$ g/mL of Torula RNA adjusted to pH 6.0 with citric acid) in order to block nonspecific hybridization sites. The following step is the hybridization with 200  $\mu$ L of HybMix+ containing 20-50 ng of DIG (digoxigenin) labeled *omd* antisense RNA probe and 5% dextran sulfate. For 48-hpf larvae, the hybridization is performed overnight at 65°C. For older larvae, incubation at 65°C lasts between 3 and 4 days. After the hybridization, larvae are thoroughly washed in 100% HybMix- (50%formamide, 5X SSC, 0.1%Tween and adjusted to pH 6.0 with citric acid) at 65°C. Several washing are carried out with an increasing concentration of SSCT and a decreasing concentration of HybMix- as follows: washes of 15 minutes at 65°C in 75% HybMix-/25% 2X

### **III. MATERIAL & METHODS**

SSCT, 50% HybMix-/50% 2X SSCT, 25% HybMix-/75% 2X SSCT and 100% 2X SSCT. Then, two washes of 30 minutes in 0.125X SSCT at 65° C are carried out. The larvae are then washed with decreasing concentration of SSCT and increasing concentration of PBST. Successive washes of 5 minutes in 75% 0.125X SSCT/25%PBST, 50% 0.125X SSCT/50%PBST and 25% 0.125X SSCT/75%PBST at room temperature are carried out. The larvae are finally washed for 10 minutes in 100% PBT at room temperature. The larvae are then incubated for minimum 2 hours in 500 µL of blocking buffer (PBST with 2% of sheep serum and 2 mg/mL BSA) at room temperature to avoid nonspecific binding of anti-DIG antibodies. The blocking buffer is replaced by the solution of anti-DIG antibodies coupled with a phosphatase (1:2000) in the blocking buffer and larvae are incubated overnight at 4°C. The following day, antibodies are removed and larvae are quickly washed once in PBST and then six times for 15 minutes in PBST at room temperature. Larvae are incubated in the staining buffer (100 mM NaCl; 50 mM MgCl<sub>2</sub>; 100 mM Tris-HCl pH 9,5; 0,5%Tween20) for 5 minutes twice and then the staining relative to the probe is revealed at room temperature with the staining buffer combined with 3.5 µL/mL Nitro Blue Tetrazolium Chloride (NBT: 100 mg/mL in 70% dimethylformamide) and 3.5 µL/mL 5-Bromo-4-chloro-3-indolyl phosphate (BCIP: 650 mg/mL in 100% dimethylformamide) reacting to generate a blue precipitate and 1 µL/mL of levamisole to reduce the background signal. The intensity of the staining is checked with a binocular microscope. The reaction is stopped by washing extensively with 5X Tris-buffered saline (TBS) 0.5%Tween (5XTBS: 250 mM Tris and 750 mM NaCl adjusted at pH 7.6). Larvae are stored in 1% PFA at 4°C until image acquisition.

**III.13 Histology of the zebrafish jaw joint**

1-year-old zebrafish were fixed with 4% PFA at 4°C for a minimum of 24 hours and were decalcified in 1M EDTA solution for 20 days. Zebrafish were dehydrated in ethanol, embedded in paraffin, and sagittally sectioned at 5 µm. Sections showing the jaw joint were stained with Toluidine Blue. OARSI score was attributed to 1 section per jaw joint as described in [264] (Table 13).

*Table 13: Guidelines adapted from OARSI for histological scoring, with Toluidine Blue staining, of OA modifications in the zebrafish.*

Zebrafish guidelines	
Score	OA damage (Toluidine Blue)
0	Normal
1	Small fibrillations without loss of cartilage
2	Fibrillations extend through the superficial layer, surface abrasion with some matrix loss within the superficial layer
3	Vertical fissures/erosion into deeper cartilage layers
4	Cartilage matrix loss, delamination of superficial layer, excavation, matrix loss in superficial and deeper layers
5	Cartilage lost, bone surface intact
6	Bone surface remodeling and deformation of articular surface contour

**III.14 Zebrafish osteoclast assay in the caudal fin**

The mutants *omd* x *TgBAC(ctsk:Citrine)* were used at 1 year for the osteoclast analysis. Their caudal fins were cut and the fin was allowed to regenerate for 7 days. Regenerated caudal fins were cut for analysis and were incubated for 20 minutes with 0.01% Alizarin red S (Sigma-Aldrich) to stain the mineralized bone matrix. Quantification of fluorescence from regenerated rays was performed using ImageJ software [277].

#### III.15 TRAP staining of the Zebrafish scales

Ontogenetic scales of 1.6-year-old fish were plucked from the flank of the zebrafish and fixed with 4% PFA at room temperature for 30 minutes. Scales were incubated for 2 hours in the TRAP staining solution. The TRAP staining solution is made freshly out of two stock solutions referred to as solutions A and B. The solution A consists of a solution of 10 mg/mL naphthol AS-MX phosphate dissolved in N, N'-dimethylformamide. The solution B is a solution of 50 mM sodium tartrate and 1.6 mM Fast Red Violet LB dissolved in 0.1M sodium acetate buffer (adjusted to pH 5.0 with 100% acetic acid). The final TRAP staining solution is made of the association of 1 part of solution A to 100 parts of solution B together. After their staining, scales were washed with PBST three times at room temperature and fixed back with 4% PFA during 30 minutes. Quantification of the TRAP staining was performed using the ZFBONE software on FIJI [278] (Fig 31).

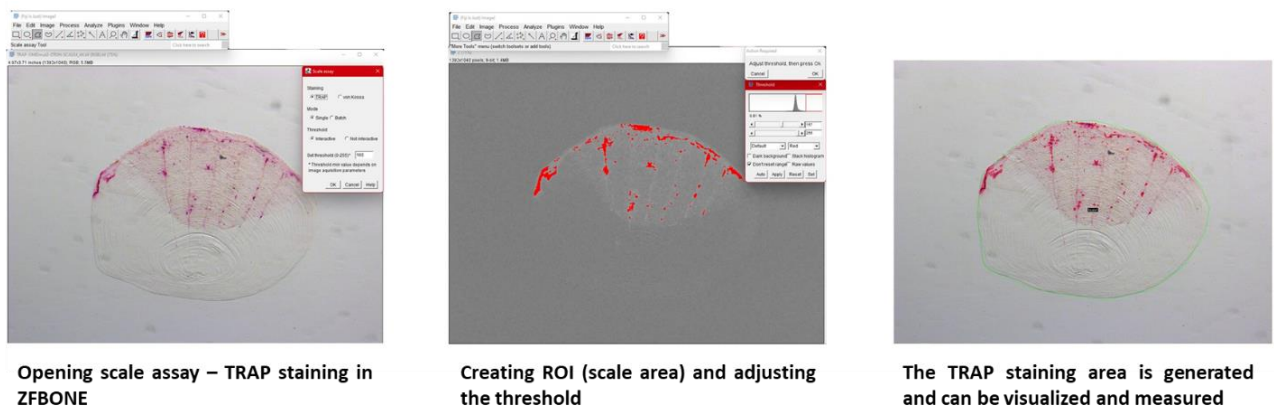


Figure 31: Representation of the TRAP staining analysis with the ZFBONE software available on FIJI.

#### III.16 Regeneration of Zebrafish scales and second harmonic generation

Zebrafish were anaesthetised and put on a wet tissue containing system water and anaesthetic in order to pluck the scales under a microscope with a watchmaker's tweezers from the midline of the lateral left flank near the dorsal fin. Zebrafish were isolated during 10

### **III. MATERIAL & METHODS**

days to allow the regeneration of their scales. After 10 days, zebrafish were immersed in 40  $\mu$ M Calcein (Sigma Aldrich) Danieau's buffer solution (pH 7.4) for two hours and washed in system water for at least 15 minutes prior to imaging. After the image acquisition, the regenerated scales (10-days) from the left flank are collected as well as the odontogenic scales (0-day) coming from the right flank. The collected elasmoid scales were fixed for 1 hour in 4% PFA and stored in PBS at 4°C before being mounted in 1% low-melting point agarose. Second harmonic generation (SHG) images were acquired using a  $\times 25/0.95$  water dipping lens, 880 nm laser excitation, and simultaneous forward and backward detection (440/20) with a Leica SP8 AOBS confocal laser scanning microscope attached to a Leica DM6000 upright epifluorescence microscope with multiphoton lasers allowing fluorescent acquisition and SHG of the same sample and z-stack acquisition (z step size 2  $\mu$ m). Microscope parameters for SHG were set as previously described [279]. Maximum projection pictures were assembled using Fiji.

#### **III.17 Fourier transform infrared (FTIR) analysis**

Measurements were carried out at the Department of Life and Environmental Sciences, Università Politecnica delle Marche, by using a Hyperion 3000 Vis-IR microscope equipped with a liquid nitrogen-cooled bidimensional focal plane array (FPA) detector coupled with an INVENIO-R interferometer (Bruker Optics GmbH, Ettlingen, Germany). The bidimensional FPA detector let simultaneously acquire infrared (IR) images ( $\sim 164 \times 164 \mu\text{m}^2$ ) containing 4096 pixel/spectra (64x64), with a spatial resolution of 2.56  $\mu$ m.

Caudal fin samples were deposited onto CaF<sub>2</sub> optical windows and let air dry for 20 minutes. The analysis was focused on the third ray of each fin, and, in particular, IR images were acquired on the edge and the first bifurcation connecting segments. Measurements were performed at room temperature in transmission mode, using a  $\times 15$  condenser/ objective, in

### **III. MATERIAL & METHODS**

the 4000-900  $\text{cm}^{-1}$  spectral region (spectral resolution 4  $\text{cm}^{-1}$ ), averaging 256 scans. Background spectra were obtained on clean regions of  $\text{CaF}_2$  optical windows with the same acquisition parameters. Raw IR images were corrected for the contribution of atmospheric  $\text{CO}_2$  and water vapor, and vector normalized in the entire spectral range for avoiding artefacts induced by local thickness variations (Atmospheric Compensation and Vector Normalization routines of OPUS 8.1 software, Bruker Optics GmbH, Ettlingen, Germany).

False color images showing the spatial distribution of collagen and hydroxyapatite within the mapped regions were obtained by integration of IR images in the 1290-1194  $\text{cm}^{-1}$  (vibrational modes of collagen, COLLAGEN maps) and 1138-1000  $\text{cm}^{-1}$  ( $\nu_1$  and  $\nu_3$  modes of  $\text{PO}_4^{3-}$  in hydroxyapatite, PHOSPHATES maps) spectral regions. To evaluate spectral differences among samples, for each IR image N. 20 IR spectra were extracted in correspondence with the edge and the first bifurcation and used to calculate the average and average  $\pm$  SD spectra (Averaging routine, OPUS 7.5 software package, Bruker Optics, Ettlingen, Germany). IR spectra were interpolated in the 1485-900  $\text{cm}^{-1}$  spectral region, multi-points baseline linear fitted, and vector normalized; spectra were then curve fitted with Gaussian functions in the same spectral range for highlighting all the underlying peaks. The position (expressed as wavenumbers) of each underlying peak was identified based on second derivative analysis and fixed before running the iterative process to obtain the best reconstructed curve (residual close to zero; bandwidth 10 to 40  $\text{cm}^{-1}$  range) (GRAMS/AI 9.1, Galactic Industries, Inc., Salem, NH, USA). The height of each underlying band was obtained and used to calculate the following spectral parameters: Mineral-to-Matrix index (MM) associated with the mineral maturity and calculated as the ratio between the intensity of the peaks at 1024  $\text{cm}^{-1}$  and 1087  $\text{cm}^{-1}$ , related to apatitic phosphates respectively in well-crystallized stoichiometric hydroxyapatite and in poorly crystalline apatite [280]; Carbonate-to-Phosphate index (C/P) related to the carbonate

### ***III. MATERIAL & METHODS***

content of bioapatite and calculated as the ratio between the intensities of the peaks at 1412  $\text{cm}^{-1}$  and 1024  $\text{cm}^{-1}$ , respectively attributed to vibrational modes of carbonate and phosphate groups; Collagen-to-Phosphate index indicating the relative amount of the organic matrix respect to the inorganic component and calculated as the ratio between the intensity of the peaks at 1340  $\text{cm}^{-1}$  and 1024  $\text{cm}^{-1}$ , corresponding respectively to the vibrational modes of proline in collagen and phosphate groups.

The bifurcation and edge areas of the caudal fin were analyzed separately as different distributions of collagen and phosphates were found in the bifurcation area. Collagen was more intensely localized in the origin of the bifurcation for 3 months and 1 year WT zebrafish, while phosphates were mainly present before the origin of the bifurcation for 3 months WT zebrafish (Fig 32).



### III. MATERIAL & METHODS

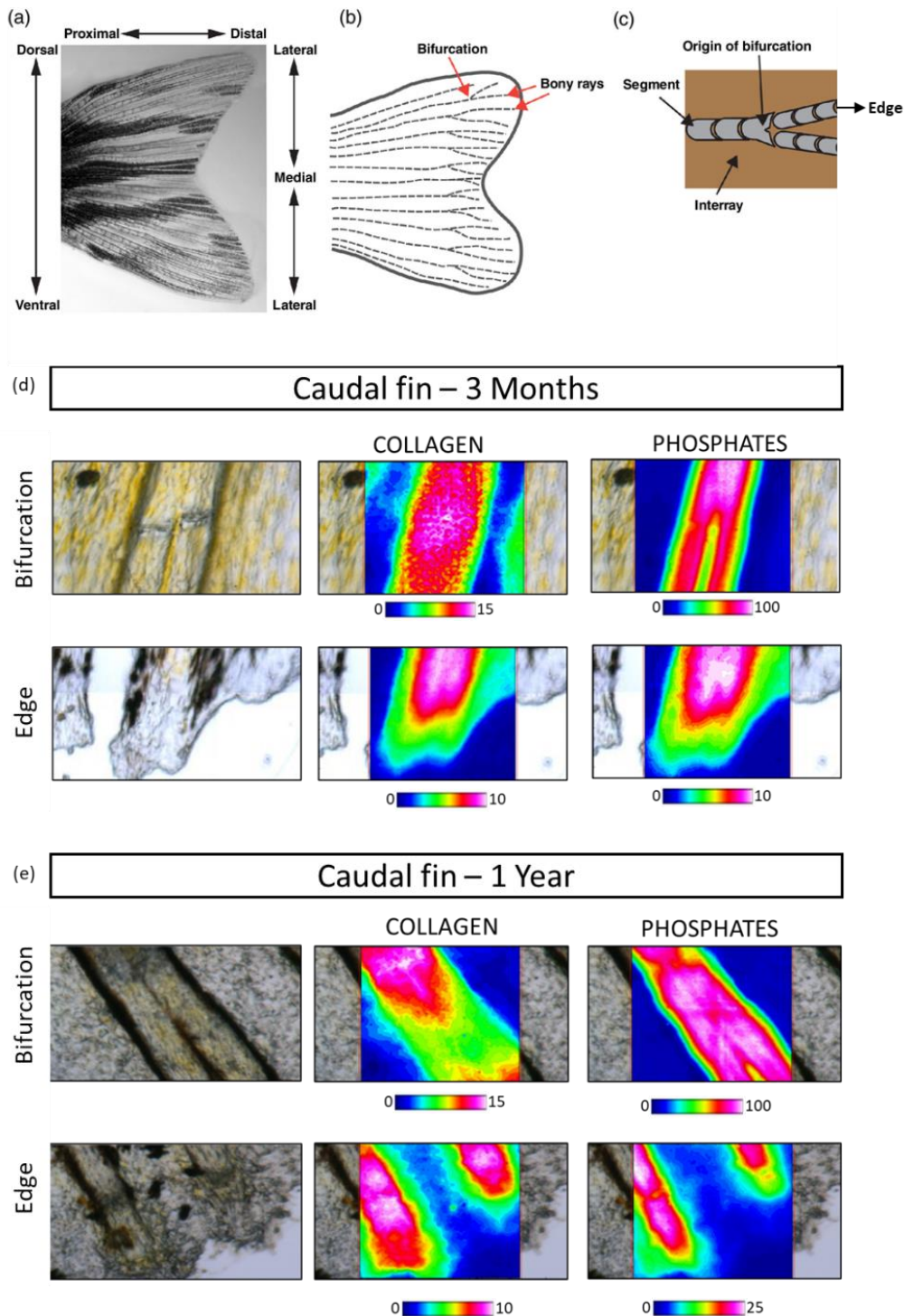


Figure 32: Description of the selected areas of the caudal fin used for the FTIR analysis (a) Brightfield image of the caudal fin of the zebrafish, (b) schematic representation of the caudal fin composed of segmented bony rays which present bifurcation. (c) Schematic representation of the bifurcation and edge areas. Figure adapted from [281] and designed by Jérémie Zappia. (d) Brightfield images of the bifurcation and edge areas of the caudal fin of 3 months WT zebrafish and associated topographical distribution of collagen and phosphate groups. (e) Brightfield images of the bifurcation and edge areas of the caudal fin of 1 year WT zebrafish and associated topographical distribution of collagen and phosphate groups.

#### **III.18 Human trabecular osteoblast culture for RNA-seq analysis**

Tibial bones were obtained from 6 male and 5 female patients undergoing total knee replacement surgery for OA. The age of the patients ranged from 58 to 89 years. All tissue samples used in this study were obtained after receiving approval from the University of Liege Medicine Faculty ethics committee (No. B70720108313, reference 2010/43) and written informed consent was obtained from each subject. Non-sclerotic trabecular bone was easily removed from the tibia with surgeon pliers and then cut into small fragments of approximately 2 mm<sup>3</sup>. Fragments were washed with Dulbecco's Modified Eagle Medium (DMEM) and then submitted to enzymatic digestions with a solution of 0.6 mg/mL clostridial collagenase IA (Sigma Aldrich) and 1% Ultrosor G (Sartorius), a serum substitute, for 240 minutes at 37°C; this solution was provided at reason of 7 mL/g of bone for correct digestion. After digestion, several washes with DMEM were performed until all the residual fat from the bone was removed. The digested bone pieces were placed in T-175 flasks (approximately 2.5 g/flask) and cultured in DMEM supplemented with 15% fetal bovine serum (FBS), 10 mM HEPES, 100 U/mL penicillin, 100 mg/mL streptomycin, and 2 mM L-glutamine until osteoblasts migrated out of bone explants. Once the cells are migrating out of the explants, the medium was replaced with fresh media containing 10% FBS, 10 mM HEPES, 100 U/ml penicillin, 100 mg/mL streptomycin, and 2 mM L-glutamine. At confluence, osteoblasts were collected by trypsinization, and seeded (22.000 cells/cm<sup>2</sup>) in 12-well plates (Nunc). Then, they were grown for 3 to 4 days, until confluence, in DMEM containing 10% FBS, 100 U/mL penicillin, 100 mg/mL streptomycin, 10 mM HEPES, 2mM L-glutamine, 50 mg/mL ascorbic acid (Sigma Aldrich), and 2 mM proline (Invitrogen). Then, osteoblasts were maintained for 3 days in differentiation media, composed of DMEM containing 100 U/mL penicillin, 100 mg/mL streptomycin, 2 mM

### III. MATERIAL & METHODS

L-glutamine, 10 mM HEPES, 2% Ultrosor G, 1 $\alpha$ ,25-Dihydroxyvitamin D3 (Sigma Aldrich), 50 mg/mL ascorbic acid, and 2 mM proline. During the 3 days in the differentiation media, osteoblasts were treated with 10 ng/mL of the human recombinant OMD (R&D systems, 2884-AD) or in its absence for the same patient, serving as its own control. A representation of the timeline of the *in vitro* culture is represented in figure 33.

Total RNA was extracted from osteoblast cultures using the RNeasy mini kit (Qiagen) following the instructions of the manufacturer. The yield of the extracted RNA was determined spectrophotometrically by measuring the optical density at 260 nm. The purity and quality of extracted RNA were further evaluated using an RNA Nano 6000 Bioanalyzer Agilent.

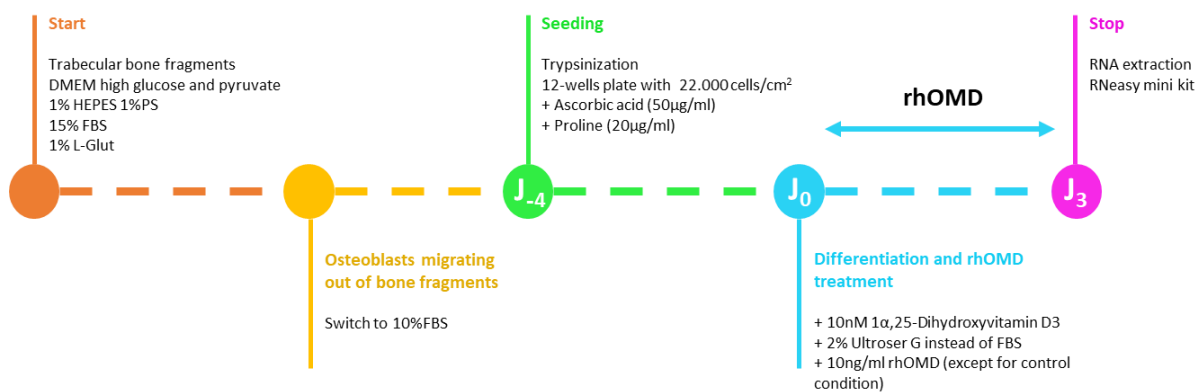


Figure 33: Representative timeline of the *in vitro* culture of trabecular osteoblasts for RNA-seq analysis.

High-quality RNAs with RNA integrity number (RIN) of >9,3 and with 100 ng of RNA from each culture were used for the RNA-seq analysis. Libraries were prepared with the Illumina Truseq stranded mRNA sample prep kit according to the manufacturer's instructions. Based on poly(A) selection of mRNAs, the coding strand information was kept. Poly(A) plus RNA was enriched using oligo(dT) beads followed by fragmentation and reverse transcription. Afterward, the 5' and 3' ends of cDNA fragments were prepared to ensure efficient ligation of "Y" adapters containing a unique barcode and primer binding sites. Finally, ligated cDNAs were

### **III. MATERIAL & METHODS**

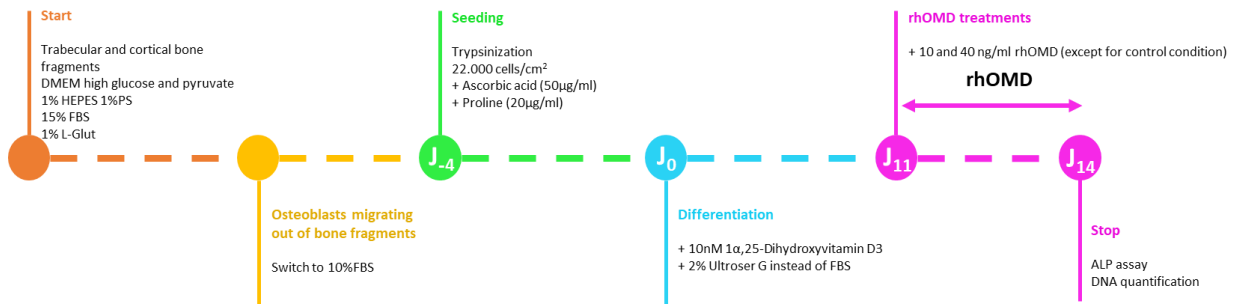
PCR-amplified to be ready for cluster generation and sequencing. Sequencing was performed on Novaseq (Illumina), paired-end reads (150-10-10-150), NovaSeq S4 V1.5 300 cycles XP workflow, generating around 20 M reads per sample. Denatured NGS library fragments were flowed across a flow cell and hybridized on a lawn of complementary Illumina adapter oligos. Complementary fragments were extended, amplified via bridge amplification PCR, and denatured, resulting in clusters of identical single-stranded library fragments. Fragments were primed and sequenced utilizing reversible terminator nucleotides. Base pairs were identified after laser excitation and fluorescence detection. Raw data were demultiplexed into individual libraries. After filtering out reads mapping to rRNA, tRNA, mitochondrial RNA, and other contaminants (e.g., adapters, etc.) using bowtie2, reads were aligned onto the human reference genome (GRCh38 and Ensembl 106 annotation) and quantified with Star to give the Counts file. Quality control of sequencing reads was assessed with FASTQC and quality control after mapping with Picard tools. Compilation of tool metrics was performed with MultiQC. Differential expression analysis was made in R (version 4.2, <https://www.R-project.org/>) using the DESeq2 package (1.36.0)[282], biomaRt package (version 2.52) [283]. Volcano plots were generated using ggplot2 (version 3.3.6). A false discovery rate (FDR) of 0.01 was used to assess the statistical significance. Pathway and biological function enrichment analysis was performed using the WEB-based "Gene Set Analysis Toolkit" (<http://www.webgestalt.org>; accessed 10 November 2022) based on the integrated GO (Gene Ontology), KEGG (Kyoto Encyclopedia of Genes and Genomes) [284,285], Panther and WikiPathways databases.

The transcriptomic data analyzed for this study are deposited in GeneExpression Omnibus (GEO) repository, under accession number GSE230198 that is publicly accessible at <https://www.ncbi.nlm.nih.gov/geo/query/acc.cgi?acc=GSE230198>.

#### **III.19 Human osteoblast culture for ALP assay and *in vitro* Alizarin red staining**

For the ALP assay and *in vitro* Alizarin red staining, trabecular, sclerotic osteoblasts, and non-sclerotic cortical bone were obtained from patients undergoing total knee replacement surgery for OA. Cortical bone was considered sclerotic if its thickness was reaching at least 2 mm and non-sclerotic if its thickness was not exceeding 1 mm. Trabecular, sclerotic, and non-sclerotic cortical bone were isolated from the tibia and then cut into small fragments of approximately 2 mm<sup>3</sup>. Fragments were put in culture as described in the section III.18 with the trabecular and non-sclerotic cortical osteoblasts seeded at 22.000 cells/cm<sup>2</sup>, and sclerotic cortical osteoblasts seeded at 17.000/cm<sup>2</sup>. Sclerotic osteoblasts were seeded at a different density because of their bigger cell size due to their sclerotic phenotype [286]. For the ALP assay, osteoblasts were cultured in the differentiation medium described in the section III.18 until 14 days and treated with 10 and 40 ng/mL rhOMD during 3 days prior to the end of the culture or in its absence for the same patient, serving as its own control. For the Alizarin red staining, the non-sclerotic and the neighboring sclerotic osteoblasts are issued of the same patients and consequently, the non-sclerotic osteoblasts served as a control for the sclerotic phenotype. Cortical osteoblasts were cultured until 17 or 21 days and treated with 10 and 40 ng/mL rhOMD during 3 days prior to the end of the culture. Finally, 2 days before the end of the culture, 10mM of  $\beta$ -glycerophosphate, the mineralization substrate, is added into the differentiation medium. A representation of the timelines of the previously explained *in vitro* cultures is represented in figure 34.

#### A) Culture design for the ALP assay



#### B) Culture design for the Alizarin red staining

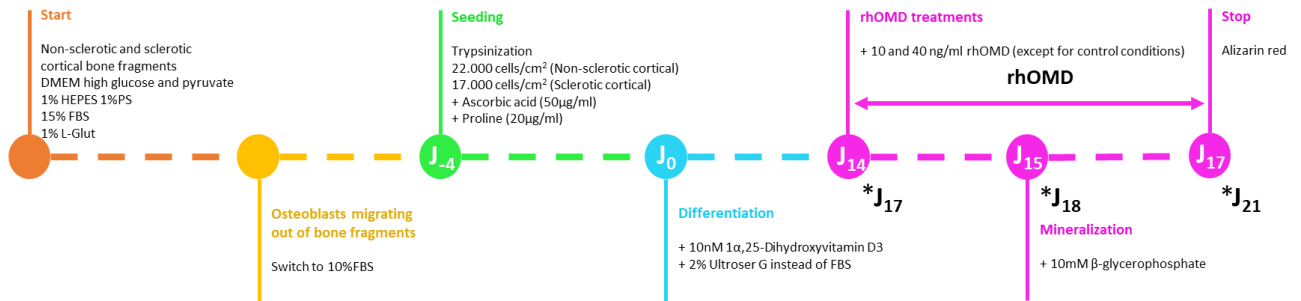


Figure 34: Representative timeline of the *in vitro* culture of trabecula and cortical osteoblasts for the ALP assay (A) and the Alizarin red staining (B). For the Alizarin red, cultures were stopped at 17, and 21 days.

#### III.20 ALP assay

At the end of the culture (14 days), cells are washed with PBS three times and 500 µL of 1 mg/mL of clostridial collagenase diluted in PBS is added during 15 minutes at 37°C to allow the collection of osteoblasts in 15 ml falcon tubes. The wells are rinsed with 500 µL of PBS and scrapped to collect every residual cell. Osteoblasts are centrifuged at 1200 rpm during 10 minutes and pellets are washed with 500µL PBS before a second centrifugation. The PBS is removed and dry pellets can be stored at -20°C until use. The pellets are suspended in 1 mL of 5 mM Tris pH 7.4 on ice. Each pellet is sonicated for 20 seconds at 50Hz and the suspension is then vortexed and transferred to a masterblock for storage at -20°C. DNA quantification is

### **III. MATERIAL & METHODS**

performed by measuring the fluorescence of bisbenzimidazole (Hoechst 33258) which binds to DNA. In a 96-well plate, 200  $\mu\text{L}$  of Hoechst's solution diluted 100 times with the DNA buffer (2M NaCl, 43.8mM  $\text{Na}_2\text{HPO}_4 \cdot 2\text{H}_2\text{O}$  and 5.5mM  $\text{KH}_2\text{PO}_4$  at pH 7.2) is added to 50  $\mu\text{L}$  of the sample. A standard solution from 10  $\mu\text{g}/\text{mL}$  to 0.625  $\mu\text{g}/\text{mL}$  of DNA is prepared by serial 2X dilutions and 50  $\mu\text{L}$  of each dilution is used with 200  $\mu\text{L}$  of the previous Hoechst's solution to create the standard curve. Each sample is measured in triplicate as well as the standard curve. After 30 to 45 minutes at room temperature and protected from the light, the fluorescence is read with the Fluoroskan Ascent FL at 355 nm of excitation and 460 nm of emission. The quantified DNA is used to normalize the ALP activity.

For the quantification of the ALP activity, 100 $\mu\text{L}$  of para-nitrophenylphosphate is added to 50  $\mu\text{L}$  of sample in a 96-well plate. In the presence of ALP, para-nitrophenylphosphate is transformed into p-nitrophenol and inorganic phosphate. A standard solution from 1000  $\mu\text{M}$  to 15.63  $\mu\text{M}$  of p-nitrophenol solution is prepared by serial 2X dilutions and 50  $\mu\text{L}$  of each dilution is used with 100  $\mu\text{L}$  of para-nitrophenylphosphate to create the standard curve. The 96-well plate is incubated at 37°C with shaking and para-nitrophenol absorbance is measured at 405nm after 10 to 15 min with the ThermoScientific MultiScan GO - Skanit RE 5.0. Results were expressed in nanomoles of para-nitrophenol released per min and  $\mu\text{g}$  of DNA.

#### **III.21 Alizarin red staining of *in vitro* osteoblast culture**

At the end of the culture (17, and 21 days), cells are washed with PBS three times, and fixed with 4% PFA for 20 min at room temperature. Afterward, they are washed three times with milliQ water. Then, cells are stained with Alizarin Red S 1% solution (Sigma Aldrich) diluted in milliQ water and adjusted to pH 4.2 with  $\text{NH}_4\text{OH}$  0.5%, during 15 minutes protected from light. Finally, cells are washed with milliQ water until the non-specific staining is removed.

#### **III.22 Solid phase binding assay**

Human recombinant RANKL (OriGene, Germany) was bound for 2 hours under constant agitation to Well-Coated™ Nickel (G-Biosciences) previously washed with PBST. Unbound protein was removed by repeated washing with PBST. RANKL-coated plates were incubated overnight at 4°C with human recombinant OMD (R&D systems). The OMD bound to the coated plate was detected using the primary biotinylated polyclonal goat antibodies anti-human OMD (R&D systems, ref: BAF2884, 0.4 µg/mL). Plates were incubated with streptavidin-POD (Roche, dilution 1:25000) for 30 minutes to allow detection. Finally, plates were read at 450 nm after applying TMB (TMBplus2, D-Tek, Denmark) for 8 minutes. The direct binding between OMD and RANKL was assessed with a fixed concentration of RANKL (0.2 µg/mL) and decreasing concentrations of OMD (1000 to 15.65 ng/mL by serial 2X dilution), with the negative control missing RANKL; and with decreasing concentrations of RANKL (800 to 6.25 ng/mL by serial 2X dilution) and fixed concentration of OMD (0.5 µg/mL), with the negative control missing OMD.

#### **III.23 Mouse osteoclast culture**

WT mice of at least 4 months of age were used to collect bone marrow cells. The bone marrow of the femur and the tibia was flushed with 10 mL of  $\alpha$ MEM containing 10% FBS, 100 U/mL penicillin, and 100 mg/mL streptomycin. Cells were strained through a 70 µm filter and then centrifuged at 1200 rpm for 7 minutes at 22°C. After centrifugation, cells were suspended in 12 mL of media containing 5ng/mL M-CSF in a petri dish and incubated overnight at 37°C. The non-adherent cells were centrifuged at 1200 rpm for 7 minutes at 4°C the day after. The cells were suspended in osteoclast differentiation medium  $\alpha$ MEM containing 10% FBS, 100 U/mL penicillin, 100 mg/mL streptomycin, 30 ng/mL M-CSF and 10 ng/mL RANKL. For the treated



### **III. MATERIAL & METHODS**

conditions, 10 and 40 ng/mL of recombinant mouse OMD (R&D systems) were pre-incubated for at least 15 minutes with RANKL and M-CSF prior to adding to the suspension of the cells. Cells were seeded (525 000 cells/cm<sup>2</sup>) in 24-well plates. Cells were maintained until 4 days of differentiation and were stained with a TRAP staining kit (Sigma Aldrich) according to the manufacturer's instructions.

#### **III.24 Assay in the serum for bone turnover markers**

The serum was extracted from blood of 16 months mice collected at the euthanasia. The level of P1NP was measured by Rat/Mouse P1NP ELISA (Immunodiagnostic Systems, Boldon, UK), and the level of TRAcP 5b by the Mouse TRAP Assay, a solid phase immunofixed enzyme activity assay (Immunodiagnostic Systems, Boldon, UK), according to the manufacturer's protocol.

#### **III.25 Western blot**

Western blots were conducted in native condition and denaturing SDS page. Serum of patients is depleted in IgG and albumin using ProteoPrep kits (Sigma Aldrich) and during this process, serum is diluted by approximately 3.3 times. Supernatants of subchondral osteoblast culture were concentrated approximately 20 times using Amicon Ultra 3 kDa 2 mL column (Millipore). The rhOMD was used as a positive control. Depleted serum (10-15µL) or osteoblasts concentrated supernatant (3 µL) were fractioned by electrophoresis on Mini-PROTEAN 12% TGX Stain-Free Precast Gels (Biorad) and transferred onto a polyvinylidene difluoride membrane. Membranes were blocked during 1 hour at room temperature with Roche Blocking Reagent, 1% in TBS (200mM Tris, 1500mM NaCl in milliQ water and adjusted at pH 7.6 with HCl). Membranes were then incubated overnight at 4°C with three antibodies raised

### **III. MATERIAL & METHODS**

against different regions of OMD, a polyclonal rabbit antibody against the 234-263 amino acids from the central region of human OMD (Thermofisher, PA5-14383) 1:1000 dilution in 0.5%; a polyclonal rabbit antibody against the 394-421 amino acids from the C-terminal region of human OMD (Thermofisher, PA5-14382) 1:1000 dilution in 0.5%, and a biotinylated polyclonal goat antiserum, affinity purified, raised against the whole OMD (R&D systems, BAF2884) 1:428 dilution in 0.5% Roche blocking reagent. The membrane is washed three times with TBS 0.1%Tween and incubated for 1 hour at room temperature with streptavidin-HRP (Roche, 1:2500 dilution) diluted in blocking solution for the detection of the antibody raised against the whole OMD protein. For the antibodies against the central and C-terminal regions of OMD, there is an incubation with goat anti-rabbit secondary antibody conjugated with HRP (Sigma Aldrich, 1:4000 dilution). Then, the membrane is washed three times with TBS 0.1%Tween and with a final wash of TBS The reaction was revealed with Luminata classico Western blotting substrate (Millipore) and the image was captured with the ChemiDoc™ MP System (Biorad) with the optimal exposure for chemiluminescence.

#### **III.26 Statistical analysis**

Results were statistically analyzed using GraphPad Prism 8.0.2 Tests performed and statistical significance are indicated in the figure legends with p values <0.05 considered statistically significant.

# **IV. MAIN RESULTS**

### **Preliminary notice**

1. This section assembles the main results of a paper which is currently under review in *Bone Research* from the Nature portfolio. The paper entitled "*Osteomodulin down-regulation is associated with osteoarthritis development*" is available in "Appendix 2".
2. The bookmark provided with the physical manuscript for the ease of the reader comes to a particular interest to navigate across the following results. The bookmark comprises the more useful abbreviations with associated descriptions and summary tables for the mouse, zebrafish, and *in vitro* models, also figuring in the section "*VII. Conclusions and future perspectives*". Summary tables were designed to improve readability regarding the comparison within the different models and between them.

### **IV.1 General growth characteristics of *Omd* KO and UP mice**

*Omd* KO mice had a lower weight and body size compared to the WT, only at 4 months. UP mice had a smaller weight than the WT at 4 months while their body size was not significantly different (Fig 35A, 35B). At 8 and 16 months, weight and size were similar in all genotypes (Fig 35A, 35B). UP mice displayed a longer femur than the KO at 8 months. The femoral length evolved differently over time between the genotypes with the UP reaching the mature size the soonest. Their femoral length was significantly increased at 8 months compared to the length at 4 months. At 16 months, each genotype reached a similar femoral length (Fig 35C, 35D). Apart from some differences in their general growth characteristics over time, overall modifications of the level of *Omd* expression did not induce gross phenotypes.

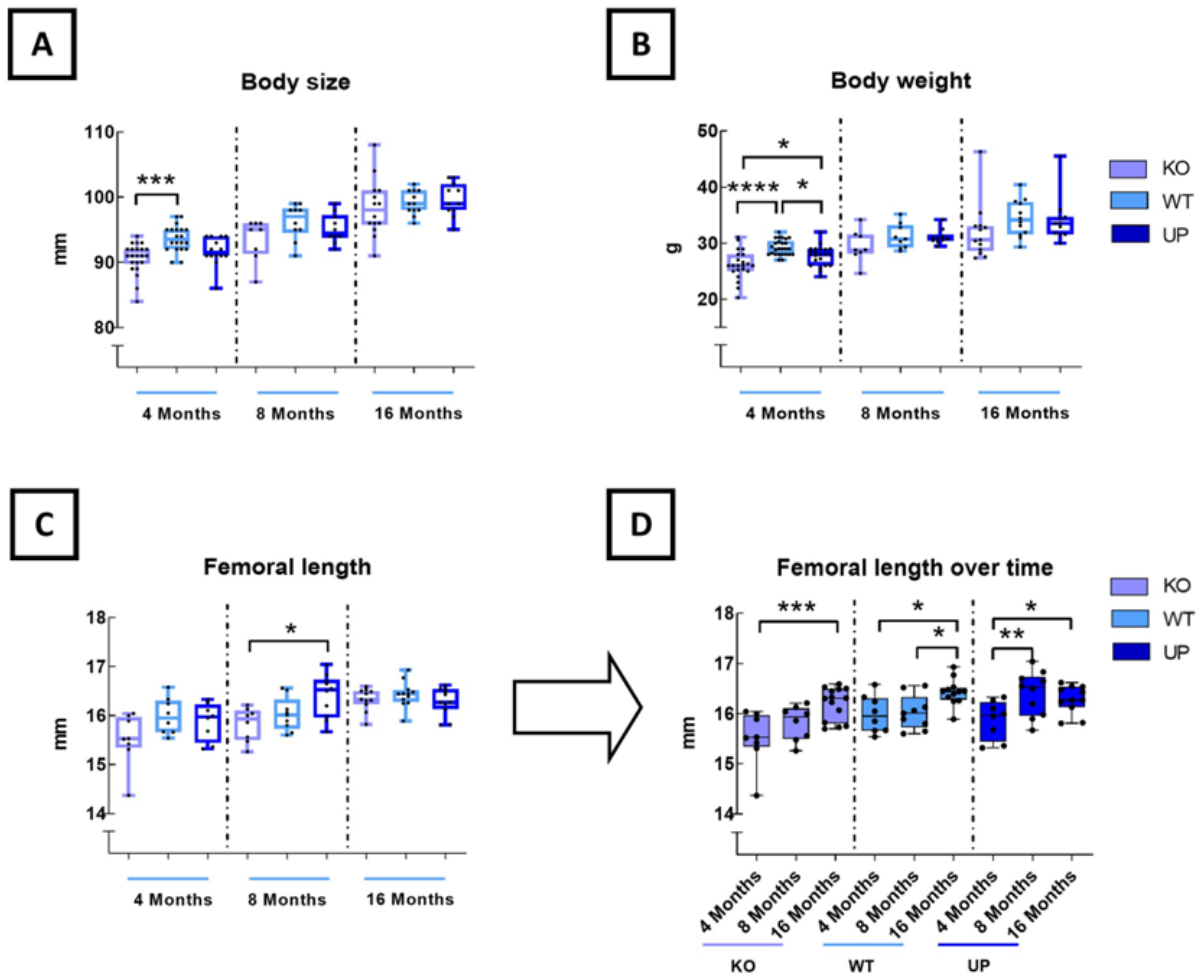
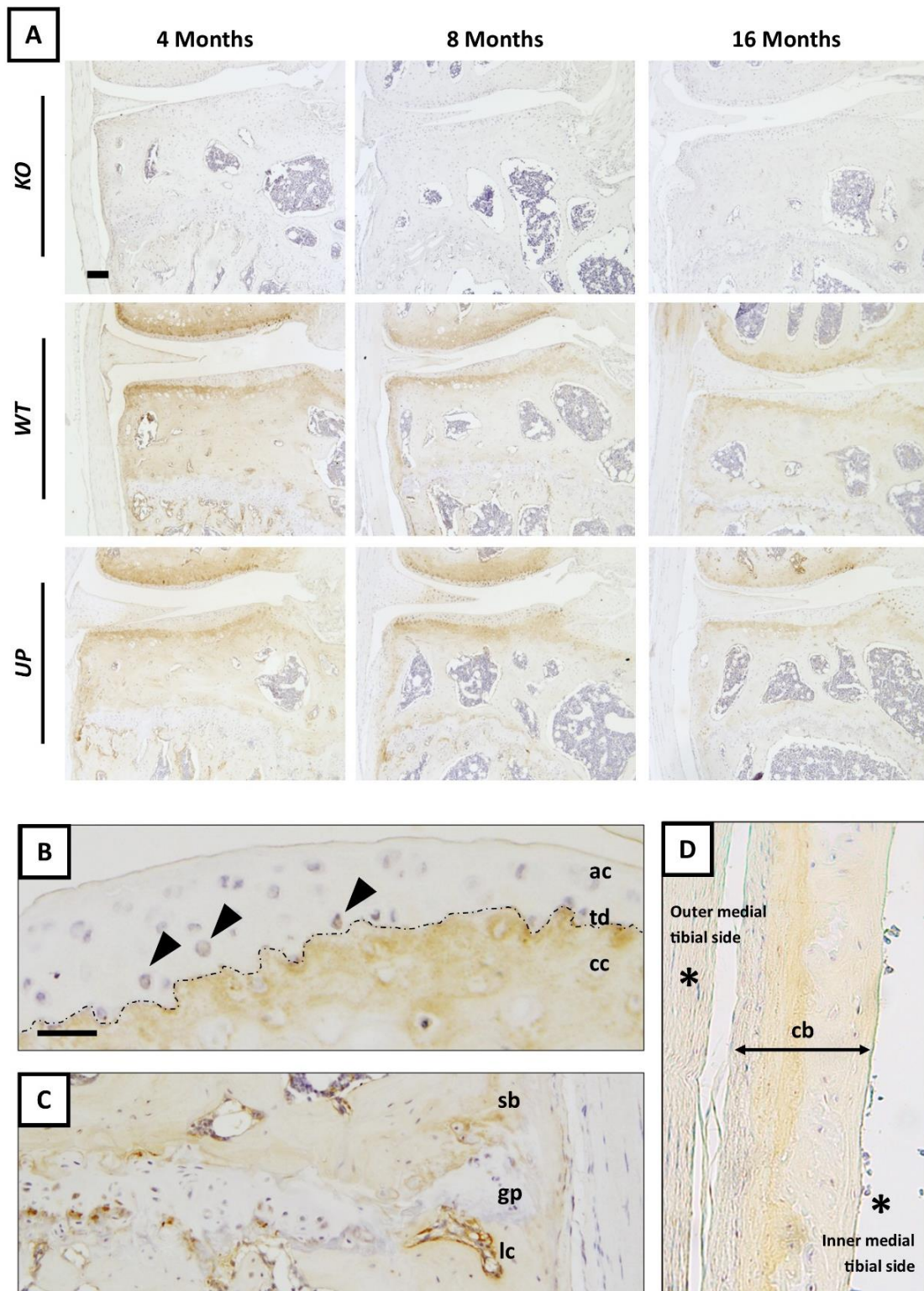


Figure 35: Macro observations of the cartilage of the knee joint of male mice. Mice that were candidates for the DMM surgery were added to the macro observations when possible. The macro observations were conducted at 4, 8 and 16 months. (A) For the body size:  $n=22$  for the KO,  $n=20$  for the WT and  $n=14$  for the UP at 4 months;  $n=8$  for the KO and  $n=10$  for the WT and UP at 8 months;  $n=14$  for the KO,  $n=12$  for the WT and  $n=11$  for the UP at 16 months. (B) For the body weight:  $n=22$  for the KO,  $n=26$  for the WT and  $n=22$  for the UP at 4 months;  $n=8$  for the KO and  $n=9$  for the WT and  $n=10$  for the UP at 8 months;  $n=13$  for the KO,  $n=12$  for the WT and  $n=11$  for the UP at 16 months. (C) For the femoral length:  $n=8$  for each genotype at 4 months;  $n=8$  for the KO and  $n=9$  for the WT and  $n=10$  for the UP at 8 months;  $n=11$  for the KO,  $n=12$  for the WT and  $n=11$  for the UP at 16 months. (D) The femoral length was displayed to show the evolution of the femurs over time within the genotypes. (A-C) Ordinary one-way ANOVA was performed to compare the body size, the body weight, and the femoral length between the genotypes, at each time-point. Kruskal-Wallis was performed when the distribution was not Gaussian. (D) Two-way ANOVA was performed to examine the influence of time on the femoral length inside each genotype. The data were plotted as a box plot showing all points with differences being considered significant at  $p$ -values  $< 0.05$  ( $*p < 0.05$ ,  $**p \leq 0.01$ ,  $***p \leq 0.001$ ,  $****p \leq 0.0001$ ).

**IV.2 OMD is mainly localized in bone and calcified cartilage in mouse knee joint tissues**

We have performed immunohistochemical detection of OMD in the knee joint of 4, 8, and 16-month-old mice. OMD was present at all ages in WT and UP mice but absent in KO mice indicating the specificity of the immunostaining (Fig 36A). OMD was strongly localized in the calcified cartilage ECM, while heterogeneous and light staining was also observed in the deep zone of the uncalcified articular cartilage ECM and in some chondrocytes (Fig 36A, 36B). In bone, the lining cells were strongly stained as well as the ECM, mostly the mineralization front (Fig 36A, 36C, 36D). The ECM and some cells in the meniscus were stained (Fig 36A). The cartilaginous ECM of the growth plate was not stained (Fig 36C). The immunostaining asserted OMD as a proteoglycan having a strong specificity for the mineralized skeletal tissues.



*Figure 36: (A) Immunostaining of OMD (in brown) in the knee joint (medial tibial plateau) of KO, WT, and UP male mice at 4, 8, and 16 months. Scale bar=100  $\mu$ m. (B-D) Zoom on specific areas from WT of 16 months. Scale bar=50  $\mu$ m. Representative pictures with n=3 for each group. (B) Uncalcified articular cartilage (ac) and calcified cartilage (cc), separated by the tidemark (td – dotted line); chondrocytes (arrowheads). (C) Subchondral bone (sb), growth plate (gp) and lining cells (lc). (D) Metaphysis of the tibia showing the cortical bone (cb), the outer medial tibial side and the inner tibial side facing the bone marrow are indicated with (\*).*



**IV.3 *Omd* influences bone and cartilage microarchitectures****IV.3.1 Effect of *Omd* on articular cartilage structure**

Histological analysis revealed that the tibial growth plate significantly decreased between 4 and 8 months in all genotypes, but further decreased between 8 and 16 months only in the WT but not in other genotypes. At 16 months, the growth plate of the KO was larger than in the WT (Fig 37A, 37B).

In the 4-month-old KO mice, the calcified cartilage layer was thinner in the medial tibial plateau and thicker in the tibial lateral plateau than in the WT (Fig 37C, 37E). The ratio of calcified cartilage/total cartilage for the medial tibial compartment of the KO was significantly lower than in the WT and UP mice at each time point (Fig 37D). In the tibial lateral plateau, this ratio was higher in the 4-month-old KO and UP mice than in the WT and in the 16-month-old KO than in the UP mice (Fig 37F). Further, this ratio decreased with age in the KO and UP genotypes while it remained stable in WT. The thickness of the cartilage (including non-calcified and calcified cartilage) was not different between genotypes except in the medial plateau of 8-month-old KO mice, in which cartilage was thinner than in WT (Fig 38). Our data showed *Omd* able to influence the cartilage microarchitecture.

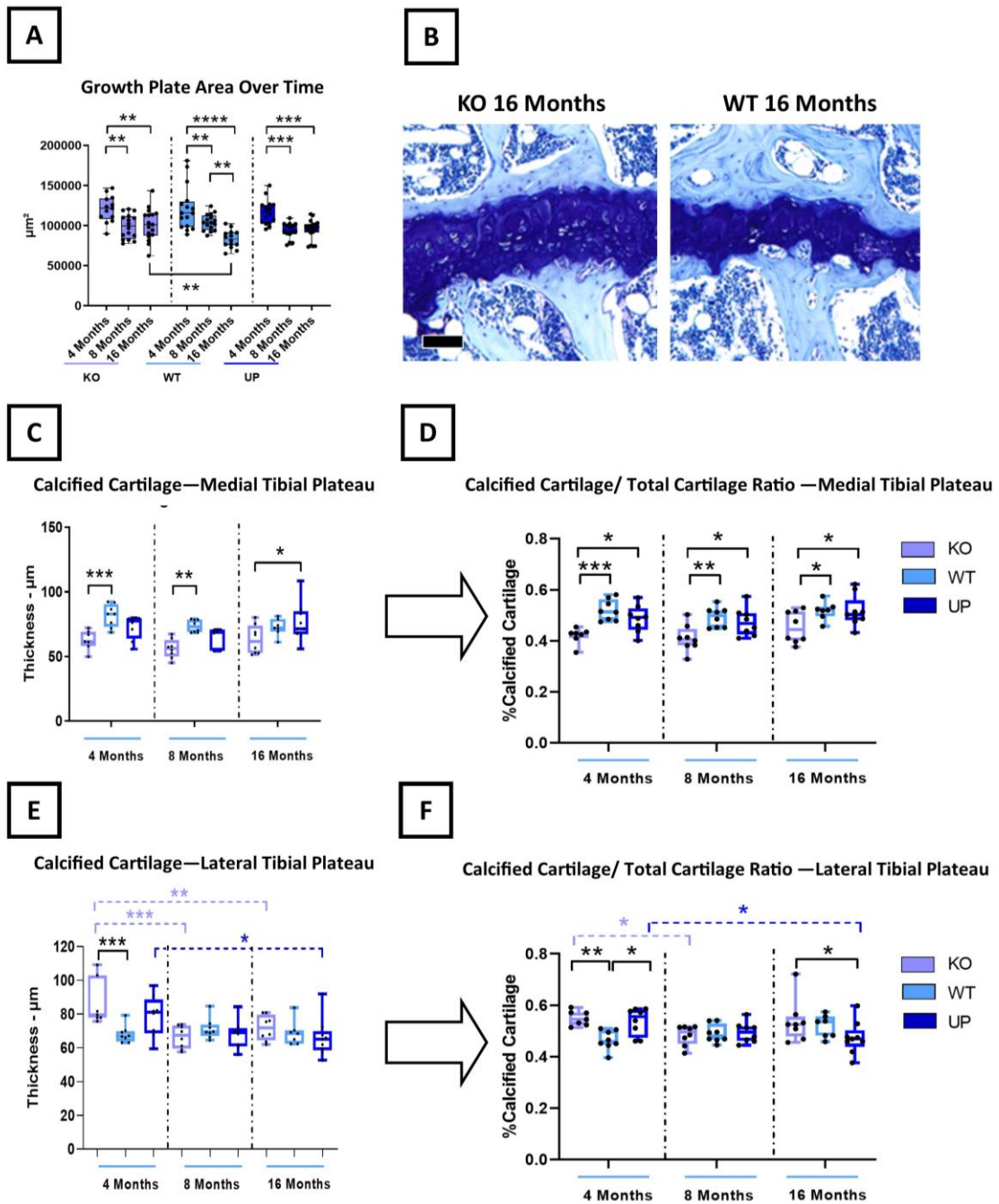


Figure 37: Histomorphometry of the cartilage was performed with QuPath at 4, 8, and 16 months. Knee joints of male mice were stained with Toluidine Blue and areas corresponding to the total cartilage, the calcified cartilage, and the growth plate were measured for the medial tibial plateau and the lateral tibial plateau. (A) Measures of the growth plate area of both medial and lateral tibial plateaus were plotted to display the evolution of the growth plate over time with  $n=13$  for the KO,  $n=16$  for the WT and UP at 4 months;  $n=16$  for the KO and WT, and  $n=15$  for the UP at 8 months;  $n=16$  for the KO,  $n=14$  for the WT and  $n=18$  for the UP at 16 months. (B) Toluidine blue of the growth plate for the KO and the WT at 16 months are represented. Scale bar=100  $\mu\text{m}$ . (C, E) The thickness of the calcified cartilage was measured on the medial and lateral plateaus from the tibia. (D, F) The ratio between the calcified cartilage and the total cartilage two was reported for both the medial and lateral plateaus.

Legend continues on the next page

#### **IV. MAIN RESULTS**

*For the medial plateau (C, D): n=7 for the KO, n=8 for the WT and UP at 4 months; n=8 for the KO and WT and n=7 for the UP at 8 months; n=8 for the KO, n=7 for the WT and n=9 for the UP at 16 months. For the lateral plateau (E, F): n=7 for the KO, n=8 for the WT and UP at 4 months; n=8 for each genotype at 8 months; n=8 for the KO, n=7 for the WT and n=9 for the UP at 16 months. Two-way ANOVA was performed to evaluate the genotype effect (in black) and the time effect inside a genotype (in the corresponding color). The data were plotted as a box plot showing all points with differences being considered significant at p-values<0.05 (\*p<0.05, \*\*p≤0.01, \*\*\*p≤0.001, \*\*\*\*p≤0.0001).*

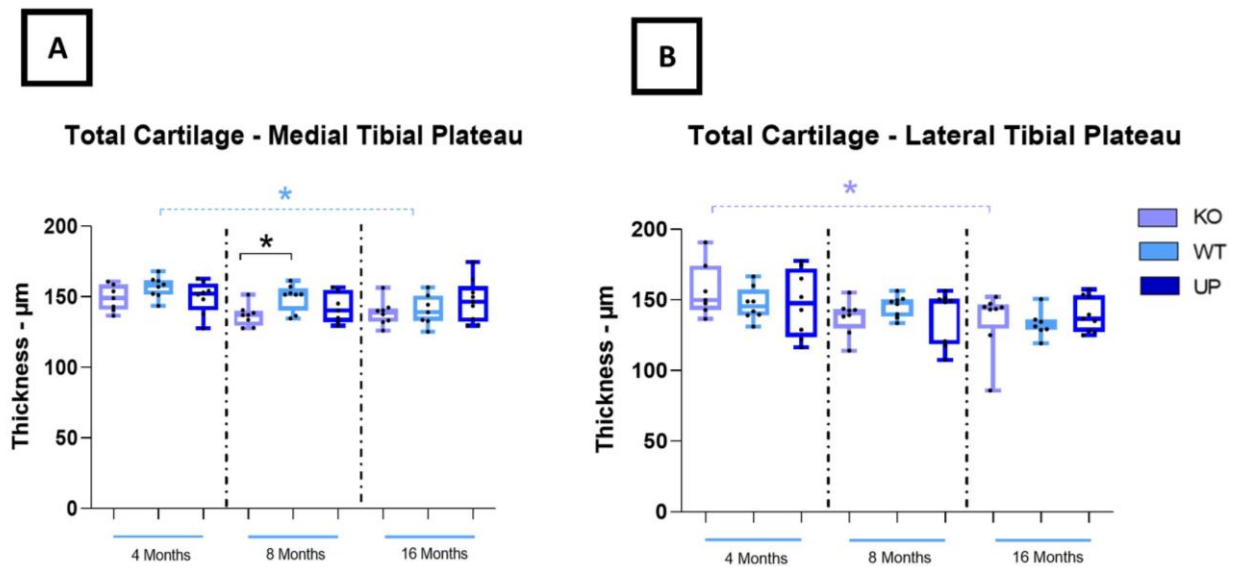


Figure 38: Histomorphometry of the cartilage was performed with QuPath at 4, 8, and 16 months. Knee joints of male mice were stained with Toluidine Blue and the thickness of the total cartilage (including non-calcified and calcified cartilage) was measured. (A) For the medial tibial plateau:  $n=7$  for the KO,  $n=8$  for the WT and UP at 4 months;  $n=8$  for the KO and WT and  $n=7$  for the UP at 8 months;  $n=8$  for the KO,  $n=7$  for the WT and  $n=9$  for the UP at 16 months. (B) For the lateral tibial plateau:  $n=7$  for the KO,  $n=8$  for the WT and UP at 4 months;  $n=8$  for all the genotypes at 8 months;  $n=8$  for the KO,  $n=7$  for the WT and  $n=9$  for the UP at 16 months. Two-way ANOVA was performed to evaluate the genotype effect (in black) and the time effect inside a genotype (in the corresponding color). The data were plotted as a box plot showing all points with differences being considered significant at  $p$ -values  $< 0.05$  ( $*p < 0.05$ ).

**IV.3.2 Effect of *Omd* on bone structure****IV.3.2.1 Metaphysis of the tibia**

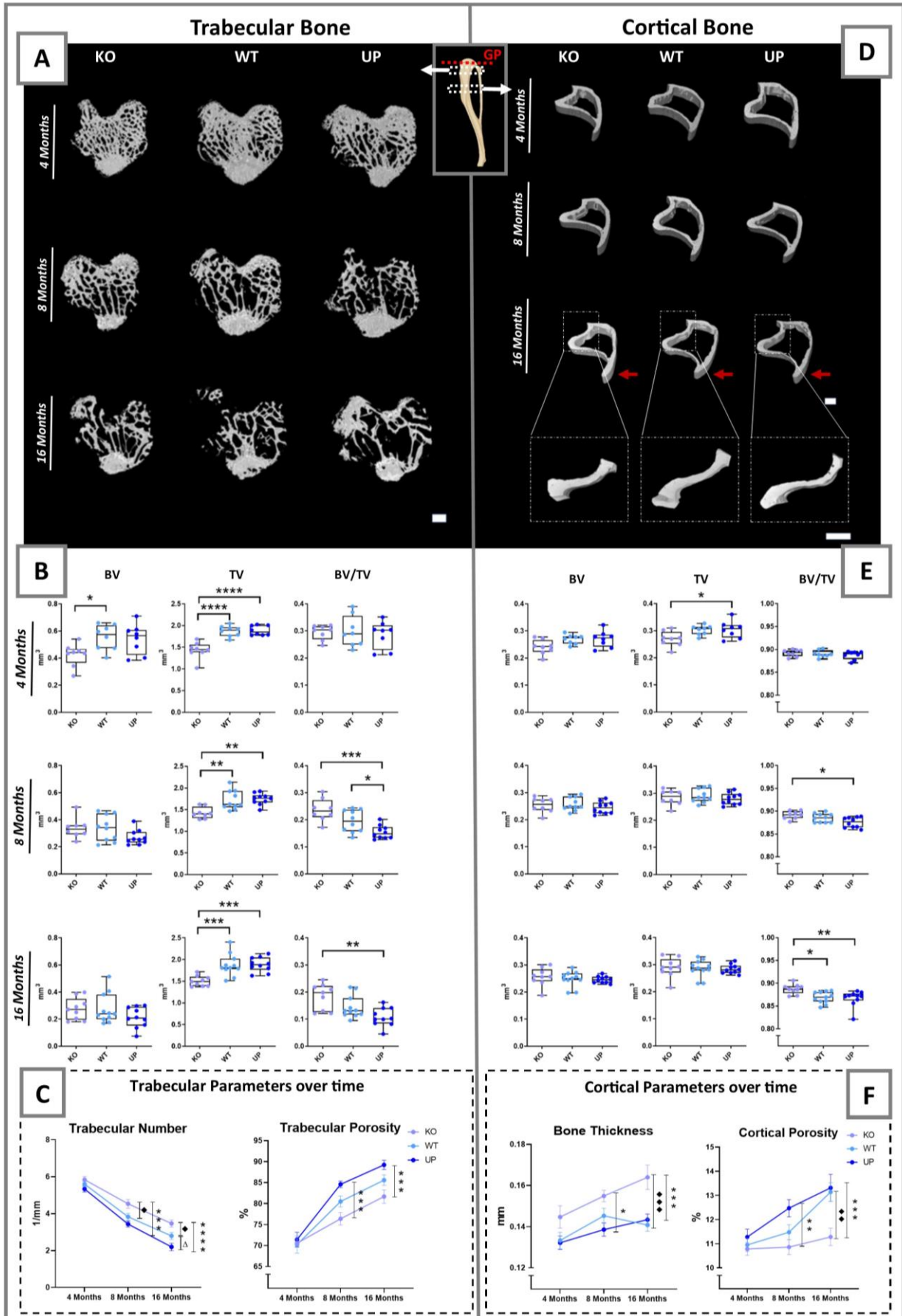
The total volume of the trabecular bone was lower in the KO than in other genotypes (Fig 39A, 39B). The trabecular BV/TV ratio was not significantly different between genotypes at 4 months. In contrast, this ratio was significantly higher in the KO than in the UP mice at 8 and 16 months and lower in UP mice than the WT at 8 months (Fig 39A, 39B). The number of trabeculae of the KO was higher at 8 and 16 months than the WT and UP while no difference was observed at 4 months (Fig 39C). The UP had significantly fewer trabeculae at 16 months compared to the WT. The porosity was lower in the KO and higher in the UP than in WT at all ages. The porosity was significantly lower in the KO at 8 and 16 months than in the UP (Fig 39C). The space between trabeculae was greater in UP than in KO mice at 16 months but no difference between genotypes was observed for the trabecular thickness. At 16 months, the structure model index of the UP mice was significantly higher than in another genotype which indicated a shift from a plate to rod-like geometry of the trabecular bone (Fig 40A).

In the cortical bone, the BV/TV ratio was higher in the KO compared to the UP mice at 8 and 16 months and to the WT at 16 months (Fig 39D, 39E). The cortical bone thickness increased with age in all genotypes but was significantly higher in the KO relative to the UP at 8 months and then relative to the WT and UP at 16 months (Fig 39F). Cortical bone porosity was also affected by *Omd* expression. The porosity was consistently the lowest in the KO and the highest in the UP mice. The cortical bone porosity was significantly lower in KO compared to the UP mice at 8 and 16 months and then compared to the WT at 16 months (Fig 39C, 39F). In addition, the tibial crest was longer in KO than in WT and UP (Fig 40B).

#### ***IV. MAIN RESULTS***

Whether in the loss of function or the overexpression of *Omd* models, both lead to interesting bone phenotypes. The KO mice conserved their bone volume better and had less porous bone while the UP mice displayed more severe loss with a decrease in the trabecular number and an altered trabecular shape, and the WT adopted an intermediate phenotype. In addition, morphological changes had been reported between genotypes with tibiae from the mutant not only being smaller and narrower but showing a dissimilar shape as well with an extended tibial crest.

# IV. MAIN RESULTS



Legend on the next page

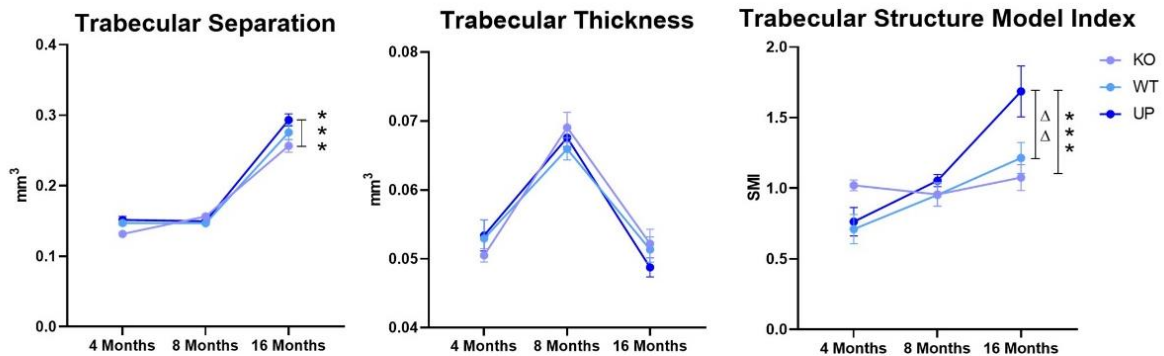
## IV. MAIN RESULTS

Figure 39:  $\mu$ CT analysis of the metaphysis of the tibia of the male mice at 4, 8 and 16 months. The trabecular bone (left) and the cortical bone (right) were analyzed separately. Regions measured for the trabecular bone and cortical bone are illustrated on the schematic tibia with the growth plate (GP), marked with a red dotted line, used as a reference for their selection. (A, D) The 3D rendering of each genotype is represented with a scale bar of 500  $\mu$ m. Red arrows indicate the tibial crest on the 16 months cortical bone. The zoom on the 16 months cortical bone illustrates the lateral side of the tibia with a scale bar of 500  $\mu$ m. (B, E) The bone parameters measured for the trabecular and cortical bone were the bone volume (BV); the total volume (TV) and their ratio (BV/TV). The data were plotted as a box plot showing all points. One-Way ANOVA was performed with differences being considered significant at  $p$ -values  $< 0.05$  (\* $p < 0.05$ , \*\* $p \leq 0.01$ , \*\*\* $p \leq 0.001$ , \*\*\*\* $p \leq 0.0001$ ). (C, F) The trabecular number, trabecular porosity, cortical thickness, and cortical porosity are represented over time. At 4 months:  $n=8$  for each genotype; at 8 months:  $n=8$  for the KO,  $n=10$  for the WT and UP; at 16 months:  $n=9$  for the KO,  $n=11$  for the WT, and  $n=10$  for the UP. Two-Way ANOVA was performed on the kinetic analysis with error bars representing  $\pm$  SEM and differences being considered significant at  $p$ -values  $< 0.05$ , \* represents significant differences between the KO and the UP,  $\blacklozenge$  represents significant differences between the KO and the WT and  $\Delta$  represents significant differences between the WT and the UP (\*/ $\blacklozenge$ / $\Delta p < 0.05$ , \*\*/ $\blacklozenge\blacklozenge$ / $\Delta p \leq 0.01$ , \*\*\*/ $\blacklozenge\blacklozenge\blacklozenge p \leq 0.001$ ).



**A**

Trabecular bone parameters over time



**B**

Cortical bone

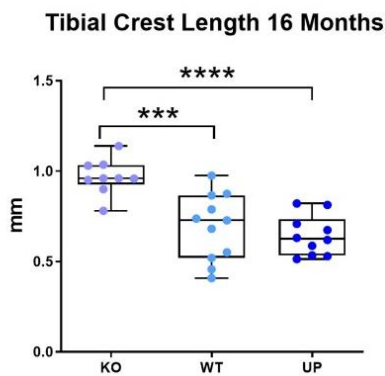


Figure 40:  $\mu$ CT analysis on the metaphysis of the tibia of the male mice at 4, 8 and 16 months (A) The trabecular bone parameters over time, with the trabecular separation, the trabecular thickness and the trabecular structure model index. Two-Way ANOVA was performed with error bars representing  $\pm$  SEM and differences being considered significant at  $p$ -values $<0.05$ , \* represents significant differences between the KO and the UP and  $\Delta$  represents significant differences between the WT and the UP (\*/ $\Delta p$  $<0.05$ , \*\*/ $\Delta p$  $\leq 0.01$ , \*\*\* $p$  $\leq 0.001$ ). (B) The length of the tibial crest of 16-month-old mice. One-Way ANOVA was performed, and the data were plotted as a box plot showing all points with differences being considered significant at  $p$ -values $<0.05$  (\* $p$  $<0.05$ , \*\* $p$  $\leq 0.01$ , \*\*\* $p$  $\leq 0.001$ , \*\*\*\* $p$  $\leq 0.0001$ ). At 4 months:  $n=8$  for each genotype; at 8 months:  $n=8$  for the KO,  $n=10$  for the WT and UP; at 16 months:  $n=9$  for the KO,  $n=11$  for the WT, and  $n=10$  for the UP.

#### ***IV. MAIN RESULTS***

The microarchitecture modifications due to the loss of function of *Omd* reflected on the bone's physical properties. The biomechanical test showed a higher whole bone strength of the KO mice tibia at 16 months, consistent with a better bone volume conservation, that could endure a higher maximal load compared to WT and UP mice. The stiffness of the KO mice was also significantly greater than the UP mice at 16 months (Fig 41).

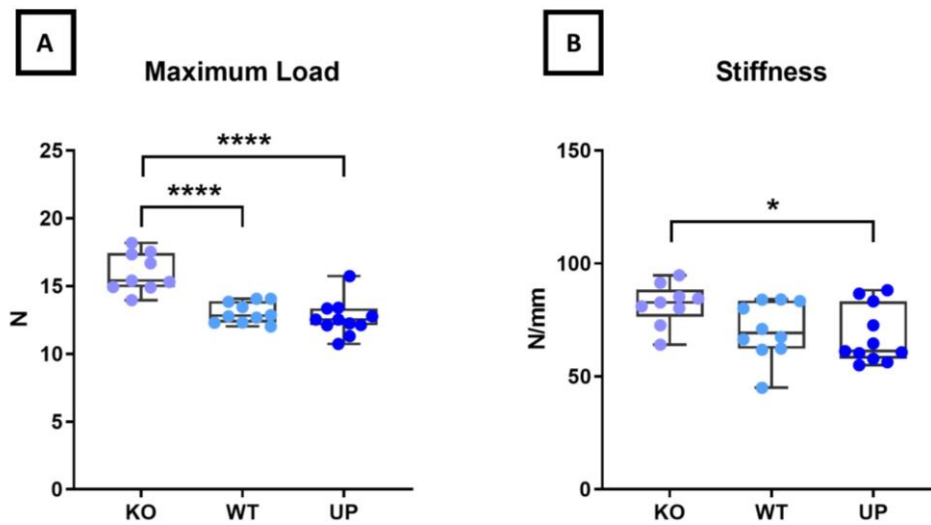
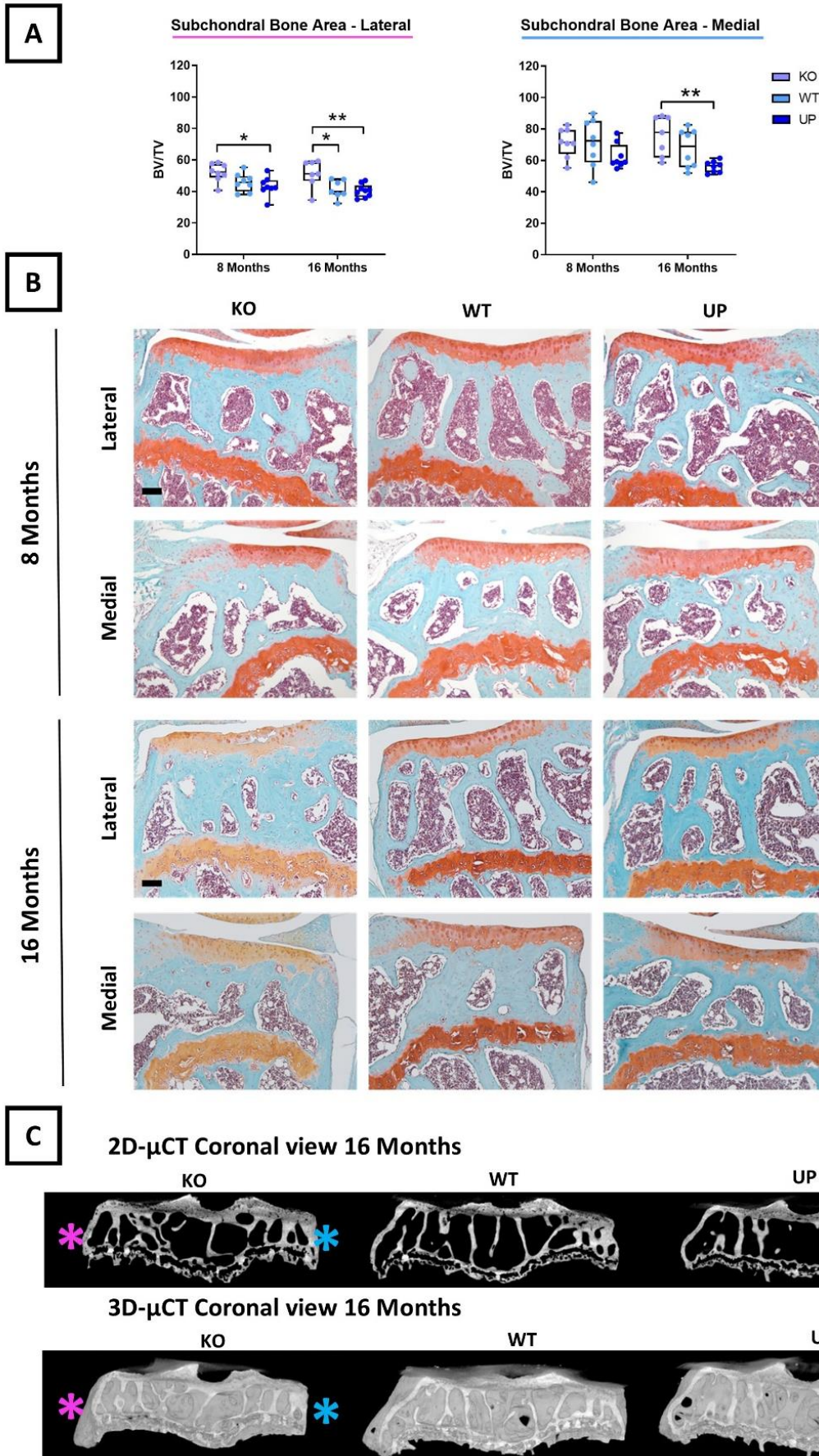


Figure 41: Biomechanical testing of the tibia from 16 months mice. (A) The maximum load (N) and (B) bone's stiffness (N/mm) were assessed using a three-point bending test with  $n=9$  for the KO,  $n=10$  for the WT and  $n=11$  for the UP. One-Way ANOVA was performed, the data were plotted as a box plot showing all points with differences being considered significant at  $p$ -values  $< 0.05$  (\* $p < 0.05$ , \*\*\*\* $p \leq 0.0001$ ).

**IV.3.2.2 Epiphysis of the tibia and the effect of *Omd* on the development of bone sclerosis**

KO mice had a greater lateral subchondral bone BV/TV ratio than the UP mice at 8 and 16 months and compared to the WT at 16 months. In the medial tibial plateau, BV/TV was more elevated in KO mice than in UP mice but only at 16 months (Fig 42A, 42B). Computed tomography illustrated that bone volume was higher in the KO than in the WT and the UP mice (Fig 42C).

*Omd* deficiency leads to a thicker bone at the tibia epiphysis and subchondral bone sclerosis. In contrast, overexpression of *Omd* by osteoblasts was associated with a decrease of bone volume. The differences between genotypes were clearly exacerbated in older mice.



Legend on the next page

#### **IV. MAIN RESULTS**

*Figure 42: (A) Histomorphometry of the subchondral bone on Safranin-O Fast Green of the knee joint of male mice at 8 and 16 months was performed with QuPath on the lateral and medial plateaus of the tibia separately. At 8 months: n=8 for each genotype; at 16 months: n=7 for the KO, n=7 for the WT, and n=9 for the UP. The data were plotted as a box plot showing all points. Two-Way ANOVA was performed with differences being considered significant at p-values<0.05 (\*p<0.05, \*\*p≤0.01). (B) Representative picture of the Safranin-O Fast Green of the knee joint of male mice showing the subchondral bone area for the lateral and medial plateau of the tibia separately. Scale bar=100 μm. (C) μCT of the subchondral bone of the tibia of the mice at 16 months. The pink asterisk indicates the lateral plateau and the blue asterisk indicates the medial plateau.*

**IV.4 *Omd* may play a beneficial role against articular degradation and prevents subchondral bone sclerosis**

To study the role of *Omd* in the pathology of OA, we compared the spontaneous development of bone and cartilage structural changes in KO, WT and UP mice during their aging, but also after destabilization of the medial meniscus. In unoperated mice, cartilage lesions appeared with aging and a higher OARSI score was observed in the medial tibial plateau of KO mice than in WT (Fig 43A). This observation was consistent with the greater loss of proteoglycans for the medial tibial plateau of KO mice compared to the WT (Fig 43B, 43C). No differences were observed in the lateral tibial plateau and femoral condyles in 16-month-old mice. In the DMM model, the lesions of the medial tibial plateau were severe and no difference between genotypes was observed (Fig 43D, 43G). Cartilage lesions were less severe in the lateral tibial plateau and KO mice tended to have a greater OARSI score than the WT (Fig 43D, 43G) but the difference was not significant (p-value=0.0585). No significant difference was observed for the scored loss of proteoglycan (Fig 43E).

In WT with DMM-induced OA, the BV/TV ratio of the subchondral bone of the medial tibial plateau was significantly higher than in non-operated mice while it was not affected in the lateral plateau. For the medial tibia, the source of variation analysis confirmed the highly significant effect of the surgery on the BV/TV ratio, but also confirmed that results were genotype-dependent. The comparison of the medial subchondral bone BV/TV ratio between genotypes in DMM groups showed that it was lower in the UP mice than in the WT. Moreover, the UP mice from the DMM group displayed a BV/TV ratio remaining similar to the non-operated WT. The two-way ANOVA comparison of the DMM model with the non-operated mice showed no interaction between the two groups which indicates that expected values are

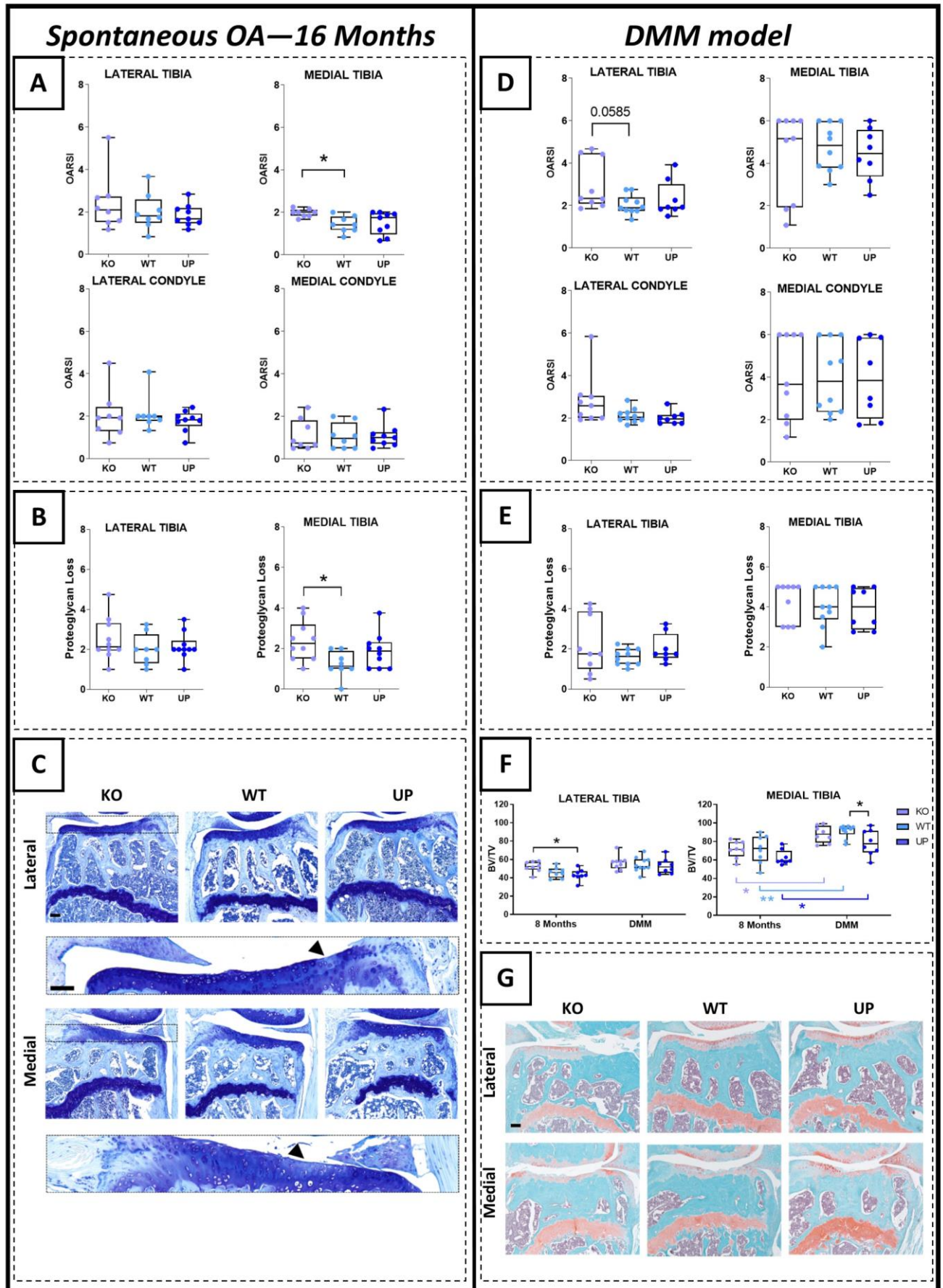
#### ***IV. MAIN RESULTS***

not related between both groups (Fig 43F, 43G). These results suggest that the expression of *Omd* helps to prevent the development of subchondral bone sclerosis associated with OA.

*Omd* would protect from the onset of subchondral sclerosis, and then, may play a role in the prevention of the subsequent articular damage, particularly for spontaneous OA.



## IV. MAIN RESULTS



## IV. MAIN RESULTS

Figure 43: Analysis of the development of OA lesions in the different genotypes after spontaneously occurring with age (left) or after the DMM (right). The spontaneous OA lesions were considered in the 16-month-old male mice and the DMM was performed on 16-week-old male mice and they were stopped at 28 weeks. (A, D): The cartilage degradation was assessed with the OARSI score (from 0 to 6) according to the OARSI recommendations. The score was attributed to the lateral and the medial tibial plateaus and to the lateral and medial condyles for the spontaneous model and the DMM model. (B, E): The score of the loss of proteoglycan (from 0 to 5) was assessed according to the OARSI recommendations for the lateral and medial tibial plateaus for the spontaneous model and the DMM model. For the OARSI score of the 16-month-old mice:  $n=8$  for the KO and the WT and  $n=9$  for the UP and for the loss of proteoglycan  $n=10$  for the KO,  $n=8$  for the WT and  $n=10$  for the UP. For the DMM model:  $n=9$  for the KO,  $n=10$  for the WT, and  $n=8$  for the UP. One-way ANOVA was performed with differences being considered significant at  $p$ -values  $<0.05$  ( $*p < 0.05$ ). (C): Illustrations of the lateral and medial plateaus stained with Toluidine Blue of the 16-month-old mice with zooms on proteoglycan loss issued from the KO and indicated by the arrowhead. Scale bar =  $100\ \mu\text{m}$ . (F): Histomorphometry of the subchondral bone on Safranin-O Fast Green of the knee joint of the DMM mice was performed with QuPath on the medial and lateral plateaus separately. Each genotype was compared to a similar age group of 8-month-old mice. At 8 months:  $n=8$  for each genotype; for the DMM:  $n=9$  for the KO,  $n=10$  for the WT, and  $n=8$  for the UP. The data were plotted as a box plot showing all points. Two-Way ANOVA was performed with differences being considered significant at  $p$ -values  $<0.05$  ( $*p < 0.05$ ,  $**p \leq 0.01$ ). (G): Illustrations of the lateral and medial plateaus stained with Safranin-O Fast Green in the DMM. Scale bar =  $100\ \mu\text{m}$ .

### **IV.5 Loss of *Omd* expression induced gait abnormalities in mice**

The gait pattern of mice was assessed at all ages using the CatWalk XT platform. At 4 months, the print area was reduced in the KO compared to the WT, and at 8 months, the print area was smaller in the KO than in the WT and UP mice. The difference between the KO and other genotypes was not significant anymore at 16 months, yet it is due to the reduced values of the WT and UP mice at 16 months while the print area of the KO remained similar at each time-point. The swing, which is the duration of no contact of the paws with the walking platform, and the single stance, defined as the duration of contact of the paws with the walking platform, were shorter in the KO mice than in other genotypes at 8 and 16 months. Finally, the intensity of the contact of paws toward the glass platform was higher in the KO compared to the WT at 8 and 16 months and compared to the UP at 8 months (Fig 44 & Appendix 3.1).

The gait analysis clearly showed that KO mice have different gait behavior than other genotypes. Their abnormal gait could be explained by their distinct bone structure and worse cartilage degradation.

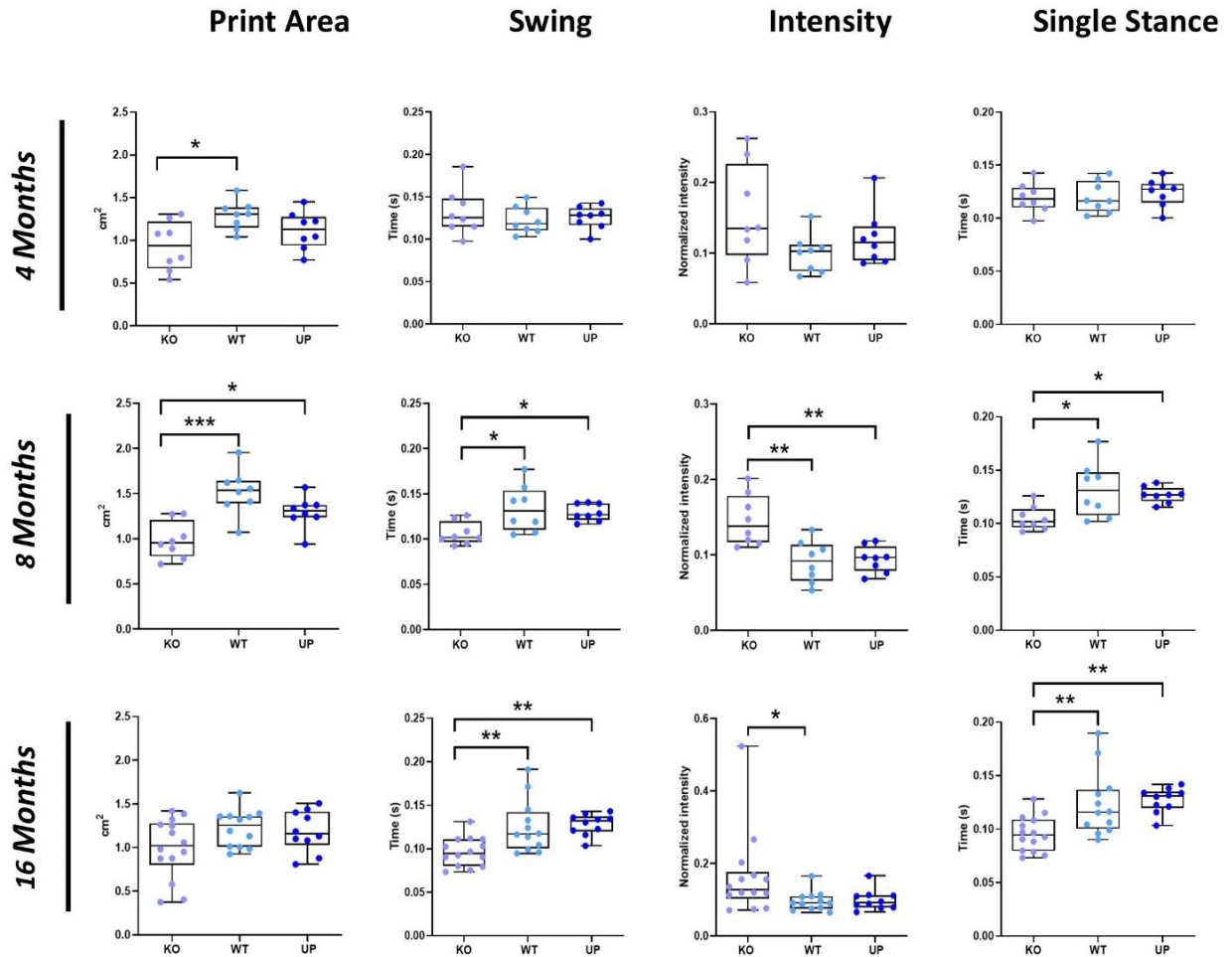


Figure 44: Analysis of the gait of 4, 8, and 16-month-old male mice with the CatWalkXT. The intensity corresponds to the mean intensity at the maximum paw contact normalized with the mean of the maximum contact paw area, the speed, and the weight of the mouse. At 4 months:  $n=8$  for each genotype; at 8 months  $n=8$  for each genotype; at 16 months:  $n=14$  for the KO,  $n=12$  for the WT and  $n=10$  for the UP. The data were plotted as a box plot showing all points. One-Way ANOVA was performed when the distribution was Gaussian and Kruskal-Wallis was performed when the distribution was not Gaussian with differences being considered significant at  $p$ -values  $< 0.05$  (\* $p < 0.05$ , \*\* $p \leq 0.01$ , \*\*\* $p \leq 0.001$ ).

### IV.6 *omd* is expressed in the zebrafish skeleton and its mutation induces articular cartilage lesions and impaired bone remodeling

The zebrafish genome presents a single homolog to the human *OMD* gene, the ortholog *omd* encoding a 401 amino acids protein presenting 46% identical and 63% similar amino acids.

We characterized the localization of *omd* expression in larvae zebrafish using whole-mount *in situ* hybridization at 48-hour post fertilization (hpf), 5-day post fertilization (dpf) and 8-dpf. We observed a strong expression of *omd* specific to craniofacial cartilages including the jaw joint during the development (Fig 45).

To gain first insights into the function of *omd* in zebrafish cartilage development, we studied the overexpression of *omd* by microinjecting 0.4 ng and 0.8 ng of its mRNA into zygotes. At 24-hpf, *omd* induced a ventralization of embryos that was not observed upon microinjection of control GFP mRNA (Fig 46A, 46B). Further, larvae injected with *omd* developed deformities at 4-dpf, mostly affecting the axial symmetry. Larvae presenting axial deformities demonstrated evident cartilage defects with abnormal development of the craniofacial cartilage (Fig 46C). As *omd* overexpression was inducing developmental defects, we designed a zebrafish *omd* mutant line (*omd*<sup>-/-</sup>) for further characterization in adults. *In situ* hybridization of *omd*<sup>-/-</sup> individuals revealed that the mutation led to the absence of *omd* mRNA in the craniofacial structures (Fig 45), indicating that no Omd protein was produced in the mutants.

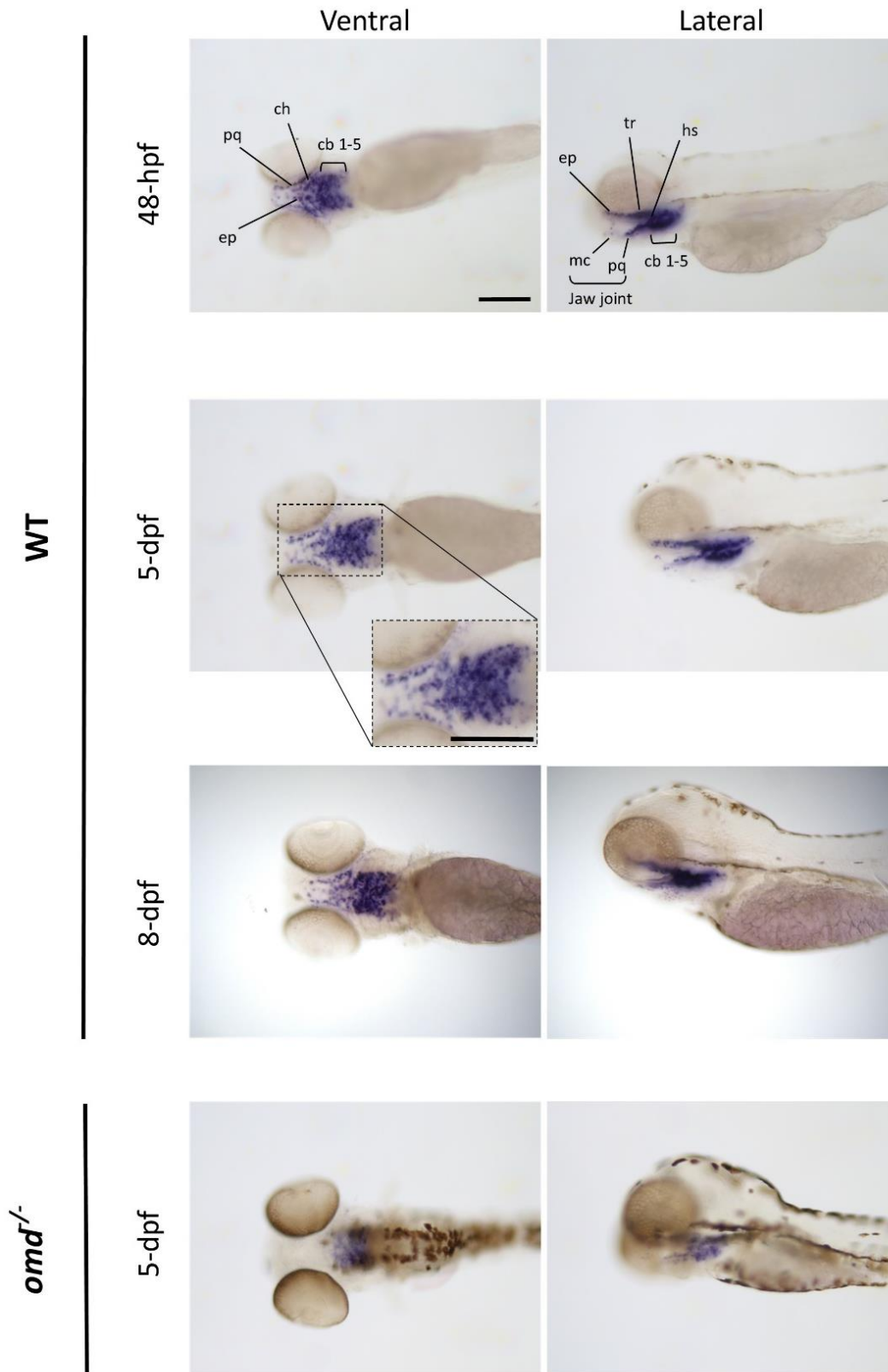


Figure 45: Whole mount in situ hybridization for the *omd* mRNA on WT zebrafish larvae at 48-hpf, 5-dpf and 8-dpf; and on *omd*<sup>-/-</sup> larvae at 5-dpf. Ventral and lateral views are illustrated. Scale bar=200  $\mu$ m. Cartilage structures are annotated as followed Ep: Ethmoid plate; Pq: Palatoquadrate; Ch: Ceratohyal; Cb: Ceratobranchial arches; Mc: Meckel's Cartilage; Tr: trabecula; Hs: Hyosymplectic cartilage. The meckel's cartilage and the palatoquadrate articulate themselves into the jaw joint.

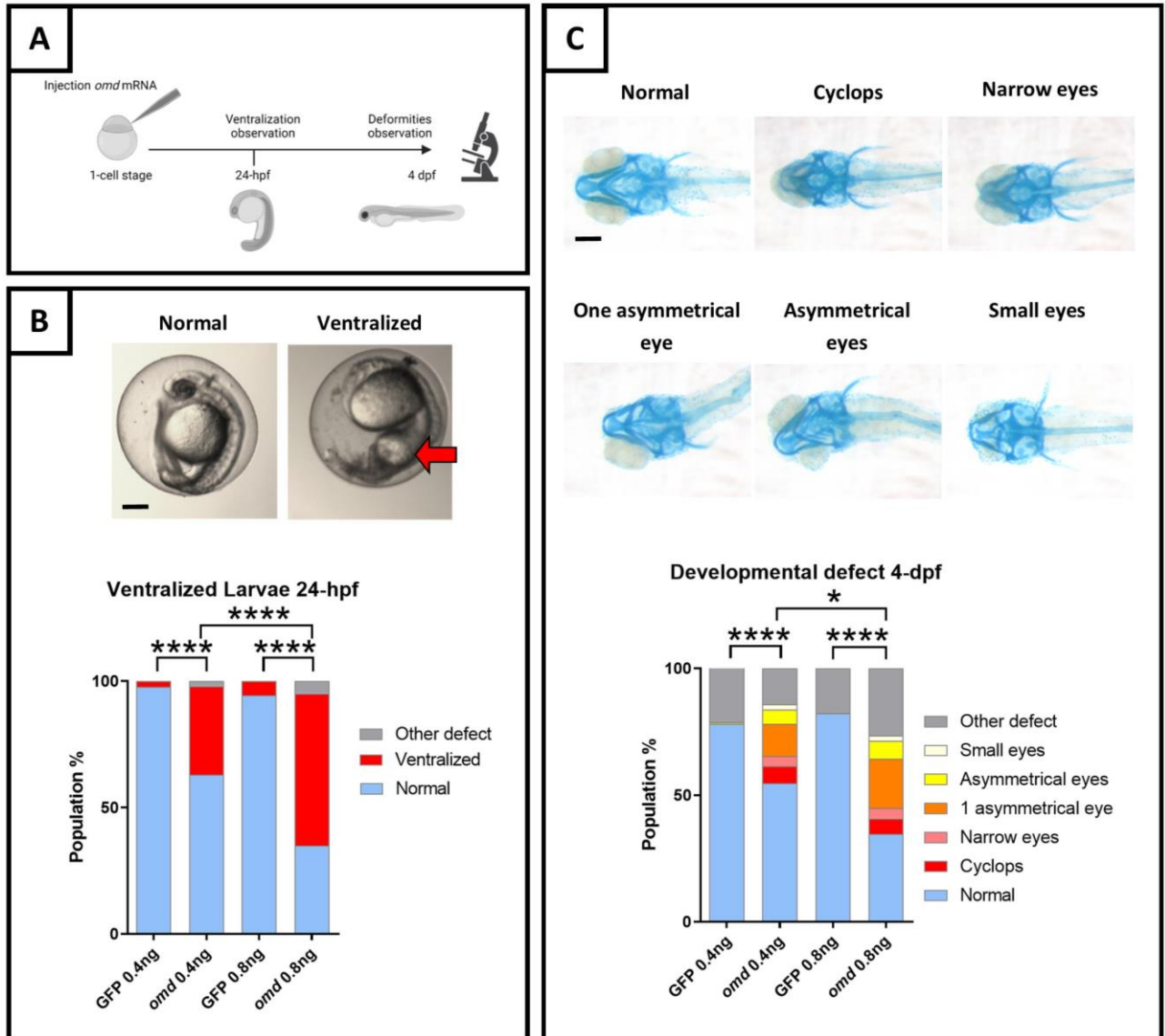
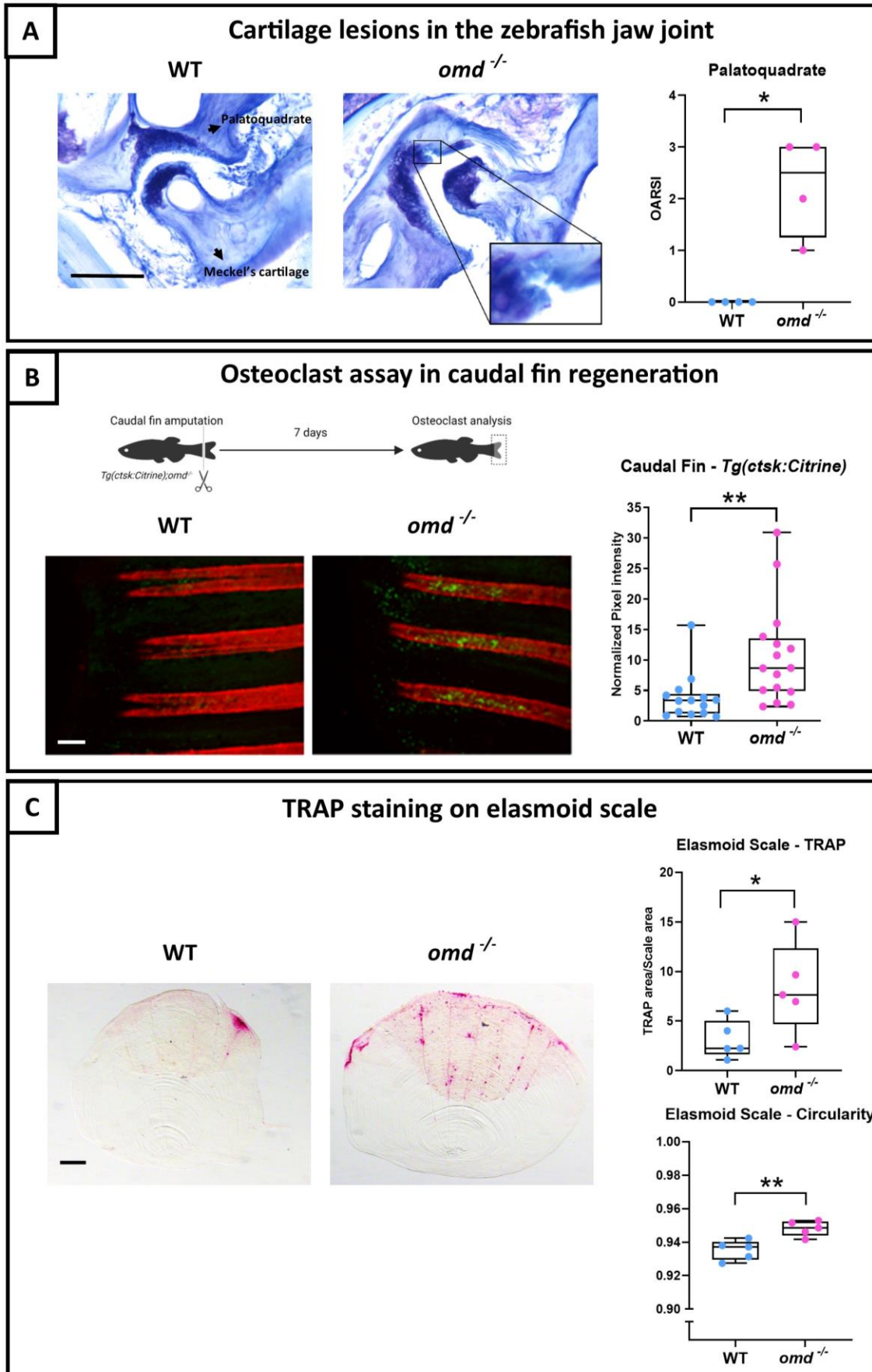


Figure 46: Analysis of the overexpression of *omd* in the zebrafish. (A) The overexpression model was generated by the injection of the zebrafish mRNA of *omd* in the 1-cell zygote followed by the observation of the ventralization at 24-hpf and the developmental deformities at 4-dpf. (B) The percentage of ventralized larvae was reported at 24-hpf after the injection of 0.4 ng ( $n=314$ ) or 0.8 ng ( $n=103$ ) of *omd*. The injection of 0.4 ng ( $n=301$ ) or 0.8 ng ( $n=72$ ) of the mRNA of the GFP served as a control. The data were plotted as a percentage of the observed class in stacked columns. A Chi-square test was performed with differences being considered significant at  $p$ -values  $< 0.05$  (\*\*\*\* $p \leq 0.0001$ ). A normal embryo and ventralized embryo with a red arrow pointing to the ventralization are illustrated. Scale bar=200  $\mu$ m. (C) The percentage of developmental deformities presented by the larvae was reported at 4-dpf after the injection of 0.4 ng ( $n=367$ ) or 0.8 ng ( $n=96$ ) of *omd*. The injection of 0.4 ng ( $n=169$ ) or 0.8 ng ( $n=79$ ) of the mRNA of the GFP served as a control. A different class of deformities was attributed: normal, cyclops, narrow eyes, one asymmetrical eye, asymmetrical eyes, small eyes and other defect which included non-specific defects. The larvae were stained with Alcian Blue and the representative illustration of each class was selected. Scale bar=200  $\mu$ m. The data were plotted as a percentage of the observed class in stacked columns. A Chi-square test was performed with differences being considered significant at  $p$ -values  $< 0.05$  (\* $p < 0.05$ , \*\*\*\* $p \leq 0.0001$ ).

#### ***IV. MAIN RESULTS***

We then compared the lubricated synovial jaw joints in one-year-old *omd*<sup>-/-</sup> zebrafish to those in WT to detect articular cartilage damage. For the palatoquadrate, the OARSI score of mutants (ranging from 1 to 3) was greater than in the WT, and clefts on their articular cartilage were observed (Fig 47A). As the murine model showed that the level of expression of *Omd* was related to the onset of the subchondral bone sclerosis and that the zebrafish displays lubricated synovial joints with similar articular degradation and subchondral bone modifications than in the physiopathology of OA [264,265], we took advantage of the zebrafish to assess the osteoclast *in vivo*. We used this model to investigate the expression of cathepsin K, a marker of osteoclasts, in the regenerating caudal fin at 7 days post-amputation, a condition associated with osteoclastogenesis. The cathepsin K expression was significantly higher in *Tg(ctsk:Citrine); omd*<sup>-/-</sup> indicating that more osteoclasts were generated in the absence of *omd* expression (Fig 47B). Furthermore, osteoclast activity was studied in elasmoid scales through TRAP staining. More TRAP staining was present on elasmoid scale of the *omd*<sup>-/-</sup>. The staining appeared to be more evenly distributed throughout the scales of the mutant and particularly localized on the edges and along the grooves of the scale. The circularity of the scales was also impacted. The scales of the *omd*<sup>-/-</sup> were more circular than in the WT (Fig 47C). The zebrafish confirmed our observations of the mouse model. The *omd* mutant zebrafish showed more severe spontaneous articular cartilage degradation in the synovial jaw joint. It also demonstrated that the regulation osteoclastogenesis was a possible mechanism of action for *Omd*.





Legend on the next page

#### **IV. MAIN RESULTS**

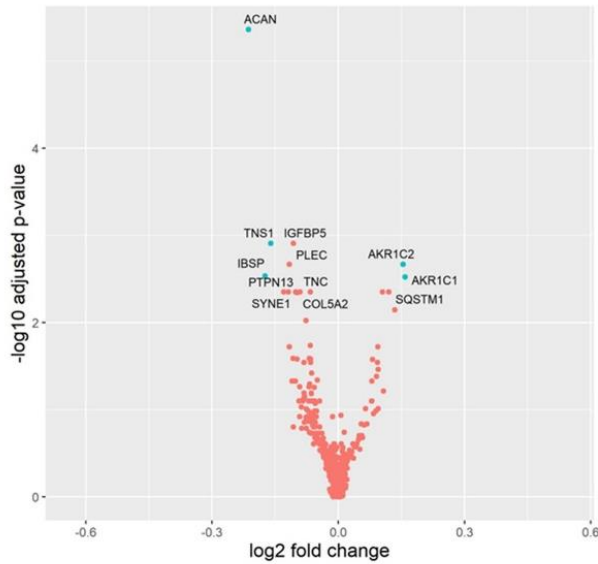
*Figure 47: The mutant deficient for omd was generated through CRISPR/Cas 9. (A) Histology of the jaw joint was performed on 1-year-old zebrafish. The OARSI score of the palatoquadrate was attributed to the jaw joint stained with Toluidine Blue with n=4 for the WT and the mutant. The data were plotted as a box plot showing all points. Mann-Whitney test was performed with differences being considered significant at p-values<0.05 (\*p<0.05). Scale bar=50µm (B) The mutant line was crossed with the Tg(ctsk:Citrine) for the osteoclasts analysis during the caudal fin regeneration. The caudal fin of 1-year-old zebrafish was cut and the regenerating fin was observed after 7 days. The osteoclasts are represented in yellow-green from the ctsk:Citrine signal and the mineralized ray were stained with Alizarin red. The data were plotted as a box plot showing all points. The pixel intensity of the regenerating rays is plotted and normalized by the background intensity with n=14 for the WT and n=16 for the mutant from two independent experiments which were pooled to perform the unpaired student t-test with differences being considered significant at p-values<0.05 (\*\*p≤0.01). Scale bar=200 µm (C) TRAP staining was performed on the elasmoid scales of 1.6-year-old zebrafish. The TRAP staining area was normalized with the total scale area. The TRAP staining and the circularity of the scales were assessed with ZFBONE - Fiji with n=5 for the WT and the mutant and with 6 to 15 scales/zebrafish analyzed. Scale bar=0.2 mm The data were plotted as a box plot showing all points. Unpaired student t-test with differences being considered significant at p-values < 0.05 (\*p < 0.05, \*\*p ≤ 0.01).*

**IV.7 OMD inhibited osteoclastogenesis by binding to RANKL**

We investigated the effects of the treatment of OMD on gene expression in cultured human primary trabecular osteoblasts. The RNA-seq revealed that only 35 genes (with  $p_{adj} < 0.05$ ) were differentially expressed after the OMD 10 ng/ml treatment, and with relatively modest fold-changes to expression (Fig 48 & Table 14). GSEA analysis using webgestalt on GO terms revealed an increase of some genes linked to the response to acid chemicals (genes *AKR1C1*, *AKR1C2*, *AKR1C3*) and a decrease of few genes involved in extracellular structure organization (GO:0043062) and ossification (genes *ACAN* and *IBSP*), and of the molecular function of actin binding. The Reactome database revealed an up-regulation of genes responsible for collagen network degradation and a down-regulation of ECM proteoglycans, ECM organization, collagen formation, and integrin cell-surface interactions.

**A**

Vulcano plot on pre-osteoblasts :  
CTL vs OMD 10 ng/ml



**B**

IBSP expression :  
CTL vs OMD 10 ng/ml

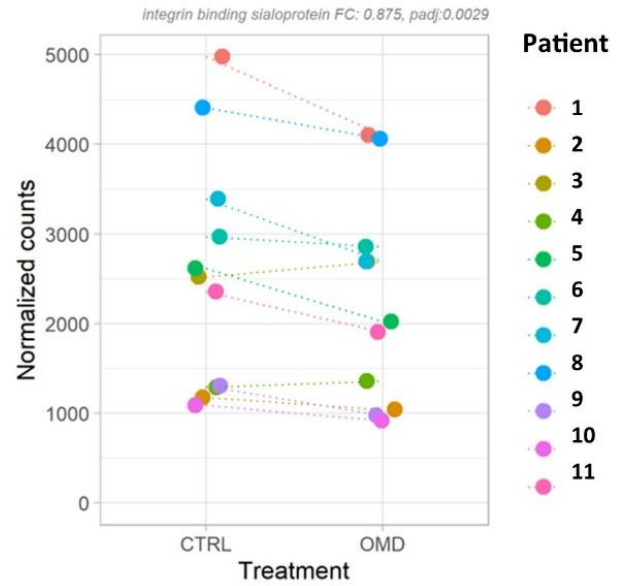


Figure 48: RNA-seq analysis of primary human pre-osteoblast cultures treated with 10 ng/ml of rhOMD during 72-h with n=11 (6 men and 5 women). (A) Vulcano plot with Threshold  $padj < 0.01$  and  $Log_2FoldChange$ . (B) IBSP gene expression comparison.

## IV. MAIN RESULTS

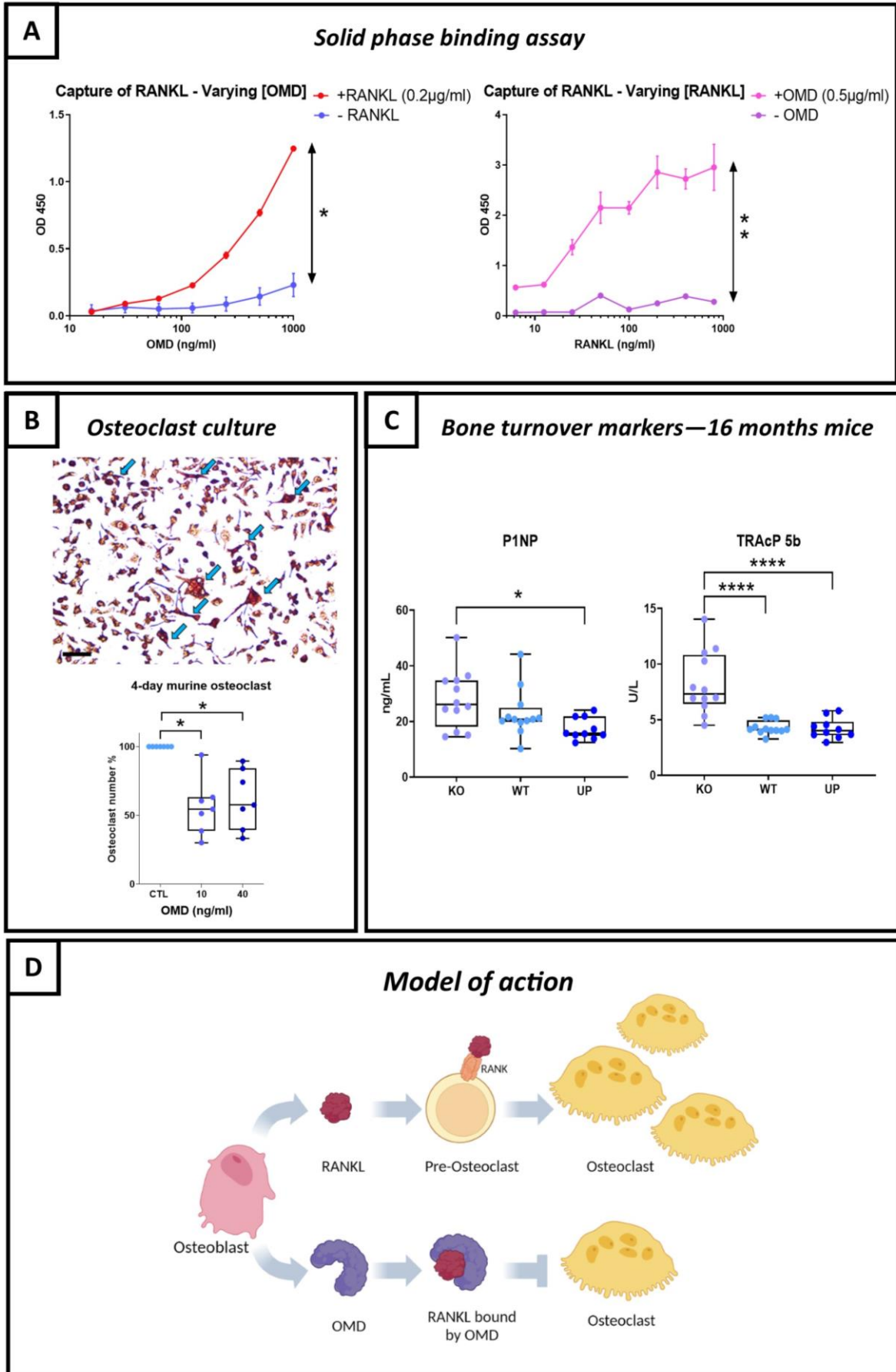
Table 14: RNA-Seq analysis of primary human pre-osteoblasts treated with 10 ng/ml of rhOMD during 72-h. List of differential gene expression, upregulated and downregulated genes sorted according to their padj. Genes with significant differential gene expression are highlighted in yellow with differences being considered significant at  $padj < 0.05$ .

DOWN REGULATED GENES						UP REGULATED GENES					
Symbol	GeneName	baseMean	log2FoldC	pvalue	padj	Symbol	GeneName	baseMean	log2FoldC	pvalue	padj
ACAN	aggreca	2411,105	-0,21316	1,15E-09	4,37E-06	AKR1C2	aldo-keto	1705,866	0,154283	2,81E-06	0,002147
IGFBP5	insulin liki	13873,32	-0,10647	9,35E-07	0,00124	AKR1C1	aldo-keto	3117,068	0,159071	5,5E-06	0,002998
TNS1	tensin 1	1957,83	-0,16004	9,75E-07	0,00124	FAM43A	family wit	3638,33	0,10487	1,54E-05	0,004463
PLEC	plectin	38057,42	-0,11604	2,58E-06	0,002147	SQSTM1	sequestos	8620,097	0,119888	1,44E-05	0,004463
IBSP	integrin bi	2395,991	-0,17361	4,61E-06	0,002933	AKR1C3	aldo-keto	1891,064	0,1345	2,99E-05	0,007134
TNC	tenascin C	105105,7	-0,0909	1,12E-05	0,004463	MMP14	matrix me	23797,94	0,094313	9,97E-05	0,019012
SYNE1	spectrin re	3486,373	-0,12999	1,2E-05	0,004463	FTL	ferritin lig	35409,69	0,081661	0,000173	0,026447
PTPN13	protein ty	3741,085	-0,11847	1,32E-05	0,004463	CLDN11	claudin 11	2835,194	0,092978	0,000203	0,028671
COL5A2	collagen t	51954,47	-0,06604	1,34E-05	0,004463	TPP1	tripeptidy	2574,102	0,095033	0,000261	0,034383
TXNIP	thioredox	15535,19	-0,10128	1,64E-05	0,004463	CLCN7	chloride v	2196,712	0,09093	0,000338	0,041542
SGCD	sarcoglyca	2555,874	-0,0979	1,78E-05	0,004539	FTH1	ferritin he	81394,98	0,080242	0,000415	0,046977
FLNB	filamin B	10552,17	-0,07663	4,24E-05	0,009514	NPC1	NPC intrac	2682,786	0,10771	0,000637	0,06077
SPTBN1	spectrin b	10107,85	-0,06612	8,62E-05	0,018268	CLTA	clathrin liq	2136,327	0,079295	0,001074	0,079648
LIMCH1	LIM and ca	1654,4	-0,11633	9,55E-05	0,019012	DVL2	dishevelle	1140,743	0,079653	0,001112	0,079648
HSPG2	heparan si	28481,36	-0,10747	0,000147	0,025749	GAS1	growth ari	5160,697	0,065182	0,001547	0,096723
SYNPO	synaptopc	3704,595	-0,06861	0,000148	0,025749	VEGFB	vascular e	1162,952	0,094535	0,00158	0,097216
HS6ST1	heparan si	1556,86	-0,09836	0,000162	0,026324	ZFP36	ZFP36 ring	3131,86	0,088973	0,001773	0,103687
LMO7	LIM domai	17862,34	-0,06548	0,000166	0,026324	BRI3	brain prot	1615,66	0,083511	0,002006	0,110923
SPTAN1	spectrin al	7236,551	-0,08121	0,000205	0,028671	GNPMB	glycoprot	5155,937	0,006262	0,002126	0,115875
COL1A2	collagen t	666596,3	-0,06554	0,00021	0,028671	MGAT4B	alpha-1,3-	2693,392	0,054505	0,003441	0,145864
COL11A1	collagen t	50162,35	-0,06306	0,000299	0,038083	SOD2	superoxid	14580,55	0,068289	0,003426	0,145864
COL5A1	collagen t	47123,68	-0,04974	0,000384	0,045765	WBP2	WW doma	1908,878	0,062006	0,003577	0,149979
MXRA5	matrix ren	2293,83	-0,10979	0,000425	0,046977	NAB2	NGFI-A bii	1215,107	0,014482	0,004731	0,180477
HELZ	helicase v	1166,073	-0,10198	0,000431	0,046977	DPP7	dipeptidy	2394,176	0,049598	0,005547	0,197423
ABI3BP	ABI family	6374,285	-0,06805	0,000477	0,050593	BOC	BOC cell a	1846,687	0,056083	0,005589	0,197423
MAP1B	microtubu	10094,58	-0,09141	0,000534	0,054225	CDC25B	cell divisi	1323,586	0,058092	0,006085	0,207729
COL8A1	collagen t	82986,12	-0,06984	0,00054	0,054225	GALNT15	polypepti	2109,369	0,048227	0,006655	0,219834
PTGIS	prostaglar	6809,253	-0,05672	0,000564	0,055138	WISP2	cellular cc	1573,634	0,006838	0,008358	0,246365
APBB2	amyloid b	4753,324	-0,06391	0,000705	0,064538	PKIG	cAMP-def	1347,838	0,04383	0,0083	0,246365
PKD1	polycystin	7354,84	-0,08114	0,000711	0,064538	KDSR	3-ketodih	1542,999	0,044489	0,008395	0,246365
MYH9	myosin he	46465,18	-0,06421	0,00074	0,065642	STAT2	signal trar	6227,577	0,034558	0,008548	0,247039
PEAK1	pseudopo	6901,382	-0,07987	0,00083	0,070926	STARD7	StAR relat	5283,118	0,037387	0,008857	0,248994
GPATCH8	G-patch di	1488,658	-0,08035	0,000837	0,070926	SLC11A2	solute car	1519,108	0,043173	0,008982	0,248994
SESN3	sestrin 3	4449,148	-0,08196	0,000931	0,075806	SLC17A5	solute car	1335,216	0,040273	0,009654	0,254005
YPEL2	yippee lik	1213,81	-0,08322	0,000934	0,075806	CEBPD	CCAAT en	1833,523	0,038947	0,01063	0,266878
COL1A1	collagen t	1158022	-0,06005	0,001002	0,079643	DUSP3	dual speci	1327,221	0,041396	0,010575	0,266878
RBMS2	RNA bindi	2232,312	-0,07013	0,001056	0,079648	GYPC	glycophor	1285,764	0,011388	0,01098	0,270709
HUWE1	HECT, UBA	6282,322	-0,09353	0,001069	0,079648	SLC6A8	solute car	1302,508	0,051077	0,011669	0,283546
TSC22D3	TSC22 don	14129,08	-0,06494	0,001126	0,079648	STOM	stomatin	3014,524	0,026907	0,01237	0,292192
HIP1	huntingtir	4042,762	-0,06478	0,001165	0,079648	ZFP36L2	ZFP36 ring	6985,44	0,009698	0,013162	0,298886
PSD3	pleckstrin	1551,104	-0,08423	0,001177	0,079648	STAT6	signal trar	6152,852	0,032288	0,013633	0,304149
MYO1B	myosin IB	4223,286	-0,0564	0,00119	0,079648	TCEAL9	transcripti	2036,363	0,012282	0,014173	0,314356
CALD1	caldesmoi	51369,15	-0,04442	0,001207	0,079648	MAP2K2	mitogen-c	5082,902	0,02987	0,014668	0,322232
BCAT1	branched	4138,794	-0,06052	0,001211	0,079648	FAM21A	WASH con	2004,276	0,026392	0,015571	0,324614
TNFRSF19	TNF recep	6751,301	-0,05444	0,001302	0,084191	SRSF6	serine anc	2807,197	0,01927	0,015866	0,327174
UBXN7	UBX doma	1479,219	-0,08739	0,001468	0,093316	SOAT1	sterol O-a	1242,091	0,016173	0,01673	0,339764
SLIT3	slit guidar	1195,11	-0,07588	0,001622	0,098215	APOD	apolipop	2303,608	0,018665	0,016663	0,339764
KIRREL	kirre like	8694,271	-0,05128	0,001766	0,103687	MTSS1	MTSS I-BA	2079,747	0,004651	0,019007	0,35199
NIN	ninein	2950,583	-0,07118	0,001794	0,103687	RNF185	ring finger	1204,454	0,023571	0,018919	0,35199
NPR3	natriuret	13269,95	-0,05616	0,001821	0,10369	FAM20C	FAM20C g	7464,93	0,036159	0,019476	0,358286
UBR5	ubiquitin	3463,241	-0,06462	0,001935	0,108555	GPX4	glutathior	4727,607	0,023814	0,0202	0,363375
CDC42EP3	CDC42 eff	11417,31	-0,05895	0,002177	0,116988	TMEM63A	transmem	1162,97	0,012537	0,020702	0,364267
SLC1A4	solute car	1846,819	-0,0919	0,002346	0,119656	INSIG1	insulin inc	4375,429	0,007516	0,022364	0,369597

#### ***IV. MAIN RESULTS***

These observations led us to explore the interaction of OMD with RANKL, which is the regulator of osteoclast differentiation, using a solid phase binding assay. These experiments revealed a clear interaction between the two proteins, which correlated to the increasing amounts of both OMD and RANKL, demonstrating that they bind directly to each other (Fig 49A). The potential biological effects of this interaction were tested on primary murine osteoclasts culture. We showed that OMD added at 10ng/ml and 40ng/ml reduced osteoclast number. No difference between 10 and 40 ng/ml of OMD was observed, both reducing the osteoclast number by 50% on average (Fig 49B). Furthermore, serum markers for bone formation (N-terminal propeptide of type I procollagen: P1NP), and osteoclast number (TRAcP 5b) showed impaired bone turnover in the KO mice at 16 months. The serum level of P1NP was significantly higher in the KO mice compared to the UP mice, and the KO mice showed significantly increased TRAcP 5b compared to the WT and UP mice (Fig 49C).

We propose a model where osteoblasts secrete OMD in the ECM to trap RANKL and prevent it from binding to the pre-osteoclast receptor RANK to inhibit their differentiation into fully committed osteoclasts. In this model, OMD depletion induces uncoupled bone remodeling, in which increased osteoclast number and bone resorption, further associated with the stimulation of bone formation, lead to subchondral bone sclerosis (Fig 49D).



Legend on the next page

## IV. MAIN RESULTS

Figure 49: (A) Solid Phase binding assay on the capture of RANKL by OMD. RANKL was coated on a plate followed by OMD addition. On the left: Binding assay with different concentrations of OMD (1000 to 15.65 ng/ml by serial 2X dilution), with 0.2  $\mu$ g/ml of coated RANKL (red curve) and negative control without RANKL (blue curve). On the right: Binding assay with different concentrations of coated RANKL (800 to 6.25 ng/ml) and 0.5  $\mu$ g/ml of given OMD (pink curve); negative control without OMD (purple curve). Wilcoxon test was performed with differences being considered significant at  $p$ -values  $< 0.05$  (\* $p < 0.05$ , \*\* $p \leq 0.01$ ). (B) Assay of the effect of OMD on primary murine osteoclast culture. The peripheral blood mononuclear cells were collected from murine bone marrow and differentiated into osteoclasts with M-CSF and RANKL. Osteoclasts were counted after 4 days of differentiation following a TRAP staining. Each point represents a mouse,  $n=7$ . The osteoclast count was represented in percentage of cells with the corresponding control set as 100%. Blue arrows point at osteoclasts. Scale bar=50  $\mu$ m. The data were plotted as a box plot showing all points. One-way ANOVA was performed with differences being considered significant at  $p$ -values  $< 0.05$  (\* $p < 0.05$ ). (C) Level of P1NP and TRAcP 5b measured in the serum of KO, WT and UP mice. The data were plotted as a box plot showing all points with  $n=12$  for the KO and WT, and  $n=10$  for the UP. One-Way ANOVA was performed when the distribution was Gaussian and Kruskal-Wallis was performed when the distribution was not Gaussian with differences being considered significant at  $p$ -values  $< 0.05$  (\* $p < 0.05$ , \*\* $p \leq 0.01$ , \*\*\*\* $p \leq 0.0001$ ). (D) Schematic representation of the mechanism of OMD on osteoclastogenesis. Osteoblasts secrete RANKL which binds to the RANK receptor on the membrane of pre-osteoclasts to induce their differentiation into osteoclasts. In parallel, osteoblasts also secrete OMD which displays the ability to capture RANKL and would prevent its binding to RANK.



# **V. DISCUSSION OF THE MAIN RESULTS**

## ***V. DISCUSSION OF THE MAIN RESULTS***

OMD is a small proteoglycan involved in bone and dental matrix mineralization but also in ectopic mineralization of other tissues, such as in arteries [225,233–235,241], suggesting it could be involved in cartilage mineralization and degradation during aging and OA.

We have previously demonstrated that osteoblasts located in the sclerotic area of OA subchondral bone produced less OMD than neighboring osteoblasts coming from the non-sclerotic area. Interestingly, OMD levels were also lower in the serum of OA patients [187]. To study the impact of *Omd* expression on bone remodeling, skeletal development and architecture, we followed mice deficient for *Omd* and mice overexpressing *Omd* during 16 months.

While the presence of OMD in bone has been previously reported [222,239], we showed for the first time that OMD is localized in mineralized tissues of the murine knee joint and is identified in calcified cartilage and tidemark. Interestingly, we observed that the calcified cartilage layer was thinner in the medial tibial compartment but thicker in the lateral tibial compartment of KO mice than in other genotypes indicating that OMD plays a key role in cartilage mineralization. The consequences of calcified cartilage thickness on cartilage degradation in OA remain controversial. One study showed that the calcified cartilage was thinning with OA, resulting in the reduction of the cartilage elastic modulus [287]. However, other studies showed that the calcified cartilage thickness increased with the progression of OA [288,289]. The presence of the more severe cartilage lesions in the medial tibial plateau of aging KO mice, where the calcified cartilage was thinner, supports the hypothesis that a thinner layer of cartilage calcified is a factor promoting cartilage degradation. Of course, this theory needs to be confirmed in other models. In the DMM OA model, there was no significant difference in cartilage damage between genotypes. This finding contrasted with the

## ***V. DISCUSSION OF THE MAIN RESULTS***

observation performed in the aging KO mice in which the cartilage lesions severity were higher in KO mice than in other genotype. This observation can be explained by the higher severity of the lesions in DMM model reflecting more of a late stage of OA. We can anticipate a ceiling effect in DMM-induced OA model because the cartilage lesions were too severe. However, considering that most of the phenotypic changes induced by the modification of the expression of *Omd* were worsened with age, the experimental design of the DMM model does not make it possible to exclude an effect of *Omd* on the articular cartilage degradation occurring at the stage set for the surgery.

At the bone level, 8 and 16-month-old KO mice had greater trabecular and cortical BV/TV than the WT while, inversely, UP mice had a reduced ratio. This finding highlights that *Omd* plays a key role in bone remodeling. More precisely, keeping the homeostatic expression of *Omd* helps to preserve its volume and structure. *Omd* overexpression not only reduced BV/TV but also increased the structure model index, which is an indicator of the altered shape of trabeculae, and led to higher bone porosity. Over time, aging was aggravating those observations. This indicates that, when overexpressed, *Omd* may turn to cause detrimental effects on skeletal tissues. In the KO, the global bone morphology was affected. Their tibia was narrower and their tibial crest longer, this morphological change may affect muscle insertion and, by so, the muscle-to-bone relationship. Further, KO mice were more prone to spontaneously develop subchondral bone sclerosis, as indicated by higher BV/TV, like in sclerotic subchondral bone in OA. The modifications of the bone microarchitecture affected the bone's physical properties as well, important features relative to the bone quality, with KO mice showing higher whole bone strength of the tibia at 16 months, an expected behavior following the observations from the  $\mu$ CT analysis.

## ***V. DISCUSSION OF THE MAIN RESULTS***

We also observed sclerosis of the subchondral bone following the DMM procedure, in all the genotypes. Yet, the subchondral bone of the medial tibia of UP mice was thinner than the KO and WT mice suggesting that *Omd* could prevent subchondral bone sclerosis in OA. Although these observations are indicating that the overexpression of *Omd* would protect from the onset of OA-associated sclerosis, we are still willing to be cautious about the efficiency of the protective effect as the BV/TV ratio is initially slightly lower in UP mice showing altered bone microarchitecture. Nonetheless, our data suggest that *Omd* plays a role in subchondral bone sclerosis, a key feature of OA, involved in cartilage degradation. Therefore, we can hypothesize that the impact of *Omd* on cartilage degradation could be secondary to its effect on bone. In the spontaneous model, the loss of function of *Omd* is associated with articular cartilage degradation, suggesting that *Omd* might prevent cartilage degeneration. This hypothesis has to be verified in a larger number of animals or a more advanced aging-related OA model where more pronounced differences with a higher articular degradation in the KO mice are anticipated.

The gait analysis with the Catwalk XT identified different motor patterns between the genotypes. The gait pattern of KO mice, including the print area, the swing, the intensity of the contact, and the single stance of paws toward the glass platform, were modified. More precisely, for their hind paws, the KO mice had a reduced print area, a shorter swing and single stance, and a higher intensity of the contact of the paw. This may result in pain, discomfort, or of mechanical disorders associated with joint damage or with skeletal tissue abnormalities. It is important to highlight that a decreased hind print area is considered the best predictor for spontaneous OA [290]. Furthermore, the single stance was reported to be significantly decreased in OA mice [291] and the swing may also be reduced with OA [292]. Our report on the gait parameters is consistent with previous observations found in the literature and

## ***V. DISCUSSION OF THE MAIN RESULTS***

corroborates the susceptibility of the KO mice to develop further OA joint damage. On the other hand, the gait patterns at 16 months may be affected by the initiation of OA leading to abnormal loading on affected limbs.

To corroborate our findings from the mice model, we studied mutant adult zebrafish which did not express *omd*. In zebrafish, we found cartilage lesions in the articular cartilage in the jaw joint. Again, this suggests that *omd* prevents spontaneous cartilage lesions during aging and that a decrease of OMD production by osteoblasts and hypertrophic chondrocytes could be deleterious for cartilage. Altogether, these findings support that a loss of OMD contributes to OA development. We have then investigated by which mechanism of action OMD could regulate bone and cartilage metabolism. Our transcriptomic data revealed that OMD is unlikely to perform its function on osteoblasts through direct gene expression regulation as very few genes were modified and with a low magnitude. It remains noteworthy to specify that among the regulated genes, *IBSP* was downregulated by OMD. *IBSP* overexpression by hypertrophic chondrocytes is associated with OA [293]. Consequently, OMD could control cartilage calcification in OA by downregulating IBSP production.

Direct binding of OMD to key bone regulatory factors is another possible mechanism of action. SLRPs are known to bind cytokines, growth factors, and ligands like RANKL [50,219]. Herein, we showed that OMD is not only enhancing the differentiation of osteoblasts [239], but is also able to bind directly to RANKL and block its biological activity on osteoclasts. Measures of bone markers in the serum of 16 months mice corroborated the elevated osteoclast number and higher bone turnover in the loss of function model. Concerning the UP mice, they showed the lowest P1NP level and it might indicate that their poor conservation of bone volume would be due to low bone formation rather than bone resorption. The mutant zebrafish model

## ***V. DISCUSSION OF THE MAIN RESULTS***

confirmed the role of *omd* in osteoclastogenesis. The number of cathepsin K positive osteoclasts increased in the regenerating caudal fin of the mutants. Further, observations of elasmoid scales, which share a similar transcriptomic profile with the mammalian skeleton including genes related to human diseases [270], highlighted higher TRAP staining and more circular scales in zebrafish lacking *omd*. As osteoclasts are inducing OMD expression in mature osteoblasts [240], OMD presents a negative feedback activity on them. Moreover, sulfated GAGs are known to inhibit the differentiation of osteoclasts and the sulfation level of OMD is higher during the ECM mineralization process [226,294]. Our findings present OMD as a novel regulator of the bone remodeling process able to protect from subchondral bone sclerosis in pathological conditions like OA. Those observations are crucial since we know that bone remodeling plays a key role in the bone-driven OA phenotype with uncoupled bone remodeling leading to impaired bone resorption and bone deposition functions, then resulting in subchondral bone sclerosis with an elevated number of osteoclasts [167,168,295]. We identified OMD as a novel player in the uncoupled bone remodeling associated with OA. Finally, we can point out that the bone and cartilage phenotypes due to the loss of function of *Omd* are consistent with other murine SLRPs-deficient models [200–203,207,208,212,219,296]. It ultimately reinforces previous statements declaring overlapping functions within the SLRP family.

In conclusion, alterations of the *OMD* expression modify the bone and cartilage metabolism and structure. OMD helps to preserve bone and cartilage integrity and a local decrease of its production leads to the development of OA mainly by increasing subchondral bone sclerosis and thinning the calcified cartilage while its overexpression alleviates the subchondral bone sclerosis. OMD is able to directly bind to RANKL and inhibit osteoclastogenesis to regulate bone remodeling and limit subchondral bone sclerosis. Our previous and current researches,

## ***V. DISCUSSION OF THE MAIN RESULTS***

making use of both *in vitro* and *in vivo* experiments either with human, mouse or zebrafish models, build a strong and compelling body of evidence of OMD being a key factor in OA associated with subchondral bone sclerosis.

# **VI. ADDITIONAL RESULTS & DISCUSSION**



## ***VI. ADDITIONAL RESULTS & DISCUSSION***

### **Preliminary notice**

Sections IV and V, presenting the main results that were selected for publication in *Bone research*, were all concerning male mice because they are showing less variability concerning the bone and cartilage biology and the development of OA. However additional data were collected on both male and female mice, and also on the zebrafish and *in vitro* models.

## ***VI. ADDITIONAL RESULTS & DISCUSSION***

### **VI.1 Further characterization of the bone phenotype by $\mu$ CT in the mouse model**

Femurs of male mice were analyzed by  $\mu$ CT for further characterization of the bone phenotype in male mice. The whole femurs of 8 and 16 months mice were reconstructed and illustrated in the figure 50. The femur of KO mice at 8 months showed a distinct phenotype concerning the femoral head that seems to conserve the calcified cartilage encapsulating the bone compared to the WT and UP mice with a fully ossified femoral head. All mice from the KO group displayed this phenotype. At 16 months, the phenotype of the femoral head of KO mice became more similar to WT and UP mice. However, the capsule of calcified cartilage still could be observed to a lesser extent. From the KO group, 2/3 of the mice showed this milder phenotype. Corroborating the visual observations, the density of the femoral head was significantly lower for the KO at 8 months when the phenotype is evident but was not significant at 16 months. A lower density for the KO at 8 months is consistent with the femoral head being less engaged in the ossification process (Fig 52A). The representation of the 16 months femurs may also indicate thicker subchondral bone from the condyle area of the knee joint in KO mice compared to the WT and especially to the UP mice. This observation would need quantification of the subchondral bone volume for confirmation (Fig 50).

## VI. ADDITIONAL RESULTS & DISCUSSION

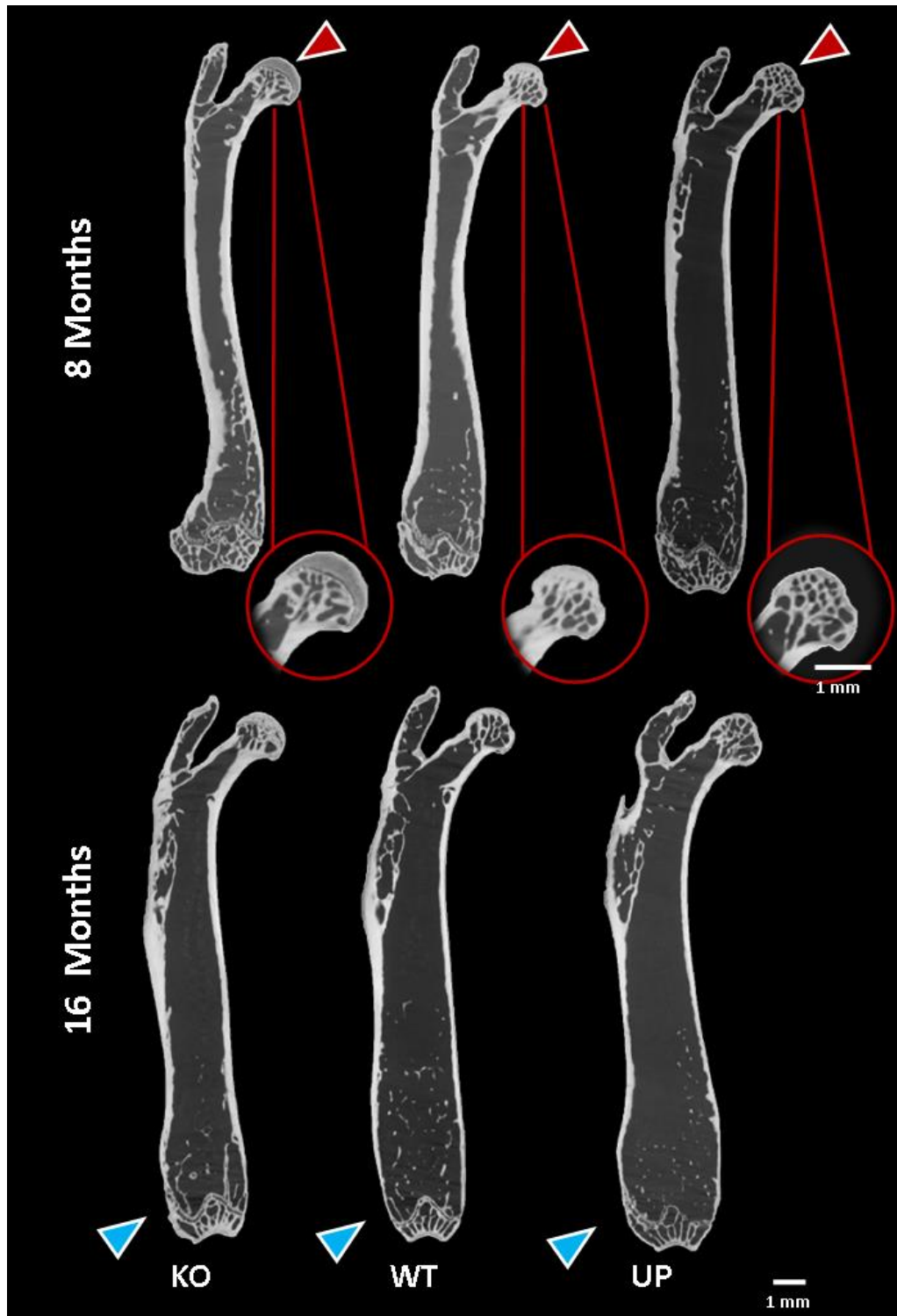


Figure 50:  $\mu$ CT analysis of the femur of male mice at 8 and 16 months with a zoom on the femoral head of 8 months mice. The red arrows point to the femoral head and highlight the distinct bone phenotype of the KO. The blue arrows point to the subchondral bone of condyles. Scale bar=1mm.

## ***VI. ADDITIONAL RESULTS & DISCUSSION***

As the  $\mu$ CT analysis from the tibia showed that the bone microarchitecture of the KO and UP mice were the most impacted at 16 months when compared to WT, analysis of the bone parameters of the femoral head and the femoral shaft was performed on 16 months mice. The volume of the trabecular bone of the femoral head, the cortical bone of the femoral shaft, and the trabecular bone of the distal epiphysis were reported as the BV, TV and BV/TV. There was a difference in the BV of the trabecular bone of the femoral head between the KO and UP mice, with the KO showing the lowest BV and the UP the greatest. The BV/TV of the trabecular bone of the femoral head showed that both the KO and the UP tended to have a higher ratio than the WT (p-value KO vs WT: 0.15; p-value UP vs WT: 0.11) (Fig 51A). For the BV/TV of the cortical bone of the femoral shaft, the KO had the greatest ratio (p-value KO vs WT: 0.05; p-value KO vs UP: 0.06) (Fig 51B). For the trabecular bone of the distal epiphysis, no distinct differences were observed for the BV, TV and the BV/TV at 16 months.

## VI. ADDITIONAL RESULTS & DISCUSSION

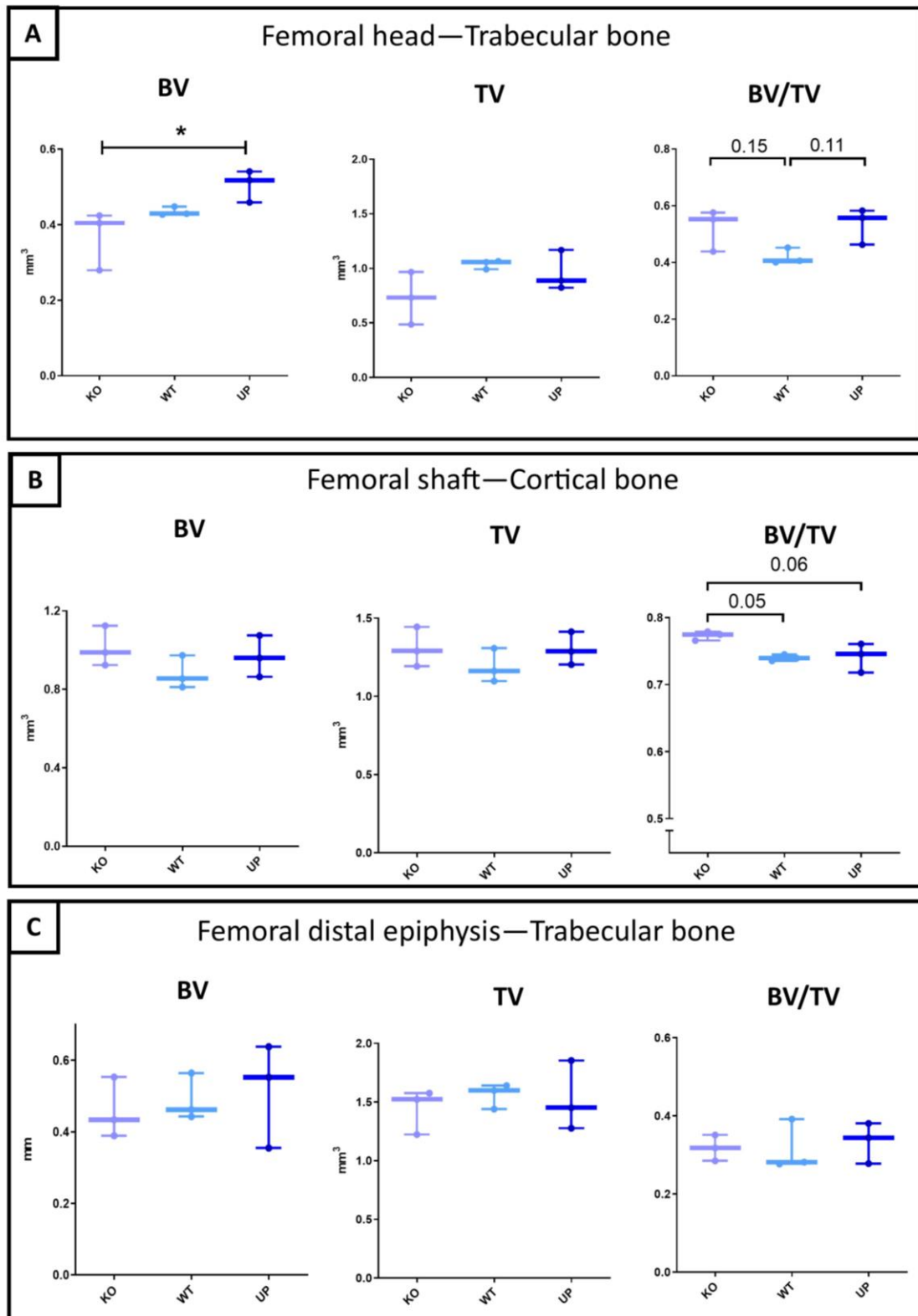


Figure 51:  $\mu$ CT analysis of the femur of 16 months male mice. For the analysis, the femoral head and the femoral shaft were separated. A) BV, TV and BV/TV of the trabecular bone of the femoral head. B) BV, TV and BV/TV of the cortical bone of the femoral shaft. C) BV, TV and BV/TV of the trabecular bone of the femoral head. B) BV, TV and BV/TV of the trabecular bone of the femoral shaft. The data were plotted as a box plot showing all points. One-Way ANOVA was performed with differences being considered significant at  $p$ -values  $< 0.05$  ( $*p < 0.05$ ,  $**p \leq 0.01$ ). For each genotype,  $n=3$ .

## ***VI. ADDITIONAL RESULTS & DISCUSSION***

The trabecular thickness of the femoral head seems to be the highest in the UP mice but was not significant (p-value UP vs WT: 0.06) (Fig 52B). Regarding the trabecular number, the femoral phenotype was consistent with the data reported from the trabecular bone of the tibia but was not significant. The KO had the greatest trabecular number and the UP the lowest in the femoral head (p-value UP vs KO: 0.1) (Fig 52C). The porosity of the trabecular bone tended to be lower in the KO and the UP mice (p-value KO vs WT: 0.15; p-value UP vs WT: 0.11) (Fig 52D). There was no difference in the trabecular separation (Fig 52E).

For the femoral shaft, there are two main parameters consistent with the observations from the tibia. First, the thickness of the cortical bone tended to be greater in the KO (p-value KO vs WT: 0.09; p-value KO vs UP: 0.14) and secondly, the porosity of the cortical bone of KO mice tended to be reduced compared to the WT and UP mice (p-value KO vs WT: 0.05; p-value KO vs UP: 0.06) (Fig 53A, 53B). Other parameters measured in the femoral distal epiphysis, such as the thickness of the trabecular bone, the number of trabeculae, the trabecular separation and the porosity of the trabecular bone did not seem to be modified by the expression of *Omd* *in vivo* (Fig 53 C-F).

Unfortunately, there is a serious limitation for the analysis conducted on femurs because only three samples could be scanned by  $\mu$ CT at 8 and 16 months for each genotype. Therefore, we should be cautious about the conclusions coming out of the analysis, especially for the data with a p-value close to the statistical threshold. Nevertheless, the phenotype of the femoral head of KO mice was very strong and corroborated the tibial phenotype, especially at 8 months, and reproduced over time between 8 and 16 months.

## VI. ADDITIONAL RESULTS & DISCUSSION

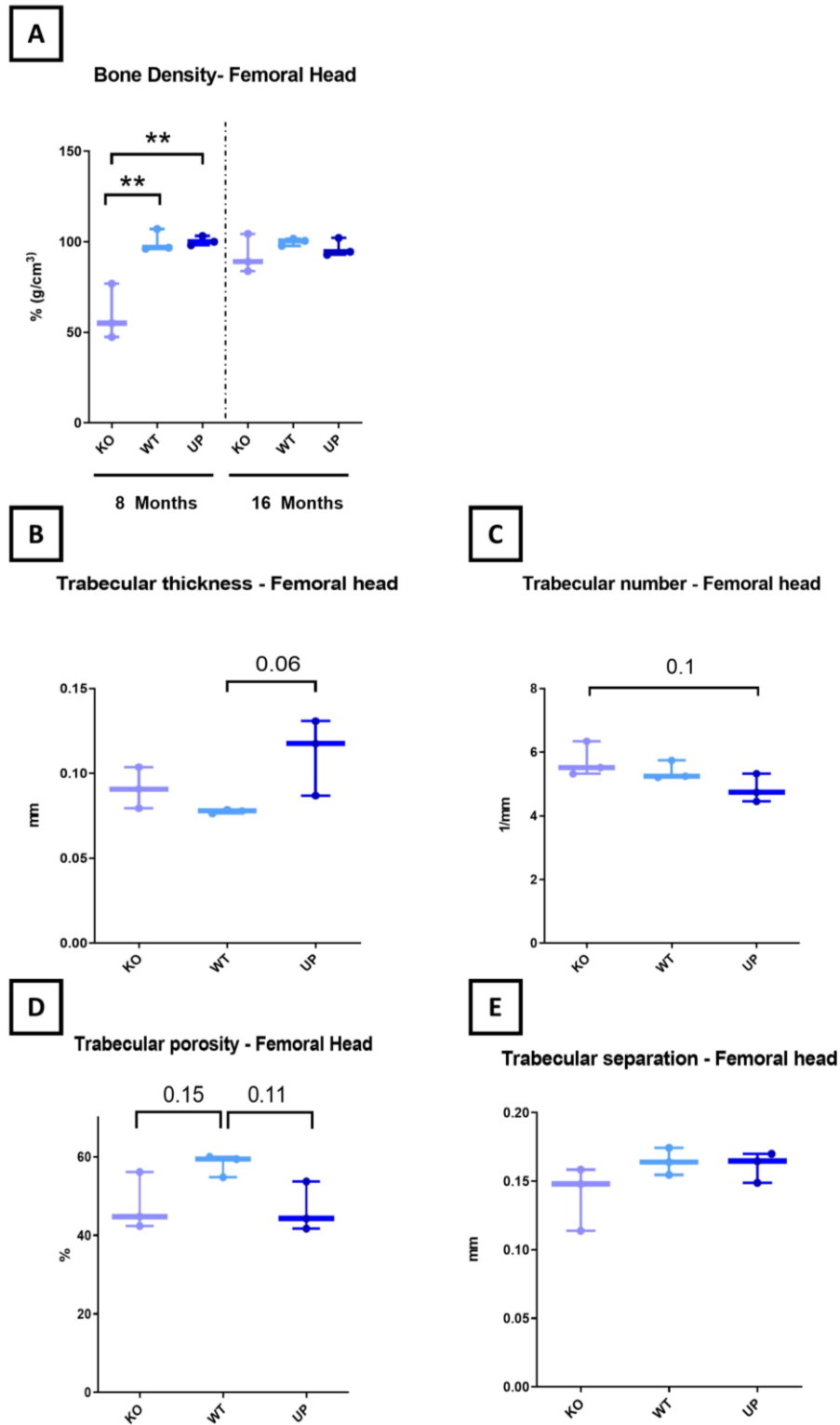


Figure 52:  $\mu$ CT analysis of the trabecular bone of the femoral head of 8 and 16 months male mice. A) the bone density of the femoral head was measured and represented as a percentage for the comparison between the genotypes at 8 months and 16 months. B) Trabecular thickness of the femoral head at 16 months. C) trabecular number at 16 months. D) Porosity of the trabecular bone at 16 months. E) Trabecular separation at 16 months. The data were plotted as a box plot showing all points. One-Way ANOVA was performed with differences being considered significant at  $p$ -values  $< 0.05$  ( $*p < 0.05$ ,  $**p \leq 0.01$ ). At 8 and 16 months,  $n=3$  for each genotype.

## VI. ADDITIONAL RESULTS & DISCUSSION

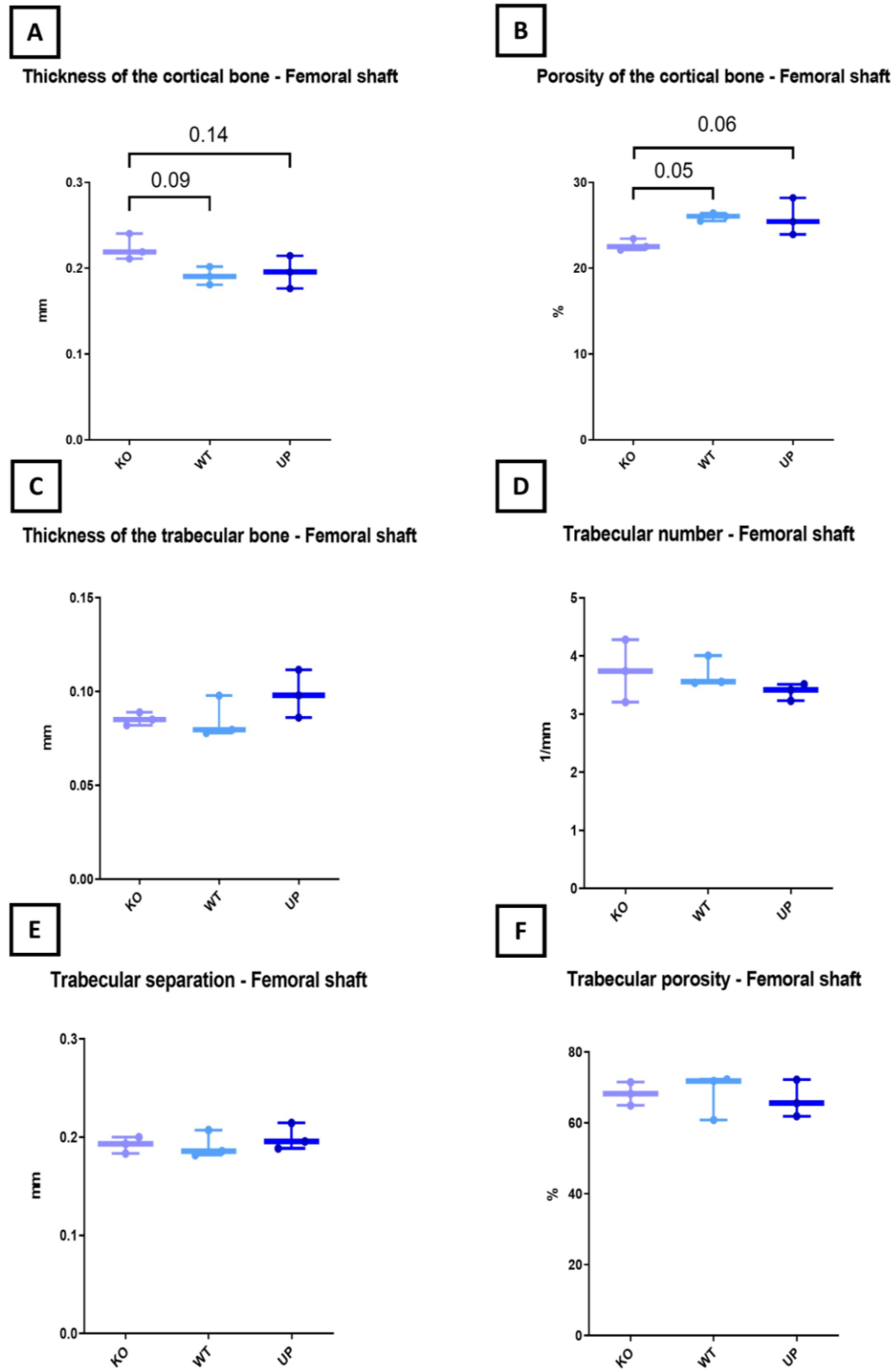


Figure 53:  $\mu$ CT analysis of the cortical and trabecular bone of the femoral shaft of 16 months male mice. A) Thickness of the cortical bone. B) Porosity of the cortical bone. C) Thickness of the trabecular bone. D) Trabecular number. E) Trabecular separation. F) Trabecular porosity. The data were plotted as a box plot showing all points. One-Way ANOVA was performed with differences being considered significant at  $p$ -values  $< 0.05$  ( $*p < 0.05$ ,  $**p \leq 0.01$ ). At 8 and 16 months,  $n=3$  for each genotype.



### **VI.2 Gait analysis of the DMM model**

The gait behavior of mice from the DMM model was assessed during the week prior to their euthanasia to evaluate if the development of severe OA would impact their gait differently according to the level of OMD. In the DMM model, the print area and the intensity of the hind paws were no more significant between the genotypes. Interestingly, the swing phase in the KO after DMM is still highly significantly decreased compared to the WT and UP mice (Fig 54). Besides the print area, the swing and the intensity of the hind paws, as reported from the mouse models over-time (4-to-16 months) in sections IV and V, the stand and the stand index were two parameters significantly increased in the WT compared to the KO and UP only in the DMM model. Other parameters from the front and hind paws were reported in “Appendix 3.2”.

Two-way ANOVA analysis on SHAM, DMM, and 8 months mice, reported a main effect from the genotype and the surgery. It showed a significant main difference between DMM groups and non-operated mice of 8 months ( $p$ -value=0.01). Data from the Catwalk XT analysis on the DMM model corroborate the indication of a gait disorder in the KO mice. Abnormal gait signs might be explained by the altered bone microarchitecture in the absence of OMD which itself might imply different muscle insertions on the elongated tibial crest of the KO. The phenotype of the femur might also be related to a form of hip instability that could be another factor explaining gait differences.

## VI. ADDITIONAL RESULTS & DISCUSSION

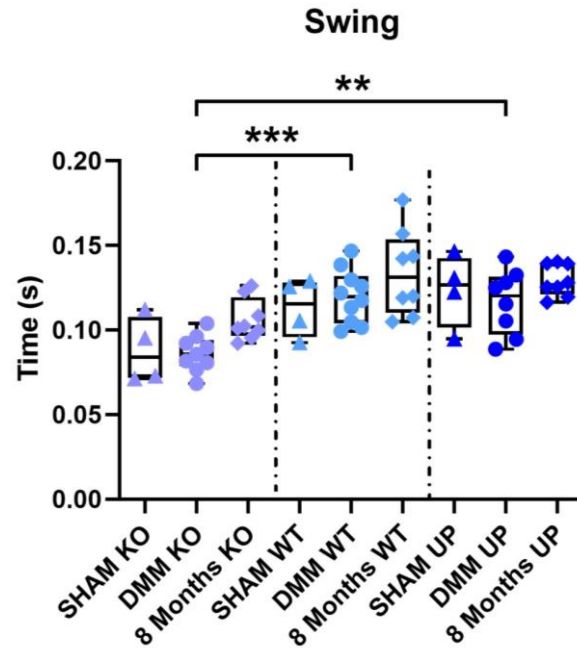


Figure 54: Analysis of the gait with the Catwalk XT of male mice from the DMM model (represented by ●) with the SHAM group (represented by ▲) and non-operated mice of 8 months (represented by ◆) as controls. The swing of the mice was reported with the data plotted as a box plot showing all points. One-Way ANOVA was performed with differences being considered significant at  $p$ -values  $< 0.05$  (\*\* $p \leq 0.01$ , \*\*\* $p \leq 0.001$ ). For the SHAM:  $n=4$  for each genotype; for the DMM:  $n=9$  for the KO,  $n=10$  for the WT and  $n=8$  for the UP. Analysis of 8 months mice was introduced in figure 44.

### **VI.3 Characterization of the functions of *Omd* in female mice**

#### **VI.3.1 General growth characteristics**

The mouse model allowed a broad characterization of the effect of the loss of *Omd* and its overexpression with a specific focus on bone and cartilage of 4, 8 and 16 months males in addition to the surgically induced OA model. During the investigation on male mice, female mice were also generated and characterized.

Following the same design as male mice, the general growth characteristic of KO, WT and UP female mice were reported with the measurement of their size, weight and femoral length. The size of female KO was shorter, first only compared to the UP at 8 months and then both to the WT and UP at 16 months (Fig 55A). However, their body weight was not significantly different at any observed time-point (Fig 55B). Concerning the femoral length, they appeared similar through each genotype at 4 and 8 months but at 16 months the female KO displayed a significantly reduced femoral length compared to the WT and UP mice (Fig 55C). The female KO was the only genotype with no further growth between 8 and 16 months (Fig 55D).

When comparing the results coming from the female and male mice, we can first highlight a difference inside a genotype due to their respective sex, as expected, but also that difference between genotypes is impacted by the attributed sex. The size of male KO was reduced at 4 months but for the female, it is at 8 and 16 months. It is the same observation with the femoral length with a distinct reduction at 16 months only in female KO.

## VI. ADDITIONAL RESULTS & DISCUSSION

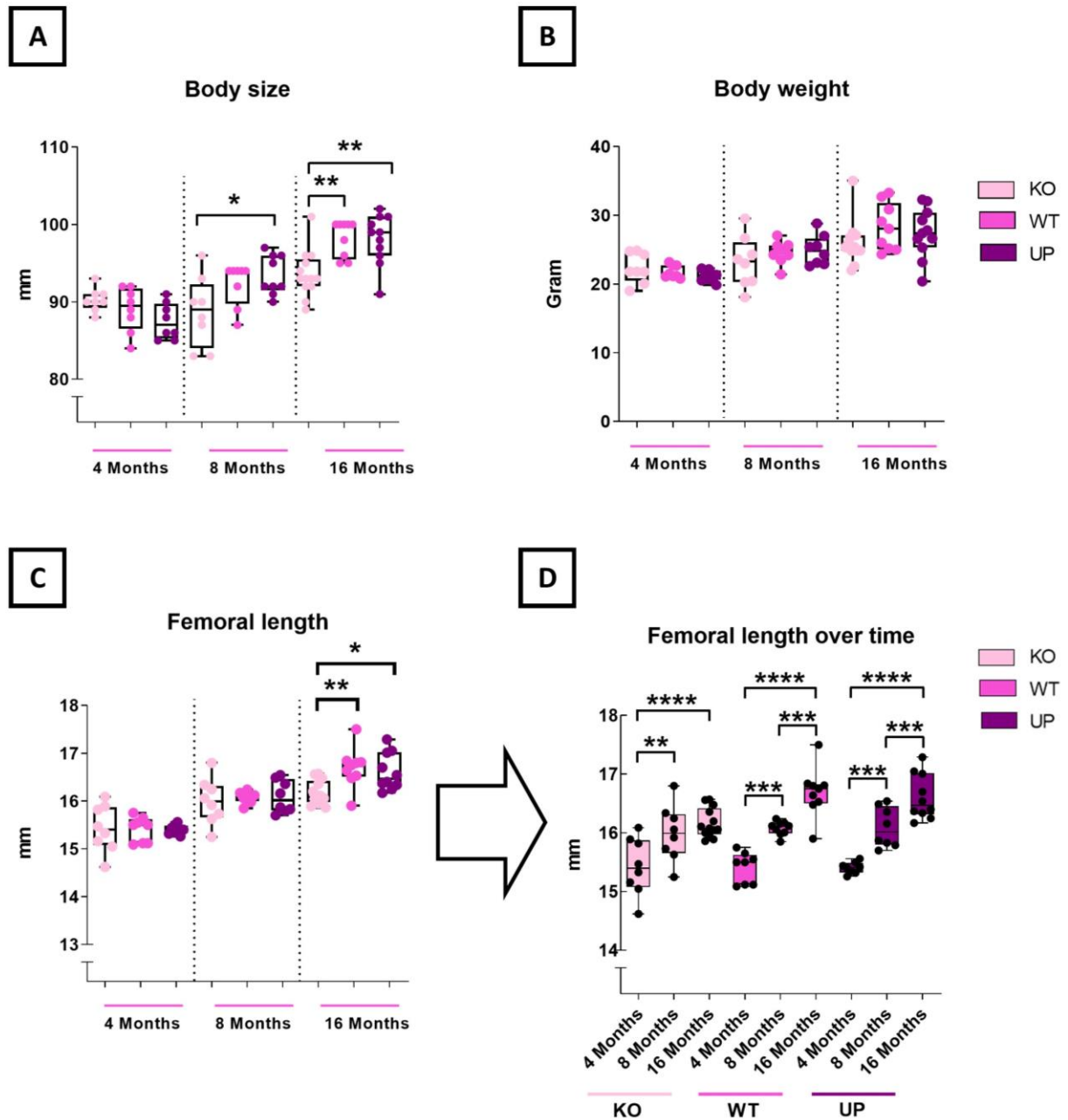


Figure 55: Macro observations of the knee joint of female mice at 4, 8 and 16 months. (A) For the body size:  $n=8$  for each genotype at 4 months.;  $n=8$  for the KO and the WT and  $n=9$  for the UP at 8 months;  $n=13$  for the KO,  $n=9$  for the WT and  $n=11$  for the UP at 16 months. (B) For the body weight:  $n=8$  for each genotype at 4 months.;  $n=8$  for the KO and the UP and  $n=9$  for the WT at 8 months;  $n=13$  for the KO,  $n=9$  for the WT and  $n=11$  for the UP at 16 months. (C) For the femoral length:  $n=8$  for each genotype at 4 months;  $n=8$  for the KO and the UP and  $n=9$  for the WT at 8 months;  $n=13$  for the KO,  $n=9$  for the WT and  $n=10$  for the UP at 16 months. (D) The femoral length was displayed to show the evolution of the femurs over time within the genotypes. (A-C) Ordinary one-way ANOVA was performed to compare the body size, the body weight, and the femoral length between the genotypes, at each time-point. Kruskal-Wallis was performed when the distribution was not Gaussian. (D) Two-way ANOVA was performed to examine the influence of time on the femoral length inside each genotype. The data were plotted as a box plot showing all points and differences being considered significant at  $p$ -values  $< 0.05$  (\* $p < 0.05$ , \*\* $p \leq 0.01$ , \*\*\* $p \leq 0.001$ , \*\*\*\* $p \leq 0.0001$ ).

## ***VI. ADDITIONAL RESULTS & DISCUSSION***

### **VI.3.2 Characterization of the bone phenotype by $\mu$ CT in female mice of 16 months**

We observed from male mice several differences among bone parameters between the KO, WT and UP mice and that they were exacerbated during the aging process with the 16 months mice showing the greatest contrast between the genotypes. Therefore, the 16 months female mice were selected in priority for the  $\mu$ CT analysis of their tibia.

3D illustration issued from the  $\mu$ CT displays the trabecular and cortical bone of female mice separately. From the 3D representations, the 16 months female KO is distinct from the WT and UP with more trabecular bone but a smaller tibia (Fig 56). The volumetric quantification for the trabecular bone corroborated this observation showing greater BV for the female KO but significantly reduced TV for the female KO compared to the UP mice. It translated in the female KO showing the greatest BV/TV ratio, clearly detached from the female WT and UP mice. For the cortical bone, no differences were reported for the BV and TV parameters while the BV/TV ratio was increased in female KO compared to the WT but not to the UP (Fig 57). Concerning the BV/TV ratio, it is a difference with the 16 months male mice for which the KO had an increased ratio compared to the WT and the UP with the UP showing even the lowest one.

## VI. ADDITIONAL RESULTS & DISCUSSION

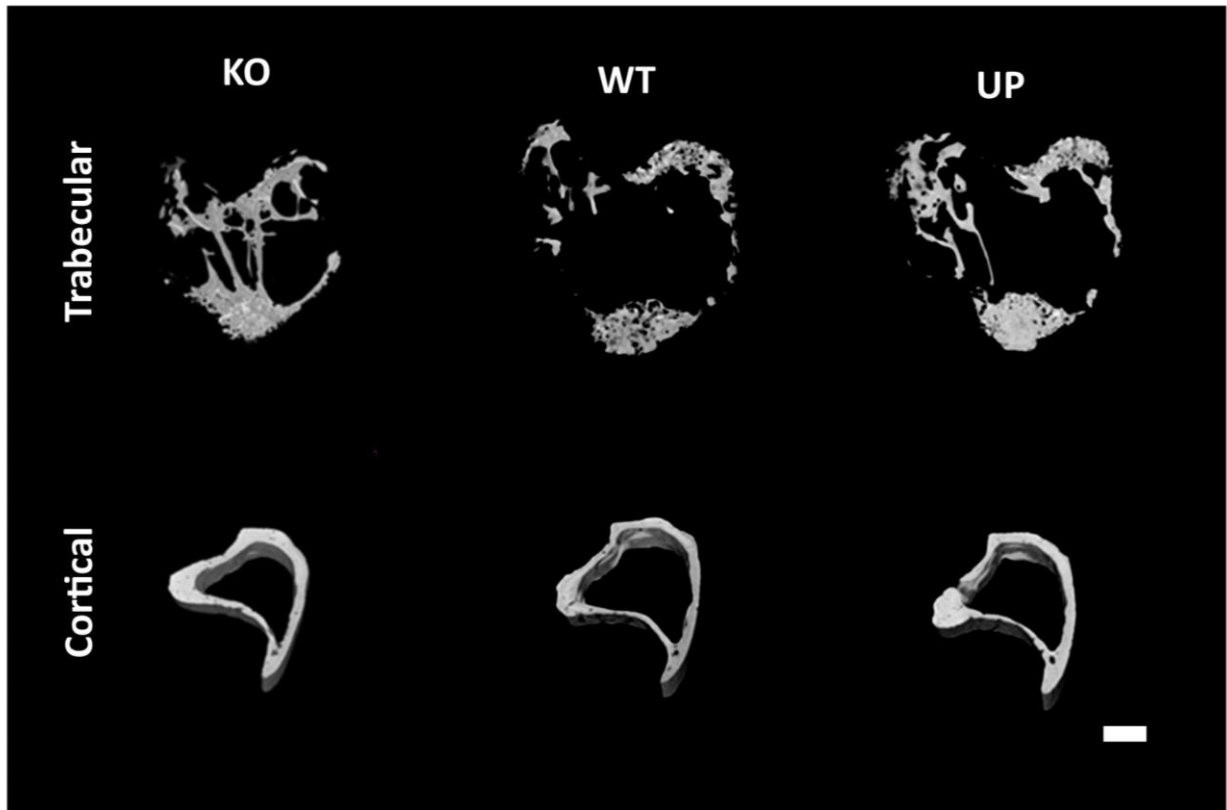


Figure 56:  $\mu$ CT 3D rendering of the tibia of female mice of 16 months for each genotype, KO, WT and UP. The trabecular and cortical bones were analyzed and represented separately. For 16 months female mice:  $n=6$  for each genotype. Scale bar= $500\ \mu\text{m}$ .

## VI. ADDITIONAL RESULTS & DISCUSSION

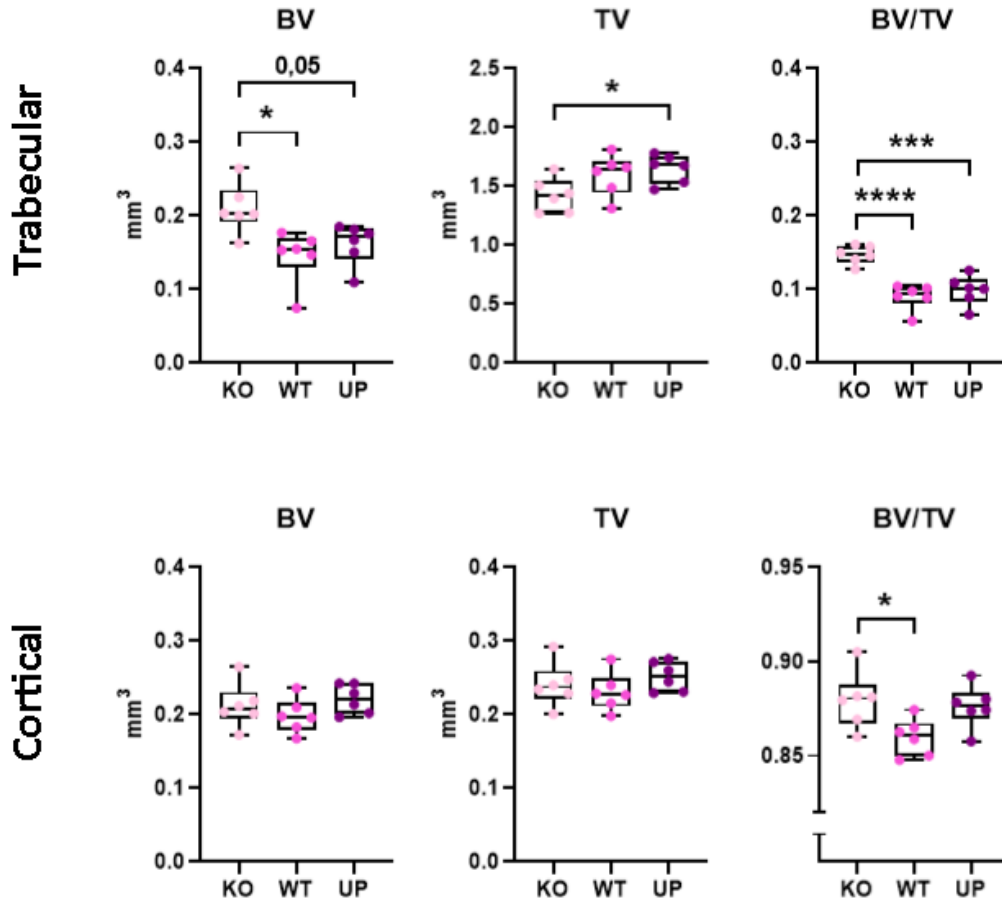


Figure 57: The bone parameters measured for the trabecular and cortical bone of 16 months female KO, WT and UP, were the bone volume (BV); the total volume (TV) and their ratio (BV/TV). The data were plotted as a box plot showing all points. One-Way ANOVA was performed with differences being considered significant at  $p$ -values  $< 0.05$  (\* $p < 0.05$ , \*\* $p \leq 0.01$ , \*\*\* $p \leq 0.001$ , \*\*\*\* $p \leq 0.0001$ ). For 16 months female mice:  $n=6$  for each genotype.

## ***VI. ADDITIONAL RESULTS & DISCUSSION***

To go further with the  $\mu$ CT analysis, additional parameters were reported for both the trabecular and cortical bones. For the trabecular bone, the female KO of 16 months showed better trabeculae conservation with a trabecular number significantly higher than the female WT and UP as it was in the male model (Fig 56, Fig 58). The trabecular separation was also impacted between the KO and the UP with the latter genotype having wider separation but the thickness of the trabeculae was similar between the genotypes. The trabecular porosity was deeply impacted in female KO showing a decreased porosity compared to the WT and UP mice (Fig 58).

Concerning the cortical bone of the 16 months female tibia, in opposition to the observation in male mice, there was no difference in their cortical thickness. Yet, the porosity of the KO was still significantly lower than the WT, as in male mice (Fig 59).



## VI. ADDITIONAL RESULTS & DISCUSSION

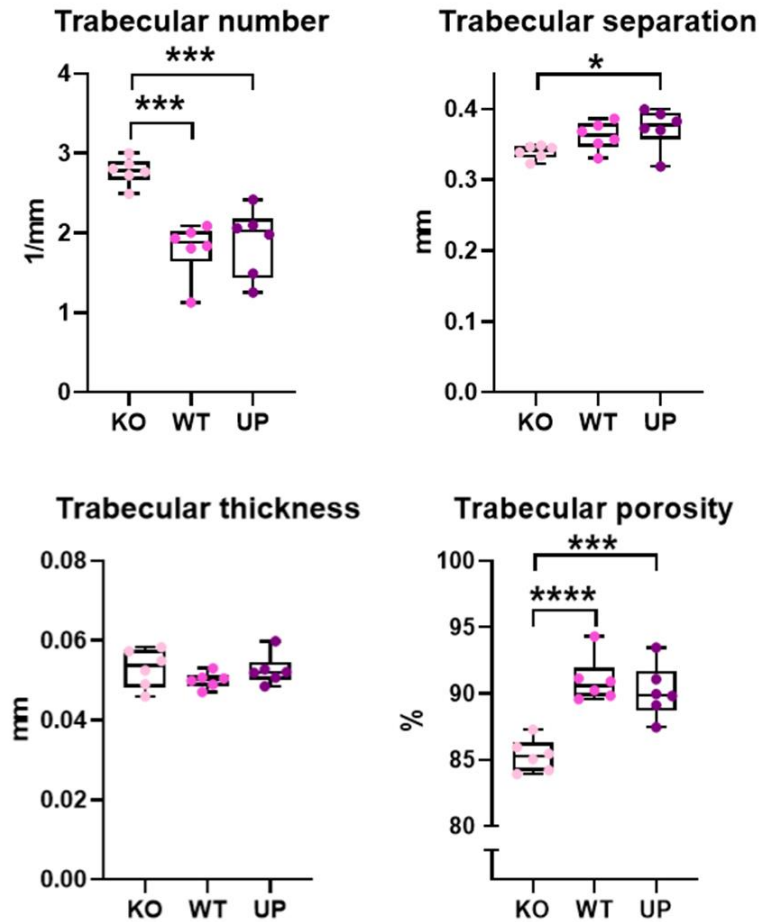


Figure 58: Additional parameters for the trabecular bone parameters were reported for the 16 months female KO, WT and UP mice. The trabecular number, separation, thickness and porosity were measured and the data were plotted as a box plot showing all points. One-Way ANOVA was performed with differences being considered significant at  $p$ -values  $< 0.05$  (\* $p < 0.05$ , \*\* $p \leq 0.01$ , \*\*\* $p \leq 0.001$ , \*\*\*\* $p \leq 0.0001$ ). For 16 months female mice:  $n=6$  for each genotype.

## VI. ADDITIONAL RESULTS & DISCUSSION

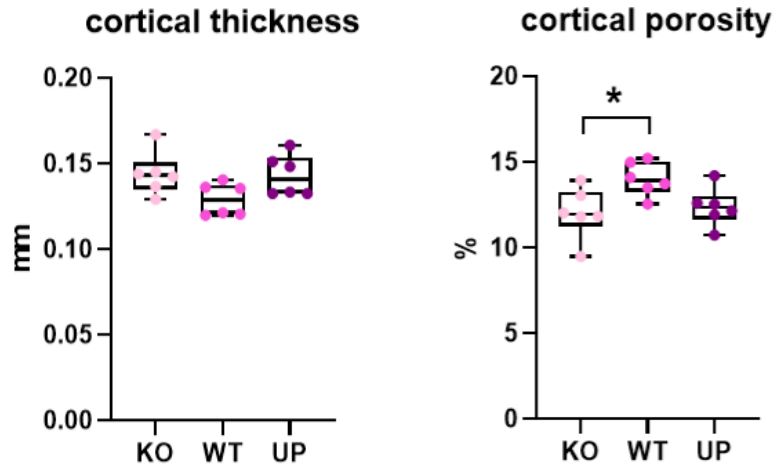


Figure 59: Additional parameters for the cortical bone were reported for the 16 months female KO, WT and UP mice. The cortical thickness and porosity were measured and the data were plotted as a box plot showing all points. One-Way ANOVA was performed with differences being considered significant at  $p$ -values  $< 0.05$  (\* $p < 0.05$ ). For 16 months female mice:  $n=6$  for each genotype.

## ***VI. ADDITIONAL RESULTS & DISCUSSION***

When comparing the effect of the expression of *Omd* on the bone microarchitecture in males and females, it came out that the outcome is also sex-dependent. For the main  $\mu$ CT parameters, comparisons of male and female mice at 16 months are displayed in figure 60 to show the sex-attributed differences in the same genotype. For the trabecular bone, female WT showed a lower BV/TV, fewer trabeculae and higher porosity than male WT, and female KO showed fewer trabeculae than KO male. Interestingly, male and female UP were showing very similar parameters and less subject to sex-attributed differences (Fig 60A). As the loss of trabecular bone volume was more pronounced in the UP genotype for the male group, it could explain their resemblance with the female groups naturally showing poorer bone volume preservation (Fig 56, 60A). The KO mice were showing greater BV/TV ratio and trabecular number, and lower trabecular porosity for both male and female mice. The less sex-attributed difference was shown for the cortical bone. Only the female WT showed a significantly thinner cortical bone compared to the male WT (Fig 60B). Trabecular and cortical bone analysis indicated that most sex-attributed differences were concerning the WT genotype. The 16 months female UP mice did not show a similar trend than their male counterpart and were adopting a closer phenotype to the WT for the trabecular bone and to the KO for the cortical bone. Regarding the similarity between the female WT and the UP mice at 16 months, it may be forced due to the nearly complete absence of trabeculae inherent in the old age of mice.

## VI. ADDITIONAL RESULTS & DISCUSSION

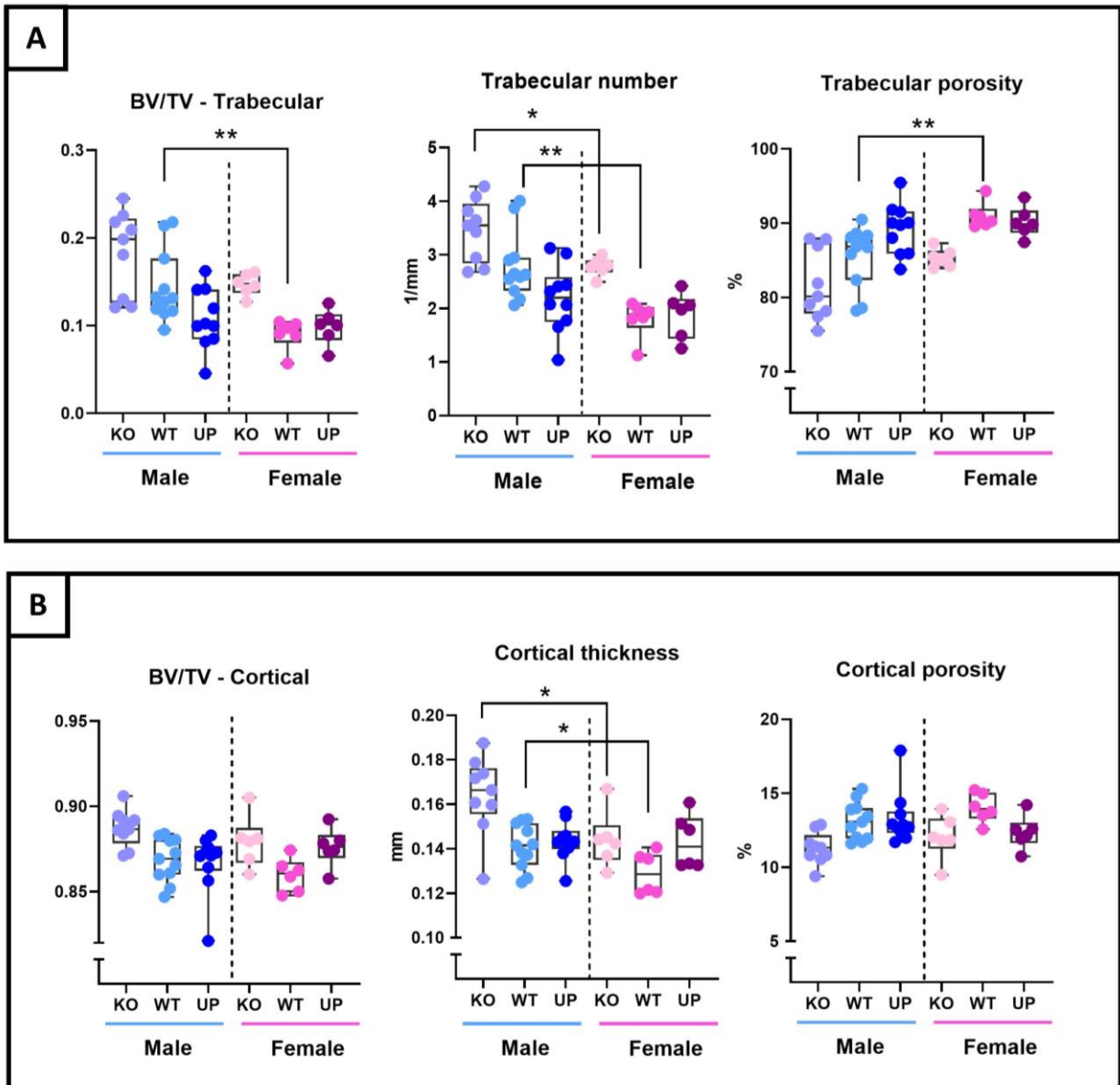


Figure 60: Comparison of the main  $\mu$ CT parameters between male and female mice at 16 months. (A) Parameters for the trabecular bone with BV/TV, trabecular number and porosity. (B) Parameters for the cortical bone with BV/TV, cortical thickness and porosity. The data were plotted as a box plot showing all points. Unpaired t-test was performed with differences being considered significant at  $p$ -values  $< 0.05$  (\* $p < 0.05$ ). Mann-Whitney was performed when the distribution was not Gaussian. For males,  $n=9$  for the KO,  $n=11$  for the WT, and  $n=10$  for the UP; for females,  $n=6$  for each genotype.

## ***VI. ADDITIONAL RESULTS & DISCUSSION***

### **VI.3.3 Characterization of the spontaneous development of OA in female mice of 16 months**

The spontaneous development of OA was assessed in 16 months female mice by scoring the loss of proteoglycan in knee sections stained with Toluidine Blue. The score was attributed to the tibia and the condyle of the medial and lateral plateaus separately (Fig 61). There was no significant difference for the different knee compartments, yet the lateral tibia of the female KO tended to show a higher score corresponding to more cartilage degradation compared to the WT (p-value=0.056) (Fig 62).

## VI. ADDITIONAL RESULTS & DISCUSSION

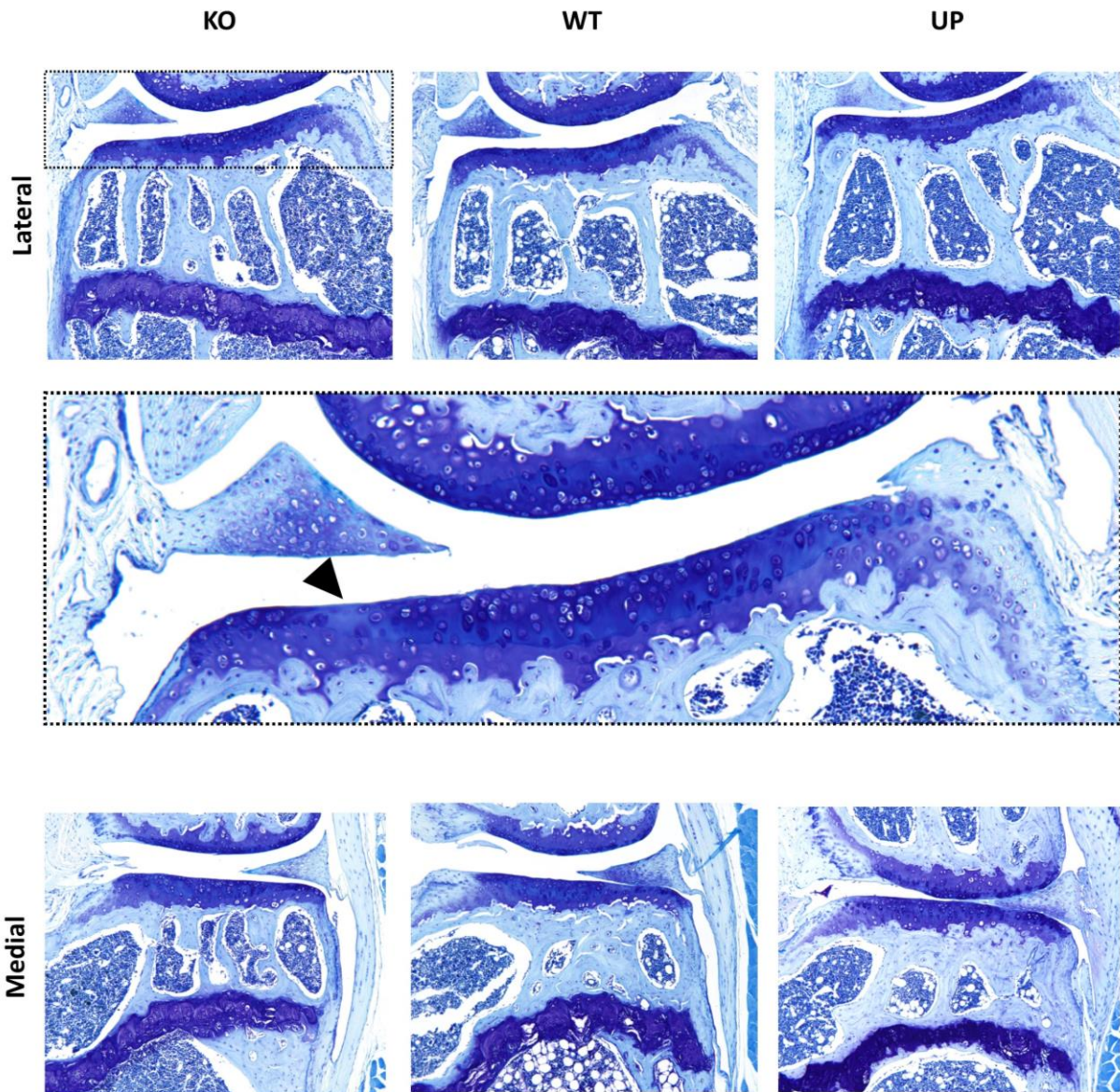


Figure 61: Analysis of the spontaneous OA development with the naturally occurring loss of proteoglycan at 16 months in female KO, WT and UP mice. The knee joint was stained with Toluidine Blue and the lateral and medial plateaus were represented separately. For the lateral tibia, a zoom on an area with a loss of Toluidine Blue staining is represented and indicated with the black arrowhead, this region is issued from a female KO mouse. For each genotype, n=8.

## VI. ADDITIONAL RESULTS & DISCUSSION

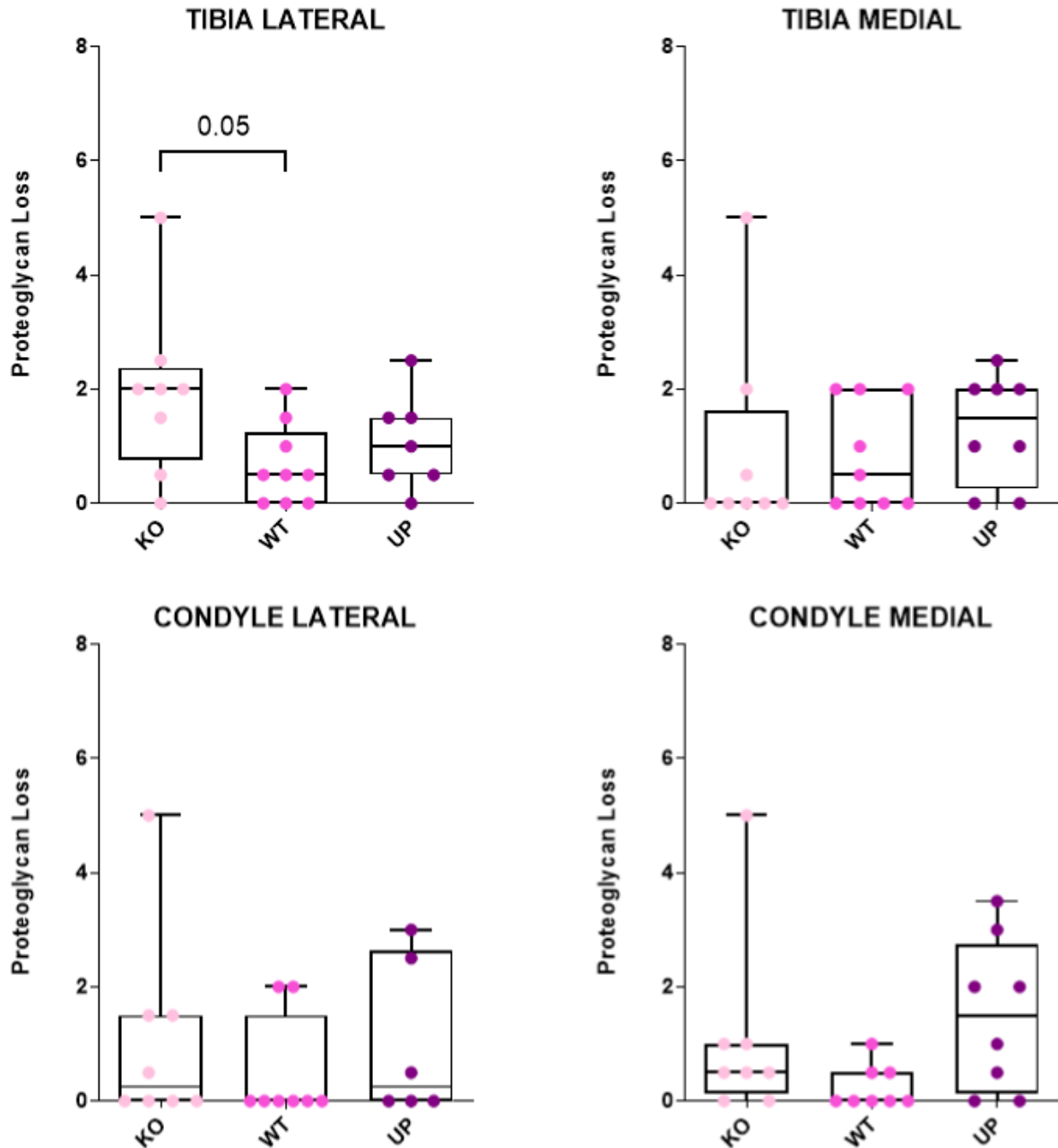


Figure 62: The spontaneous cartilage degradation of 16 months female mice was assessed from the knee joint sections that were stained with Toluidine Blue to score the loss of proteoglycan. The score (from 0 to 5) was attributed to the lateral and the medial tibial plateaus and to the lateral and medial condyles according to the OARSI recommendations. The data were plotted as a box plot showing all points. One-way ANOVA was performed with differences being considered significant at  $p$ -values  $< 0.05$  ( $*p < 0.05$ ). Kruskal-Wallis was performed when the distribution was not Gaussian. For each genotype,  $n=8$ .

## ***VI. ADDITIONAL RESULTS & DISCUSSION***

Interestingly, when comparing the proteoglycan loss of male and female mice at 16 months, there was a distinct development of OA related to the sex but in the opposite direction of the observations reported from humans. In mice, it is males that develop OA prematurely or show more severe cartilage damage than females and the score of the lateral tibia of male and female WT mice corroborated this previous information. The comparison of the score of male and female UP mice followed the same pattern as the WT, but there was no significant difference between the score of the male and female KO mice. For the medial plateau, the comparison of male and female mice for the WT and UP genotypes did not show a significant difference anymore while the score of female KO is significantly reduced compared to the male KO. We should highlight that the KO is the only genotype with a decreased score for the female in the medial tibia compared to the male one but it is also the male KO that showed increased naturally occurring cartilage degradation for the medial compartment compared to the WT (Fig 63).



## VI. ADDITIONAL RESULTS & DISCUSSION

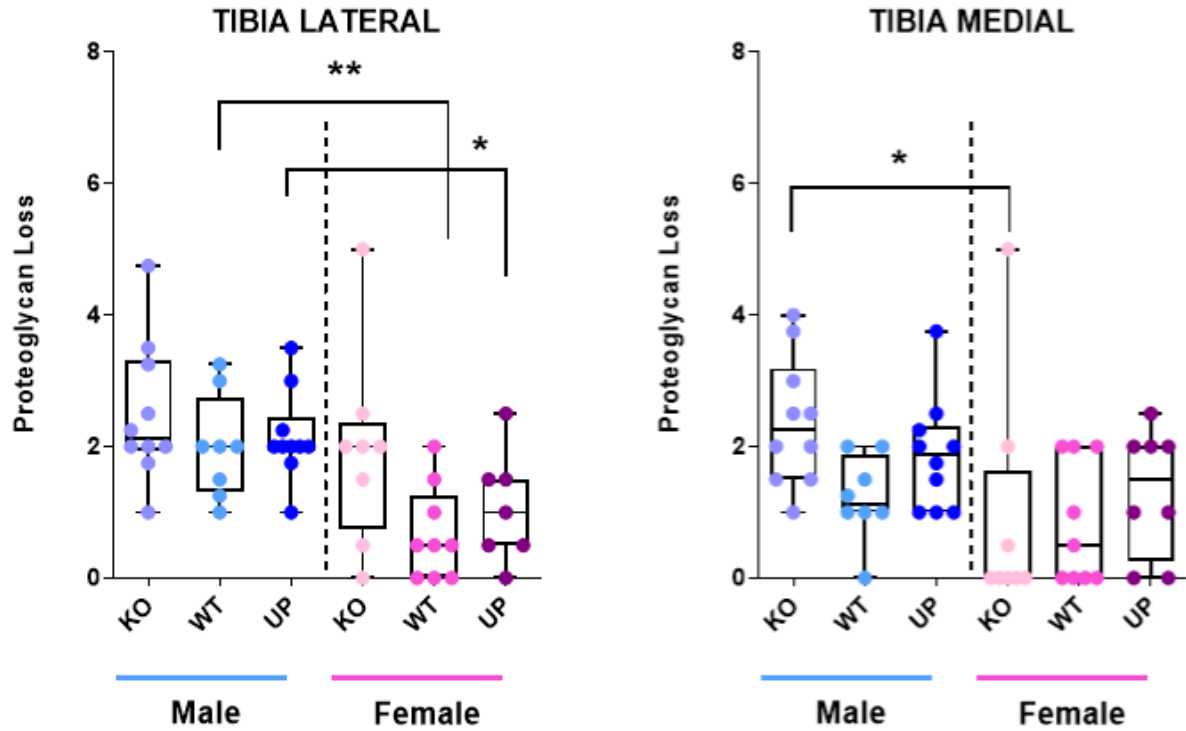


Figure 63: Comparison of the spontaneous cartilage degradation of 16 months male and female mice for the lateral and medial tibia. The data were plotted as a box plot showing all points. Unpaired t-test was performed with differences being considered significant at  $p$ -values  $< 0.05$  (\* $p < 0.05$ ). Mann-Whitney was performed when the distribution was not Gaussian. For males,  $n=10$  for the KO and the UP,  $n=8$  for the WT; for females,  $n=8$  for each genotype.

## ***VI. ADDITIONAL RESULTS & DISCUSSION***

### **VI.3.4 Gait analysis of female mice**

The gait parameters of female mice were analyzed over time at 4, 8 and 16 months. The print area, the swing, which is the duration of absence of paw contact toward the walking platform, and the intensity of hind paws were reported in figure 64. The print area of the female KO was smaller than WT and UP at 4 months but not at 8 and 16 months. Standing by the observation made in male mice, the swing was strongly impacted in female KO mice and was shortened compared to the WT at 8 months and to the UP at 8 and 16 months. The paw intensity was not significantly different between the genotypes even if there was a trend indicating a higher paw intensity for the female KO in comparison to the WT at 4 months (p-value=0.056). Lastly, for the single stance, female KO showed a shorter phase than the WT at 4 months and than the UP mice at 4 and 16 months. Other parameters from the front and hind paws were reported in “Appendix 3.3”

The modifications of the gait behavior between the genotypes in females roughly recapitulated the observations from male mice. Then, data from the Catwalk XT issued from female mice reaffirmed a disorder in the gait behavior from the KO mice.

## VI. ADDITIONAL RESULTS & DISCUSSION

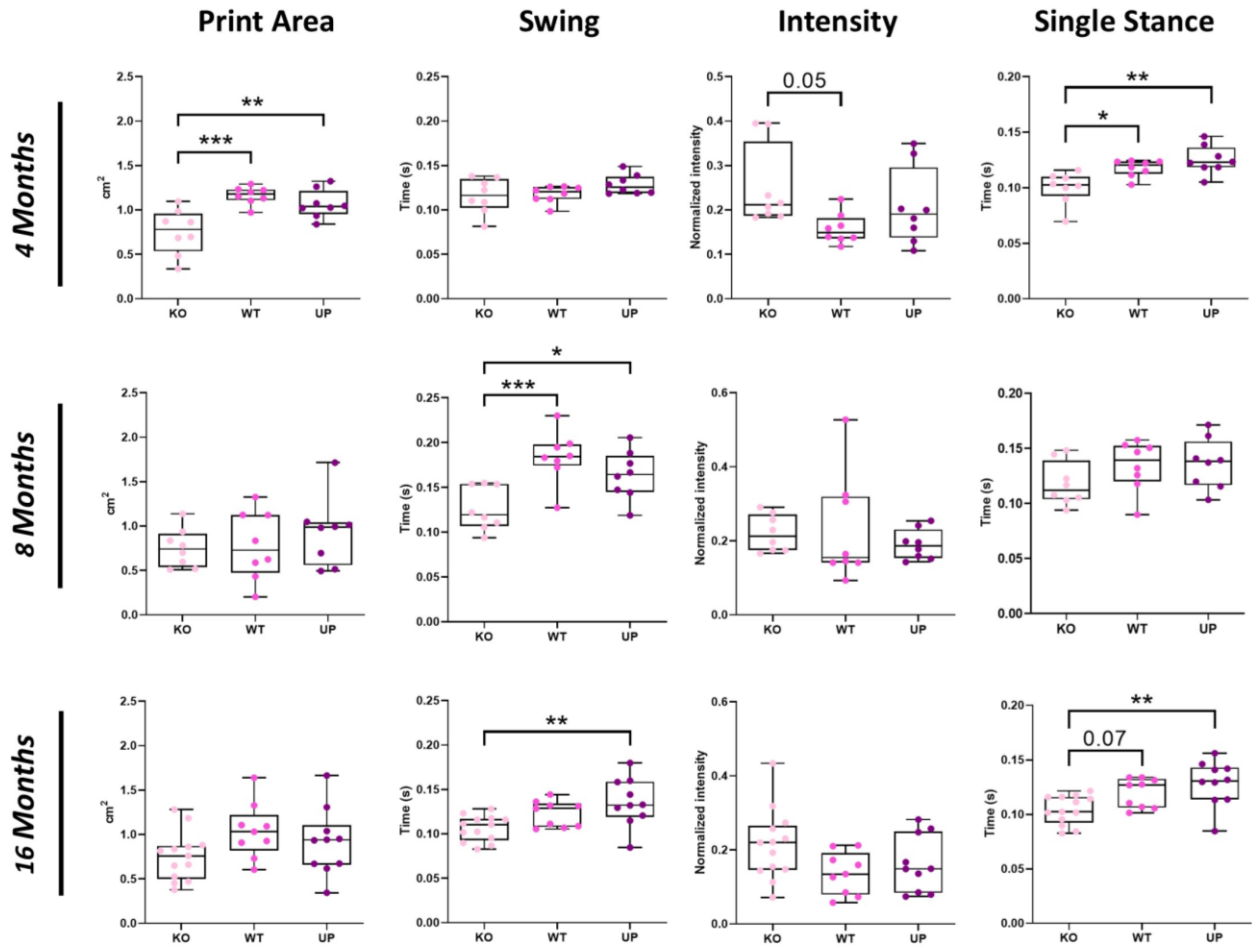


Figure 64: Analysis of the gait of 4, 8, and 16-month-old female mice with the CatWalkXT. The intensity corresponds to the mean intensity at the maximum paw contact normalized with the mean of the maximum contact paw area, the speed, and the weight of the mouse. At 4 months:  $n=8$  for each genotype; at 8 months  $n=8$  for each genotype; at 16 months:  $n=13$  for the KO,  $n=9$  for the WT and  $n=10$  for the UP. The data were plotted as a box plot showing all points. One-Way ANOVA was performed when the distribution was gaussian and Kruskal-Wallis was performed when the distribution was not gaussian with differences being considered significant at  $p$ -values  $< 0.05$  (\* $p < 0.05$ , \*\* $p \leq 0.01$ , \*\*\* $p \leq 0.001$ ).

## ***VI. ADDITIONAL RESULTS & DISCUSSION***

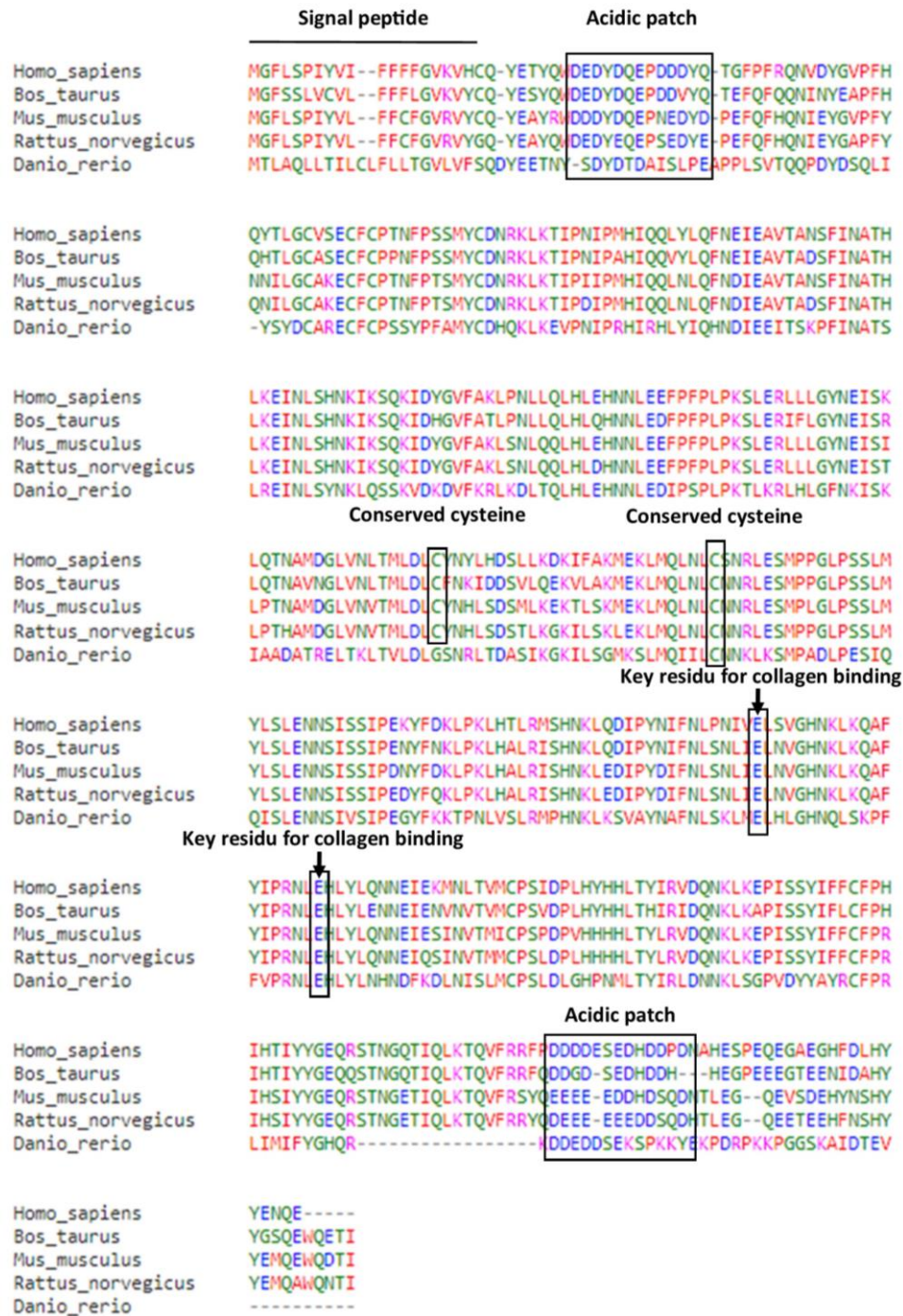
### **VI.4 Further characterization of the loss of function of *omd* in the zebrafish**

#### **VI.4.1 Multiple alignment comparison**

The study of bone and cartilage biology, and especially OA, in the zebrafish model might appear surprising but this model proved itself for genetic studies and establishing study design unfeasible in mammals as introduced in the background section.

To begin with, several pieces of information can be drawn from the comparison of the protein sequence of OMD between vertebrae. Multiple alignment analysis was performed with Kalign in *Homo sapiens*, *Bos taurus*, *Mus musculus*, *Rattus norvegicus* and *Danio rerio* (Zebrafish) with the matrix reporting the percentage of identity between them (Fig 65). The multiple alignment parameters are available in "Appendix 4". From the multiple alignment, we can observe that the specific feature of OMD, such as the wide acidic patches and the key residues of glutamic acid (Amino acid: E), are highly conserved in all vertebrae. SLRPs have conserved cysteine clusters specific to their class and OMD has two more central cysteine residues which are unique to this SLRP member. This feature is conserved among vertebrae, except that the zebrafish retains only the second conserved central cysteine. The identity matrix indicates a well-conserved protein among vertebrae, with 79.9% of identity between the human and the mouse; 48.36% of identity between the human and the zebrafish and 46.45% of identity between the mouse and the zebrafish. As expected, there is higher conservation between the human and the mouse than for the zebrafish. The multiple alignment analysis suggests that OMD has conserved functions in bone and cartilage in vertebrae.

## VI. ADDITIONAL RESULTS & DISCUSSION



Percent Identity Matrix - created by Clustal2.1

1: Homo_sapiens	100.00	82.97	79.90	79.90	48.36
2: Bos_taurus	82.97	100.00	76.90	77.86	48.09
3: Mus_musculus	79.90	76.90	100.00	91.25	46.45
4: Rattus_norvegicus	79.90	77.86	91.25	100.00	47.72
5: Danio_erio	48.36	48.09	46.45	47.72	100.00

Figure 65: Multiple alignment of the protein ostemodulin in homo sapiens, bos taurus, mus musculus, rattus norvegicus and danio rerio with Kalign and the associated identity matrix in percentage. The signal peptide, acidic patches, specific cysteines identified in [297] and key residues for collagen binding identified in [247] are highlighted in the sequences alignment.

## ***VI. ADDITIONAL RESULTS & DISCUSSION***

### **VI.4.2 Characterization of early stages of the mutant *omd***

From the section IV and V, it was established that the ectopic overexpression of *omd* had a strong impact on the early development of larvae. A high percentage of the injected larvae were ventralized and they developed various deformities, impairing the axial symmetry, by 4-dpf. As the overexpression model of *omd* was inducing a detrimental phenotype, the loss of function of *omd* was designed by its mutation through the CRISPR/Cas9 technique.

The skeletal development of the early stages of the zebrafish was characterized for the *omd* mutant. Alcian blue staining was performed at 5, 8 and 14-dpf to observe the craniofacial cartilaginous structures and no evident phenotype could be isolated from the mutant (Fig 66-68). For the examination of the craniofacial bones, larvae were stained with Alizarin red at 8-dpf in order to compare larvae already well engaged in the mineralization, but again, there was no evident phenotype (Fig 69).

Deleterious effects were not identified following the loss of function of *omd* during the early development of the zebrafish, in opposition to the overexpression model. Consequently, as disclosed in the section *“IV.6 omd is expressed in the zebrafish skeleton and its mutation induces articular cartilage lesions and impaired bone remodeling”*, the bone biology of the *omd* mutant was studied in adult zebrafish. The characterization of the *omd* mutant in adult zebrafish corroborated early spontaneous OA lesions in the mutant and revealed increased osteoclastogenesis and/or osteoclast activity.

## VI. ADDITIONAL RESULTS & DISCUSSION

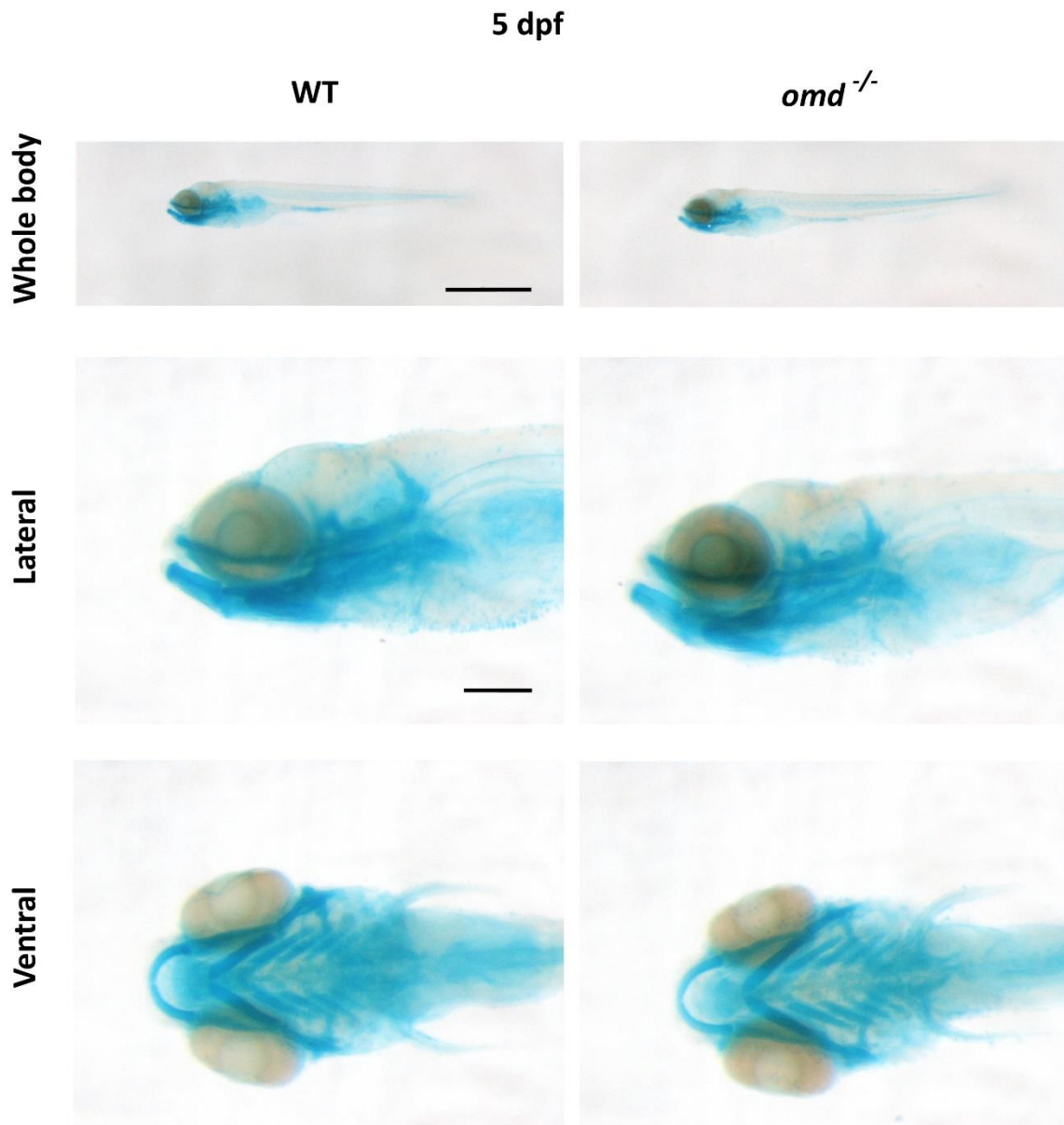


Figure 66: Alcian blue staining of 5-dpf WT and *omd*<sup>-/-</sup> larvae showing the whole larvae (Zoom 1.6X), scale bar=1mm; and the craniofacial cartilaginous structures in the lateral and ventral view (Zoom 6.3X), scale bar=200 $\mu$ m.

## VI. ADDITIONAL RESULTS & DISCUSSION

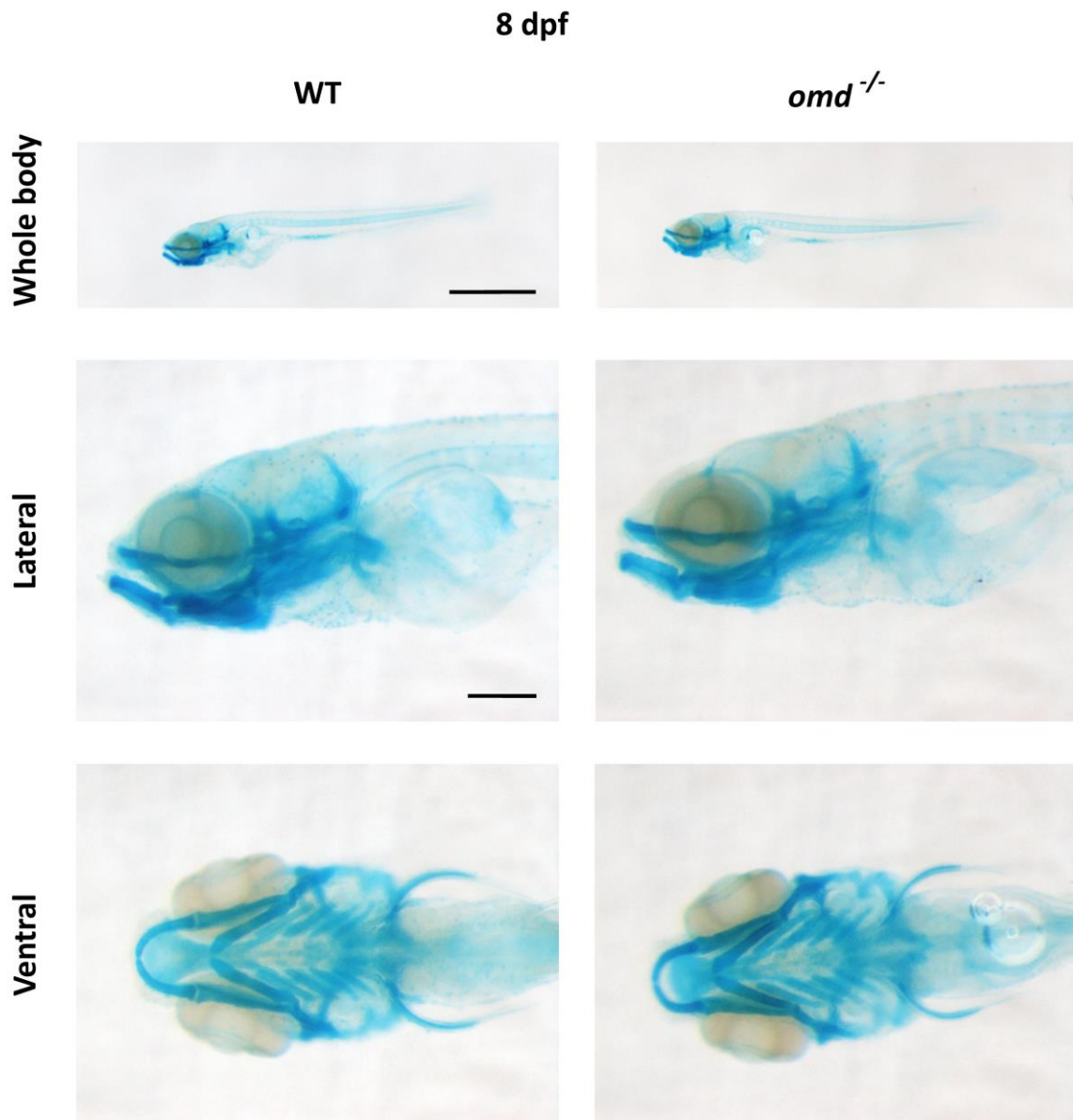


Figure 67: Alcian blue staining of 8-dpf WT and *omd*<sup>-/-</sup> larvae showing the whole larvae (Zoom 1.6X), scale bar=1mm; and the craniofacial cartilaginous structures in the lateral and ventral view (Zoom 6.3X), scale bar=200 $\mu$ m.



## VI. ADDITIONAL RESULTS & DISCUSSION

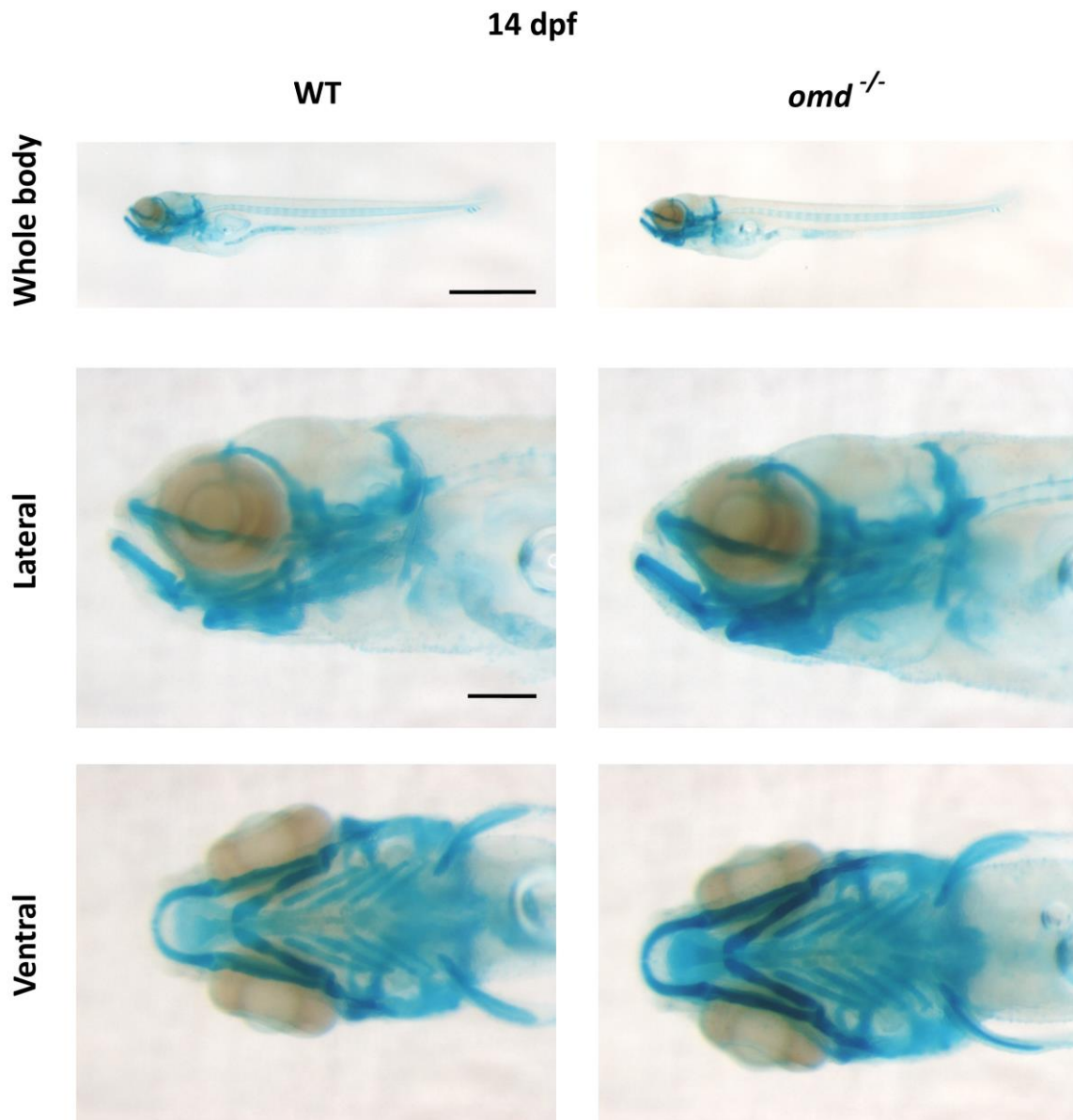


Figure 68: Alcian blue staining of 14-dpf WT and *omd*<sup>-/-</sup> larvae showing the whole larvae (Zoom 1.6X), scale bar=1mm; and the craniofacial cartilaginous structures in the lateral and ventral view (Zoom 6.3X), scale bar=200 $\mu$ m.

## VI. ADDITIONAL RESULTS & DISCUSSION

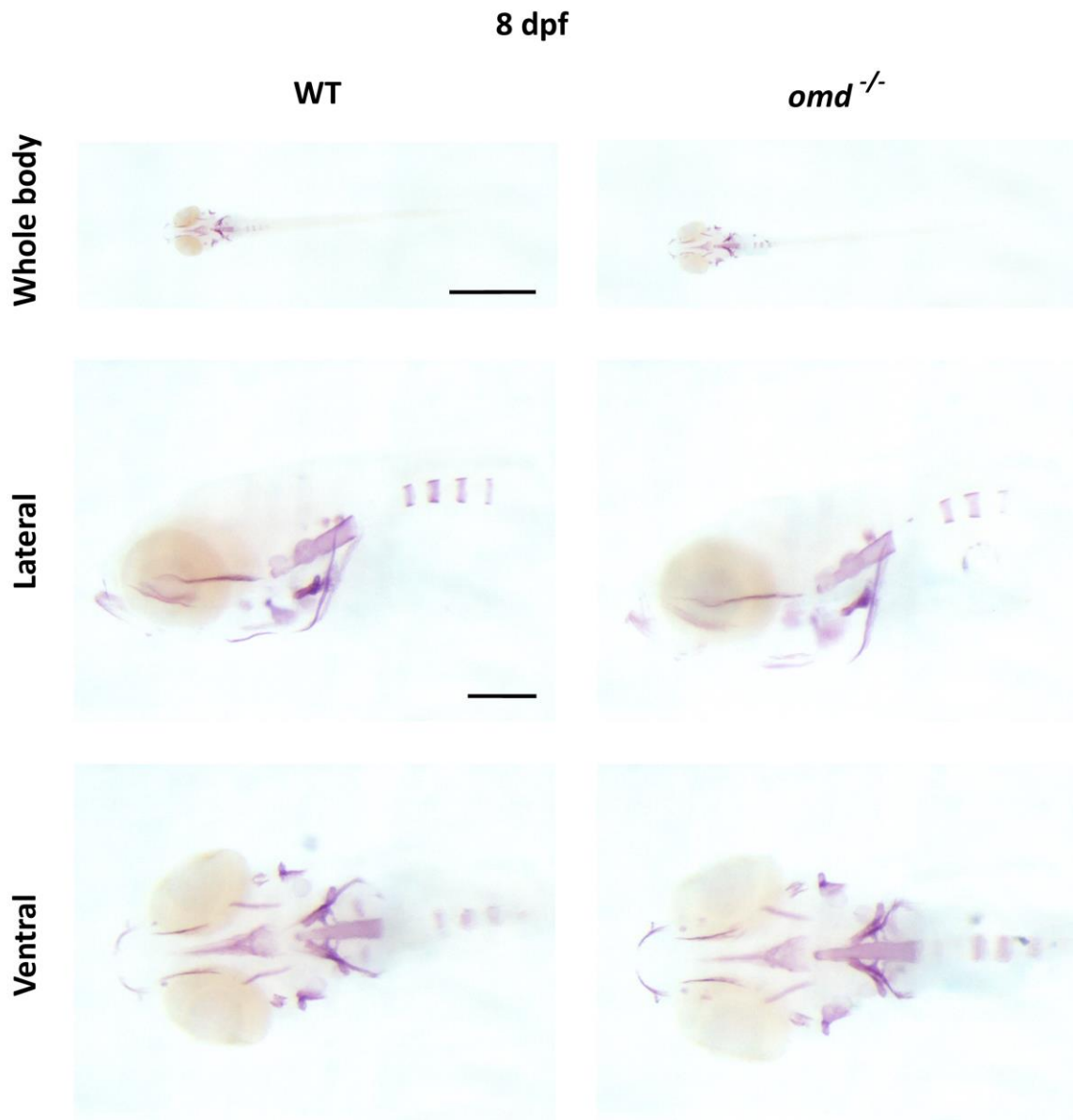


Figure 69: Alizarin red staining of 8-dpf WT and *omd*<sup>-/-</sup> larvae showing the whole larvae (Zoom 1.6X), scale bar=1mm; and the craniofacial mineralized structures in the lateral and ventral view (Zoom 6.3X), scale bar=200 $\mu$ m.

**VI.4.3 Characterization of the bone matrix components of the mutant *omd***

The Fourier transform infrared (FTIR) method, a vibrational spectroscopic technique, allows the study of the mineral component of the bone matrix. Here we reported the Mineral-to-Matrix index (MM), which is associated with mineral maturity; the Carbonate-to-Phosphate index (C/P), which is related to the carbonate content of bioapatite; and the Collagen-to-Phosphate index (COLL/P), which indicates the relative amount of the organic matrix in comparison to the inorganic component. These parameters were analyzed in the caudal fin of 3-month-old and 1-year-old zebrafish. The caudal fin presents bony rays with bifurcations and this specific area and the edge of the caudal fin were used separately to generate their corresponding FTIR spectrum because of their different distribution of collagen and phosphates (Fig 70) [298].

## VI. ADDITIONAL RESULTS & DISCUSSION

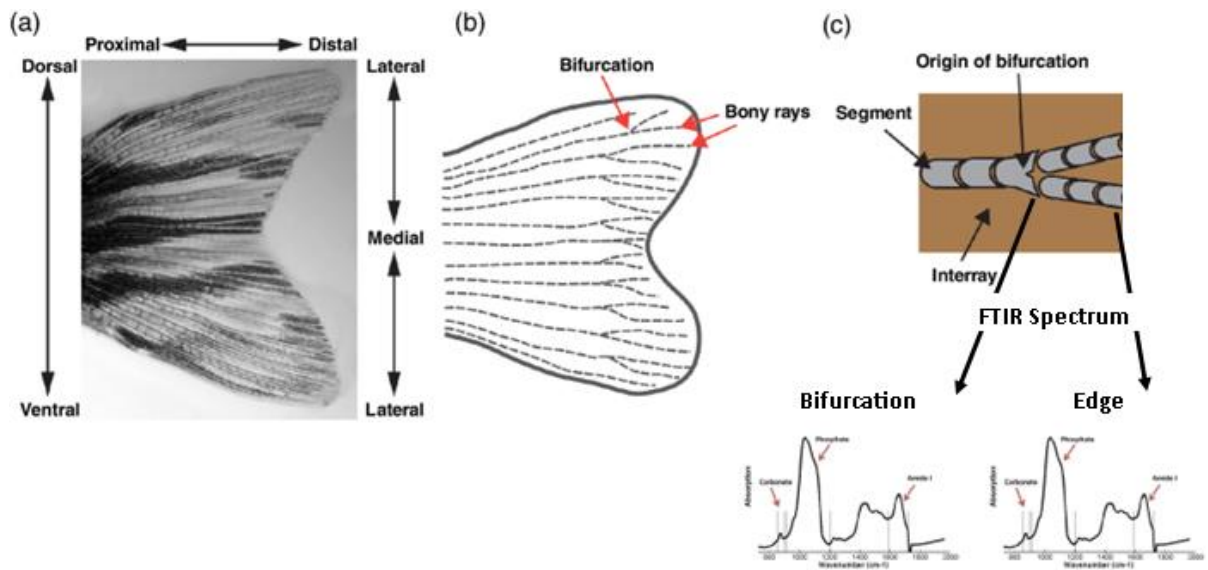


Figure 70: Study design of the FTIR analysis of the caudal fin of zebrafish. (a) Brightfield image of the caudal fin of the zebrafish, (b) schematic representation of the caudal fin composed of segmented bony rays which present bifurcation. (c) Schematic representation of the region investigated with FTIR spectra generated for the bifurcation area and the edge of the fin separately. Figure adapted from [281] and designed by Jérémie Zappia.

## ***VI. ADDITIONAL RESULTS & DISCUSSION***

The FTIR analysis indicated that the MM ratio of 3-month-old zebrafish was reduced both for the bifurcation and the edge of the caudal fin while the COLL/P ratio was especially increased for the bifurcation area (Fig 71). The COLL/P ratio for 1-year-old zebrafish was elevated as well in the bifurcation area of the mutant but the MM parameter became similar between the WT and the mutant (Fig 72). The lower MM ratio of the mutant at 3 months indicates a lower mineral maturity (transition of the nanocrystalline structure of the hydroxyapatite to a well-crystallized mineral) of the bone matrix which is not surprising due to the anticipated function of Omd in the mineralization. However, the mutant recovers the poor mineralization maturity phenotype in the caudal fin as the MM ratio becomes similar between the WT and the mutant at 1-year-old. The COLL/P ratio being greater in the mutant is reinforcing the importance of Omd for the bone matrix and corresponds to lower mineralization of the bony ray. Altogether, the data acquired on the zebrafish model showed that the loss of function of *omd* did not generate evident bone deformities but lowered the quality of the bone mineral component.

## VI. ADDITIONAL RESULTS & DISCUSSION

### BIFURCATION

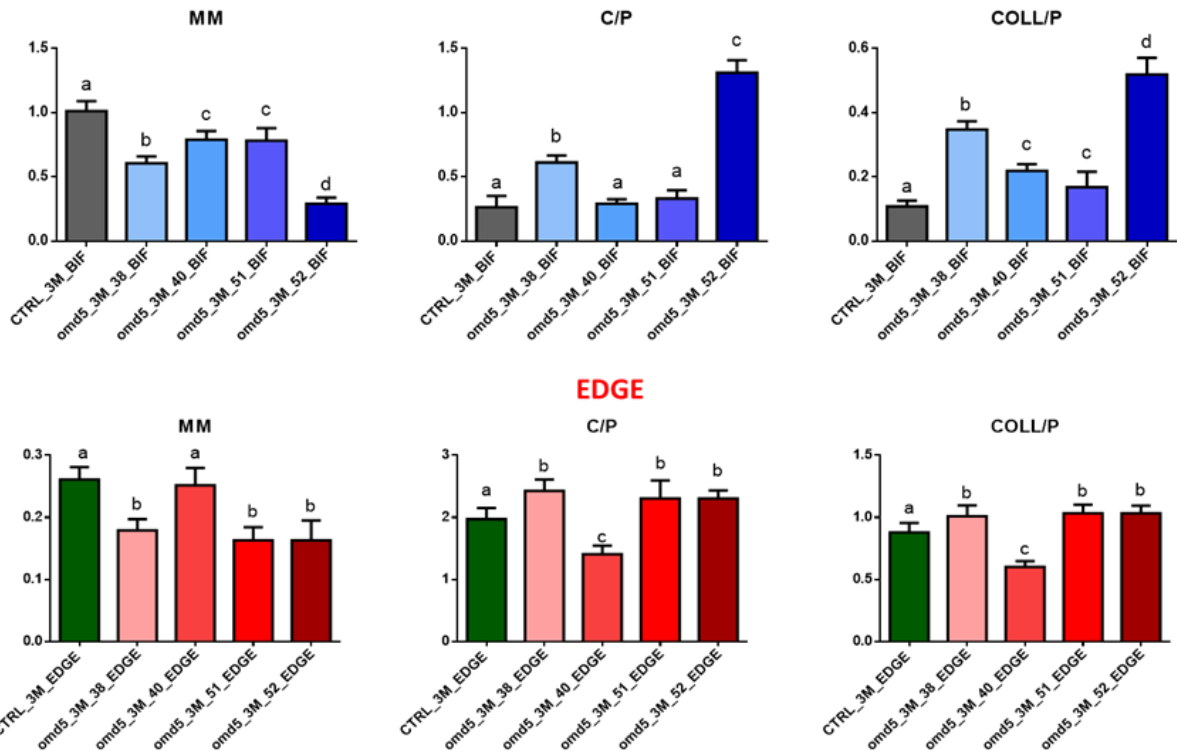


Figure 71: FTIR analysis with the reported parameters being MM, C/P and COLL/P ratios from the bifurcation area and the edge of the caudal fin of 3 months zebrafish. For the analysis,  $n=4$  for WT and  $omd^{-/-}$ . The low variability of the WT samples allowed us to pool them for their comparison with the mutant. Different letters above the bar plot represent statistical significance while the same letter indicates an absence of significance.

## VI. ADDITIONAL RESULTS & DISCUSSION

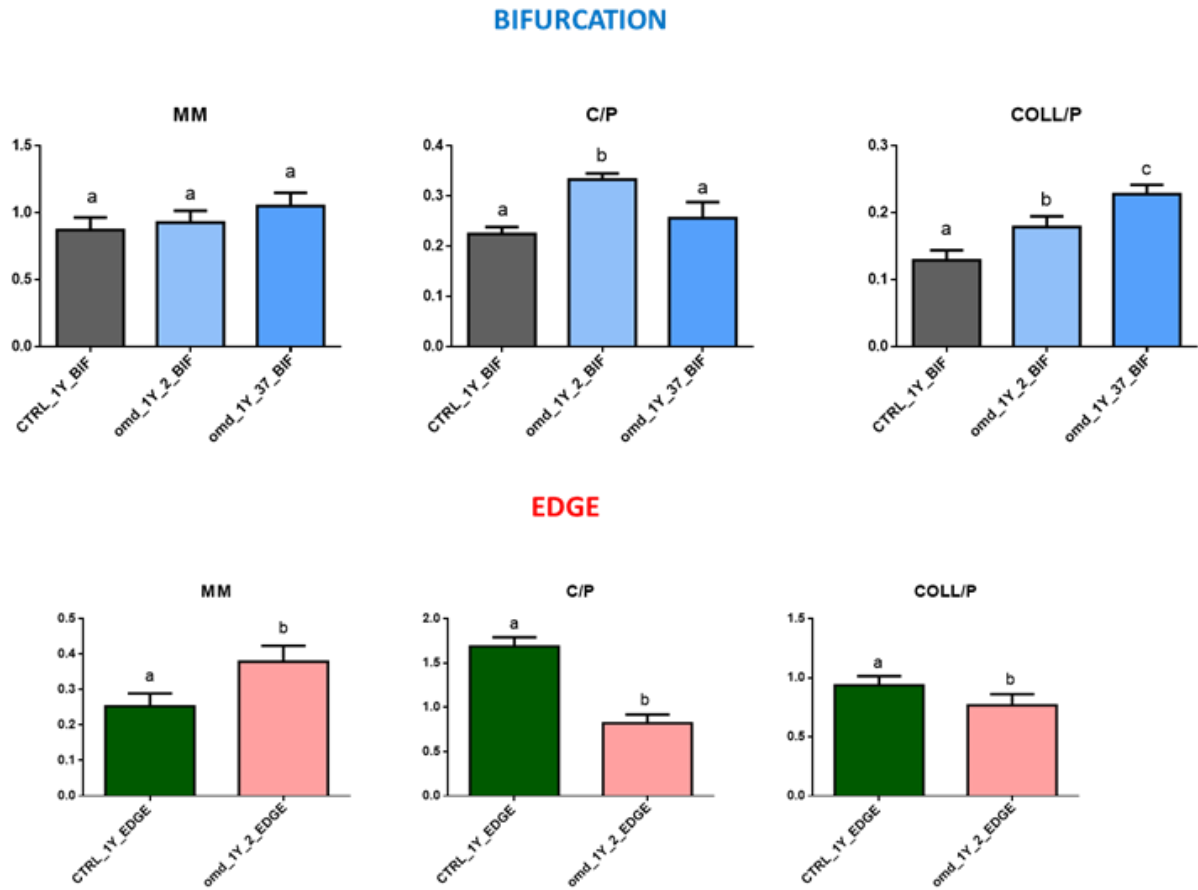


Figure 72: FTIR analysis with the reported parameters being MM, C/P and COLL/P ratios from the bifurcation area and the edge of the caudal fin of 1-year-old zebrafish. For the analysis,  $n=2$  for WT and  $omd^{-/-}$ . The low variability of the WT samples allowed us to pool them for their comparison with the mutant. Different letters above the bar plot represent statistical significance while the same letter indicates an absence of significance.

## ***VI. ADDITIONAL RESULTS & DISCUSSION***

### **VI.4.4 Characterization of the regeneration of elasmoid scales of the mutant *omd***

The zebrafish model is extensively used to study the regeneration of diverse organs. By plucking out the elasmoid scales from their right flank to assess the osteoclast activity and localization (data presented in “*IV.6 omd is expressed in the zebrafish skeleton and its mutation induces articular cartilage lesions and impaired bone remodeling*”), it was the opportunity to follow the regenerative ability of the elasmoid scale in the *omd* mutant. The study design is illustrated in figure 73A, where the regenerating and the otongenetic scales of adult zebrafish are observed after 10 days following a calceine treatment. The calceine is incorporated in the newly mineralized matrix translating into more intense fluorescence in the regenerating scales in respect to the otongenetic ones as observed in the illustration (Fig 73B).

The scales of the WT regenerate in a highly organized fashion, similar to the pattern and localization of the otongenetic scales. In contrast, the mutant showed disorganized regenerating scales which appeared to sprout from random areas or developing with a considerable delay. Although the scale regeneration is disturbed in the mutant, they accumulated calceine in a similar way to the WT which is indicating that the mineralization process of their regenerating scales is occurring. The otongenetic scales from the mutant serving as controls showed that they naturally adopt a well-organized pattern and that the disorganization is specific to the regeneration (Fig 73B).



## VI. ADDITIONAL RESULTS & DISCUSSION

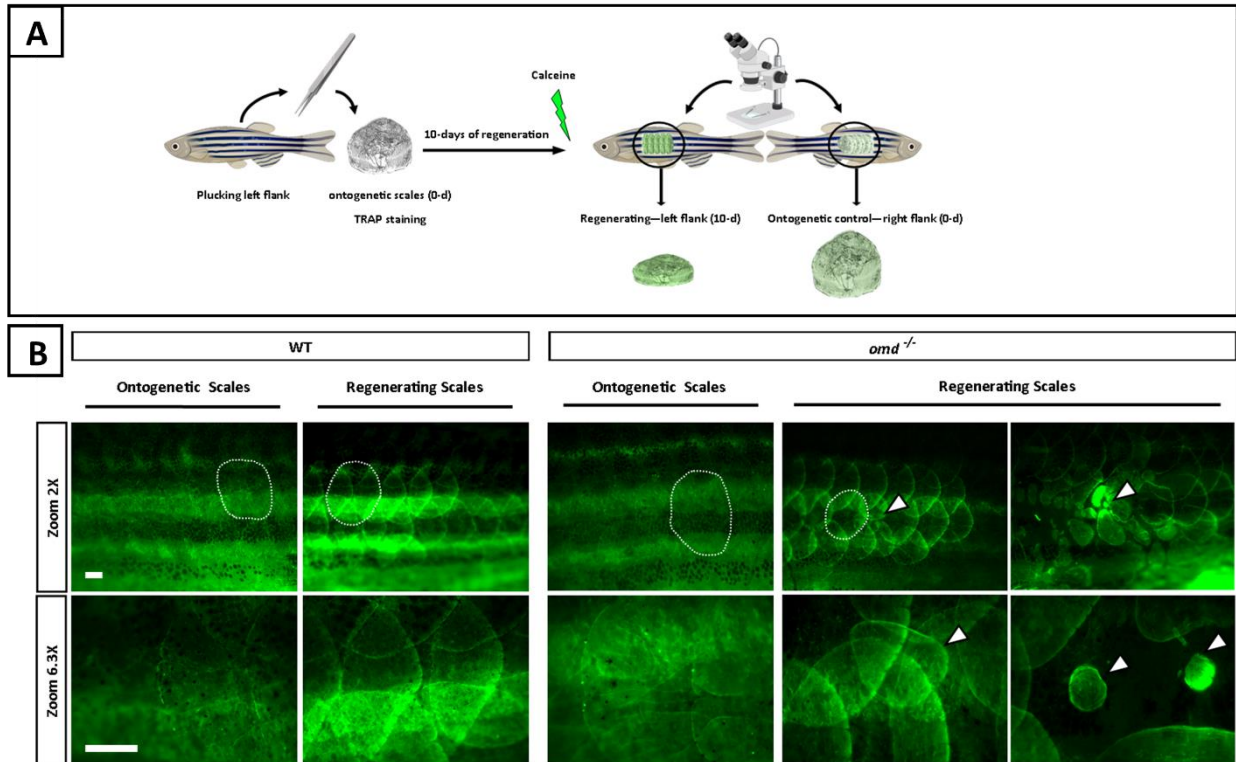
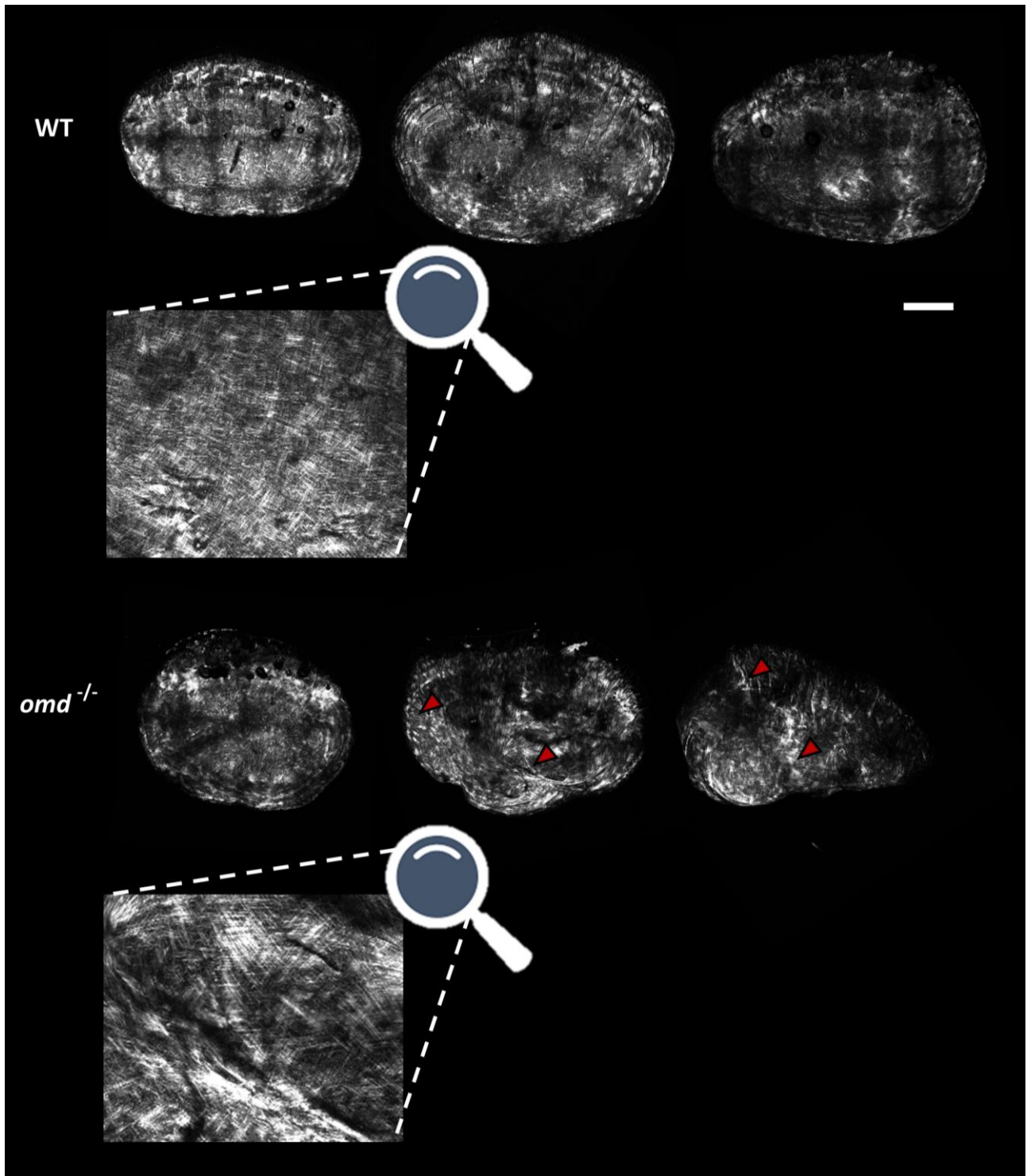


Figure 73: Analysis of the elasmoid scales regeneration in 1.6-year-old zebrafish. A) Schematic representation of the study design with the scales being plucked out from the right flank of the zebrafish. These ontogenetic scales were used for the TRAP staining presented in the main research paper. After 10 days to allow the regeneration of the scales, zebrafish were treated with calceine incorporating the newly mineralized matrix. The analysis of regenerating scales could be observed from the right flank while the left flank served as a control with ontogenetic scales. B) Comparison of the regenerating scales and ontogenetic scales from the WT and *omd*<sup>-/-</sup> with  $n=5$  for each genotype. White dotted lines delimit a scale. White arrowheads are pointing to disorganized regenerating scales. Scale bar=500 $\mu$ m.

## ***VI. ADDITIONAL RESULTS & DISCUSSION***

Second harmonics generation microscopy was used to visualize the structure of the regenerating scales with their organization of collagen fibrils (absorbing at 880 nm). The collagen network achieves an extreme level of organization resembling a plywood-like structure. In the scales, the network of collagen fibrils is easily observed, as demonstrated in the regenerating scales of the WT. However, the collagen network of the mutant scales is less organized and the plywood-like structure is lost in several regions which could explain their peculiar morphology. The loss of collagen organization in the absence of OMD was reported by [246,247] and our *in vivo* data confirmed this effect (Fig 74).



*Figure 74: Multiphoton forward scattering (second harmonic generation (SHG), 880 nm wavelength) for the visualization of regenerating scales and zoom on the organization of collagen fibrils for the 1.6-year-old WT and  $omd^{-/-}$  zebrafish. Red arrowheads highlight highly disorganized collagen fibrils area For each genotype,  $n=5$ . Scale bar=500 $\mu$ m.*

### **VI.5 Additional data from *in vitro* models**

#### **VI.5.1 Effect of OMD treatment on human osteoblast culture**

The RNA-seq analysis conducted on primary human trabecular pre-osteoblasts treated with rhOMD established that its effect on gene expression is low (Fig 48 & Table 14). Therefore, it is unlikely that OMD undertakes its function through direct gene regulation, or at least on trabecular bone. However, we could argue that rhOMD treatments might not be optimal because the recombinant protein, despite borrowing the human sequence, is lacking some post-translational modifications compared to the OMD secreted by osteoblasts, as indicated by the western blot analysis performed with commercially available antibodies (Appendix 5). While produced *in vitro* by eukaryotic murine cells, differential post-translational events are occurring on the core protein when compared to the human sequence following the prediction of UniProt. Yet, as reviewed [50], post-translational events contribute to the biological functions of SLRPs. Also, we cannot exclude that OMD could modulate the gene expression of other cell types. Besides, it is what we reported when comparing the ALP activity of osteoblasts originating either from cortical bone or trabecular bone. The rhOMD treatment was able to increase the ALP activity in osteoblast culture issued from the cortical bone at 10 and 40 ng/mL but not in culture issued from trabecular bone neither at 10 nor at 40 ng/mL (Fig 75). Nonetheless, the augmentation of ALP activity of cortical osteoblasts was subtle. Then, we can anticipate that the function of OMD may adopt some specificity between the cortical and trabecular bone.

## VI. ADDITIONAL RESULTS & DISCUSSION

Osteoblast from cortical bone - 14 days

Osteoblast from trabecular bone - 14 days

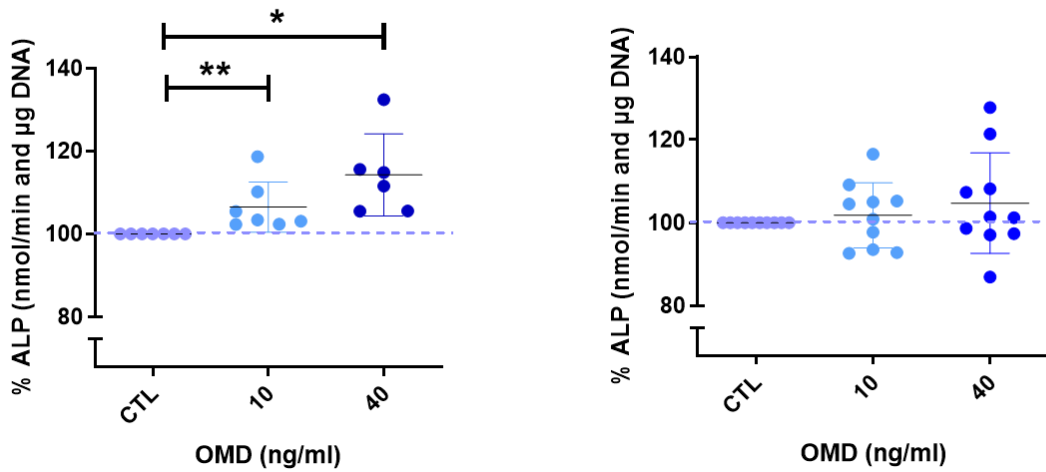


Figure 75: Primary human osteoblasts from cortical and trabecular bone were used for monolayer culture with osteogenic medium during 14 days. Osteoblasts were treated with 10 or 40 ng/mL of rhOMD, or none (CTL), during 3 days prior to the analysis of the ALP activity reported in percentage. Each point represents a unique patient with error bars representing  $\pm$ SD. Paired one-way ANOVA was performed with differences being considered significant at  $p$ -values  $< 0.05$  (\* $p < 0.05$ , \*\* $p \leq 0.01$ ). For the cortical osteoblasts,  $n=7$  for the CTL and 10 ng/mL and  $n=6$  for 40 ng/mL; for the trabecular osteoblast,  $n=10$  for each condition.

**VI.5.2 Rescue of the sclerotic phenotype in cortical osteoblast culture**

Previous work from the mSKIL laboratory identified OMD as the top protein downregulated during subchondral bone sclerosis when compared to the neighboring non-sclerotic area [187]. Therefore, cortical osteoblast cultures were designed in order to assess the potential rescue of the sclerotic phenotype of rhOMD treatment. The sclerotic phenotype can be observed following Alizarin red staining, showing a lack or a delay of mineralization by the sclerotic cortical osteoblasts [286]. We showed that rhOMD treatments on sclerotic osteoblasts enhanced their potential of mineralization compared to the untreated conditions reinforcing the key function of OMD during the development of subchondral bone sclerosis (Fig 76).

## VI. ADDITIONAL RESULTS & DISCUSSION

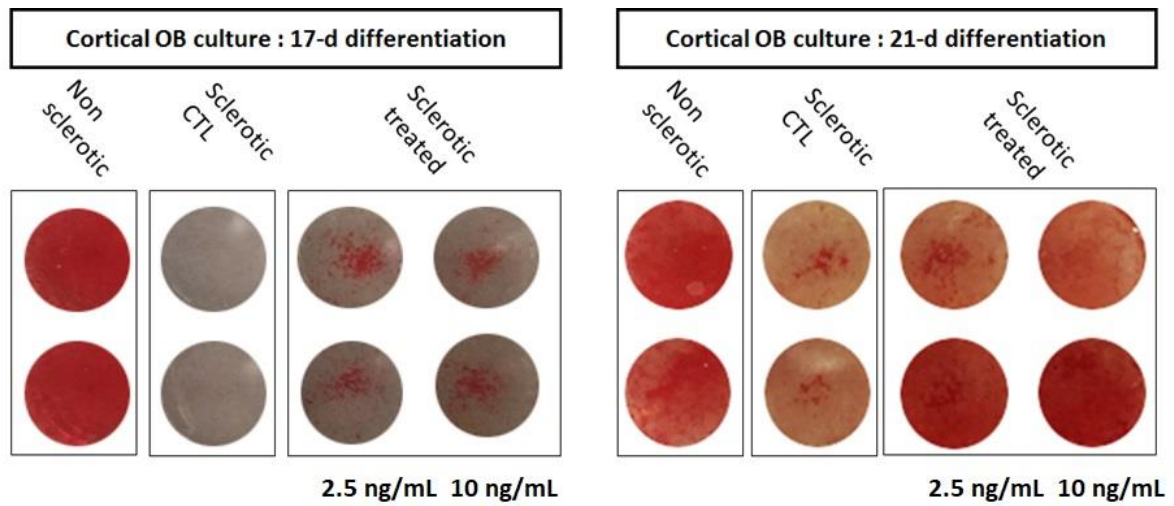


Figure 76: Alizarin red staining on cortical osteoblasts, either from the non-sclerotic area or the neighboring sclerotic subchondral bone, after 17 days and 21 days of differentiation in osteogenic medium. Sclerotic osteoblasts were treated with 2.5 or 10 ng/mL of rhOMD, or none (CTL), during their 3 last days of differentiation. For 17-days,  $n=2$ , and for 21-days,  $n=1$ .

# **VII. CONCLUSIONS & FUTURE PERSPECTIVES**



## VII. CONCLUSIONS & FUTURE PERSPECTIVES

The work conducted during this thesis shed light on the functions of OMD from the SLRP family. Most of our observations are issued from *in vivo* models in mice and zebrafish. Besides, the *in vitro* assays gave valuable insights on the mechanical route taken by OMD to orchestrate its functions. Tables 15 to 19 summarize the effects of the loss of function of *Omd*, its overexpression, and its treatment on primary cell cultures to seize an overall representation.

Table 15: Summary of the bone parameters over time in the male mouse models

			KO vs UP	KO vs WT	UP vs WT
Trabecular bone	BV/TV	4-Months			
		8-Months	↑		↓
		16-Months	↑		
	Trabecular Number	4-Months			
		8-Months	↑	↑	
		16-Months	↑	↑	↓
Porosity	4-Months				
	8-Months				
	16-Months	↓			
Cortical bone	BV/TV	4-Months			
		8-Months	↑		
		16-Months	↑	↑	
	Thickness	4-Months			
		8-Months	↑		
		16-Months	↑	↑	
Porosity	4-Months				
	8-Months	↓			
	16-Months	↓	↓		
Biomechanic	Maximal Load	16-Months	↑	↑	
	Stiffness	16-Months	↑		
Bone turnover	P1NP	16-Months	↑		
	TRAcP 5b	16-Months	↑	↑	

Table 16: Summary of the cartilage parameters over time in the male mouse models

			KO vs UP	KO vs WT	UP vs WT
Cartilage	Growth plate area	4-Months			
		8-Months			
		16-Months		↑	
	Calcified Cartilage/Total Cartilage - Lateral	4-Months		↑	↑
		8-Months			
		16-Months	↑		
Calcified Cartilage/Total Cartilage - Medial	4-Months	↓	↓		
	8-Months	↓	↓		
	16-Months	↓	↓		

Table 17: Summary of OA parameters in the male mouse models (Spontaneous & DMM)

			KO vs UP	KO vs WT	UP vs WT
Cartilage	OARSI - Lateral	16-Months			
		DMM			
	OARSI - Medial	16-Months		↑	
		DMM			
PG loss - Lateral	16-Months		↑		
	DMM				
Subchondral bone sclerosis	BV/TV - Lateral	8-Months	↑		
		16-Months	↑	↑	
	BV/TV - Medial	8-Months			
		16-Months	↑		↓

Table 18: Summary of the characterization of the zebrafish models, with the microinjection of *omd* mRNA (UP) and the mutant (KO)

			KO vs WT	UP vs WT	
Development	Ventralization	24-Hpf	Na	↑	
		4-Dpf	Na	↑	
	Developmental defect	5-Dpf		Na	
		8-Dpf		Na	
Cartilage	OARSI – Jaw joint	1-Year	↑	Na	
		14-Dpf		Na	
	Bone remodeling	Osteoclast number	1-Year	↑	Na
		TRAP	1.6-Years	↑	Na
Scale regeneration	Defect	1.6-Years	↑	Na	
FTIR	Mineral-to-Matrix	3-Months	↓	Na	
		1-Year		Na	
	Carbonate-to-Phosphate	3-Months		Na	
		1-Year		Na	
	Collagen-to-Phosphate	3-Months	↑	Na	
		1-Year		Na	

Table 19: Summary of the *in vitro* models (murine and human primary cell culture)

			Treated vs CTL
Murine osteoclast	Number	5-Days	↓
Human trabecular osteoblast	ALP activity	14-Days	
Human cortical osteoblast	ALP activity	14-Days	↑
	Sclerotic phenotype	17/21-Days	↓

Color key	
↑	Significant increase ( $p < 0.05$ )
↓	Significant decrease ( $p < 0.05$ )
	Non significant
Na	Not applicable

## ***VII. CONCLUSIONS & FUTURE PERSPECTIVES***

Our data corroborated the deep relationship of OMD with the mineralized tissues including bone but also calcified cartilage. In skeletal tissues, OMD safeguards the bone and cartilage metabolisms and controls their microarchitectures. The absence of OMD was accompanied by higher bone volume and by spontaneous sclerosis of the subchondral bone as well. This bone feature is linked to OA. Interestingly,  $\mu$ CT analysis of the tibial metaphysis of STR/Ort mice, a strain developing spontaneous OA, revealed higher bone volume in STR/Ort than in the WT corroborating our findings [299,300]. The DMM model demonstrated that *Omd* overexpression reduced subchondral bone sclerosis suggesting that OMD may be a key player in its development. The further development of cartilage lesions may be secondary, following the modification of the subchondral bone structure [98,163,164,255–258]. In addition, the *in vivo* data are supported by a previous analysis of the secretome showing the decreased synthesis of OMD by human osteoblasts from the sclerotic bone area compared to neighboring non-sclerotic osteoblasts [180]. We can point out that the secretome analysis was conducted only on male patients but, following our *in vivo* observations on mice, females also display a specific bone phenotype due to the absence of OMD. According to our research, OMD would be an interesting marker in the context of subchondral bone-driven OA [106]. By positioning OMD as a factor actively implied in bone and cartilage homeostasis, we are not only identifying a new target for OA research but we are also contributing to raise awareness on the importance of the matrisome. ECM proteins, in addition to their functions for the matrix assembly and creating the cell environment, influence cell behavior and fate through cell-to-matrix interactions. Keeping a balanced ECM environment prevents pathological development and diseases. This research also underlines the importance of deepening our knowledge of the matrisome with the aim of discovering new biomarkers and therapeutic targets of OA [301–303]. Modifications of OMD could represent a signature to follow, part of

## ***VII. CONCLUSIONS & FUTURE PERSPECTIVES***

a bony fingerprint and future pre-clinical studies might turn OMD into an opportunity for the development of a diagnostic tool for subchondral-bone driven OA helping the difficult challenge of phenotyping OA patients.

Concerning the mechanisms by which OMD undertakes its functions, our work showed that it was consistent with the role of biological reservoirs assigned to SLRPs [50]. OMD binds directly to RANKL, the master differentiation factor for osteoclastogenesis. OMD would regulate the availability of RANKL by trapping it within the ECM. The action of OMD on osteoclasts would depend on its sulfation profile, with greater inhibition of osteoclasts associated with a higher level of sulfation during ECM mineralization. [226,294,304]. This model of action could explain the increased osteoclast number in the absence of OMD. Although it is counterintuitive that increased bone resorption is correlated with bone sclerosis, several studies showed that both are correlated. There is uncoupled bone remodeling in OA with increased osteoclast number and bone resorption inducing recruitment of osteoprogenitors leading to abnormal bone formation and ultimately to sclerosis. Targeting bone remodeling is then considered a promising perspective for OA treatment, either in early or advanced OA, especially in the context of subchondral bone-driven OA phenotype [295].

Aiming therapeutic perspectives, the mode of action of OMD could prove to be of particular interest by trapping cytokines and growth factors such as RANKL, BMP2, and possibly TGF- $\beta$ 1 [195]. OMD would finely control their bioavailability assuring subchondral bone homeostasis. This approach could be specifically useful to avoid adverse effects coming with the modulation of pleiotropic and major molecular pathways remaining a double-edged sword. For instance, therapies preventing uncoupled bone remodeling by targeting the inhibition of TGF- $\beta$ 1 showed beneficial effects against OA in rodent models [167,175,305–308]. The development

## ***VII. CONCLUSIONS & FUTURE PERSPECTIVES***

of antibodies against TGF- $\beta$ 1 or even treatment with a native antagonist like noggin seems appealing therapeutic strategies and showed encouraging results in animal models. However, serious adverse effects cannot be neglected with articular cartilage getting damaged when stepping outside the therapeutic window or when using a higher dose of the inhibitor [167,309], and with healthy articular cartilage adopting OA phenotype under TGF- $\beta$ 1 activation [310,311]. Shifting our attention to downstream regulators, like OMD, might bring new perspectives to combine the best of both worlds in the context of OA therapies. The preliminary data from *in vitro* cortical culture of sclerotic osteoblasts comforts this auspicious message by showing a partial rescue of the pathological phenotype. If downstream regulators, like OMD, are proposed to fine-tune the cellular response, then we also have to think about how to deliver it. We can envisage adding OMD to bone substitute material, directly injected into the subchondral bone, which is resorbed and replaced by healthy bone to repair bone defects [312]. OMD could also be added to the scaffold injected alongside with MSCs in the subchondral bone, originally designed to enhance their survival and beneficial effects on OA [313].

Besides, I would like to bring attention to new bioengineered scaffolds developed and used for bone defects that could profit from the same perspective. The implanted scaffold needs to direct the bone healing response by providing a substrate for adhesion and proliferation to the cells and directing their fate [314,315]. Among the key factors to consider for scaffold engineering, there are the growth factors but also the ECM proteins which are essential for correct osteoinduction [40]. Recent studies are already showing potential applications for OMD. For instance, poly(L-lactide-co- $\epsilon$ -caprolactone) scaffolds functionalized with demineralized dentine mimicking natural bone regeneration mechanism, release OMD helping bone regeneration mechanism [316]. A newly designed coating of polysaccharide

## ***VII. CONCLUSIONS & FUTURE PERSPECTIVES***

carboxymethyl cellulose and the non-steroid anti-inflammatory drug diclofenac on AISI 316LVM stainless steel that is used in orthopaedic medicine showed better control of drug release with increased *OMD* expression and higher osteointegration rate [317].

To go further with the mode of action of OMD, I have to address the direct effect of OMD on the ECM structure happening concomitantly to its reservoir functions with growth factors and cytokines. It was previously described that OMD has the ability to directly bind to type I collagen. OMD regulates fibrillogenesis by controlling the rate of fibril formation which reduces the diameter of collagen fibrils and avoids twisted fibrils [246,247]. The control over collagen fibrillogenesis appears to be a primordial function of OMD as both glutamic acids identified in collagen binding are highly conserved among vertebrae. The loss of OMD would jeopardize the ECM biophysical properties of mineralized tissues and would result in abnormal mechanical loading on the articular surface which promotes OA development. The downregulation of OMD in subchondral bone sclerosis fits the observation of thicker collagen fibrils made in the murine DMM model. It is associating the loss of OMD with degenerative collagenous modifications during OA [318]. The control over collagen fibrillogenesis might also be partly responsible for the microarchitectural modifications of the cortical and trabecular bone in the *Omd* mutant and overexpressing mice in comparison to the WT. Supporting this statement, the results from the zebrafish model indicate structural disorganization of collagen fibrils. This direct interaction with collagen only increases the therapeutic interest that can be brought to OMD, whether for treatments or in the case of bioengineering.

The observations made on the zebrafish confirm the efficiency of this model to translate OA phenotype. The mutation of *omd* in the zebrafish led to cartilaginous lesions of the synovial jaw joint. Showing similar functions and a similar pattern of expression in the zebrafish is

## **VII. CONCLUSIONS & FUTURE PERSPECTIVES**

especially interesting as it underlines the important roles of OMD worth being conserved. Using the zebrafish as OA model is extremely recent (late 2010's [264]), making us privileged pioneers, and may certainly arise new research opportunities, especially for the regeneration of the articular cartilage that will represent exciting challenges to translate to regenerative medicine in human. Looking at the overexpression of *omd* in the zebrafish, it clearly demonstrated that ectopic expression of *omd* appears to induce deleterious effects in the development. This phenotype is consistent with the deformities of the dorsoventral axis following the injection of *decorin* mRNA in zebrafish [319]. Again, I will link this phenotype to the regulation of the bioavailability of growth factors knowing OMD binds to BMP2 to help its activation and that ectopic BMP2 induces the ventralization of embryos [195,320].

Finally, we have extensively studied OMD under the magnifying glass of OA, associating its loss with the initiation of subchondral bone sclerosis; nonetheless, OMD might be related to other musculoskeletal disorders such as osteoporosis. Reporting a significative diminution of bone volume under overexpression of *Omd* in aged mice forced us to envisage a relationship with osteoporosis. Other members of the SLRP family are related to osteoporosis, for example, the mutation of biglycan is associated with its early onset while its activation alleviates its progression through the BMP pathway [202,321,322].

In conclusion, our *in vitro* and *in vivo* research has yielded a strong and compelling body of evidence that OMD helps preserve bone and cartilage integrity, and is an active player in sclerosis-associated subchondral bone in OA. OMD would prevent sclerosis by regulating osteoclastogenesis and the structure of the collagen network. OMD could be a relevant biomarker of subchondral bone-driven OA phenotype and a therapeutic target. This perspective is a step towards a personalized approach to OA management.

## VII. CONCLUSIONS & FUTURE PERSPECTIVES

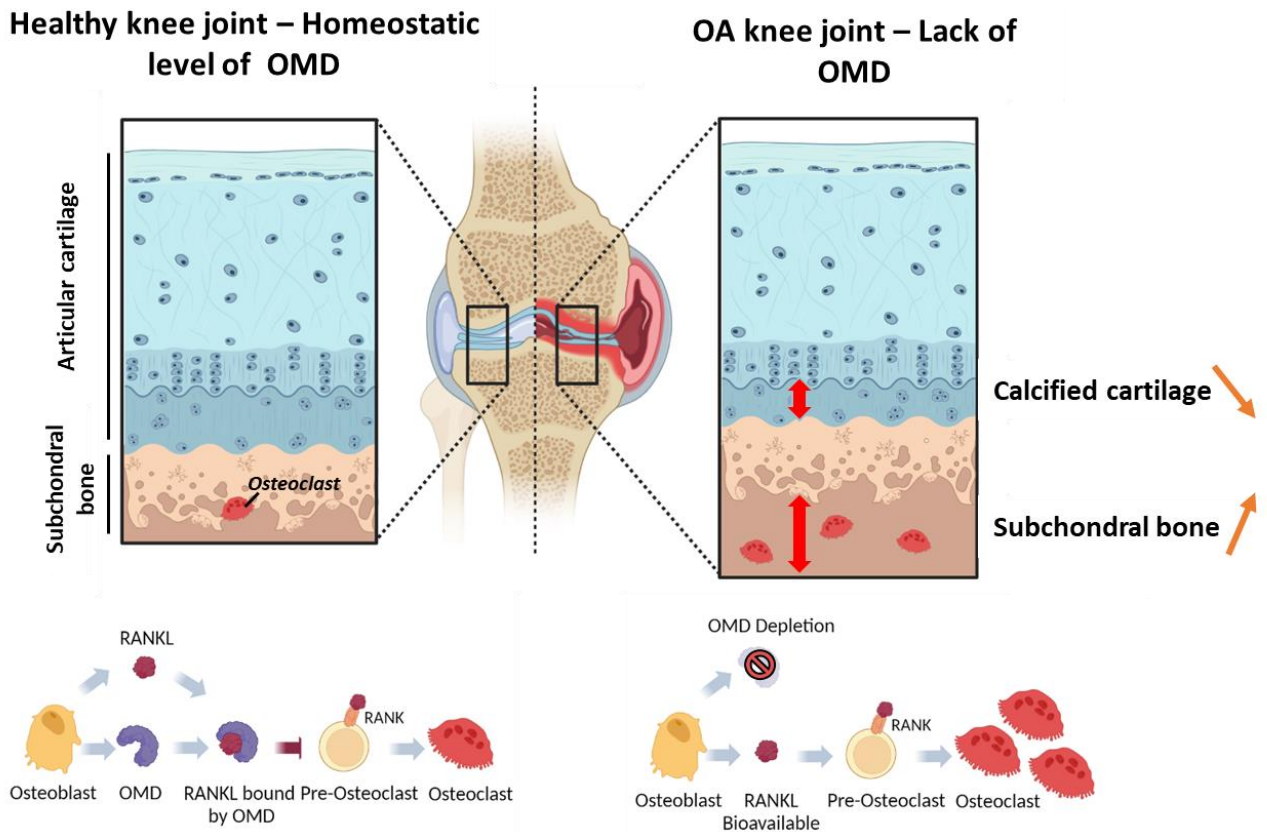


Figure 77: Graphical representation of the effect of the lack of OMD in the murine knee joint. Left: in the healthy knee joint, the secretion of OMD in the ECM allows the regulation of bone remodeling. OMD found in mineralized tissues traps RANKL to control its bioavailability and tempers osteoclastogenesis. Right: The lack of OMD increases the availability of RANKL inducing the formation of osteoclasts in the subchondral bone and lead to uncoupled bone remodeling. Increased bone resorption stimulates osteoblast activity and bone formation resulting in the subchondral bone sclerosis associated with OA. The bone and cartilage architectures are impaired in the absence of OMD. The calcified cartilage of the medial tibial plateau is reduced and the overall bone volume is increased. Figure designed by Jérémie Zappia with Biorender.

### Highlights :

- ⇒ OMD is localized in mineralized tissues of the knee joint, including calcified cartilage and subchondral bone
- ⇒ OMD regulates bone and cartilage microarchitectures impacting physical properties
- ⇒ Lack of OMD promotes subchondral bone sclerosis while its overexpression alleviates its onset
- ⇒ OMD may be beneficial against articular degradation in OA
- ⇒ OMD acts as a bioreservoir in the ECM, binding RANKL to regulate its availability and inhibiting osteoclastogenesis; thus safeguarding the bone remodeling balance and helping to prevent subchondral bone sclerosis.

# **VIII. BIBLIOGRAPHY**



## VIII. BIBLIOGRAPHY

- 1 Zhou R, Guo Q, Xiao Y, *et al.* Endocrine role of bone in the regulation of energy metabolism. *Bone Res.* 2021;**9**. doi:10.1038/s41413-021-00142-4
- 2 Su N, Yang J, Xie Y, *et al.* Bone function, dysfunction and its role in diseases including critical illness. *Int J Biol Sci.* 2019;**15**. doi:10.7150/ijbs.27063
- 3 Lefebvre V, Bhattaram P. Vertebrate skeletogenesis. In: *Current Topics in Developmental Biology.* 2010. doi:10.1016/S0070-2153(10)90008-2
- 4 Karsenty G, Oury F. Regulation of male fertility by the bone-derived hormone osteocalcin. *Mol Cell Endocrinol.* 2014;**382**. doi:10.1016/j.mce.2013.10.008
- 5 Han Y, You X, Xing W, *et al.* Paracrine and endocrine actions of bone - The functions of secretory proteins from osteoblasts, osteocytes, and osteoclasts. *Bone Res.* 2018;**6**. doi:10.1038/s41413-018-0019-6
- 6 Quilhac A. An overview of cartilage histology. In: *Vertebrate Skeletal Histology and Paleohistology.* 2021. doi:10.1201/9781351189590-7
- 7 Boyce BF, Zuscik MJ, Xing L. Biology of Bone and Cartilage. In: *Genetics of Bone Biology and Skeletal Disease.* Elsevier 2018. 173–95. doi:10.1016/B978-0-12-804182-6.00011-3
- 8 Goldring MB, Tsuchimochi K, Ijiri K. The control of chondrogenesis. *J Cell Biochem.* 2006;**97**. doi:10.1002/jcb.20652
- 9 Yang X, Tian S, Fan L, *et al.* Integrated regulation of chondrogenic differentiation in mesenchymal stem cells and differentiation of cancer cells. *Cancer Cell Int* 2022;**22**:169. doi:10.1186/s12935-022-02598-8
- 10 Chen H, Tan XN, Hu S, *et al.* Molecular Mechanisms of Chondrocyte Proliferation and Differentiation. *Front Cell Dev Biol.* 2021;**9**. doi:10.3389/fcell.2021.664168
- 11 Song H, Park KH. Regulation and function of SOX9 during cartilage development and regeneration. *Semin Cancer Biol.* 2020;**67**. doi:10.1016/j.semcancer.2020.04.008
- 12 Zhao Q, Eberspaecher H, Lefebvre V, *et al.* Parallel expression of Sox9 and Col2a1 in cells undergoing chondrogenesis. *Developmental Dynamics* 1997;**209**. doi:10.1002/(SICI)1097-0177(199708)209:4<377::AID-AJA5>3.0.CO;2-F
- 13 Akiyama H, Chaboissier MC, Martin JF, *et al.* The transcription factor Sox9 has essential roles in successive steps of the chondrocyte differentiation pathway and is required for expression of Sox5 and Sox6. *Genes Dev* 2002;**16**. doi:10.1101/gad.1017802
- 14 Healy C, Uwanogho D, Sharpe PT. Regulation and role of Sox9 in cartilage formation. *Developmental Dynamics* 1999;**215**. doi:10.1002/(SICI)1097-0177(199905)215:1<69::AID-DVDY8>3.0.CO;2-N
- 15 Nishimura R, Hata K, Matsubara T, *et al.* Regulation of bone and cartilage development by network between BMP signalling and transcription factors. *J Biochem.* 2012;**151**. doi:10.1093/jb/mvs004
- 16 Nishimura R, Wakabayashi M, Hata K, *et al.* Osterix regulates calcification and degradation of chondrogenic matrices through matrix metalloproteinase 13 (MMP13) expression in association with transcription factor Runx2 during endochondral ossification. *Journal of Biological Chemistry* 2012;**287**. doi:10.1074/jbc.M111.337063

## VIII. BIBLIOGRAPHY

- 17 Hallett SA, Ono W, Ono N. Growth plate chondrocytes: Skeletal development, growth and beyond. *Int J Mol Sci.* 2019;**20**. doi:10.3390/ijms20236009
- 18 Ding M, Lu Y, Abbassi S, *et al.* Targeting Runx2 expression in hypertrophic chondrocytes impairs endochondral ossification during early skeletal development. *J Cell Physiol* 2012;**227**. doi:10.1002/jcp.24045
- 19 Park J, Gebhardt M, Golovchenko S, *et al.* Dual pathways to endochondral osteoblasts: A novel chondrocyte-derived osteoprogenitor cell identified in hypertrophic cartilage. *Biol Open* 2015;**4**. doi:10.1242/bio.201411031
- 20 Qin X, Jiang Q, Nagano K, *et al.* Runx2 is essential for the transdifferentiation of chondrocytes into osteoblasts. *PLoS Genet* 2020;**16**. doi:10.1371/journal.pgen.1009169
- 21 Rashid H, Chen H, Javed A. Runx2 is required for hypertrophic chondrocyte mediated degradation of cartilage matrix during endochondral ossification. *Matrix Biol Plus* 2021;**12**. doi:10.1016/j.mbplus.2021.100088
- 22 Stickens D, Behonick DJ, Ortega N, *et al.* Altered endochondral bone development in matrix metalloproteinase 13-deficient mice. *Development* 2004;**131**. doi:10.1242/dev.01461
- 23 Clarke B. Normal bone anatomy and physiology. *Clin J Am Soc Nephrol.* 2008;**3 Suppl 3**. doi:10.2215/CJN.04151206
- 24 Feng X. Chemical and Biochemical Basis of Cell-Bone Matrix Interaction in Health and Disease. *Curr Chem Biol* 2009;**3**. doi:10.2174/187231309788166398
- 25 Black JD, Tadros BJ. Bone structure: from cortical to calcium. *Orthop Trauma* 2020;**34**. doi:10.1016/j.mporth.2020.03.002
- 26 Galea GL, Zein MR, Allen S, *et al.* Making and shaping endochondral and intramembranous bones. *Developmental Dynamics.* 2021;**250**. doi:10.1002/dvdy.278
- 27 Tam WL, Luyten FP, Roberts SJ. From skeletal development to the creation of pluripotent stem cell-derived bone-forming progenitors. *Philosophical Transactions of the Royal Society B: Biological Sciences.* 2018;**373**. doi:10.1098/rstb.2017.0218
- 28 Gilbert SF. *Developmental Biology. Osteogenesis: The Development of Bones. Development Biology: 6th edition* 2000.
- 29 Eames BF, Sharpe PT, Helms JA. Hierarchy revealed in the specification of three skeletal fates by Sox9 and Runx2. *Dev Biol* 2004;**274**. doi:10.1016/j.ydbio.2004.07.006
- 30 Duan X, Bradbury SR, Olsen BR, *et al.* VEGF stimulates intramembranous bone formation during craniofacial skeletal development. *Matrix Biology* 2016;**52–54**. doi:10.1016/j.matbio.2016.02.005
- 31 Hara ES, Nagaoka N, Okada M, *et al.* Distinct Morphologies of Bone Apatite Clusters in Endochondral and Intramembranous Ossification. *Adv Biol* 2022;**2200076**. doi:10.1002/adbi.202200076
- 32 Safadi FF, Barbe MF, Abdelmagid SM, *et al.* Bone structure, development and bone biology. In: *Bone Pathology.* 2009. doi:10.1007/978-1-59745-347-9\_1

## VIII. BIBLIOGRAPHY

- 33 Maes C, Kronenberg HM. Bone Development and Remodeling. In: *Endocrinology: Adult and Pediatric*. Elsevier 2016. 1038-1062.e8. doi:10.1016/B978-0-323-18907-1.00060-3
- 34 Knowles HJ, Moskovsky L, Thompson MS, *et al*. Chondroclasts are mature osteoclasts which are capable of cartilage matrix resorption. *Virchows Archiv* 2012;**461**. doi:10.1007/s00428-012-1274-3
- 35 Romeo SG, Alawi KM, Rodrigues J, *et al*. Endothelial proteolytic activity and interaction with non-resorbing osteoclasts mediate bone elongation. *Nat Cell Biol* 2019;**21**. doi:10.1038/s41556-019-0304-7
- 36 Kusumbe AP, Ramasamy SK, Adams RH. Coupling of angiogenesis and osteogenesis by a specific vessel subtype in bone. *Nature* 2014;**507**. doi:10.1038/nature13145
- 37 Zhou X, von der Mark K, Henry S, *et al*. Chondrocytes Transdifferentiate into Osteoblasts in Endochondral Bone during Development, Postnatal Growth and Fracture Healing in Mice. *PLoS Genet* 2014;**10**. doi:10.1371/journal.pgen.1004820
- 38 Yang L, Tsang KY, Tang HC, *et al*. Hypertrophic chondrocytes can become osteoblasts and osteocytes in endochondral bone formation. *Proc Natl Acad Sci U S A* 2014;**111**. doi:10.1073/pnas.1302703111
- 39 Wolff LI, Hartmann C. A Second Career for Chondrocytes—Transformation into Osteoblasts. *Curr Osteoporos Rep*. 2019;**17**. doi:10.1007/s11914-019-00511-3
- 40 Zhu G, Zhang T, Chen M, *et al*. Bone physiological microenvironment and healing mechanism: Basis for future bone-tissue engineering scaffolds. *Bioact Mater*. 2021;**6**. doi:10.1016/j.bioactmat.2021.03.043
- 41 Buckwalter JA, Glimcher MJ, Cooper RR, *et al*. Bone biology. Part I: Structure, blood supply, cells, matrix, and mineralization. *Journal of Bone and Joint Surgery*. 1995;**77**. doi:10.2106/00004623-199508000-00019
- 42 Schrof S, Varga P, Galvis L, *et al*. 3D Raman mapping of the collagen fibril orientation in human osteonal lamellae. *J Struct Biol* 2014;**187**. doi:10.1016/j.jsb.2014.07.001
- 43 Lin X, Patil S, Gao YG, *et al*. The Bone Extracellular Matrix in Bone Formation and Regeneration. *Front Pharmacol*. 2020;**11**. doi:10.3389/fphar.2020.00757
- 44 Murshed M. Mechanism of bone mineralization. *Cold Spring Harb Perspect Med* 2018;**8**. doi:10.1101/CSHPERSPECT.A031229
- 45 Zaichick V, Tzaphlidou M. Determination of calcium, phosphorus, and the calcium/phosphorus ratio in cortical bone from the human femoral neck by neutron activation analysis. *Applied Radiation and Isotopes* 2002;**56**. doi:10.1016/S0969-8043(02)00066-0
- 46 Gasser JA, Kneissel M. Bone physiology and biology. In: *Molecular and Integrative Toxicology*. 2017. doi:10.1007/978-3-319-56192-9\_2
- 47 Garnero P. The Role of Collagen Organization on the Properties of Bone. *Calcif Tissue Int* 2015;**97**. doi:10.1007/s00223-015-9996-2
- 48 Wu M, Crane JS. *Biochemistry, Collagen Synthesis*. 2018.

## VIII. BIBLIOGRAPHY

- 49 Gorski JP. Biochemistry of Non-collagenous Proteins of Bone. 2021. doi:10.1007/978-3-030-76283-4\_8
- 50 Zappia J, Joiret M, Sanchez C, *et al.* From translation to protein degradation as mechanisms for regulating biological functions: A review on the SLRP family in skeletal tissues. *Biomolecules* 2020;**10**. doi:10.3390/biom10010080
- 51 Burr DB. Bone Morphology and Organization. In: *Basic and Applied Bone Biology*. 2019. doi:10.1016/b978-0-12-813259-3.00001-4
- 52 Alford AI, Kozloff KM, Hankenson KD. Extracellular matrix networks in bone remodeling. *International Journal of Biochemistry and Cell Biology*. 2015;**65**. doi:10.1016/j.biocel.2015.05.008
- 53 Zhao B, Ivashkiv LB. Negative regulation of osteoclastogenesis and bone resorption by cytokines and transcriptional repressors. *Arthritis Res Ther*. 2011;**13**. doi:10.1186/ar3379
- 54 Park-Min KH. Mechanisms involved in normal and pathological osteoclastogenesis. *Cellular and Molecular Life Sciences*. 2018;**75**. doi:10.1007/s00018-018-2817-9
- 55 Wilson SR, Peters C, Saftig P, *et al.* Cathepsin K activity-dependent regulation of osteoclast actin ring formation and bone resorption. *Journal of Biological Chemistry* 2009;**284**. doi:10.1074/jbc.M805280200
- 56 Ballanti P, Minisola S, Pacitti MT, *et al.* Tartrate-resistant acid phosphate activity as osteoclastic marker: Sensitivity of cytochemical assessment and serum assay in comparison with standardized osteoclast histomorphometry. *Osteoporosis International* 1997;**7**. doi:10.1007/BF01623458
- 57 Itzstein C, Coxon FP, Rogers MJ. The regulation of osteoclast function and bone resorption by small GTPases. *Small GTPases* 2011;**2**. doi:10.4161/sgtp.2.3.16453
- 58 Ross FP. Osteoclast Biology and Bone Resorption. In: *Primer on the Metabolic Bone Diseases and Disorders of Mineral Metabolism: Seventh Edition*. 2009. doi:10.1002/9780470623992.ch3
- 59 McDonald MM, Khoo WH, Ng PY, *et al.* Osteoclasts recycle via osteomorphs during RANKL-stimulated bone resorption. *Cell* 2021;**184**. doi:10.1016/j.cell.2021.02.002
- 60 Bolamperti S, Villa I, Rubinacci A. Bone remodeling: an operational process ensuring survival and bone mechanical competence. *Bone Res* 2022;**10**:48. doi:10.1038/s41413-022-00219-8
- 61 Y. A, Valds-Flores M, Orozco L, *et al.* Molecular Aspects of Bone Remodeling. In: *Topics in Osteoporosis*. 2013. doi:10.5772/54905
- 62 Kennedy OD, Herman BC, Laudier DM, *et al.* Activation of resorption in fatigue-loaded bone involves both apoptosis and active pro-osteoclastogenic signaling by distinct osteocyte populations. *Bone* 2012;**50**. doi:10.1016/j.bone.2012.01.025
- 63 Komori T. Cell death in Chondrocytes, osteoblasts, and osteocytes. *Int J Mol Sci*. 2016;**17**. doi:10.3390/ijms17122045
- 64 Ek-Rylander B, Flores M, Wendel M, *et al.* Dephosphorylation of osteopontin and bone sialoprotein by osteoclastic tartrate-resistant acid phosphatase. Modulation of osteoclast adhesion in vitro. *Journal of Biological Chemistry* 1994;**269**. doi:10.1016/s0021-9258(17)36541-9

## VIII. BIBLIOGRAPHY

- 65 Vääräniemi J, Halleen JM, Kaarlonen K, *et al.* Intracellular machinery for matrix degradation in bone-resorbing osteoclasts. *Journal of Bone and Mineral Research* 2004;**19**. doi:10.1359/JBMR.040603
- 66 Costa AG, Cusano NE, Silva BC, *et al.* Cathepsin K: Its skeletal actions and role as a therapeutic target in osteoporosis. *Nat Rev Rheumatol.* 2011;**7**. doi:10.1038/nrrheum.2011.77
- 67 Juneja P, Munjal A, Hubbard JB. Anatomy , Joints. *StatPearls [Internet]* 2022.
- 68 Wang W, Ye R, Xie W, *et al.* Roles of the calcified cartilage layer and its tissue engineering reconstruction in osteoarthritis treatment. *Front Bioeng Biotechnol* 2022;**10**. doi:10.3389/fbioe.2022.911281
- 69 Jung CK. Articular cartilage: Histology and physiology. In: *Techniques in Cartilage Repair Surgery.* 2014. doi:10.1007/978-3-642-41921-8\_2
- 70 Sophia Fox AJ, Bedi A, Rodeo SA. The basic science of articular cartilage: Structure, composition, and function. *Sports Health* 2009;**1**. doi:10.1177/1941738109350438
- 71 Eschweiler J, Horn N, Rath B, *et al.* The biomechanics of cartilage-an overview. *Life* 2021;**11**. doi:10.3390/life11040302
- 72 Saito T. The superficial zone of articular cartilage. *Inflamm Regen* 2022;**42**:14. doi:10.1186/s41232-022-00202-0
- 73 Kozhemyakina E, Zhang M, Ionescu A, *et al.* Identification of a Prg4-expressing articular cartilage progenitor cell population in mice. *Arthritis and Rheumatology* 2015;**67**. doi:10.1002/art.39030
- 74 Rhee DK, Marcelino J, Baker M, *et al.* The secreted glycoprotein lubricin protects cartilage surfaces and inhibits synovial cell overgrowth. *Journal of Clinical Investigation* 2005;**115**. doi:10.1172/JCI200522263
- 75 Oliveira Silva M, Gregory JL, Ansari N, *et al.* Molecular Signaling Interactions and Transport at the Osteochondral Interface: A Review. *Front Cell Dev Biol.* 2020;**8**. doi:10.3389/fcell.2020.00750
- 76 Mayan MD, Gago-Fuentes R, Carpintero-Fernandez P, *et al.* Articular chondrocyte network mediated by gap junctions: Role in metabolic cartilage homeostasis. *Ann Rheum Dis* 2015;**74**. doi:10.1136/annrheumdis-2013-204244
- 77 Chen C, Tambe DT, Deng L, *et al.* Biomechanical properties and mechanobiology of the articular chondrocyte. *Am J Physiol Cell Physiol.* 2013;**305**. doi:10.1152/ajpcell.00242.2013
- 78 Sebastian A, McCool JL, Hum NR, *et al.* Single-cell RNA-seq reveals transcriptomic heterogeneity and post-traumatic osteoarthritis-associated early molecular changes in mouse articular chondrocytes. *Cells* 2021;**10**. doi:10.3390/cells10061462
- 79 Ji Q, Zheng Y, Zhang G, *et al.* Single-cell RNA-seq analysis reveals the progression of human osteoarthritis. *Ann Rheum Dis* 2019;**78**. doi:10.1136/annrheumdis-2017-212863
- 80 Maroudas A, Schneiderman R. “Free” and “exchangeable” or “trapped” and “non-exchangeable” water in cartilage. *Journal of Orthopaedic Research* 1987;**5**. doi:10.1002/jor.1100050117

## VIII. BIBLIOGRAPHY

- 81 Alcaide-Ruggiero L, Molina-Hernández V, Granados MM, *et al.* Main and minor types of collagens in the articular cartilage: The role of collagens in repair tissue evaluation in chondral defects. *Int J Mol Sci* 2021;**22**. doi:10.3390/ijms222413329
- 82 Orozco GA, Tanska P, Florea C, *et al.* A novel mechanobiological model can predict how physiologically relevant dynamic loading causes proteoglycan loss in mechanically injured articular cartilage. *Sci Rep* 2018;**8**. doi:10.1038/s41598-018-33759-3
- 83 Zylinska B, Sobczynska-Rak A, Lisiacka U, *et al.* Structure and pathologies of articular cartilage. *In Vivo (Brooklyn)*. 2021;**35**. doi:10.21873/invivo.12388
- 84 Roughley PJ, Mort JS. The role of aggrecan in normal and osteoarthritic cartilage. *J Exp Orthop* 2014;**1**. doi:10.1186/s40634-014-0008-7
- 85 Roughley PJ. Articular cartilage and changes in arthritis noncollagenous proteins and proteoglycans in the extracellular matrix of cartilage. *Arthritis Res.* 2001;**3**. doi:10.1186/ar326
- 86 Roseman S. Reflections on Glycobiology. *Journal of Biological Chemistry.* 2001;**276**. doi:10.1074/jbc.R100053200
- 87 Poole CA. Articular cartilage chondrons: Form, function and failure. *J Anat.* 1997;**191**. doi:10.1017/S0021878297002185
- 88 Wilusz RE, Sanchez-Adams J, Guilak F. The structure and function of the pericellular matrix of articular cartilage. *Matrix Biology.* 2014;**39**. doi:10.1016/j.matbio.2014.08.009
- 89 Vincent TL, McClurg O, Troeberg L. The Extracellular Matrix of Articular Cartilage Controls the Bioavailability of Pericellular Matrix-Bound Growth Factors to Drive Tissue Homeostasis and Repair. *Int J Mol Sci* 2022;**23**:6003. doi:10.3390/ijms23116003
- 90 Y. Z, Garciadiego-Czares D, Parra- Cid C, *et al.* Cartilage Tissue Engineering: The Role of Extracellular Matrix (ECM) and Novel Strategies. In: *Regenerative Medicine and Tissue Engineering*. 2013. doi:10.5772/55917
- 91 Zhou H, Yuan L, Xu Z, *et al.* Mimicking the Composition and Structure of the Osteochondral Tissue to Fabricate a Heterogeneous Three-Layer Scaffold for the Repair of Osteochondral Defects. *ACS Appl Bio Mater* 2022;**5**. doi:10.1021/acsabm.1c01152
- 92 Khanarian NT, Boushell MK, Spalazzi JP, *et al.* FTIR-I compositional mapping of the cartilage-to-bone interface as a function of tissue region and age. *Journal of Bone and Mineral Research* 2014;**29**. doi:10.1002/jbmr.2284
- 93 Pouran B, Raoof A, de Winter DAM, *et al.* Topographic features of nano-pores within the osteochondral interface and their effects on transport properties –a 3D imaging and modeling study. *J Biomech* 2021;**123**. doi:10.1016/j.jbiomech.2021.110504
- 94 Tang T, Landis W, Raguin E, *et al.* A 3D Network of Nanochannels for Possible Ion and Molecule Transit in Mineralizing Bone and Cartilage. *Adv Nanobiomed Res* 2022;**2**:2100162. doi:10.1002/anbr.202100162
- 95 Hoemann C, Lafantaisie-Favreau C-H, Lascau-Coman V, *et al.* The Cartilage-Bone Interface. *Journal of Knee Surgery* 2012;**25**:085–98. doi:10.1055/s-0032-1319782
- 96 Madry H, van Dijk CN, Mueller-Gerbl M. The basic science of the subchondral bone. *Knee Surgery, Sports Traumatology, Arthroscopy* 2010;**18**. doi:10.1007/s00167-010-1054-z

## VIII. BIBLIOGRAPHY

- 97 Sanchez C, Pesesse L, Gabay O, *et al.* Regulation of subchondral bone osteoblast metabolism by cyclic compression. *Arthritis Rheum* 2012;**64**. doi:10.1002/art.33445
- 98 Chen Y, Hu Y, Yu YE, *et al.* Subchondral Trabecular Rod Loss and Plate Thickening in the Development of Osteoarthritis. *Journal of Bone and Mineral Research* 2018;**33**. doi:10.1002/jbmr.3313
- 99 Scanzello CR. Synovial Structure and Physiology in Health and Disease. In: *Synovial Fluid Analysis and The Evaluation of Patients With Arthritis*. Cham: : Springer International Publishing 2022. 5–19. doi:10.1007/978-3-030-99612-3\_2
- 100 D. Smith M. The Normal Synovium. *Open Rheumatol J* 2012;**5**. doi:10.2174/1874312901105010100
- 101 Long H, Liu Q, Yin H, *et al.* Prevalence Trends of Site-Specific Osteoarthritis From 1990 to 2019: Findings From the Global Burden of Disease Study 2019. *Arthritis and Rheumatology* Published Online First: 2022. doi:10.1002/art.42089
- 102 Loeser RF, Goldring SR, Scanzello CR, *et al.* Osteoarthritis: A disease of the joint as an organ. *Arthritis Rheum.* 2012;**64**. doi:10.1002/art.34453
- 103 Dell’Isola A, Allan R, Smith SL, *et al.* Identification of clinical phenotypes in knee osteoarthritis: a systematic review of the literature. *BMC Musculoskelet Disord* 2016;**17**. doi:10.1186/s12891-016-1286-2
- 104 Mobasheri A, van Spil WE, Budd E, *et al.* Molecular taxonomy of osteoarthritis for patient stratification, disease management and drug development: Biochemical markers associated with emerging clinical phenotypes and molecular endotypes. *Curr Opin Rheumatol.* 2019;**31**. doi:10.1097/BOR.0000000000000567
- 105 Arden N, Nevitt MC. Osteoarthritis: Epidemiology. *Best Pract Res Clin Rheumatol.* 2006;**20**. doi:10.1016/j.berh.2005.09.007
- 106 Henrotin Y. Osteoarthritis in year 2021: biochemical markers. *Osteoarthritis Cartilage.* 2022;**30**. doi:10.1016/j.joca.2021.11.001
- 107 Mobasheri A, Saarakkala S, Finnilä M, *et al.* Recent advances in understanding the phenotypes of osteoarthritis. *F1000Res.* 2019;**8**. doi:10.12688/f1000research.20575.1
- 108 Deveza LA, Melo L, Yamato TP, *et al.* Knee osteoarthritis phenotypes and their relevance for outcomes: a systematic review. *Osteoarthritis Cartilage.* 2017;**25**. doi:10.1016/j.joca.2017.08.009
- 109 Angelini F, Widera P, Mobasheri A, *et al.* Osteoarthritis endotype discovery via clustering of biochemical marker data. *Ann Rheum Dis* 2022;**81**. doi:10.1136/annrheumdis-2021-221763
- 110 van Helvoort EM, van Spil WE, Jansen MP, *et al.* Cohort profile: The Applied Public-Private Research enabling OsteoArthritis Clinical Headway (IMI-APPROACH) study: a 2-year, European, cohort study to describe, validate and predict phenotypes of osteoarthritis using clinical, imaging and biochemical markers. *BMJ Open* 2020;**10**. doi:10.1136/bmjopen-2019-035101
- 111 Yuan C, Pan Z, Zhao K, *et al.* Classification of four distinct osteoarthritis subtypes with a knee joint tissue transcriptome atlas. *Bone Res* 2020;**8**. doi:10.1038/s41413-020-00109-x

- 112 Steinberg J, Southam L, Fontalis A, *et al.* Linking chondrocyte and synovial transcriptional profile to clinical phenotype in osteoarthritis. *Ann Rheum Dis* 2021;**80**. doi:10.1136/annrheumdis-2020-219760
- 113 Coutinho De Almeida R, Mahfouz A, Mei H, *et al.* Identification and characterization of two consistent osteoarthritis subtypes by transcriptome and clinical data integration. *Rheumatology (United Kingdom)* 2021;**60**. doi:10.1093/rheumatology/keaa391
- 114 Glyn-Jones S, Palmer AJR, Agricola R, *et al.* Osteoarthritis. *The Lancet* 2015;**386**:376–87. doi:10.1016/S0140-6736(14)60802-3
- 115 Peters AE, Akhtar R, Comerford EJ, *et al.* The effect of ageing and osteoarthritis on the mechanical properties of cartilage and bone in the human knee joint. *Sci Rep* 2018;**8**. doi:10.1038/s41598-018-24258-6
- 116 Pritzker KPH, Gay S, Jimenez SA, *et al.* Osteoarthritis cartilage histopathology: Grading and staging. *Osteoarthritis Cartilage* 2006;**14**. doi:10.1016/j.joca.2005.07.014
- 117 Pearson RG, Kurien T, Shu KSS, *et al.* Histopathology grading systems for characterisation of human knee osteoarthritis - reproducibility, variability, reliability, correlation, and validity. *Osteoarthritis Cartilage* 2011;**19**. doi:10.1016/j.joca.2010.12.005
- 118 Custers RJH, Creemers LB, Verbout AJ, *et al.* Reliability, reproducibility and variability of the traditional Histologic/Histochemical Grading System vs the new OARSI Osteoarthritis Cartilage Histopathology Assessment System. *Osteoarthritis Cartilage* 2007;**15**. doi:10.1016/j.joca.2007.04.017
- 119 Pauli C, Whiteside R, Heras FL, *et al.* Comparison of cartilage histopathology assessment systems on human knee joints at all stages of osteoarthritis development. *Osteoarthritis Cartilage* 2012;**20**. doi:10.1016/j.joca.2011.12.018
- 120 Waldstein W, Perino G, Gilbert SL, *et al.* OARSI osteoarthritis cartilage histopathology assessment system: A biomechanical evaluation in the human knee. *Journal of Orthopaedic Research* 2016;**34**. doi:10.1002/jor.23010
- 121 Pesesse L, Sanchez C, Delcour JP, *et al.* Consequences of chondrocyte hypertrophy on osteoarthritic cartilage: Potential effect on angiogenesis. *Osteoarthritis Cartilage* 2013;**21**. doi:10.1016/j.joca.2013.08.018
- 122 Lu J, Zhang H, Cai D, *et al.* Positive-Feedback Regulation of Subchondral H-Type Vessel Formation by Chondrocyte Promotes Osteoarthritis Development in Mice. *Journal of Bone and Mineral Research* 2018;**33**. doi:10.1002/jbmr.3388
- 123 Bonde H v., Talman MLM, Kofoed H. The area of the tidemark in osteoarthritis - A three-dimensional stereological study in 21 patients. *APMIS* 2005;**113**. doi:10.1111/j.1600-0463.2005.apm\_113506.x
- 124 Suri S, Gill SE, de Camin SM, *et al.* Neurovascular invasion at the osteochondral junction and in osteophytes in osteoarthritis. *Ann Rheum Dis* 2007;**66**. doi:10.1136/ard.2006.063354
- 125 Tchetina E v., Squires G, Poole AR. Increased type II collagen degradation and very early focal cartilage degeneration is associated with upregulation of chondrocyte differentiation related genes in early human articular cartilage lesions. *Journal of Rheumatology* 2005;**32**.



- 126 Stöve J, Huch K, Günther KP, *et al.* Interleukin-1 $\beta$  induces different gene expression of stromelysin, aggrecan and tumor-necrosis-factor-stimulated gene 6 in human osteoarthritic chondrocytes in vitro. *Pathobiology* 2000;**68**. doi:10.1159/000055915
- 127 Neidel J, Zeidler U. Independent effects of interleukin 1 on proteoglycan synthesis and proteoglycan breakdown of bovine articular cartilage in vitro. *Agents Actions* 1993;**39**. doi:10.1007/BF01975718
- 128 Lefebvre V, Peeters-Joris C, Vaes G. Modulation by interleukin 1 and tumor necrosis factor  $\alpha$  of production of collagenase, tissue inhibitor of metalloproteinases and collagen types in differentiated and dedifferentiated articular chondrocytes. *BBA - Molecular Cell Research* 1990;**1052**. doi:10.1016/0167-4889(90)90145-4
- 129 Chadjichristos C, Ghayor C, Kypriotou M, *et al.* Sp1 and Sp3 transcription factors mediate interleukin-1 $\beta$  down-regulation of human type II collagen gene expression in articular chondrocytes. *Journal of Biological Chemistry* 2003;**278**. doi:10.1074/jbc.M303541200
- 130 Vinatier C, Domínguez E, Guicheux J, *et al.* Role of the inflammation-autophagy-senescence integrative network in Osteoarthritis. *Front Physiol.* 2018;**9**. doi:10.3389/fphys.2018.00706
- 131 McCulloch K, Litherland GJ, Rai TS. Cellular senescence in osteoarthritis pathology. *Aging Cell.* 2017;**16**. doi:10.1111/acel.12562
- 132 Lambert C, Zappia J, Sanchez C, *et al.* The Damage-Associated Molecular Patterns (DAMPs) as Potential Targets to Treat Osteoarthritis: Perspectives From a Review of the Literature. *Front Med (Lausanne)* 2021;**7**. doi:10.3389/fmed.2020.607186
- 133 Liu B, Zhang M, Zhao J, *et al.* Imbalance of M1/M2 macrophages is linked to severity level of knee osteoarthritis. *Exp Ther Med* 2018;**16**. doi:10.3892/etm.2018.6852
- 134 Chen Y, Jiang W, Yong H, *et al.* Macrophages in osteoarthritis: Pathophysiology and therapeutics. *Am J Transl Res* 2020;**12**.
- 135 Kalchishkova N, Fürst CM, Heinega D, *et al.* NC4 domain of cartilage-specific collagen IX inhibits complement directly due to attenuation of membrane attack formation and indirectly through binding and enhancing activity of complement inhibitors C4B-binding protein and factor H. *Journal of Biological Chemistry* 2011;**286**. doi:10.1074/jbc.M111.242834
- 136 Klatt AR, Paul-Klausch B, Klinger C, *et al.* A critical role for collagen II in cartilage matrix degradation: Collagen II induces pro-inflammatory cytokines and MMPS in primary human chondrocytes. *Journal of Orthopaedic Research* 2009;**27**. doi:10.1002/jor.20716
- 137 Avenoso A, Bruschetta G, D'Ascola A, *et al.* Hyaluronan Fragmentation During Inflammatory Pathologies: A Signal that Empowers Tissue Damage. *Mini-Reviews in Medicinal Chemistry* 2019;**20**. doi:10.2174/1389557519666190906115619
- 138 Schaefer L, Babelova A, Kiss E, *et al.* The matrix component biglycan is proinflammatory and signals through Toll-like receptors 4 and 2 in macrophages. *Journal of Clinical Investigation* 2005;**115**. doi:10.1172/JCI23755
- 139 Sjöberg AP, Manderson GA, Mörgelin M, *et al.* Short leucine-rich glycoproteins of the extracellular matrix display diverse patterns of complement interaction and activation. *Mol Immunol* 2009;**46**. doi:10.1016/j.molimm.2008.09.018

## VIII. BIBLIOGRAPHY

- 140 Iqbal SM, Leonard C, Regmi SC, *et al.* Lubricin/Proteoglycan 4 binds to and regulates the activity of Toll-Like Receptors in Vitro. *Sci Rep* 2016;**6**. doi:10.1038/srep18910
- 141 Su SL, Tsai CD, Lee CH, *et al.* Expression and regulation of Toll-like receptor 2 by IL-1 $\beta$  and fibronectin fragments in human articular chondrocytes. *Osteoarthritis Cartilage* 2005;**13**. doi:10.1016/j.joca.2005.04.017
- 142 Hwang HS, Park SJ, Cheon EJ, *et al.* Fibronectin fragment-induced expression of matrix metalloproteinases is mediated by MyD88-dependent TLR-2 signaling pathway in human chondrocytes. *Arthritis Res Ther* 2015;**17**. doi:10.1186/s13075-015-0833-9
- 143 Homandberg GA, Hui F. Association of proteoglycan degradation with catabolic cytokine and stromelysin release from cartilage cultured with fibronectin fragments. *Arch Biochem Biophys* 1996;**334**. doi:10.1006/abbi.1996.0461
- 144 Millerand M, Berenbaum F, Jacques C. Danger signals and inflammaging in osteoarthritis. *Clin Exp Rheumatol*. 2019;**37**.
- 145 Pfander D, Swoboda B, Kirsch T. Expression of early and late differentiation markers (proliferating cell nuclear antigen, syndecan-3, annexin VI, and alkaline phosphatase) by human osteoarthritic chondrocytes. *American Journal of Pathology* 2001;**159**. doi:10.1016/S0002-9440(10)63024-6
- 146 Fuerst M, Bertrand J, Lammers L, *et al.* Calcification of articular cartilage in human osteoarthritis. *Arthritis Rheum* 2009;**60**. doi:10.1002/art.24774
- 147 Kühn K, D’Lima DD, Hashimoto S, *et al.* Cell death in cartilage. *Osteoarthritis Cartilage*. 2004;**12**. doi:10.1016/j.joca.2003.09.015
- 148 Guilak F, Nims RJ, Dicks A, *et al.* Osteoarthritis as a disease of the cartilage pericellular matrix. *Matrix Biology*. 2018;**71–72**. doi:10.1016/j.matbio.2018.05.008
- 149 Ma B, van Blitterswijk CA, Karperien M. A Wnt/ $\beta$ -catenin negative feedback loop inhibits interleukin-1-induced matrix metalloproteinase expression in human articular chondrocytes. *Arthritis Rheum* 2012;**64**. doi:10.1002/art.34425
- 150 Yang Y, Topol L, Lee H, *et al.* Wnt5a and Wnt5b exhibit distinct activities in coordinating chondrocyte proliferation and differentiation. *Development*. 2003;**130**. doi:10.1242/dev.00324
- 151 Huang G, Chubinskaya S, Liao W, *et al.* Wnt5a induces catabolic signaling and matrix metalloproteinase production in human articular chondrocytes. *Osteoarthritis Cartilage* 2017;**25**. doi:10.1016/j.joca.2017.05.018
- 152 Ge X, Shi R, Ma X. The secreted protein WNT5A regulates condylar chondrocyte proliferation, hypertrophy and migration. *Arch Oral Biol* 2017;**82**. doi:10.1016/j.archoralbio.2017.06.019
- 153 Wang X, Cornelis FMF, Lories RJ, *et al.* Exostosin-1 enhances canonical Wnt signaling activity during chondrogenic differentiation. *Osteoarthritis Cartilage* 2019;**27**. doi:10.1016/j.joca.2019.07.007
- 154 Cherifi C, Monteagudo S, Lories RJ. Promising targets for therapy of osteoarthritis: a review on the Wnt and TGF- $\beta$  signalling pathways. *Ther Adv Musculoskelet Dis*. 2021;**13**. doi:10.1177/1759720X211006959

## VIII. BIBLIOGRAPHY

- 155 Du X, Cai L, Xie J, *et al.* The role of TGF-beta3 in cartilage development and osteoarthritis. *Bone Res* 2023;**11**:2. doi:10.1038/s41413-022-00239-4
- 156 Marcacci M, Andriolo L, Kon E, *et al.* Aetiology and pathogenesis of bone marrow lesions and osteonecrosis of the knee. *EFORT Open Rev* 2016;**1**. doi:10.1302/2058-5241.1.000044
- 157 Gobbi A, Dallo I, Frank RM, *et al.* A review of bone marrow lesions in the arthritic knee and description of a technique for treatment. *Journal of Cartilage and Joint Preservation*. 2021;**1**. doi:10.1016/j.jcjp.2021.100021
- 158 Guerhazi A, Niu J, Hayashi D, *et al.* Prevalence of abnormalities in knees detected by MRI in adults without knee osteoarthritis: Population based observational study (Framingham Osteoarthritis Study). *BMJ (Online)* 2012;**345**. doi:10.1136/bmj.e5339
- 159 Bowes MA, McLure SWD, Wolstenholme CBH, *et al.* Osteoarthritic bone marrow lesions almost exclusively collocate with denuded cartilage: A 3D study using data from the Osteoarthritis Initiative. *Ann Rheum Dis* 2016;**75**. doi:10.1136/annrheumdis-2015-208407
- 160 Muratovic D, Findlay DM, Cicuttini FM, *et al.* Bone marrow lesions in knee osteoarthritis: regional differences in tibial subchondral bone microstructure and their association with cartilage degeneration. *Osteoarthritis Cartilage* 2019;**27**. doi:10.1016/j.joca.2019.07.004
- 161 Lowitz T, Museyko O, Bousson V, *et al.* Bone marrow lesions identified by MRI in knee osteoarthritis are associated with locally increased bone mineral density measured by QCT. *Osteoarthritis Cartilage* 2013;**21**. doi:10.1016/j.joca.2013.04.006
- 162 Cohen-Solal M, Funck-Brentano T, Hay E. Animal models of osteoarthritis for the understanding of the bone contribution. *Bonekey Rep* 2013;**2**. doi:10.1038/bonekey.2013.156
- 163 Hu W, Chen Y, Dou C, *et al.* Microenvironment in subchondral bone: Predominant regulator for the treatment of osteoarthritis. *Ann Rheum Dis*. 2021;**80**. doi:10.1136/annrheumdis-2020-218089
- 164 Zamli Z, Robson Brown K, Tarlton JF, *et al.* Subchondral bone plate thickening precedes chondrocyte apoptosis and cartilage degradation in spontaneous animal models of osteoarthritis. *Biomed Res Int* 2014;**2014**. doi:10.1155/2014/606870
- 165 Shiraishi K, Chiba K, Okazaki N, *et al.* In vivo analysis of subchondral trabecular bone in patients with osteoarthritis of the knee using second-generation high-resolution peripheral quantitative computed tomography (HR-pQCT). *Bone* 2020;**132**. doi:10.1016/j.bone.2019.115155
- 166 Sanchez C, Deberg MA, Piccardi N, *et al.* Subchondral bone osteoblasts induce phenotypic changes in human osteoarthritic chondrocytes. *Osteoarthritis Cartilage* 2005;**13**. doi:10.1016/j.joca.2005.07.012
- 167 Zhen G, Wen C, Jia X, *et al.* Inhibition of TGF- $\beta$  signaling in mesenchymal stem cells of subchondral bone attenuates osteoarthritis. *Nat Med* 2013;**19**. doi:10.1038/nm.3143
- 168 Dai G, Xiao H, Liao J, *et al.* Osteocyte TGF $\beta$ 1-Smad2/3 is positively associated with bone turnover parameters in subchondral bone of advanced osteoarthritis. *Int J Mol Med* 2020;**46**. doi:10.3892/ijmm.2020.4576

## VIII. BIBLIOGRAPHY

- 169 Kennedy OD, Laudier DM, Majeska RJ, *et al.* Osteocyte apoptosis is required for production of osteoclastogenic signals following bone fatigue in vivo. *Bone* 2014;**64**. doi:10.1016/j.bone.2014.03.049
- 170 Li J, Xue J, Jing Y, *et al.* SOST Deficiency Aggravates Osteoarthritis in Mice by Promoting Sclerosis of Subchondral Bone. *Biomed Res Int* 2019;**2019**. doi:10.1155/2019/7623562
- 171 Zhou Y, Wang T, Hamilton JL, *et al.* Wnt/ $\beta$ -catenin Signaling in Osteoarthritis and in Other Forms of Arthritis. *Curr Rheumatol Rep.* 2017;**19**. doi:10.1007/s11926-017-0679-z
- 172 Mazur CM, Woo JJ, Yee CS, *et al.* Osteocyte dysfunction promotes osteoarthritis through MMP13-dependent suppression of subchondral bone homeostasis. *Bone Res* 2019;**7**. doi:10.1038/s41413-019-0070-y
- 173 Chu L, Liu X, He Z, *et al.* Articular Cartilage Degradation and Aberrant Subchondral Bone Remodeling in Patients with Osteoarthritis and Osteoporosis. *Journal of Bone and Mineral Research* 2020;**35**. doi:10.1002/jbmr.3909
- 174 Peng Y, Wu S, Li Y, *et al.* Type H blood vessels in bone modeling and remodeling. *Theranostics.* 2020;**10**. doi:10.7150/thno.34126
- 175 Cui Z, Crane J, Xie H, *et al.* Halofuginone attenuates osteoarthritis by inhibition of TGF- $\beta$  activity and H-type vessel formation in subchondral bone. *Ann Rheum Dis* 2016;**75**. doi:10.1136/annrheumdis-2015-207923
- 176 Zhang H, Wang H, Zeng C, *et al.* mTORC1 activation downregulates FGFR3 and PTH/PTHrP receptor in articular chondrocytes to initiate osteoarthritis. *Osteoarthritis Cartilage* 2017;**25**. doi:10.1016/j.joca.2016.12.024
- 177 Zhang Y, Vasheghani F, Li YH, *et al.* Cartilage-specific deletion of mTOR upregulates autophagy and protects mice from osteoarthritis. *Ann Rheum Dis* 2015;**74**. doi:10.1136/annrheumdis-2013-204599
- 178 Lin C, Liu L, Zeng C, *et al.* Activation of mTORC1 in subchondral bone preosteoblasts promotes osteoarthritis by stimulating bone sclerosis and secretion of CXCL12. *Bone Res* 2019;**7**. doi:10.1038/s41413-018-0041-8
- 179 Ni GX, Li Z, Zhou YZ. The role of small leucine-rich proteoglycans in osteoarthritis pathogenesis. *Osteoarthritis Cartilage.* 2014;**22**. doi:10.1016/j.joca.2014.04.026
- 180 Mochida Y, Kaku M, Yoshida K, *et al.* Podocan-like protein: A novel small leucine-rich repeat matrix protein in bone. *Biochem Biophys Res Commun* 2011;**410**:333–8. doi:10.1016/j.bbrc.2011.05.150
- 181 Yano K, Washio K, Tsumanuma Y, *et al.* The role of Tsukushi (TSK), a small leucine-rich repeat proteoglycan, in bone growth. *Regen Ther* 2017;**7**. doi:10.1016/j.reth.2017.08.001
- 182 Madisen L, Neubauer M, Plowman G, *et al.* Molecular Cloning of a Novel Bone-Forming Compound: Osteoinductive Factor. *DNA Cell Biol* Published Online First: 1990. doi:10.1089/dna.1990.9.303
- 183 Lee NJ, Ali N, Zhang L, *et al.* Osteoglycin, a novel coordinator of bone and glucose homeostasis. *Mol Metab* 2018;**13**. doi:10.1016/j.molmet.2018.05.004

## VIII. BIBLIOGRAPHY

- 184 Melrose J, Fuller ES, Roughley PJ, *et al.* Fragmentation of decorin, biglycan, lumican and keratocan is elevated in degenerate human meniscus, knee and hip articular cartilages compared with age-matched macroscopically normal and control tissues. *Arthritis Res Ther* Published Online First: 2008. doi:10.1186/ar2453
- 185 Young AA, Smith MM, Smith SM, *et al.* Regional assessment of articular cartilage gene expression and small proteoglycan metabolism in an animal model of osteoarthritis. *Arthritis Res Ther* Published Online First: 2005. doi:10.1186/ar1756
- 186 Bock HC, Michaeli P, Bode C, *et al.* The small proteoglycans decorin and biglycan in human articular cartilage of late-stage osteoarthritis. *Osteoarthritis Cartilage* Published Online First: 2001. doi:10.1053/joca.2001.0420
- 187 Sanchez C, Mazzucchelli G, Lambert C, *et al.* Comparison of secretome from osteoblasts derived from sclerotic versus non-sclerotic subchondral bone in OA: A pilot study. Published Online First: 2018. doi:10.1371/journal.pone.0194591
- 188 Tanaka N, Tashiro T, Katsuragawa Y, *et al.* Expression of minor cartilage collagens and small leucine rich proteoglycans may be relatively reduced in osteoarthritic cartilage. *BMC Musculoskelet Disord* 2019;**20**. doi:10.1186/s12891-019-2596-y
- 189 Aigner T, Fundel K, Saas J, *et al.* Large-scale gene expression profiling reveals major pathogenetic pathways of cartilage degeneration in osteoarthritis. *Arthritis Rheum* 2006;**54**. doi:10.1002/art.22174
- 190 Tío L, Martel-Pelletier J, Pelletier JP, *et al.* Characterization of opticin digestion by proteases involved in osteoarthritis development. *Joint Bone Spine* Published Online First: 2014. doi:10.1016/j.jbspin.2013.05.007
- 191 Barreto G, Senturk B, Colombo L, *et al.* Lumican is upregulated in osteoarthritis and contributes to TLR4-induced pro-inflammatory activation of cartilage degradation and macrophage polarization. *Osteoarthritis Cartilage* 2020;**28**. doi:10.1016/j.joca.2019.10.011
- 192 Hildebrand A, Romaris M, Rasmussen M, *et al.* Interaction of the small interstitial proteoglycans biglycan, decorin and fibromodulin with transforming growth factor  $\beta$ . *Biochemical Journal* Published Online First: 1994. doi:10.1042/bj3020527
- 193 Ohta K, Lupo G, Kuriyama S, *et al.* Tsukushi functions as an organizer inducer by inhibition of BMP activity in cooperation with chordin. *Dev Cell* 2004;**7**. doi:10.1016/j.devcel.2004.08.014
- 194 Morris SA, Almeida AD, Tanaka H, *et al.* Tsukushi modulates Xnr2, FGF and BMP signaling: Regulation of *Xenopus* germ layer formation. *PLoS One* 2007;**2**. doi:10.1371/journal.pone.0001004
- 195 Lin W, Zhu X, Gao L, *et al.* Osteomodulin positively regulates osteogenesis through interaction with BMP2. *Cell Death Dis* 2021;**12**. doi:10.1038/s41419-021-03404-5
- 196 Yamaguchi Y, Mann DM, Ruoslahti E. Negative regulation of transforming growth factor- $\beta$  by the proteoglycan decorin. *Nature* 1990;**346**. doi:10.1038/346281a0
- 197 Mochida Y, Parisuthiman D, Yamauchi M. Biglycan is a positive modulator of BMP-2 induced osteoblast differentiation. In: *Advances in Experimental Medicine and Biology*. 2006. doi:10.1007/978-0-387-34133-0\_7

## VIII. BIBLIOGRAPHY

- 198 Takeuchi Y, Kodama Y, Matsumoto T. Bone matrix decorin binds transforming growth factor- $\beta$  and enhances its bioactivity. *Journal of Biological Chemistry* 1994;**269**. doi:10.1016/s0021-9258(18)31681-8
- 199 Kresse H, Schnherr E. Proteoglycans of the extracellular matrix and growth control. *J Cell Physiol.* 2001;**189**. doi:10.1002/jcp.10030
- 200 Ameye L, Aria D, Jepsen K, *et al.* Abnormal collagen fibrils in tendons of biglycan/fibromodulin-deficient mice lead to gait impairment, ectopic ossification, and osteoarthritis. *The FASEB Journal* 2002;**16**. doi:10.1096/fj.01-0848com
- 201 Nuka S, Zhou W, Henry SP, *et al.* Phenotypic characterization of epiphycan-deficient and epiphycan/biglycan double-deficient mice. *Osteoarthritis Cartilage* 2010;**18**. doi:10.1016/j.joca.2009.11.006
- 202 Xu T, Bianco P, Fisher LW, *et al.* Targeted disruption of the biglycan gene leads to an osteoporosis-like phenotype in mice. *Nat Genet* 1998;**20**. doi:10.1038/1746
- 203 Corsi A, Xu T, Chen XD, *et al.* Phenotypic effects of biglycan deficiency are linked to collagen fibril abnormalities, are synergized by decorin deficiency, and mimic Ehlers-Danlos-like changes in bone and other connective tissues. *Journal of Bone and Mineral Research* 2002;**17**. doi:10.1359/jbmr.2002.17.7.1180
- 204 Kilts T, Ameye L, Syed-Picard F, *et al.* Potential roles for the small leucine-rich proteoglycans biglycan and fibromodulin in ectopic ossification of tendon induced by exercise and in modulating rotarod performance. *Scand J Med Sci Sports* 2009;**19**. doi:10.1111/j.1600-0838.2009.00909.x
- 205 Furukawa T, Ito K, Nuka S, *et al.* Absence of biglycan accelerates the degenerative process in mouse intervertebral disc. *Spine (Phila Pa 1976)* 2009;**34**. doi:10.1097/BRS.0b013e3181b7c7ec
- 206 Han B, Li Q, Wang C, *et al.* Differentiated activities of decorin and biglycan in the progression of post-traumatic osteoarthritis. *Osteoarthritis Cartilage* 2021;**29**. doi:10.1016/j.joca.2021.03.019
- 207 Gill MR, Oldberg Å, Reinholt FP. Fibromodulin-null murine knee joints display increased incidences of osteoarthritis and alterations in tissue biochemistry. *Osteoarthritis Cartilage* 2002;**10**. doi:10.1053/joca.2002.0527
- 208 Jepsen KJ, Wu F, Peragallo JH, *et al.* A syndrome of joint laxity and impaired tendon integrity in lumican- and fibromodulin-deficient mice. *Journal of Biological Chemistry* 2002;**277**. doi:10.1074/jbc.M205398200
- 209 Li Q, Han B, Wang C, *et al.* Mediation of Cartilage Matrix Degeneration and Fibrillation by Decorin in Post-traumatic Osteoarthritis. *Arthritis & Rheumatology* 2020;**72**:1266–77. doi:10.1002/art.41254
- 210 Boote C, Ma Q, Goh KL. Age-dependent mechanical properties of tail tendons in wild-type and mimecan gene-knockout mice – A preliminary study. *J Mech Behav Biomed Mater* 2023;**139**:105672. doi:10.1016/j.jmbbm.2023.105672
- 211 Farrán A, Valverde-Franco G, Tío L, *et al.* In vivo effect of opticin deficiency in cartilage in a surgically induced mouse model of osteoarthritis. *Sci Rep* 2018;**8**. doi:10.1038/s41598-017-18047-w

## VIII. BIBLIOGRAPHY

- 212 Hesse L, Stordalen GA, Wenglén C, *et al.* The Skeletal Phenotype of Chondroadherin Deficient Mice. *PLoS One* 2013;**8**. doi:10.1371/journal.pone.0063080
- 213 Batista MA, Nia HT, Önerfjord P, *et al.* Nanomechanical phenotype of chondroadherin-null murine articular cartilage. *Matrix Biology* 2014;**38**. doi:10.1016/j.matbio.2014.05.008
- 214 Wadhwa S, Embree M, Ameye L, *et al.* Mice deficient in biglycan and fibromodulin as a model for temporomandibular joint osteoarthritis. In: *Cells Tissues Organs*. 2006. doi:10.1159/000091375
- 215 Wadhwa S, Embree MC, Kilts T, *et al.* Accelerated osteoarthritis in the temporomandibular joint of biglycan/ fibromodulin double-deficient mice. *Osteoarthritis Cartilage* 2005;**13**. doi:10.1016/j.joca.2005.04.016
- 216 Embree M, Ono M, Kilts T, *et al.* Role of subchondral bone during early-stage experimental TMJ osteoarthritis. *J Dent Res* 2011;**90**. doi:10.1177/0022034511421930
- 217 Chen J, Gupta T, Barasz JA, *et al.* Analysis of microarchitectural changes in a mouse temporomandibular joint osteoarthritis model. *Arch Oral Biol* 2009;**54**. doi:10.1016/j.archoralbio.2009.10.001
- 218 Embree MC, Kilts TM, Ono M, *et al.* Biglycan and fibromodulin have essential roles in regulating chondrogenesis and extracellular matrix turnover in temporomandibular joint osteoarthritis. *American Journal of Pathology* Published Online First: 2010. doi:10.2353/ajpath.2010.090450
- 219 Kram V, Kilts TM, Bhattacharyya N, *et al.* Small leucine rich proteoglycans, a novel link to osteoclastogenesis. *Sci Rep* Published Online First: 2017. doi:10.1038/s41598-017-12651-6
- 220 Lee JY, Park SJ, Kim DA, *et al.* Muscle-Derived Lumican Stimulates Bone Formation via Integrin  $\alpha 2\beta 1$  and the Downstream ERK Signal. *Front Cell Dev Biol* 2020;**8**. doi:10.3389/fcell.2020.565826
- 221 Lee JY, Kim DA, Kim EY, *et al.* Lumican Inhibits Osteoclastogenesis and Bone Resorption by Suppressing Akt Activity. *Int J Mol Sci* 2021;**22**. doi:10.3390/ijms22094717
- 222 Wendel M, Sommarin Y, Heinegård D. Bone matrix proteins: Isolation and characterization of a novel cell-binding keratan sulfate proteoglycan (osteadherin) from bovine bone. *Journal of Cell Biology* 1998;**141**:839–47. doi:10.1083/jcb.141.3.839
- 223 Sommarin Y, Wendel M, Shen Z, *et al.* Osteoadherin, a cell-binding keratan sulfate proteoglycan in bone, belongs to the family of leucine-rich repeat proteins of the extracellular matrix. *Journal of Biological Chemistry* Published Online First: 1998. doi:10.1074/jbc.273.27.16723
- 224 Wendel M, Sommarin Y, Heinegård D. Characterization of osteoadherin - A novel, cell binding keratan sulfate proteoglycan from bone. *Acta Orthop*. 1995. doi:10.3109/17453679509157655
- 225 Couble ML, Bleicher F, Farges JC, *et al.* Immunodetection of osteoadherin in murine tooth extracellular matrices. *Histochem Cell Biol* 2004;**121**. doi:10.1007/s00418-003-0608-2
- 226 R.V. S, M.-L. O, S. M, *et al.* The glycosylation profile of osteoadherin alters during endochondral bone formation. *Bone* 2013.
- 227 Nikdin H, Olsson ML, Hulténby K, *et al.* Osteoadherin accumulates in the predentin towards the mineralization front in the developing tooth. *PLoS One* 2012;**7**. doi:10.1371/journal.pone.0031525

## VIII. BIBLIOGRAPHY

- 228 Juchtmans N, Dhollander AAM, Coudenys J, *et al.* Brief report: Distinct dysregulation of the small leucine-rich repeat protein family in osteoarthritic acetabular labrum compared to articular cartilage. *Arthritis and Rheumatology* 2015;**67**:435–41. doi:10.1002/art.38930
- 229 Zhang W, Zhang S, Yan P, *et al.* A single-cell transcriptomic landscape of primate arterial aging. *Nat Commun* 2020;**11**. doi:10.1038/s41467-020-15997-0
- 230 Papadaki V, Asada K, Watson JK, *et al.* Two secreted proteoglycans, activators of urothelial cell–cell adhesion, negatively contribute to bladder cancer initiation and progression. *Cancers (Basel)* 2020;**12**. doi:10.3390/cancers12113362
- 231 Yoon SH, Bae YS, Oh SP, *et al.* Altered hippocampal gene expression, glial cell population, and neuronal excitability in aminopeptidase P1 deficiency. *Sci Rep* 2021;**11**. doi:10.1038/s41598-020-79656-6
- 232 Belluoccio D, Etich J, Rosenbaum S, *et al.* Sorting of growth plate chondrocytes allows the isolation and characterization of cells of a defined differentiation status. *Journal of Bone and Mineral Research* 2010;**25**. doi:10.1002/jbmr.30
- 233 Gonçalves I, Oduor L, Matthes F, *et al.* Osteomodulin Gene Expression Is Associated with Plaque Calcification, Stability, and Fewer Cardiovascular Events in the CPIP Cohort. *Stroke* 2022;**29**. doi:10.1161/STROKEAHA.121.037223
- 234 Skenteris NT, Seime T, Witasp A, *et al.* Osteomodulin is a novel gene in cardiovascular calcification. *Atherosclerosis* 2021;**331**. doi:10.1016/j.atherosclerosis.2021.06.271
- 235 Skenteris NT, Seime T, Witasp A, *et al.* Osteomodulin attenuates smooth muscle cell osteogenic transition in vascular calcification. *Clin Transl Med* 2022;**12**. doi:10.1002/ctm2.682
- 236 Hamaya E, Fujisawa T, Tamura M. Osteoadherin serves roles in the regulation of apoptosis and growth in MC3T3-E1 osteoblast cells. *Int J Mol Med* 2019;**44**. doi:10.3892/ijmm.2019.4376
- 237 Lin W, Gao L, Jiang W, *et al.* The role of osteomodulin on osteo/odontogenic differentiation in human dental pulp stem cells. *BMC Oral Health* 2019;**19**. doi:10.1186/s12903-018-0680-6
- 238 Noack C, Hempel U, Preissler C, *et al.* Prostaglandin E2 impairs osteogenic and facilitates adipogenic differentiation of human bone marrow stromal cells. *Prostaglandins Leukot Essent Fatty Acids* 2015;**94**. doi:10.1016/j.plefa.2014.11.008
- 239 Rehn AP, Cerny R, Sugars R v., *et al.* Osteoadherin is upregulated by mature osteoblasts and enhances their in vitro differentiation and mineralization. *Calcif Tissue Int* 2008;**82**:454–64. doi:10.1007/s00223-008-9138-1
- 240 Ninomiya K, Miyamoto T, Imai J ichi, *et al.* Osteoclastic activity induces osteomodulin expression in osteoblasts. *Biochem Biophys Res Commun* 2007;**362**:460–6. doi:10.1016/j.bbrc.2007.07.193
- 241 Buchaille R, Couble ML, Magloire H, *et al.* Expression of the small leucine-rich proteoglycan osteoadherin/osteomodulin in human dental pulp and developing rat teeth. *Bone* 2000;**27**. doi:10.1016/S8756-3282(00)00310-0
- 242 Rehn AP, Chalk AM, Wendel M. Differential regulation of osteoadherin (OSAD) by TGF- $\beta$ 1 and BMP-2. *Biochem Biophys Res Commun* 2006;**349**. doi:10.1016/j.bbrc.2006.08.133
- 243 Dong T, Lin W, Zhu X, *et al.* Osteomodulin protects dental pulp stem cells from cisplatin-induced apoptosis in vitro. *Stem Cell Rev Rep* 2023;**19**:188–200. doi:10.1007/s12015-022-10399-9



- 244 Kuttapitiya A, Assi L, Laing K, *et al.* Microarray analysis of bone marrow lesions in osteoarthritis demonstrates upregulation of genes implicated in osteochondral turnover, neurogenesis and inflammation. *Ann Rheum Dis* 2017;**76**. doi:10.1136/annrheumdis-2017-211396
- 245 Xu Y, Gu Y, Ji W, *et al.* Activation of the extracellular-signal-regulated kinase (ERK)/c-Jun N-terminal kinase (JNK) signal pathway and osteogenic factors in subchondral bone of patients with knee osteoarthritis. *Ann Transl Med* 2021;**9**. doi:10.21037/atm-21-1215
- 246 Tashima T, Nagatoishi S, Sagara H, *et al.* Osteomodulin regulates diameter and alters shape of collagen fibrils. *Biochem Biophys Res Commun* 2015;**463**. doi:10.1016/j.bbrc.2015.05.053
- 247 Tashima T, Nagatoishi S, Caaveiro JMM, *et al.* Molecular basis for governing the morphology of type-I collagen fibrils by Osteomodulin. *Commun Biol* 2018;**1**. doi:10.1038/s42003-018-0038-2
- 248 Manivong S, Cullier A, Audigie F, *et al.* New trends for osteoarthritis: Biomaterials, models and modeling. *Drug Discov Today* 2023;:103488. doi:10.1016/j.drudis.2023.103488
- 249 Cope PJ, Ourradi K, Li Y, *et al.* Models of osteoarthritis: the good, the bad and the promising. *Osteoarthritis Cartilage*. 2019;**27**. doi:10.1016/j.joca.2018.09.016
- 250 McCoy AM. Animal Models of Osteoarthritis: Comparisons and Key Considerations. *Vet Pathol* 2015;**52**. doi:10.1177/0300985815588611
- 251 Glasson SS, Blanchet TJ, Morris EA. The surgical destabilization of the medial meniscus (DMM) model of osteoarthritis in the 129/SvEv mouse. *Osteoarthritis Cartilage* 2007;**15**. doi:10.1016/j.joca.2007.03.006
- 252 Glasson SS, Chambers MG, Van Den Berg WB, *et al.* The OARSI histopathology initiative – recommendations for histological assessments of osteoarthritis in the mouse. *Osteoarthritis Cartilage* 2010;**18**:S17–23. doi:10.1016/j.joca.2010.05.025
- 253 Yamamoto K, Shishido T, Masaoka T, *et al.* Morphological studies on the ageing and osteoarthritis of the articular cartilage in C57 black mice. *J Orthop Surg (Hong Kong)* 2005;**13**. doi:10.1177/230949900501300103
- 254 McNulty MA, Loeser RF, Davey C, *et al.* Histopathology of naturally occurring and surgically induced osteoarthritis in mice. *Osteoarthritis Cartilage* 2012;**20**. doi:10.1016/j.joca.2012.05.001
- 255 Staines KA, Poulet B, Wentworth DN, *et al.* The STR/ort mouse model of spontaneous osteoarthritis – an update. *Osteoarthritis Cartilage*. 2017;**25**. doi:10.1016/j.joca.2016.12.014
- 256 Sanada Y, Ikuta Y, Ding C, *et al.* Senescence-accelerated mice prone 8 (SAMP8) in male as a spontaneous osteoarthritis model. *Arthritis Res Ther* 2022;**24**:235. doi:10.1186/s13075-022-02916-5
- 257 Malaise O, Tachikart Y, Constantinides M, *et al.* Mesenchymal stem cell senescence alleviates their intrinsic and senosuppressive paracrine properties contributing to osteoarthritis development. *Aging* 2019;**11**. doi:10.18632/aging.102379
- 258 Nagira K, Ikuta Y, Shinohara M, *et al.* Histological scoring system for subchondral bone changes in murine models of joint aging and osteoarthritis. *Sci Rep* 2020;**10**. doi:10.1038/s41598-020-66979-7

## VIII. BIBLIOGRAPHY

- 259 Huang H, Skelly JD, Ayers DC, *et al.* Age-dependent Changes in the Articular Cartilage and Subchondral Bone of C57BL/6 Mice after Surgical Destabilization of Medial Meniscus. *Sci Rep* 2017;**7**. doi:10.1038/srep42294
- 260 Fang H, Huang L, Welch I, *et al.* Early Changes of Articular Cartilage and Subchondral Bone in The DMM Mouse Model of Osteoarthritis. *Sci Rep* 2018;**8**. doi:10.1038/s41598-018-21184-5
- 261 Tonelli F, Bek JW, Besio R, *et al.* Zebrafish: A Resourceful Vertebrate Model to Investigate Skeletal Disorders. *Front Endocrinol (Lausanne)*. 2020;**11**. doi:10.3389/fendo.2020.00489
- 262 Howe K, Clark MD, Torroja CF, *et al.* The zebrafish reference genome sequence and its relationship to the human genome. *Nature* Published Online First: 2013. doi:10.1038/nature12111
- 263 Dietrich K, Fiedler IAK, Kurzyukova A, *et al.* Skeletal Biology and Disease Modeling in Zebrafish. *Journal of Bone and Mineral Research*. 2021;**36**. doi:10.1002/jbmr.4256
- 264 Askary A, Smeeton J, Paul S, *et al.* Ancient origin of lubricated joints in bony vertebrates. Published Online First: 2016. doi:10.7554/eLife.16415.001
- 265 Smeeton J, Natarajan N, Anderson T, *et al.* Regeneration of Jaw Joint Cartilage in Adult Zebrafish. *Front Cell Dev Biol* 2022;**9**. doi:10.3389/fcell.2021.777787
- 266 Mitchell RE, Huitema LFA, Skinner REH, *et al.* New tools for studying osteoarthritis genetics in zebrafish. *Osteoarthritis Cartilage* 2013;**21**:269–78. doi:10.1016/j.joca.2012.11.004
- 267 Lawrence EA, Kague E, Aggleton JA, *et al.* The mechanical impact of *col11a2* loss on joints; *col11a2* mutant zebrafish show changes to joint development and function, which leads to early-onset osteoarthritis. *Philosophical Transactions of the Royal Society B: Biological Sciences* 2018;**373**:20170335. doi:10.1098/rstb.2017.0335
- 268 Juryneć MJ, Sawitzke AD, Beals TC, *et al.* A hyperactivating proinflammatory RIPK2 allele associated with early-onset osteoarthritis. *Hum Mol Genet* 2018;**27**:2383–91. doi:10.1093/hmg/ddy132
- 269 Pasqualetti S, Banfi G, Mariotti M. The zebrafish scale as model to study the bone mineralization process. *J Mol Histol* 2012;**43**. doi:10.1007/s10735-012-9425-z
- 270 Bergen DJM, Tong Q, Shukla A, *et al.* Regenerating zebrafish scales express a subset of evolutionary conserved genes involved in human skeletal disease. *BMC Biol* 2022;**20**. doi:10.1186/s12915-021-01209-8
- 271 Henke K, Farmer DT, Niu X, *et al.* Genetically engineered zebrafish as models of skeletal development and regeneration. *Bone* 2023;**167**:116611. doi:10.1016/j.bone.2022.116611
- 272 Woitowich NC, Woodruff TK. Implementation of the NIH Sex-Inclusion Policy: Attitudes and Opinions of Study Section Members. *J Womens Health* 2019;**28**. doi:10.1089/jwh.2018.7396
- 273 Bankhead P, Loughrey MB, Fernández JA, *et al.* QuPath: Open source software for digital pathology image analysis. *Sci Rep* 2017;**7**. doi:10.1038/s41598-017-17204-5
- 274 Tiede-Lewis LAM, Xie Y, Hulbert MA, *et al.* Degeneration of the osteocyte network in the C57BL/6 mouse model of aging. *Aging* 2017;**9**. doi:10.18632/aging.101308

## VIII. BIBLIOGRAPHY

- 275 Jepsen KJ, Silva MJ, Vashishth D, *et al.* Establishing biomechanical mechanisms in mouse models: Practical guidelines for systematically evaluating phenotypic changes in the diaphyses of long bones. *Journal of Bone and Mineral Research*. 2015;**30**. doi:10.1002/jbmr.2539
- 276 Garrick JM, Costa LG, Cole TB, *et al.* Evaluating Gait and Locomotion in Rodents with the CatWalk. *Curr Protoc* 2021;**1**. doi:10.1002/cpz1.220
- 277 Rasband WS. ImageJ: Image processing and analysis in Java. *Astrophysics Source Code Library* 2012.
- 278 Tarasco M, Cordelières FP, Cancela ML, *et al.* ZFBONE: An ImageJ toolset for semi-automatic analysis of zebrafish bone structures. *Bone* 2020;**138**. doi:10.1016/j.bone.2020.115480
- 279 Chen X, Nadiarynkh O, Plotnikov S, *et al.* Second harmonic generation microscopy for quantitative analysis of collagen fibrillar structure. *Nat Protoc* 2012;**7**. doi:10.1038/nprot.2012.009
- 280 Farlay D, Boivi G. Bone Mineral Quality. In: *Osteoporosis*. 2012. doi:10.5772/29091
- 281 Sehring IM, Weidinger G. Recent advancements in understanding fin regeneration in zebrafish. *Wiley Interdiscip Rev Dev Biol*. 2020;**9**. doi:10.1002/wdev.367
- 282 Love MI, Huber W, Anders S. Moderated estimation of fold change and dispersion for RNA-seq data with DESeq2. *Genome Biol* 2014;**15**. doi:10.1186/s13059-014-0550-8
- 283 Durinck S, Spellman PT, Birney E, *et al.* Mapping identifiers for the integration of genomic datasets with the R/ Bioconductor package biomaRt. *Nat Protoc* 2009;**4**. doi:10.1038/nprot.2009.97
- 284 Kanehisa M, Goto S. KEGG: Kyoto Encyclopedia of Genes and Genomes. *Nucleic Acids Res*. 2000;**28**. doi:10.1093/nar/28.1.27
- 285 Kanehisa M, Sato Y, Kawashima M. KEGG mapping tools for uncovering hidden features in biological data. *Protein Science* 2022;**31**. doi:10.1002/pro.4172
- 286 Sanchez C, Deberg MA, Bellahcène A, *et al.* Phenotypic characterization of osteoblasts from the sclerotic zones of osteoarthritic subchondral bone. *Arthritis Rheum* 2008;**58**. doi:10.1002/art.23159
- 287 Fan X, Wu X, Trevisan Franca De Lima L, *et al.* The deterioration of calcified cartilage integrity reflects the severity of osteoarthritis—A structural, molecular, and biochemical analysis. *FASEB Journal* 2022;**36**. doi:10.1096/fj.202101449R
- 288 Hayami T, Pickarski M, Zhuo Y, *et al.* Characterization of articular cartilage and subchondral bone changes in the rat anterior cruciate ligament transection and meniscectomized models of osteoarthritis. *Bone* 2006;**38**. doi:10.1016/j.bone.2005.08.007
- 289 Deng B, Wang F, Yin L, *et al.* Quantitative study on morphology of calcified cartilage zone in OARSI 0~4 cartilage from osteoarthritic knees. *Curr Res Transl Med* 2016;**64**. doi:10.1016/j.retram.2016.01.009
- 290 Poulet B, De Souza R, Knights CB, *et al.* Modifications of gait as predictors of natural osteoarthritis progression in Str/Ort mice. *Arthritis and Rheumatology* 2014;**66**. doi:10.1002/art.38616

## VIII. BIBLIOGRAPHY

- 291 Muramatsu Y, Sasho T, Saito M, *et al.* Preventive effects of hyaluronan from deterioration of gait parameters in surgically induced mice osteoarthritic knee model. *Osteoarthritis Cartilage* 2014;**22**. doi:10.1016/j.joca.2014.03.016
- 292 Makii Y, Asaka M, Setogawa S, *et al.* Alteration of gait parameters in a mouse model of surgically induced knee osteoarthritis. *Journal of Orthopaedic Surgery* 2018;**26**. doi:10.1177/2309499018768017
- 293 Pesesse L, Sanchez C, Walsh DA, *et al.* Bone sialoprotein as a potential key factor implicated in the pathophysiology of osteoarthritis. *Osteoarthritis Cartilage* 2014;**22**. doi:10.1016/j.joca.2014.01.010
- 294 Salbach J, Kliemt S, Rauner M, *et al.* The effect of the degree of sulfation of glycosaminoglycans on osteoclast function and signaling pathways. *Biomaterials* 2012;**33**. doi:10.1016/j.biomaterials.2012.08.028
- 295 Geurts J, Patel A, Hirschmann MT, *et al.* Elevated marrow inflammatory cells and osteoclasts in subchondral osteosclerosis in human knee osteoarthritis. *Journal of Orthopaedic Research* 2016;**34**. doi:10.1002/jor.23009
- 296 Chen XD, Bian X, Teslovich TM, *et al.* Dissection of the sets of genes that control the behavior of biglycan-deficient pre-osteoblasts using oligonucleotide microarrays. *Bone* 2005;**37**. doi:10.1016/j.bone.2005.04.006
- 297 Sommarin Y, Wendel M, Shen Z, *et al.* Osteoadherin, a Cell-binding Keratan Sulfate Proteoglycan in Bone, Belongs to the Family of Leucine-rich Repeat Proteins of the Extracellular Matrix\*. 1998. <http://www.jbc.org/> (accessed 18 Dec 2019).
- 298 Sojan JM, Gioacchini G, Giorgini E, *et al.* Zebrafish caudal fin as a model to investigate the role of probiotics in bone regeneration. *Sci Rep* 2022;**12**:8057. doi:10.1038/s41598-022-12138-z
- 299 Pasold J, Engelmann R, Keller J, *et al.* High bone mass in the STR/ort mouse results from increased bone formation and impaired bone resorption and is associated with extramedullary hematopoiesis. *J Bone Miner Metab* 2013;**31**. doi:10.1007/s00774-012-0394-9
- 300 Javaheri B, Razi H, Piles M, *et al.* Sexually dimorphic tibia shape is linked to natural osteoarthritis in STR/Ort mice. *Osteoarthritis Cartilage* 2018;**26**. doi:10.1016/j.joca.2018.03.008
- 301 Hynes RO, Naba A. Overview of the matrisome—An inventory of extracellular matrix constituents and functions. *Cold Spring Harb Perspect Biol* Published Online First: 2012. doi:10.1101/cshperspect.a004903
- 302 Sainio A, Järveläinen H. Extracellular matrix-cell interactions: Focus on therapeutic applications. *Cell Signal* 2020;**66**. doi:10.1016/j.cellsig.2019.109487
- 303 Naba A, Clauser KR, Ding H, *et al.* The extracellular matrix: Tools and insights for the ‘omics’ era. *Matrix Biology*. 2016;**49**:10–24. doi:10.1016/j.matbio.2015.06.003
- 304 Salbach-Hirsch J, Ziegler N, Thiele S, *et al.* Sulfated glycosaminoglycans support osteoblast functions and concurrently suppress osteoclasts. *J Cell Biochem* 2014;**115**. doi:10.1002/jcb.24750

## VIII. BIBLIOGRAPHY

- 305 Zheng L, Pi C, Zhang J, *et al.* Aberrant activation of latent transforming growth factor- $\beta$  initiates the onset of temporomandibular joint osteoarthritis. *Bone Res* 2018;**6**. doi:10.1038/s41413-018-0027-6
- 306 Chen R, Mian M, Fu M, *et al.* Attenuation of the progression of articular cartilage degeneration by inhibition of TGF- $\beta$ 1 signaling in a mouse model of osteoarthritis. *American Journal of Pathology* 2015;**185**. doi:10.1016/j.ajpath.2015.07.003
- 307 Thomas M, Fronk Z, Gross A, *et al.* Losartan attenuates progression of osteoarthritis in the synovial temporomandibular and knee joints of a chondrodysplasia mouse model through inhibition of TGF- $\beta$ 1 signaling pathway. *Osteoarthritis Cartilage* 2019;**27**. doi:10.1016/j.joca.2018.12.016
- 308 Wang YJ, Shen M, Wang S, *et al.* Inhibition of the TGF- $\beta$ 1/Smad signaling pathway protects against cartilage injury and osteoarthritis in a rat model. *Life Sci.* 2017;**189**. doi:10.1016/j.lfs.2017.09.022
- 309 Wen L, Gao M, He Z, *et al.* Noggin, an inhibitor of bone morphogenetic protein signaling, antagonizes TGF- $\beta$ 1 in a mouse model of osteoarthritis. *Biochem Biophys Res Commun* 2021;**570**. doi:10.1016/j.bbrc.2021.07.044
- 310 Zhao W, Wang T, Luo Q, *et al.* Cartilage degeneration and excessive subchondral bone formation in spontaneous osteoarthritis involves altered TGF- $\beta$  signaling. *Journal of Orthopaedic Research* 2016;**34**. doi:10.1002/jor.23079
- 311 Shen J, Li J, Wang B, *et al.* Deletion of the transforming growth factor  $\beta$  Receptor type II gene in articular chondrocytes leads to a progressive osteoarthritis-like phenotype in mice. *Arthritis Rheum* 2013;**65**. doi:10.1002/art.38122
- 312 Colon DA, Yoon BJV, Russell TA, *et al.* Assessment of the injection behavior of commercially available bone BSMs for Subchondroplasty<sup>®</sup> procedures. *Knee* 2015;**22**. doi:10.1016/j.knee.2015.06.017
- 313 Pasculli RM, Kenyon CD, Berrigan WA, *et al.* Mesenchymal stem cells for subchondral bone marrow lesions: From bench to bedside. *Bone Rep* 2022;**17**. doi:10.1016/j.bonr.2022.101630
- 314 Richbourg NR, Peppas NA, Sikavitsas VI. Tuning the biomimetic behavior of scaffolds for regenerative medicine through surface modifications. *J Tissue Eng Regen Med.* 2019;**13**. doi:10.1002/term.2859
- 315 Hu C, Ashok D, Nisbet DR, *et al.* Bioinspired surface modification of orthopedic implants for bone tissue engineering. *Biomaterials.* 2019;**219**. doi:10.1016/j.biomaterials.2019.119366
- 316 Munir A, Døskeland A, Avery SJ, *et al.* Efficacy of copolymer scaffolds delivering human demineralised dentine matrix for bone regeneration. *J Tissue Eng* 2019;**10**. doi:10.1177/2041731419852703
- 317 Maver U, Xhanari K, Žižek M, *et al.* Carboxymethyl cellulose/diclofenac bioactive coatings on AISI 316LVM for controlled drug delivery, and improved osteogenic potential. *Carbohydr Polym* 2020;**230**. doi:10.1016/j.carbpol.2019.115612
- 318 Natalie Y. Structural changes in the collagen network of joint tissues in late stages of murine OA.

## VIII. BIBLIOGRAPHY

- 319 Zoeller JJ, Pimtong W, Corby H, *et al.* A central role for decorin during vertebrate convergent extension. *Journal of Biological Chemistry* 2009;**284**. doi:10.1074/jbc.M808991200
- 320 Kishimoto Y, Lee KH, Zon L, *et al.* The molecular nature of zebrafish swirl: BMP2 function is essential during early dorsoventral patterning. *Development* 1997;**124**. doi:10.1242/dev.124.22.4457
- 321 Chen XD, Shi S, Xu T, *et al.* Age-related osteoporosis in biglycan-deficient mice is related to defects in bone marrow stromal cells. *Journal of Bone and Mineral Research* 2002;**17**. doi:10.1359/jbmr.2002.17.2.331
- 322 Jin SL, Bai YM, Zhao BY, *et al.* Silencing of miR-330-5p stimulates osteogenesis in bone marrow mesenchymal stem cells and inhibits bone loss in osteoporosis by activating Bgn-mediated BMP/Smad pathway. *Eur Rev Med Pharmacol Sci* 2020;**24**. doi:10.26355/eurrev\_202004\_20987

# **IX. APPENDICES**

**Appendix 1: Review on the SLRP family in the skeletal tissues.**





Review

---

# From Translation to Protein Degradation as Mechanisms for Regulating Biological Functions: A Review on the SLRP Family in Skeletal Tissues

---

J r mie Zappia, Marc Joiret, Christelle Sanchez, C cile Lambert, Liesbet Geris, Marc Muller and Yves Henrotin



Review

# From Translation to Protein Degradation as Mechanisms for Regulating Biological Functions: A Review on the SLRP Family in Skeletal Tissues

Jérémie Zappia <sup>1</sup>, Marc Joiret <sup>2</sup>, Christelle Sanchez <sup>1</sup>, Cécile Lambert <sup>1</sup>, Liesbet Geris <sup>2</sup>, Marc Muller <sup>3</sup> and Yves Henrotin <sup>1,4,5,\*</sup>

<sup>1</sup> Bone and Cartilage Research Unit, Arthropôle Liège, Center for Interdisciplinary research on Medicines (CIRM) Liège, Liège University, Institute of Pathology, CHU Sart-Tilman, 4000 Liège, Belgium; jzappia@uliege.be (J.Z.); christelle.sanchez@uliege.be (C.S.); cecile.lambert@uliege.be (C.L.)

<sup>2</sup> Biomechanics Research Unit, B34 GIGA-R, In Silico Medicine, Liège University, CHU Sart-Tilman, 4000 Liège, Belgium; marc.joiret@uliege.be (M.J.); Liesbet.Geris@uliege.be (L.G.)

<sup>3</sup> Laboratory for Organogenesis and Regeneration (LOR), GIGA-Research, Liège University, Avenue de l'Hôpital, B-4000 Liège, Belgium; m.muller@uliege.be

<sup>4</sup> Physical therapy and Rehabilitation department, Princess Paola Hospital, Vivalia, B-6900 Marche-en-Famenne, Belgium

<sup>5</sup> Artialis SA, GIGA Tower, Level 3, CHU Sart-Tilman, 4000 Liège, Belgium

\* Correspondence: yhenrotin@uliege.be; Tel.: +32-4-3665937

Received: 2 December 2019; Accepted: 26 December 2019; Published: 3 January 2020



**Abstract:** The extracellular matrix can trigger cellular responses through its composition and structure. Major extracellular matrix components are the proteoglycans, which are composed of a core protein associated with glycosaminoglycans, among which the small leucine-rich proteoglycans (SLRPs) are the largest family. This review highlights how the codon usage pattern can be used to modulate cellular response and discusses the biological impact of post-translational events on SLRPs, including the substitution of glycosaminoglycan moieties, glycosylation, and degradation. These modifications are listed, and their impacts on the biological activities and structural properties of SLRPs are described. We narrowed the topic to skeletal tissues undergoing dynamic remodeling.

**Keywords:** small leucine-rich proteoglycans; codon usage; post-translational event; glycosaminoglycan; glycosylation; catabolism

## 1. Introduction

The extracellular matrix (ECM) is a three-dimensional network of extracellular macromolecules that provides structural and biochemical support to surrounding cells. More than a physical support tissue, the ECM is a dynamic structure that not only depends on but also regulates cell behavior and functions. Any change in its composition may reflect a disease state or may initiate a disease [1–3]. Glycoproteins, collagens, and proteoglycans are the main components of the ECM, and they constitute the “core matrisome” encompassing almost 300 proteins in mammals. This matrisome contains 35 proteoglycans including small leucine-rich proteoglycans (SLRPs). The majority of SLRPs control ECM assembly by regulating collagen fibrillogenesis [4–6]. In addition, SLRPs are able to control and interact with various cytokines in the extracellular space and bind to cellular receptors [7–10].

In this review, the SLRP family’s codon usage was investigated. The codon usage is commonly associated to pathological or stress conditions. In many coding sequences, the usage patterns of rare versus common synonymous codons are nonrandom and under selection pressure. Synonymous rare codons can enhance co-translational protein folding, increasing the likelihood of forming the

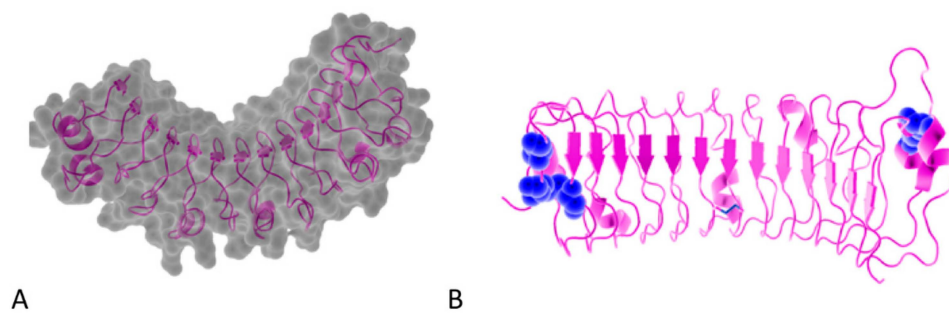
native protein structure and suppressing alternatively folded structures [11–14]. They increase the time available for post-translational chemical reactions to occur on specific residues upstream in the oriented sequence (N-terminal toward C-terminal), even before the protein translation is fully completed, adding an extra layer to the dynamic translational control [15]. Here, the coding DNA sequence (CDS) of 17 SLRP proteins, for which the human CDS is known, were data-mined for their codon usage for seven amino acid residues deemed relevant to characterize the SLRP family.

Post-translational modifications are defined as the set of modifications that happen on the core protein such as the addition of a chemical group or the cleavage of a sequence of amino acid residues. The regulation of post-translational modifications was shown to play a role in the modulation of cell biological functions [16]. There are more than 200 different types of post-translational modifications, the most common within SLRPs being glycanation, glycosylation, and enzymatic or oxidative degradation. Changes in SLRPs are associated with certain pathologies, and the pattern of these modifications could be used as a biomarker to diagnose diseases and predict their progression [6,9].

This review describes the impact of the SLRP codon usage pattern and their post-translational modifications on the homeostasis of skeletal tissues. These two regulatory pathways are key cellular mechanisms for adaptation to stress and pathological conditions. Herein, the human skeletal system is defined as all the bony, ligamentous, fibrous and cartilaginous elements that together make up the skeleton and its attachment.

## 2. The SLRP Family: Classification and Structure

Proteoglycans are complex macromolecules composed of a core protein covalently decorated by glycosaminoglycan (GAG) chains on serines or threonines. The small core protein has a molecular weight between 36 kDa and 77 kDa and is characterized by a variable number of central leucine-rich repeat (LRR) domains, each made of one  $\alpha$ -helix and one  $\beta$ -strand. SLRPs are solenoid-like proteins with a horseshoe shape. Their concave face is formed of  $\beta$ -sheets, while the convex surface is formed of  $\alpha$ -helices, where each LRR provides one  $\beta$ -sheet and one  $\alpha$ -helix that correspond to one turn of the solenoid-like structure, the hydrophobic residues of the LRR facing inside. This structure is favorable to protein–protein interaction where the inner concave face is ideal to capture a ligand [17–19] (Figure 1A). The consensus sequence of LRR is LXXLXLXXNXL, where L is a leucine, an isoleucine, a valine, or another hydrophobic amino acid; N is an asparagine; and X is any amino acid. LRRs are composed of variable amino acid sequences across the SLRP family, ranging in size from 20 to 29 residues, with 24 residues being the most representative [18,19]. The N and C-terminal regions of the protein flanking the central LRR domain are rich in cysteine residues. The N-terminal domain contains four cysteines spaced by a varying number of amino acids. This N-terminal domain shows variability within the SLRP family. The cysteines present in this cluster form a disulfide bond between the first LRR and a  $\beta$ -hairpin. The C-terminal domain generally contains two cysteines [20]. The C-terminal end includes the two C-terminal LRRs with the penultimate one called the ear-repeat. The ear-repeat is the longest LRR that is laterally extended from the main axis of the core protein to form the ear [18,19] (Figure 1B). Ear-repeats are thought to be involved in ligand recognition and in the structural folding of the protein. As an example, a truncated decorin lacking C-terminal end residues is associated with congenital stromal corneal dystrophy. This mutated decorin is insoluble and retained in the cell, leading to an endoplasmic reticulum stress and an unfolded protein response [21].



**Figure 1.** (A). Osteomodulin in 3D view (PDB id: 5YQ5) with PyMol showing the horseshoe shape with 13  $\beta$ -sheets on the concave side and 13  $\alpha$ -helices on the convex side. (B). Osteomodulin in 3D view (PDB id: 5YQ5) with PyMol showing cystein residues (in blue) of the protein near the N-terminal (C66, C68–C78 on the left) and C-terminal end (C321–C353 on the right downstream of the ear-repeat). The secondary structure's graphical representations showing the small leucine-rich proteoglycans (SLRPs) salient features were carried out with the PyMol software (PyMOL™ 2.3.1—Incentive Product Copyright Schrodinger, LLC) and using home-made Python scripts to display relevant amino acids in chosen colors.

The SLRP family is composed of 18 members that have been classified into five distinct classes according to their structural and functional properties and their chromosomal organization. The five classes are divided into canonical and non-canonical classes. The presence of the ear-repeat is a feature of all the canonical SLRPs. The classes I–III (13 members) include the canonical SLRPs and the classes IV–V (5 members) include the non-canonical SLRPs [9,19] (Table 1).

Glycosaminoglycans (GAGs) are long linear polysaccharides made of repeated disaccharide units consisting of an amino sugar (N-acetylgalactosamine or N-acetylglucosamine) and an uronic acid (glucuronic acid or iduronic acid), on the basis of which they can be classified. They are synthesized through a complex enzymatic pathway starting from the addition of four monosaccharides (xylose, galactose, galactose, and glucuronic acid) on the hydroxyl group of a serine, except for the keratan sulfate (see below). This tetrasaccharide is the linker to which the different additional units are attached to form the diverse GAGs; additional diversity is generated through epimerization, sulfation, and deacetylation [22]. Keratan sulfate addition results either from an N or an O-glycosylation via three different possible linkers, from which the chain elongation occurs. Interestingly, keratan sulfate might be associated with a tyrosine sulfation pattern, as the two coincide in the same SLRPs each time. GAG biosynthesis and modifications mainly take place in the Golgi apparatus [22,23]. GAGs are subject to degradation within lysosomes where different enzymes such as exohydrolase and endoenzymes catabolize them to oligosaccharides with further desulfation steps [24,25].

Many GAG side chains may be attached to SLRP core proteins, mainly to the N-terminal part. These GAG modifications are often similar for an SLRP class and therefore can be used for their characterization (Table 1). GAG chains are involved in the structure, the conformational stability, Ref. [26] and the secretory process of SLRPs [27].

**Table 1.** Classification of the SLRP family in five classes; BGN: Biglycan; DCN: Decorin; ASP: Asporin; ECM2: Extracellular Matrix Protein 2; ECMX: Extracellular Matrix Protein X; LUM: Lumican; KTN: Keratocan; FMOD: Fibromodulin; OMD: Osteomodulin; PRELP: Proline/arginine-rich end leucine-rich repeat protein; EPN: Epiphycan; OGN: Osteoglycin; OPTC: Opticin; CHAD: Chondroadherin; NYX: Nyctalopin; TSK: Tsukushi; PODN: Podocan; PODNL: Podocan-like protein. The N-terminal cysteine cluster is a major feature for the classification of this family. The 3D representations are resolved by X-ray diffraction and are publicly available on protein data base repositories such as Protein Data Bank (PDB: <https://www.rcsb.org/>). The 3D structures can be displayed and viewed with the PyMol software (Schrödinger LCC, version 2.1.1), illustrating the horseshoe shape with lateral asparagines (N shown in red thanks to a home-made Python script). X-Ray crystallographic analysis for the SLRP family members of class III and class IV are not yet available. The different post-translational modifications are listed by each SLRP family member. All information was cross-checked with the UniProt database [28]. LRR: leucine-rich repeat.

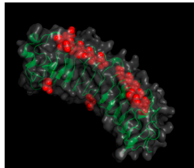
Class	N-End Cysteine Motif	3D Representation and PDB ID	Member	GAG Type/Glycosylation	Other	Ref.
I	CX <sub>3</sub> CXCX <sub>6</sub> C	 ID: 1XKU	BGN	Chondroitin sulfate Dermatan sulfate N-linked oligosaccharide O-linked oligosaccharide		[29–32]
			DCN	Chondroitin sulfate Dermatan sulfate N-linked oligosaccharide O-linked oligosaccharide		[30–34]
		ASP	N-linked oligosaccharide O-linked oligosaccharide		[35]	
		ECM2	N-linked oligosaccharide No data on potential GAG	ECM2 has a peculiarity in its motif with only 2 conserved cysteines.	[19,31]	
		ECMX	No data on potential GAG or glycosylation		[31]	

Table 1. Cont.

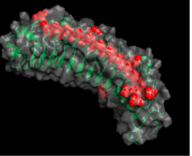
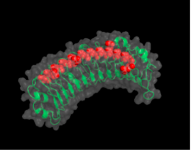
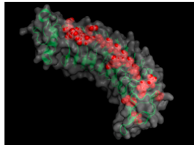
Class	N-End Cysteine Motif	3D Representation and PDB ID	Member	GAG Type/Glycosylation	Other	Ref.	
II	CX <sub>3</sub> CXCX <sub>9</sub> C	 ID: 5MX0	LUM	Keratan sulfate	Tyrosine sulfation	[36–38]	
			KTN	Poly-lactosamine N-linked oligosaccharide		[39]	
			FMOD	Keratan sulfate Poly-lactosamine N-linked oligosaccharide	Tyrosine sulfation Acidic patch	[38,40–42]	
			 ID: 5YQ5	OMD		Keratan sulfate N-linked oligosaccharide	[38,43–45]
				PRELP		N-linked oligosaccharide	Basic patch
III	CX <sub>2</sub> CXCX <sub>6</sub> C		EPN	Chondroitin sulfate Dermatan sulfate N-linked oligosaccharide O-linked oligosaccharide	LRRs with only seven repeats Tyrosine sulfation Acidic patch	[30,31]	
			OGN	Keratan sulfate Chondroitin sulfate Dermatan sulfate N-linked oligosaccharide	LRRs with only seven repeats Tyrosine sulfation	[31,48–52]	
			OPTC	N-linked oligosaccharide O-linked oligosaccharide		[31,53,54]	

Table 1. Cont.

Class	N-End Cysteine Motif	3D Representation and PDB ID	Member	GAG Type/Glycosylation	Other	Ref.
IV	CX <sub>3</sub> CXCX <sub>6-17</sub> C	 ID: 5MX1	CHAD	Keratan sulfate O-linked oligosaccharide		[31,55]
			NYX TSK	N-linked oligosaccharide		[31]
V	CX <sub>3-4</sub> CXCX <sub>9</sub> C		PODN	N-linked oligosaccharide	High number of LRR with 20 repeats Acidic patch	[9,56,57]
			PODNL		High number of LRR with 21 repeats	[58]

### 3. SLRP Codon Usage Patterns May Fine-Tune Selective Translation Pathways during Cellular Stress Conditions

The SLRP family members share common structural features as described in the classification and structure section and partially illustrated in Table 1. Here, we conducted a biostatistical and bioinformatics exploratory analysis of the SLRP family members based on the codon usage of the genes encoding 17 members of the family.

Biases in codon usage have been documented to play a role in the translational fine-tuning of protein expression levels for cells undergoing stress conditions. This fine-tuning involves enzymatic modifications (i.e., reprogramming) of specific t-RNAs on their U34 wobble-base [59]. These t-RNA U34 wobble-base modifications affect the elongation rate during translation for transcripts that have a specific pattern of codon usage, resulting in a selective increase in the translation of specific proteins by the cytoplasmic pool of ribosomes. A well-known example [60] is the modified U34 wobble-base called  $mcm^5$ -s<sup>2</sup>-U34 (methoxy-carbonyl-methyl-5, thio-2 uridine 34), which is catalyzed by three successive enzymes targeting the original uridine t-ribonucleobase (U34-t-RNA): acetyltransferase elongator (Elp1-6), methyltransferase TRM9-like domain of alkylation repair homolog (ALKBH8), and the cytosolic thiouridylase homolog 1 and 2 (Ctu1/2). This modified t-RNA  $mcm^5$ -s<sup>2</sup>-U34 wobble-base will eventually base pair to the transcript cognate codons whose third base ends preferentially with an A instead of a G, thus resulting in a privileged base pairing with the rarely used codons for lysine, glutamine, and glutamate.

In yeasts, this mechanism has been shown to enhance the translation of proteins involved in hypoxic stress responses [61]. In melanoma cancer cells, it has been shown to enhance the expression of HIF1- $\alpha$  and of other proteins enriched in the codon usage patterns that happen to be promoted in tumor cells resistant to targeted therapy [62].

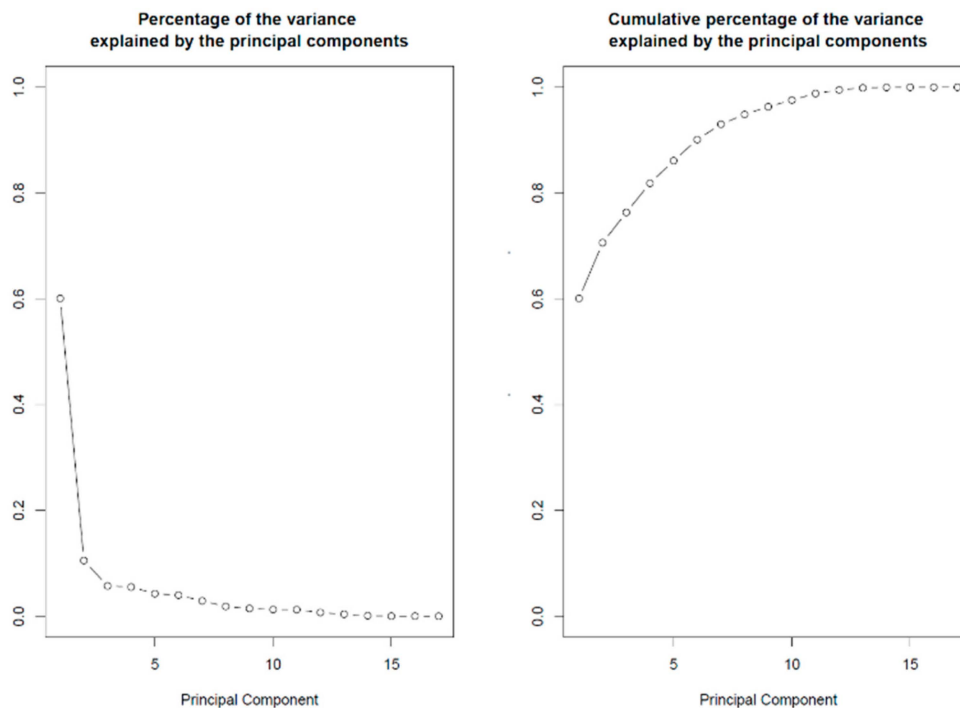
Even in the absence of enzymatic tRNA modifications, the usage of rare codons may be required to slow down the translating ribosome to increase the available time for proper folding of the nascent protein or to increase the likelihood of chemical additions (e.g., hypothetical glycanation tagging) on specific residues located upstream in the sequence being translated for later post-translational purposes.

The coding DNA sequences (CDS) of 17 SLRP proteins ( $n = 17$  observations) were data-mined for their codon usage of seven amino acid residues deemed relevant to characterize the SLRP family: cysteine (C:Cys), lysine (K:Lys), glutamine (Q:Gln), glutamate (E:Glu), asparagine (N:Asn), aspartate (D:Asp), and of course leucine (L:Leu). The genetic code degeneracy associated to these amino acid residues reads as follows: cysteine, two codons: UGC, UGU; lysine, two codons: AAA, AAG; glutamine, two codons: CAA, CAG; glutamate, two codons: GAA, GAG; asparagine, two codons: AAU, AAC; aspartate, two codons: GAU, GAC; and finally leucine, six codons: UUA, UUG, CUA, CUC, CUG, and CUU. The subset of all these investigated codons contains 18 codons ( $p = 18$  variables).

The coding DNA sequences (CDS) of 17 members of the SLRP family (all SLRP members except the class I protein ECMX, whose CDS sequence was not found) were extracted from the Ensembl human genome repository (GRCh38.p12 assembly) in FASTA format. The complete coding sequences were collected with the longest possible open reading frame (ORF) starting from start codon AUG and ending at the most downstream occurrence of one of the three possible stop codons (UAA, UAG, UGA). We processed each sequence to count the total number of codons in the longest open reading frame, to count the codon usage of the seven aforementioned amino acid residues and to compute the codon usage frequencies of the corresponding 18 codons under investigation with a home-made Python program using BioPython modules (importing SeqIO, IUPAC, codonTable and suffix trees). The data were exported and then retrieved in R for further statistical analysis. The codon frequencies revealed different bias patterns in codon usage between the SLRP family members, on which an unsupervised statistical learning analysis was performed [63]. The results of the principal component analysis (PCA) are presented below. The PCA was conducted with the `prcomp` function in R and graphically represented with the `biplot` function in R (both functions in software package 'stats' in R version 3.5.2. R Core Team, 2014. <https://www.r-project.org/>). Figure 2 displays the percentage of the



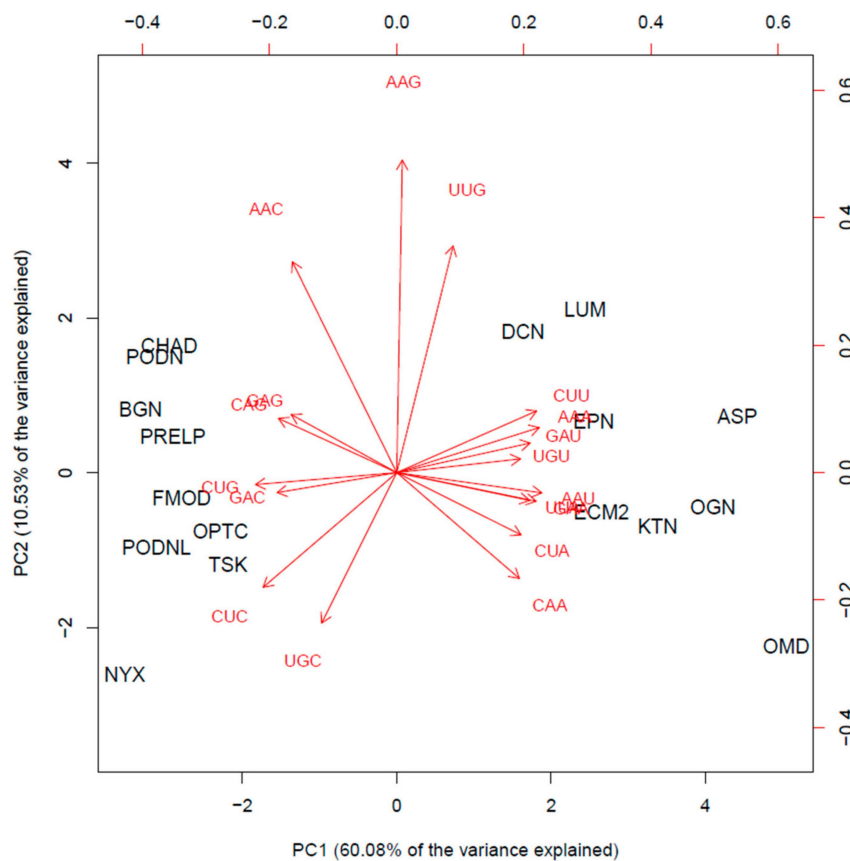
variance that is explained by the principal components (PCs). The first two PCs explain 60.08% and 10.53% of the variance, while together they explain more than 70.6% of the data variance.



**Figure 2.** Percentage of variance explained by the PCs. Left panel: The first two components explain 60.08% and 10.53% of the variance, respectively. Right panel: Cumulative percentage of the variance explained. The first two components explain  $60.08 + 10.53 = 70.6\%$  of the variance in codon usage between SLRP family members' proteins.

In a graphical representation, orthogonal loading vectors tend to be less correlated with each other than co-linear or almost co-linear loading vectors (vectors pointing in the same, or opposite direction), which are interpreted as highly correlated variable features.

The biplot on Figure 3 displays a 2D representation of the scores for the 17 protein members from the SLRP family (in black) projected along the first two principal components and a representation of the 18 loading vectors for the codon usage features (red arrowed vectors). It shows that the SLRP family mainly clusters in two groups and that osteomodulin and nyctalopin appear as outlying members of the SLRP family. There seems to be at least two clusters with different codon usage patterns. In cluster 1 (left part of the biplot), the chondroadherin (CHAD), biglycan (BGN), Prelp (PRELP), fibromodulin (FMOD), opticin (OPTC), tsukushi (TSK), podocan (PODN), podocan like protein 1 (PDNL), and nyctalopin (NYX) mature mRNA transcripts all present a similarly biased codon usage pattern represented in Table 2. Cluster 2 (right part of the biplot) is made of decorin (DCN), lumican (LUM), epiphycan (EPN), asporin (ASP), ECM2, osteoglycin (OGN), keratocan (KTN) and osteomodulin (OMD). Its codon usage pattern contrasts with that of cluster 1 and is represented in Table 2.



**Figure 3.** Biplot: scores of the 17 members of the SLRP family (in black) projected on the first two PCs (bottom and left first two PC scores), and red arrows indicate the loading vectors in the space of the codon usage frequency features (top and right axes first two PC loadings).

**Table 2.** Representation of the biased codon usage patterns of the mature mRNA transcripts among Cluster 1 and Cluster 2 of the SLRP family. Over-represented codons are colored in green and marked by a '+'; under-represented codons are colored in red and marked by a '-'.

		Cluster 1	Cluster 2
Leucine	CUG	+	-
	CUC	+	-
	CUU	-	+
	CUA	-	+
	UUG	-	+
	UUA	-	+
Glutamate	GAG	+	-
	GAA	-	+
Glutamine	CAG	+	-
	CAA	-	+
Lysine	AAG	+	-
	AAA	-	+
Aspartate	GAC	+	-
	GAU	-	+
Asparagine	AAC	+	-
	AAU	-	+
Cysteine	UGC	+	-
	UGU	-	+

In Cluster 2, it is noted that osteomodulin appears to have a strong codon usage bias. Indeed, leucine (L), in addition to CUU, is significantly encoded by the rare CUA, and the three K, Q, and E

amino acid residues are mostly encoded by the unusual codons ending with the AA dinucleotide. Thus, their codon usage is strongly biased toward the A-ending codons, which are known to preferentially base pair with the modified mcm<sup>5</sup>s<sup>2</sup>-U34 tRNA. Therefore, we suspect that the osteomodulin protein translation rate would be enhanced in cells undergoing hypoxic stress or mechanical stress via enzymatic reprogramming of the wobble U34 in the cognate t-RNA decoding leucine, glutamine, glutamate, and lysine residues. Supplementary Figures S1 and S2 show the codon usage biased patterns contrasting osteomodulin with the other members of the SLRP family for leucine and for the triplet glutamine, glutamate, and lysine amino acids residues.

Due to a similar though less extreme codon usage bias, it is hypothesized that asporin, osteoglycin, keratocan, and ECM2 could also have their translation rate enhanced in cellular stress conditions. The occurrence of re-programming of the wobble-base U34 tRNA under stress conditions has not yet been checked experimentally in the context of skeletal or cartilaginous tissues. Experimental validation is required to investigate whether this cascade of events results in differential levels of protein expression in the SLRP family under cellular stress conditions.

#### 4. Roles of SRLP GAG Moieties in Fibrillogenesis

A major feature of the SLRPs is their interaction with collagen fibrils in the ECM. Although they bind through their core protein, their GAGs are also functional actors. GAG moieties were shown to interact directly with collagen and to modulate their fibrillogenesis [64,65]. High-resolution scanning electron microscopy indicates that these interactions are periodic and GAG chains bound to the collagen surface can form interfibrillar elastic bridges and belts around fibrils. GAGs regulate the fibril diameter and the interfibrillar spacing, and they also assemble the collagen fibrils, thus generating a network that organizes the ECM [64,66–68]. In the interfibrillar space, a majority of GAGs is oriented spanning adjacent fibrils, while also interacting together to form antiparallel structures called “shape modules” and keeping collagen fibrils at defined distances [66,69–71].

Data from *in vivo* studies also suggest collagen fibril regulation through the presence of GAGs. The glycanation of decorin plays a critical role in the early stages of fibrillogenesis and reduces the collagen fibril diameter. In Ehlers–Danlos syndrome, the decrease of galactosyltransferase activity impairs the glycanation of decorin and biglycan, and collagen fibrillogenesis is decreased [72–74]. In contrast, decorin dermatan sulfate-deficient knock-in mice, where the site of GAG attachment was mutated, fail to express any variation of the collagen fibril diameter. Although we cannot exclude compensation by other SLRPs associated with dermatan sulfate in the mouse model or the lack of functional conservation of GAGs between human and mouse [75], this discrepancy indicates that more studies are required to clarify the role of SRLPs’ GAG chains.

A model has been proposed in which GAG bridges could manage mechanical stress, namely occurring in tendons that are biological structures transmitting large forces between muscles and bones. GAG bridges are supposed to play a role in force control through fibril-to-fibril interactions during loading. In addition, decorin enhances mechanical properties by reducing fibrils aggregation during polymerization [76]. Therefore, SLRPs could protect collagen fibrils against excessive mechanical strains [77–80]. However, this model is subject to controversy. Indeed, several studies have found that the enzymatic removal of GAGs did not affect the mechanical properties of collagen fibrils [71,81–83] except for pathological post-injury tendons [84]. Controversially, another investigation of the collagen mechanical response in both native and GAG-depleted tendons in mouse proposed a model where GAGs promote the fibrils sliding under straining conditions by isolating individual fibrils to bear the load [85]. This conflicting evidence leaves the question open about the complex functions of the GAG and SLRP extrafibrillar network in ECM assembly.

Besides direct interaction and fibril organization, GAGs have a protective role. When SLRPs are bound to collagen fibrils, their GAGs protect collagen fibrils in acidic conditions against cathepsin K, conferring on them putative functions during bone resorption [86].

## 5. SLRP GAG Moieties: Fingerprints of the Tissue Status and Active Players

The diversity of SLRP's GAG moieties is a characteristic of the tissue and can serve to track its status. Furthermore, the same SLRP displays different forms via the absence or presence and diversity of its GAGs.

In articular cartilage, intervertebral disc, and dental tissue, biglycan and decorin may be represented under a proteoglycan or a non-proteoglycan form [87–89]. Immunoblots before and after the removal of glycanation have revealed two forms of biglycan lacking GAG whose abundance is low in juveniles in the articular cartilage and in the intervertebral disc but increases in adults until they become predominant. The abundance of the biglycan proteoglycan form appears to be stable through life [87,88]. However, for decorin, its non-proteoglycan form is always a minor component, even though there is also an increase related to age [88]. In cortical bone, the level of decorin glycanation decreases with age [90]. Finally, the decorin GAG length is reduced in the tendon fascicle of old mice [91].

The glycanation of fibromodulin is modified by aging, similar to decorin and biglycan. The proteoglycan form is present in juvenile human articular cartilage, and the GAG chains are shortened through the aging process until they are mostly represented by the non-proteoglycan form in mature cartilage. However, fibromodulin continues to be substituted with N-linked oligosaccharide [92].

It appears that lumican, a keratan sulfated SLRP, goes through the same age-related mechanism in human articular cartilage. The increased representation of the non-glycanated form of lumican is due to a lack of keratan sulfate synthesis by mature chondrocytes. It is interesting to point out that aggrecan conserves its keratan sulfate chains in mature cartilage, demonstrating that chondrocytes are still able to synthesize [93,94]. In human cultured chondrocytes, it was shown that growth factors/cytokines were able to modulate the GAG chain length and sulfation of lumican by regulating the cell metabolism. IL-1 $\beta$  induces the production of a non-glycanated lumican, whereas the length of GAG chains in glycanated forms is modulated by basic fibroblast growth factor (bFGF), insulin growth factor (IGF)-1, and transforming growth factor (TGF) $\beta$  [95].

Osteomodulin presents a different pattern of changing glycosylation profiles among keratan sulfated SLRPs, in that it varies through endochondral bone formation and its biomineralization process. In non-mineralized ECM, osteomodulin is non-glycanated and N-glycosylated, whereas in mineralized ECM, the keratan sulfate modification of osteomodulin increases with bone maturation [96].

It was suggested that the changes in growth factor/cytokine synthesis with aging could be one mechanism explaining the post-translational GAG modifications of SLRPs [95]. Non-glycanated SLRPs can also result from the degradation of a glycanated precursor, as demonstrated by the N-terminal sequence analysis of SLRPs coming from intervertebral disc tissue [87].

In addition to the presence or absence of glycanation, the nature of the GAG chains substituted to the SLRP core is also changing during bone development, and therefore could be associated with different functions. In cultured alveolar bone cells, biglycan is conjugated mainly with dermatan sulfate during the cell proliferation phase and switches to only chondroitin sulfate chains during the mineralization phase. Similarly, decorin carries many dermatan sulfate chains during early bone matrix formation but later associates only with chondroitin sulfate during mineralization [97]. The same changing profiles occur in dental tissue, where in the predentine, biglycan and decorin are mostly associated with dermatan sulfate, whereas in the predentine/dentine interface, the chondroitin sulfate becomes predominant, and in the dentine itself, it is the only GAG chain identifiable [89], while keratan sulfate distribution in the predentine forms a gradient with a maximum toward the mineralization front [98]. Moreover, the position of the sulfate within the GAG also varies within these tissues, and the GAG length is longer in the dentine than in the predentine and in the dentine/predentine interface [89]. Interestingly, GAG components are active players in the mechanical properties of the dental tissues such as stiffness and ductility due to their physicochemical properties, their location, and also by modulating the collagen structure through interfibrillar bridges. GAGs are key factors in the dentin's ability to recover under strain and deformation events in a time-dependent manner

and contribute to the dental tissues' longevity and conservation of their mechanical integrity. GAGs are also thought to play a role in the mineralization; in dentine, chondroitin sulfate may allow the mineralization process through sequestering calcium ions. These mechanisms might be displayed in other mineralized tissues [99–103].

The nature of the GAG can also help to discriminate a tissue, e.g., decorin and biglycan are mostly associated with dermatan sulfate in the annulus fibrosus, but with chondroitin sulfate in the cartilage end-plate [87]. Moreover, the modifications occurring on SLRPs could be used to assess the differentiation stage of cells. In C2C12 mouse cells treated with the bone morphogenetic protein (BMP)-2, modifications to the decorin GAG chains' length take place during the differentiation from myoblast to osteoblast. In addition to being upregulated, decorin has longer GAG chains in induced cells [104].

Defective glycanation is correlated with pathological states, for instance in geroderma osteodysplastica. In the organism model corresponding to this pathology characterized by the early onset of osteoporosis, decorin and biglycan are glycanated to a lesser extent, and it is suggested that this defect is involved in the abnormal gain of periosteum thickness [90]. Equine degenerative suspensory ligament desmitis (DSL), which affects tendons, ligaments, and other connective tissues and resembles Ehlers–Danlos syndrome, correlates with the accumulation of decorin carrying abnormally glycosylated GAG chains [105]. In this case, chondroitin sulfate replaces the normal dermatan sulfate, and this modification leads to a reduced TGF- $\beta$ 1 binding affinity and the production of antibodies against decorin. There is no change in the level of dermatan sulfate epimerase, the enzyme in charge of the dermatan sulfate synthesis; however, in DSL, the tendon is associated with high levels of BMP-2, which may enhance proteoglycan production [106,107].

Furthermore, ECM assembly may be influenced by post-translational modifications affecting molecular interactions. These interactions in turn may regulate signaling pathways. The GAG chains of biglycan enhance the binding of calvarial osteoblastic cells from mouse to BMP-4. Consequently, the signaling pathway is more strongly activated, with an increased phosphorylation of Smad 1/5/8 and upregulation of a set of osteoblastic markers such as Cbfa1 (Runx2), osteopontin, bone sialoprotein (BSP) and osteocalcin. Therefore, biglycan plays a role in osteoblast differentiation as a cytokine reservoir thanks to its GAG chains [108]. Biglycan GAGs also play a crucial role on the Erk pathway promoting osteoblast differentiation, as no phosphorylation of Erk is observed when murine pre-osteoblasts are treated with biglycan lacking GAGs [109]. It is conceivable that the age-related evolution of SLRP GAGs is correlated with their balancing function on growth factors as, in juveniles, the osteoblast differentiation process needs to be active and fully functional [108]. Surprisingly, a study showed that although all forms of biglycan positively affect BMP-2 signaling in C2C12 myogenic cells, even if non-glycanated forms are more efficient, only the biglycan lacking GAG induces osteogenesis in a rat mandible-deficient model. The studies concluded that the biglycan positive effect on BMP-2 is inhibited by its GAG moieties. However, it is important to highlight that the cells in these studies are not at the same differentiation stages nor the same cell lines, but a role of GAGs dependent on the type of BMP cannot be excluded [108,110,111].

## 6. Other SLRP Post-Translational Events in Skeletal Tissues

### 6.1. Sulfation

Sulfated tyrosines were identified in fibromodulin, osteomodulin, lumican, and opticin [38,112]. The tyrosine sulfate domain of SLRPs is interacting with proteins, mimicking heparin via the highly negative charge produced in combination with acidic amino acids. Fibromodulin and osteomodulin were shown to bind heparin-binding protein through this specific domain, and the affinity varies via the sulfated tyrosine residues number and their position. When present on the fibromodulin N-terminal domain, it attracts the MMP-13 protease and guides the cleavage of the domain [113,114]. This specific domain is involved in the fibrillogenesis process. Fibromodulin can bind to collagen type I

by both its LRR and its N-terminal tyrosine sulfated domain, which allows it to interact simultaneously with two collagen molecules. That feature may be useful in the assembly and networking of the ECM. The sulfated domain affects the collagen fibril formation and induces a shortened lag phase, thus affecting the arrangement of collagen molecules into highly organized fibrils structures [115].

### 6.2. SLRP Degradation and Cleavage in Skeletal Tissues

In addition to their glycosylation and glycanation, SLRPs degradation interferes with their biological functions and adds a level of complexity to their network. In this part, we will discuss the degradation mechanisms of SLRPs and the impact on their biological functions.

Several MMPs have been recognized to cleave SLRP members *in vitro*. MMP-2, MMP-3, and MMP-7 can cleave the human recombinant decorin. Interestingly, MMP-2 and MMP-3 show decreased efficiency when decorin is lacking its GAG. The consequences of substrate affinity variation with respect to post-translational modification combined with the increase of non-glycanated forms through aging remains unclear [116]. Membrane-type matrix metalloproteinase-1 (MT1-MMP) can induce cleavage of the human recombinant lumican [117]. Fibromodulin is cleaved in the N-terminal region containing sulfated tyrosine when cartilage degradation is induced. MMP-13 can cleave fibromodulin in the region interacting with collagen fibrils [113,118]. MMP-13 is also able to cleave biglycan, opticin, and to a lesser extent, lumican and decorin. In the latter cases, the degradation products are of low abundance despite proven direct interaction between MMP-13 and decorin [119–121]. In human cartilage, MMP-1-2-3-7-8-9 were shown to be part of opticin catabolism with different proteolytic efficiencies, with MMP-2 and MMP-7 being the most efficient [122]. MMP-9 and MMP-12 can cleave biglycan, and the fragments produced appear to be relevant neo-epitopes associated with dysregulated ECM remodeling pathogenesis. Indeed, the biglycan fragments were increased in *ex vivo* degraded cartilage explants and in the serum of a rheumatoid arthritis (RA) rat model [123]. In addition to the MMPs, ADAMTS-4, ADAMTS-5, and granzyme B can be mentioned as efficient enzymes that cleave some SLRPs, as it was proven for biglycan, decorin, and opticin [122,124–126]. Chondroadherin can be digested by the serine protease HTRA1 in degenerated human intervertebral discs [127].

The various locations of the cleavage sites lead to numerous possibilities of SLRP fragments to be produced (Table 3). For instance, biglycan is processed in its N-terminal region [88,128] within its core, namely in its fifth LRR by ADAMTS-4 and ADAMTS-5 [124] and in its C-terminal region by MMPs [119]. The biological importance of this large variety of fragments remains an under-examined field and needs further research.

**Table 3.** Specific cleavage sites among the SLRP family in the skeletal tissues.

SLRP	Species	Cleavage Site	Protease	Technique	In Vivo Data	Ref
Decorin	Human	S241-L242	MMP2	N-terminal sequencing	-	[116]
		S241-L242	MMP3	N-terminal sequencing	-	
		D31-A32	MMP7	N-terminal sequencing	-	
		E274-L273	MMP7	N-terminal sequencing	-	
		S240-L241	MMP-13	N-terminal sequencing	Comparison with WB on cartilage	[119]
	Bovine	M200-K201	-	N-terminal sequencing	Extracted from fresh matrix tendon	[129]
		A209-D210	-			
		Q218-G219	-		Extracted from medium of cultured tendon	

Table 3. Cont.

SLRP	Species	Cleavage Site	Protease	Technique	In Vivo Data	Ref
Biglycan	Human	G177-V178	MMP-13	N-terminal sequencing	Comparison with WB on cartilage	[119]
	Bovine	N187-C188	ADAMTS-4 ADAMTS-5	N-terminal sequencing	Comparison with WB on cartilage	[124]
Fibromodulin	Human	Y63-T64	MMP-13	Data not shown	Data not shown	[113]
	Bovine	Y63-A64	MMP-13	Mass spectrometry	Extracted from cartilage explant	[113]
Opticin	Human	T87-S88	MMP-2 MMP-7	N-terminal sequencing	Comparison with WB on cartilage	[122]
		E443-L444	MMP-2 MMP-7			
		G114-L115	MMP-2 MMP-7	Prediction from [120]		
		A20-S21 E32-Q33	MMP-7 MMP-7	N-terminal sequencing		
Chondroadherin	Human	G104-L105 P109-A110	MMP-13 MMP-13	N-terminal sequencing	Comparison with WB on human cartilage; IHC on human cartilage and synovial membrane	[120]
		I80-Y81	HTRA1	Mass spectrometry	Comparison with WB on discs tissue	[127]

Corroborating the in vitro data, there is evidence that SLRPs are degraded in vivo. During the aging process, decorin and biglycan undergo degradation in bovine tendons [130]. Degraded biglycan, lumican, keratocan, and opticin fragments were found in human articular cartilage, while decorin and fibromodulin fragments were found in remodeling tissues from ovine intervertebral discs after a lesion [119,120,131]. The team of Zhen et al. (2008) [132] characterized several MMPs and ADAMTS that carry out the proteolysis of SLRPs; among them were biglycan, decorin, fibromodulin, osteoglycin, and PRELP. They showed that in human cartilage, biglycan, fibromodulin, and PRELP are cleaved by MMP-2, MMP-3, MMP-8, MMP-9, MMP-12, MMP-13, ADAMTS-4, and ADAMTS-5. Decorin can be digested by the same proteases except for MMP-9, lumican by MMP-12 and ADAMTS-4, and osteoglycin by MMP-2, MMP-8, and ADAMTS-4 [132]. The processing of SLRPs occurs in human knee, hip articular cartilage, and meniscus, as it was shown for decorin, biglycan, lumican, and keratocan. This fragmentation process is increased in tissues undergoing degradation, and there is a slight increase related with the aging process but not in every tissue. However, fewer fragments were found in tissues for fibromodulin. Interestingly, but not unexpectedly, fragments observed after in vitro cleavage of biglycan and decorin by MMP-13 correspond to the fragments characterized in vivo, in contrast to the fibromodulin fragments. Yet, it must be highlighted that a majority of the in vivo, so-called naturally occurring fragments do not correlate with fragments generated in vitro. This suggests that besides all the enzymes already identified to cleave the SLRPs, additional unknown enzymes may be involved in their degradation [119,133,134].

This phenomenon may lead to the alteration of ECM homeostasis and its biomechanical properties, and hence damage skeletal tissues over time [119,124,133,135,136]. An increased proteolysis of chondroadherin has also been observed in the scoliotic disc of some adolescent patients and in adult degenerative discs when compared to normal discs. The fragmentation of chondroadherin is also characteristic of the disease, the cleavage site-specific for disc degeneration is represented in Table 2, making the chondroadherin fragment an efficient biomarker [127,137]. In addition, other SLRPs present enhanced fragmentation patterns in pathological human and canine intervertebral discs [138–140].

Interestingly, the SLRP fragment pattern has been characterized in serum of osteoarthritic (OA) and RA patients and in the serum of animals with experimentally induced OA. This observation indicates a relationship between these pathologies and the SLRP degradation. The fragmentation pattern is more than a global OA feature; it is also specific to the SLRP member and the joint localization. For example, more cleavage products are detected in OA hip than in OA knee articular cartilage

for decorin, biglycan, lumican, and keratocan [133,136,141]. The extent of fibromodulin and opticin degradation by MMP-13 is correlated with the severity of the cartilage damage [113,119,120,142]. Knowing that almost all the members of the SLRP family are involved in collagen interaction as previously reviewed by Chen and Birk, 2013 [6], and that they have a protective function on collagen fibrils, their degradation could lead to the exposure of the MMP-13 cleavage site on the collagen, indicating a predisposition for the initiation of cartilage damage [113,118–120]. Consolidating this hypothesis, it was demonstrated that the maximal biglycan processing in the medial meniscus outer zone is concomitant with collagenolysis [126,143]. Moreover, treatment with RS 110–2481, an MMP-13 inhibitor, prevents not only SLRP degradation but also collagenolysis [119,144]. The loss of SLRPs weakens the cartilage's mechanical properties [119,136].

It appears that SLRP fragments are of interest to unravel the mechanism of OA, and some could be specifically beneficial to study. High levels of biglycan were found in synovial fluid, which is located in the joint cavities of OA and RA patients [145,146]. Treatments with soluble biglycan were reported to induce an inflammatory response in human chondrocytes through TLR-4 and NF- $\kappa$ B activation, enhancing the catabolic response in cartilage explants depending on their OA stage [146,147]. It was also demonstrated that cartilage neo-angiogenesis associated with inflammation [148] is related to the degradation of opticin, which is an inhibitor of angiogenesis, by regulating the adhesiveness of endothelial cells. In OA cartilage, opticin is a substrate for several proteases, and particularly MMP-7 [120,122,149].

The cleavage of SLRPs also impacts the accumulation of growth factors in the ECM. SLRPs are known to bind several growth factors, such as TGF- $\beta$ , FGF, and BMP, and block their biological activity [150]. Direct evidence of active TGF- $\beta$ 1 being released from decorin and biglycan upon cleavage by granzyme B, a protease that accumulates in the extracellular space during inflammation, was demonstrated. TGF- $\beta$ 1 was also released from decorin after proteolysis by MMP-2, MMP-3, or MMP-7. Biglycan, asporin, and fibromodulin were also found to bind TGF- $\beta$ , giving them the possibility to release it when cleaved [151,152]. Moreover, in SLRP knockout mice, there is an excessive activation of TGF- $\beta$ 1 signaling, leading to an impaired control on osteoprogenitor cells and chondrogenesis. These data suggest a mechanism by which the modulation of the bioavailability of cytokines such as TGF- $\beta$ 1 can correlate to the development or even the initiation of OA [8,116,125,153].

### 6.3. SLRP Intracellular Degradation Pathways

The intracellular catabolism requires the lysosomal system, and SLRPs can accumulate within cells when lysosomes are inhibited [129,154–158]. This mechanism appears to be partially competitive between SLRPs. The internalizing process is receptor-mediated, and the core protein involving the LRR structure is the ligand for the putative 51kDa and 26 kDa human receptors of endocytosis located at the plasma membrane and in the endosomal compartment. Furthermore, the presence of GAG modification adds a supplemental layer of control, as its presence negatively affects the uptake [159–163]. Interactions between SLRPs and other ECM proteins also interfere with the endocytosis, as only free SLRPs are degraded through the internal pathway [164]. Additional human receptors possibly involved in endocytosis were later characterized in a different cell type for decorin or biglycan, suggesting redundancy in receptors involved in SLRP endocytosis. The putative receptors encompass the first discovered 51 kDa and 26 kDa [159]; a 110 kDa receptor [165]; the IGFR [166], and the class A scavenger receptor [167]. In addition, for decorin, it was suggested that several endocytic pathways can be used such as the clathrin-dependant pathway and the Tfr/recycling pathway. It also appears that endocytosis is dependent on the signaling role of EGFR, the PI-3 kinase signaling, and the lipid rafts [168].

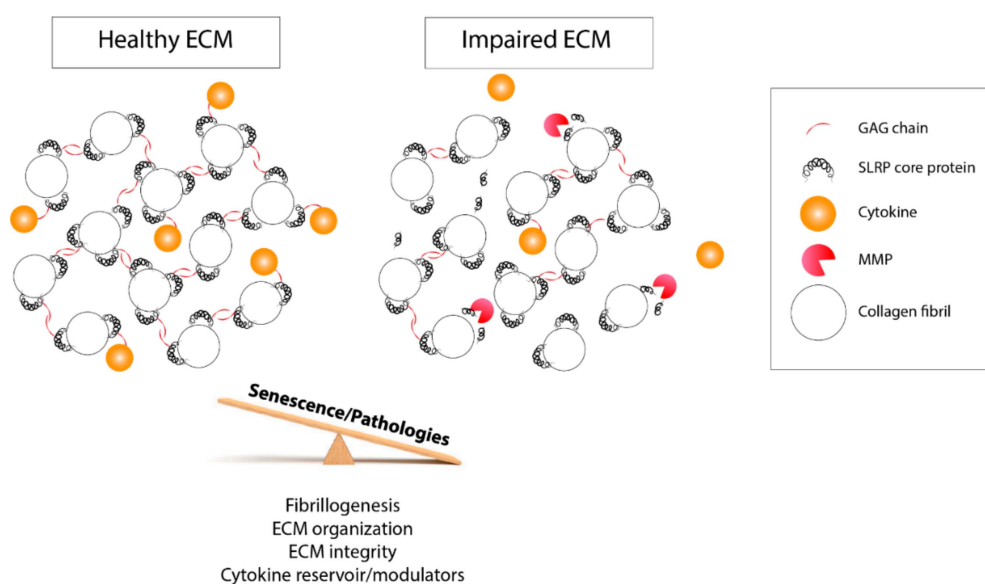
## 7. Conclusions

There is a great variability in codon usage among the SLRP coding sequences. This may impact the structure and stability of these proteoglycans. According to their codon usage, it appears that SLRPs split into two main clusters. However, it is currently unclear whether this variability in codon usage



plays a functional role at all. Further investigations are required to shed light on the causal mechanisms or chain of events by which codon usage may affect the differential SLRP translation rate and how codon usage is associated with pathological conditions. In summary, current assumptions, which are not necessarily mutually exclusive, are that rare codon usage clusters in the SLRP sequences are required to increase the time available to allow for proper folding or for adequate *in vivo* co-translational chemical tagging on specific amino acid residues for post-translational purposes, or to cause differential sensitivity to enzymatic tRNA modifications that occur under stressed conditions.

Similarly, there is great variability of glycosylation, GAG, and sulfotyrosine patterns, as well in the SLRP fragments detected. All are subject to changes according to the related tissue, age, and pathological conditions. These heterogeneous post-translational events can contribute to various structural and biological functions of SLRPs. Accordingly, one can define SLRPs as highly versatile components of the ECM. The presence of GAGs and sulfated tyrosine domain conditions their interactions with collagens and ECM proteins, and it can be considered as a factor in ECM assembly and integrity. They are also modulating cytokine activity and availability by sequestering them and are bringing a higher level of subtlety to the cellular response (Figure 4). Moreover, the presence of distinct and precise GAG motifs is involved in specific functions in different cellular contexts [169].



**Figure 4.** Schematic representation of the biological functions of post-translational modifications impacted by aging and pathology development. On the left panel, GAG side chains and the tyrosine sulfate-rich domain of SLRPs help to maintain the ECM biomechanical properties and the fibrillogenesis and organize the collagen fibrils. They regulate the cell response and their homeostasis through their interaction with cytokines and modulate their accessibility. On the right panel, following an imbalanced control of the post-translational events and MMP-driven degradation, the ECM biological properties are disturbed, which impedes the bioavailability of cytokines that are free to leave the ECM. This latter case can be prompted by a disease condition or the aging process.

Concerning the SLRP catabolism, it plays a role in cell responses as well by regulating the bioavailability of the molecules under the control of SLRPs. SLRPs themselves can lose their functions and properties under this process. The catabolism can be affected by aging and impaired by pathologies such as Ehlers–Danlos syndrome, OA, RA, or Kashin–Beck disease [170]. SLRPs form a protective coat protecting the ECM from collagenolysis induced by MMPs. Interestingly, alteration of the ECM content appears to be an early step in the progression of a pathology disrupting the ECM properties and functions and later deregulates the cell homeostasis (Figure 4). SLRP fragments can be soluble and circulate in biological fluid, where they might trigger a biological response in other tissues. This means that SLRPs could be actors in aging-related musculoskeletal and rheumatic diseases and could be

therapeutic targets. They could also be potential soluble biomarkers that are useful for the diagnosis and prognosis of disease progression as well as predictive of therapeutic response. Indeed, numerous SLRP fragments were identified through mass spectrometry to have the potential to be unique neopeptides characterizing pathologic conditions such as cartilage degradation and OA onset [132,171–175]. In particular, a biglycan neopeptide issued from MMP cleavage measured in rat serum is correlated with pathologies involving imbalanced ECM remodeling [123]. These features could be tracked down to follow the initiation and development of pathologies that are hard to diagnose at an early stage.

In summary, post-translational events encompass a large number of modifications in the SLRP core proteins. They help ECM assembly and are involved in the ECM physicochemical properties and remodeling. They are also required by cells to regulate responses with higher precision. They are valuable fingerprints of the tissues and a characterizing tool that can be used as biomarkers. Here, we focused on the SLRP post-translational events and degradation in skeletal tissues; however, they exert their modulation of biological functions in other tissues as well. Unfortunately, few studies discuss their functions and take them into account when analyzing results. Given the findings summarized in this review, we conclude that their biological functions are too often underestimated, and we hope that future studies will be more careful to consider the impact of post-translational events on biological functions and include them in their design.

**Supplementary Materials:** The supplementary materials are available online at <http://www.mdpi.com/2218-273X/10/1/80/s1>.

**Funding:** This research was funded by the F.R.S.-FNRS for the “EOS: The Excellence of Science -Join-t-against-Osteoarthritis”, grant number 30480119, and by a research grant from the Osteoarthritis Foundation. M.M. is a Maître de Recherche at FNRS.

**Acknowledgments:** The authors would like to thank Sing-E Lee from the University of Liège—Department of Life Sciences—GIGA for critically reading of the manuscript.

**Conflicts of Interest:** The authors declare no conflict of interest.

## References

1. Hynes, R.O.; Naba, A. Overview of the matrisome—An inventory of extracellular matrix constituents and functions. *Cold Spring Harb. Perspect. Biol.* **2012**, *4*, 4903. [CrossRef] [PubMed]
2. Bonnans, C.; Chou, J.; Werb, Z. Remodelling the extracellular matrix in development and disease. *Nat. Rev. Mol. Cell Biol.* **2014**, *15*, 786–801. [CrossRef] [PubMed]
3. Naba, A.; Clauser, K.R.; Ding, H.; Whittaker, C.A.; Carr, S.A.; Hynes, R.O. The extracellular matrix: Tools and insights for the “omics” era. *Matrix Biol.* **2016**, *49*, 10–24. [CrossRef] [PubMed]
4. Kalamajski, S.; Oldberg, A. The role of small leucine-rich proteoglycans in collagen fibrillogenesis. *Matrix Biol.* **2010**, *29*, 248–253. [CrossRef]
5. Nikitovic, A.; Aggelidakis, J.; Young, M.F.; Iozzo, R.V.; Karamanos, N.K.; Tzanakakis, G.N. The Biology of Small Leucine-rich Proteoglycans in Bone Pathophysiology. *J. Biol. Chem.* **2012**, *287*, 33926–33933. [CrossRef]
6. Chen, S.; Birk, D.E. The regulatory roles of small leucine-rich proteoglycans in extracellular matrix assembly. *FEBS J.* **2013**, *280*, 2120–2137. [CrossRef]
7. Chen, X.-D.; Fisher, L.W.; Robey, P.G.; Young, M.F. The small leucine-rich proteoglycan biglycan modulates BMP-4-induced osteoblast differentiation. *FASEB J.* **2004**, *18*, 948–958. [CrossRef]
8. Bi, Y.; Stuelten, C.H.; Kilts, T.; Wadhwa, S.; Iozzo, R.V.; Robey, P.G.; Chen, X.-D.; Young, M.F. Extracellular Matrix Proteoglycans Control the Fate of Bone Marrow Stromal Cells. *J. Biol. Chem.* **2005**, *280*, 30481–30489. [CrossRef]
9. Schaefer, L.; Iozzo, R. V Biological Functions of the Small Leucine-rich Proteoglycans: From Genetics to Signal Transduction. *J. Biol. Chem.* **2008**, *283*, 21305–21309. [CrossRef]
10. Kram, V.; Kilts, T.M.; Bhattacharyya, N.; Li, L.; Young, M.F. Small leucine rich proteoglycans, a novel link to osteoclastogenesis. *Sci. Rep.* **2017**, *7*, 12627. [CrossRef]
11. Marín, M. Folding at the rhythm of the rare codon beat. *Biotechnol. J.* **2008**, *3*, 1047–1057. [CrossRef] [PubMed]
12. Plotkin, J.B.; Kudla, G. Synonymous but not the same: The causes and consequences of codon bias. *Nat. Rev. Genet.* **2011**, *12*, 32–42. [CrossRef] [PubMed]

13. Sherman, M.Y.; Qian, S.-B. Less is more: Improving proteostasis by translation slow down. *Trends Biochem. Sci.* **2013**, *38*, 585–591. [[CrossRef](#)] [[PubMed](#)]
14. Brule, C.E.; Grayhack, E.J. Synonymous Codons: Choose Wisely for Expression. *Trends Genet.* **2017**, *33*, 283–297. [[CrossRef](#)]
15. Chan, C.; Pham, P.; Dedon, P.C.; Begley, T.J. Lifestyle modifications: Coordinating the tRNA epitranscriptome with codon bias to adapt translation during stress responses. *Genome Boil.* **2018**, *19*, 228. [[CrossRef](#)]
16. Duan, G.; Walther, D. The Roles of Post-translational Modifications in the Context of Protein Interaction Networks. *PLoS Comput. Boil.* **2015**, *11*, e1004049. [[CrossRef](#)]
17. Schaefer, L.; Schaefer, R.M. Proteoglycans: From structural compounds to signaling molecules. *Cell Tissue Res.* **2010**, *339*, 237–246. [[CrossRef](#)]
18. Iozzo, R.V.; Goldoni, S.; Berendsen, A.D.; Young, M.F. Small Leucine-Rich Proteoglycans. In *The Extracellular Matrix: An Overview*; Springer: Berlin/Heidelberg, Germany, 2011; pp. 197–231.
19. McEwan, P.A.; Scott, P.G.; Bishop, P.N.; Bella, J. Structural correlations in the family of small leucine-rich repeat proteins and proteoglycans. *J. Struct. Boil.* **2006**, *155*, 294–305. [[CrossRef](#)]
20. Kobe, B. The leucine-rich repeat as a protein recognition motif. *Curr. Opin. Struct. Boil.* **2001**, *11*, 725–732. [[CrossRef](#)]
21. Chen, S.; Sun, M.; Iozzo, R.V.; Kao, W.W.-Y.; Birk, D.E. Intracellularly-retained decorin lacking the C-terminal ear repeat causes ER stress: A cell-based etiological mechanism for congenital stromal corneal dystrophy. *Am. J. Pathol.* **2013**, *183*, 247–256. [[CrossRef](#)]
22. Prydz, K.; Dalen, K.T. Synthesis and sorting of proteoglycans. *J. Cell Sci.* **2000**, *113*, 193–205.
23. Funderburgh, J.L. Keratan Sulfate Biosynthesis. *IUBMB Life* **2002**, *54*, 187–194. [[CrossRef](#)] [[PubMed](#)]
24. Fuller, M.; Meikle, P.J.; Hopwood, J.J. Glycosaminoglycan degradation fragments in mucopolysaccharidosis I. *Glycobiology* **2004**, *14*, 443–450. [[CrossRef](#)] [[PubMed](#)]
25. Ernst, S.; Langer, R.; Cooney, C.L.; Sasisekharan, R. Enzymatic Degradation of Glycosaminoglycans. *Crit. Rev. Biochem. Mol. Boil.* **1995**, *30*, 387–444. [[CrossRef](#)]
26. Krishnan, P.; Hocking, A.M.; Scholtz, J.M.; Pace, C.N.; Holik, K.K.; McQuillan, D.J. Distinct secondary structures of the leucine-rich repeat proteoglycans decorin and biglycan. Glycosylation-dependent conformational stability. *J. Boil. Chem.* **1999**, *274*, 10945–10950. [[CrossRef](#)] [[PubMed](#)]
27. Seo, N.-S.; Hocking, A.M.; Höök, M.; McQuillan, D.J. Decorin Core Protein Secretion Is Regulated by N-Linked Oligosaccharide and Glycosaminoglycan Additions. *J. Boil. Chem.* **2005**, *280*, 42774–42784. [[CrossRef](#)]
28. Bateman, A. UniProt: A worldwide hub of protein knowledge. *Nucleic Acids Res.* **2019**, *28*, 32.
29. Fisher, L.W.; Termine, J.D.; Young, M.F. Deduced protein sequence of bone small proteoglycan I (biglycan) shows homology with proteoglycan II (decorin) and several nonconnective tissue proteins in a variety of species. *J. Boil. Chem.* **1989**, *264*, 4571–4576.
30. Johnson, H.J.; Rosenberg, L.; Choi, H.U.; Garza, S.; Höök, M.; Neame, P.J. Characterization of epiphycan, a small proteoglycan with a leucine-rich repeat core protein. *J. Boil. Chem.* **1997**, *272*, 18709–18717. [[CrossRef](#)]
31. Iozzo, R.V.; Schaefer, L. Proteoglycan form and function: A comprehensive nomenclature of proteoglycans. *Matrix Boil.* **2015**, *42*, 11–55. [[CrossRef](#)]
32. Roughley, P.J.; White, R.J. Dermatan sulphate proteoglycans of human articular cartilage. The properties of dermatan sulphate proteoglycans I and II. *Biochem. J.* **1989**, *262*, 823–827. [[CrossRef](#)] [[PubMed](#)]
33. Krusius, T.; Ruoslahti, E. Primary structure of an extracellular matrix proteoglycan core protein deduced from cloned cDNA. *Proc. Natl. Acad. Sci. USA* **1986**, *83*, 7683–7687. [[CrossRef](#)] [[PubMed](#)]
34. Klein, J.A.; Meng, L.; Zaia, J. Deep sequencing of complex proteoglycans: A novel strategy for high coverage and sitespecific identification of glycosaminoglycanlinked peptides. *Mol. Cell. Proteom.* **2018**, *17*, 1578–1590. [[CrossRef](#)] [[PubMed](#)]
35. Lorenzo, P.; Aspberg, A.; Önnarfjord, P.; Bayliss, M.T.; Neame, P.J.; Heinegård, D. Identification and Characterization of Asporin. *J. Boil. Chem.* **2001**, *276*, 12201–12211. [[CrossRef](#)] [[PubMed](#)]
36. Blochberger, T.C.; Vergnes, J.P.; Hempel, J.; Hassell, J.R. cDNA to chick lumican (corneal keratan sulfate proteoglycan) reveals homology to the small interstitial proteoglycan gene family and expression in muscle and intestine. *J. Boil. Chem.* **1992**, *267*, 347–352.
37. Cornuet, P.K.; Blochberger, T.C.; Hassell, J.R. Molecular polymorphism of lumican during corneal development. *Investig. Ophthalmol. Vis. Sci.* **1994**, *35*, 870–877.

38. Önnerfjord, P.; Heathfield, T.F.; Heinegård, D. Identification of Tyrosine Sulfation in Extracellular Leucine-rich Repeat Proteins Using Mass Spectrometry. *J. Biol. Chem.* **2004**, *279*, 26–33. [[CrossRef](#)]
39. Corpuz, L.M.; Funderburgh, J.L.; Funderburgh, M.L.; Bottomley, G.S.; Prakash, S.; Conrad, G.W. Molecular cloning and tissue distribution of keratocan. Bovine corneal keratan sulfate proteoglycan 37A. *J. Biol. Chem.* **1996**, *271*, 9759–9763. [[CrossRef](#)]
40. Oldberg, A.; Antonsson, P.; Lindblom, K.; Heinegård, D. A collagen-binding 59-kd protein (fibromodulin) is structurally related to the small interstitial proteoglycans PG-S1 and PG-S2 (decorin). *EMBO J.* **1989**, *8*, 2601–2604. [[CrossRef](#)]
41. Antonsson, P.; Heinegård, D.; Oldberg, A. Posttranslational Modifications of Fibromodulin. *J. Biol. Chem.* **1991**, *267*, 6132–6136.
42. Plaas, A.H.; Wong-Palms, S. Biosynthetic mechanisms for the addition of poly lactosamine to chondrocyte fibromodulin. *J. Biol. Chem.* **1993**, *268*, 26634–26644.
43. Wendel, M.; Sommarin, Y.; Heinegård, D. Characterization of osteoadherin—a novel, cell binding keratan sulfate proteoglycan from bone. *Acta Orthop. Scand.* **1995**, *66*, 77. [[CrossRef](#)]
44. Wendel, M.; Sommarin, Y.; Heinegård, D. Bone Matrix Proteins: Isolation and Characterization of a Novel Cell-binding Keratan Sulfate Proteoglycan (Osteoadherin) from Bovine Bone. *J. Cell Biol.* **1998**, *141*, 839–847. [[CrossRef](#)] [[PubMed](#)]
45. Sommarin, Y. Osteoadherin, a Cell-binding Keratan Sulfate Proteoglycan in Bone, Belongs to the Family of Leucine-rich Repeat Proteins of the Extracellular Matrix. *J. Biol. Chem.* **1998**, *273*, 16723–16729. [[CrossRef](#)] [[PubMed](#)]
46. Bengtsson, E.; Neame, P.J.; Heinegård, D.; Sommarin, Y. The Primary Structure of a Basic Leucine-rich Repeat Protein, PRELP, Found in Connective Tissues. *J. Biol. Chem.* **1995**, *270*, 25639–25644. [[CrossRef](#)]
47. Bengtsson, E.; Aspberg, A.; Heinegård, D.; Sommarin, Y.; Spillmann, D. The Amino-terminal Part of PRELP Binds to Heparin and Heparan Sulfate. *J. Biol. Chem.* **2000**, *275*, 40695–40702. [[CrossRef](#)]
48. Bentz, H.; Nathan, R.M.; Rosen, D.M.; Armstrong, R.M.; Thompson, A.Y.; Segarini, P.R.; Mathews, M.C.; Dasch, J.R.; Piez, K.A.; Seyedin, S.M. Purification and characterization of a unique osteoinductive factor from bovine bone. *J. Biol. Chem.* **1989**, *264*, 20805–20810.
49. Funderburgh, J.L.; Corpuz, L.M.; Roth, M.R.; Funderburgh, M.L.; Tasheva, E.S.; Conrad, G.W. Mimecan, the 25-kDa corneal keratan sulfate proteoglycan, is a product of the gene producing osteoglycin. *J. Biol. Chem.* **1997**, *272*, 28089–28095. [[CrossRef](#)]
50. Kampmann, A.; Fernández, B.; Deindl, E.; Kubin, T.; Pipp, F.; Eitenmüller, I.; Hofer, I.E.; Schaper, W.; Zimmermann, R. The proteoglycan osteoglycin/mimecan is correlated with arteriogenesis. *Mol. Cell. Biochem.* **2009**, *322*, 15–23. [[CrossRef](#)]
51. Rienks, M.; Papageorgiou, A.; Wouters, K.; Verhesen, W.; van Leeuwen, R.; Carai, P.; Summer, G.; Westermann, D.; Heymans, S. A novel 72-kDa leukocyte-derived osteoglycin enhances the activation of toll-like receptor 4 and exacerbates cardiac inflammation during viral myocarditis. *Cell. Mol. Life Sci.* **2017**, *74*, 1511–1525. [[CrossRef](#)]
52. Madisen, L.; Neubauer, M.; Plowman, G.; Rosen, D.; Segarini, P.; Dasch, J.; Thompson, A.; Ziman, J.; Bentz, H.; Purchio, A. Molecular Cloning of a Novel Bone-Forming Compound: Osteoinductive Factor. *DNA Cell Biol.* **1990**, *9*, 303–309. [[CrossRef](#)] [[PubMed](#)]
53. Reardon, A.J.; Le Goff, M.; Briggs, M.D.; McLeod, D.; Sheehan, J.K.; Thornton, D.J.; Bishop, P.N. Identification in vitreous and molecular cloning of opticin, a novel member of the family of leucine-rich repeat proteins of the extracellular matrix. *J. Biol. Chem.* **2000**, *275*, 2123–2129. [[CrossRef](#)] [[PubMed](#)]
54. Hobby, P.; Wyatt, M.K.; Gan, W.; Bernstein, S.; Tomarev, S.; Slingsby, C.; Wistow, G. Cloning, modeling, and chromosomal localization for a small leucine-rich repeat proteoglycan (SLRP) family member expressed in human eye. *Mol. Vis.* **2000**, *6*, 72–78. [[PubMed](#)]
55. Neame, P.J.; Sommarin, Y.; Boynton, R.E.; Heinegård, D. The structure of a 38-kDa leucine-rich protein (chondroadherin) isolated from bovine cartilage. *J. Biol. Chem.* **1994**, *269*, 21547–21554.
56. Shimizu-Hirota, R.; Sasamura, H.; Kuroda, M.; Kobayashi, E.; Saruta, T. Functional characterization of podocan, a member of a new class in the small leucine-rich repeat protein family. *FEBS Lett.* **2004**, *563*, 69–74. [[CrossRef](#)]

57. Ross, M.D.; Bruggeman, L.A.; Hanss, B.; Marras, D.; Klotman, M.E.; Sunamoto, M.; Klotman, P.E. Podocan, a Novel Small Leucine-rich Repeat Protein Expressed in the Sclerotic Glomerular Lesion of Experimental HIV-associated Nephropathy. *J. Boil. Chem.* **2003**, *278*, 33248–33255. [[CrossRef](#)]
58. Mochida, Y.; Kaku, M.; Yoshida, K.; Katafuchi, M.; Atsawasuwan, P.; Yamauchi, M. Podocan-like protein: A novel small leucine-rich repeat matrix protein in bone. *Biochem. Biophys. Res. Commun.* **2011**, *410*, 333–338.
59. Endres, L.; Dedon, P.C.; Begley, T.J. Codon-biased translation can be regulated by wobble-base tRNA modification systems during cellular stress responses. *RNA Biol.* **2015**, *12*, 603–614. [[CrossRef](#)]
60. Rapino, F.; Delaunay, S.; Zhou, Z.; Chariot, A.; Close, P. tRNA Modification: Is Cancer Having a Wobble? *Trends Cancer* **2017**, *3*, 249–252. [[CrossRef](#)]
61. Hou, Y.-M.; Gamper, H.; Yang, W. Post-transcriptional modifications to tRNA—a response to the genetic code degeneracy. *RNA* **2015**, *21*, 642–644. [[CrossRef](#)]
62. Rapino, F.; Delaunay, S.; Rambow, F.; Zhou, Z.; Tharun, L.; De Tullio, P.; Sin, O.; Shostak, K.; Schmitz, S.; Piepers, J.; et al. Codon-specific translation reprogramming promotes resistance to targeted therapy. *Nat.* **2018**, *558*, 605–609. [[CrossRef](#)] [[PubMed](#)]
63. James, G.; Witten, D.; Hastie, T.; Tibshirani, R. *An Introduction to Statistical Learning*; Springer: New York, NY, USA, 2013; Volume 112, p. 18.
64. Raspanti, M.; Viola, M.; Forlino, A.; Tenni, R.; Gruppi, C.; Tira, M.E. Glycosaminoglycans show a specific periodic interaction with type I collagen fibrils. *J. Struct. Boil.* **2008**, *164*, 134–139. [[CrossRef](#)] [[PubMed](#)]
65. Tatara, Y.; Kakizaki, I.; Suto, S.; Ishioka, H.; Negishi, M.; Endo, M. Chondroitin sulfate cluster of epiphycan from salmon nasal cartilage defines binding specificity to collagens. *Glycobiology* **2015**, *25*, 557–569. [[CrossRef](#)] [[PubMed](#)]
66. Lewis, P.N.; Pinali, C.; Young, R.D.; Meek, K.M.; Quantock, A.J.; Knupp, C. Structural Interactions between Collagen and Proteoglycans Are Elucidated by Three-Dimensional Electron Tomography of Bovine Cornea. *Structure* **2010**, *18*, 239–245. [[CrossRef](#)]
67. Parfitt, G.J.; Pinali, C.; Young, R.D.; Quantock, A.J.; Knupp, C. Three-dimensional reconstruction of collagen–proteoglycan interactions in the mouse corneal stroma by electron tomography. *J. Struct. Boil.* **2010**, *170*, 392–397. [[CrossRef](#)]
68. Stamov, D.R.; Müller, A.; Wegrowski, Y.; Brezillon, S.; Franz, C.M.; Müller, A. Quantitative analysis of type I collagen fibril regulation by lumican and decorin using AFM. *J. Struct. Boil.* **2013**, *183*, 394–403. [[CrossRef](#)]
69. Scott, J.E. Extracellular matrix, supramolecular organisation and shape. *J. Anat.* **1995**, *187*, 259–269.
70. Scott, J.E.; Thomlinson, A.M. The structure of interfibrillar proteoglycan bridges ('shape modules') in extracellular matrix of fibrous connective tissues and their stability in various chemical environments. *J. Anat.* **1998**, *192*, 391–405. [[CrossRef](#)]
71. Lujan, T.J.; Underwood, C.J.; Henninger, H.B.; Thompson, B.M.; Weiss, J.A. Effect of dermatan sulfate glycosaminoglycans on the quasi-static material properties of the human medial collateral ligament. *J. Orthop. Res.* **2007**, *25*, 894–903. [[CrossRef](#)]
72. Seidler, D.G.; Faiyaz-UI-Haque, M.; Hansen, U.; Yip, G.W.; Zaidi, S.H.E.; Teebi, A.S.; Kiesel, L.; Götte, M. Defective glycosylation of decorin and biglycan, altered collagen structure, and abnormal phenotype of the skin fibroblasts of an Ehlers–Danlos syndrome patient carrying the novel Arg270Cys substitution in galactosyltransferase I ( $\beta$ 4GalT-7). *J. Mol. Med.* **2006**, *84*, 583–594. [[CrossRef](#)]
73. Rühland, C.; Schönherr, E.; Robenek, H.; Hansen, U.; Iozzo, R.V.; Bruckner, P.; Seidler, D.G. The glycosaminoglycan chain of decorin plays an important role in collagen fibril formation at the early stages of fibrillogenesis. *FEBS J.* **2007**, *274*, 4246–4255. [[CrossRef](#)] [[PubMed](#)]
74. Malfait, F.; Kariminejad, A.; Van Damme, T.; Gauche, C.; Syx, D.; Merhi-Soussi, F.; Gulberti, S.; Symoens, S.; Vanhauwaert, S.; Willaert, A.; et al. Defective initiation of glycosaminoglycan synthesis due to B3GALT6 mutations causes a pleiotropic Ehlers–Danlos-syndrome-like connective tissue disorder. *Am. J. Hum. Genet.* **2013**, *92*, 935–945. [[CrossRef](#)] [[PubMed](#)]
75. Moffatt, P.; Geng, Y.; Lamplugh, L.; Nanci, A.; Roughley, P.J. Absence of the dermatan sulfate chain of decorin does not affect mouse development. *J. Negat. Results Biomed.* **2017**, *16*, 7. [[CrossRef](#)] [[PubMed](#)]
76. Reese, S.P.; Underwood, C.J.; Weiss, J.A. Effects of decorin proteoglycan on fibrillogenesis, ultrastructure, and mechanics of type I collagen gels. *Matrix Boil.* **2013**, *32*, 414–423. [[CrossRef](#)] [[PubMed](#)]
77. Scott, J.E. Elasticity in extracellular matrix 'shape modules' of tendon, cartilage, etc. A sliding proteoglycan-filament model. *J. Physiol.* **2003**, *553*, 335–343. [[CrossRef](#)] [[PubMed](#)]

78. Redaelli, A.; Vesentini, S.; Soncini, M.; Vena, P.; Mantero, S.; Montevercchi, F. Possible role of decorin glycosaminoglycans in fibril to fibril force transfer in relative mature tendons—A computational study from molecular to microstructural level. *J. Biomech.* **2003**, *36*, 1555–1569. [[CrossRef](#)]
79. Vesentini, S.; Redaelli, A.; Montevercchi, F.M. Estimation of the binding force of the collagen molecule-decorin core protein complex in collagen fibril. *J. Biomech.* **2005**, *38*, 433–443. [[CrossRef](#)]
80. Liao, J.; Vesely, I. Skewness angle of interfibrillar proteoglycans increases with applied load on mitral valve chordae tendineae. *J. Biomech.* **2007**, *40*, 390–398. [[CrossRef](#)]
81. Lujan, T.J.; Underwood, C.J.; Jacobs, N.T.; Weiss, J.A. Contribution of glycosaminoglycans to viscoelastic tensile behavior of human ligament. *J. Appl. Physiol.* **2009**, *106*, 423–431. [[CrossRef](#)]
82. Fessel, G.; Snedeker, J.G. Equivalent stiffness after glycosaminoglycan depletion in tendon—An ultra-structural finite element model and corresponding experiments. *J. Theor. Boil.* **2011**, *268*, 77–83. [[CrossRef](#)]
83. Svensson, R.B.; Hassenkam, T.; Hansen, P.; Kjaer, M.; Magnusson, S.P. Tensile Force Transmission in Human Patellar Tendon Fascicles Is Not Mediated by Glycosaminoglycans. *Connect. Tissue Res.* **2011**, *52*, 415–421. [[CrossRef](#)] [[PubMed](#)]
84. Choi, R.K.; Smith, M.M.; Martin, J.H.; Clarke, J.L.; Dart, A.J.; Little, C.B.; Clarke, E.C. Chondroitin sulphate glycosaminoglycans contribute to widespread inferior biomechanics in tendon after focal injury. *J. Biomech.* **2016**, *49*, 2694–2701. [[CrossRef](#)] [[PubMed](#)]
85. Rigozzi, S.; Müller, R.; Stemmer, A.; Snedeker, J. Tendon glycosaminoglycan proteoglycan sidechains promote collagen fibril sliding—AFM observations at the nanoscale. *J. Biomech.* **2013**, *46*, 813–818. [[CrossRef](#)] [[PubMed](#)]
86. Tatara, Y.; Suto, S.; Itoh, K. Novel roles of glycosaminoglycans in the degradation of type I collagen by cathepsin K. *Glycobiology* **2017**, *27*, 1089–1098. [[CrossRef](#)]
87. Johnstone, B.; Markopoulos, M.; Neame, P.; Caterson, B. Identification and characterization of glycanated and non-glycanated forms of biglycan and decorin in the human intervertebral disc. *Biochem. J.* **1993**, *292*, 661–666. [[CrossRef](#)]
88. Roughley, P.J.; White, R.J.; Magny, M.C.; Liu, J.; Pearce, R.H.; Mort, J.S. Non-proteoglycan forms of biglycan increase with age in human articular cartilage. *Biochem. J.* **1993**, *295*, 421–426. [[CrossRef](#)]
89. Waddington, R.; Hall, R.; Embery, G.; Lloyd, D. Changing profiles of proteoglycans in the transition of pre-dentine to dentine. *Matrix Boil.* **2003**, *22*, 153–161. [[CrossRef](#)]
90. Chan, W.L.; Steiner, M.; Witkos, T.; Egerer, J.; Busse, B.; Mizumoto, S.; Pestka, J.M.; Zhang, H.; Hausser, I.; Khayal, L.A.; et al. Impaired proteoglycan glycosylation, elevated TGF- $\beta$  signaling, and abnormal osteoblast differentiation as the basis for bone fragility in a mouse model for gerodermia osteodysplastica. *PLoS Genet.* **2018**, *14*, e1007242. [[CrossRef](#)]
91. Derwin, K.A.; Soslowsky, L.J.; Kimura, J.H.; Plaas, A.H. Proteoglycans and glycosaminoglycan fine structure in the mouse tail tendon fascicle. *J. Orthop. Res.* **2001**, *19*, 269–277. [[CrossRef](#)]
92. Roughley, P.J.; White, R.J.; Cs-Szabó, G.; Mort, J.S. Changes with age in the structure of fibromodulin in human articular cartilage. *Osteoarthr. Cartil.* **1996**, *4*, 153–161. [[CrossRef](#)]
93. Santer, V.; White, R.J.; Roughley, P.J. O-linked oligosaccharides of human articular cartilage proteoglycan. *BBA Gen. Subj.* **1982**, *716*, 277–282. [[CrossRef](#)]
94. Grover, J.; Chen, X.N.; Korenberg, J.R.; Roughley, P.J. The human lumican gene. Organization, chromosomal location, and expression in articular cartilage. *J. Boil. Chem.* **1995**, *270*, 21942–21949. [[CrossRef](#)] [[PubMed](#)]
95. Melching, L.I.; Roughley, P.J. Modulation of keratan sulfate synthesis on lumican by the action of cytokines on human articular chondrocytes. *Matrix Boil.* **1999**, *18*, 381–390. [[CrossRef](#)]
96. Sugars, R.V.; Olsson, M.L.; Marchner, S.; Hulthenby, K.; Wendel, M. The glycosylation profile of osteoadherin alters during endochondral bone formation. *Bone* **2013**, *53*, 459–467. [[CrossRef](#)] [[PubMed](#)]
97. Waddington, R.J.; Roberts, H.C.; Sugars, R.V.; Schönherr, E. Differential roles for small leucine-rich proteoglycans in bone formation. *Eur Cell Mater* **2003**, *6*, 12–21. [[CrossRef](#)] [[PubMed](#)]
98. Goldberg, M.; Rapoport, O.; Septier, D.; Palmier, K.; Hall, R.; Embery, G.; Young, M.; Ameye, L. Proteoglycans in pre-dentine: The last 15 micrometers before mineralization. *Connect. Tissue Res.* **2003**, *44*, 184–188. [[CrossRef](#)]
99. Ho, S.P.; Sulyanto, R.M.; Marshall, S.J.; Marshall, G.W. The cementum–dentin junction also contains glycosaminoglycans and collagen fibrils. *J. Struct. Boil.* **2005**, *151*, 69–78. [[CrossRef](#)]
100. Bertassoni, L.E.; Stankoska, K.; Swain, M.V. Insights into the structure and composition of the peritubular dentin organic matrix and the lamina limitans. *Micron* **2012**, *43*, 229–236. [[CrossRef](#)]

101. Bertassoni, L.E.; Kury, M.; Rathsam, C.; Little, C.B.; Swain, M.V. The role of proteoglycans in the nanoindentation creep behavior of human dentin. *J. Mech. Behav. Biomed. Mater.* **2015**, *55*, 264–270. [[CrossRef](#)]
102. Dorvee, J.R.; Gerkowicz, L.; Bahmanyar, S.; Deymier-Black, A.; Veis, A. Chondroitin sulfate is involved in the hypercalcification of the organic matrix of bovine peritubular dentin. *Arch. Oral Biol.* **2016**, *62*, 93–100. [[CrossRef](#)]
103. Farina, A.P.; Vidal, C.M.P.; Cecchin, D.; Aguiar, T.R.; Bedran-Russo, A.K. Structural and biomechanical changes to dentin extracellular matrix following chemical removal of proteoglycans. *Odontology* **2019**, *107*, 316–323. [[CrossRef](#)] [[PubMed](#)]
104. Gutierrez, J.; Osses, N.; Brandan, E. Changes in secreted and cell associated proteoglycan synthesis during conversion of myoblasts to osteoblasts in response to bone morphogenetic protein-2: Role of decorin in cell response to BMP-2. *J. Cell Physiol.* **2006**, *206*, 58–67. [[CrossRef](#)] [[PubMed](#)]
105. Halper, J.; Kim, B.; Khan, A.; Yoon, J.H.; Mueller, P.O.E. Degenerative suspensory ligament desmitis as a systemic disorder characterized by proteoglycan accumulation. *BMC Vet. Res.* **2006**, *2*, 12. [[CrossRef](#)] [[PubMed](#)]
106. Kim, B.; Yoon, J.H.; Zhang, J.; Mueller, P.E.; Halper, J. Glycan profiling of a defect in decorin glycosylation in equine systemic proteoglycan accumulation, a potential model of progeroid form of Ehlers-Danlos syndrome. *Arch. Biochem. Biophys.* **2010**, *501*, 221–231. [[CrossRef](#)]
107. Young, M.; Moshood, O.; Zhang, J.; Sarbacher, C.A.; Mueller, P.O.E.; Halper, J. Does BMP2 play a role in the pathogenesis of equine degenerative suspensory ligament desmitis? *BMC Res. Notes* **2018**, *11*, 672. [[CrossRef](#)]
108. Ye, Y.; Hu, W.; Guo, F.; Zhang, W.; Wang, J.; Chen, A. Glycosaminoglycan chains of biglycan promote bone morphogenetic protein-4-induced osteoblast differentiation. *Int. J. Mol. Med.* **2012**, *30*, 1075–1080. [[CrossRef](#)]
109. Wang, X.; Harimoto, K.; Xie, S.; Cheng, H.; Liu, J.; Wang, Z. Matrix protein biglycan induces osteoblast differentiation through extracellular signal-regulated kinase and Smad pathways. *Boil. Pharm. Bull.* **2010**, *33*, 1891–1897. [[CrossRef](#)]
110. Miguez, P.; Terajima, M.; Nagaoka, H.; Mochida, Y.; Yamauchi, M. Role of Glycosaminoglycans of Biglycan in BMP-2 Signaling. *Biochem. Biophys. Res. Commun.* **2011**, *405*, 262–266. [[CrossRef](#)]
111. Miguez, P.; Terajima, M.; Nagaoka, H.; Ferreira, J.; Braswell, K.; Ko, C.; Yamauchi, M. Recombinant Biglycan Promotes Bone Morphogenetic Protein-induced Osteogenesis. *J. Dent. Res.* **2014**, *93*, 406–411. [[CrossRef](#)]
112. Kanan, Y.; Siefert, J.C.; Kinter, M.; Al-Ubaidi, M.R. Complement factor H, vitronectin, and opticin are tyrosine-sulfated proteins of the retinal pigment epithelium. *PLoS ONE* **2014**, *9*, e105409. [[CrossRef](#)]
113. Heathfield, T.F.; Önnarfjord, P.; Dahlberg, L.; Heinegård, D. Cleavage of Fibromodulin in Cartilage Explants Involves Removal of the N-terminal Tyrosine Sulfate-rich Region by Proteolysis at a Site That Is Sensitive to Matrix Metalloproteinase-13. *J. Biol. Chem.* **2004**, *279*, 6286–6295. [[CrossRef](#)] [[PubMed](#)]
114. Tillgren, V.; Önnarfjord, P.; Haglund, L.; Heinegård, D. The Tyrosine Sulfate-rich Domains of the LRR Proteins Fibromodulin and Osteoadherin Bind Motifs of Basic Clusters in a Variety of Heparin-binding Proteins, Including Bioactive Factors. *J. Biol. Chem.* **2009**, *284*, 28543–28553. [[CrossRef](#)] [[PubMed](#)]
115. Tillgren, V.; Mörgelin, M.; Önnarfjord, P.; Kalamajski, S.; Aspberg, A. The Tyrosine Sulfate Domain of Fibromodulin Binds Collagen and Enhances Fibril Formation. *J. Biol. Chem.* **2016**, *291*, 23744–23755. [[CrossRef](#)] [[PubMed](#)]
116. Imai, K.; Hiramatsu, A.; Fukushima, D.; Pierschbacher, M.D.; Okada, Y. Degradation of decorin by matrix metalloproteinases: Identification of the cleavage sites, kinetic analyses and transforming growth factor- $\beta$ 1 release. *Biochem. J.* **1997**, *322*, 809–814. [[CrossRef](#)]
117. Li, Y.; Aoki, T.; Mori, Y.; Ahmad, M.; Miyamori, H.; Takino, T.; Sato, H. Cleavage of Lumican by Membrane-Type Matrix Metalloproteinase-1 Abrogates This Proteoglycan-Mediated Suppression of Tumor Cell Colony Formation in Soft Agar. *Cancer Res.* **2004**, *64*, 7058–7064. [[CrossRef](#)]
118. Geng, Y.; McQuillan, D.; Roughley, P.J. SLRP interaction can protect collagen fibrils from cleavage by collagenases. *Matrix Biol.* **2006**, *25*, 484–491. [[CrossRef](#)]
119. Monfort, J.; Tardif, G.; Reboul, P.; Mineau, F.; Roughley, P.; Pelletier, J.-P.; Martel-Pelletier, J. Degradation of small leucine-rich repeat proteoglycans by matrix metalloproteinase-13: Identification of a new biglycan cleavage site. *Arthritis Res. Ther.* **2006**, *8*, 26. [[CrossRef](#)]

120. Monfort, J.; Tardif, G.; Roughley, P.; Reboul, P.; Boileau, C.; Bishop, P.; Pelletier, J.-P.; Martel-Pelletier, J. Identification of opticin, a member of the small leucine-rich repeat proteoglycan family, in human articular tissues: A novel target for MMP-13 in osteoarthritis. *Osteoarthr. Cartil.* **2008**, *16*, 749–755. [[CrossRef](#)]
121. Zhang, L.; Yang, M.; Yang, N.; Cavey, G.; Davidson, P.; Gibson, G. Molecular Interactions of MMP-13 C-Terminal Domain with Chondrocyte Proteins. *Connect. Tissue Res.* **2010**, *51*, 230–239. [[CrossRef](#)]
122. Tio, L.; Martel-Pelletier, J.; Pelletier, J.-P.; Bishop, P.N.; Roughley, P.; Farran, A.; Benito, P.; Monfort, J. Characterization of opticin digestion by proteases involved in osteoarthritis development. *Jt. Bone Spine* **2014**, *81*, 137–141. [[CrossRef](#)]
123. Genovese, F.; Barascuk, N.; Larsen, L.; Larsen, M.R.; Nawrocki, A.; Li, Y.; Zheng, Q.; Wang, J.; Veidal, S.S.; Leeming, D.J.; et al. Biglycan fragmentation in pathologies associated with extracellular matrix remodeling by matrix metalloproteinases. *Fibrogenesis Tissue Repair* **2013**, *6*, 9. [[CrossRef](#)] [[PubMed](#)]
124. Melching, L.; Fisher, W.; Lee, E.; Mort, J.; Roughley, P. The cleavage of biglycan by aggrecanases. *Osteoarthr. Cartil.* **2006**, *14*, 1147–1154. [[CrossRef](#)] [[PubMed](#)]
125. Boivin, W.A.; Shackelford, M.; Vanden Hoek, A.; Zhao, H.; Hackett, T.L.; Knight, D.A.; Granville, D.J. Granzyme B Cleaves Decorin, Biglycan and Soluble Betaglycan, Releasing Active Transforming Growth Factor- $\beta$ 1. *PLoS ONE* **2012**, *7*, 33163. [[CrossRef](#)]
126. Fuller, E.; Little, C.B.; Melrose, J. Interleukin-1 $\alpha$  induces focal degradation of biglycan and tissue degeneration in an in-vitro ovine meniscal model. *Exp. Mol. Pathol.* **2016**, *101*, 214–220. [[CrossRef](#)] [[PubMed](#)]
127. Akhatib, B.; Onnerfjord, P.; Gawri, R.; Ouellet, J.; Jarzem, P.; Heinegård, D.; Mort, J.; Roughley, P.; Haglund, L. Chondroadherin Fragmentation Mediated by the Protease HTRA1 Distinguishes Human Intervertebral Disc Degeneration from Normal Aging. *J. Biol. Chem.* **2013**, *288*, 19280–19287. [[CrossRef](#)] [[PubMed](#)]
128. Scott, I.C.; Imamura, Y.; Pappano, W.N.; Troedel, J.M.; Recklies, A.D.; Roughley, P.J.; Greenspan, D.S. Bone Morphogenetic Protein-1 Processes Probiglycan. *J. Biol. Chem.* **2000**, *275*, 30504–30511. [[CrossRef](#)]
129. Samiric, T.; Ilic, M.Z.; Handley, C.J. Characterisation of proteoglycans and their catabolic products in tendon and explant cultures of tendon. *Matrix Biol.* **2004**, *23*, 127–140. [[CrossRef](#)]
130. Rees, S.G.; Flannery, C.R.; Little, C.B.; Hughes, C.E.; Caterson, B.; Dent, C.M. Catabolism of aggrecan, decorin and biglycan in tendon. *Biochem. J.* **2000**, *350*, 181–188. [[CrossRef](#)]
131. Melrose, J.; Smith, S.M.; Fuller, E.S.; Young, A.A.; Roughley, P.J.; Dart, A.; Little, C.B. Biglycan and fibromodulin fragmentation correlates with temporal and spatial annular remodelling in experimentally injured ovine intervertebral discs. *Eur. Spine J.* **2007**, *16*, 2193–2205. [[CrossRef](#)]
132. Zhen, E.Y.; Brittain, I.J.; Laska, D.A.; Mitchell, P.G.; Sumer, E.U.; Karsdal, M.A.; Duffin, K.L. Characterization of metalloprotease cleavage products of human articular cartilage. *Arthritis Rheum.* **2008**, *58*, 2420–2431. [[CrossRef](#)]
133. Melrose, J.; Fuller, E.S.; Roughley, P.J.; Smith, M.M.; Kerr, B.; Hughes, C.E.; Caterson, B.; Little, C.B. Fragmentation of decorin, biglycan, lumican and keratocan is elevated in degenerate human meniscus, knee and hip articular cartilages compared with age-matched macroscopically normal and control tissues. *Arthritis Res. Ther.* **2008**, *10*, 79. [[CrossRef](#)] [[PubMed](#)]
134. Shu, C.C.; Flannery, C.R.; Little, C.B.; Melrose, J. Catabolism of Fibromodulin in Developmental Rudiment and Pathologic Articular Cartilage Demonstrates Novel Roles for MMP-13 and ADAMTS-4 in C-terminal Processing of SLRPs. *Int. J. Mol. Sci.* **2019**, *20*, 579. [[CrossRef](#)] [[PubMed](#)]
135. Cs-Szabo, G.; Roughley, P.J.; Plaas, A.H.K.; Glant, T.T. Large and small proteoglycans of osteoarthritic and rheumatoid articular cartilage. *Arthritis Rheum.* **1995**, *38*, 660–668. [[CrossRef](#)] [[PubMed](#)]
136. Young, A.A.; Smith, M.M.; Smith, S.M.; Cake, M.A.; Ghosh, P.; Read, R.A.; Melrose, J.; Sonnabend, D.H.; Roughley, P.J.; Little, C.B. Regional assessment of articular cartilage gene expression and small proteoglycan metabolism in an animal model of osteoarthritis. *Arthritis Res. Ther.* **2005**, *7*, 852–861. [[CrossRef](#)] [[PubMed](#)]
137. Haglund, L.; Ouellet, J.; Roughley, P. Variation in Chondroadherin Abundance and Fragmentation in the Human Scoliotic Disc. *Spine* **2009**, *34*, 1513–1518. [[CrossRef](#)]
138. Brown, S.; Melrose, J.; Caterson, B.; Roughley, P.; Eisenstein, S.M.; Roberts, S. A comparative evaluation of the small leucine-rich proteoglycans of pathological human intervertebral discs. *Spine J.* **2012**, *21*, 154–159.
139. Erwin, W.M.; DeSouza, L.; Funabashi, M.; Kawchuk, G.; Karim, M.Z.; Kim, S.; Mädler, S.; Matta, A.; Wang, X.; Mehrkens, K.A. The biological basis of degenerative disc disease: Proteomic and biomechanical analysis of the canine intervertebral disc. *Arthritis Res.* **2015**, *17*, 240. [[CrossRef](#)]



140. Bisson, D.G.; Lama, P.; Abduljabbar, F.; Rosenzweig, D.H.; Saran, N.; Ouellet, J.A.; Haglund, L. Facet joint degeneration in adolescent idiopathic scoliosis. *JOR Spine* **2018**, *1*, 1016. [[CrossRef](#)]
141. Bock, H.; Michaeli, P.; Bode, C.; Schultz, W.; Kresse, H.; Herken, R.; Miosge, N. The small proteoglycans decorin and biglycan in human articular cartilage of late-stage osteoarthritis. *Osteoarthr. Cartil.* **2001**, *9*, 654–663. [[CrossRef](#)]
142. Goldring, M.B.; Otero, M.; Plumb, D.A.; Dragomir, C.; Favero, M.; El Hachem, K.; Hashimoto, R.; Roach, H.I.; Olivotto, E.; Borzi, R.M.; et al. Roles of inflammatory and anabolic cytokines in cartilage metabolism: Signals and multiple effectors converge upon MMP-13 regulation in osteoarthritis. *Cells Mater.* **2011**, *21*, 202.
143. Fuller, E.; Smith, M.; Little, C.; Melrose, J. Zonal differences in meniscus matrix turnover and cytokine response. *Osteoarthr. Cartil.* **2012**, *20*, 49–59. [[CrossRef](#)] [[PubMed](#)]
144. Billingham, R.C.; Dahlberg, L.; Ionescu, M.; Reiner, A.; Bourne, R.; Rorabeck, C.; Mitchell, P.; Hambor, J.; Diekmann, O.; Tschesche, H.; et al. Enhanced cleavage of type II collagen by collagenases in osteoarthritic articular cartilage. *J. Clin. Investig.* **1997**, *99*, 1534–1545. [[CrossRef](#)] [[PubMed](#)]
145. Frey, H.; Schroeder, N.; Manon-Jensen, T.; Iozzo, R.V.; Schaefer, L. Biological interplay between proteoglycans and their innate immune receptors in inflammation. *FEBS J.* **2013**, *280*, 2165–2179. [[CrossRef](#)] [[PubMed](#)]
146. Barreto, G.; Soyninen, A.; Ylinen, P.; Sandelin, J.; Konttinen, Y.T.; Nordström, D.C.; Eklund, K.K. Soluble biglycan: A potential mediator of cartilage degradation in osteoarthritis. *Arthritis Res.* **2015**, *17*, 379. [[CrossRef](#)]
147. Avenoso, A.; D'Ascola, A.; Scuruchi, M.; Mandraffino, G.; Calatroni, A.; Saitta, A.; Campo, S.; Campo, G.M. The proteoglycan biglycan mediates inflammatory response by activating TLR-4 in human chondrocytes: Inhibition by specific siRNA and high polymerized Hyaluronan. *Arch. Biochem. Biophys.* **2018**, *640*, 75–82. [[CrossRef](#)]
148. Bonnet, C.S.; Walsh, D.A. Osteoarthritis, angiogenesis and inflammation. *Rheumatology* **2005**, *44*, 7–16. [[CrossRef](#)]
149. Le Goff, M.M.; Sutton, M.J.; Slevin, M.; Latif, A.; Humphries, M.J.; Bishop, P.N. Opticin exerts its anti-angiogenic activity by regulating extracellular matrix adhesiveness. *J. Boil. Chem.* **2012**, *287*, 28027–28036. [[CrossRef](#)]
150. Merline, R.; Schaefer, R.M.; Schaefer, L. The matricellular functions of small leucine-rich proteoglycans (SLRPs). *J. Cell Commun. Signal.* **2009**, *3*, 323–335. [[CrossRef](#)]
151. Hildebrand, A.; Romaris, M.; Rasmussen, L.M.; Heinegård, D.; Twardzik, D.R.; Border, W.A.; Ruoslahti, E. Interaction of the small interstitial proteoglycans biglycan, decorin and fibromodulin with transforming growth factor  $\beta$ . *Biochem. J.* **1994**, *302*, 527–534. [[CrossRef](#)]
152. Kizawa, H.; Kou, I.; Iida, A.; Sudo, A.; Miyamoto, Y.; Fukuda, A.; Mabuchi, A.; Kotani, A.; Kawakami, A.; Yamamoto, S.; et al. An aspartic acid repeat polymorphism in asporin inhibits chondrogenesis and increases susceptibility to osteoarthritis. *Nat. Genet.* **2005**, *37*, 138–144. [[CrossRef](#)]
153. Embree, M.C.; Kiltz, T.M.; Ono, M.; Inkson, C.A.; Syed-Picard, F.; Karsdal, M.A.; Oldberg, A.; Bi, Y.; Young, M.F. Biglycan and Fibromodulin Have Essential Roles in Regulating Chondrogenesis and Extracellular Matrix Turnover in Temporomandibular Joint Osteoarthritis. *Am. J. Pathol.* **2010**, *176*, 812–826. [[CrossRef](#)] [[PubMed](#)]
154. Campbell, M.A.; Handley, C.J.; Hascall, V.C.; Campbell, R.A.; Lowther, D.A. Turnover of proteoglycans in cultures of bovine articular cartilage. *Arch. Biochem. Biophys.* **1984**, *234*, 275–289. [[CrossRef](#)]
155. Campbell, M.A.; Winter, A.D.; Ilic, M.Z.; Handley, C.J. Catabolism and Loss of Proteoglycans from Cultures of Bovine Collateral Ligament. *Arch. Biochem. Biophys.* **1996**, *328*, 64–72. [[CrossRef](#)] [[PubMed](#)]
156. Winter, A.D.; Campbell, M.A.; Robinson, H.; Handley, C.J. Catabolism of newly synthesized decorin by explant cultures of bovine ligament. *Matrix Boil.* **2000**, *19*, 129–138. [[CrossRef](#)]
157. Samiric, T.; Ilic, M.Z.; Handley, C.J. Large aggregating and small leucine-rich proteoglycans are degraded by different pathways and at different rates in tendon. *JBC J. Boil. Inorg. Chem.* **2004**, *271*, 3612–3620. [[CrossRef](#)] [[PubMed](#)]
158. Ilic, M.Z.; Carter, P.; Tyndall, A.; Dudhia, J.; Handley, C.J. Proteoglycans and catabolic products of proteoglycans present in ligament. *Biochem. J.* **2005**, *385*, 381–388. [[CrossRef](#)]
159. Hausser, H.; Hoppe, W.; Rauch, U.; Kresse, H. Endocytosis of a small dermatan sulphate proteoglycan. Identification of binding proteins. *Biochem. J.* **1989**, *263*, 137–142. [[CrossRef](#)]
160. Hausser, H. Binding of heparin and of the small proteoglycan decorin to the same endocytosis receptor proteins leads to different metabolic consequences. *J. Cell Boil.* **1991**, *114*, 45–52. [[CrossRef](#)]

161. Hausser, H.; Ober, B.; Quentin-Hoffmann, E.; Schmidt, B.; Kresse, H. Endocytosis of Different Members of the Small Chondroitin/Dermatan Sulfate Proteoglycan Family. *J. Biol. Chem.* **1992**, *267*, 11559–11564.
162. Hausser, H.; Schönherr, E.; Müller, M.; Liszio, C.; Bin, Z.; Fisher, L.W.; Kresse, H. Receptor-Mediated Endocytosis of Decorin: Involvement of Leucine-Rich Repeat Structures. *Arch. Biochem. Biophys.* **1998**, *349*, 363–370. [[CrossRef](#)]
163. Hausser, H.; Kresse, H. Decorin endocytosis: Structural features of heparin and heparan sulphate oligosaccharides interfering with receptor binding and endocytosis. *Biochem. J.* **1999**, *344*, 827–835. [[CrossRef](#)] [[PubMed](#)]
164. Schmidt, G.; Hausser, H.; Kresse, H. Extracellular accumulation of small dermatan sulphate proteoglycan II by interference with the secretion-recapture pathway. *Biochem. J.* **1990**, *266*, 591–595. [[PubMed](#)]
165. Feugaing, D.D.S.; Kresse, H.; Greb, R.R.; Götte, M. A Novel 110-kDa Receptor Protein is Involved in Endocytic Uptake of Decorin by Human Skin Fibroblasts. *Sci. World J.* **2006**, *6*, 35–52. [[CrossRef](#)] [[PubMed](#)]
166. Schönherr, E.; Sunderkotter, C.; Iozzo, R.; Schaefer, L. Decorin, a Novel Player in the Insulin-like Growth Factor System. *J. Biol. Chem.* **2005**, *280*, 15767–15772. [[CrossRef](#)] [[PubMed](#)]
167. Santiago-García, J.; Kodama, T.; Pitas, R.E. The class A scavenger receptor binds to proteoglycans and mediates adhesion of macrophages to the extracellular matrix. *J. Biol. Chem.* **2003**, *278*, 6942–6946. [[CrossRef](#)] [[PubMed](#)]
168. Feugaing, D.; Tammi, R.; Echtermeyer, F.; Stenmark, H.; Kresse, H.; Smollich, M.; Schönherr, E.; Kiesel, L.; Götte, M. Endocytosis of the dermatan sulfate proteoglycan decorin utilizes multiple pathways and is modulated by epidermal growth factor receptor signaling. *Biochimie* **2007**, *89*, 637–657. [[CrossRef](#)]
169. Townley, R.A.; Bülow, H.E. Deciphering functional glycosaminoglycan motifs in development. *Curr. Opin. Struct. Biol.* **2018**, *50*, 144–154. [[CrossRef](#)]
170. Wang, M.; Xue, S.; Fang, Q.; Zhang, M.; He, Y.; Zhang, Y.; Lammi, M.J.; Cao, J.; Chen, J. Expression and localization of the small proteoglycans decorin and biglycan in articular cartilage of Kashin-Beck disease and rats induced by T-2 toxin and selenium deficiency. *Glycoconj. J.* **2019**, *36*, 1–9. [[CrossRef](#)]
171. Cillero-Pastor, B.; Eijkel, G.B.; Kiss, A.; Blanco, F.J.; Heeren, R.M.A.; Garcia, F.J.B. Matrix-assisted laser desorption ionization-imaging mass spectrometry: A new methodology to study human osteoarthritic cartilage. *Arthritis Rheum.* **2013**, *65*, 710–720. [[CrossRef](#)]
172. Balakrishnan, L.; Nirujogi, R.S.; Ahmad, S.; Bhattacharjee, M.; Manda, S.S.; Renuse, S.; Kelkar, D.S.; Subbannayya, Y.; Raju, R.; Goel, R.; et al. Proteomic analysis of human osteoarthritis synovial fluid. *Clin. Proteom.* **2014**, *11*, 6. [[CrossRef](#)]
173. Peffers, M.J.; Cillero-Pastor, B.; Eijkel, G.B.; Clegg, P.D.; Heeren, R.M. Matrix assisted laser desorption ionization mass spectrometry imaging identifies markers of ageing and osteoarthritic cartilage. *Arthritis Res. Ther.* **2014**, *16*, 110. [[CrossRef](#)] [[PubMed](#)]
174. Peffers, M.; McDermott, B.; Clegg, P.; Riggs, C. Comprehensive protein profiling of synovial fluid in osteoarthritis following protein equalization. *Osteoarthr. Cartil.* **2015**, *23*, 1204–1213. [[CrossRef](#)] [[PubMed](#)]
175. Peffers, M.J.; Thornton, D.J.; Clegg, P.D. Characterization of neopeptides in equine articular cartilage degradation. *J. Orthop. Res.* **2016**, *34*, 106–120. [[CrossRef](#)] [[PubMed](#)]



**Appendix 2: Main paper “Osteomodulin down-regulation is associated with osteoarthritis development”.**

## Osteomodulin down-regulation is associated with osteoarthritis development

Jérémie Zappia<sup>1\*</sup>, Qiao Tong<sup>2</sup>, Renée Van der Cruyssen<sup>3,4</sup>, Frederique M. F. Cornelis<sup>5</sup>, Cécile Lambert<sup>1</sup>, Tiago Pinto Coelho<sup>6,7</sup>, Juliane Grisart<sup>8</sup>, Erika Kague<sup>2</sup>, Rik J. Lories<sup>5,9</sup>, Marc Muller<sup>10</sup>, Dirk Elewaut<sup>3,4</sup>, Chrissy L. Hammond<sup>2</sup>, Christelle Sanchez<sup>1</sup>, Yves Henrotin<sup>1,8,11</sup>.

1 MusculoSkeletal Innovative Research Lab, Center for Interdisciplinary Research on Medicines, Université de Liège, Liège, Belgium,

2 School of Physiology, Pharmacology, and Neuroscience, University of Bristol, Bristol, England, UK,

3 Department of Biomedical Molecular Biology, Ghent University, Ghent, Belgium,

4 Laboratory for Molecular Immunology and Inflammation, Department of Rheumatology, Ghent University Hospital, Ghent, Belgium,

5 Laboratory of Tissue Homeostasis and Disease, Skeletal Biology and Engineering Research Center, Department of Development and Regeneration, KU Leuven, Leuven, Belgium,

6 Cardiovascular Sciences, Groupe Interdisciplinaire de Génoprotéomique Appliquée, Université de Liège, Liège, Belgium,

7 Division of Nephrology, CHU of Liège, Université de Liège, Liège, Belgium,

8 Artialis SA, Tour GIGA, CHU Sart-Tilman, Liège, Belgium,

9 Division of Rheumatology, University Hospitals Leuven, Leuven, Belgium,

10 Laboratoire d'Organogenèse et Régénération, Groupe Interdisciplinaire de Génoprotéomique Appliquée, Université de Liège, Liège, Belgium

11 Physical Therapy and Rehabilitation Department, Princess Paola Hospital, Vivalia, Marche-en-Famenne, Belgium

**Corresponding author** : Jérémie Zappia; tel +32 4 366 58 69 |

### **AUTHORS CONTRIBUTIONS**

J.Z, C.L.H, C.S and Y.H were responsible for study design. J.Z supervised murine *in vivo* experiments. J.Z and F.M.F.C supervised the DMM model. J.Z and T.P.C supervised the CatWalk XT experiment. J.Z and M.M developed the mutant zebrafish line. J.Z, Q.T, J.G and E.K supervised zebrafish *in vivo* experiments. J.Z and R.V.d.C performed the *in vitro* experiments. J.Z wrote the manuscript. R.J.L, M.M, D.E and C.L.H. provided resources and advised on research studies. C.S and C.L advised on research studies. J.Z, C.S and Y.H analyzed the results. Y.H acquired funding, verified data and assisted in writing the manuscript and acts as guarantor. All authors approved the final manuscript.

### **KEYWORDS**

Osteomodulin, Cartilage, Subchondral bone, Osteoclast, Osteoarthritis.

**ABSTRACT**

Abnormal subchondral bone remodeling leading to sclerosis is a main feature of osteoarthritis (OA) and Osteomodulin (OMD), a proteoglycan involved in extracellular matrix mineralization, is associated to the sclerotic phenotype. However, the functions of OMD remain poorly understood, specifically *in vivo*. We used knock-out and overexpressing male mice for *Omd* and mutant zebrafish to study its roles in bone and cartilage metabolism and in the development of OA. The expression of *Omd* is deeply correlated to bone and cartilage microarchitectures affecting the bone volume and the onset of subchondral bone sclerosis and spontaneous cartilage lesions. Mechanistically, OMD binds to RANKL and inhibits osteoclastogenesis; thus controlling the balance of the bone remodeling. In conclusions, OMD is a key factor in subchondral bone sclerosis associated with OA. It participates in bone and cartilage homeostasis acting on the regulation of osteoclastogenesis. Targeting OMD may be a promising new and personalized approach for OA.

**INTRODUCTION**

Osteoarthritis (OA) is a degenerative joint disease with a high prevalence affecting 527.8 million people worldwide in 2019<sup>1</sup>. OA, being a major source of handicap, is a public health challenge and a rising societal burden due to the aging population and increasing life expectancy<sup>1</sup>. OA is a heterogeneous disease originating from multifactorial causes with different subtypes of patients linked to distinct phenotypes<sup>2,3</sup>. It is associated with pathologic changes in all the joint tissues including subchondral bone, cartilage, meniscus and synovium<sup>4</sup>. One of the main OA features is subchondral bone sclerosis which results from impaired subchondral bone remodeling driven by excessive mechanical loading. Bone sclerosis is associated with abnormalities in bone matrix biochemistry and mechanical properties that contribute to OA pathophysiology. Among these abnormalities, loss of matrix elasticity, abnormal mineralization, modification of the proteomic landscape with impaired cytokine production such as increased Transforming growth factor  $\beta$  and Interleukin 6 levels, overexpression of proteases, and decreased synthesis of small proteoglycans are well documented<sup>5-8</sup>. These changes are associated with the "bone-driven" OA phenotype<sup>3,4</sup>.

The Small Leucine-rich Proteoglycans (SLRPs) are intricately related to bone's physical properties and can be used as a fingerprint of its health status<sup>9</sup>. The majority of SLRPs control the organization of the collagen fibrils and, through the extracellular matrix (ECM), interact directly with cytokines acting as a reservoir and a regulator of their bioavailability<sup>10-15</sup>. Mice deficient for the SLRPs biglycan, fibromodulin, epiphygan, lumican, and chondroadherin demonstrated the protective role of these proteoglycans on the bone and cartilage matrix or osteoblasts; many of the knock-out mutants showed premature or more pronounced OA<sup>16-24</sup>. In contrast, the knock-out for opticon was associated with an inhibition of cartilage damage in an OA model<sup>25</sup>. Until now, the role played by osteomodulin (OMD), also known as osteoadherin, in OA pathophysiology is poorly documented.

OMD is a keratan sulfate proteoglycan and a member of the SLRP family. OMD was originally isolated and characterized from bone and shown to be strongly expressed by osteoblasts<sup>26-28</sup>. Even though *OMD* is considered to be mainly expressed in bone, its expression has been observed in other cell types such as articular chondrocytes and fibrochondrocytes<sup>29</sup>. It is involved in the mineralization process by binding to osteoblasts through the  $\alpha_v\beta_3$  integrin and by stabilizing Bone morphogenetic protein 2 (BMP2) ligands on their membrane receptors<sup>28,30,31</sup>. A secretome analysis comparing osteoblasts from sclerotic and non-sclerotic areas of OA patients performed in our laboratory has shown that OMD is one of the major proteins downregulated by sclerotic osteoblasts in culture<sup>8</sup>. Mature osteoblasts show enhanced expression of *OMD* when osteoclast activity is increased<sup>32</sup>.

For the first time, knock-out mice for *Omd*, here referred to as KO, and mice with *Omd* gain-of-function in osteoblasts, hereafter referred to as UP, were used to decipher the roles of *Omd* on bone remodeling and OA pathophysiology. We followed the development of OA in aging mice and after the destabilization of the medial meniscus (DMM). We have focused on the subchondral bone as a lack of

OMD was reported to be related to bone sclerosis<sup>8</sup>. In addition, we used the zebrafish model to study the role of *omd* in development and bone remodeling. Finally, using *in vitro* models we deepened our investigation of the relationship between OMD and osteoclastogenesis.

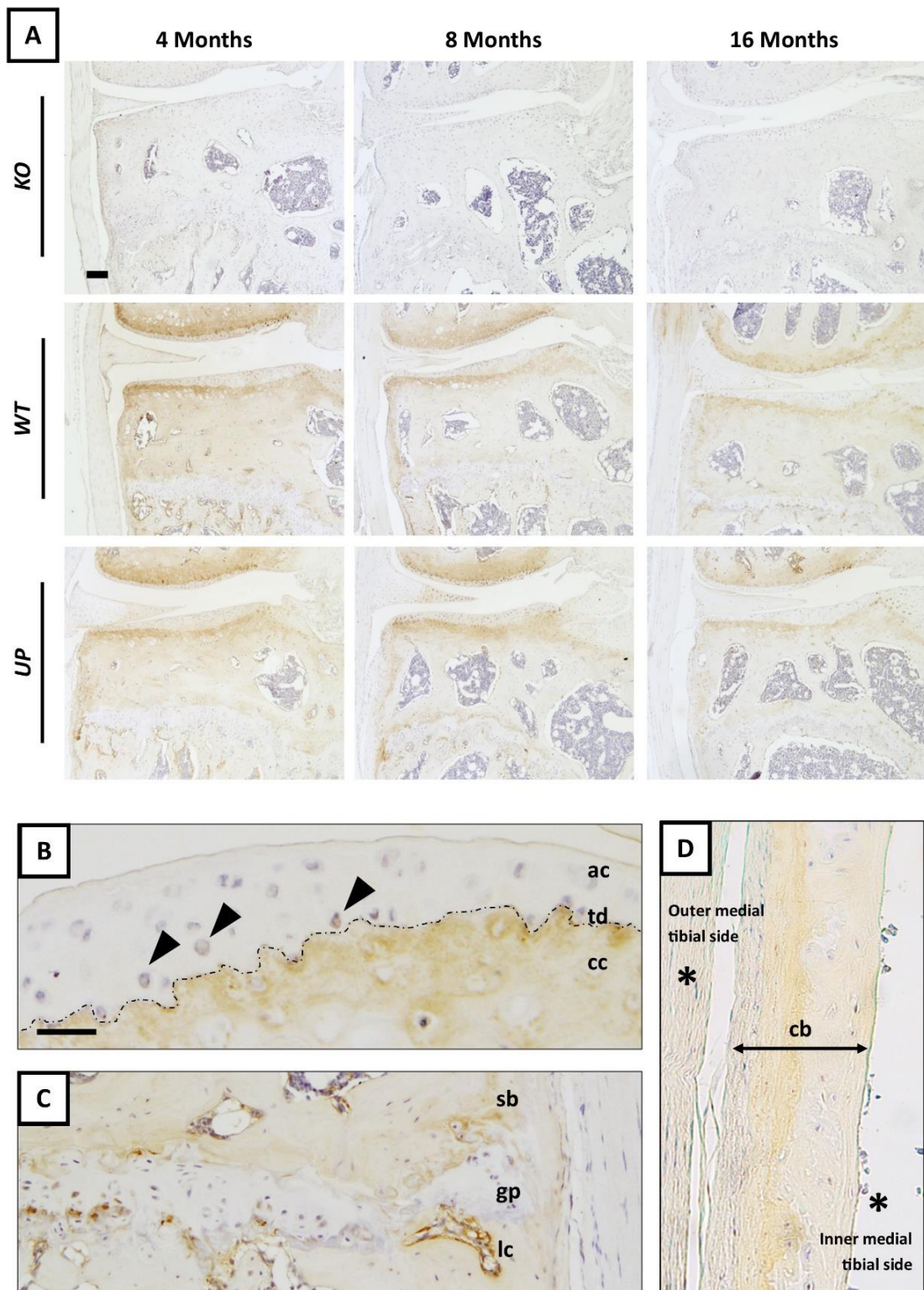
### **RESULTS**

#### **General growth characteristics of *Omd* KO and UP mice**

*Omd* KO mice had a lower weight and body size compared to the WT, only at 4 months. UP mice had a smaller weight than the WT at 4 months while their body size was not significantly different (Supplemental Fig 1A, 1B). At 8 and 16 months, weight and size were similar in all genotypes (Supplemental Fig 1A, 1B). UP mice displayed a longer femur than the KO at 8 months. The femoral length evolved differently over time between the genotypes with the UP reaching the mature size the soonest. Their femoral length was significantly increased at 8 months compared to the length at 4 months. At 16 months, each genotype reached a similar femoral length (Supplemental Fig 1C, 1D). Apart from some differences in their general growth characteristics over time, overall modifications of the level of *Omd* expression did not induce gross phenotypes.

#### **OMD is mainly localized in bone and calcified cartilage in mouse knee joint tissues**

We have performed immunohistochemical detection of OMD in the knee joint of 4, 8, and 16-month-old mice. OMD was present at all ages in WT and UP mice but absent in KO mice indicating the specificity of the immunostaining (Fig 1A). OMD was strongly localized in the calcified cartilage ECM, while heterogeneous and light staining was also observed in the deep zone of the uncalcified articular cartilage ECM and in some chondrocytes (Fig 1A, 1B). In bone, the lining cells were strongly stained as well as the ECM, mostly the mineralization front (Fig 1A, 1C, 1D). The ECM and some cells in the meniscus were stained (Fig 1A). The cartilaginous ECM of the growth plate was not stained (Fig 1C). The immunostaining asserted OMD as a proteoglycan having a strong specificity for the mineralized skeletal tissues.



*Figure 1: (A) Immunostaining of OMD (in brown) in the knee joint (medial tibial plateau) of KO, WT, and UP male mice at 4, 8, and 16 months. Scale bar=100  $\mu$ m. (B-D) Zoom on specific areas from WT of 16 months. Scale bar=50  $\mu$ m. Representative pictures with n=3 for each group. (B) Uncalcified articular cartilage (ac) and calcified cartilage (cc), separated by the tidemark (td - dotted line); chondrocytes (arrowheads). (C) Subchondral bone (sb), growth plate (gp) and lining cells (lc). (D) Metaphysis of the tibia showing the cortical bone (cb), the outer medial tibial side and the inner tibial side facing the bone marrow are indicated with (\*).*

***Omd* influences bone and cartilage microarchitectures**Effect of *Omd* on articular cartilage structure

Histological analysis revealed that the tibial growth plate significantly decreased between 4 and 8 months in all genotypes, but further decreased between 8 and 16 months only in the WT but not in other genotypes. At 16 months, the growth plate of the KO was larger than in the WT (Fig 2A, 2B).

In the 4-month-old KO mice, the calcified cartilage layer was thinner in the medial tibial plateau and thicker in the tibial lateral plateau than in the WT (Fig 2C, 2E). The ratio of calcified cartilage/total cartilage for the medial tibial compartment of the KO was significantly lower than in the WT and UP mice at each time point (Fig 2D). In the tibial lateral plateau, this ratio was higher in the 4-month-old KO and UP mice than in the WT and in the 16-month-old KO than in the UP mice (Fig 2F). Further, this ratio decreased with age in the KO and UP genotypes while it remained stable in WT. The thickness of the cartilage (including non-calcified and calcified cartilage) was not different between genotypes except in the medial plateau of 8-month-old KO mice, in which cartilage was thinner than in WT (Supplemental Fig 2). Our data showed *Omd* able to influence the cartilage microarchitecture.



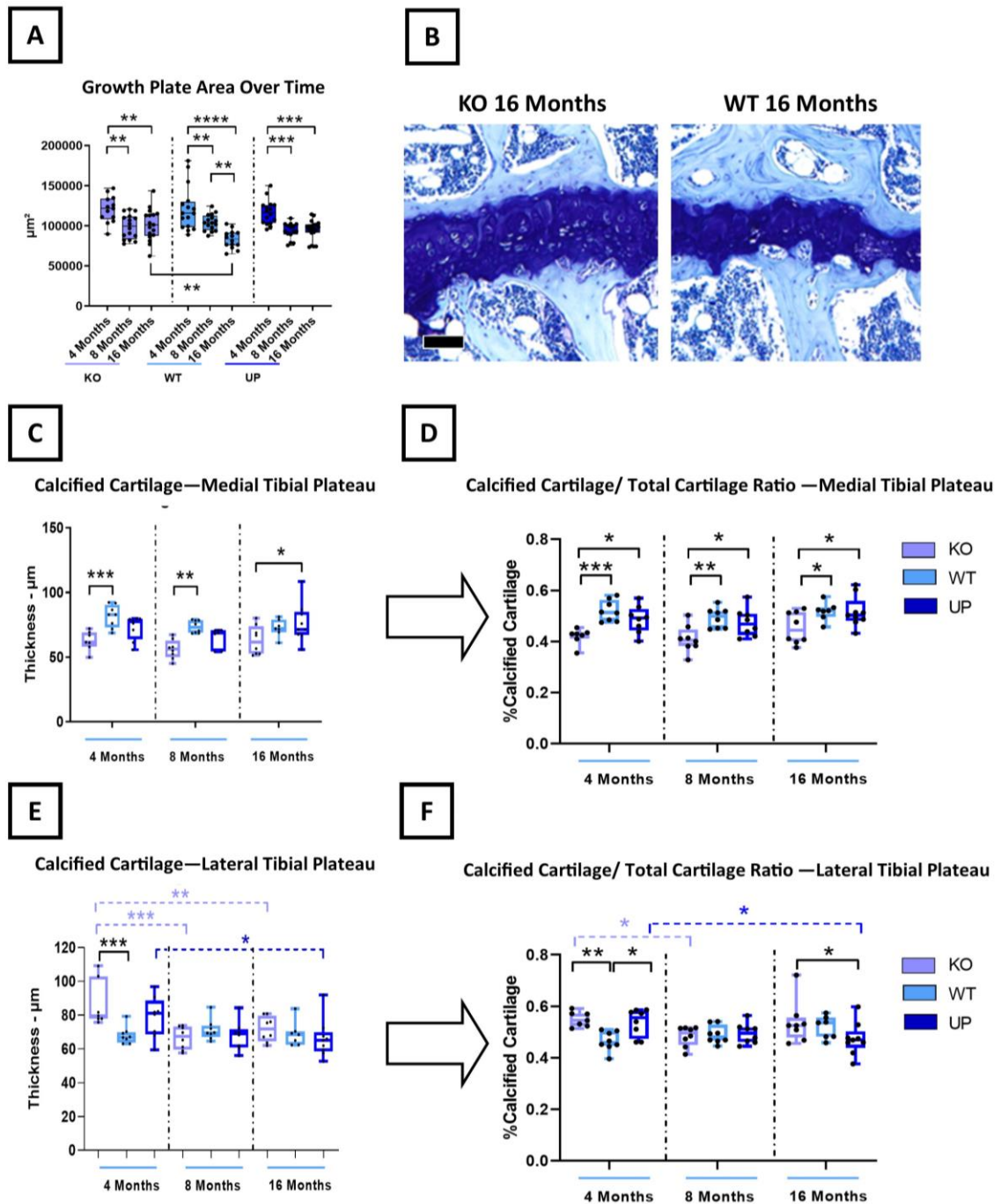


Figure 2: Histomorphometry of the cartilage was performed with QuPath at 4, 8, and 16 months. Knee joints of male mice were stained with Toluidine Blue and areas corresponding to the total cartilage, the calcified cartilage, and the growth plate were measured for the medial tibial plateau and the lateral tibial plateau. (A) Measures of the growth plate area of both medial and lateral tibial plateaus were plotted to display the evolution of the growth plate over time with  $n=13$  for the KO,  $n=16$  for the WT and UP at 4 months;  $n=16$  for the KO and WT, and  $n=15$  for the UP at 8 months;  $n=16$  for the KO,  $n=14$  for the WT and  $n=18$  for the UP at 16 months. (B) Toluidine blue of the growth plate for the KO and the WT at 16 months are represented. Scale bar=100  $\mu\text{m}$ . (C, E) The thickness of the calcified cartilage was measured on the medial and lateral plateaus from the tibia. (D, F) The ratio between the calcified cartilage and the total cartilage two was reported for both the medial and lateral plateaus. For the medial plateau (C, D):  $n=7$  for the KO,  $n=8$  for the WT and UP at 4 months;  $n=8$  for the KO and WT and  $n=7$  for the UP at 8 months;  $n=8$  for the KO,  $n=7$  for the WT and  $n=9$  for the UP at 16 months. For the lateral plateau (E, F):  $n=7$  for the KO,  $n=8$  for the WT and UP at 4 months;  $n=8$  for each genotype at 8 months;  $n=8$  for the KO,  $n=7$  for the WT and  $n=9$  for the UP at 16 months. Two-way ANOVA was performed to evaluate the genotype effect (in black) and the time effect inside a genotype (in the corresponding color). The data were plotted as a box plot showing all points with differences being considered significant at  $p$ -values  $< 0.05$  (\* $p < 0.05$ , \*\* $p \leq 0.01$ , \*\*\* $p \leq 0.001$ , \*\*\*\* $p \leq 0.0001$ ).

### Effect of *Omd* on bone structure

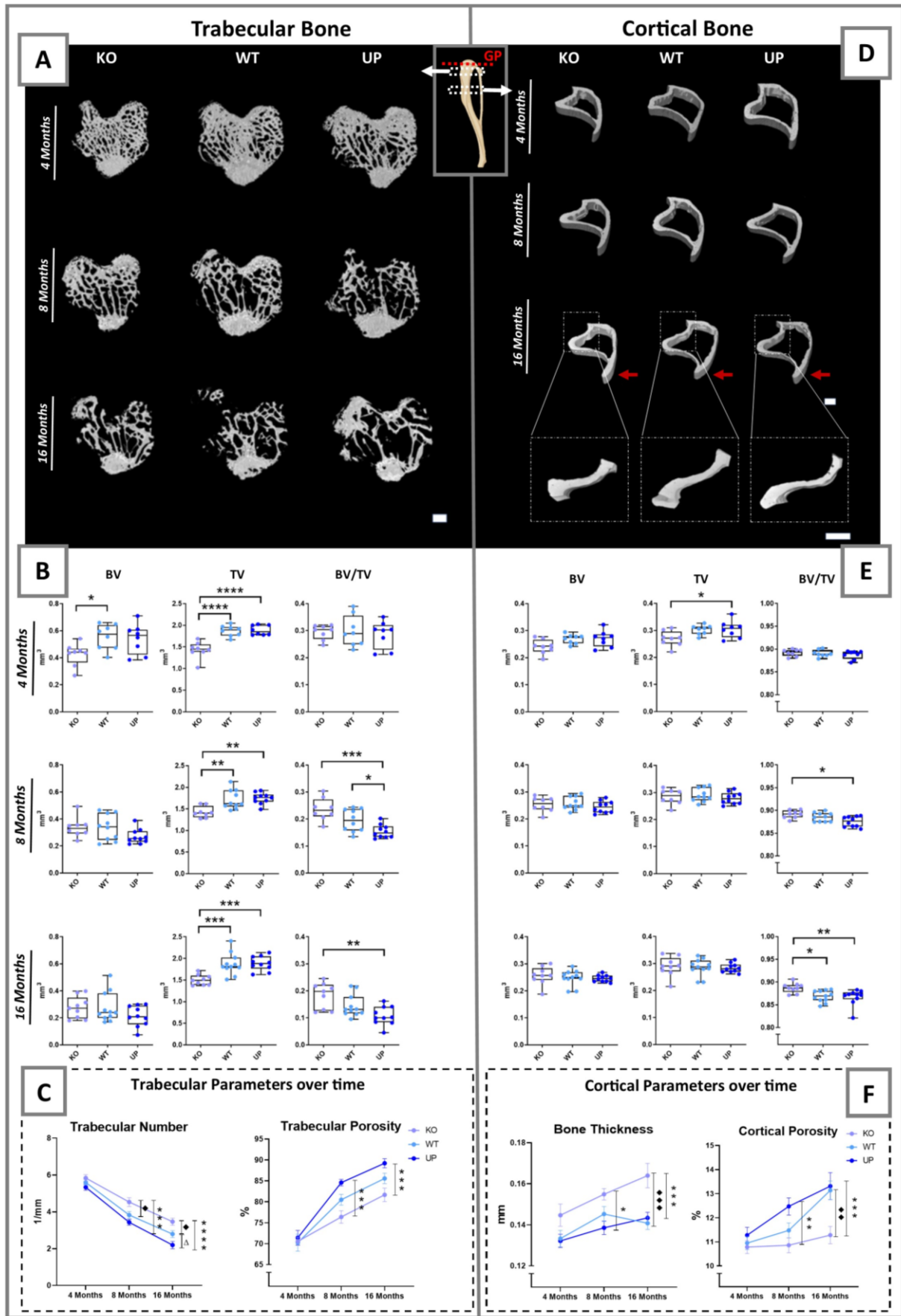
#### *Metaphysis of the tibia*

The total volume of the trabecular bone was lower in the KO than in other genotypes (Fig 3A, 3B). The trabecular BV/TV ratio was not significantly different between genotypes at 4 months. In contrast, this ratio was significantly higher in the KO than in the UP mice at 8 and 16 months and lower in UP mice than the WT at 8 months (Fig 3A, 3B). The number of trabeculae of the KO was higher at 8 and 16 months than the WT and UP while no difference was observed at 4 months (Fig 3C). The UP had significantly fewer trabeculae at 16 months compared to the WT. The porosity was lower in the KO and higher in the UP than in WT at all ages. The porosity was significantly lower in the KO at 8 and 16 months than in the UP (Fig 3C). The space between trabeculae was greater in UP than in KO mice at 16 months but no difference between genotypes was observed for the trabecular thickness. At 16 months, the structure model index of the UP mice was significantly higher than in another genotype which indicated a shift from a plate to rod-like geometry of the trabecular bone (Supplemental Fig 3A).

In the cortical bone, the BV/TV ratio was higher in the KO compared to the UP mice at 8 and 16 months and to the WT at 16 months (Fig 3D, 3E). The cortical bone thickness increased with age in all genotypes but was significantly higher in the KO relative to the UP at 8 months and then relative to the WT and UP at 16 months (Fig 3F). Cortical bone porosity was also affected by *Omd* expression. The porosity was consistently the lowest in the KO and the highest in the UP mice. The cortical bone porosity was significantly lower in KO compared to the UP mice at 8 and 16 months and then compared to the WT at 16 months (Fig 3C, 3F). In addition, the tibial crest was longer in KO than in WT and UP (Supplemental Fig 3B).

Whether in the loss of function or the overexpression of *Omd* models, both lead to interesting bone phenotypes. The KO mice conserved their bone volume better and had less porous bone while the UP mice displayed more severe loss with a decrease in the trabecular number and an altered trabecular shape, and the WT adopted an intermediate phenotype. In addition, morphological changes had been reported between genotypes with tibiae from the mutant not only being smaller and narrower but showing a dissimilar shape as well with an extended tibial crest.

The microarchitecture modifications due to the loss of function of *Omd* reflected on the bone's physical properties. The biomechanical test showed a higher whole bone strength of the KO mice tibia at 16 months, consistent with a better bone volume conservation, that could endure a higher maximal load compared to WT and UP mice. The stiffness of the KO mice was also significantly greater than the UP mice at 16 months (Supplemental Fig 4).



## IX. APPENDICES

Figure 3:  $\mu$ CT analysis of the metaphysis of the tibia of the male mice at 4, 8 and 16 months. The trabecular bone (left) and the cortical bone (right) were analyzed separately. Regions measured for the trabecular bone and cortical bone are illustrated on the schematic tibia with the growth plate (GP), marked with a red dotted line, used as a reference for their selection. (A, D) The 3D rendering of each genotype is represented with a scale bar of 500  $\mu$ m. Red arrows indicate the tibial crest on the 16 months cortical bone. The zoom on the 16 months cortical bone illustrates the lateral side of the tibia with a scale bar of 500  $\mu$ m. (B, E) The bone parameters measured for the trabecular and cortical bone were the bone volume (BV); the total volume (TV) and their ratio (BV/TV). The data were plotted as a box plot showing all points. One-Way ANOVA was performed with differences being considered significant at  $p$ -values $<0.05$  (\* $p$  $<0.05$ , \*\* $p$  $\leq 0.01$ , \*\*\* $p$  $\leq 0.001$ , \*\*\*\* $p$  $\leq 0.0001$ ). (C, F) The trabecular number, trabecular porosity, cortical thickness, and cortical porosity are represented over time. At 4 months:  $n=8$  for each genotype; at 8 months:  $n=8$  for the KO,  $n=10$  for the WT and UP; at 16 months:  $n=9$  for the KO,  $n=11$  for the WT, and  $n=10$  for the UP. Two-Way ANOVA was performed on the kinetic analysis with error bars representing  $\pm$  SEM and differences being considered significant at  $p$ -values $<0.05$ , \* represents significant differences between the KO and the UP,  $\blacklozenge$  represents significant differences between the KO and the WT and  $\Delta$  represents significant differences between the WT and the UP (\*/ $\blacklozenge$ / $\Delta$  $p$  $<0.05$ , \*\*/ $\blacklozenge$ / $\Delta$  $p$  $\leq 0.01$ , \*\*\*/ $\blacklozenge$ / $\Delta$  $p$  $\leq 0.001$ ).

### *Epiphysis of the tibia and the effect of Omd on the development of bone sclerosis*

KO mice had a greater lateral subchondral bone BV/TV ratio than the UP mice at 8 and 16 months and compared to the WT at 16 months. In the medial tibial plateau, BV/TV was more elevated in KO mice than in UP mice but only at 16 months (Figure 4A, 4B). Computed tomography illustrated that bone volume was higher in the KO than in the WT and the UP mice (Fig 4C).

*Omd* deficiency leads to a thicker bone at the tibia epiphysis and subchondral bone sclerosis. In contrast, overexpression of *Omd* by osteoblasts was associated with a decrease of bone volume. The differences between genotypes were clearly exacerbated in older mice.

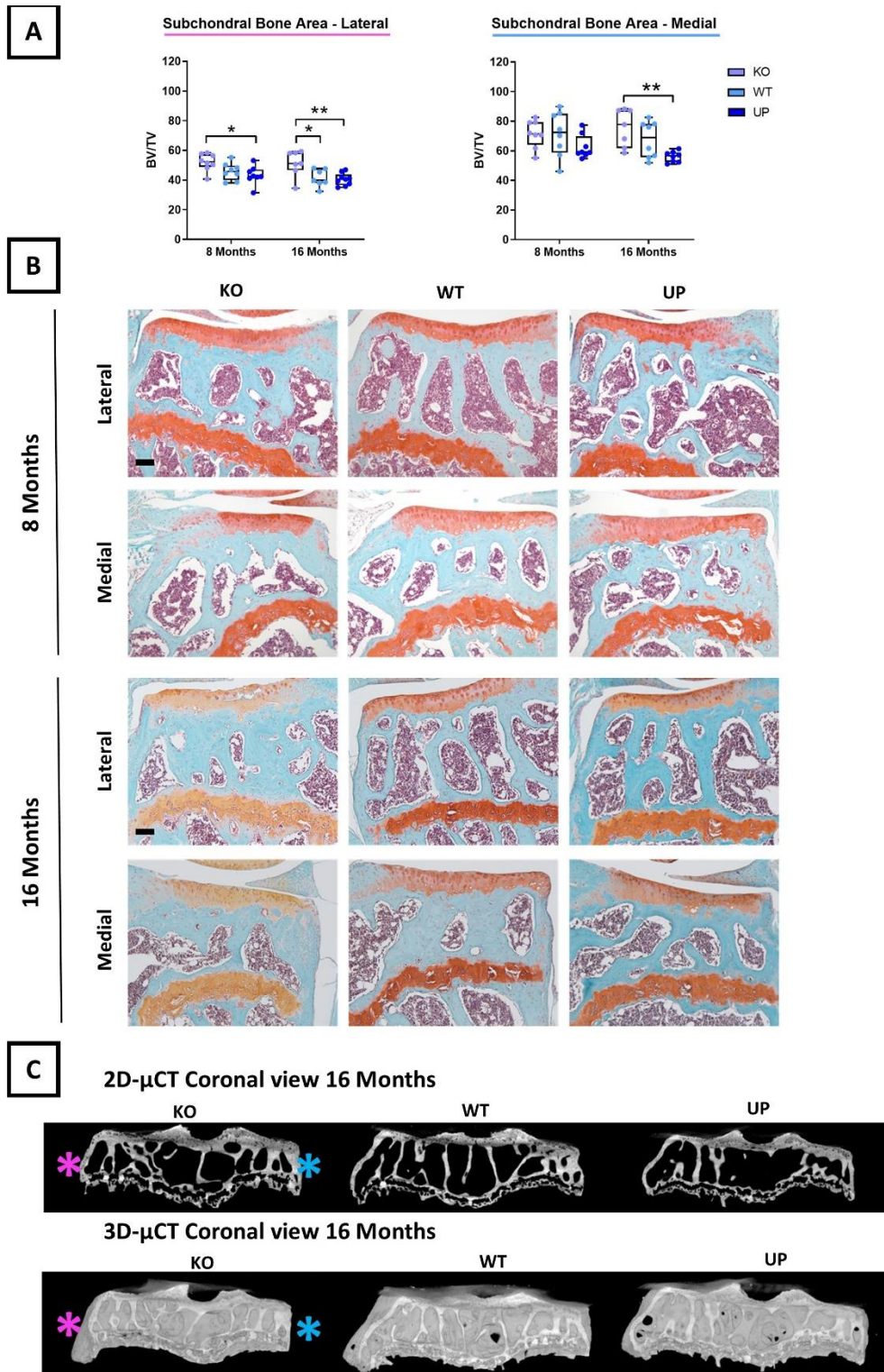


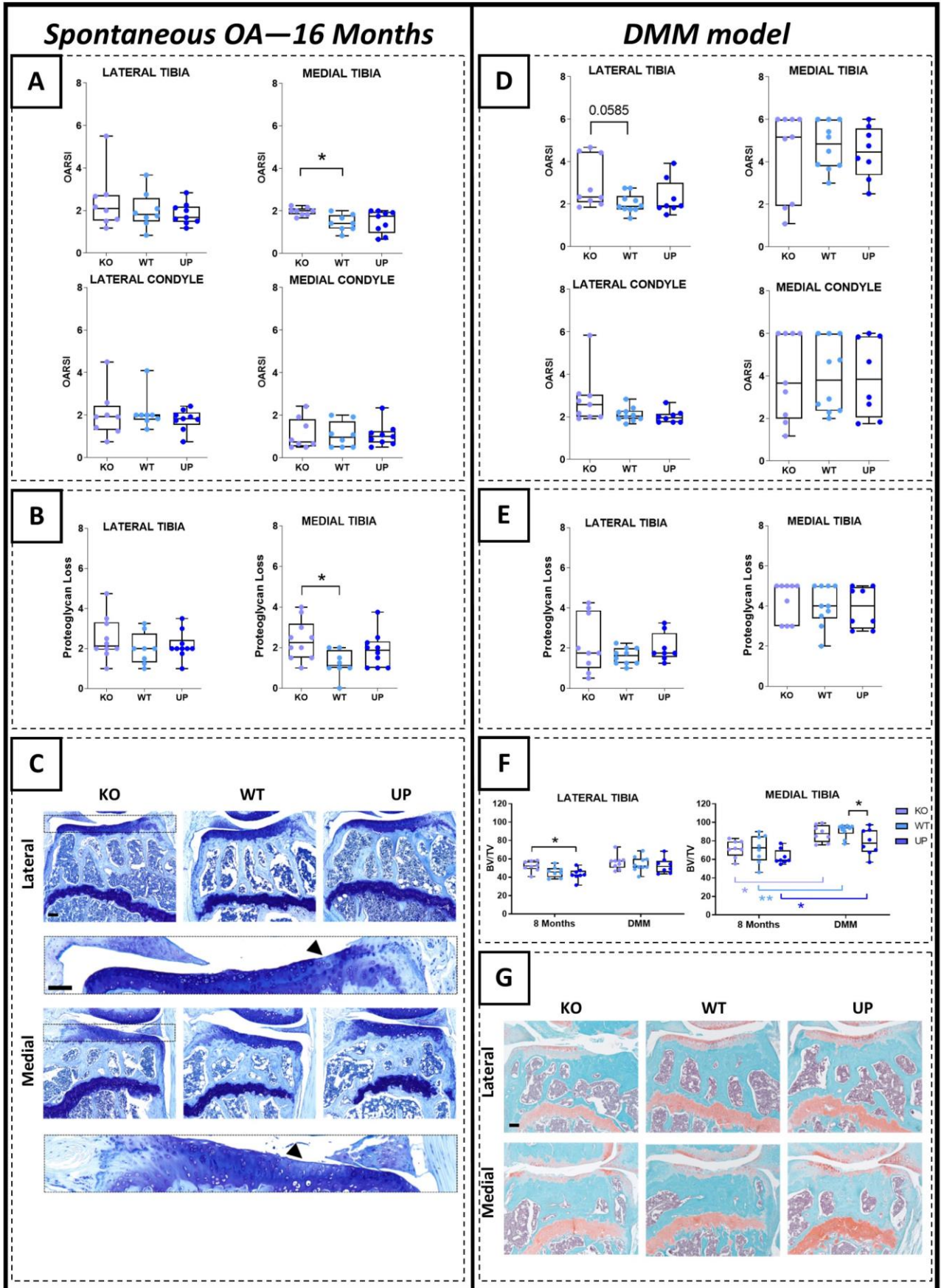
Figure 4: (A) Histomorphometry of the subchondral bone on Safranin-O Fast Green of the knee joint of male mice at 8 and 16 months was performed with QuPath on the lateral and medial plateaus of the tibia separately. At 8 months:  $n=8$  for each genotype; at 16 months:  $n=7$  for the KO,  $n=7$  for the WT, and  $n=9$  for the UP. The data were plotted as a box plot showing all points. Two-Way ANOVA was performed with differences being considered significant at  $p$ -values  $< 0.05$  ( $*p < 0.05$ ,  $**p \leq 0.01$ ). (B) Representative picture of the Safranin-O Fast Green of the knee joint of male mice showing the subchondral bone area for the lateral and medial plateau of the tibia separately. Scale bar =  $100 \mu\text{m}$ . (C)  $\mu$ CT of the subchondral bone of the tibia of the mice at 16 months. The pink asterisk indicates the lateral plateau and the blue asterisk indicates the medial plateau.

### ***Omd* may play a beneficial role against articular degradation and prevents subchondral bone sclerosis**

To study the role of *Omd* in the pathology of OA, we compared the spontaneous development of bone and cartilage structural changes in KO, WT and UP mice during their aging, but also after destabilization of the medial meniscus. In unoperated mice, cartilage lesions appeared with aging and a higher OARSI score was observed in the medial tibial plateau of KO mice than in WT (Fig 5A). This observation was consistent with the greater loss of proteoglycans for the medial tibial plateau of KO mice compared to the WT (Fig 5B, 5C). No differences were observed in the lateral tibial plateau and femoral condyles in 16-month-old mice. In the DMM model, the lesions of the medial tibial plateau were severe and no difference between genotypes was observed (Fig 5D, 5G). Cartilage lesions were less severe in the lateral tibial plateau and KO mice tended to have a greater OARSI score than the WT (Fig 5D, 5G) but the difference was not significant (p-value=0.0585). No significant difference was observed for the scored loss of proteoglycan (Fig 5E).

In WT with DMM-induced OA, the BV/TV ratio of the subchondral bone of the medial tibial plateau was significantly higher than in non-operated mice while it was not affected in the lateral plateau. For the medial tibia, the source of variation analysis confirmed the highly significant effect of the surgery on the BV/TV ratio, but also confirmed that results were genotype-dependent. The comparison of the medial subchondral bone BV/TV ratio between genotypes in DMM groups showed that it was lower in the UP mice than in the WT. Moreover, the UP mice from the DMM group displayed a BV/TV ratio remaining similar to the non-operated WT. The two-way ANOVA comparison of the DMM model with the non-operated mice showed no interaction between the two groups which indicates that expected values are not related between both groups (Fig 5F, 5G). These results suggest that the expression of *Omd* helps to prevent the development of subchondral bone sclerosis associated with OA.

*Omd* would protect from the onset of subchondral sclerosis, and then, may play a role in the prevention of the subsequent articular damage, particularly for spontaneous OA.



## IX. APPENDICES

Figure 5: Analysis of the development of OA lesions in the different genotypes after spontaneously occurring with age (left) or after the DMM (right). The spontaneous OA lesions were considered in the 16-month-old male mice and the DMM was performed on 16-week-old male mice and they were stopped at 28 weeks. (A, D): The cartilage degradation was assessed with the OARSI score (from 0 to 6) according to the OARSI recommendations. The score was attributed to the lateral and the medial tibial plateaus and to the lateral and medial condyles for the spontaneous model and the DMM model. (B, E): The score of the loss of proteoglycan (from 0 to 5) was assessed according to the OARSI recommendations for the lateral and medial tibial plateaus for the spontaneous model and the DMM model. For the OARSI score of the 16-month-old mice:  $n=8$  for the KO and the WT and  $n=9$  for the UP and for the loss of proteoglycan  $n=10$  for the KO,  $n=8$  for the WT and  $n=10$  for the UP. For the DMM model:  $n=9$  for the KO,  $n=10$  for the WT, and  $n=8$  for the UP. One-way ANOVA was performed with differences being considered significant at  $p$ -values  $<0.05$  ( $*p < 0.05$ ). (C): Illustrations of the lateral and medial plateaus stained with Toluidine Blue of the 16-month-old mice with zooms on proteoglycan loss issued from the KO and indicated by the arrowhead. Scale bar =  $100\ \mu\text{m}$ . (F): Histomorphometry of the subchondral bone on Safranin-O Fast Green of the knee joint of the DMM mice was performed with QuPath on the medial and lateral plateaus separately. Each genotype was compared to a similar age group of 8-month-old mice. At 8 months:  $n=8$  for each genotype; for the DMM:  $n=9$  for the KO,  $n=10$  for the WT, and  $n=8$  for the UP. The data were plotted as a box plot showing all points. Two-Way ANOVA was performed with differences being considered significant at  $p$ -values  $<0.05$  ( $*p < 0.05$ ,  $**p \leq 0.01$ ). (G): Illustrations of the lateral and medial plateaus stained with Safranin-O Fast Green in the DMM. Scale bar =  $100\ \mu\text{m}$ .

### Loss of *Omd* expression induced gait abnormalities in mice

The gait pattern of mice was assessed at all ages using the CatWalk XT platform. At 4 months, the print area was reduced in the KO compared to the WT, and at 8 months, the print area was smaller in the KO than in the WT and UP mice. The difference between the KO and other genotypes was not significant anymore at 16 months, yet it is due to the reduced values of the WT and UP mice at 16 months while the print area of the KO remained similar at each time-point. The swing, which is the duration of no contact of the paws with the walking platform, and the single stance, defined as the duration of contact of the paws with the walking platform, were shorter in the KO mice than in other genotypes at 8 and 16 months. Finally, the intensity of the contact of paws toward the glass platform was higher in the KO compared to the WT at 8 and 16 months and compared to the UP at 8 months (Fig 6 & Supplementary Table 1).

The gait analysis clearly showed that KO mice have different gait behavior than other genotypes. Their abnormal gait could be explained by their distinct bone structure and worse cartilage degradation.



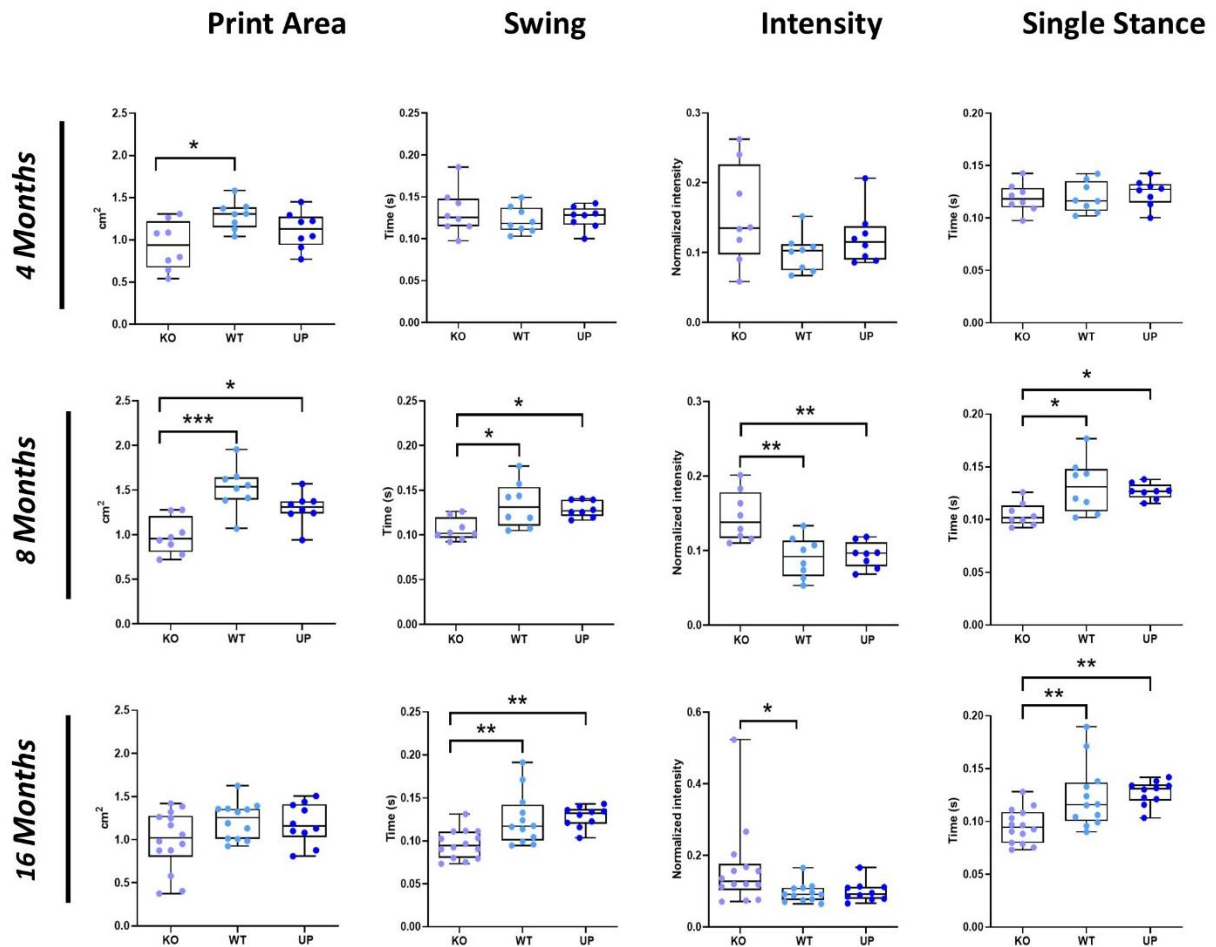


Figure 6: Analysis of the gait of 4, 8, and 16-month-old male mice with the CatWalkXT. The intensity corresponds to the mean intensity at the maximum paw contact normalized with the mean of the maximum contact paw area, the speed, and the weight of the mouse. At 4 months:  $n=8$  for each genotype; at 8 months  $n=8$  for each genotype; at 16 months:  $n=14$  for the KO,  $n=12$  for the WT and  $n=10$  for the UP. The data were plotted as a box plot showing all points. One-Way ANOVA was performed when the distribution was Gaussian and Kruskal-Wallis was performed when the distribution was not Gaussian with differences being considered significant at  $p$ -values  $< 0.05$  (\* $p < 0.05$ , \*\* $p \leq 0.01$ , \*\*\* $p \leq 0.001$ ).

### ***omd* is expressed in the zebrafish skeleton and its mutation induces articular cartilage lesions and impaired bone remodeling**

The zebrafish genome presents a single homolog to the human *OMD* gene, the ortholog *omd* encoding a 401 amino acids protein presenting 46% identical and 63% similar amino acids.

We characterized the localization of *omd* expression in larvae zebrafish using whole-mount *in situ* hybridization at 48-hour post fertilization (hpf), 5-day post fertilization (dpf) and 8-dpf. We observed a strong expression of *omd* specific to craniofacial cartilages including the jaw joint during the development (Supplemental Fig 5).

To gain first insights into the function of *omd* in zebrafish cartilage development, we studied the overexpression of *omd* by microinjecting 0.4 ng and 0.8 ng of its mRNA into zygotes. At 24-hpf, *omd* induced a ventralization of embryos that was not observed upon microinjection of control GFP mRNA (Supplemental Fig 6A, 6B). Further, larvae injected with *omd* developed deformities at 4-dpf, mostly affecting the axial symmetry. Larvae presenting axial deformities demonstrated evident cartilage defects with abnormal development of the craniofacial cartilage (Supplemental Fig 6C). As *omd* overexpression was inducing developmental defects, we designed a zebrafish *omd* mutant line (*omd*

<sup>-/-</sup>) for further characterization in adults. *In situ* hybridization of *omd*<sup>-/-</sup> individuals revealed that the mutation led to the absence of *omd* mRNA in the craniofacial structures (Supplemental Fig 5), indicating that no Omd protein was produced in the mutants.

We then compared the lubricated synovial jaw joints in one-year-old *omd*<sup>-/-</sup> zebrafish to those in WT to detect articular cartilage damage. For the palatoquadrate, the OARSI score of mutants (ranging from 1 to 3) was greater than in the WT, and clefts on their articular cartilage were observed (Fig 7A). As the murine model showed that the level of expression of *Omd* was related to the onset of the subchondral bone sclerosis and that the zebrafish displays lubricated synovial joints with similar articular degradation and subchondral bone modifications than in the physiopathology of OA<sup>33,34</sup>, we took advantage of the zebrafish to assess the osteoclast *in vivo*. We used this model to investigate the expression of cathepsin K, a marker of osteoclasts, in the regenerating caudal fin at 7 days post-amputation, a condition associated with osteoclastogenesis. The cathepsin K expression was significantly higher in *Tg(ctsk:Citrine); omd*<sup>-/-</sup> indicating that more osteoclasts were generated in the absence of *omd* expression (Fig 7B). Furthermore, osteoclast activity was studied in elasmoid scales through TRAP staining. More TRAP staining was present on elasmoid scale of the *omd*<sup>-/-</sup>. The staining appeared to be more evenly distributed throughout the scales of the mutant and particularly localized on the edges and along the grooves of the scale. The circularity of the scales was also impacted. The scales of the *omd*<sup>-/-</sup> were more circular than in the WT (Fig 7C).

The zebrafish confirmed our observations of the mouse model. The *omd* mutant zebrafish showed more severe spontaneous articular cartilage degradation in the synovial jaw joint. It also demonstrated that the regulation osteoclastogenesis was a possible mechanism of action for Omd.

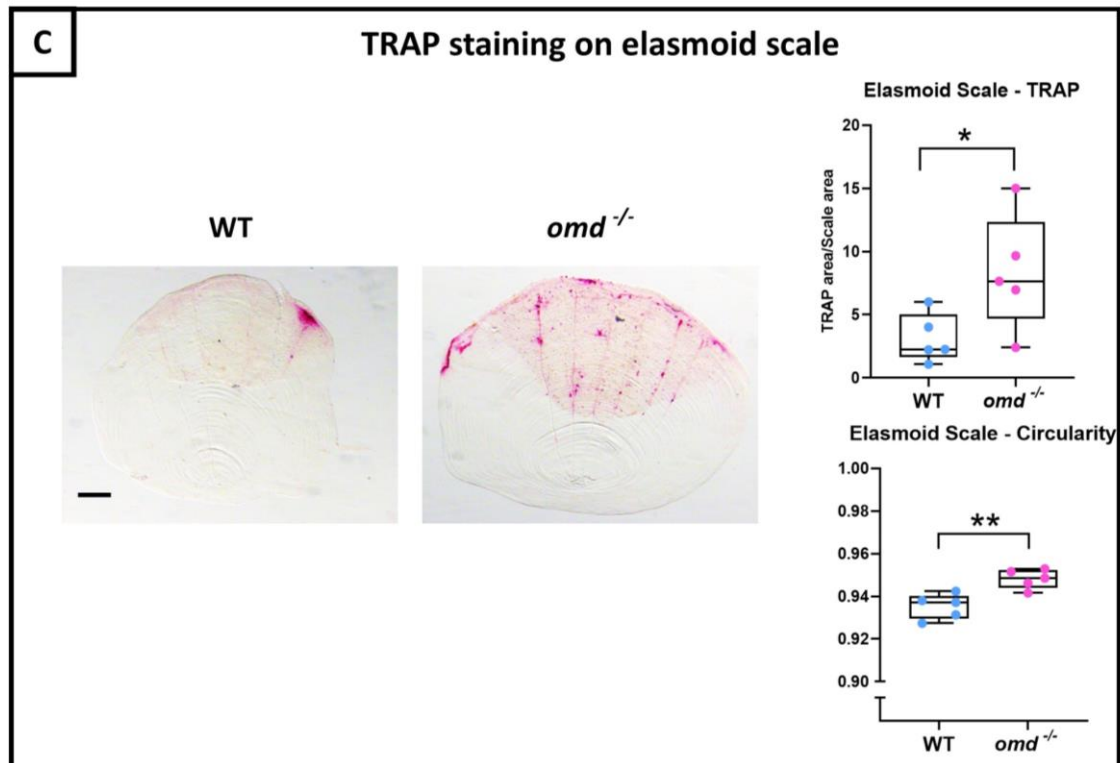
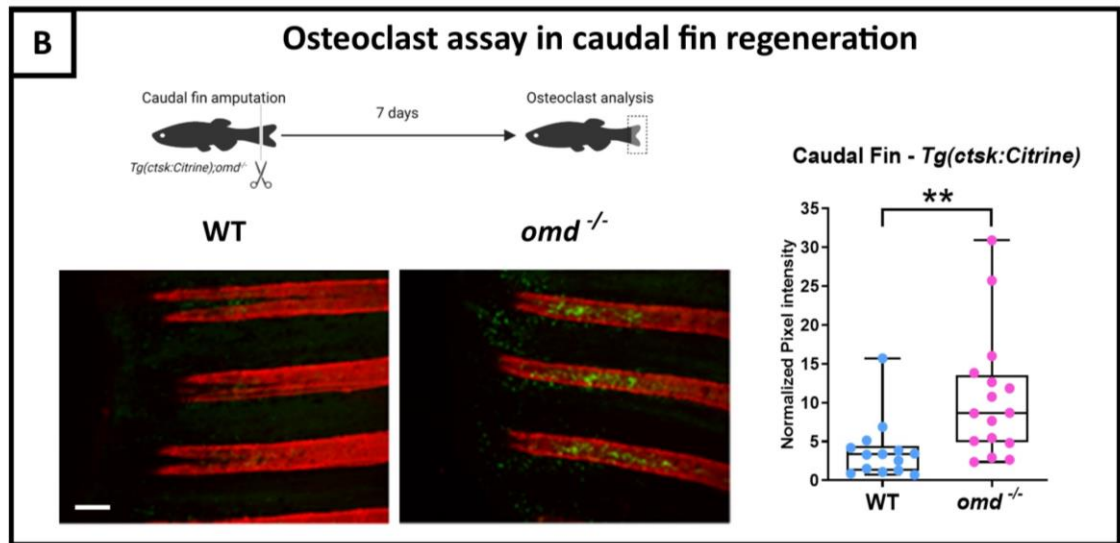
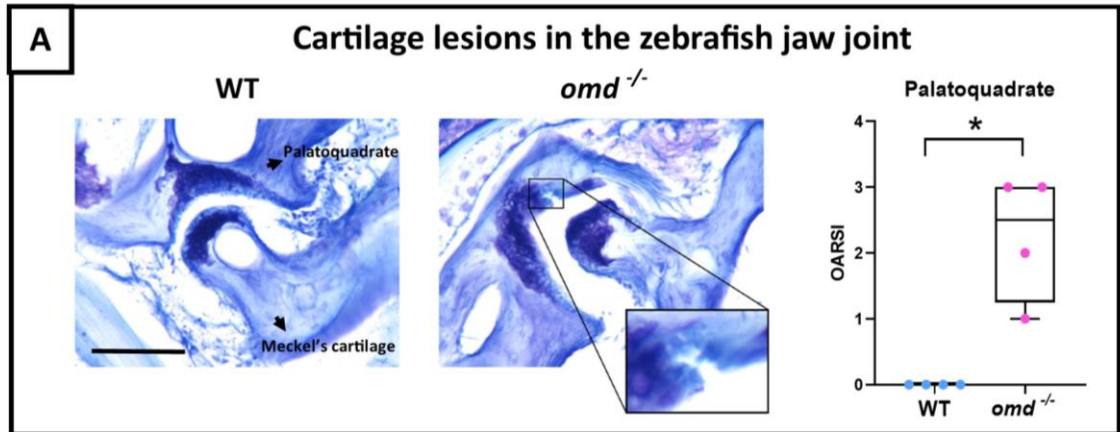


Figure 7: The mutant deficient for *omd* was generated through CRISPR/Cas 9. (A) Histology of the jaw joint was performed on 1-year-old zebrafish. The OARSJ score of the palatoquadrate was attributed to the jaw joint stained with Toluidine Blue with  $n=4$  for the WT and the mutant. The data were plotted as a box plot showing all points. Mann-Whitney test was performed with differences being considered significant at  $p$ -values  $< 0.05$  ( $*p < 0.05$ ). Scale bar =  $50\mu\text{m}$  (B) The mutant line was crossed with the *Tg(ctsk:Citrine)* for the osteoclasts analysis during the caudal fin regeneration. The caudal fin of 1-year-old zebrafish was cut and the regenerating fin was observed after 7 days. The osteoclasts are represented in yellow-green from the *ctsk:Citrine* signal and the mineralized ray were stained with Alizarin red. The data were plotted as a box plot showing all points. The pixel intensity of the regenerating rays is plotted and normalized by the background intensity with  $n=14$  for the WT and  $n=16$  for the mutant from two independent experiments which were pooled to perform the unpaired student  $t$ -test with differences being considered significant at  $p$ -values  $< 0.05$  ( $**p \leq 0.01$ ). Scale bar =  $200\mu\text{m}$  (C) TRAP staining was performed on the elasmoid scales of 1.6-year-old zebrafish. The TRAP staining area was normalized with the total scale area. The TRAP staining and the circularity of the scales were assessed with ZFBONE - Fiji with  $n=5$  for the WT and the mutant and with 6 to 15 scales/zebrafish analyzed. Scale bar =  $0.2\text{ mm}$  The data were plotted as a box plot showing all points. Unpaired student  $t$ -test with differences being considered significant at  $p$ -values  $< 0.05$  ( $*p < 0.05$ ,  $**p \leq 0.01$ ).

### OMD inhibited osteoclastogenesis by binding to RANKL

We investigated the effects of the treatment of OMD on gene expression in cultured human primary trabecular osteoblasts. The RNA-seq revealed that only 35 genes (with  $\text{padj} < 0.05$ ) were differentially expressed after the OMD 10 ng/ml treatment, and with relatively modest fold-changes to expression (Supplemental Fig 7 & Supplementary Table 2). GSEA analysis using webgestalt on GO terms revealed an increase of some genes linked to the response to acid chemicals (genes *AKR1C1*, *AKR1C2*, *AKR1C3*) and a decrease of few genes involved in extracellular structure organization (GO:0043062) and ossification (genes *ACAN* and *IBSP*), and of the molecular function of actin binding. The Reactome database revealed an up-regulation of genes responsible for collagen network degradation and a down-regulation of ECM proteoglycans, ECM organization, collagen formation, and integrin cell-surface interactions.

These observations led us to explore the interaction of OMD with RANKL, which is the regulator of osteoclast differentiation, using a solid phase binding assay. These experiments revealed a clear interaction between the two proteins, which correlated to the increasing amounts of both OMD and RANKL, demonstrating that they bind directly to each other (Fig 8A). The potential biological effects of this interaction were tested on primary murine osteoclasts culture. We showed that OMD added at 10ng/ml and 40ng/ml reduced osteoclast number. No difference between 10 and 40 ng/ml of OMD was observed, both reducing the osteoclast number by 50% on average (Fig 8B). Furthermore, serum markers for bone formation (N-terminal propeptide of type I procollagen: P1NP), and osteoclast number (TRAcP 5b) showed impaired bone turnover in the KO mice at 16 months. The serum level of P1NP was significantly higher in the KO mice compared to the UP mice, and the KO mice showed significantly increased TRAcP 5b compared to the WT and UP mice (Fig 8C).

We propose a model where osteoblasts secrete OMD in the ECM to trap RANKL and prevent it from binding to the pre-osteoclast receptor RANK to inhibit their differentiation into fully committed osteoclasts. In this model, OMD depletion induces uncoupled bone remodeling, in which increased osteoclast number and bone resorption, further associated with the stimulation of bone formation, lead to subchondral bone sclerosis (Fig 8D).

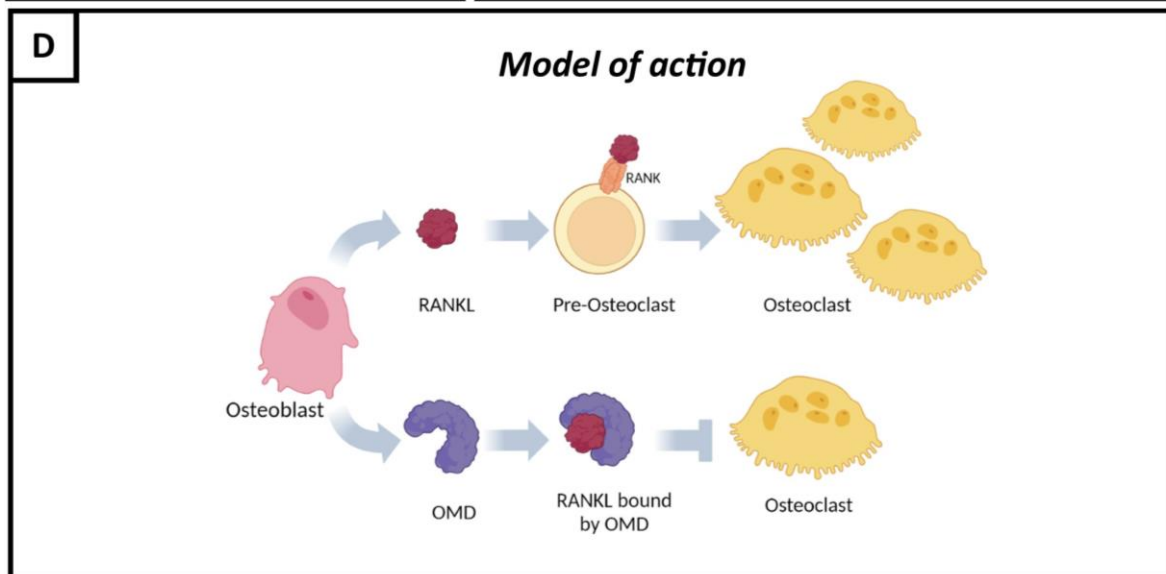
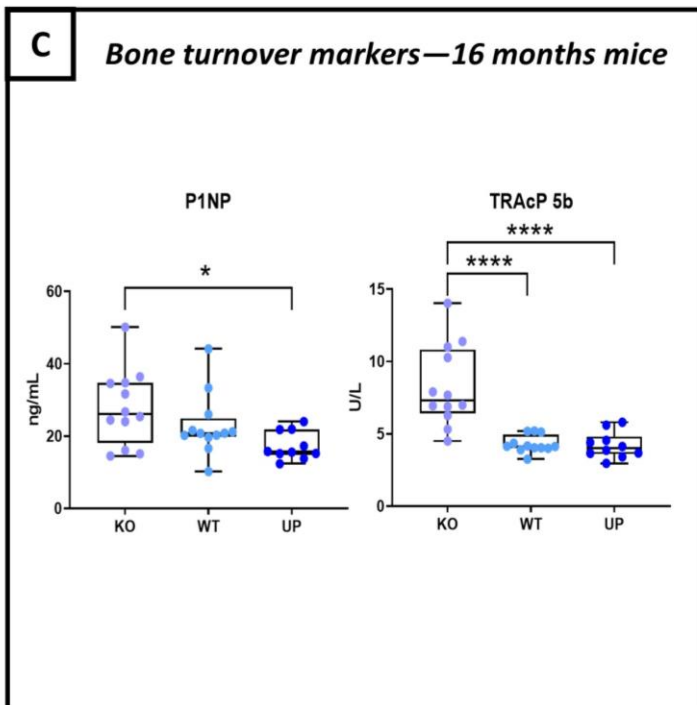
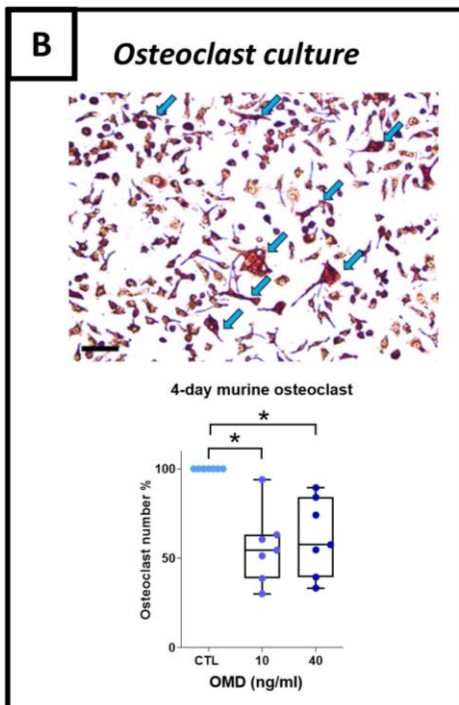
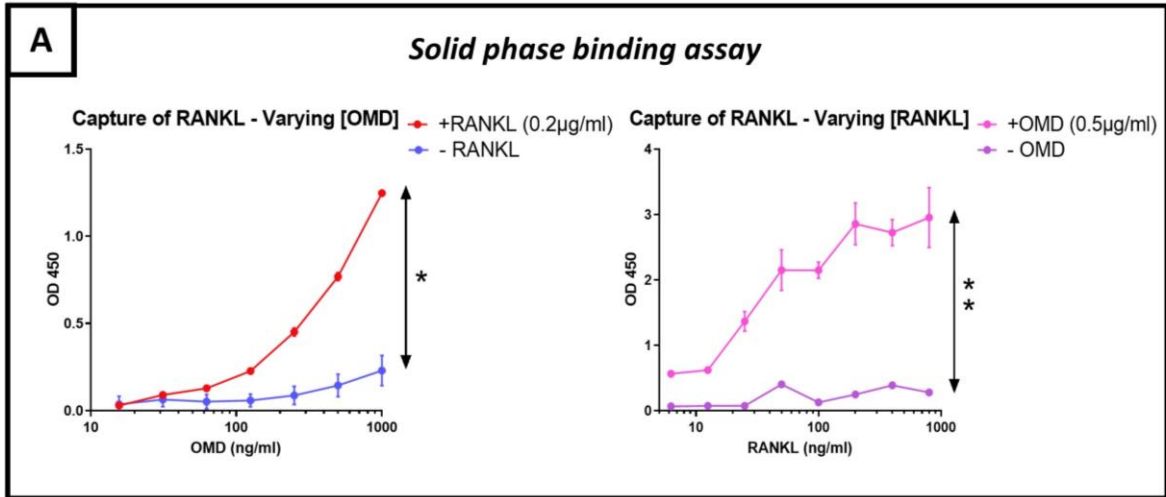


Figure 8: (A) Solid Phase binding assay on the capture of RANKL by OMD. RANKL was coated on a plate followed by OMD addition. On the left: Binding assay with different concentrations of OMD (1000 to 15.65 ng/ml by serial 2X dilution), with 0.2 µg/ml of coated RANKL (red curve) and negative control without RANKL (blue curve). On the right: Binding assay with different concentrations of coated RANKL (800 to 6.25 ng/ml) and 0.5 µg/ml of given OMD (pink curve); negative control without OMD (purple curve). Wilcoxon test was performed with differences being considered significant at  $p$ -values  $< 0.05$  ( $*p < 0.05$ ,  $**p \leq 0.01$ ). (B) Assay of the effect of OMD on primary murine osteoclast culture. The peripheral blood mononuclear cells were collected from murine bone marrow and differentiated into osteoclasts with M-CSF and RANKL. Osteoclasts were counted after 4 days of differentiation following a TRAP staining. Each point represents a mouse,  $n=7$ . The osteoclast count was represented in percentage of cells with the corresponding control set as 100%. Blue arrows point at osteoclasts. Scale bar=50 µm. The data were plotted as a box plot showing all points. One-way ANOVA was performed with differences being considered significant at  $p$ -values  $< 0.05$  ( $*p < 0.05$ ). (C) Level of P1NP and TRAcP 5b measured in the serum of KO, WT and UP mice. The data were plotted as a box plot showing all points with  $n=12$  for the KO and WT, and  $n=10$  for the UP. One-Way ANOVA was performed when the distribution was Gaussian and Kruskal-Wallis was performed when the distribution was not Gaussian with differences being considered significant at  $p$ -values  $< 0.05$  ( $*p < 0.05$ ,  $**p \leq 0.01$ ,  $***p \leq 0.0001$ ). (D) Schematic representation of the mechanism of OMD on osteoclastogenesis. Osteoblasts secrete RANKL which binds to the RANK receptor on the membrane of pre-osteoclasts to induce their differentiation into osteoclasts. In parallel, osteoblasts also secrete OMD which displays the ability to capture RANKL and would prevent its binding to RANK.

## DISCUSSION

OMD is a small proteoglycan involved in bone and dental matrix mineralization but also in ectopic mineralization of other tissues, such as in arteries<sup>35-39</sup>, suggesting it could be involved in cartilage mineralization and degradation during aging and OA.

We have previously demonstrated that osteoblasts located in the sclerotic area of OA subchondral bone produced less OMD than neighboring osteoblasts coming from the non-sclerotic area. Interestingly, OMD levels were also lower in the serum of OA patients<sup>8</sup>. To study the impact of *Omd* expression on bone remodeling, skeletal development and architecture, we followed mice deficient for *Omd* and mice overexpressing *Omd* during 16 months.

While the presence of OMD in bone has been previously reported<sup>31,40</sup>, we showed for the first time that OMD is localized in mineralized tissues of the murine knee joint and is identified in calcified cartilage and tidemark. Interestingly, we observed that the calcified cartilage layer was thinner in the medial tibial compartment but thicker in the lateral tibial compartment of KO mice than in other genotypes indicating that OMD plays a key role in cartilage mineralization. The consequences of calcified cartilage thickness on cartilage degradation in OA remain controversial. One study showed that the calcified cartilage was thinning with OA, resulting in the reduction of the cartilage elastic modulus<sup>41</sup>. However, other studies showed that the calcified cartilage thickness increased with the progression of OA<sup>42,43</sup>. The presence of the more severe cartilage lesions in the medial tibial plateau of aging KO mice, where the calcified cartilage was thinner, supports the hypothesis that a thinner layer of cartilage calcified is a factor promoting cartilage degradation. Of course, this theory needs to be confirmed in other models. In the DMM OA model, there was no significant difference in cartilage damage between genotypes. This finding contrasted with the observation performed in the aging KO mice in which the cartilage lesions severity were higher in KO mice than in other genotype. This observation can be explained by the higher severity of the lesions in DMM model reflecting more of a late stage of OA. We can anticipate a ceiling effect in DMM-induced OA model because the cartilage lesions were too severe. However, considering that most of the phenotypic changes induced by the modification of the expression of *Omd* were worsened with age, the experimental design of the DMM model does not make it possible to exclude an effect of *Omd* on the articular cartilage degradation occurring at the stage set for the surgery.

At the bone level, 8 and 16-month-old KO mice had greater trabecular and cortical BV/TV than the WT while, inversely, UP mice had a reduced ratio. This finding highlights that *Omd* plays a key role in bone remodeling. More precisely, keeping the homeostatic expression of *Omd* helps to preserve its volume and structure. *Omd* overexpression not only reduced BV/TV but also increased the structure model index, which is an indicator of the altered shape of trabeculae, and led to higher bone porosity. Over

time, aging was aggravating those observations. This indicates that, when overexpressed, *Omd* may turn to cause detrimental effects on skeletal tissues. In the KO, the global bone morphology was affected. Their tibia was narrower and their tibial crest longer, this morphological change may affect muscle insertion and, by so, the muscle-to-bone relationship. Further, KO mice were more prone to spontaneously develop subchondral bone sclerosis, as indicated by higher BV/TV, like in sclerotic subchondral bone in OA. The modifications of the bone microarchitecture affected the bone's physical properties as well, important features relative to the bone quality, with KO mice showing higher whole bone strength of the tibia at 16 months, an expected behavior following the observations from the  $\mu$ CT analysis.

We also observed sclerosis of the subchondral bone following the DMM procedure, in all the genotypes. Yet, the subchondral bone of the medial tibia of UP mice was thinner than the KO and WT mice suggesting that *Omd* could prevent subchondral bone sclerosis in OA. Although these observations are indicating that the overexpression of *Omd* would protect from the onset of OA-associated sclerosis, we are still willing to be cautious about the efficiency of the protective effect as the BV/TV ratio is initially slightly lower in UP mice showing altered bone microarchitecture. Nonetheless, our data suggest that *Omd* plays a role in subchondral bone sclerosis, a key feature of OA, involved in cartilage degradation. Therefore, we can hypothesize that the impact of *Omd* on cartilage degradation could be secondary to its effect on bone. In the spontaneous model, the loss of function of *Omd* is associated with articular cartilage degradation, suggesting that *Omd* might prevent cartilage degeneration. This hypothesis has to be verified in a larger number of animals or a more advanced aging-related OA model where more pronounced differences with a higher articular degradation in the KO mice are anticipated.

The gait analysis with the Catwalk XT identified different motor patterns between the genotypes. The gait pattern of KO mice, including the print area, the swing, the intensity of the contact, and the single stance of paws toward the glass platform, were modified. More precisely, for their hind paws, the KO mice had a reduced print area, a shorter swing and single stance, and a higher intensity of the contact of the paw. This may result in pain, discomfort, or of mechanical disorders associated with joint damage or with skeletal tissue abnormalities. It is important to highlight that a decreased hind print area is considered the best predictor for spontaneous OA<sup>44</sup>. Furthermore, the single stance was reported to be significantly decreased in OA mice<sup>45</sup> and the swing may also be reduced with OA<sup>46</sup>. Our report on the gait parameters is consistent with previous observations found in the literature and corroborates the susceptibility of the KO mice to develop further OA joint damage. On the other hand, the gait patterns at 16 months may be affected by the initiation of OA leading to abnormal loading on affected limbs.

To corroborate our findings from the mice model, we studied mutant adult zebrafish which did not express *omd*. In zebrafish, we found cartilage lesions in the articular cartilage in the jaw joint. Again, this suggests that *omd* prevents spontaneous cartilage lesions during aging and that a decrease of OMD production by osteoblasts and hypertrophic chondrocytes could be deleterious for cartilage. Altogether, these findings support that a loss of OMD contributes to OA development. We have then investigated by which mechanism of action OMD could regulate bone and cartilage metabolism. Our transcriptomic data revealed that OMD is unlikely to perform its function on osteoblasts through direct gene expression regulation as very few genes were modified and with a low magnitude. It remains noteworthy to specify that among the regulated genes, *IBSP* was downregulated by OMD. *IBSP* overexpression by hypertrophic chondrocytes is associated with OA<sup>47</sup>. Consequently, OMD could control cartilage calcification in OA by downregulating *IBSP* production.

Direct binding of OMD to key bone regulatory factors is another possible mechanism of action. SLRPs are known to bind cytokines, growth factors, and ligands like RANKL<sup>9,24</sup>. Herein, we showed that OMD is not only enhancing the differentiation of osteoblasts<sup>31</sup>, but is also able to bind directly to RANKL and block its biological activity on osteoclasts. Measures of bone markers in the serum of 16 months mice

corroborated the elevated osteoclast number and higher bone turnover in the loss of function model. Concerning the UP mice, they showed the lowest P1NP level and it might indicate that their poor conservation of bone volume would be due to low bone formation rather than bone resorption. The mutant zebrafish model confirmed the role of *omd* in osteoclastogenesis. The number of cathepsin K positive osteoclasts increased in the regenerating caudal fin of the mutants. Further, observations of elasmoid scales, which share a similar transcriptomic profile with the mammalian skeleton including genes related to human diseases<sup>48</sup>, highlighted higher TRAP staining and more circular scales in zebrafish lacking *omd*. As osteoclasts are inducing OMD expression in mature osteoblasts<sup>32</sup>, OMD presents a negative feedback activity on them. Moreover, sulfated GAGs are known to inhibit the differentiation of osteoclasts and the sulfation level of OMD is higher during the ECM mineralization process<sup>49,50</sup>. Our findings present OMD as a novel regulator of the bone remodeling process able to protect from subchondral bone sclerosis in pathological conditions like OA. Those observations are crucial since we know that bone remodeling plays a key role in the bone-driven OA phenotype with uncoupled bone remodeling leading to impaired bone resorption and bone deposition functions, then resulting in subchondral bone sclerosis with an elevated number of osteoclasts<sup>51-53</sup>. We identified OMD as a novel player in the uncoupled bone remodeling associated with OA. Finally, we can point out that the bone and cartilage phenotypes due to the loss of function of *Omd* are consistent with other murine SLRPs-deficient models<sup>16-24</sup>. It ultimately reinforces previous statements declaring overlapping functions within the SLRP family.

In conclusion, alterations of the *OMD* expression modify the bone and cartilage metabolism and structure. OMD helps to preserve bone and cartilage integrity and a local decrease of its production leads to the development of OA mainly by increasing subchondral bone sclerosis and thinning the calcified cartilage while its overexpression alleviates the subchondral bone sclerosis. OMD is able to directly bind to RANKL and inhibit osteoclastogenesis to regulate bone remodeling and limit subchondral bone sclerosis. Our previous and current researches, making use of both *in vitro* and *in vivo* experiments either with human, mouse or zebrafish models, build a strong and compelling body of evidence of OMD being a key factor in OA associated with subchondral bone sclerosis.

## METHODS

### Mouse strains and housing

The mutant mouse strain deficient for *Omd* used for this research project, C57BL/6 *Omd*<sup>tm1Lex</sup>/*Mmucd*, RRID: MMRRC\_011749-UCD, was obtained from the Mutant Mouse Resource and Research Center (MMRRC) at the University of California at Davis, a NIH-funded strain repository, and was donated to the MMRRC by Lexicon Genetics Incorporated. The mutation targeted the coding exons 1 and 2 by homologous recombination. The genotyping protocol from MMRRC was applied. The overexpressing mouse strain for *Omd* used for this research project, C57BL/6 *Tg(Bglap-Omd)1Kieg*, EMMA ID EM:02120, was obtained from the European Mouse Mutant Archive (EMMA), a repository supported by the national research programs and by the EC's Research and Innovation programme Horizon 2020. The transgenic line expressed *Omd* under the osteocalcin promoter in addition to its natural expression, hence *Omd* overexpression is only osteoblast-specific. Strains were crossed with the WT C57BL/6 to maintain the line. Transgenic, WT, and mutant mice were maintained on a 12-hour-light/dark cycle with food and water supplied *ad libitum*. To ease the nomenclature in the paper, we refer to the *Omd* deficient mice as "KO" and to the *Tg(Bglap-Omd)* as "UP". The ethical committee of the University of Liège approved all experimental procedures (reference no. 19-2090).

### Mouse model of OA

Post-traumatic OA was induced by DMM on UP, WT, and KO strains at 16 weeks. The surgical transection of the medial menisco-tibial ligament of the right knee was performed in order to induce mild instability of the knee<sup>54</sup>. The mice were euthanized 12 weeks after surgery and their knees histologically analyzed.



For spontaneous OA, UP, WT, and KO mice were euthanized at 16 months and their knees histologically analyzed.

### **Knee joint histology and histomorphometry**

Knee joints of the mice, at 4, 8, 16 months, and 28 weeks from the DMM model, were fixed for 24 hours in 4% paraformaldehyde at 4°C, followed by decalcification in hydrochloric acid (DC2 medium; Labonord) for 2 hours and 30 minutes at 4 °C then washed in Milli-Q water overnight at 4°C before embedding in paraffin. Coronal sections of 5 µm were cut within the central area with 3 sections of at least 80 µm apart selected for the analysis with the Safranin-O Fast-Green staining. An additional central section was used for the Toluidine Blue staining. Each compartment of the knee joint was scored by two readers following OARSI guidelines for the mouse model as described in<sup>55</sup> and the mean score from the 3 sections was calculated.

Histomorphometry of the sections was performed with the software QuPath version 0.3.2<sup>56</sup>. The sections were photographed at the magnification of 10X. The cartilage histomorphometry analysis was performed on the section stained with Toluidine Blue. The total cartilage, the calcified cartilage, the plate length, and the growth plate area were measured. For the growth plate, the area was measured inside a consistent circle of a fixed size under the articular plateau. The subchondral bone area analysis was performed on the 3 sections stained with the Safranin-O Fast-Green. The bone area was measured under the tibial plateau according to its length and the bone marrow area was removed. The measured region of interest (ROI) is explained in Supplemental Figure 8.

### **Immunohistochemistry**

Epitope retrieval was performed using the chondroitinase ABC (50 units/ml, Sigma-Aldrich) in 60mM sodium acetate and 100mM Tris (pH 8) for 30 min at 37°C. Animal-Free Blocking Solution (Cell Signaling Technology, dilution 5X) was used to block the sections prior overnight incubation with the primary polyclonal goat antibodies anti-mouse OMD (R&D systems, AF3308, 0.8 µg/mL) in Antibody diluent (Dako, S2022). The sections were then incubated for 30 minutes with the secondary polyclonal rabbit antibody anti-goat coupled with HRP (DakoP0449, dilution 1:400) diluted in Antibody diluent. The revelation of the secondary antibody was determined by using DAB (Cell Signaling Technology, 8059) for 2 minutes. Sections were counterstained by the Hematoxyline of Carazzi (Sigma-Aldrich) for 4 minutes.

### **Micro-computed tomography (µCT) and image analysis**

Tibiae from mice were dislocated and fixed for 24 hours in 4% paraformaldehyde at 4°C and transferred into phosphate-buffered saline (PBS) for storage, at 4°C. Samples were imaged using the Phoenix NanoTom M (GE Measurement and Control Solutions, Germany). A target of diamond was applied, and scans were operated at a voltage of 60 kV and a current of 170 µA, voxel size of 3µm. A filter of aluminum of 0.2 mm was used to reduce beam hardening during the acquisition. The exposure time was 500 ms, and 1800 images were acquired over 360° using the fast scan mode (frame averaging = 1; image skip = 0). During reconstruction (Datos|x, GE Measurement, and Control Solutions), we applied a beam hardening correction of 8. After reconstruction, scans were oriented in the same plane, using DataViewer (Bruker MicroCT, Kontich, Belgium). Images were analyzed using CTAn (Bruker MicroCT, Kontich, Belgium). For the assessment of the trabecular architecture, we selected 150 images (450 µm height) starting at 30 µm below the growth plate level. Using 3D analysis, the trabecular volume (BV), total ROI volume (TV), number of trabeculae, porosity, and the structure model index (SMI) were calculated. For analysis of the cortical architecture, we selected 100 images (300 µm height) starting at 1500 µm below the growth plate level and corresponding to the mid-shaft. Using 3D analysis, the BV, TV, cortical thickness, porosity and tibial crest length were calculated. 3D visualization was performed using CTvox (Bruker MicroCT, Kontich, Belgium). The subchondral bone of the tibia,

showing a coronal view of the medial and lateral plateau, was also visualized in 3D using CTVox and a 2-D visualization was generated using DataViewer.

### **CatWalk XT**

The gait analysis of the mice was performed using the CatWalk XT System (Noldus, Netherlands; software version XT 10.5). The CatWalk XT platform was placed in a dark and silent environment to enhance the quality of the recording and reduce animal stress. The same detection settings were used for each mouse: camera gain of 18.99 dB, green intensity threshold of 0.1, detection threshold of 0.1 a.U, red ceiling light of 17.2 V, and green walkway light of 16.5 V. The gait was recorded, and the CatWalk XT software automatically labeled the footprint and generated the various associated gait parameters for the compliant runs. A compliant run was defined as a run where the mouse did not stop while going through the walkway with at least 12 footprints, the maximum variation was set at 60% and the speed was comprised between 10 and 45 cm/s. At least 3 runs for each mouse were recorded and the data represent the mean value. The data from the left and right paws were pooled for the front and hind paws to simplify the run parameter visualization.

### **Zebrafish husbandry and strains**

Zebrafish (*Danio rerio*) were raised in standard conditions as described in <sup>57</sup>. Mutant lines deficient for *omd* were generated using CRISPR-Cas9 mutagenesis with the guide RNA 5'-CAA-GAG-CTG-CGC-CAATG-TCA-3'. The gRNAs targeting *omd* were incubated with Cas9 protein (Thermo Fisher Scientific) before microinjections into 1-cell stage zygotes. The mutation targeted the START codon. The reporter line used to visualize osteoclasts is the transgenic line *TgBAC(ctsk:Citrine)* <sup>58</sup> and was kindly provided by Prof. Stefan Schulte-Merker. The ethical committee of the University of Liège approved all experimental procedures (references no. 16-1961 and 19-2133).

### **Injection of mRNA of *omd* in the Zebrafish**

For *omd* overexpression, zebrafish *omd* mRNA and *GFP* mRNA, serving as a control, were microinjected into 1-cell stage zygotes. The following primers were used to generate the *omd* mRNA: forward 5'-CGA GAG AGA TAT TCA ATC CCA CAG-3' and reverse 5'-TCA ACC AAC AAG GAA TGG AAG-3'. The T7 promoter sequence for *in vitro* mRNA synthesis with the kit mMessage mMACHINE<sup>®</sup>T7 Ultra (Invitrogen) was added afterward with a nested PCR- using the forward primer : 5'-GCG AAT TGT AAT ACG ACT CAC TAT AGG GCC ACC ATG ACA TTG GCG CAG-3'. Fertilized eggs were injected with either 0.4 ng or 0.8 ng of mRNA. Phenotypic characterization was performed at 24-hpf and 4-dpf. At 4-dpf, the larvae were fixed with 4% PFA ON at 4°C and then stained with Alcian blue as described in <sup>59</sup>.

### **Whole-mount *in situ* hybridization in the Zebrafish**

Zebrafish larvae at 48-hpf, 5-dpf and 8-dpf were used for whole-mount *in situ* hybridization. Larvae were raised in presence of 0.003% of 1-phenyl-2-thiourea until 5-dpf to avoid pigmentation development. Larvae were fixed overnight in 4% of PFA at 4°C and stored in 100% methanol at -20°C until use. Visible *in situ* hybridizations were performed as described in <sup>60</sup> with a digestion step with the Proteinase K (Thermo Scientific) at 40 µg/ml during 30 minutes at 37°C for the 48-hpf larvae, at 50 µg/ml during 30 minutes at room temperature, at 40 µg/ml during 50 minutes at room temperature for the 8-dpf larvae.

### **Histology of the zebrafish jaw joint**

1-year-old zebrafish were fixed with 4% PFA at 4°C for a minimum of 24 hours and were decalcified in 1 M EDTA solution for 20 days. Zebrafish were dehydrated in ethanol, embedded in paraffin, and sagittally sectioned at 5 µm. Sections showing the jaw joint were stained with Toluidine Blue. OARS1 score was attributed to 1 section per jaw joint as described in <sup>33</sup>.

### **Zebrafish osteoclast assay in the caudal fin**

The mutants *omd x TgBAC(ctsk:Citrine)* were used at 1 year for the osteoclast analysis. Their caudal fins were cut and the fin was allowed to regenerate for 7 days. Regenerated caudal fins were cut for analysis and were incubated for 20 minutes with 0,01% alizarin red S (Sigma-Aldrich) to stain the mineralized bone matrix. Quantification of fluorescence from regenerated rays was performed using ImageJ software <sup>61</sup>.

### **TRAP staining of the zebrafish scales**

Ontogenetic scales of 1.6-year-old fish were plucked from the flank of the zebrafish and fixed with 4% PFA at room temperature for 30 minutes. Scales were incubated for 2 hours in the TRAP staining solution as described in <sup>62</sup>. Quantification of the TRAP staining was performed using the ZFBONE software on FIJI <sup>63</sup>.

### **Human trabecular osteoblast culture and RNA-seq analysis**

Tibial bones were obtained from 6 male and 5 female patients undergoing total knee replacement surgery for OA. The age of the patients ranged from 58 to 89 years. All tissue samples used in this study were obtained after receiving approval from the University of Liege Medicine Faculty ethics committee (No. B70720108313, reference 2010/43) and written informed consent was obtained from each subject. Non-sclerotic trabecular bone was easily removed from the tibia with surgeon pliers and enzymatically processed to get digested bone pieces cultured as described in <sup>64</sup>. At confluence, osteoblasts were collected by trypsinization, and seeded (22.000 cells/cm<sup>2</sup>) in 12-well plates (Nunc). Osteoblasts were cultured until confluence, then switched into differentiation media as described in <sup>64</sup> during three days in the presence of 10ng/ml of the human recombinant OMD (R&D systems, 2884-AD) or its absence for the same patient, serving as its own control.

Total RNA was extracted from osteoblast cultures, with RNA quality indicator scores (RIN) of 9.3; and RNA-seq for differential gene expression analyses was performed with a false Discovery Rate (FDR) of 0.01 to assess the statistical significance. as described in <sup>65</sup>.

### **Solid phase binding assay**

Human recombinant RANKL (OriGene, Germany) was bound for 2 hours under constant agitation to Well-Coated™ Nickel (G-Biosciences) previously washed with PBST. Unbound protein was removed by repeated washing with PBST. RANKL-coated plates were incubated overnight at 4°C with human recombinant OMD (R&D systems). The OMD bound to the coated plate was detected using the primary biotinylated polyclonal goat antibodies anti-human OMD (R&D systems, ref: BAF2884, 0.4 µg/ml). Plates were incubated with streptavidin-POD (Roche, dilution 1:25000) for 30 minutes to allow the detection. Finally, plates were read at 450 nm after applying TMB (TMBplus2, D-Tek, Denmark) for 8 minutes. The direct binding between OMD and RANKL was assessed with a fixed concentration of RANKL (0,2 µg/ml) and decreasing concentrations of OMD (1000 to 15,65 ng/l by serial 2X dilution), with the negative control missing RANKL; and with decreasing concentrations of RANKL (800 to 6,25 ng/ml by serial 2X dilution) and fixed concentration of OMD (0,5µg/ml), with the negative control missing OMD.

### **Mouse osteoclast culture**

WT mice of at least 4 months of age were used to collect bone marrow cells. The bone marrow of the femur and the tibia was flushed with 10ml of  $\alpha$ MEM containing 10% FBS, 100 U/ml penicillin, and 100 mg/ml streptomycin. Cells were strained through a 70 µm filter and then centrifuged at 1200 rpm for 7 minutes at 22°C. After centrifugation, cells were suspended in 12 ml of media containing 5ng/ml M-CSF in a petri dish and incubated overnight at 37°C. The non-adherent cells were centrifuged at 1200 rpm for 7 minutes at 4°C the day after. The cells were suspended in osteoclast differentiation medium  $\alpha$ MEM containing 10% FBS, 100 U/ml penicillin, 100 mg/ml streptomycin, 30 ng/ml M-CSF and 10 ng/ml

RANKL. For the treated conditions, 10 and 40 ng/ml of recombinant mouse OMD (R&D systems) were pre-incubated for at least 15 minutes with RANKL and M-CSF prior to adding to the suspension of the cells. Cells were seeded (525 000 cells/cm<sup>2</sup>) in 24-well plates. Cells were maintained until 4 days of differentiation and were stained with a TRAP staining kit (Sigma Aldrich) according to the manufacturer's instructions.

### **Assay in the serum for bone turnover markers**

The serum was extracted from blood of 16 months mice collected at the euthanasia. The level of P1NP was measured by Rat/Mouse P1NP ELISA (Immunodiagnostic Systems, Boldon, UK), and the level of TRAcP 5b by the Mouse TRAP Assay, a solid phase immunofixed enzyme activity assay (Immunodiagnostic Systems, Boldon, UK), according to the manufacturer's protocol.

### **Mechanical testing**

The biomechanical properties of the tibia of 16 months mice were determined using a three-point bending test in an Instron 5565 tensile testing machine. Tibiae were stored in PBS, and the remaining soft tissues and fibulae were carefully removed. The samples were assessed at room temperature on a special holding device on their anteroposterior axis. Force was applied on the midpoint of the tibia diaphysis with a 100 N load cell, at 8 mm separation (span length) with a perpendicular constant speed of 0.05 mm/s and with a preload of 1 N, until it fractured. From the load-deformation curve, the values for the maximal load (N) and stiffness (N/mm) were obtained<sup>66</sup>.

### **Statistical analysis**

Results were statistically analyzed using GraphPad Prism 6.0. Tests performed and statistical significance are indicated in the figure legends with *p values* <0.05 considered statistically significant.

## **DATA AVAILABILITY**

Data generated and analyzed during this study are included in this published article (and its supplementary information files).

The scripts generated for the histomorphometry analysis using Qupath are deposited in GitHub and publicly accessible for the cartilage (Toluidine Blue) and the bone (Safranin-O Fast Green) analysis respectively at: <https://doi.org/10.5281/zenodo.7898818> ; <https://doi.org/10.5281/zenodo.7899774>.

The transcriptomic data analyzed for this study are deposited in GeneExpression Omnibus (GEO) repository, under accession number GSE230198 that is publicly accessible at <https://www.ncbi.nlm.nih.gov/geo/query/acc.cgi?acc=GSE230198>.

## **BIBLIOGRAPHY**

1. Long, H. et al. Prevalence Trends of Site-Specific Osteoarthritis From 1990 to 2019: Findings From the Global Burden of Disease Study 2019. *Arthritis and Rheumatology* (2022). doi:10.1002/art.42089.
2. Dell'Isola, A., Allan, R., Smith, S. L., Marreiros, S. S. P. & Steultjens, M. Identification of clinical phenotypes in knee osteoarthritis: a systematic review of the literature. *BMC Musculoskelet Disord* 17, (2016).
3. Mobasheri, A. et al. Molecular taxonomy of osteoarthritis for patient stratification, disease management and drug development: Biochemical markers associated with emerging clinical phenotypes and molecular endotypes. *Current Opinion in Rheumatology* vol. 31 Preprint at <https://doi.org/10.1097/BOR.0000000000000567> (2019).

## ***IX. APPENDICES***

4. Loeser, R. F., Goldring, S. R., Scanzello, C. R. & Goldring, M. B. Osteoarthritis: A disease of the joint as an organ. *Arthritis and Rheumatism* vol. 64 Preprint at <https://doi.org/10.1002/art.34453> (2012).
5. Shabestari, M. et al. Altered protein levels in bone marrow lesions of hip osteoarthritis: Analysis by proteomics and multiplex immunoassays. *Int J Rheum Dis* 23, (2020).
6. Maruotti, N., Corrado, A. & Cantatore, F. P. Osteoblast role in osteoarthritis pathogenesis. *Journal of Cellular Physiology* vol. 232 Preprint at <https://doi.org/10.1002/jcp.25969> (2017).
7. Stewart, H. L. & Kawcak, C. E. The importance of subchondral bone in the pathophysiology of osteoarthritis. *Frontiers in Veterinary Science* vol. 5 Preprint at <https://doi.org/10.3389/fvets.2018.00178> (2018).
8. Sanchez, C. et al. Comparison of secretome from osteoblasts derived from sclerotic versus non-sclerotic subchondral bone in OA: A pilot study. (2018) doi:10.1371/journal.pone.0194591.
9. Zappia, J. et al. From translation to protein degradation as mechanisms for regulating biological functions: A review on the SLRP family in skeletal tissues. *Biomolecules* 10, (2020).
10. Tashima, T., Nagatoishi, S., Sagara, H., Ohnuma, S. I. & Tsumoto, K. Osteomodulin regulates diameter and alters shape of collagen fibrils. *Biochem Biophys Res Commun* 463, (2015).
11. Chen, S. & Birk, D. E. The regulatory roles of small leucine-rich proteoglycans in extracellular matrix assembly. *FEBS Journal* Preprint at <https://doi.org/10.1111/febs.12136> (2013).
12. Chen, X. D., Fisher, L. W., Robey, P. G. & Young, M. F. The small leucine-rich proteoglycan biglycan modulates BMP-4-induced osteoblast differentiation. *FASEB Journal* (2004) doi:10.1096/fj.03-0899com.
13. Bi, Y. et al. Extracellular Matrix Proteoglycans Control the Fate of Bone Marrow Stromal Cells\*. (2005) doi:10.1074/jbc.M500573200.
14. Kalamajski, S. & Oldberg, A. The role of small leucine-rich proteoglycans in collagen fibrillogenesis. *Matrix Biology* vol. 29 248–253 Preprint at <https://doi.org/10.1016/j.matbio.2010.01.001> (2010).
15. Schaefer, L. & Iozzo, R. v. Biological Functions of the Small Leucine-rich Proteoglycans: From Genetics to Signal Transduction \*. (2008) doi:10.1074/jbc.R800020200.
16. Hesse, L. et al. The Skeletal Phenotype of Chondroadherin Deficient Mice. *PLoS One* 8, (2013).
17. Jepsen, K. J. et al. A syndrome of joint laxity and impaired tendon integrity in lumican- and fibromodulin-deficient mice. *Journal of Biological Chemistry* 277, (2002).
18. Gill, M. R., Oldberg, Å. & Reinholt, F. P. Fibromodulin-null murine knee joints display increased incidences of osteoarthritis and alterations in tissue biochemistry. *Osteoarthritis Cartilage* 10, (2002).

## ***IX. APPENDICES***

19. Corsi, A. et al. Phenotypic effects of biglycan deficiency are linked to collagen fibril abnormalities, are synergized by decorin deficiency, and mimic Ehlers-Danlos-like changes in bone and other connective tissues. *Journal of Bone and Mineral Research* 17, (2002).
20. Ameye, L. et al. Abnormal collagen fibrils in tendons of biglycan/fibromodulin-deficient mice lead to gait impairment, ectopic ossification, and osteoarthritis. *The FASEB Journal* 16, (2002).
21. Nuka, S. et al. Phenotypic characterization of epiphykan-deficient and epiphykan/biglycan double-deficient mice. *Osteoarthritis Cartilage* 18, (2010).
22. Xu, T. et al. Targeted disruption of the biglycan gene leads to an osteoporosis-like phenotype in mice. *Nat Genet* 20, (1998).
23. Chen, X. D., Bian, X., Teslovich, T. M., Stephan, D. A. & Young, M. F. Dissection of the sets of genes that control the behavior of biglycan-deficient pre-osteoblasts using oligonucleotide microarrays. *Bone* 37, (2005).
24. Kram, V., Kilts, T. M., Bhattacharyya, N., Li, L. & Young, M. F. Small leucine rich proteoglycans, a novel link to osteoclastogenesis. *Sci Rep* (2017) doi:10.1038/s41598-017-12651-6.
25. Farrán, A. et al. In vivo effect of opticin deficiency in cartilage in a surgically induced mouse model of osteoarthritis. *Sci Rep* 8, (2018).
26. Wendel, M., Sommarin, Y. & Heinegård, D. Characterization of osteoadherin - A novel, cell binding keratan sulfate proteoglycan from bone. *Acta Orthopaedica Preprint* at <https://doi.org/10.3109/17453679509157655> (1995).
27. Wendel, M., Sommarin, Y. & Heinegård, D. Bone Matrix Proteins: Isolation and Characterization of a Novel Cell-binding Keratan Sulfate Proteoglycan (Osteoadherin) from Bovine Bone. *The Journal of Cell Biology* vol. 141 <http://www.jcb.org> (1998).
28. Sommarin, Y., Wendel, M., Shen, Z., Hellman, U. & Heinegård, D. Osteoadherin, a cell-binding keratan sulfate proteoglycan in bone, belongs to the family of leucine-rich repeat proteins of the extracellular matrix. *Journal of Biological Chemistry* (1998) doi:10.1074/jbc.273.27.16723.
29. Juchtmans, N. et al. Brief report: Distinct dysregulation of the small leucine-rich repeat protein family in osteoarthritic acetabular labrum compared to articular cartilage. *Arthritis and Rheumatology* 67, 435–441 (2015).
30. Lin, W. et al. Osteomodulin positively regulates osteogenesis through interaction with BMP2. *Cell Death Dis* 12, (2021).
31. Rehn, A. P., Cerny, R., Sugars, R. v., Kaukua, N. & Wendel, M. Osteoadherin is upregulated by mature osteoblasts and enhances their in vitro differentiation and mineralization. *Calcif Tissue Int* 82, 454–464 (2008).
32. Ninomiya, K. et al. Osteoclastic activity induces osteomodulin expression in osteoblasts. *Biochem Biophys Res Commun* 362, 460–466 (2007).
33. Askary, A. et al. Ancient origin of lubricated joints in bony vertebrates. (2016) doi:10.7554/eLife.16415.001.

## ***IX. APPENDICES***

34. Smeeton, J. et al. Regeneration of Jaw Joint Cartilage in Adult Zebrafish. *Front Cell Dev Biol* 9, (2022).
35. Gonçalves, I. et al. Osteomodulin Gene Expression Is Associated with Plaque Calcification, Stability, and Fewer Cardiovascular Events in the CPIP Cohort. *Stroke* 29, (2022).
36. Couble, M. L. et al. Immunodetection of osteoadherin in murine tooth extracellular matrices. *Histochem Cell Biol* 121, (2004).
37. Buchaille, R., Couble, M. L., Magloire, H. & Bleicher, F. Expression of the small leucine-rich proteoglycan osteoadherin/osteomodulin in human dental pulp and developing rat teeth. *Bone* 27, (2000).
38. Skenteris, N. T. et al. Osteomodulin is a novel gene in cardiovascular calcification. *Atherosclerosis* 331, (2021).
39. Skenteris, N. T. et al. Osteomodulin attenuates smooth muscle cell osteogenic transition in vascular calcification. *Clin Transl Med* 12, (2022).
40. Wendel, M., Sommarin, Y. & Heinegård, D. Bone matrix proteins: Isolation and characterization of a novel cell-binding keratan sulfate proteoglycan (osteoadherin) from bovine bone. *Journal of Cell Biology* 141, 839–847 (1998).
41. Fan, X. et al. The deterioration of calcified cartilage integrity reflects the severity of osteoarthritis—A structural, molecular, and biochemical analysis. *FASEB Journal* 36, (2022).
42. Hayami, T. et al. Characterization of articular cartilage and subchondral bone changes in the rat anterior cruciate ligament transection and meniscectomized models of osteoarthritis. *Bone* 38, (2006).
43. Deng, B. et al. Quantitative study on morphology of calcified cartilage zone in OARSI 0~4 cartilage from osteoarthritic knees. *Curr Res Transl Med* 64, (2016).
44. Poulet, B. et al. Modifications of gait as predictors of natural osteoarthritis progression in Str/Ort mice. *Arthritis and Rheumatology* 66, (2014).
45. Muramatsu, Y. et al. Preventive effects of hyaluronan from deterioration of gait parameters in surgically induced mice osteoarthritic knee model. *Osteoarthritis Cartilage* 22, (2014).
46. Makii, Y. et al. Alteration of gait parameters in a mouse model of surgically induced knee osteoarthritis. *Journal of Orthopaedic Surgery* 26, (2018).
47. Pesesse, L. et al. Bone sialoprotein as a potential key factor implicated in the pathophysiology of osteoarthritis. *Osteoarthritis Cartilage* 22, (2014).
48. Bergen, D. J. M. et al. Regenerating zebrafish scales express a subset of evolutionary conserved genes involved in human skeletal disease. *BMC Biol* 20, (2022).
49. Salbach, J. et al. The effect of the degree of sulfation of glycosaminoglycans on osteoclast function and signaling pathways. *Biomaterials* 33, (2012).
50. R.V., S., M.-L., O., S., M., K., H. & M., W. The glycosylation profile of osteoadherin alters during endochondral bone formation. *Bone* (2013).

51. Geurts, J. et al. Elevated marrow inflammatory cells and osteoclasts in subchondral osteosclerosis in human knee osteoarthritis. *Journal of Orthopaedic Research* 34, (2016).
52. Zhen, G. et al. Inhibition of TGF- $\beta$  signaling in mesenchymal stem cells of subchondral bone attenuates osteoarthritis. *Nat Med* 19, (2013).
53. Dai, G. et al. Osteocyte TGF $\beta$ 1-Smad2/3 is positively associated with bone turnover parameters in subchondral bone of advanced osteoarthritis. *Int J Mol Med* 46, (2020).
54. Glasson, S. S., Blanchet, T. J. & Morris, E. A. The surgical destabilization of the medial meniscus (DMM) model of osteoarthritis in the 129/SvEv mouse. *Osteoarthritis Cartilage* 15, (2007).
55. Glasson, S. S., Chambers, M. G., van den Berg, W. B. & Little, C. B. The OARSI histopathology initiative - recommendations for histological assessments of osteoarthritis in the mouse. *Osteoarthritis Cartilage* 18, (2010).
56. Bankhead, P. et al. QuPath: Open source software for digital pathology image analysis. *Sci Rep* 7, (2017).
57. Aleström, P. et al. Zebrafish: Housing and husbandry recommendations. *Lab Anim* 54, (2020).
58. Bussmann, J. & Schulte-Merker, S. Rapid BAC selection for tol2-mediated transgenesis in zebrafish. *Development* 138, (2011).
59. Walker, M. B. & Kimmel, C. B. A two-color acid-free cartilage and bone stain for zebrafish larvae. *Biotechnic and Histochemistry* 82, (2007).
60. Hauptmann G & Gerster T. Two-color whole-mount in situ hybridization to vertebrate and *Drosophila* embryos. *Trends in Genetics* vol. 10 Preprint at [https://doi.org/10.1016/0168-9525\(90\)90008-T](https://doi.org/10.1016/0168-9525(90)90008-T) (1994).
61. Rasband, W. S. ImageJ: Image processing and analysis in Java. *Astrophysics Source Code Library* (2012).
62. Ethiraj, L. P. et al. Colorimetric and fluorescent TRAP assays for visualising and quantifying fish osteoclast activity. *European Journal of Histochemistry* 66, (2022).
63. Tarasco, M., Cordelières, F. P., Cancela, M. L. & Laizé, V. ZFBONE: An ImageJ toolset for semi-automatic analysis of zebrafish bone structures. *Bone* 138, (2020).
64. Sanchez, C. et al. Osteoblasts from the sclerotic subchondral bone downregulate aggrecan but upregulate metalloproteinases expression by chondrocytes. This effect is mimicked by interleukin-6, -1 $\beta$  and oncostatin M pre-treated non-sclerotic osteoblasts. *Osteoarthritis Cartilage* (2005) doi:10.1016/j.joca.2005.03.008.
65. Sanchez, C. et al. Curcuma longa and Boswellia serrata Extracts Modulate Different and Complementary Pathways on Human Chondrocytes In Vitro: Deciphering of a Transcriptomic Study. *Front Pharmacol* 13, (2022).
66. Jepsen, K. J., Silva, M. J., Vashishth, D., Guo, X. E. & Van Der Meulen, M. C. H. Establishing biomechanical mechanisms in mouse models: Practical guidelines for



systematically evaluating phenotypic changes in the diaphyses of long bones. *Journal of Bone and Mineral Research* vol. 30 Preprint at <https://doi.org/10.1002/jbmr.2539> (2015).

### **ACKNOWLEDGMENTS**

The authors acknowledge the mouse facility of the University of Liege for the help provided during the housing as well as the zebrafish facility of the University of Liège and of Bristol. The authors acknowledge the GIGA University of Liège Genomic Next Generation Sequencing platform for having performed the RNA sequencing. The authors acknowledge the GIGA University of Liège Immunohistology platform and the Bristol University Histology platform for the help provided with the sample preparation. The authors acknowledge Prof. Stefan Schulte-Merker for having kindly provided the transgenic zebrafish line *TgBAC(ctsk:Citrine)*. The KU Leuven X-ray Computed Tomography Core facility is acknowledged for the 3D image acquisition and quantitative post-processing tools (<http://www.xct.kuleuven.be>). The Hercules fund of the FWO is acknowledged for their financial support of the project I013518N “The KU Leuven X-ray computed tomography center: a versatile and structured way to unravel the material structures and dynamic processes”. The authors acknowledge Carla Geeroms for her help during the X-ray computed tomography data acquisition. The authors acknowledge MaJEB sprl (Liège, Belgium) for their help provided with the biomechanical testing of the tibiae. The authors acknowledge Ratish Raman, Prescilia Centonze, Clémentine Lausberg, Lisa Carton and Laura Massoz for technical support.

### **AUTHORS CONTRIBUTIONS**

J.Z, C.L.H, C.S and Y.H were responsible for the study design. J.Z supervised murine *in vivo* experiments. J.Z and F.M.F.C supervised the DMM model. J.Z and T.P.C supervised the CatWalk XT experiment. J.Z and M.M developed the mutant zebrafish line. J.Z, Q.T, J.G and E.K supervised zebrafish *in vivo* experiments. J.Z and R.V.d.C performed the *in vitro* experiments. J.Z performed the bone marker assay. J.Z and C.S supervised the biomechanical testing. J.Z wrote the manuscript. R.J.L, M.M, D.E and C.L.H. provided resources and advised on research studies. C.S and C.L advised on research studies. J.Z, C.S and Y.H analyzed the results. Y.H acquired funding, verified data and assisted in writing the manuscript and acts as guarantor. All authors approved the final manuscript.

### **COMPETING INTERESTS**

None declared.

### **FUNDING**

This work was funded by the F.R.S.-FNRS for the “EOS: The Excellence of Science -Join-t-against-Osteoarthritis”, grant number 30480119, by a research grant from the Osteoarthritis Foundation and by the University of Liege (Fonds Léon Fredericq and Fonds Speciaux à la Recherche). CLH EK and QT were funded by Versus Arthritis senior fellowship 21937. MM is a Maître de Recherche at the Fonds National de Recherche Scientifique (FNRS).

### **CORRESPONDENCE**

Correspondence and requests for materials should be addressed to Yves Henrotin.

**Appendix 3: Supplemental table of the CatWalk XT analysis.**

Parameters of the front paws and the hinds paws were reported. The first column corresponds to the gait parameter with its specific unit; the second column corresponds to the genotype, the third column corresponds to the reported value, the fourth, fifth and sixth columns are the reported p-values between KO and WT, KO and UP, WT and UP respectively. One-Way ANOVA was performed when the distribution was Gaussian and Kruskal-Wallis was performed when the distribution was not Gaussian with differences being considered significant at p-values < 0.05 (\*p < 0.05, \*\*p ≤ 0.01, \*\*\*p ≤ 0.001).

## IX. APPENDICES

Appendix 3.1: Analysis of the gait development from the CatWalkXT of 4, 8 and 16 month-old male mice. At 4 months: n=8 for each genotype; at 8 months: n=8 for each genotype; at 16 months: n=14 for the KO, n=12 for the WT and n=10 for the UP.

### 4 months : Front Paws

Parameter	Genotype	Value	KO vs WT	KO vs UP	UP vs WT
Stand Index	KO	-3,135	0,6056	0,9594	0,7708
	WT	-2,702			
	UP	-3,012			
Stand (s)	KO	0,1982	0,9999	0,9999	0,9999
	WT	0,1968			
	UP	0,1825			
Max Contact Area (cm <sup>2</sup> )	KO	1,172	0,4027	<b>0,0033 (**)</b>	0,0610
	WT	1,073			
	UP	0,8901			
Print Area (cm <sup>2</sup> )	KO	1,364	0,3367	<b>0,0032 (**)</b>	0,0762
	WT	1,233			
	UP	1,024			
Swing (s)	KO	0,1191	<b>0,0400 (*)</b>	<b>0,0362 (*)</b>	0,9999
	WT	0,1475			
	UP	0,1427			
Swing Speed (cm)	KO	75,67	0,5725	0,5373	0,9999
	WT	66,77			
	UP	67,95			
Stride Length (cm)	KO	8,430	0,2212	0,1306	0,9499
	WT	9,074			
	UP	9,188			
Step Cycle (s)	KO	0,3153	0,7737	0,9999	0,9999
	WT	0,3429			
	UP	0,3206			
Single Stance	KO	0,1191	<b>0,0296 (*)</b>	<b>0,0362 (*)</b>	0,9999

## IX. APPENDICES

(s)	WT	0,1443			
	UP	0,1412			
Initial dual stance (s)	KO	0,03823	0,0935	<b>0,0021 (**)</b>	0,2172
	WT	0,02829			
	UP	0,02049			
Terminal dual stance (s)	KO	0,03836	<b>0,0470 (*)</b>	<b>0,0047 (**)</b>	0,5603
	WT	0,02713			
	UP	0,02255			
Base of support (cm)	KO	2,106	<b>0,0140 (*)</b>	0,4637	0,1610
	WT	1,688			
	UP	1,944			
Intensity	KO	0,08859	0,5010	0,0521	0,1401
	WT	0,09884			
	UP	0,1272			

### 4 months : Hind Paws

Parameter	Genotype	Value	KO vs WT	KO vs UP	UP vs WT
Stand Index	KO	-10,62	<b>0,0061 (**)</b>	<b>0,0153 (*)</b>	0,9136
	WT	-7,544			
	UP	7,903			
Stand (s)	KO	0,1850	0,0931	0,5373	0,9999
	WT	0,2091			
	UP	0,1975			
Max Contact Area (cm <sup>2</sup> )	KO	0,7649	<b>0,0134 (*)</b>	0,1267	0,5320
	WT	1,074			
	UP	0,9663			
Print Area (cm <sup>2</sup> )	KO	0,9344	<b>0,0142 (*)</b>	0,2787	0,2975
	WT	1,292			
	UP	1,116			

**IX. APPENDICES**

Swing (s)	KO	0,1319	0,6208	0,7914	0,9560
	WT	0,1226			
	UP	0,1254			
Swing Speed (cm/s)	KO	67,92	0,4127	0,5038	0,9999
	WT	77,41			
	UP	74,37			
Stride Length (cm)	KO	8,330	0,4284	0,0898	0,6104
	WT	8,783			
	UP	9,126			
Step Cycle (s)	KO	0,3108	0,7731	0,8602	0,9855
	WT	0,3285			
	UP	0,3243			
Single Stance (s)	KO	0,1191	0,9914	0,7499	0,8200
	WT	0,1200			
	UP	0,1242			
Initial dual stance (s)	KO	0,03142	0,0535	0,3594	0,9999
	WT	0,04169			
	UP	0,03783			
Terminal dual stance (s)	KO	0,03356	0,0778	0,5038	0,9999
	WT	0,04485			
	UP	0,03976			
Base of support (cm)	KO	3,516	0,8857	0,8160	0,9893
	WT	3,609			
	UP	3,637			
Intensity	KO	0,1530	0,1829	0,9999	0,8192
	WT	0,09976			
	UP	0,1218			

## IX. APPENDICES

### 8 months : Front Paws

Parameter	Genotype	Value	KO vs WT	KO vs UP	UP vs WT
Stand Index	KO	-2,976	0,4716	0,9999	0,9999
	WT	-2,397			
	UP	-2,732			
Stand (s)	KO	0,2172	0,5961	0,9099	0,3607
	WT	0,2356			
	UP	0,2095			
Max Contact Area (cm <sup>2</sup> )	KO	1,030	<b>0,0120 (*)</b>	0,7729	0,0529
	WT	1,256			
	UP	1,079			
Print Area (cm <sup>2</sup> )	KO	1,178	<b>0,0140 (*)</b>	0,6791	0,0832
	WT	1,451			
	UP	1,252			
Swing (s)	KO	0,1229	0,1553	<b>0,0486 (*)</b>	0,9999
	WT	0,1500			
	UP	0,1533			
Swing Speed (cm/s)	KO	68,47	0,7632	0,7452	0,9995
	WT	64,77			
	UP	64,60			
Stride Length (cm)	KO	7,929	0,1938	<b>0,0336 (*)</b>	0,6403
	WT	8,892			
	UP	9,379			
Step Cycle (s)	KO	0,3408	0,1686	0,6090	0,9999
	WT	0,3842			
	UP	0,3604			
Single Stance (s)	KO	0,1228	0,1430	0,0535	0,9999
	WT	0,1481			
	UP	0,1516			

## IX. APPENDICES

Initial dual stance (s)	KO	0,04792	0,8489	0,0759	0,2054
	WT	0,04300			
	UP	0,02712			
Terminal dual stance (s)	KO	0,04756	0,9554	0,0559	0,0986
	WT	0,04531			
	UP	0,02831			
Base of support (cm)	KO	2,002	0,5068	0,5391	0,9984
	WT	1,864			
	UP	1,870			
Intensity	KO	0,1131	0,9999	0,6093	0,9999
	WT	0,09739			
	UP	0,09320			

### 8 months : Hind Paws

Parameter	Genotype	Value	KO vs WT	KO vs UP	UP vs WT
Stand Index	KO	-8,854	0,2133	0,1638	0,9867
	WT	-6,898			
	UP	-6,723			
Stand (s)	KO	0,2285	0,6897	0,8393	0,3614
	WT	0,2456			
	UP	0,2168			
Max Contact Area (cm <sup>2</sup> )	KO	0,7735	<b>0,0002 (***)</b>	<b>0,0150 (*)</b>	0,1838
	WT	1,281			
	UP	1,092			
Print Area (cm <sup>2</sup> )	KO	0,9831	<b>0,0002 (***)</b>	<b>0,0230 (*)</b>	0,1125
	WT	1,519			
	UP	1,293			
Swing (s)	KO	0,1061	<b>0,0105 (*)</b>	<b>0,0345 (*)</b>	0,8521
	WT	0,1339			

**IX. APPENDICES**

	UP	0,1293			
Swing Speed (cm/s)	KO	75,28	0,6475	0,9999	0,9999
	WT	67,74			
	UP	73,17			
Stride Length (cm)	KO	7,764	0,2493	<b>0,0447 (*)</b>	0,6284
	WT	8,665			
	UP	9,174			
Step Cycle (s)	KO	0,2879	0,2139	0,9999	0,8662
	WT	0,3027			
	UP	0,2862			
Single Stance (s)	KO	0,1050	<b>0,0104 (*)</b>	<b>0,0390 (*)</b>	0,8197
	WT	0,1320			
	UP	0,1270			
Initial dual stance (s)	KO	0,06246	0,7260	0,2462	0,6554
	WT	0,05460			
	UP	0,04554			
Terminal dual stance (s)	KO	0,06126	0,8707	0,2389	0,4838
	WT	0,05661			
	UP	0,04579			
Base of support (cm)	KO	3,917	0,7297	0,9999	0,9999
	WT	4,024			
	UP	4,007			
Intensity	KO	0,1461	<b>0,0016 (**)</b>	<b>0,0027 (**)</b>	0,9722
	WT	0,09121			
	UP	0,09427			



## IX. APPENDICES

### 16 months : Front Paws

Parameter	Genotype	Value	KO vs WT	KO vs UP	UP vs WT
Stand Index	KO	-3,510	0,6897	<b>0,0414 (*)</b>	0,6034
	WT	-2,574			
	UP	-2,114			
Stand (s)	KO	0,2083	0,6504	0,2633	0,7525
	WT	0,2245			
	UP	0,2388			
Max Contact Area (cm <sup>2</sup> )	KO	0,9117	0,1656	0,0987	0,9345
	WT	1,022			
	UP	1,045			
Print Area (cm <sup>2</sup> )	KO	1,037	0,1390	0,1265	0,9889
	WT	1,166			
	UP	1,177			
Swing (s)	KO	0,1127	<b>0,0110 (*)</b>	<b>0,0005 (***)</b>	0,4263
	WT	0,1430			
	UP	0,1565			
Swing Speed (cm/s)	KO	80,19	0,1677	<b>0,0057 (**)</b>	0,2918
	WT	69,05			
	UP	59,08			
Stride Length (cm)	KO	8,130	<b>0,0114 (*)</b>	0,4293	0,2553
	WT	9,176			
	UP	8,580			
Step Cycle (s)	KO	0,3204	0,1834	<b>0,0251 (*)</b>	0,5799
	WT	0,3673			
	UP	0,3957			
Single Stance (s)	KO	0,1102	<b>0,0255 (*)</b>	<b>0,0008 (***)</b>	0,7841
	WT	0,1422			
	UP	0,1545			

## IX. APPENDICES

Initial dual stance (s)	KO	0,04890	0,2393	0,6400	0,9999
	WT	0,03957			
	UP	0,04172			
Terminal dual stance (s)	KO	0,04986	0,1950	0,4125	0,9226
	WT	0,03952			
	UP	0,04196			
Base of support (cm)	KO	2,189	0,4017	<b>0,0357 (*)</b>	0,3963
	WT	2,040			
	UP	1,875			
Intensity	KO	0,1370	0,2138	0,5193	0,9999
	WT	0,1060			
	UP	0,1091			

### 16 months : Hind Paws

Parameter	Genotype	Value	KO vs WT	KO vs UP	UP vs WT
Stand Index	KO	-7,240	0,9999	0,9999	0,9999
	WT	-6,534			
	UP	-6,784			
Stand (s)	KO	0,2204	0,5801	0,0985	0,4962
	WT	0,2418			
	UP	0,2683			
Max Contact Area (cm <sup>2</sup> )	KO	0,7817	0,0566	0,1145	0,9754
	WT	1,007			
	UP	0,9853			
Print Area (cm <sup>2</sup> )	KO	0,9933	0,1083	0,2277	0,9543
	WT	1,221			
	UP	1,186			
Swing (s)	KO	0,09631	<b>0,0040 (**)</b>	<b>0,0029 (**)</b>	0,9565
	WT	0,1255			

## ***IX. APPENDICES***

	UP	0,1281			
Swing Speed (cm/s)	KO	87,05	0,1386	<b>0,0180 (*)</b>	0,5844
	WT	76,67			
	UP	70,93			
Stride Length (cm)	KO	7,936	<b>0,0091 (**)</b>	0,0951	0,6900
	WT	9,013			
	UP	8,707			
Step Cycle (s)	KO	0,3133	0,1067	<b>0,0051 (**)</b>	0,3767
	WT	0,3637			
	UP	0,3991			
Single Stance (s)	KO	0,09559	<b>0,0055 (**)</b>	<b>0,0028 (**)</b>	0,9146
	WT	0,1236			
	UP	0,1273			
Initial dual stance (s)	KO	0,06292	0,8214	0,9999	0,3389
	WT	0,05523			
	UP	0,06931			
Terminal dual stance (s)	KO	0,06289	0,8660	0,7988	0,5267
	WT	0,05807			
	UP	0,06924			
Base of support (cm)	KO	3,916	0,9984	0,7295	0,7733
	WT	3,908			
	UP	3,796			
Intensity	KO	0,1646	<b>0,0418 (*)</b>	0,1269	0,9999
	WT	0,09608			
	UP	0,09931			

## IX. APPENDICES

Appendix 3.2: Analysis of the gait from the CatWalkXT of the mice from the DMM model. For the SHAM: n=4 for each genotype; for the DMM: n=9 for the KO, n=10 for the WT and n=8 for the UP.

### Front Paws - DMM

Parameter	Genotype	Value	KO vs WT	KO vs UP	UP vs WT
Stand Index	KO	-3,527	<b>0,0039 (**)</b>	0,2697	0,1716
	WT	-2,063			
	UP	-2,844			
Stand (s)	KO	0,1799	<b>0,0027 (**)</b>	0,1712	0,2154
	WT	0,2460			
	UP	0,2146			
Max Contact Area (cm <sup>2</sup> )	KO	1,081	0,9576	0,6728	0,4947
	WT	1,093			
	UP	1,043			
Print Area (cm <sup>2</sup> )	KO	1,209	>0,9999	>0,9999	0,8197
	WT	1,229			
	UP	1,206			
Swing (s)	KO	0,09160	<b>&lt;0,0001 (****)</b>	<b>0,0298(*)</b>	<b>0,0093 (**)</b>
	WT	0,1436			
	UP	0,1157			
Swing Speed (cm)	KO	98,76	<b>&lt;0,0001 (****)</b>	<b>0,0084 (**)</b>	0,1580
	WT	66,11			
	UP	77,93			
Stride Length (cm)	KO	8,292	0,4047	0,9997	0,4406
	WT	8,830			
	UP	8,302			
Step Cycle (s)	KO	0,2727	<b>&lt;0,0001 (****)</b>	0,0546	<b>0,0059 (**)</b>
	WT	0,3913			
	UP	0,3228			
Single Stance	KO	0,09473	<b>&lt;0,0001 (****)</b>	0,0565	<b>0,0013 (**)</b>

**IX. APPENDICES**

(s)	WT	0,1439			
	UP	0,1135			
Initial dual stance (s)	KO	0,04362	0,7529	0,8643	0,9840
	WT	0,05079			
	UP	0,04904			
Terminal dual stance (s)	KO	0,04031	>0,9999	0,9347	>0,9999
	WT	0,04569			
	UP	0,04968			
Base of support (cm)	KO	2,122	0,2874	0,9787	0,4107
	WT	1,947			
	UP	2,098			
Intensity	KO	0,1158	0,9133	0,9703	0,9870
	WT	0,1202			
	UP	0,1185			

## IX. APPENDICES

### Hind Paws - DMM

Parameter	Genotype	Value	KO vs WT	KO vs UP	UP vs WT
Stand Index	KO	-7,010	<b>0,0110 (*)</b>	>0,9999	<b>0,0179 (*)</b>
	WT	-4,891			
	UP	-6,977			
Stand (s)	KO	0,1740	<b>0,0003 (***)</b>	0,2933	<b>0,0207 (*)</b>
	WT	0,2601			
	UP	0,2043			
Max Contact Area (cm <sup>2</sup> )	KO	1,113	0,6981	0,6895	0,2500
	WT	1,176			
	UP	1,045			
Print Area (cm <sup>2</sup> )	KO	1,257	0,2776	0,7046	0,0687
	WT	1,376			
	UP	1,193			
Swing (s)	KO	0,08614	<b>0,0002 (***)</b>	<b>0,0013 (**)</b>	0,8933
	WT	0,1200			
	UP	0,1166			
Swing Speed (cm/s)	KO	93,71	<b>0,0014 (**)</b>	<b>0,0231 (*)</b>	>0,9999
	WT	74,43			
	UP	77,32			
Stride Length (cm)	KO	7,922	0,3319	0,7465	0,7918
	WT	8,633			
	UP	8,302			
Step Cycle (s)	KO	0,2584	<b>&lt;0,0001 (****)</b>	<b>0,0214 (*)</b>	<b>0,0045 (**)</b>
	WT	0,3779			
	UP	0,3127			
Single Stance (s)	KO	0,08514	<b>0,0020 (**)</b>	0,3912	0,2388
	WT	0,1173			
	UP	0,09370			

**IX. APPENDICES**

Initial dual stance (s)	KO	0,04474	0,0789	0,4030	0,6694
	WT	0,06605			
	UP	0,05772			
Terminal dual stance (s)	KO	0,04490	0,0630	0,8075	0,2370
	WT	0,07185			
	UP	0,05237			
Base of support (cm)	KO	3,907	0,5067	0,9644	0,3796
	WT	4,107			
	UP	3,859			
Intensity	KO	0,1074	>0,9999	>0,9999	>0,9999
	WT	0,1042			
	UP	0,1254			

**Front and Hind Paws - SHAM**

<b>Parameter</b>	<b>Genotype</b>	<b>Front value</b>	<b>Hind value</b>
Stand Index	KO	-3,236	-5,266
	WT	-1,785	-5,727
	UP	-2,469	-5,151
Stand (s)	KO	0,1904	0,2090
	WT	0,2525	0,2518
	UP	0,2471	0,2598
Max Contact Area (cm <sup>2</sup> )	KO	1,056	1,117
	WT	1,049	1,146
	UP	1,124	1,254
Print Area (cm <sup>2</sup> )	KO	1,159	1,267
	WT	1,248	1,346
	UP	1,351	1,474
Swing (s)	KO	0,1147	0,08786
	WT	0,1350	0,1132
	UP	0,1448	0,1236
Swing Speed (cm/s)	KO	80,32	92,90
	WT	67,42	75,13
	UP	70,13	76,81
Stride Length (cm)	KO	8,342	7,825
	WT	8,363	8,124
	UP	9,136	9,116
Step Cycle (s)	KO	0,3025	0,2943
	WT	0,3918	0,3652
	UP	0,3879	0,3885
Single Stance (s)	KO	0,1048	0,09309
	WT	0,1421	0,1128
	UP	0,1391	0,1146



**IX. APPENDICES**

Initial dual stance (s)	KO	0,03827	0,06270
	WT	0,05332	0,06337
	UP	0,04911	0,05288
Terminal dual stance (s)	KO	0,04874	0,05359
	WT	0,05200	0,07344
	UP	0,05416	0,07819
Base of support (cm)	KO	2,275	4,088
	WT	1,924	4,318
	UP	1,928	3,826
Intensity	KO	0,1186	0,1143
	WT	0,1225	0,1114
	UP	0,1136	0,09972

## IX. APPENDICES

Appendix 3.3: Analysis of the gait development from the CatWalkXT of 4, 8 and 16 month-old female mice. At 4 months: n=8 for each genotype; at 8 months n=8 for each genotype; at 16 months: n=13 for the KO, n=9 for the WT and n=10 for the UP.

### 4 months : Front Paws

Parameter	Genotype	Value	KO vs WT	KO vs UP	UP vs WT
Stand Index	KO	-3,488	0,7455	0,2188	0,5901
	WT	-3,168			
	UP	-2,738			
Stand (s)	KO	0,2024	0,4592	0,9825	0,3632
	WT	0,1840			
	UP	0,2051			
Max Contact Area (cm <sup>2</sup> )	KO	0,9518	0,3304	0,8428	0,1325
	WT	1,059			
	UP	0,9107			
Print Area (cm <sup>2</sup> )	KO	1,109	0,3960	0,8097	0,1497
	WT	1,219			
	UP	1,058			
Swing (s)	KO	0,1187	<b>0,0208 (*)</b>	<b>0,0009 (***)</b>	0,3725
	WT	0,1397			
	UP	0,1495			
Swing Speed (cm)	KO	71,21	0,1058	<b>0,0035 (**)</b>	0,2780
	WT	63,51			
	UP	57,85			
Stride Length (cm)	KO	7,823	0,4225	0,5358	0,9788
	WT	8,343			
	UP	8,263			
Step Cycle (s)	KO	0,3199	0,9950	0,2592	0,2998
	WT	0,3218			
	UP	0,3520			
Single Stance	KO	0,1160	<b>0,0332 (*)</b>	<b>0,0015 (**)</b>	0,3736

## IX. APPENDICES

(s)	WT	0,1379			
	UP	0,1490			
Initial dual stance (s)	KO	0,04123	<b>0,0196 (*)</b>	0,0954	0,7279
	WT	0,02333			
	UP	0,02796			
Terminal dual stance (s)	KO	0,04392	<b>0,0093 (**)</b>	<b>0,0359 (*)</b>	0,8152
	WT	0,02384			
	UP	0,02757			
Base of support (cm)	KO	1,939	<b>0,0229 (*)</b>	<b>0,0441 (*)</b>	0,9494
	WT	1,681			
	UP	1,708			
Intensity	KO	0,2506	0,0561	0,4930	0,4051
	WT	0,1580			
	UP	0,2072			

### 4 months : Hind Paws

Parameter	Genotype	Value	KO vs WT	KO vs UP	UP vs WT
Stand Index	KO	-8,232	0,7100	0,7050	>0,9999
	WT	-7,639			
	UP	-7,633			
Stand (s)	KO	0,1895	0,6142	0,2263	0,7345
	WT	0,2050			
	UP	0,2172			
Max Contact Area (cm <sup>2</sup> )	KO	0,5930	<b>&lt;0,0001 (***)</b>	<b>0,0032 (**)</b>	0,2927
	WT	1,003			
	UP	0,8838			
Print Area (cm <sup>2</sup> )	KO	0,7521	<b>0,0142 (*)</b>	0,2787	0,2975
	WT	1,163			

## **IX. APPENDICES**

	UP	1,066			
Swing (s)	KO	0,1159	0,9688	0,1920	0,2820
	WT	0,1176			
	UP	0,1287			
Swing Speed (cm/s)	KO	66,11	0,5136	0,9713	0,3851
	WT	71,42			
	UP	65,02			
Stride Length (cm)	KO	7,299	0,1609	0,3245	0,9002
	WT	8,122			
	UP	7,933			
Step Cycle (s)	KO	0,3040	0,6679	0,1163	0,4523
	WT	0,3191			
	UP	0,3405			
Single Stance (s)	KO	0,09993	<b>0,0198 (*)</b>	<b>0,0011 (**)</b>	0,4396
	WT	0,1176			
	UP	0,1251			
Initial dual stance (s)	KO	0,04143	0,9336	0,9566	0,9973
	WT	0,04395			
	UP	0,04346			
Terminal dual stance (s)	KO	0,04448	0,9862	0,9996	0,9904
	WT	0,04571			
	UP	0,04468			
Base of support (cm)	KO	3,822	0,5331	0,9913	0,6097
	WT	3,628			
	UP	3,800			
Intensity	KO	0,2506	0,0561	0,4930	0,4051
	WT	0,1580			
	UP	0,2072			

## IX. APPENDICES

### 8 months : Front Paws

Parameter	Genotype	Value	KO vs WT	KO vs UP	UP vs WT
Stand Index	KO	-3,362	0,9263	0,8754	0,9922
	WT	-3,607			
	UP	-3,685			
Stand (s)	KO	0,2134	0,9746	0,5626	0,4365
	WT	0,2088			
	UP	0,2353			
Max Contact Area (cm <sup>2</sup> )	KO	0,8711	0,4164	0,2494	0,9329
	WT	1,001			
	UP	1,037			
Print Area (cm <sup>2</sup> )	KO	1,020	0,2191	0,1342	0,9564
	WT	1,219			
	UP	1,251			
Swing (s)	KO	0,1313	<b>0,0009 (***)</b>	<b>0,0009 (***)</b>	0,9998
	WT	0,1614			
	UP	0,1612			
Swing Speed (cm/s)	KO	68,16	0,3072	0,0639	0,6517
	WT	60,20			
	UP	55,50			
Stride Length (cm)	KO	8,385	0,2922	0,8694	0,5627
	WT	9,223			
	UP	8,660			
Step Cycle (s)	KO	0,3428	0,5954	0,1873	0,6843
	WT	0,3660			
	UP	0,3859			
Single Stance (s)	KO	0,1303	<b>0,0044 (**)</b>	<b>0,0030 (**)</b>	0,9843
	WT	0,1578			
	UP	0,1590			

## IX. APPENDICES

Initial dual stance (s)	KO	0,04106	<b>0,0316 (*)</b>	0,3438	0,4058
	WT	0,02398			
	UP	0,03214			
Terminal dual stance (s)	KO	0,04321	<b>0,0436 (*)</b>	0,2619	0,6016
	WT	0,02583			
	UP	0,03236			
Base of support (cm)	KO	1,984	0,9924	0,1978	0,9999
	WT	1,867			
	UP	1,767			
Intensity	KO	0,1529	0,0845	0,1796	0,9109
	WT	0,1126			
	UP	0,1200			

### 8 months : Hind Paws

Parameter	Genotype	Value	KO vs WT	KO vs UP	UP vs WT
Stand Index	KO	-8,251	0,9878	0,9996	0,9917
	WT	-8,065			
	UP	-8,218			
Stand (s)	KO	0,2135	0,0687	0,5605	0,3987
	WT	0,1602			
	UP	0,1900			
Max Contact Area (cm <sup>2</sup> )	KO	0,6008	0,9523	0,5129	0,6941
	WT	0,6460			
	UP	0,7704			
Print Area (cm <sup>2</sup> )	KO	0,7523	0,9829	0,5526	0,6607
	WT	0,7824			
	UP	0,9318			
Swing (s)	KO	0,1264	<b>0,0009 (***)</b>	<b>0,0293 (*)</b>	0,3084
	WT	0,1840			

## **IX. APPENDICES**

	UP	0,1637			
Swing Speed (cm/s)	KO	67,85	<b>0,0071 (**)</b>	<b>0,0050 (**)</b>	0,9880
	WT	49,41			
	UP	48,61			
Stride Length (cm)	KO	8,107	0,8986	0,9034	0,6635
	WT	8,397			
	UP	7,824			
Step Cycle (s)	KO	0,3385	0,9999	0,9999	0,8192
	WT	0,3364			
	UP	0,3496			
Single Stance (s)	KO	0,1178	0,3098	0,2359	0,9828
	WT	0,1342			
	UP	0,1361			
Initial dual stance (s)	KO	0,04752	<b>0,0034 (**)</b>	0,1980	0,4719
	WT	0,01151			
	UP	0,02415			
Terminal dual stance (s)	KO	0,04731	<b>0,0056 (**)</b>	0,1431	0,7737
	WT	0,01211			
	UP	0,02339			
Base of support (cm)	KO	3,549	0,4415	<b>0,0296 (*)</b>	0,7737
	WT	3,900			
	UP	4,141			
Intensity	KO	0,2206	0,9761	0,7881	0,6640
	WT	0,2303			
	UP	0,1902			

## IX. APPENDICES

### 16 months : Front Paws

Parameter	Genotype	Value	KO vs WT	KO vs UP	UP vs WT
Stand Index	KO	-3,976	0,9999	0,9999	0,9999
	WT	-3,204			
	UP	-3,011			
Stand (s)	KO	0,2097	0,6024	0,3315	0,0817
	WT	0,1971			
	UP	0,2280			
Max Contact Area (cm <sup>2</sup> )	KO	0,7388	<b>0,0260 (*)</b>	0,4830	0,6980
	WT	0,9566			
	UP	0,8649			
Print Area (cm <sup>2</sup> )	KO	0,8610	<b>0,0123 (*)</b>	0,1416	0,9999
	WT	1,113			
	UP	1,023			
Swing (s)	KO	0,1210	<b>0,0007 (***)</b>	<b>0,0001 (****)</b>	<b>0,0382 (*)</b>
	WT	0,1449			
	UP	0,1606			
Swing Speed (cm/s)	KO	68,22	0,9967	0,1350	0,2076
	WT	67,87			
	UP	59,39			
Stride Length (cm)	KO	7,690	<b>0,0019 (**)</b>	<b>0,0287 (*)</b>	0,5200
	WT	9,374			
	UP	8,856			
Step Cycle (s)	KO	0,3319	0,9487	<b>0,0056 (**)</b>	<b>0,0232 (*)</b>
	WT	0,3370			
	UP	0,3866			
Single Stance (s)	KO	0,1209	<b>0,0014 (**)</b>	<b>0,0001 (****)</b>	<b>0,0387 (*)</b>
	WT	0,1433			
	UP	0,1589			



## IX. APPENDICES

Initial dual stance (s)	KO	0,04403	<b>0,0029 (**)</b>	0,2008	0,1798
	WT	0,02316			
	UP	0,03424			
Terminal dual stance (s)	KO	0,04450	<b>0,0148 (*)</b>	0,2254	0,4170
	WT	0,02571			
	UP	0,03422			
Base of support (cm)	KO	1,984	0,5752	0,9999	0,6193
	WT	2,102			
	UP	1,985			
Intensity	KO	0,1586	0,1293	0,1672	0,1672
	WT	0,1224			
	UP	0,1259			

### 16 months : Hind Paws

Parameter	Genotype	Value	KO vs WT	KO vs UP	UP vs WT
Stand Index	KO	-7,541	0,6956	0,9442	0,5418
	WT	-8,323			
	UP	-7,241			
Stand (s)	KO	0,2161	0,9835	0,2915	0,2763
	WT	0,2129			
	UP	0,2438			
Max Contact Area (cm <sup>2</sup> )	KO	0,5934	0,1671	0,5921	0,6705
	WT	0,8206			
	UP	0,7098			
Print Area (cm <sup>2</sup> )	KO	0,7503	0,1043	0,4452	0,6633
	WT	1,041			
	UP	0,9144			
Swing (s)	KO	0,1062	0,1345	<b>0,0029 (**)</b>	0,3206
	WT	0,1227			

## ***IX. APPENDICES***

	UP	0,1356			
Swing Speed (cm/s)	KO	72,90	0,6743	0,5576	0,2019
	WT	76,99			
	UP	68,05			
Stride Length (cm)	KO	7,493	<b>0,0070 (**)</b>	0,0766	0,5577
	WT	9,027			
	UP	8,515			
Step Cycle (s)	KO	0,3224	0,8446	<b>0,0056 (**)</b>	<b>0,0392 (*)</b>
	WT	0,3317			
	UP	0,3770			
Single Stance (s)	KO	0,1042	0,0778	<b>0,0026 (**)</b>	0,4401
	WT	0,1197			
	UP	0,1288			
Initial dual stance (s)	KO	0,05393	0,7384	0,9945	0,7087
	WT	0,04650			
	UP	0,05489			
Terminal dual stance (s)	KO	0,05565	0,5119	0,9734	0,4307
	WT	0,04429			
	UP	0,05783			
Base of support (cm)	KO	3,729	0,2061	0,0786	0,8819
	WT	4,028			
	UP	4,115			
Intensity	KO	0,2137	0,0871	0,3010	0,7660
	WT	0,1369			
	UP	0,1627			

## Appendix 4: Multiple alignment parameters.

<b>Program</b> kalign <b>Version</b> 3.3.1	<b>Number of Sequences</b> 5	<b>Launched Date</b> Sun, Feb 26, 2023 at 21:47:23 <b>End Date</b> Sun, Feb 26, 2023 at 21:47:26	<b>Input Sequences</b> kalign-I20230226-214822-0719-56238491-p1m.input <b>Output Result</b> kalign-I20230226-214822-0719-56238491-p1m.output
---	---------------------------------	---	---

### Command

```
$APPBIN/kalign:3.3.1 /kalign -i kalign-I20230226-214822-0719-56238491-p1m.sequence --format clu -o kalign-I20230226-214822-0719-56238491-p1m.output --gpo 11.0 --gpe 4.0 --tgpe 2.0
```

### Input Parameters

Sequence Type

protein

Alignment format

clu

Gap Open Penalty

11.0

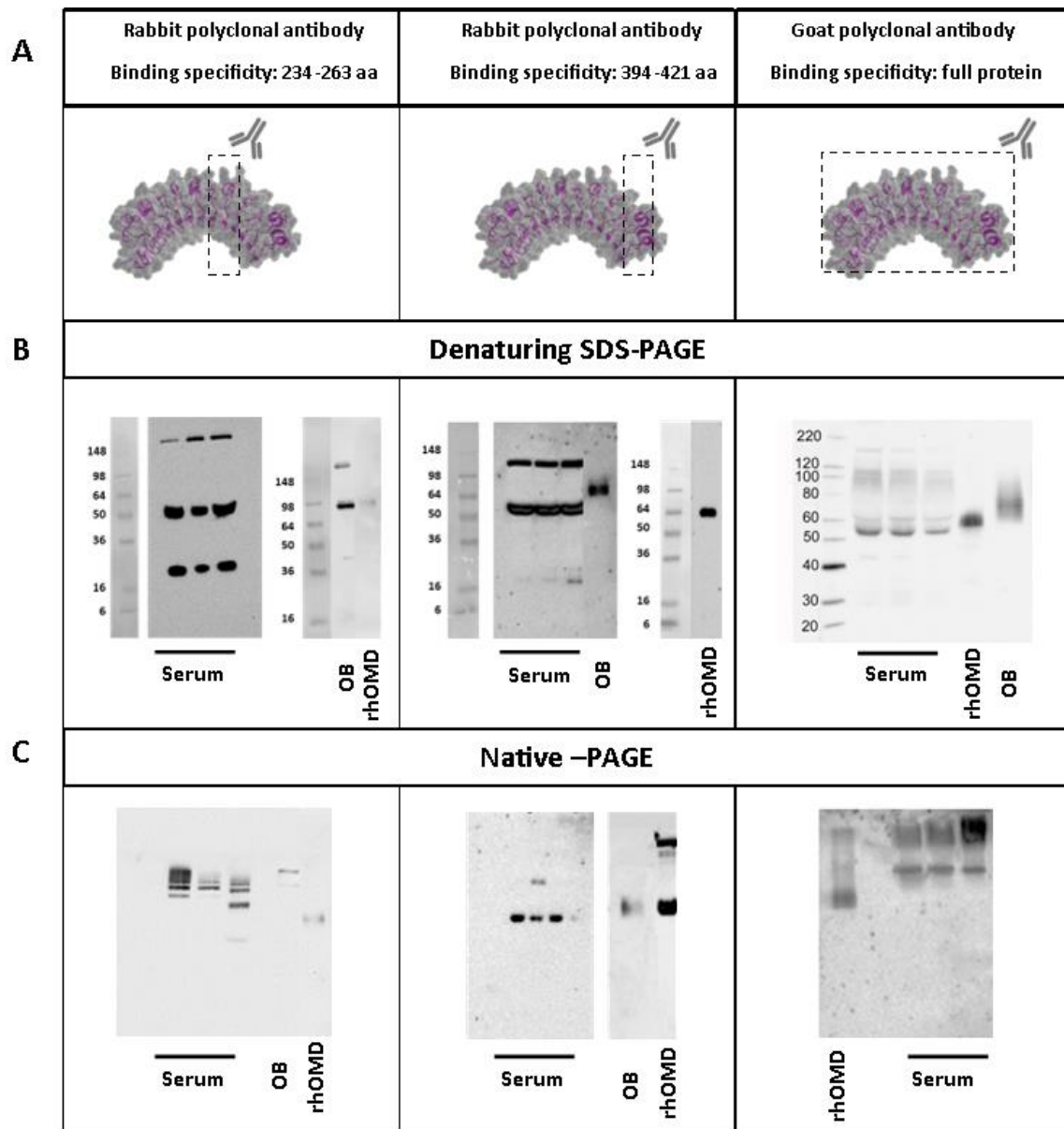
Gap Extension Penalty

4.0

Terminal Gap Penalties

2.0

## Appendix 5: Western blot from commercially available antibodies against OMD.



Appendix 5: (A) Western blot analysis with three different antibodies raised against OMD: specific to the central region, the C-terminal region and to the whole OMD. Western blots were conducted under denaturing condition (B) and native condition (C). For the antibody against the central region in SDS page: 10  $\mu$ L of serum, 3  $\mu$ L of osteoblast supernatant (OB) and 100 ng rhOMD; for the native condition: 10  $\mu$ L of serum, 3  $\mu$ L OB, 300 ng rhOMD. For the antibody against the C-terminal region in SDS page: 15  $\mu$ L of serum, 3  $\mu$ L OB and 15 ng rhOMD; for the native condition: 15  $\mu$ L of serum, 3  $\mu$ L OB, 100 ng rhOMD. For the antibody against the whole OMD: the image is from [187]; for the native condition: 10  $\mu$ L of serum and 3 ng of rhOMD. For the SDS page, the protein standard used as the ladder is SeeBlue™ (5  $\mu$ L) but no ladder can be used in native condition as the fragments migrate according to their isoelectric point and 3D structure. Sera from three different patients were used and patients were uncharacterized for musculoskeletal disorders.



# Summary

**Purpose:** To investigate the roles of osteomodulin (OMD), a small proteoglycan known for controlling collagen fibrils organization in bone, in the development of osteoarthritis (OA) associated with subchondral bone sclerosis.

**Methods:** Loss of function and overexpressing mice for *Omd* aged 4, 8, and 16 months were used to study *Omd* roles in bone and cartilage metabolism and answer whether mice develop spontaneous OA. Surgical destabilization of the medial meniscus (DMM) model was performed to investigate its role in mechanically-induced OA. Additionally, we used *omd* overexpression as well as a mutant deficiency for *omd* in the zebrafish model to study *omd* effects on skeletal metabolism and cartilage development. Finally, *in vitro* models were used to further study OMD in osteoclastogenesis.

**Results:** *Omd* regulated bone and cartilage microarchitectures. Knock-out mice showed thinner calcified cartilage in the medial tibial plateau, and their growth plate was thicker at 16 months compared to WT. Both trabecular and cortical bone volume/total volume ratios were increased in the *Omd* knock-out mice and they showed a reduced percentage of porosity. The trabecular number of the knock-out mice was increased while their trabecular total volume was decreased. Further, their cortical bone showed increased thickness, and a higher whole bone strength. Knock-out mice were more prone to develop cartilage lesions spontaneously. Interestingly, *Omd* knock-out mice developed subchondral bone sclerosis spontaneously while overexpressing mice showed less subchondral bone sclerosis in the DMM OA model. At 16 months, *Omd*-overexpressing mice had the less trabecular number and a greater structure-model index for their trabecular bone geometry. The zebrafish model showed that the ectopic overexpression of *omd* induced developmental defects with abnormal cartilage structures. Further, we studied the development of OA in zebrafish, an animal model that develop OA features in the synovial jaw joint during aging and which is an excellent genetic model to study OA. We showed that adult zebrafish lacking *omd* were more prone to articular cartilage degeneration. Furthermore, mutant zebrafish showed increased mature osteoclasts generation and increased TRAP staining revealing a higher osteoclast activity. Impaired osteoclastogenesis might be involved in the defects involved during scale regeneration. Our zebrafish results are supported by our *in vitro* experiments where we demonstrated that OMD bound to RANKL and inhibited osteoclastogenesis.

**Conclusions:** OMD is a key factor in subchondral bone sclerosis associated with OA. This small proteoglycan participates in bone and cartilage homeostasis notably by acting on the regulation of osteoclastogenesis.